

Biomembrane Electrochemistry

ADVANCES IN CHEMISTRY SERIES **235**

Biomembrane Electrochemistry

Martin Blank, EDITOR
Columbia University

Igor Vodyanoy, EDITOR
Office of Naval Research

Publication Date: May 5, 1994 | doi: 10.1021/ba-1994-0235.fw001



American Chemical Society, Washington, DC 1994



Biomembrane electrochemistry

Library of Congress

Biomembrane electrochemistry / [edited by] Martin Blank, Igor Vodyanoy.

p. cm.—(Advances in chemistry series, ISSN 0065-2393; 235)

Includes bibliographical references and indexes.

ISBN 0-8412-2524-9

1. Cell membranes—Electric properties. 2. Bioelectrochemistry.


I. Blank, Martin, 1933— II. Vodyanoy, Igor, 1947— . III. Series.

QH601.B545 1993

574.875—dc20

93-24348

CIP

The paper used in this publication meets the minimum requirements of American National Standard for Information Sciences—Permanence of Paper for Printed Library Materials, ANSI Z39.48-1984. 

Copyright © 1994

American Chemical Society

All Rights Reserved. The appearance of the code at the bottom of the first page of each chapter in this volume indicates the copyright owner's consent that reprographic copies of the chapter may be made for personal or internal use or for the personal or internal use of specific clients. This consent is given on the condition, however, that the copier pay the stated per-copy fee through the Copyright Clearance Center, Inc., 27 Congress Street, Salem, MA 01970, for copying beyond that permitted by Sections 107 or 108 of the U.S. Copyright Law. This consent does not extend to copying or transmission by any means—graphic or electronic—for any other purpose, such as for general distribution, for advertising or promotional purposes, for creating a new collective work, for resale, or for information storage and retrieval systems. The copying fee for each chapter is indicated in the code at the bottom of the first page of the chapter.

The citation of trade names and/or names of manufacturers in this publication is not to be construed as an endorsement or as approval by ACS of the commercial products or services referenced herein; nor should the mere reference herein to any drawing, specification, chemical process, or other data be regarded as a license or as a conveyance of any right or permission to the holder, reader, or any other person or corporation, to manufacture, reproduce, use, or sell any patented invention or copyrighted work that may in any way be related thereto. Registered names, trademarks, etc., used in this publication, even without specific indication thereof, are not to be considered unprotected by law.

PRINTED IN THE UNITED STATES OF AMERICA

American Chemical Society
Library
 1155 16th St., N.W.
 Washington, D.C. 20036

1994 Advisory Board

Advances in Chemistry Series

M. Joan Comstock, *Series Editor*

Robert J. Alaimo
Procter & Gamble Pharmaceuticals

Douglas R. Lloyd
The University of Texas at Austin

Mark Arnold
University of Iowa

Cynthia A. Maryanoff
R. W. Johnson Pharmaceutical
Research Institute

David Baker
University of Tennessee

Julius J. Menn
Plant Sciences Institute,
U.S. Department of Agriculture

Arindam Bose
Pfizer Central Research

Roger A. Minear
University of Illinois
at Urbana-Champaign

Robert F. Brady, Jr.
Naval Research Laboratory

Margaret A. Cavanaugh
National Science Foundation

Vincent Pecoraro
University of Michigan

Arthur B. Ellis
University of Wisconsin at Madison

Marshall Phillips
Delmont Laboratories

Dennis W. Hess
Lehigh University

George W. Roberts
North Carolina State University

Hiroshi Ito
IBM Almaden Research Center

A. Truman Schwartz
Macalaster College

Madeleine M. Joullie
University of Pennsylvania

John R. Shapley
University of Illinois
at Urbana-Champaign

Lawrence P. Klemann
Nabisco Foods Group

L. Somasundaram
DuPont

Gretchen S. Kohl
Dow-Corning Corporation

Michael D. Taylor
Parke-Davis Pharmaceutical Research

Bonnie Lawlor
Institute for Scientific Information

Peter Willett
University of Sheffield (England)

FOREWORD

The ADVANCES IN CHEMISTRY SERIES was founded in 1949 by the American Chemical Society as an outlet for symposia and collections of data in special areas of topical interest that could not be accommodated in the Society's journals. It provides a medium for symposia that would otherwise be fragmented because their papers would be distributed among several journals or not published at all.

Papers are reviewed critically according to ACS editorial standards and receive the careful attention and processing characteristic of ACS publications. Volumes in the ADVANCES IN CHEMISTRY SERIES maintain the integrity of the symposia on which they are based; however, verbatim reproductions of previously published papers are not accepted. Papers may include reports of research as well as reviews, because symposia may embrace both types of presentation.

ABOUT THE EDITORS



MARTIN BLANK received a B.S. in chemistry from City College of New York, a Ph.D. in physical chemistry from Columbia University, and a Ph.D. in colloid science from Cambridge University. In England, he developed a strong interest in the physical chemistry of biological membranes and biopolymers, and he has pursued this interest for more than 30 years in the Department of Physiology and Cellular Biophysics at Columbia University, as well as through appointments in several academic, industrial, and U.S. government settings. He has had appointments at Cambridge University, the Weizmann Institute (Israel), the University of California—Berkeley, The Hebrew University (Israel), Monash University (Australia), the Frumkin Institute of Electrochemistry (the former Soviet Union), and the Tata Institute (India). His industrial research experience has included work at California Research Corporation, Esso Research and Engineering, and Unilever research labs in both England and the Netherlands. While at the U.S. Office of Naval Research (ONR) in London and in Arlington, Virginia, he developed and managed a research program on biological membrane electrochemistry. He has been a consultant to the ONR and to the Electric Power Research Institute. His research has been on transport, electrochemistry, and rheology of protein and lipid surface films, and he has also developed theoretical models of monolayer permeation, hemoglobin equilibria, and the ion fluxes during electrical excitation in nerve membranes.

Recently, he has become interested in the effects of environmental electromagnetic fields on protein synthesis in cells and on the function of the “ion pump” enzyme. He has written more than 150 papers and reviews and edited eight books on electrical properties of biological systems. He is currently working on a volume based on the fourth Erice (Italy) course on nerve–muscle function and is the editor-in-chief for the *Proceedings of the First World Congress on Electricity and Magnetism in Biology in Medicine*.

Over the years, he has organized many meetings, including the first Gordon Research Conference on Bioelectrochemistry, and has been active in the American Chemical Society (Division of Colloid and Surface Chemistry), the Electrochemical Society (chairman, Organic and Biological Division), the Bioelectrochemical Society (president), and the Bioelectromagnetics Society. He has also served for many years on the editorial boards of several journals,

including the *Journal of the Electrochemical Society* (divisional editor for biology) and *Bioelectrochemistry and Bioenergetics* (North American editor).



IGOR VODYANOY is a manager of the Sensory Biology and Biophysics Program of the Office of Naval Research (ONR). He received his education from Leningrad Polytechnic Institute in Russia (now St. Petersburg Polytechnic Institute) in solid-state physics and studied biophysics at the Institute of Cytology of the U.S.S.R. Academy of Sciences in Leningrad. His early work in physics was research on new materials for radioelectronics. In Leningrad, he started to work on biophysical mechanisms of carrier-mediated membrane charge transfer. The work was carried out at the Institute of Semiconductors and at the Leningrad Nuclear Institute. In

1977, he performed original measurements of equilibrium electronic noise in artificial bilayers doped with an ion carrier and demonstrated that this system shows complete correspondence between noise and impedance. He entered the United States in 1979, has been at the University of California at Irvine for nine years, and joined ONR in 1988. He had a visiting appointment at Ben-Gurion University in Israel. He currently holds a joint appointment at the University of California and the National Institutes of Health. In more recent years, he has studied ion channel former proteins; their molecular mechanisms of action; and their interaction with a membrane. He was one of the organizers of the bilateral U.S.–U.S.S.R. symposia on membrane charge transfer and sensory biophysics.

PREFACE

THE FUNDAMENTAL MEMBRANE PROCESSES OF LIVING CELLS, for example, generation of ion gradients, sensory transductance, conduction of impulses, and energy transduction, are electrical in nature. Each process involves charge movement in a specialized protein structure, where part of the protein forms a channel for conduction of ions. The opening of the channel is controlled by changes in physical factors such as the electrical potential across the membrane or the binding of signaling (e.g., neurotransmitter or hormone) molecules and ions to specific receptor or enzyme sites. The many structural similarities between different protein assemblies suggest that there is a general design and that specific functions are based on variations of that design.

A number of channel protein structures are known in considerable detail, so their function can be studied in relation to structure, and models for which structure and properties can be characterized together can be constructed. Experimental approaches to this problem have tended to focus on the specific functions of each protein rather than on the general physical aspects of the problem. An approach based on electrochemical concepts and techniques emphasizes the general properties of the different structures and provides insights into the electrochemical nature of the charge-transfer phenomena in all channel systems.

For these reasons, the Office of Naval Research initiated in October 1986 an Accelerated Research Initiative of electrochemical research on biological and model membranes. The 5-year program explored the physical basis of biological sensory and energy-transducing processes by focusing on the electrochemical properties of integral membrane proteins (i.e., channel structures) associated with ion-transport processes. The major research areas covered were interfaces and lipid layers, channels (structure and function), and signal transduction. This volume contains papers from that program, as well as some related studies.

The electrochemical emphasis in the study of channels has led to some useful generalizations about the physical properties of integral membrane proteins and some of the specialized properties that depend on unique structures. The findings were presented and discussed at contractor's meetings in November 1988 at Belmont House in Elkridge, Maryland, and in April 1991 at Airlie House in Airlie, Virginia. Many research papers were published as a result of

this program. This volume summarizes the most important research accomplishments of the program and indicates the critical problems that require further research.

MARTIN BLANK
Department of Physiology
and Cellular Biophysics
Columbia University
New York, NY 10032

IGOR VODYANOV
Biology Division
Office of Naval Research
800 North Quincy
Arlington, VA 22214-5000

Interaction Forces between Membrane Surfaces

Role of Electrostatic Concepts

Max L. Berkowitz and K. Raghavan

Department of Chemistry, University of North Carolina, Chapel Hill, NC 27599

We briefly review the role electrostatic concepts play in the theoretical description of forces acting between membrane surfaces. A special emphasis is given to a discussion on the nature of the hydration force.

THE MOST IMPORTANT FORCES ACTING BETWEEN MEMBRANE SURFACES are van der Waals, electrostatic, and hydration. The first two forces are explained by the Derjaguin–Landau–Verwey–Overbeek (DLVO) theory (1); the existence of the hydration force was anticipated before it was measured (2). The van der Waals force is always attractive and displays a power law distance dependence, whereas the electrostatic and hydration forces are repulsive and exponentially decay with distance. The electrostatic force describes the interaction between charged membrane surfaces when the separation between surfaces is above 10 molecular solvent diameters. The hydration force acts between charged and uncharged membrane surfaces and at distances below 10 molecular solvent diameters; its value dominates the values of van der Waals and electrostatic forces (3). The term “hydration” reflects the belief that the force is due to the structure of water between the surfaces. Electrostatic and hydration forces are similar in some respects: both are exponential and repulsive and their theoretical description involves coupling electrostatic concepts and ideas borrowed from statistical mechanics. Although the nature of the electrostatic force is solidly established, this is not the case for the hydration force. To illustrate the role the electrostatic

0065-2393/94/0235-0003\$08.54/0
© 1994 American Chemical Society

concepts play in the description of the interaction between the membrane surfaces, we will describe the theory of the electrostatic and hydration forces. The description of the electrostatic force will be brief because details can be found in the excellent book by Verwey and Overbeek (1). The main emphasis of this review will be on the description of the hydration force.

Electrostatic Force

Because molecules at an aqueous–membrane interface often carry a net charge, electrostatics must be an important component of the theory that explains the functioning of this interface. Also, because a very large number of molecules constitute the interface, it is anticipated that the theory couples the electrostatic concepts with the concepts of statistical mechanics. Among the theories that illustrate this coupling, we find the rather simple but surprisingly successful Gouy–Chapman theory (4). The successes and failures of the Gouy–Chapman theory in explaining the properties of biological membranes are detailed in the recent review by McLaughlin (5).

Gouy–Chapman Theory. The first theory that successfully treated the electric double layer present at a phase boundary was the Gouy–Chapman theory (4). In its simplest version it considers an interface between a homogeneously charged solid surface and an ionic solution. The ions in the solution are modeled as point charges and the solvent is modeled as a dielectric continuum with dielectric constant ϵ . To simplify the description of the theory we consider a symmetric $z:z$ electrolyte solution. Place the surface charge at plane $x = 0$ and let the space charge due to mobile ions extend from $x = 0$ to infinity. The starting equation in the Gouy–Chapman theory is Poisson's equation, which couples the space-charge density ρ with the electrostatic potential ψ :

$$\epsilon \nabla^2 \psi = -4\pi\rho \quad (1)$$

where ϵ is the dielectric constant of the medium and ∇^2 is the Laplace operator. At this point the Gouy–Chapman theory assumes that the average concentration of ions at a given point can be obtained from the average value of the electrostatic potential at the same point through the application of the Boltzmann distribution; that is,

$$n_- = n_0 \exp(ze\psi/kT) \quad (2)$$

$$n_+ = n_0 \exp(-ze\psi/kT) \quad (3)$$

where n_0 is the bulk concentration of ions, n_- (n_+) are local concentrations of negative (positive) ions, e is the electronic charge, k is the Boltzmann

constant, T is the temperature of the system, and z is the valency of the ions. The total charge density ρ is then given by the expression

$$\rho = ze(n_+ - n_-) = -2zen_0 \sinh(ze\psi/kT) \quad (4)$$

Substitution of 4 into eq 1 results in the Poisson–Boltzmann equation:

$$\epsilon \nabla^2 \psi = 8\pi zen_0 \sinh(ze\psi/kT) \quad (5)$$

Equation 5 the fundamental equation of Gouy–Chapman theory. When $ze\psi \ll kT$, eq 5 can be linearized. The resulting equation is

$$\nabla^2 \psi = \frac{8\pi z^2 e^2 n_0 \psi}{\epsilon kT} = \frac{\psi}{\lambda_D^2} \quad (6)$$

where λ_D , which is usually called the Debye length, is given by the expression

$$\lambda_D^2 = \epsilon kT / 8\pi z^2 e^2 n_0 \quad (7)$$

For a flat interface, ψ is a function of x only. Using the boundary conditions that $\psi = 0$ and $d\psi/dx = 0$ when $x \rightarrow \infty$, the following exact solution for the $z:z$ electrolyte at the flat interface can be obtained:

$$\psi = \frac{2kT}{ze} \ln \frac{1 + \alpha \exp(-x/\lambda_D)}{1 - \alpha \exp(-x/\lambda_D)} \quad (8)$$

where

$$\alpha = \frac{\exp(ze\psi_0/2kT) - 1}{\exp(ze\psi_0/2kT) + 1} \quad (9)$$

ψ_0 is the potential at the surface ($x = 0$). For $ze\psi_0/kT \ll 1$, eq 9 predicts the exponential decay of the potential:

$$\psi = \psi_0 \exp(-x/\lambda_D) \quad (10)$$

Equation 10 can be obtained directly from the linearized Poisson–Boltzmann equation.

An important connection between the surface potential, surface charge density σ , and the density of ions can be established. Because the system is electroneutral, we can write

$$\sigma = \int_0^\infty \rho \, dx = \frac{\epsilon}{4\pi} \int_0^\infty \frac{d^2\psi}{dx^2} \, dx = -\frac{\epsilon}{4\pi} \left(\frac{d\psi}{dx} \right)_{x=0} \quad (11)$$

Equation 11 is often called the contact value theorem. Combining eqs 8 and 11, we get the desired relationship:

$$\sigma = \sqrt{\frac{2n_0\epsilon kT}{\pi}} \sinh\left(\frac{ze\psi_0}{2kT}\right) \quad (12)$$

For the biomembrane surfaces the situation $ze\psi_0 \gg kT$ often occurs. In this limit, eq 12 is simplified and has the form

$$n(0) = n_0 \exp(ze\psi_0/kT) = 2\pi\sigma^2/\epsilon kT \quad (13)$$

Equation 13 predicts that the concentration of counterions at the surface of the membrane, $n(0)$, is proportional to the square of the membrane charge density and is independent on the valency and the bulk concentration of the ions. Equation 13 together with other predictions from Gouy–Chapman theory are subject to experimental verification. The agreement between the Gouy–Chapman theory and the experiment is rather nice, considering how simple it is. The recent review by McLaughlin (5) should be consulted for further details of the experimental tests, successes, and limitations of Gouy–Chapman theory.

From the rigorous treatment of the double-layer problem on the molecular level, it becomes clear that the Gouy–Chapman theory of the interface is equivalent to a mean field solution of a simple primitive model (PM) of electrolytes at the interface (6). To consider the correlation between ions, integral equations that describe the PM are devised and solved in different approximations. An “exact solution” of the PM of the electrolyte can be obtained from the computer simulations. This solution can be compared with the solutions obtained from different integral equations. For detailed discussion of this topic, refer to the review by Carnie and Torrie (6). In many cases, the molecular description of the solvent must be introduced into the theory to explain the complexity of the observed phenomena. The analytical treatment in such cases is very involved, but initial success has already been achieved. Some of the theoretical developments along these lines were reviewed by Blum (7).

Double-Layer Interaction. When two charged surfaces approach each other their electrical double layers start to overlap and, as a result, the surfaces experience a repulsive force. For flat surfaces the forces can be explained in terms of the osmotic pressure due to the difference in the ionic concentration in the region between the plates and the concentration in the bulk region. Therefore, we can write (1)

$$p = kT(n_+ + n_- - 2n_0) = 2n_0kT[\cosh(ze\psi_m/kT) - 1] \quad (14)$$

where p is the disjoining pressure and ψ_m is the potential at the midplane between the surfaces separated by a distance h . If $ze\psi_m/kT \ll 1$, the cosh term in eq 14 can be expanded and the following expression for the pressure can be obtained:

$$p = n_0 kT (ze\psi_m/kT)^2 \quad (15)$$

When the distance between the plates is large ($h/\lambda_D \gg 1$), we can show that $\psi_m \sim 2\psi(x = h/2)$ (1). Therefore, at these conditions we get from eqs 8 and 9 that

$$ze\psi_m/kT = 8\alpha \exp(-h/2\lambda_D) \quad (16)$$

Substitution of eq 16 into eq 15 produces the final result for the disjoining pressure:

$$p = 64n_0 kT \alpha^2 \exp(-h/\lambda_D) \quad (17)$$

where α is given by eq 9. Equation 17 is an often quoted result of the DLVO theory that predicts that at distances greater than the Debye length the repulsive pressure between charged membranes decays exponentially, and the decay length is given by the Debye length.

Hydration Forces

Experimental Results. The DLVO theory, which is based on a continuum description of matter, explains the nature of the forces acting between membrane surfaces that are separated by distances beyond 10 molecular solvent diameters. When the interface distance is below 10 solvent diameters the continuum picture breaks down and the molecular nature of the matter should be taken into account. Indeed the experiment shows that for these distances the forces acting between the molecularly smooth surfaces (e.g., mica) have an oscillatory character (8). The oscillations of the force are correlated to the size of the solvent, and obviously reflect the molecular nature of the solvent. In the case of the rough surfaces, or more specifically biomembrane surfaces, the solvation force displays a monotonic behavior. It is the nature of this solvation force (if the solvent is water, then the force is called hydration force) that still remains a puzzle. The hydration (solvation) forces have been measured by using the surface force apparatus (9) and by the osmotic stress method (10, 11). Forces between phosphatidylcholine (PC) bilayers have been measured using both methods and good agreement was found.

The general picture that emerges from the experiments is that up to distances ~ 3 nm lipid bilayers in water repel each other with an exponen-

tially decaying force. The decay constant of the force varies from the value less than 0.1 nm to above 0.3 nm (3). If the lipids are neutral, the repulsion is eventually balanced by the attractive van der Waals forces of DLVO theory. If the lipids are charged, the repulsion continues but with a decay constant compatible with the value obtained from the double-layer theory. The addition of ions to water can, in some cases, provoke the appearance of an attractive force (3), a phenomenon of obvious relevance to membrane fusion.

The previously described measurements have been performed on lipids in aqueous solutions, but lipid bilayers also swell in some other solvents (12) and the results of such measurements compare quite well with the aqueous case. In addition, hydration (solvation) forces act between DNA polyelectrolytes (13) and polysaccharides (14). These facts make the interpretation of the forces even more complicated and it is no wonder that different approaches to explain the nature of this solvation force exist. So far no truly *ab initio* theory has been proposed. The existing theories include models based on the electrostatic approach, the free energy approach, and an approach based on the entropic or protrusion model.

Electrostatic Models. The solvated phospholipid bilayer can be considered as an electrostatic problem, where water is modeled as a dielectric continuum (with $\epsilon \approx 80$) enclosed between surfaces that represent the phospholipid membranes. The head groups of the membrane molecules can be represented by dipoles and the tails can be represented by a dielectric continuum ($\epsilon \approx 2$). The repulsion hydration force is due to the interaction of the zwitterions of the head groups with the image charges. The first analysis of such an electrostatic model was performed by Jonsson and Wennerstrom (JW; 15). Because the head groups of the membrane molecules are mobile, JW represented the zwitterions as a two-dimensional fluid described by a radial distribution $g(r)$. To simplify the problem, JW assumed that the surface separation was large and that there was no correlation between the surfaces. From their analysis JW concluded that the force due to the images strongly depended on the character of the pair distribution function. The force had an exponential decay when the correlation between the zwitterions was strong. For the uncorrelated zwitterions, the force followed the power law. Because the calculated value of the force was of the same magnitude as in the experiment, JW considered their theory a success. The theory proposed by JW was extended by Kjellander (16), who investigated the model in greater detail by removing some overrestrictive assumptions. Kjellander concluded that the force was strongly dependent on the model used for $g(r)$ and that the agreement between the JW results and the experiment was fortuitous. Moreover, Kjellander showed that a change in the location of the dielectric discontinuities with respect to the location of the zwitterions caused the results to undergo a dramatic change.

The electrostatic model proposed by JW was later thoroughly analyzed in a series of works performed by the "Swedish-Australian group" (17-19), where exact formal treatment and approximate methods were used to solve the problem. The authors of these papers considered two electrostatic models. In the first model they investigated the interaction between two planar surfaces (separated by a distance h) with mobile ions adsorbed onto them (the net surface charge was zero). The surfaces were immersed in the dielectric continuum with the dielectric constant ϵ_1 . Behind each surface a different dielectric medium (with the dielectric constant ϵ_2) was placed. In the second model the mobile ions were replaced by mobile dipoles that were oriented perpendicular to the surfaces. In both models the motion of the particles was restricted to the well-defined plane. From the analytical treatment, which included images and correlations, the following asymptotic results for the pressure were obtained for the first model:

1. When $\epsilon_1 = \epsilon_2$ (no image charges are present in the system), the interaction arises from the charge fluctuations. The pressure, P , is attractive and displays an asymptotic behavior:

$$P \sim -T/h^3 \quad (h \rightarrow \infty) \quad (18)$$

The pressure is independent of the ion concentration and ionic radii; it only depends on the temperature T and the distance between the layers.

2. When $\epsilon_1 \neq \epsilon_2$, image charges are present in the system. The image repulsion between electroneutral planes is exactly canceled by the static van der Waals interaction, and the leading term for the total pressure is exactly the same as in the previous case.

In the second model (and in the case that $\epsilon_1 \neq \epsilon_2$), the pressure between surfaces arises from dipole correlations and dielectric images. Asymptotically the pressure is

$$P \sim -A/h^3 + B/h^4 - C/h^5 \quad (h \rightarrow \infty) \quad (19)$$

The van der Waals pressure is not screened and it dominates at large distances; the second term is due to image repulsion, and the third term is due to the attraction between dipoles on different surfaces.

These asymptotic results were compared with numerical results obtained by solving the hypernetted chain equation (HNC) for the pair distribution function, with Monte Carlo (MC) simulations and with a mean field approximation. The agreement between the numerical results and the asymptotic results was fairly good at distances above $h \approx 1.5$ nm. Substitution of the

parameters that correspond to the zwitterionic lipid lamellae into the foregoing pressure expressions resulted in the attractive total pressure.

We have concluded that the electrostatic model proposed by JW is quite an interesting model by itself, but it is very sensitive to the fine details of the system and, therefore, cannot explain the quite generally measured exponential dependence of hydration forces on the surface separation.

Free Energy Approach. Nearly immediately after the publication of the first data on the hydration force (10), Marcelja and Radic (MR) proposed a very elegant theory to explain the nature of the observed strong force (20). According to MR theory the force is due to the modification of water structure near the membrane–water interface. The water molecules near the interface differ from the water molecules in the bulk: they are more “ordered.” To describe this “order,” one can introduce an order parameter $\eta(x)$ and perform a Landau-type expansion of the free energy density $g(x)$; that is,

$$g = g_0 + a\eta^2 + c(\partial\eta/\partial x)^2 + \dots \quad (20)$$

where g_0 is the free energy density in bulk water, and a and c are constants. The corresponding minimization problem results in the differential equation

$$d^2\eta(x)/dx^2 - (a/c)\eta(x) = 0 \quad (21)$$

Assume now that the interfaces are positioned at $x = h/2$ and $x = -h/2$ and that $\eta(h/2) = -\eta(-h/2) = \eta_0$. The minimization of free energy density given by equation 20 subject to these boundary conditions results in the following form for the order parameter:

$$\eta(x) = \eta_0 \sinh(\kappa x) / \sinh(\kappa h/2) \quad (22)$$

where $\kappa = (c/a)^{1/2}$. The excess free energy per unit area, ΔG , is

$$\Delta G = \int_{-h/2}^{h/2} (g - g_0) dx = (ac)^{1/2} \eta_0^2 \coth(h\kappa/2) \quad (23)$$

The pressure, p , is given by the derivative of the excess free energy:

$$p = - \frac{\partial \Delta G}{\partial h} = \frac{p_0}{\sinh^2(\kappa h/2)} \quad (24)$$

For $\kappa h \gg 1$, the repulsion follows the exponential law:

$$p = 4p_0 \exp(-\kappa h) = 4p_0 \exp(-h/\lambda) \quad (25)$$

where $\lambda = 1/\kappa$. From the derivation described previously, it follows that the value of p_0 (the pressure when the surfaces are at close contact) is determined by the degree the surface orders the water and, therefore, depends on the properties of the surface. The decay parameter λ is determined by the degree the ordering is propagated through water and, therefore, according to MR theory (20) characterizes water only.

Marcelja and Radic (20) did not specify what quantity plays the role of the order parameter. Many different variables can be considered as candidates for this role, but the orientational polarization of water has the greatest appeal. Indeed, in later publications Gruen and Marcelja (21) explicitly considered this quantity as an order parameter in the problem. An emphasis on the orientational polarization allows easy construction of an intuitive picture for the origin of the hydration force, and this picture is given in Figure 1. As can be seen from this figure, due to the preferential orientation and symmetry, the resulting dipole to the left of the midplane OO' repels the dipole to the right of the midplane. The net result is a repulsive force.

The MR theory predicts that the decay constant is independent of the nature of the surface, but the experimental data show that this is not the case and that the decay constant does depend on the nature of the surface (3). Recently, Kornyshev and Leikin (KL; 22) extended the Marcelja–Radic theory and demonstrated how this dependence can be explained. They replaced the homogeneous boundary conditions used in Marcelja–Radic theory by the inhomogeneous boundary conditions. According to Kornyshev and Leikin, the description of the inhomogeneous character of the bound-

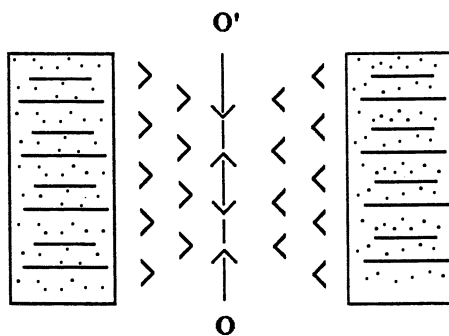


Figure 1. Pictorial representation of the Marcelja–Radic theory.

aries is measured by the correlation function

$$S_{ij}(R) = \frac{1}{2} \langle \delta\eta_i(r+R) \delta\eta_j(r) + \delta\eta_j(r+R) \delta\eta_i(r) \rangle \quad (26)$$

where R is the lateral coordinate and i, j label the surfaces. In reference 22 the authors show that only $S_{ii}(R)$ contribute to the repulsion force. The Fourier transform of this correlation function, $S_{ii}(Q)$ (usually called the structure factor), which is defined as

$$S_{ii}(Q) = \int dR S_{ii}(R) \exp(-iQR) \quad (27)$$

determines the inhomogeneous contribution to the hydration pressure P_{inh} , which is given by the expressions

$$P_{inh}(h) = P_1(h) + P_2(h) \quad (28)$$

$$P_i(h) = \frac{c}{2\pi} \int_0^\infty dQ \frac{QS_{ii}(Q)}{\sinh^2[h(\kappa^2 + Q^2)^{1/2}]} \quad (29)$$

In eq 29, $1/\kappa$ is the characteristic decay length for the pure water. As reference 22 pointed out, $S_{ii}(R)$ displays periodic oscillations with some wavenumber q_* , modulated by a decaying envelope of some characteristic width ξ . Then $S_{ii}(Q)$ has a maximum centered at $Q = q_*$ with a width ξ^{-1} . In this situation when $\xi^2 \gg h(\kappa^2 + q_*^2)^{1/2}$ (22), the main contribution to the integral is given by $Q = q_*$, so that we obtain

$$P_i(h) = \frac{c \langle [\delta p_i(R)]^2 \rangle}{\sinh^2[h(\kappa^2 + q_*^2)^{1/2}]} = \frac{p_0}{\sinh^2(\kappa_{eff} h)} \quad (30)$$

This equation is very similar to eq (24), the main result of Marcelja-Radic theory. The difference between the eqs 24 and 30 is that eq 30 clearly shows that the decay constant of the hydration force depends on the nature of the interface. Equation 30 is obtainable from MR theory if the constants a and c in eq 21 are assumed to be interface specific. Equation 30 justifies this assumption.

In the opposite limit when $\xi^2 \ll h(\kappa^2 + q_*^2)^{1/2}$, the main contribution to the integral is due to the region near $Q \sim \kappa$. The decay length is then $(2\kappa)^{-1}$. In the intermediate case there is no single decay length, but there is

a superposition of exponentials. Because the variation of h in the experiment is rather narrow (22), it might be considered as an apparent exponential with an effective decay length that lies between two limits,

$$\frac{1}{2(\kappa^2 + q_*^2)^{1/2}} < \lambda_{\text{eff}} < \frac{1}{2\kappa} \quad (31)$$

Kornyshev and Leikin (22) also proposed the following three qualitative rules that describe the variation of the decay length and the strength of the hydration force:

1. With the increase of the correlation range of the surface structure factor, the effective decay range of the hydration repulsion decreases.
2. At a large fixed distance between the surfaces, the increase of the correlation range of the surface structure factor leads to the decrease in the absolute value of the force.
3. The variation of the observable effective decay lengths is limited from below and above. The lower limit is the period for the surface perturbation distribution divided by 4π ; the upper limit is one-half of the water correlation length.

Kornyshev and Leikin show that these rules correlate well with the experimental data (22).

Because the Landau-type expansion has an empirical character, justification on molecular grounds is important. Gruen and Marcelja (21) attempted to justify the expansion and discovered that the polarization of water had to be assumed is nonlocal; that is, instead of the local equation connecting the polarization \mathbf{P} and Maxwell field \mathbf{E} at point \mathbf{r}

$$\mathbf{P}(\mathbf{r}) = \chi \mathbf{E}(\mathbf{r}) \quad (32)$$

the nonlocal counterpart should be considered:

$$\mathbf{P}(\mathbf{r}) = \int \chi(\mathbf{r}, \mathbf{r}') \mathbf{E}(\mathbf{r}') d\mathbf{r}' \quad (33)$$

In equations 32 and 33, χ is the susceptibility of the medium. Expressed in the Fourier space, the Maxwell field \mathbf{E} and the polarization \mathbf{P} are related by

$$4\pi \mathbf{P}(\mathbf{k}) = (\epsilon(\mathbf{k}) - \mathbf{I}) \mathbf{E}(k) \quad (34)$$

where $\epsilon(\mathbf{k})$ is the wave-vector-dependent dielectric tensor and \mathbf{I} is the unit tensor. From the minimization of the free energy density Gruen and Marcelja (21) obtained the following form for the dielectric function $\epsilon(\mathbf{k})$:

$$\epsilon(\mathbf{k}) = \left(\epsilon_{\infty} + \frac{\epsilon_0 - \epsilon_{\infty}}{1 + \xi^2 k^2 \epsilon_0 / \epsilon_{\infty}} \right) \mathbf{I} \quad (35)$$

where ϵ_0 and ϵ_{∞} are the static and high-frequency dielectric constants, respectively, and ξ is a decay length, the value of which is fixed to secure agreement with the measured forces. This form for the dielectric function was used extensively in nonlocal electrostatic theories that attempted to explain the hydration repulsion (23–25). Very recently, it was pointed out that the form for the dielectric function given by eq 35 may be incorrect and, therefore, the theories based on this form may be incorrect also (26).

Protrusion Model for the Hydration Force. Recently Israelachvili and Wennerstrom (IW) proposed that the origin of the hydration force is due to the head-group protrusion of the phospholipid molecules into the solvent region (27), and, therefore, the force is more akin to a “steric” force acting between polymer-covered surfaces. Because such an explanation of the nature of the hydration force does not involve electrostatic concepts, we will not present the IW theory here. A detailed description of a protrusion model is available in a recent review by Israelachvili and Wennerstrom (28), and a critique of IW theory of protrusions can be found in Parsegian and Rand (29).

Computer Modeling

Marcelja–Radic theory and its extensions (20–22) and Jonsson–Wennerstrom theory and its extensions (15–19) do not address the problem of the hydration force on the level of a detailed molecular Hamiltonian. Due to the complexity of the problem perhaps only a computer simulation technique can provide a description on this level. The tremendous usefulness of computer methods in the study of DNA and protein molecules (30, 31) inspires the hope that simulations will also play an important role in the study of biomembrane molecules. The first computer simulations to study the problem of hydration force on phospholipid molecules were performed by Scott (32, 33) and by Kjellander and Marcelja (34, 35). Because these studies were performed seven to eight years ago, the researchers were limited by the computer power available. As a result, the simulations were performed with

simplified models of membrane molecules and the dynamics was restricted. For example, in the simulations of Kjellander and Marcelja (34, 35) the dynamics of water molecules in the presence of fixed lecithin head groups was performed for a rather short run (8 ps). In these simulations the orientational polarization propagated in a damped oscillatory manner some 1 nm from each membrane surface. This observation was used by Israelachvili and Wennerstrom (27) as an argument against Marcelja–Radic theory, which predicts an exponential decay of the polarization (20). However, because Kjellander and Marcelja simulations were performed for rather short runs, we question if the oscillating polarization profiles observed in these simulations are due to the limited statistics. Another pertinent question is if the monotonically repulsive hydration force between bilayers could be a smeared-out oscillatory force, due to thermal motion and roughness of the mobile head group (27). To answer these questions we recently performed two molecular dynamics simulations: simulations A and B, each 96 ps long. (A detailed description by K. Raghavan and M. Berkowitz is being prepared and will be given elsewhere.) In simulation A we considered a bilayer composed of 32 dilauroylphosphatidylethanolamine (DLPE) molecules and 362 water molecules at $T = 285$ K. Each layer of the bilayer consisted of 16 molecules and the layers were separated by a distance ~ 1.4 nm. The force field was

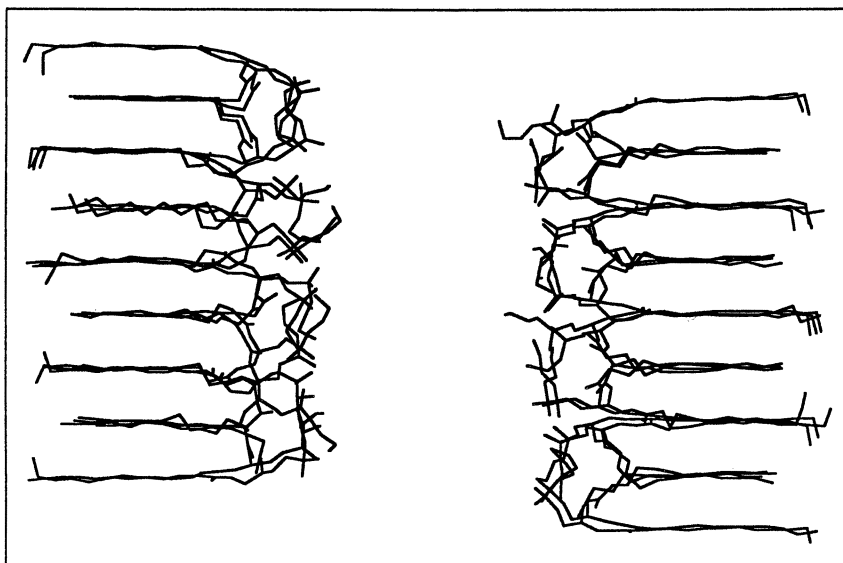


Figure 2. A snapshot of the molecular dynamics unit cell that consists of 32 DLPE molecules in gel phase and 362 water molecules. For clarity the water molecules are not displayed in the figure.

taken from the AMBER software package (36). In this simulation we made some improvements in modeling the DLPE bilayer since our last simulations (37): In the previous simulations the hydrocarbon atoms of the chain were held fixed; in the present simulation A all the atoms are moving. To concentrate on the head-group motion we considered the bilayer to be in a gel phase; therefore, the spacing between the molecules was adjusted so that the area per DLPE molecule was 0.41 nm^2 (area in the gel phase). A snapshot from the simulation is given in Figure 2. In simulation B we kept the DLPE molecules rigid and in the crystal phase.

The distribution of densities for water oxygen (relative to the density of bulk water) along the x axis (axis perpendicular to the bilayer surface) is shown in Figure 3. Figure 4 displays the density and the location of the atoms in the head group of the phospholipid molecules. One of the most difficult problems to be resolved when dealing with the rough surfaces is to decide how to measure the intersurface distance. In the present simulations, guided by Figure 3, we positioned the boundaries of the surfaces at $x = 0.14 \text{ nm}$

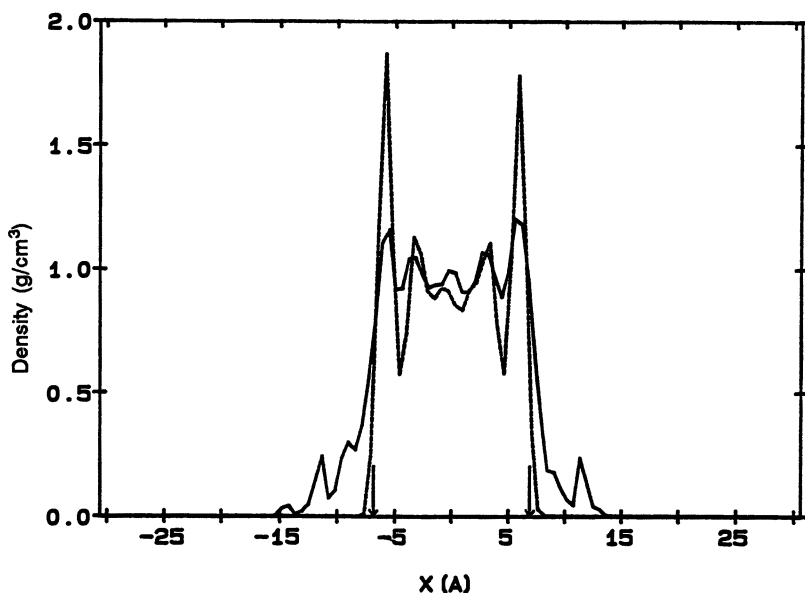


Figure 3. Water oxygen densities from the simulations A (solid line) and B (dashed line) in units of grams per cubic centimeter between DLPE surfaces as a function of distance along the bilayer normal (given in angstroms). The arrows point to the location of the membrane surfaces (see the text).

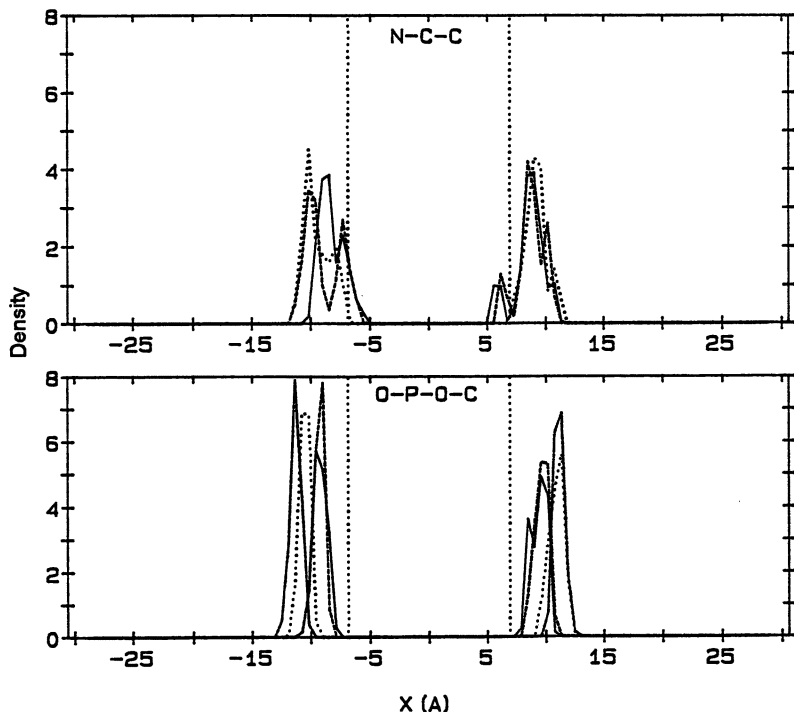


Figure 4. The densities (in arbitrary units) of the atoms that comprise the backbone of the DLPE molecules in the simulation A as a function of distance along bilayer normal. The dotted vertical line is at the location of the membrane surfaces. Key: Upper panel: Solid line is for N atom, dashed line is for C atom connected to N, and dotted line is for the other C atom. Lower panel: Solid line is for the first O atom, dashed line is for the P atom, dotted line is for the O atom connected to P atom and C atom, and dot-dashed line is for C atom.

(roughly the radius of the water molecule) away from the positions that correspond to the water adsorption peaks at the membrane surfaces. As we can see from Figures 3 and 4, the head-group atoms slightly protrude into the water and water penetrates ~ 0.5 nm from the surface into the head-group region in simulation A. The weak layering of water is still present in the system. When the surface is rigid (simulation B), the close packing arrangement of the head groups does not allow water penetration, and a strong water adsorption at the surface, as indicated by the sharp intense peaks in the density, is observed. In this case the density oscillations of water are still

strong even beyond the first layer. Figure 5 shows the orientational polarization profiles along the bilayer normal obtained from the simulations A and B. Similar to the density profiles, much sharper polarization oscillations are observed in the simulation with rigid DLPE molecules. Although the oscillations in the polarization profile from a gel simulation are reduced compared to the oscillations observed by Kjellander and Marcelja (34), they are still present in our simulation. The main conclusion we draw from the comparison of water properties obtained in simulations A and B is that the structure and packing of the head groups of the membrane molecules dramatically influence the properties of water molecules embedded between membrane surfaces. This conclusion is in agreement with Kornyshev and Leikin theory (22).

Because our simulations were performed on a rather small sample and only for 96 ps, it is possible that we did not sample enough of the configuration space of the system. To avoid some of the effects due to this problem we performed another 96-ps simulation (simulation C) in which the phospholipid molecules were again kept in gel phase, but were initially prepared in a different configuration. The symmetrized polarization profile obtained from

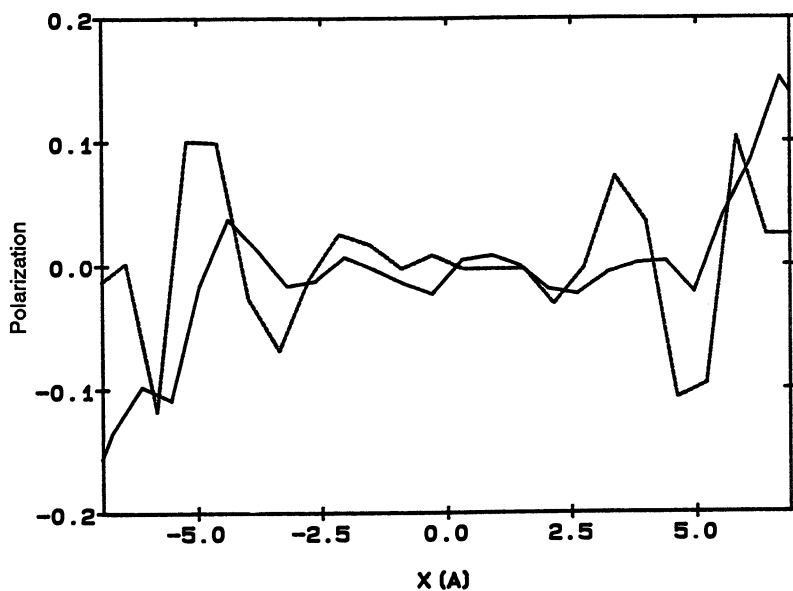


Figure 5. Polarization of water in the direction normal to the DLPE surface from simulations A (solid line) and B (dashed line).

averaging the two gel simulations (simulations A and C) is presented in Figure 6 together with the fit of this profile to a functional form given by eq 22. The dependence of the decay length κ on the character of the interface is assumed. This assumption is justified by Kornyshev–Leikin theory [see the foregoing discussion on Kornyshev–Leikin theory (22)]. In general, the polarization data from the simulations are fitted to the equation

$$\eta(x) = \alpha \sinh[(x - x_0)/\lambda_{\text{eff}}] \quad (36)$$

where a is a fit constant and x_0 is the value of the coordinate in the middle of the bilayer ($x_0 = 0$ in eq 22). The polarization profile obtained from our simulations does not show as much oscillation as the profile from the simulation of Kjellander and Marcelja (34), but it is still not monotonically decaying as predicted by eq 36. Nevertheless the decay exponent for the polarization obtained from the fit is of the same value as the exponent found

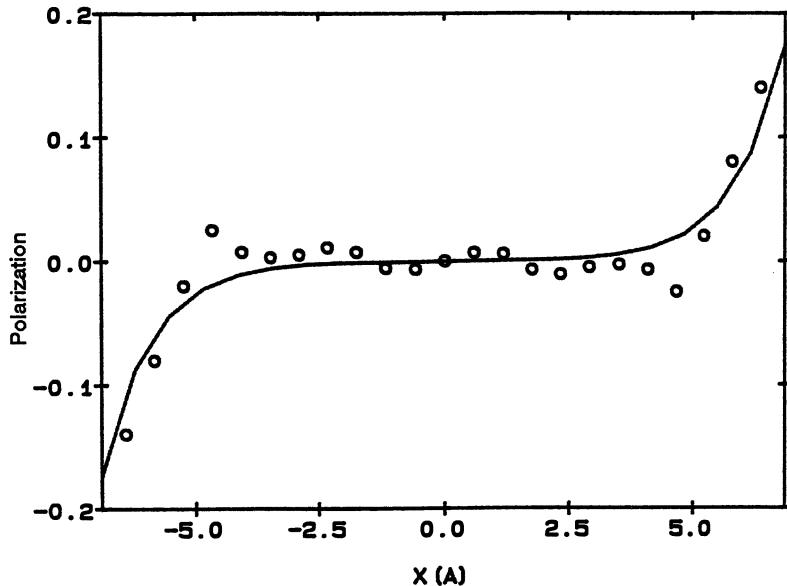


Figure 6. Data points that represent the orientational polarization of water between DLPE bilayers obtained by averaging the results from simulations A and C (see text). The dashed line is a fit to a functional form given by eq 36.

in different experiments involving PE molecules in gel phase [the experimental decay length in the region 0.08–0.12 nm (3)].

A better sampling of the motion of the configuration space of the system can be done when the membrane molecules are in a liquid crystalline phase. Therefore, to study the behavior of water between the membrane surfaces, we analyzed the data from the recent simulations of a liquid crystalline phase of dipalmitoylphosphatidylcholine (DPPC) molecules (38) and from an extension of this simulation (S. J. Marrink, M. Berkowitz, and H. J. C. Berendsen, unpublished). Some of the results from these works are shown in Figures 7–11. Figure 7 displays the density of phosphorus (P) and nitrogen (N) atoms of the head groups together with the profile for water density. As the figure indicates, the phospholipid molecules are well solvated. The vertical lines on this figure indicate the positions of the surfaces, which were found using the following procedure. First we obtained the average positions of P atom and of

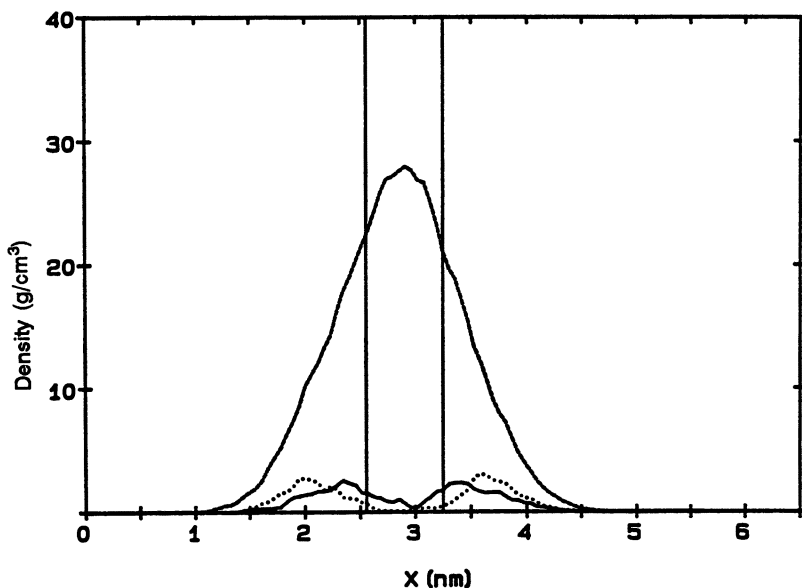


Figure 7. The N atom (solid line), P atom (dotted line), and water densities (dashed line) from a simulation of DPPC–water interface as a function of distance along the bilayer normal (in units of nanometers). The membrane surfaces (solid vertical lines) are placed according to the prescription in the text and are shown by vertical lines. In this simulation the distance between surfaces is ~ 0.6 nm.

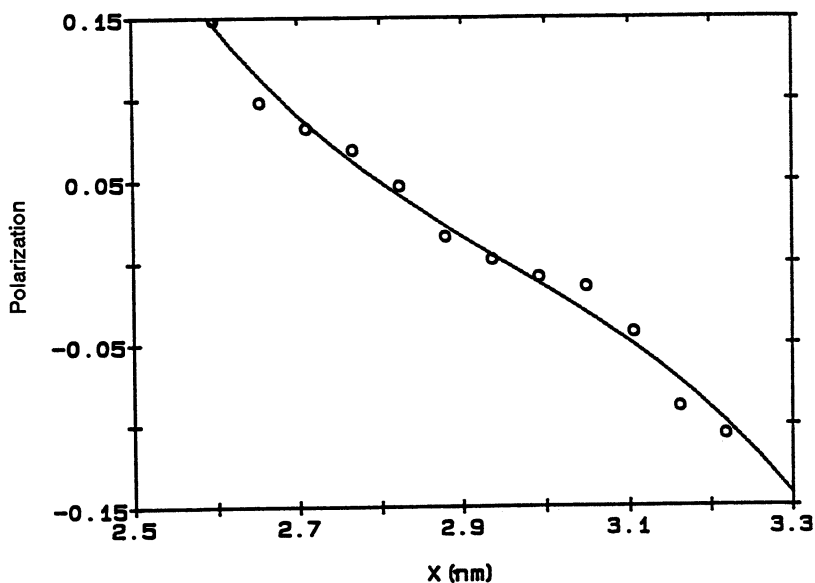


Figure 8. Data points that represent the orientational polarization of water between DPPC bilayers. The dashed line is a fit to a functional form given by eq 36.

N atoms from their respective distributions. Then we found the midpoint between these positions, and finally we placed the membrane wall at a distance 0.5 nm away from the midpoint toward the water. This procedure used to locate the position of the membrane surface agrees well with the procedure used in the experiments with X-rays (11). The density profile of water, which is also shown on the figure is smooth and does not display any oscillations. It is, therefore, not that surprising that the orientational polarization of water is also smooth and, moreover, can be very nicely fitted to a functional form given by eq 36, as shown in Figure 8. The exponent for the polarization decay obtained from the fit has the value of 0.26 nm, which is relatively close to the experimental value of 0.21 nm (3). Figures 9 and 10 are similar to Figures 7 and 8, but they are obtained from a simulation with a larger separations between DPPC membrane surfaces. Again the fit of the water polarization profile obtained from the simulation to the functional form of eq 36 is good. According to theory the exponent of the polarization decay should not depend on the distance between membranes, and, indeed, from our simulations we observe this to be true (the decay constant obtained from

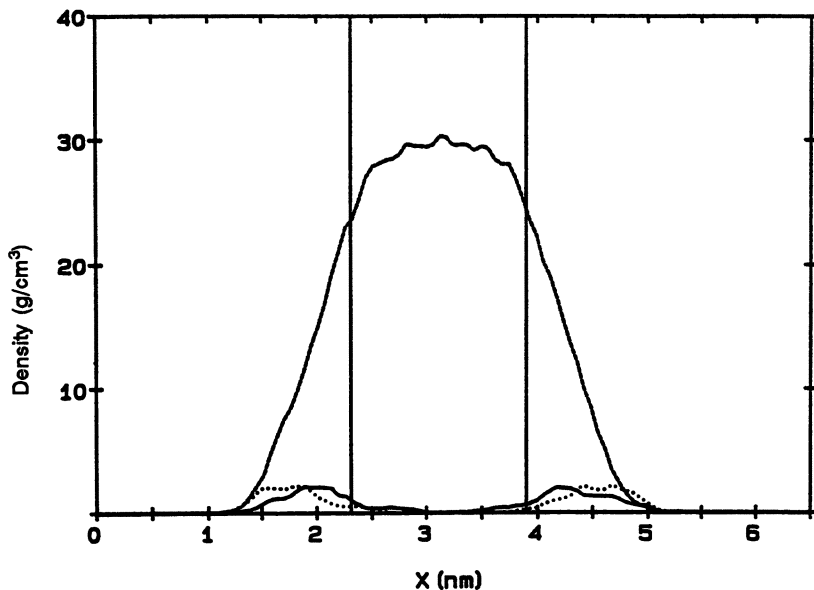


Figure 9. Same as Figure 7, only for the distance ~ 1.6 nm between DPPC surfaces.

a simulation with a larger separation of DPPC molecules is found to be ~ 0.21 nm). Considering that we deal with measurements of rather limited accuracy due to the fit and statistics, we conclude that the agreement between the exponents from the two simulations of DPPC molecules is good.

The major result from our analysis of DPPC simulation is that the orientational polarization of water displays a monotonic behavior. Therefore, the statement that computer simulations always show an oscillatory polarization profile of water seems to be incorrect. To understand better the nature of what is happening in the simulations with liquid crystalline DPPC, we display a snapshot from the simulation in Figure 11. This figure clearly shows protrusions of the phospholipid molecules from the bilayer surface. We think that the role of these protrusions is to "roughen" the surface. Rough surfaces destroy the layered packing arrangement of water molecules; as the result we observe the exponential decay of the force due to the smearing out of the oscillations. Therefore, our explanation of the nature of hydration force in some way combines the pictures presented by free energy theories (20–22) with the IW (27) theory. We emphasize that, contrary to the IW view expressed in reference 27, we believe that the force is due to the orientational order in the solvent.

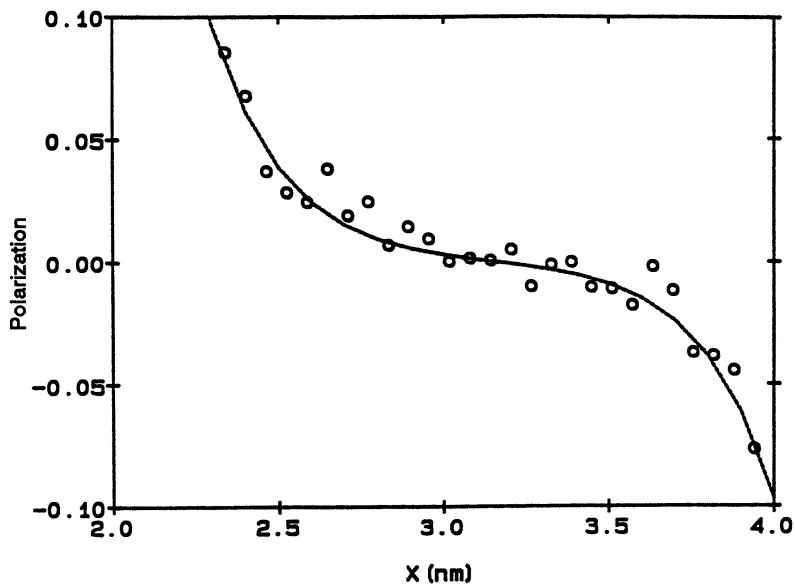


Figure 10. Same as Figure 8, only for the distance ~ 1.6 nm between DPPC surfaces.

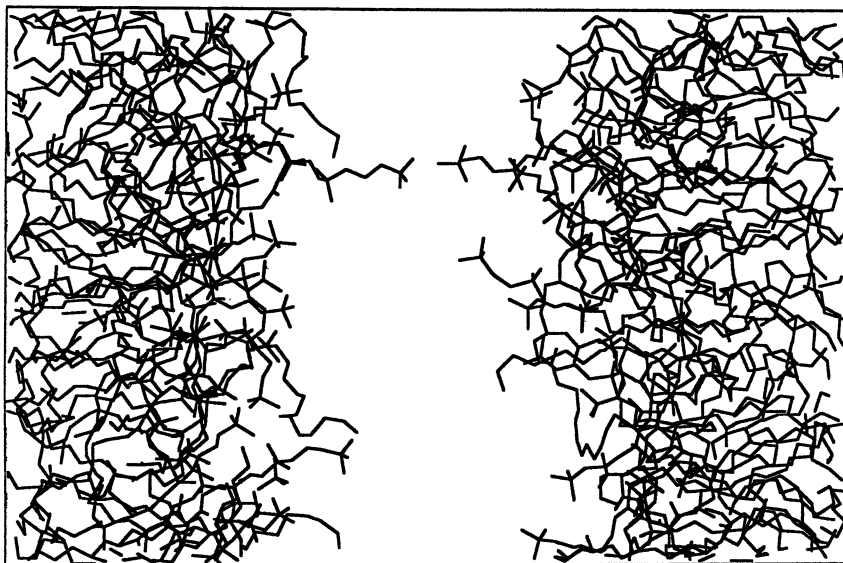


Figure 11. A snapshot from a simulation of liquid crystalline DPPC bilayer in water. For clarity water is not shown in the simulation.

Acknowledgment

This work was supported by a grant from the Office of Naval Research. The simulations were performed on the CRAY-YMP at the North Carolina Supercomputer Center.

References

1. Verwey, E. J. W.; Overbeek, J. Th. G. *Theory of Stability of Colloids*; Elsevier: Amsterdam, Netherlands, 1948.
2. Langmuir, I. *J. Chem. Phys.* **1938**, *6*, 873.
3. Rand, R. P.; Parsegian, V. A. *Biochim. Biophys. Acta* **1989**, *988*, 351.
4. Gouy, G. *J. Phys. (Paris)* **1910**, *9*, 457; Chapman, D. L. *Philos. Mag.* **1913**, *25*, 475.
5. McLaughlin, S. *Annu. Rev. Biophys. Chem.* **1989**, *18*, 113.
6. Carnie, S. L.; Torrie, G. M. *Adv. Chem. Phys.* **1984**, *56*, 141.
7. Blum, L. *Adv. Chem. Phys.* **1990**, *78*, 171.
8. Christenson, H. K.; Horn, R. G.; Israelachvili, J. N. *J. Colloid Interface Sci.* **1982**, *88*, 79.
9. Marra, J.; Israelachvili, J. N. *Biochemistry* **1985**, *24*, 4608.
10. LeNeveu, D. M.; Rand, R. P.; Parsegian, V. A. *Nature (London)* **1976**, *259*, 601.
11. McIntosh, T. J.; Simon, S. A. *Biochemistry* **1986**, *25*, 4058.
12. McIntosh, T. J.; Magid, A. D.; Simon, S. A. *Biochemistry* **1989**, *28*, 7904.
13. Rau, D. C.; Lee, B.; Parsegian, V. A. *Proc. Natl. Acad. Sci. U.S.A.* **1984**, *81*, 2621.
14. Rau, D. C.; Parsegian, V. A. *Science (Washington, D.C.)* **1990**, *249*, 1278.
15. Jonsson, B.; Wennerstrom, H. *J. Chem. Soc. Faraday Trans. 2* **1983**, *79*, 19.
16. Kjellander, R. *J. Chem. Soc.* **1984**, *80*, 1323.
17. Attard, P.; Mitchell, D. J. *Chem. Phys. Lett.* **1987**, *133*, 347.
18. Attard, P.; Kjellander, R.; Mitchell, D. J. *Chem. Phys. Lett.* **1987**, *139*, 219.
19. Attard, P.; Kjellander, R.; Mitchell, D. J.; Jonsson, B. *J. Chem. Phys.* **1988**, *89*, 1664.
20. Marcelja, S.; Radic, N. *Chem. Phys. Lett.* **1976**, *42*, 129.
21. Gruen, D. W. R.; Marcelja, S. *J. Chem. Soc. Faraday Trans. 2* **1983**, *79*, 211, 225.
22. Kornyshev, A. A.; Leikin, S. *Phys. Rev. A* **1989**, *40*, 6431.
23. Kornyshev, A. A. *Electrochim. Acta* **1981**, *26*, 1.
24. Belaya, M. L.; Feigel'man, M. V.; Levadny, V. G. *Chem. Phys. Lett.* **1986**, *126*, 361.
25. Kornyshev, A. A. *J. Electroanal. Chem.* **1986**, *204*, 79.
26. Attard, P.; Dongquig, W.; Patey, G. N. *Chem. Phys. Lett.* **1990**, *172*, 69.
27. Israelachvili, J. N.; Wennerstrom, H. *Langmuir* **1990**, *6*, 873.
28. Israelachvili, J. N.; Wennerstrom, H. *J. Phys. Chem.* **1992**, *96*, 520.
29. Parsegian, V. A.; Rand, R. P. *Langmuir* **1991**, *7*, 1299.
30. McCammon, J. A.; Harvey, S. C. *Dynamics of Proteins and Nucleic Acids*; Cambridge University Press: Cambridge, England, 1987.
31. Brooks, C. L., III; Karplus, M.; Pettitt, M. *Adv. Chem. Phys.* **1988**, *71*, 1.

32. Scott, H. L. *Chem. Phys. Lett.* **1984**, *109*, 570.
33. Scott, H. L. *Biochem. Biophys. Acta* **1985**, *814*, 327.
34. Kjellander, R.; Marcelja, S. *Chem. Scr.* **1985**, *25*, 73.
35. Kjellander, R.; Marcelja, S. *Chem. Phys. Lett.* **1985**, *120*, 393.
36. Singh, U. C.; Weiner, P. K.; Caldwell, J. K.; Kollman, P. K. Program AMBER, University of California, San Francisco, CA, Version 3.1, 1987.
37. Raghavan, K.; Rami Reddy, M.; Berkowitz, M. *Langmuir* **1992**, *8*, 233.
38. Egberts, E., Ph.D. Thesis, Groningen, Netherlands, 1988.

RECEIVED for review January 29, 1991. ACCEPTED revised manuscript September 30, 1992.

Time-Resolved Dynamics of Proton Diffusion at a Water–Membrane Interface

Menachem Gutman

Laser Laboratory for Fast Reactions in Biology, Department of Biochemistry, The George S. Wise Faculty of Life Sciences, Tel Aviv University, Tel Aviv 69978, Israel

The manner in which protons diffuse is a reflection of the physical properties of the environment, the geometry of the diffusion space, and the chemical composition of the surface that defines the reaction space. The biomembrane, with heterogeneous surface composition and dielectric discontinuity normal to the surface, markedly alters the dynamics of proton transfer reactions that proceed close to its surface. Time-resolved measurements of fast, diffusion-controlled reactions of protons with chromophores and fluorophores allow us to gauge the physical, chemical, and geometric characteristics of thin water layers enclosed between phospholipid membranes. Combination of the experimental methodology and the mathematical formalism for analysis renders this procedure an accurate tool for evaluating the properties of the special environment of the water–membrane interface, where the proton-coupled energy transformation takes place.

THE STUDY OF PROTON DIFFUSION ON MEMBRANE SURFACES can be satisfied with different levels of elaboration. The initial step is acquisition of experimental transients that reflect the proton diffusion process. The study continues with analysis of the observation to obtain time constants and diffusion coefficients, and ends with transformation of diffusion measurements into a tool for investigation of the chemical and physical properties of the environment where the diffusion takes place.

0065-2393/94/0235-0027\$08.00/0
© 1994 American Chemical Society

We shall describe the various steps in the evolution of the methods and knowledge of proton diffusion on the membrane surface. The methods used for our studies all emanate from one basic technique—the laser-induced proton pulse (1). The common step of the various forms of this method is a pulse excitation of aromatic alcohols (ΦOH), such as naphthols, sulfonated naphthols, or pyranine (8-hydroxypyrene-1,3,6-trisulfonate), to their first excited electronic singlet state (ΦOH^*). In this state the compound is very acidic and the hydroxyl proton dissociates in subnanosecond dynamics.

The reaction of the proton with the environment is monitored by its interaction with pH indicators, dye release by the ground-state anion of the proton (ΦO^-), or even the geminate recombination of H^+ with the excited anion (ΦO^{*-}) (for reviews, *see* references 2 and 3).

The capability to measure transient signals directly coupled with protonation of a distinct chromophore is further exploited by insertion of the chromophore into defined microenvironments. Gutman et al. (4) used this method to trap the proton emitter, pyranine, in aqueous layers of multilamellar liposomes to measure the diffusion of protons in ultrathin layers in the microsecond time scale. The same system was investigated with a 1000-fold time resolution to monitor the reaction within 2 ns after dissociation of the proton (5). In a similar way, by attachment of dye to a protein, we measured the diffusion of protons within a proteinaceous cavity (6). Thus the versatility of the method is limited only by the ingenuity of the experimentalist as to how to place the proton emitter or detector at the site of interest.

Diffusion within Thin Water Layers

Pyranine has three sulfono groups and is a very water soluble dye. When dry phospholipids are swelled in dilute solutions of pyranine (2 mM or less), multilamellar vesicles are formed where the dye is entrapped, almost exclusively, in the outer aqueous layers. A suspension of such vesicles in water provides a model for the water layers that exist in the folding of mitochondria membranes or the packed lamellae of thylakoids.

When the dye in the thin water layer is laser pulsed, its proton is rapidly ejected and, after rapid relaxation to ground state, an ion pair H^+ and ΦO^- is formed. The strong absorption of the ΦO^- anion (at 450 nm) fades rapidly (within a few microseconds) due to its reaction with the proton, and the system relaxes to its initial prepulse state. Typical traces are shown in Figure 1. The two traces correspond to recombination in unstressed vesicles, where the width of the water layer is 25 Å, and under strong osmotic pressure (applied by sucrose), which squeezes the water layer to ~ 10 Å (7). Both signals exhibit a rise time, unresolved at that time frame, followed by well-resolved relaxation.

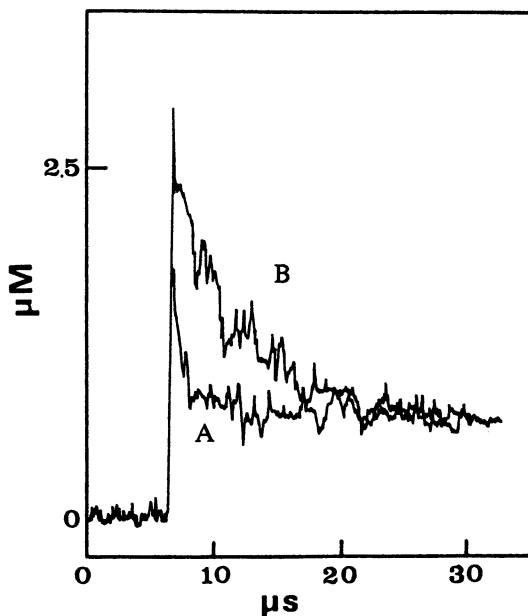


Figure 1. Transient absorption measurement of reprotonation of pyranine anion trapped within the hydration layers of phosphatidylcholine multilamellar vesicles. A, Vesicles suspended in 10-mM mesylate buffer, pH 5.7. B, Vesicles under osmotic pressure applied by 1.6-M sucrose (4.7×10^7 dyn/cm²) in 10-mM mesylate pH 5.7.

The analysis of the dynamics assumes the water layer to be infinitely thin, approximated by a two-dimensional space. The dynamics of a diffusion-controlled reaction in a two-dimensional space is given by Hardt's analytic expression (8), which predicts that the relaxation rate (γ) will vary almost linearly with the two-dimensional concentration $[\Phi O^-]_{(2)}$ of the reactants:

$$\gamma = \frac{D_{(2)} 2\pi N [\Phi O^-]_{(2)}}{\ln(1/R_{AB} \sqrt{\pi N [\Phi O^-]_{(2)}})} \quad (1)$$

where $D_{(2)}$ is the two-dimensional diffusion coefficient of H^+ (diffusion of ΦO^- is assumed to be negligible), N is Avogadro's number, and R_{AB} is the collision distance.

The results of many experiments, similar to those depicted in Figure 1, are drawn in Figure 2 in accordance with eq 1. As predicted, a straight line correlates the experimental value of the rate constant (γ) with the amplitude. The slope of these lines corresponds to the two-dimensional diffusion coefficient of H^+ . The different slopes imply that the diffusion coefficient of

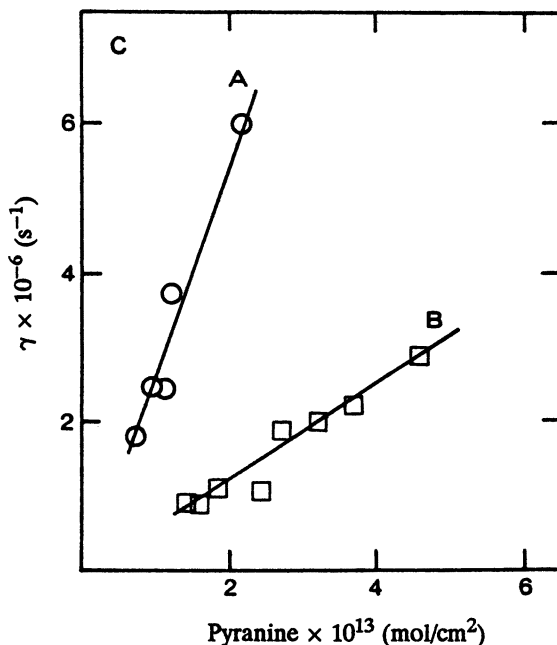


Figure 2. Dependence of the observed rate of reprotonation on the two-dimensional concentration of pyranine anion in the hydration layer. The rate constant (γ) was calculated from the experiments carried out as in Figure 1. The concentration of the anion was calculated from the amplitude of the transient and the dye-lipid ratio of the preparation. The magnitude of the amplitude was varied by modulation of the excitation pulse energy by glass filters. Measurements were carried out in the absence of sucrose, A, and in the presence of 0.57-M sucrose (1.5×10^7 dyn/cm²), B.

protons near a membrane is not constant; it varies with the width of the aqueous layer. The value measured for the unpressed structure is

$$D_{(2)} = 2.5 \pm 0.5 \times 10^{-5} \text{ cm}^2/\text{s}$$

This value is definitely smaller than the value given by Prats et al. (9), who estimated the proton diffusion coefficient on a lipid interface to be 20 times larger than in bulk water (*see* also reference 10).

The slower diffusion coefficient derived from the dynamics of the proton anion reactions, measured under osmotic pressure (curve B in Figure 2), implies a complex relationship between the external pressure and the ordering of water in the hydration layer. As the width shrinks, the capacity of protons to diffuse within the space by a random walk is diminished.

The interpretation of this observation is not simple and calls for evaluation of two more parameters: the interaction of protons with surface groups

and the effect of the geometry of the reaction space on the dynamics of the reaction.

Interaction of Protons with Surface Groups

The surface of a biomembrane is not inert. It is covered by a multitude of groups that have a wide range of pK values. Each phospho moiety, even zwitterionic ones, can bind a single proton with $pK = 2.25$. The carboxyl of phosphatidylserine has a higher proton affinity ($pK = 4.5$), whereas proteins and phosphatidic acids provide sites with pK values above 7. The multiplicity of proton binding sites dramatically affects the capacity of the proton to propagate along a surface. For instance, free protons bound to a phospholipid or protein are practically immobile. Thus the *apparent* diffusion coefficient (D_{app}) of protons near a surface will be much smaller than that of protons in bulk; it will be roughly proportional to the fraction of free protons at the interface. The precise expression derived by Junge and McLaughlin (12) also accounts for the presence of mobile buffer molecules (substrates, adenosine 5'-triphosphate (ATP), adenosine 5'-diphosphate (ADP), etc., present under physiological conditions). The detailed expression for the diffusion of extra H^+ (or OH^-) near a buffered surface is given by

$$D_{app} = D_{H^+} \left(\frac{2.3[H^+]}{\beta_{tot}} \right) + D_{OH^-} \left(\frac{2.3[OH^-]}{\beta_{tot}} \right) + \frac{\sum D_i \beta_i}{\beta_{tot}} \quad (2)$$

where D_{H^+} , D_{OH^-} , and D_i are the diffusion coefficients of H^+ , OH^- , and all other buffers (fixed and mobile) present in the system. β_{tot} is the total buffer capacity and β_i is the buffer capacity of the various individual buffer moieties. From this expression one can see that near neutrality, where $[H^+] \sim [OH^-] \sim 10^{-7}$ M, even 1 mM of mobile buffer will suffice to function as the main carrier of acidity.

Although the presence of buffering moieties on membrane surfaces reduces the apparent diffusion coefficient of a proton, it can enhance the probability that protons in the bulk phase will interact with groups on a membrane surface. This feature is demonstrated by the experiments presented in Figure 3. The measured parameter in these experiments was the protonation of a pH indicator adsorbed to the surface of a micelle made of uncharged detergent (Brij 58). The protons were released in the bulk from a hydrophilic proton emitter, 2-naphthol-3,6-disulfonate. The protons released in the bulk react by a diffusion-controlled reaction with the micelle-bound indicator and lead to a fast protonation phase. The perturbation then relaxes,

on a larger time scale, both by dissociation of the proton from the indicator and through collisional proton transfer between the indicator and the anionic state (ΦO^-) of the proton emitter. That scenario is depicted in curve A of Figure 3. Trace B in Figure 3 was measured under the same conditions except that the micelles were spiked with six molecules (averaged for the population) of the zwitterionic neutral phospholipid, phosphatidylcholine. The signal of the protonation of the indicator is larger, which demonstrates that the neutral phospholipid somehow enhanced the probability of proton-indicator interaction.

The mechanism of the enhancement is the rapid exchange of protons between adjacent surface groups. When two charged sites are packed together on a surface so that they are a few angstroms apart, their Coulomb cages can merge into a double minimum potential well (13, 14). In such an extended cage, the proton can rapidly shuttle between the sites. When the density of these sites is sufficiently high to form an effective network, the "search" becomes very efficient, which represents a reduction of dimension of the search space (15, 16). The effective rate of proton exchange between

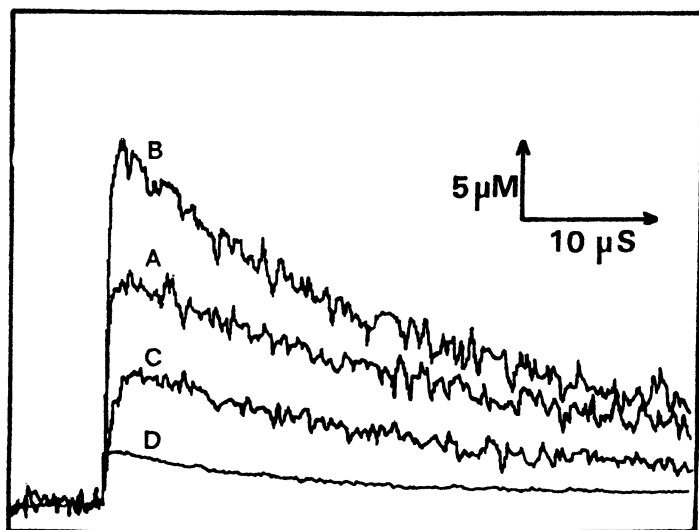


Figure 3. The effect of phospholipid head group on the protonation dynamics of an indicator adsorbed on a surface of neutral micelle. The indicator, bromocresol green, was adsorbed on Brij-58 micelles at a ratio of one per micelle. The pulse protonation, measured at pH 7.3, was initiated by photoexcitation of a water-soluble proton emitter 2-naphthol-3,6-disulfonate (2 mM). The reaction was followed spectrophotometrically. A, control; no phospholipids added. B, phosphatidylcholine added to amount of 6 molecules per micelle. C, phosphatidylserine added to 6 molecules per micelle. D, phosphatidic acid added to 6 molecules per micelle. For more details see Nachliel and Gutman (11).

nearby surface groups is a function of the proton binding site density on the surface. As a result, we observe a “concentration” dependence. The larger the density of sites, the more efficient is the mechanism. The apparent correlation factor, as measured for mixed micelles (17), pure lipid surfaces (11), or protein (18) is $\sim 10^{10} \text{ M}^{-1} \text{ s}^{-1}$; that is, as fast as a diffusion-controlled reaction. This process bestows a “proton antenna” property on any surface.

It must be stressed that the exchange of protons between adjacent groups has no surface-enhanced directionality. A proton dissociating from one moiety can reach either the bulk or the nearby surface moiety, which sets a limit to the effectiveness of the proton antenna. Even with transfer efficiency as high as 90%, after $n = 9$ passages the probability that the proton will remain on the surface dwindles to e^{-1} . Because the length of a Coulomb radius on the surface is $l \approx 10 \text{ \AA}$, the dimension of the effective search distance is $d = l\sqrt{n} = 30 \text{ \AA}$.

The efficiency of the proton antenna of a surface is a function of the $\text{p}K$ of the collecting groups. Very basic moieties ($\text{p}K \gg \text{pH}$) will be constantly protonated and, thus, noneffective in the exchange. More acidic moieties ($\text{p}K \sim \text{pH}$) will be in the proper ionization state to accept the proton and keep it for a few microseconds, which renders the proton less mobile. This is clearly seen in traces C and D of Figure 3. Neither phosphatidylserine ($\text{p}K = 4.5$) nor phosphatidic acid ($\text{p}K = 8.0$) function as components of proton antennas. The dwell time of protons on these groups is sufficiently long to inhibit propagation along on the surface.

Effect of Geometric Constraints on Proton Binding Dynamics

At present the highest resolution of diffusion-controlled proton binding reactions is attained by monitoring the time-resolved fluorescence signals of reversible proton dissociation from the excited state of proton emitters (18–21). These measurements monitor, at real time, the subnanosecond events of the dissociation of protons from ΦOH^* with sensitivity so high that the recombination event of $\Phi\text{O}^{*-} + \text{H}^+$ can be observed. The high accuracy experiments of Huppert et al. (19–21) were reconstructed by Agmon’s mathematical treatment. The procedure is a numerical solution of the Debye–Smoluchowski operator that describes the translational diffusion of the proton within the electrostatic field of the excited anion. For a proton in spherical symmetry, the program calculates the probability of stepping inward [from r_i to $r(i - 1)$] and outward [to $r(i + 1)$], and the influx of protons to $r(i)$ from the two adjacent shells. These probabilities are given by the gradient of the electrochemical potential of the proton, which is the combination of the electrostatic potential and the entropic gain of a proton moving to a larger volume as r increases.

The primary advantage, and beauty, of this treatment is that the control parameters of the program are purely stochastic. These stochastic elements are blended by the computation algorithm to produce averaged values such as density probabilities or radial possibilities with macroscopic interpretabilities.

The reaction space pertinent to our system is depicted in Figure 4. The proton is assumed to dissociate in the aqueous layer and diffuse in a three-dimensional space until its diffusion sphere contacts both membranes. At that point the diffusion loses its three-dimensional property and assumes a cylindrical configuration that, with respect to the volume increment between two shells, is identical to a two-dimensional diffusion. The shift from a three- to a two-dimensional space has a marked effect on the diffusion dynamics: In the three-dimensional space the density of a particle in a concentric shell varies as r^{-3} , whereas in the two-dimensional space the density varies as r^{-2} . Consequently the concentration gradient in three-dimensional space is larger and drives a better diffusion away from the center.

The second factor associated with the shift to the two-dimensional regime is the reactivity of the proton with the surface group. The effect of transferring the reacting pair from the ideal spherical symmetric environment of bulk water to the confined space between the phospholipid plates is shown in Figure 5. The lower curve depicts the fluorescence decay dynamics of pyranine in bulk water. After a fast relaxation of the ΦOH^* fluorescence, due to its dissociation, we observe a long shallow tail due to geminate recombination. Between membranes (made of dipalmitoylphosphatidylcholine (DPPC) or DPPC plus cholesterol) the tail is more pronounced, which indicates a higher probability of proton- ΦO^{*-} encounter.

Figure 6 depicts the observed dynamics using a logarithmic scale. This figure also includes the reconstructed fluorescence dynamics generated by Agmon's algorithm. The five curves drawn in the figure were calculated with the same microscopic parameters, with the exception that the width of the

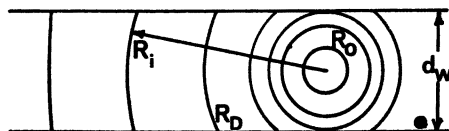


Figure 4. Schematic presentation of the reaction space for proton-excited pyranine anion recombination in the thin water layer between phospholipid membranes of multilamellar vesicles. The proton release is depicted at the center of the layer and diffuses in concentric shells. When the diffusion radius (R_i) exceeds the distance to the membrane ($d_w/2$), the shape of the diffusion space deviates from spherical symmetry and approaches cylindrical symmetry. R_0 is the reaction radius, R_d is the unscreened Debye radius of pyranine ($R_d = 28.3 \text{ \AA}$). d_w in this scheme is 30 \AA , and the size of the water molecules is drawn to scale.

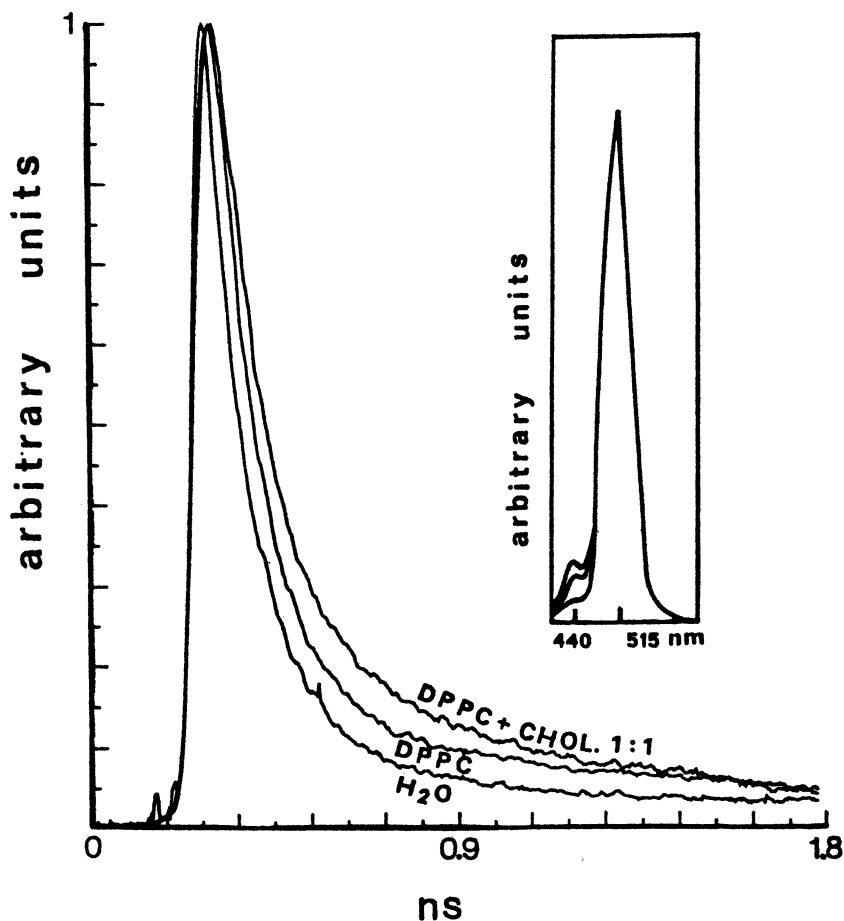


Figure 5. Time-resolved fluorescence of pyranine at the wavelength of maximum ΦOH^* emission. The dye was excited by a 10-ps laser pulse ($\lambda = 335 \text{ nm}$) and the fluorescence was recorded with a streak camera and multichannel analyzer as detailed by Pines et al. (19). The traces correspond to fluorescence decay dynamics measured for pyranine in water, entrapped in the aqueous layers of multilamellar vesicles made of DPPC or those made of DPPC plus cholesterol (1:1). Inset: Steady-state fluorescence spectra of the samples shown in the main frame. The spectra were normalized to have the same value at 515 nm where emission of ΦO^{*-} is maximal. This presentation emphasizes the incremental emission of the membranal preparation at 440 nm. The three curves correspond to dye dissolved in water (lowermost curve), entrapped in DPPC vesicles (middle curve), or in DPPC plus cholesterol vesicles (uppermost curve).

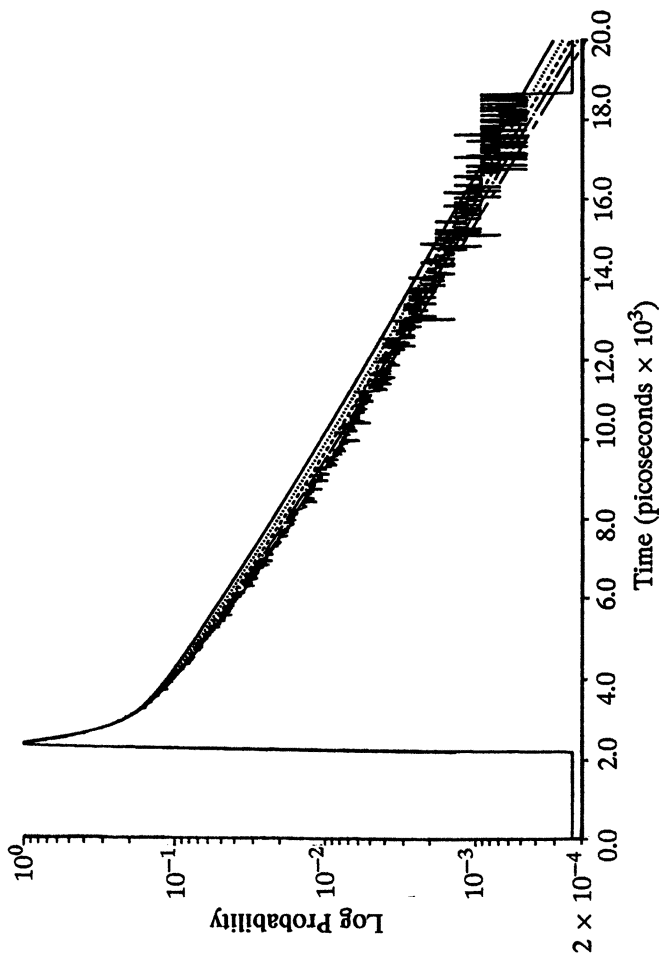


Figure 6. Time-resolved fluorescence of ΦOH^* state of pyranine as measured when trapped in the aqueous layers of multilamellar liposome made of DPPC plus cholesterol at 1:1 ratio. The fluorescence signal, recorded over 20 ns, is presented on a logarithmic amplitude scale. The overlaid curves are theoretically reconstructed dynamics, calculated according to Agmon's formalism (19-21) and modified to account for the geometry depicted in Figure 4. The lowermost curve was calculated for $d_w = 30 \text{ \AA}$. In the other curves, d_w decreases by equal decrements of 2.5 \AA to $d_w = 20 \text{ \AA}$ (upper curve). Even at the first decrement the predicted curve deviates from the margin determined by the experimental noise in the time range of $t \sim 8 \text{ ps}$, where the signal is still $\sim 5\%$ of the maximal amplitude.

aqueous layer (*see* Figure 4) was varied from 30 [corresponding to with the value determined by Rand and Parsegian (22)] to 20 Å.

The curve calculated for the actual width of the hydration layer is an accurate replication of the observed signal measured over the whole dynamic range of more than 3 orders of magnitude. The curves, with smaller gaps between the membranes where the two-dimensional diffusion was established earlier, differ systematically from the experimental curves. All the curves exhibit a slower fading of the ΦOH^* species, which indicates that the shift of the escape regime (from three to two dimensional) has a marked effect on the dynamics. Thus the time-resolved measurement supplemented by the numerical analysis provides an alternative method for measuring the width of the aqueous layer. This method, unlike X-ray scattering (7, 22) or electron density maps (23), gauges the effective width of the diffusion space and is free from assumptions associated with the interpretation of the X-ray scattering data (*see* references 22 and 23).

Another aspect of the intermembranal water phase that can be elucidated by the time-resolved proton transfer dynamics is the intensity of the electrostatic forces. The thin layer of a high dielectric fluid sandwiched between the low dielectric lipid plates, each covered by positive and negative charges, forms a very complex medium for calculation of electrostatic interaction (24, 25).

Figure 7 demonstrates how the time-resolved fluorescence measurement can provide an *empirical* method for determination of the intensity of electrostatic attraction within the thin water layer. The experimental curve, as in Figure 6, is recorded for the proton-pyranine anion trapped between membranes (30 Å apart) made of phosphatidylcholine plus cholesterol at 1:1 ratio. The computed curves were drawn for a range of dielectric constants of the varying interbilayer space ($\epsilon_{\text{eff}} = 78$) (lowermost curve) down to $\epsilon_{\text{eff}} = 39$ (uppermost curve). The value $\epsilon_{\text{eff}} = 78$ represents the situation that assumes no dielectric boundary and no image charge effect. The deviation of the predicted curve from the experimental curve is clear evidence for the role of image charges in the intermembranal space.

The uppermost curve was calculated for $\epsilon_{\text{eff}} = 39$, which would have been the dielectric constant for a charge adsorbed to the dielectric boundary between water ($\epsilon = 78$) and lipid ($\epsilon = 2$). The corresponding curve is far from reality. Near the best fit curve (corresponding to $\epsilon_{\text{eff}} = 52$), the shape of the line is extremely sensitive to the dielectric constant, and deviations as small as 10% can grossly distort the curve.

These calculations represent the phase where the diffusion of protons gradually loses its role as a subject of interest and is transformed into a method for evaluating the complex environment of the aqueous phase in contact with biomembranes.

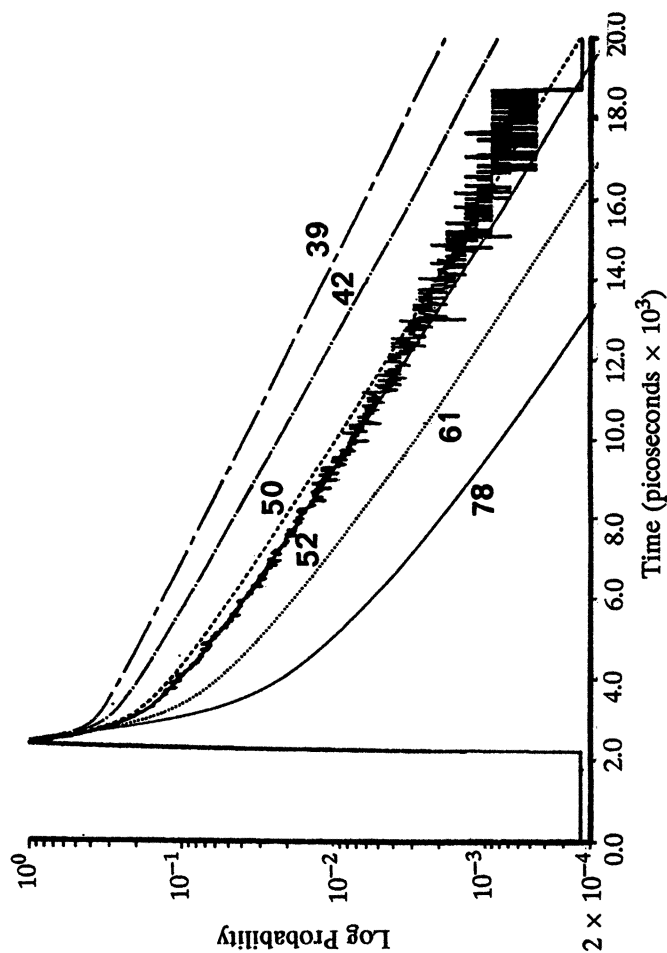


Figure 7. Effect of the intensity of the electrostatic potential on the geminate recombination that takes place in the aqueous layer between DPPC plus cholesterol membranes 30 Å apart. The experimental curve is accurately reconstructed with a $\epsilon_{eff} = 52$; the other curves correspond to ϵ_{eff} values labeled. Note near the best fit value how close the control of ϵ_{eff} on the shape of the curve is.

Summary and Conclusions

We have demonstrated how studies of proton transfer on membrane surfaces evolved from the phase of data acquisition to the level of biophysical evaluation of the diffusion space matrix, an evaluation that is based on recognition of the paramount role of dielectric discontinuities and the geometry of the reaction space.

These studies can evolve further. The biochemist and the physiologist are much more interested in the protein and lipid elements of the biomembrane than in the aqueous phase adjacent to it. These components can be investigated through measurements of the effective dielectric constants on their surface.

If the dielectric constant of the aqueous phase enclosed inside the heme binding site of apomyoglobin can be measured and the dielectric constant of the protein is deduced from that data (26), there is no reason why the same procedure cannot be applied to membrane proteins. If the geminate recombination of proton-excited pyranine anion can be monitored in the anion channel of the Pho-E protein (27), the interior of other channels can also be investigated.

No doubt these experiments are not simple and the theoretical work is formidable, but the goal is significant and the method is reliable, so that one day the results will be followed by "Discussion".

Acknowledgment

This research was supported by the U.S. Navy Office of Naval Research under Contract N00014-89-J-1622.

References

1. Gutman, M. *Methods Biochem. Anal.* **1984**, *30*, 1–103.
2. Gutman, M. *Methods Enzymol.* **1986**, *127*, 522–538.
3. Gutman, M.; Nachliel, E. *Biochim. Biophys. Acta* **1990**, *1055*, 391–414.
4. Gutman, M.; Nachliel, E.; Moshich, S. *Biochemistry* **1989**, *28*, 2936–2946.
5. Rochel, S.; Nachliel, E.; Huppert, D.; Gutman, M. *J. Membr. Biol.* **1990**, *118*, 225–232.
6. Yam, R.; Nachliel, E.; Kiryati, S.; Gutman, M.; Huppert, D. *Biophys. J.* **1991**, *59*, 4–11.
7. Parsegian, V.; Rand, R. P.; Fuller, N.; Rao, D. C. *Methods Enzymol.* **1986**, *127*, 400–416.
8. Hardt, S. *Biophys. Chem.* **1979**, *10*, 234–248.
9. Prats, M.; Tocanne, J. F.; Teissie, J. *Eur. J. Biochem.* **1987**, *162*, 379–385.
10. Kasianowicz, J.; Benz, R.; Gutman, M.; McLaughlin, S. *J. Membr. Biol.* **1987**, *99*, 228–274.
11. Nachliel, E.; Gutman, M. *J. Am. Chem. Soc.* **1988**, *110*, 2629–2635.
12. Junge, W.; McLaughlin, S. *Biochim. Biophys. Acta* **1987**, *890*, 1–5.

13. Matthew, J. B.; Richards, F. M. *Biochemistry* **1982**, *21*, 4989–4994.
14. Leberle, K.; Kempf, I.; Zundel, G. *Biophys. J.* **1989**, *55*, 637–648.
15. Adam, G.; Delbruck, M. In *Structural Chemistry and Molecular Biology*; Rich, A.; Davidson, N., Eds.; Freeman: San Francisco, CA, 1968; p 198.
16. Berg, H. C.; Purcell, E. M. *Biophys. J.* **1977**, *20*, 193–219.
17. Gutman, M.; Nachliel, E. *Biochemistry* **1985**, *24*, 2941–2946.
18. Yam, R.; Nachliel, E.; Gutman, M. *J. Am. Chem. Soc.* **1988**, *110*, 2636–2640.
19. Pines, E.; Huppert, D.; Agmon, N. *J. Chem. Phys.* **1988**, *88*, 5620–5630.
20. Agmon, N.; Pines, E.; Huppert, D. *J. Chem. Phys.* **1988**, *88*, 5631–5638.
21. Huppert, D.; Pines, E.; Agmon, N. *J. Opt. Soc. Am. B* **1990**, *7*, 1546–1550.
22. Rand, R. P.; Parsegian, V. A. *Biochim. Biophys. Acta* **1989**, *988*, 351–376.
23. McIntosh, T. J.; Magid, A. D.; Simon, S. A. *Biochemistry* **1989**, *28*, 17–25.
24. Kjellander, R.; Marcelja, S. *J. Chem. Phys.* **1988**, *88*, 7138–7146.
25. Berkowitz, M. Chapter 1 in this book.
26. Gutman, M.; Shimoni, E.; Tsfadia, Y. In *Electron and Proton Transfer in Chemistry and Biology*; Muller, A.; Ratojczak, H.; Junge, W.; Diemann, E., Eds.; Elsevier: Amsterdam, Netherlands, 1992; Vol. 78, pp 273–285.
27. Gutman, M.; Tsfadia, Y.; Masad, A.; and Nachliel, E. *Biochim. Biophys. Acta* **1992**, *1109*, 141–148.

RECEIVED for review March 8, 1991. ACCEPTED revised manuscript July 20, 1992.

Role of Water in Proton Conductance across Model and Biological Membranes

D. W. Deamer¹ and M. Akeson²

¹Department of Zoology, University of California, Davis, CA 95616

²Laboratory of Molecular Biology, National Institutes of Health, Bethesda, MD 20892

Proton conductance across model and biological membranes can be understood in terms of proton translocation along chains of hydrogen-bonded water molecules. This translocation mechanism accounts for the unexpectedly high permeability of lipid bilayers to proton flux, which seems to occur through rare transient defects in the bilayer barrier. The nature of the proton-conducting channel of the F_1F_0 adenosine 5'-triphosphate (ATP) synthase is unknown, but may use a similar translocation mechanism. We have tested the gramicidin channel as a model of such proton conductance. The channel consists of a single chain of hydrogen-bonded water molecules, and its proton conductance at saturation is near 140 pA, or 10^9 H^+ /s. Assuming that an adequate supply of protons is made available to the putative channel, this rate easily supports proton transport requirements of the F_1F_0 ATP synthase during ATP synthesis. However, at neutral pH ranges diffusion of free protons probably could not maintain an adequate supply at the channel mouth. Other sources of protons must therefore be postulated.

THE NATURE OF THE PERMEABILITY BARRIER AND THE BASIC MECHANISM of ion permeation are understood only in the most general sense even though the first measurements of ionic flux across lipid bilayer membranes were conducted 25 years ago. Establishing a permeation mechanism is difficult because the fluid lipid bilayer is described in terms of average motions of

0065-2393/94/0235-0041\$08.00/0
© 1994 American Chemical Society

many lipid hydrocarbon chains. This description makes it difficult to deduce the conformation or activity of a lipid molecule as it interacts with an ion, for instance, the permeation of a single potassium ion. The flux of potassium ions across a liposome membrane is readily measured, either as radioactively labeled species or with a potassium-sensitive electrode. The flux is slow—about 10^{-9} the rate of water permeation down equivalent gradients—but nonetheless occurs. What happens when a potassium ion approaches the bilayer? Is the bilayer indifferent, or does it become deformed by the immense electrostatic energy associated with the ion? How does the ion enter the bilayer phase? Does it dissolve in some sense, in a manner analogous to a permeating water molecule, or does it require a substantial transmembrane defect before it can find its way across?

We were forced to address such questions 10 years ago when we observed that pH gradients across liposome membranes decayed at rates much greater than expected from our knowledge of other cation permeation rates (1). For example, a potassium ion gradient has a decay half-time measured in hours, whereas an unbuffered hydrogen ion gradient in the same system decays in less than a second if counterion current is not limiting. The apparent discrepancy between proton and potassium permeation rates has intrinsic interest, but also has more general implications because the generation and maintenance of hydrogen ion gradients are central bioenergetic events in all cells.

What underlying mechanism might account for the vastly greater permeability of lipid bilayer membranes to protons? There is no obvious difference between solvated forms of potassium and hydrogen ions. Both would be “seen” by the membrane as a positive charge surrounded by several water molecules. However, there are important differences in the way a hydrogen ion might be translocated across a membrane. First, unlike any other cation, a hydrogen ion has an equivalent anion; that is, translocation of a hydroxide ion across a membrane in one direction is essentially indistinguishable from the translocation of a hydrogen ion in the other direction. Second, hydrogen ion equivalents have the capacity to move along chains of hydrogen bonds, as exemplified by protonic conductance in ice (2, 3). In liquid water as well, the ionic mobility of protons is about seven times that of other cations because of hydrogen ion diffusion through transient clusters of hydrogen-bonded water molecules.

The unique ability of hydrogen ions to move along hydrogen-bonded chains suggested a possible flux mechanism that would differentiate between the permeation of protons and other cations. Perhaps ions do not “dissolve” in the bilayer to cross the membrane. Instead, transient hydrated defects may be produced by thermal fluctuations in the lipid, and ions could then cross the membrane barrier by diffusion through the defects. If water molecules in the defects are associated by hydrogen bonding, protons could cross the

defect not by diffusion, as all other ions must, but instead by hydrogen-bond exchange along the associated water molecules.

The concept of transient hydrated defects in lipid bilayers with high selectivity for protons suggests a second possibility: If there were some way to produce a relatively long-lived chain of hydrogen-bonded water molecules across a membrane, the result would be a proton-conducting channel. Such a channel would have important implications for the function of certain biological membranes. For example, the F_0 subunit of coupling membranes directs protons in such a way that previously synthesized adenosine 5'-triphosphate (ATP) is released from binding sites on the F_1 subunit. We can ask how protons move through the F_0 subunit: Do they diffuse through a channel by a process resembling that of other ion channel conductance? An alternative is that proton transfer occurs along hydrogen-bonded chains of water within F_0 .

In the discussion to follow, we will address the following questions:

1. What is the mechanism of the proton conduction across lipid bilayers?
2. What are the proton-conducting properties of known hydrogen-bonded chains?
3. Can we relate these properties to models for proton conductance by the F_0 subunit?

Characteristics of Proton Flux across Bilayers

Proton flux across lipid bilayers can be measured by a variety of techniques. For example, a buffered pH gradient can be established across liposome membranes, and the rate of decay of the gradient can be monitored by any of several methods. Early measurements were carried out by monitoring pH shifts in the external medium with a glass electrode (1); later measurements used pH-sensitive dyes such as pyranine, carboxyfluorescein, and 9-aminoacridine (4–6). Cafiso and Hubbell (7) used spin labels very effectively, and Perkins and Cafiso (8) conducted an extensive series of measurements with this system.

In a typical experiment, proton flux might be driven by placing liposomes that contain pH 8 buffer in a solution buffered at pH 6, so that the initial proton flux is driven by 10^{-6} -M protons outside and 10^{-6} hydroxide ions inside. Buffers are required to make the decay rate of pH gradients sufficiently slow so that initial rates can be conveniently estimated. It is also necessary to release proton diffusion potentials by addition of valinomycin or a permeant anion; otherwise the proton flux will be limited by counterion flux (9).

It is not known whether protons or hydroxide ions conduct the primary ionic current under these conditions, and Nichols and Deamer (1) suggested

the term “net proton flux” to indicate this uncertainty. However, if significant conductance occurred by simple diffusion of hydroxide ions across the bilayer, the decay of a pH gradient would be expected to have kinetics controlled by the permeability of the hydroxide anion, which should resemble that of other monovalent anions like chloride. As we will see, this expectation is inconsistent with evidence in hand, so for the purposes of our discussion we will assume that all the current is carried as protons.

Under these conditions, a typical measured proton flux might be in the range of 10^{-15} mol/(cm² s). To compare this value with that of potassium, 1 M potassium ion (as potassium sulfate) could be trapped inside the same liposomes, and potassium efflux into 1 M choline sulfate could be measured with a potassium-sensitive electrode. A typical result might again be in the range of 10^{-15} mol/(cm² s). The proton permeability anomaly now becomes clear: The same flux is measured for both potassium ion and protons, yet the proton flux is driven by a concentration of protons 6 orders of magnitude less than the concentration of potassium ions. Estimates of the relative permeabilities of the bilayer to protons and potassium using these flux data yield values of 10^{-6} cm/s for protons and 10^{-12} cm/s for potassium ion.

A second characteristic of proton flux makes such calculations of proton permeability coefficients useful only for comparisons of permeability at defined pH values. Imagine in the preceding experiment that we measured potassium ion flux down 10-fold gradients: 1.0–0.1-, 0.1–0.01-, and 0.01–0.001-MK⁺. The flux would decrease by an order of magnitude with each 10-fold decrease in potassium concentration. Now imagine that we measured proton conductance across lipid bilayers down 10-fold proton gradients: pH 6–7, 7–8, and 8–9. When this experiment was carried out, the unexpected result was that the flux was relatively independent of pH (1). This observation was confirmed and extended by Gutknecht (10), who measured voltage-driven proton current across planar lipid membranes at pH values ranging from 2 to 11 and found again that current was essentially independent of pH; current varied approximately 10-fold over 9 orders of magnitude difference in proton concentration. Any mechanism proposed for the proton flux anomaly must take this observation into account, which has proven to be a surprisingly difficult task.

Models for Proton Conductance in Bilayers

Before discussing possible mechanisms of proton conductance, it is worth introducing the more general question of ion flux. The bilayer barrier to free diffusion of ions was first considered by Parsegian (11), who treated the hydrocarbon phase as solvent in which an ion might dissolve. The energy requirement can be calculated in terms of the Born energy necessary to move

a monovalent cation from water (dielectric constant = 80) into the hydrocarbon phase of a lipid bilayer (dielectric constant = 2). Parsegian showed that the energy was in the range of 40 kcal/mol for a typical ionic solute like sodium.

This substantial energy requirement helps us to understand why a lipid bilayer 5 nm thick represents such an effective barrier to ionic diffusion. The barrier can be overcome by providing a hydrated channel, so that a continuous high dielectric pathway exists across the bilayer. For example, Parsegian showed that a hydrated 0.5-nm-diameter "pore" reduced the Born energy barrier to 6.7 kcal. The gramicidin channel, a classic example of such a pore, contains a single chain of water molecules that permits ions to diffuse with greatly reduced energy requirements.

We can now ask whether the Born energy calculation can predict the experimental measurement of an actual ion flux. Hauser et al. (12) trapped radioactive sodium ion in sonicated liposome preparations [now referred to as small unilamellar vesicles (SUV)] and measured the sodium ion efflux over periods up to a month. The measured rates were then compared with theoretical rates predicted from Born energy considerations. The unexpected result was that the measured permeability constant was 3 orders of magnitude greater than the calculated value. To explain this discrepancy, Hauser et al. proposed that sodium ions leaked out, not by dissolving in the bilayer phase and diffusing across, but instead by leaking through some very substantial defect.

Our laboratory (13) and others (14) have confirmed and extended the earlier measurements of cation permeability across liposome membranes [large unilamellar vesicles (LUV)] and values in the range of 10^{-12} cm/s have been reported. These values are much greater than predicted from Born energy considerations, which is again consistent with the presence of transient defects in lipid bilayers. Such defects need not be common events to account for ion permeation rates. One can readily calculate from the measured flux of sodium, potassium, and protons (10^{-15} mol)/(cm² s) that one ion will, on average, pass through the area occupied by a single phospholipid (0.7 nm²) every two days. By contrast, several thousand water molecules pass through the same area every second!

Proton permeability can now be compared with the permeability of other cations in lipid bilayer systems, specifically liposomes (Table I) (15–21). First, it is important to note that the intrinsic proton permeability of a given lipid bilayer depends on its physical state (gel or fluid) and the size of the vesicles. This dependence means that the proton permeability of lipid bilayers can vary by as much as 3 orders of magnitude when small vesicles composed of relatively saturated lipid ($P = 10^{-7}$ cm/s) are compared to large vesicles composed of highly unsaturated lipid ($P = 10^{-4}$ cm/s). The permeability is not strongly dependent on the lipid head group.

Table I. Comparison of Permeabilities of Protons and Other Ions in Model and Biological Membranes

<i>Membrane</i> ^a	<i>P</i> (cm/s)	<i>Reference</i>
Protons		
<i>Large vesicles (LUV)</i>		
Egg PC:PA 9:1	1.4×10^{-4}	1
Mixed plant PL	1.4×10^{-4}	15
Egg PC	0.7×10^{-5}	8
Synthetic DAPC	1.8×10^{-5}	8
Synthetic DMPA ($T < T_m$)	10^{-5}	16
($T > T_m$)	10^{-3}	16
<i>Small vesicles (SUV)</i>		
Egg PC	5.9×10^{-7}	8
<i>Planar lipid membranes</i>		
Bacterial PE	10^{-5}	10
Diphytanoyl PC	4×10^{-6}	10
<i>Biological membranes</i>		
Sarcoplasmic reticulum	10^{-3}	17
Muscle sarcolemma	10^{-3}	18
Mitochondria	10^{-3}	1, 19
Brush border membranes	5×10^{-3}	20
Other Ions		
SUV, egg PC, Na ⁺	10^{-14}	12
LUV, egg PC, Na ⁺	10^{-12}	14
SUV, egg PC, Cl ⁻	10^{-11}	21

^a Abbreviations: PC, phosphatidylcholine; PA, phosphatidic acid; PL, phospholipid; DAPC, diarachidonylphosphatidylcholine; DMPA, dimyristoylphosphatidic acid; PE, phosphatidylethanolamine.

The permeability of liposomes to other cations also seems to depend on the size of the vesicle: In small vesicles, sodium permeability ranges around 10^{-14} cm/s, whereas in large vesicles, sodium permeability is about 100-fold greater. The permeability of lipid bilayers to monovalent anions like chloride is consistently higher; typical values are in the range of 10^{-10} cm/s. The question of greater anion permeability has been addressed by Flewelling and Hubbell (22), who concluded that permeability is in part a function of a dipole potential at the bilayer surface that favors permeation of anions.

Several estimates of proton permeability of biological membranes have been made. These estimates are generally greater than the permeability of lipid bilayers, as might be expected if the presence of integral proteins produces defects in the bilayer barrier that permit substantial proton leakage. However, even though the permeability to protons is high, the concentration of protons in a typical biological system is so low (0.1 μ M) that significant proton currents do not occur. For instance, Mitchell and Moyle (23) showed that the proton *conductance* (not permeability) of mitochondrial membranes was no greater than that of other cations. The conclusion is that a coupling

membrane provides a sufficient barrier to proton flux follows, even though it may be 6 orders of magnitude more permeable to protons than to other ions (1).

We can now summarize our conclusions regarding proton permeation of lipid bilayers:

1. Lipid bilayers have an anomalously high permeability to protons relative to other monovalent cations.
2. The high permeability, however, is balanced by the very low concentration that drives proton flux in typical membranes, so the conductance is low. This situation permits coupling membranes like those of mitochondria to maintain proton gradients even though proton permeability is high.
3. The proton permeability is affected by lipid composition and vesicle size over about 3 orders of magnitude.
4. Proton flux across bilayers has the unique property that it is independent of proton concentration.
5. Proton flux is linearly proportional to the magnitude of the concentration gradient driving the flux.
6. The conductance mechanism is understandable in terms of transient hydrated defects in the bilayer that allow protons to translocate along hydrogen-bonded water chains. Other cations are able to permeate through such defects, but by diffusion, rather than hydrogen-bond translocation. If the defects are short-lived, the high relative permeability of protons could, therefore, be accounted for by protons finding their way through a rare transient defect, whereas more slowly diffusing cations could not.

Proton Channels in Biological Membranes

Electrochemical proton gradients are central to many bioenergetic processes, particularly energy coupling. To produce such gradients, coupling membranes contain proton "pumps" that are activated by ATP, electron transport, or light as energy sources. Examples include bacteriorhodopsin; the proton ATPases of membranes such as lysosomes, gastric mucosa, and secretory vesicles; the proton pumps coupled to electron transport enzymes such as cytochrome oxidase; and the F_1F_0 ATP synthase of coupling membranes. Such proton pumps must have some means to translocate protons across lipid bilayers, and the bilayer must in turn provide a sufficient barrier to proton leakage, as previously discussed. In the second portion of this review we will focus on the F_0 subunit.

**American Chemical Society
Library**

1155 16th St., N.W.

In Biomembrane Electrochemistry, Blank, M., et al.;
Advances in Chemistry; American Chemical Society, Washington, DC, 1994.

The F_1F_0 ATP synthases produce ATP at the expense of electrochemical proton gradients generated by the electron transport systems in coupling membranes. The F_1F_0 structures are similar in bacteria, chloroplasts, and mitochondria (24), and it is likely that the proton flux mechanism is essentially the same in all three membranes. Some primary characteristics of proton flux in ATP synthases are a $1200 \text{ H}^+/\text{s}$ current requirement (25) and $\text{H}^+/\text{Na}^+ = 10^7$ selectivity (26) for the CF_0 channel. Conserved amino acids required for proton permeation are *a* subunits Arg₂₁₀, His₂₄₅, and Ser₂₀₆ (27) and *c* subunit Asp₆₁ (28).

There are three alternative mechanisms by which protons might cross the F_0 subunits during ATP synthesis. One possibility is that the protons pass individually through a channel by a mechanism similar to the diffusion of other cations through known transmembrane channels. However, true diffusion of individual protons through a classical ion channel seems unlikely. Even in a disordered environment like water, proton mobility occurs largely by hydrogen bond exchange; diffusion is only a minor component. This situation suggests that some form of translocation along hydrogen-bonded chains is plausible.

The earliest suggestion that protons may be conducted by a hopping mechanism along amino acid residues of membrane proteins was the "proton wire" concept of Nagle and Morowitz (29). Cox et al. (30) and Senior (24) proposed models in which a network of such residues is present along the aligned surfaces of α -helices in the F_0 subunit. Although this is an attractive hypothesis, no such wire-like arrangements of amino acids have yet been detected. Furthermore, obligatory proton conductance along wires of amino acid residues is inconsistent with evidence that Na^+ currents can also drive ATP synthesis (31, 32). Sodium ions would not be expected to move within a hydrogen-bonded chain of amino acid residues by the same hydrogen-bond exchange mechanism available to protons.

The third alternative is proton exchange along hydrogen-bonded water molecules (33–35). In bacteriorhodopsin, for example, a recent structural model at 3.5-Å resolution strongly suggests that water molecules form a narrow channel and are involved in proton delivery to the chromophore (36). The remainder of this review will discuss chains of hydrogen-bonded water molecules as potential proton translocators and describe some initial tests of the concept.

The first question concerns the physical nature of such a channel in the F_0 subunit. A useful model is provided by the work of Lear et al. (37, 38), who found that synthetic serine-leucine peptides form ion-conducting channels in planar lipid membranes. The channels apparently are produced when α -helical configurations of the peptides form clusters within the bilayer. For instance, when a 21 residue peptide $\text{H}_2\text{N}-(\text{LSSLSSL})_3-\text{CONH}_2$ was incorporated into a planar lipid bilayer membrane, channels appeared that had cation conducting properties that resembled those of the acetylcholine

receptor. Channel lifetimes in 0.5-M KCl ranged around 5 ms, with conductances of 70 pS (4.2×10^7 ions/s) at 100-mV potentials. Significantly, peptides with one of the serines replaced by a leucine formed highly selective proton channels with a conductance of 120 pS and lifetimes in the range of 1 ms. Computer modeling suggested that the proton channel is a trimeric or tetrameric aggregate of α -helices, whereas the cation conducting channel is hexameric or larger.

How might this knowledge be applied to proton flux through the F_0 subunit? The F_0 subunit of the *E. coli* ATP synthase is composed of approximately 10 α -helical *c* subunits associated with one *a* subunit and two *b* subunits (27). It seems reasonable to suggest as a working hypothesis that the *c* subunits encircle the *a* subunit. Their α -helices and those of the *a* subunit would then form complexes within the lipid bilayer with proton-conducting characteristics similar to those described in the model system of Lear et al. If the complexes are tetramers of associated α -helices, chains of hydrogen-bonded water molecules would be able to translocate protons across the assembled F_0 subunit.

Gramicidin as a Proton-Conducting Channel

How can we go about testing the concept that chains of hydrogen-bonded water could represent the proton-conducting channel of F_0 ? A relatively simple test concerns the rate of proton conductance relative to ATP synthesis. Using this approach, Junge and co-workers (25) measured proton flux rates through the CF_0 channel. After correcting for the large fraction ($\sim 97\%$) of channels that do not conduct proton current, the unit conductance was estimated to be 169 fS at an external pH of 7.5, and 100-mV driving potential. This conductance is approximately 2×10^5 protons per channel per second, which is more than sufficient to accommodate even the highest ATP synthesis rates (1200 H^+ /s) during photophosphorylation.

We can now ask a more specific question: Can a single chain of hydrogen-bonded water molecules conduct enough protons to supply measured rates of ATP synthesis? The gramicidin channel is able to provide some insight here. Gramicidin A produces ion-conducting channels in lipid bilayers when two gramicidin molecules form head-to-head hydrogen-bonded pairs that span the membrane (39, 40). The channel contains a single strand of 10–12 water molecules, and is highly selective for monovalent cations. Myers and Haydon (41) first measured cation conductance characteristics of the gramicidin channel and found that proton conductance was greater than expected. It was therefore proposed that protons were translocated by moving along hydrogen-bonded water, similar to the mechanism known to occur in ice. Levitt et al. (42) measured streaming potentials produced when water is pushed through the channel by translocating ions. Potassium and sodium ions

produced the expected streaming potentials, but proton flux did not. This observation supported the original conjecture of Myers and Haydon that protons moved by a hopping mechanism along hydrogen-bonded water molecules in the channel, rather than by diffusion.

The gramicidin channel thus offers a model system for investigating properties of proton conductance along hydrogen-bonded waters. We can now address the question of the maximum rate at which a single strand of hydrogen-bonded water molecules can transport protons. If we find that under no conditions are protons transported sufficiently fast to account for ATP synthesis by F_1F_0 , then we must consider alternative conductance mechanisms. We can also ask how the proton selectivity of the gramicidin channel compares with that measured in the F_0 subunit. If the selectivities are similar, we can draw some conclusions about the nature of the F_0 channel, but if the selectivities are vastly different, we will need to consider what properties of the F_0 channel might produce such a difference.

The experiments described in the following text were carried out on gramicidin channels in a glycerol monooleate-cholesterol membrane (43). Channel open times of about 1 s were typically observed, similar to those first described by Hladky and Haydon (26). We compared single channel proton currents under several conditions, including varying the potential driving the current and varying the concentration of protons (in the form of HCl from 0.01 to 7 M). Our results are summarized as follows:

- **Single channel currents:** 1.4 pA in 0.01 M HCl; 6.0 pA in 0.1 M HCl; 45 pA in 1 M HCl
- **Saturation current:** 140 pA in 4 M HCl or 10^9 protons per second per channel
- **Activation energy:** 20 ± 3 kJ/mol

When proton currents through gramicidin single channels were compared in HCl solutions of varying concentration, we found three distinct conductance regimes: a shoulder at 0.01 M HCl, a linear relationship between 0.1 and 2.0 M HCl, and saturation above 4 M. The saturation of the channel appears to be due to a rate-limiting property of the channel itself, rather than some property of the bulk phase in supplying protons to the channel. The saturating current in 4 M HCl is near 140 pA, equivalent to 10^9 protons per second per channel. This is 10^6 times faster than the proton transfer rate required to ATP synthesis and about 10^3 times faster than the maximum protonic current in CF_0 (25).

We conclude that a chain of hydrogen-bonded water molecules is able to translocate protons at a rate sufficient for measured ATP synthesis if the proton supply from the bulk phase is adequate. In the physiological pH range, the question of proton supply to a putative proton channel becomes

central. Our current-voltage data show that proton flux in the gramicidin channel is limited by supply from the bulk phase at pH ranges higher than 2 (43). Proton supply to the F_0 channel from the thylakoid lumen (pH 5) and from the cytosol bathing the mitochondrial membrane (pH 7.5) would, therefore, limit proton flux. Would this supply be adequate to account for measured ATP synthesis rates? The proton motive force in chloroplasts and mitochondria is about 200 mV. At pH 2 and 200-mV applied potential, proton current through a gramicidin channel is 1.1 pA or 6.9×10^6 H^+ per channel per second. The proton current in a population of gramicidin channels appears to decrease linearly with pH below 2 (44). Therefore, at pH 5 (the pH of the chloroplast thylakoid lumen; 45), proton flux through the gramicidin channel would be 6.9×10^3 H^+ per channel per second. If we assume that the gramicidin channel is a plausible model for proton conductance in F_0 , this value is sufficient for the maximum rate of ATP synthesis in CF_0CF_1 of intact chloroplasts.

An adequate proton supply to an F_0 subunit channel in the mitochondrial ATP synthase is less certain. Using the same logic as before, proton supply from the cytosol at pH 7.5 would be only 20 H^+ per channel per second. This discrepancy might be overcome by a much wider channel mouth, a slower rate of ATP synthesis per enzyme, or some additional mechanism by which protons are supplied to the mitochondrial ATP synthase. One possibility is that in mitochondria, where ATP synthesis (and therefore proton flux) is driven by a membrane potential, hydrolysis of water at the channel mouth could be a major source for protons. Kasianowicz et al. (46) found it necessary to invoke this possibility to account for the observed rates of protonophore-mediated proton conductance across lipid bilayers.

The last question to be considered here is whether hydrogen-bonded water molecules account for the extreme proton selectivity (10^7) observed in F_0 . First, it is important to note that the proton selectivity observed by Lill et al. (25) in CF_0 is not due to an anomalously high proton conductance, but rather to the apparent failure of Na^+ or K^+ to permeate the channel even at 300-mM electrolyte concentration. CF_0 effectively excludes all ions except protons. Exclusion of this sort could result from any of several underlying characteristics of the conductance mechanism. For instance, ions larger than the diameter of the channel might be rejected, or there may be specific binding to a site in the channel (an energy well) and failure of that site to bind other ions (47, 48).

Rejection of an ion by size seems unlikely for the F_0 subunit. That is, such a channel must be at least 2.5 Å in diameter to accommodate water molecules, but then would resemble gramicidin, which does not exclude Na^+ or K^+ ions with diameters significantly less than 2.5 Å. A proton selectivity ratio of 100 would be expected rather than 10^7 (CF_0).

Water chains that extend only part way across the membrane, such as those postulated to lead to the chromophore in bacteriorhodopsin (37) are

more likely to account for an extreme proton selectivity. To permeate a channel containing a single chain of water molecules, alkali cations must push water molecules through the channel (42). If displacement of water molecules were prevented by some physical property of the channel, K^+ or Na^+ flux would be inhibited. A second possibility is that amino acids within the channel could specifically interact with protons. For example, the amino groups of arginine and histidine readily form bonds with protons but have very low affinities for alkali cations (49). Alternatively, the $-NH_2$ groups and carboxylates in F_0 could coordinate with hydrated protons and select against alkali cations as do certain crown ethers (33).

We can now summarize our results with the gramicidin channel and relate them to the F_0 subunit:

1. The proton conductance of the gramicidin channel has at least three rate-limiting conditions that depend on proton concentration. In the neutral pH range, the rate-limiting step appears to be proton production by hydrolysis of water at the channel mouth. At moderate proton concentrations (pH 2–5) conductance is limited by proton diffusion to the channel. At high proton concentrations (pH 0–2) conductance is limited by translocation along hydrogen-bonded water chains in the channel.
2. The gramicidin channel conductance saturates at 140 pA (530 pS) of protonic current in 4-M HCl.
3. The gramicidin channel was tested as a model for proton conductance in the F_0 subunit under the assumptions that the channel resembled those channels produced by synthetic α -helical peptides in lipid bilayers and that proton translocation occurred along chains of hydrogen-bonded water molecules. The measured proton conductance at saturation is more than sufficient to transport protons through the F_0 subunit in quantities that would support known ATP synthesis rates. At physiological pH ranges the rate-limiting step appears to be proton diffusion to the channel, rather than the channel itself. Finally, the F_0 channel must be much more restrictive than gramicidin to alkali cation permeation due to either a partial water strand or to selectivity at an internal binding site.

References

1. Nichols, J. W.; Deamer, D. W. *Proc. Natl. Acad. Sci. U.S.A.* **1980**, *77* 2038–2042.
2. Eigen, M.; DeMaeyer, L. *Proc. R. Soc. London Ser. A* **1958**, *247*, 505–533.

3. Nagle, J. F.; Tristram-Nagle, S. *J. Memb. Biol.* **1983**, *74*, 1–14.
4. Nichols, J. W.; Hill, M. W.; Bangham, A. D.; Deamer, D. W. *Biochim. Biophys. Acta* **1980**, *596*, 393–399.
5. Deamer, D. W.; Gutknecht, J. *Methods Enzymol.* **1986**, *127*, 471–480.
6. Clement, N. R.; Gould, J. M. *Biochemistry* **1981**, *20*, 1534–1539.
7. Cafiso, D. S.; Hubbell, W. L. *Biophys. J.* **1983**, *44*, 49–57.
8. Perkins, W. R.; Cafiso, D. S. *Biochemistry* **1986**, *25*, 2270–2276.
9. Deamer, D. W.; Nichols, J. W. *Proc. Natl. Acad. Sci. U.S.A.* **1983**, *80*, 165–168.
10. Gutknecht, J. *J. Memb. Biol.* **1984**, *82*, 105–112.
11. Parsegian, A. *Nature (London)* **1969**, *221*, 844–846.
12. Hauser, H.; Oldani, D.; Phillips, M. C. *Biochemistry* **1973**, *12*, 4507–4517.
13. Barchfeld, G.; Deamer, D. W. *Biochim. Biophys. Acta* **1988**, *944*, 40–48.
14. Mimms, L. T.; Zampighi, G.; Nozaki, Y.; Tanford, C.; Reynolds, J. A. *Biochemistry* **1981**, *20*, 833–850.
15. Rossignol, M.; Grignon, N. Grignon, C. *Biochim. Biophys. Acta* **1982**, *684*, 195–199.
16. Elamrani, K.; Blume, A. *Biochim. Biophys. Acta* **1983**, *727*, 22–30.
17. Meissner, G.; Young, R. C. *J. Biol. Chem.* **1980**, *244*, 6814–6820.
18. Izutsu, K. T. *J. Physiol. (London)* **1972**, *221*, 15–27.
19. Krishnamoorthy, G.; Hinkle, P. *Biochemistry* **1984**, *23*, 1640–1645.
20. Ives, H. E.; Verkman, A. S. *Am. J. Physiol.* **1985**, *248*, F78–F86.
21. Papahadjopoulos, D.; Nir, S.; Ohki, S. *Biochim Biophys. Acta* **1972**, *266*, 561–583.
22. Flewelling, R. F.; Hubbell, W. L. *Biophys. J.* **1986**, *49*, 531–540.
23. Mitchell, P.; Moyle, J. *Biochem. J.* **1967**, *104*, 588–592.
24. Senior, A. E. *Physiol. Rev.* **1988**, *177*–231.
25. Lill, H.; Engelbrecht, S.; Schonknecht, G.; Junge, W. *Eur. J. Biochem.* **1986**, *160*, 627–634.
26. Hladky, S. B.; Haydon, D. A. *Biochim. Biophys. Acta* **1972**, *274*, 294–312.
27. Fillingame, R. H.; Miller, M. J.; Fraga, D.; Girvin, M. E. *Biophys. J.* **1990**, *57*, 201a.
28. Cain, B. D.; Simoni, R. D. *J. Biol. Chem.* **1988**, *263*, 6606–6612.
29. Nagle, J. F.; Morowitz, H. J. *Proc. Natl. Acad. Sci. U.S.A.* **1978**, *75*, 298–302.
30. Cox, G. B.; Fimmel, A. L.; Gibson, F.; Hatch, L. *Biochim. Biophys. Acta* **1986**, *849*, 62–69.
31. Laubinger, W.; Deckers-Hebestreit, G.; Altendorf, K.; Dimroth, P. *Biochemistry* **1990**, *29*, 5458–5463.
32. Boyer, P. D. *Trends Biochem. Sci.* **1988**, *13*, 5–7.
33. Hoppe, J.; Sebald, W. *Biochim. Biophys. Acta* **1984**, *768*, 1–27.
34. Schulten, Z.; Schulten, K. *Eur. Biophys. J.* **1985**, *11*, 149–155.
35. Deamer, D. W.; Nichols, J. W. *J. Membr. Biol.* **1989**, *107*, 91–104.
36. Henderson, R.; Baldwin, J. M.; Ceska, T. A.; Zemlin, F.; Beckmann, E.; Downing, K. H. *J. Mol. Biol.* **1990**, *213*, 899–929.
37. Lear, J. D.; Wasserman, Z. R.; DeGrado, W. F. *Science (Washington, D.C.)* **1988**, *240*, 1177–1181.
38. DeGrado, W. F.; Lear, J. D. *Biopolymers* **1990**, *29*, 2065–2213.
39. Cornell, B. J. *Bioenerg. Biomembr.* **1987**, *19*, 655–676.
40. Urry, D. W.; Goodall, M. C.; Glickson, J. D.; Mayers, D. F. *Proc. Natl. Acad. Sci. U.S.A.* **1971**, *68*, 1907–1911.
41. Myers, V. B.; Haydon, D. A. *Biochim. Biophys. Acta* **1972**, *274*, 313–322.

42. Levitt, D. G.; Elias S. R.; Hautman, J. M. *Biochim. Biophys. Acta* **1978**, *512*, 436–451.
43. Akeson, M.; Deamer, D. W. *Biophys. J.* **1991**, *60*, 101–109.
44. Eisenman, G.; Enos, B.; Sandblom, J.; Haggland, J. *Ann. N.Y. Acad. Sci.* **1980**, *339*, 8–20.
45. Althoff, G.; Lill, H.; Junge, W. *J. Membr. Biol.* **1989**, *108*, 263–271.
46. Kasianowicz, J.; Benz, R.; McLaughlin, S. *J. Membr. Biol.* **1987**, *95*, 73–89.
47. Tsien, R. W.; Hess, P.; McCleskey, E. W.; Rosenberg, R. L. *Annu. Rev. Biophys. Biophys. Chem.* **1987**, *16*, 265–290.
48. Eisenman, G.; Dali, J. A. *Annu. Rev. Biophys. Biophys. Chem.* **1987**, *16*, 205–226.
49. Williams, R. J. P. *Annu. Rev. Biophys. Biophys. Chem.* **1988**, *17*, 71–97.

RECEIVED for review January 29, 1991. ACCEPTED revised manuscript June 24, 1992.

Interfacial Ion Transport between Immiscible Liquids

Petr Vanýsek

Department of Chemistry, Northern Illinois University, DeKalb, IL 60115

The interface between two immiscible liquids is used as a characteristic boundary for study of charge equilibrium, adsorption, and transport. Interfacial potential differences across the liquid-liquid boundary are explained theoretically and documented in experimental studies with fluorescent, potential-sensitive dyes. The results show that the presence of an inert salt or a physiological electrolyte is essential for the function of the dyes. Impedance measurements are used for studies of bovine serum albumin (BSA) adsorption on the interface. Methods for determination of liquid-liquid capacitance influenced by the presence of BSA are shown. The potential of zero charge of the interface was obtained for 0–200 ppm of BSA. The impedance behavior is also discussed as a function of pH. A recent new approach, using a microinterface for interfacial ion transport, is outlined.

Liquid-Liquid Interfaces and Electrochemistry

Interfaces between two immiscible solutions with dissolved electrolytes, which are most interesting to workers in several disciplines, cover theoretical physical electrochemistry and analytical applications for sensor design. These interfaces are used in interpretation of processes that occur in biological membranes and in biological systems. The interface between two immiscible electrolyte solutions was studied for the first time at least 100 years ago by Nernst (1), who performed the experiments that provide the theoretical basis for current potentiometric and voltammetric studies of interfaces. In 1963, Blank and Feig (2) suggested that an interface between two immiscible liquids could be used as a model (at least as a crude approximation) for

0065-2393/94/0235-0055\$09.26/0
© 1994 American Chemical Society

one-half of a biological membrane. Later Koryta et al. (3) suggested that such an interface should behave similarly as an interface between an electronic conductor (i.e., an electrode) and a bathing solution. Koryta was also the first to abbreviate the interface between two immiscible electrolyte solutions as ITIES. Experimental measurements revealed that this predicted similarity is real, and the field of experimental electrochemistry on ITIES gained recognition and practitioners.

The similarities between ITIES and conventional electrode electrochemistry provide an arsenal of electrochemical techniques that have been previously tested in the more common electroanalytical chemistry and physical electrochemistry. To understand the similarities between ITIES and electrode electrochemistry, it is more useful to look at the differences first. Faradaic current flow through an electrochemical cell is associated with redox processes that occur at the electrode surface. The functional analog of an electrode surface in ITIES is the interface itself. However, the net current observed when the interface is polarized from an outside electric source is not a result of a redox process at the interface; rather, it is an effect that is caused by an ion transport through the interface, from one phase to another.

Figure 1 illustrates the difference in the cause of current flow experienced on an electrode and on the ITIES. Sufficiently negative potential applied to the metal electrode (Figure 1A) will cause reduction of the analyte in the bathing solution. An electron will leave the electrode and reduce the dissolved species Fe^{3+} to Fe^{2+} . Overall charge balance is achieved and overall flow of negative charge from the electrode to the solution is observed. To complete the circuit, an oxidation of some species, often even the solvent, has to occur on the counter electrode. Figure 1B considers the case of ITIES with a picrate anion present in both phases. Electric potential applied between the two electrodes will result in a potential difference on the liquid interface. If the potential on the aqueous side is positive enough, the picrate anion will be carried from the nonaqueous (nitrobenzene) phase to water and its transport will appear in the outside electric circuit as a flow of negative charge from the bottom of the cell to the top. Overall charge balance is maintained by reduction of any available material of the nonaqueous phase and oxidation of some available species in the aqueous phase on surfaces of the current-carrying platinum electrodes.

Liquid-Liquid Interfaces in Interfacial Ion Transport

From the principle governing current-potential response of liquid-liquid electrochemistry, it follows that the interface between the two immiscible electrolytes can be treated in a manner similar to solid electrodes. It must be stressed again that it is ion transport across the interface, and not an electrode redox process, that determines the potential and current character-

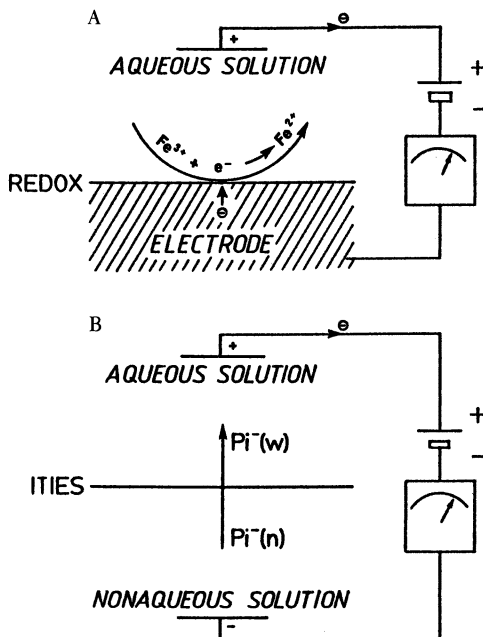


Figure 1. Comparison of the interface between an electronically conductive electrode and a solution (reduction of Fe^{3+}) (A) and the interface between two immiscible solutions of electrolytes (ITIES) during current flow in a closed electric circuit [transport of picrate (Pi^-) from nonaqueous phase (n) to water (w)] (B). (Reproduced from reference 4. Copyright 1990 American Chemical Society.)

istics of the system. With this fact in mind, it is possible to employ, in some modified fashion, all the techniques used with electronic electrodes in the studies of immiscible electrolyte interfaces.

Figure 2 is a diagram of a typical cell used in the studies of immiscible electrolytes. The investigated interface is formed in the narrow part of the cell. To allow positioning of the interface within the desired location, a screw-driven plunger that varies the volume of the bottom part can be used. In voltammetric studies, care must be taken to eliminate voltage drop within the solutions. Because the resistance of the solvents should be eliminated, a four-electrode potentiostat with a pair of reference and counter electrodes should be used. The measured or controlled potential difference resides between the tips of the two reference electrodes; thus, the potential across the liquid-liquid (LL) interface is monitored.

A number of techniques have been applied to the interface in recent years. For the detailed list and explanations, several reviews are suggested (4-11). Typical evidence of interfacial ion transport is illustrated by Figure 3, where the transport of acetylcholine cation is observed between water and

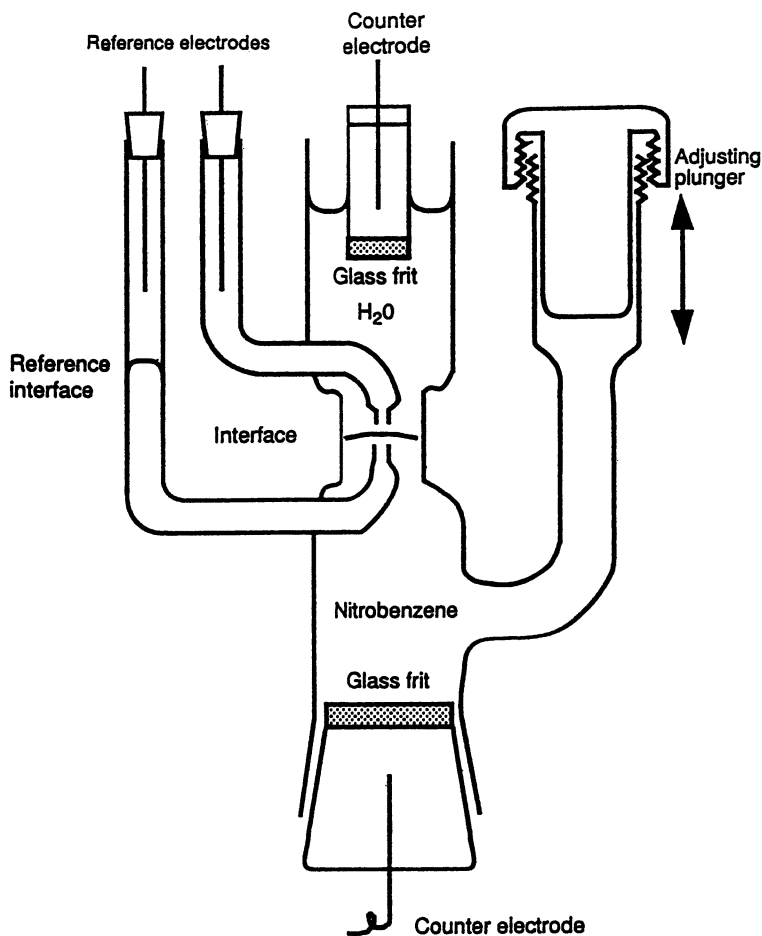


Figure 2. Apparatus used for potentiometric and voltammetric studies on the interface between two immiscible electrolyte solutions. (Reproduced from reference 4. Copyright 1990 American Chemical Society.)

nitrobenzene (curve 2). The potentials of the peaks are separated by 60 mV, which signifies a reversible process in the sense that the transported ion can move, with only thermodynamic restrictions, from one phase to another. A process that could be called irreversible is observed in the cases when the ion, upon transport to the other phase, undergoes some change that prevents its rapid return upon differential change of potential. Often this irreversibility occurs when the ion forms an insoluble precipitate in the opposite phase or when adsorption of the ion or its reaction product takes place on the interface. Curve 1 in Figure 3 corresponds to a voltammetric curve of the supporting electrolytes only. A voltammogram depicts a dynamic dependence

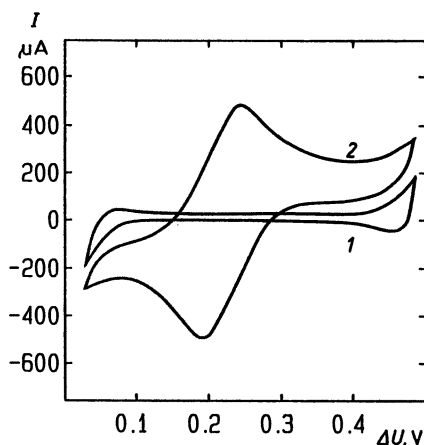


Figure 3. Ion transport voltammogram of acetylcholine cation. Curve 1 is the voltammogram of supporting electrolytes only: 1 mol/L LiCl in water and 0.025 mol/L tetrabutylammonium tetraphenylborate in nitrobenzene. Curve 2 is the voltammogram after the addition of 0.011 mol/L acetylcholine chloride to water. Scan rate 12.5 mV s. (Reproduced with permission from reference 9. Copyright 1984 The Electrochemical Society.)

of current I on applied potential ΔU . In comparison with metal electrodes, the LL interfaces allow much narrower potential window in which analytes can be studied. This narrow window is one disadvantage noted in electroanalytical applications of the technique.

Subsequently, the water–nitrobenzene interface will be described and experimentally studied. The reason for using nitrobenzene, which is not a physiologically occurring environment, is its high relative permittivity ($\epsilon = 34.8$ at 25 °C), which makes it very convenient for performing many studies. When the experimental techniques are perfected, in particular, when high resistance of less polar solvents can be overcome, the conclusions and experience can be explained to naturally occurring lipophilic environments with lower relative permittivity.

Potentiometry on the Water–Nitrobenzene Interface in the Presence of Oxacyanine Dyes

The membrane or interfacial potential, particularly in biological applications, is often determined from the change in fluorescence of added carbocyanine dyes (12, 13). The fluorescence intensity of the dyes depends on the solvent in which the dyes are present. When the dyes are used as potential-sensitive probes, their fluorescent intensity is a function of the interfacial potential across the membrane. We studied the behavior of dye transport on a phase boundary between water and nitrobenzene to better understand the principles of the potential dye partitioning as a function of interfacial potential (14).

Carbocyanine dyes are salts that have fluorescent cations. To use this fluorescent property to indicate biological membrane potential, the dye cation

is added as a potentiometric indicator to a suspension of cells. If the inside of the cell has a negative potential with respect to the solution surrounding the cell, some of the dye cations will be transported across the cell membrane. The fluorescent intensity of the dye that moves from the extracellular liquid into the cell through the cell membrane decreases due to fluorescence quenching in a different dielectric medium or due to adsorption of the dye onto the membrane or other cell structure. This decrease in fluorescent intensity is proportional to the membrane potential and provides a relatively noninvasive and simple method of determining the cell membrane potential. A suitable technique that can be used to calibrate these probes independently in vitro and to understand their behavior can be found in liquid-liquid electrochemistry research.

Interfacial Potential. The relationship that describes ionic equilibrium on the ITIES and accounts for all the present ions was first described by Hung (15). The derivation is based on the equality of the electrochemical potentials in either phase for all ions involved and the requirement of electroneutrality in each solvent. The equation is given as a summation over all present ions, i :

$$\sum_{i=1}^j z_i m_i \left/ \left\{ V_\alpha + V_\beta \frac{\gamma_i^\alpha}{\gamma_i^\beta} \exp \left[\frac{z_i F}{RT} (\Delta_\beta^\alpha \phi - \Delta_\beta^\alpha \phi_i^0) \right] \right\} \right. = 0 \quad (1)$$

where z_i is the charge of the ion, m_i is the total number of moles of the ion i in both phases, V_α and V_β are the volumes of phases α (aqueous) and β (nitrobenzene), γ_i^α and γ_i^β are the activity coefficients of the ion, $\Delta_\beta^\alpha \phi$ is the potential difference on the interface defined as $\Delta \phi = \phi^\alpha - \phi^\beta$, and $\Delta_\beta^\alpha \phi_i^0$ is the standard potential of transfer of the individual ion from phase α to phase β . T is absolute temperature expressed in kelvins, R is the molar gas constant (8.31441 J/(mol K)), and F is the Faraday constant (96,484.6 C/mol).

The standard potential of transfer for an individual ion, $\Delta_\beta^\alpha \phi_i^0$, is not amenable to thermodynamic measurement. Its value can be determined by measuring the distribution ratio of its salt, for which the Gibbs free energy of transfer of the counterion is already known. From the experimentally accessible partition coefficient of the salt, the standard Gibbs free energy of transfer of the salt, $\Delta G_{\text{tr, salt}}^{0, \alpha \rightarrow \beta}$, from phase α to phase β is calculated as

$$\Delta G_{\text{tr, salt}}^{0, \alpha \rightarrow \beta} = RT \ln \frac{a_{\text{salt}}(\alpha)}{a_{\text{salt}}(\beta)} \quad (2)$$

using the activities a of the salt in phases α and β . The standard Gibbs free energy of transport of a salt is the sum of the $\Delta G_{tr,i}^{0,\alpha \rightarrow \beta}$ of both ions, so

$$\Delta G_{tr,i}^{0,\alpha \rightarrow \beta} = \Delta G_{tr,salt}^{0,\alpha \rightarrow \beta} - \Delta G_{tr,counterion}^{0,\alpha \rightarrow \beta} \quad (3)$$

Equation 3 allows the values for individual ions to be calculated from the knowledge of the Gibbs energies of transfer for other individual ions. This chain calculation requires an a priori knowledge of the value for one ion, which is, in a rigorous thermodynamic sense, impossible. It is usually assumed that tetraphenylarsonium (TPAs⁺) and tetraphenylborate (TPB⁻) partition in the same ratio in any pair of solvents (16). Then it holds that

$$\Delta G_{tr,TPAs^+} = \Delta G_{tr,TPB^-} = (1/2) \Delta G_{tr,TPAsTPB} \quad (4)$$

The quantity $\Delta G_{tr,TPAsTPB}$ is experimentally accessible from a partition ratio for the salt itself and was used to calculate individual Gibbs energies of transfer for many ions (17). Table I lists the values used in this work. A corresponding standard potential of transfer for an individual ion is calculated from the standard Gibbs free energy for the transfer of individual ion from phase α to the phase β as

$$\Delta_{\beta}^{\alpha} \varphi_i^0 = \Delta G_{tr,i}^{0,\alpha \rightarrow \beta} / z_i F \quad (5)$$

Table I. Standard Potentials of Transfer between Water and Nitrobenzene for Ions Used in the Potentiometry Measurements

<i>Ion</i>	$\Delta_{\beta}^{\alpha} \varphi_i^0$ (mV)	<i>Reference</i>
Li ⁺	+395	51
Na ⁺	+354	51
H ⁺	+337	51
TMA ⁺	+35	51
TEA ⁺	-59	51
TBA ⁺	-248	51
DiOC ₁ (3) ⁺	-310	21
TPAs ⁺	-372	51
DiOC ₂ (5) ⁺	-400	21
CV ⁺	-410	52
Cl ⁻	-324	51
I ⁻	-195	51
TPB ⁻	+372	51

Equation 1 provides a comprehensive description of the equilibrium on liquid-liquid interfaces, but it cannot be solved explicitly for $\Delta_{\beta}^{\alpha}\phi$ without some assumption when more than two ions are involved. For more than two ions the implicit form can be solved numerically. We used a TK-Plus Solver (Universal Technical Systems, Rockford, IL) software for a personal computer.

Reference Interface. Any system that measures the potential of the liquid-liquid interface has to have a pair of reference electrodes connected to it. The aqueous phase is usually connected to a simple electrode of the second kind; the state of the nonaqueous phase is usually explored by the so-called reference interface, which is, in essence, an ion-selective electrode. The reference interface is a liquid-liquid boundary that shares a common ion (usually a cation, denoted here B_1) of a constant and usually known concentration. The interfacial potential can be calculated as

$$\Delta_{\beta}^{\alpha}\phi = \Delta_{\beta}^{\alpha}\phi_{B_1^+}^0 + \frac{RT}{F} \ln \left(\frac{c^{\alpha}}{c^{\beta}} \right) \quad (6)$$

under the assumption that

$$\left(\frac{c^{\alpha}}{c^{\beta}} \right)^2 \exp \left(\frac{2F}{RT} \Delta_{\beta}^{\alpha}\phi_{B_1^+}^0 \right) \gg 4 \left(1 + \frac{c^{\alpha}}{c^{\beta}} \right) \exp \left\{ \frac{F}{RT} (\Delta_{\beta}^{\alpha}\phi_{B_1^+}^0 + \Delta_{\beta}^{\alpha}\phi_{A^-}^0) \right\} \quad (7)$$

The counterions of the supporting electrolytes are A_1^- in phase α and A_2^- in phase β . Condition 7 has to be fulfilled for either counterion; thus it is designated A^- . After the two phases are brought into contact, some repartitioning of the salts occurs. The concentrations c^{α} and c^{β} denote the salt concentrations after the repartitioning; the values of c^{α} and c^{β} are not easily obtained. However, for the purpose of the inequality test eq 7, the initial concentration values before repartitioning can be used. Statement 6 is often used in the literature, but the prerequisite and the meaning of the assumption 7, first made by Hung (15), is never fully quantified. The repartitioning does not interfere with the test condition. However, it does cause significant deviation in calculated interfacial potentials in situations when inequality 7 is not fulfilled. Our calculations reveal that for a reference system consisting of tetrabutylammonium chloride (TBACl) in water and tetrabutylammonium tetraphenylborate (TBATPB) in nitrobenzene at 0.01-mol/L initial (formal) concentrations, the left-hand side of eq 7 is actually only 2.4 times greater than the right-hand side. As a result, the interfacial potential for equal concentrations in both phases, calculated from eq 6, is -248 mV, whereas the actual value obtained from eq 1 is -245.7 mV. Considering the experimental uncertainty, this difference is acceptable. It must be emphasized that

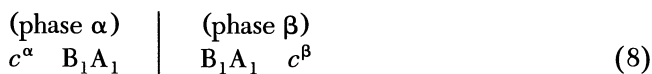
any new reference system should be tested for the validity of condition 7. For example, when tetraphenylarsonium (TPAs^+) is the common ion in a water–nitrobenzene reference interface, the approximately calculated value is -372 mV, a significant difference from the exact value -335.5 mV (18).

Interfacial Potential of the Reference Interface. The value of the potential of the reference interface is determined by the relative concentrations of the common ion, B_1^+ , in the two phases. Thus, this interface responds to changes at the working interface through the change in the concentration of B_1^+ in the organic phase. The practical merit of the reference interface is not only that its potential can be calculated, but also its indifference to outside perturbations. For example, an attempt to change the -245.7 -mV equilibrium potential of a 0.01 -mol/L $\text{TBA}^+-\text{TBA}^+$ reference interface by 10 mV would require repartition of 20.5% of all ions present in the system, a rather significant impediment to the potential change (19, 20).

Other Ions in the System. Consider what happens to the potential of the reference interface if another ion is added to the nonaqueous phase. This experimental condition will arise from ion redistribution on the working interface. Iterative calculations account for the effect of the dye in the nonaqueous phase on the reference interface. The result shows that if the dye concentration changes from 10^{-2} to 10^{-6} mol/L while the supporting electrolyte concentrations are held constant at 0.01 mol/L, the interface experiences only a 1 -mV change. This change is so small that for actual work the potential of this interface can be considered constant.

The tetrabutylammonium chloride–tetrabutylammonium tetraphenylborate junction of equal concentrations in aqueous and oil phase are commonly used as the practical reference for LL measurements. Often the interfacial potentials are expressed in relative terms as the potential vs. the TBA^+ ion selective electrode. Potentials thus expressed are 245.7 mV lower than if they were expressed relative to the tetraphenylarsonium–tetraphenylborate convention, which de facto determines the practical standard scale for ITIES studies.

Nonpolarizable Interface. It is important to realize that in the case when only one salt of the type B_1A_1 is present, at respective concentrations c^α and c^β in phases α and β , as in the cell



the interfacial potential will be independent of the total salt concentration. Equation 1 can be solved explicitly for one salt in this cell. If the charge on

the cation is $+n$ and the charge on the anion is $-m$, then the interfacial potential can be calculated from the standard potentials of transfer of the individual ions $\Delta_{\beta}^{\alpha}\varphi$:

$$\Delta_{\beta}^{\alpha}\varphi = \frac{m(\Delta_{\beta}^{\alpha}\varphi_{B_1^+}^0) + n(\Delta_{\beta}^{\alpha}\varphi_{A_1^-}^0)}{m + n} \quad (9)$$

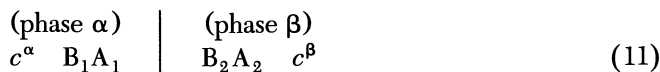
If both the cation and the anion are univalent, eq 9 simplifies to

$$\Delta_{\beta}^{\alpha}\varphi = \frac{1}{2}(\Delta_{\beta}^{\alpha}\varphi_A^0 - + \Delta_{\beta}^{\alpha}\varphi_B^0) \quad (10)$$

This system behaves like a nonpolarizable interface. The salt concentration ratio will not be affected by potential applied from an extraneous source. The equilibrium potential depends only on the standard potentials of transfer of the ions; in particular, it does not depend on the initial concentrations (c^{α} and c^{β}) nor is it a function of the phase volumes. Therefore, if only one salt is present in a LL system, the system is not amenable to potentiometric studies. It is thus essential that a supporting electrolyte be present to observe a potentiometric response of a third ion. The need to have a supporting electrolyte is similar to the need of immobilized ions in an ion exchanger membrane of an ion-selective electrode; it also explains why it is essential that a supporting electrolyte or physiological concentration of salts must be present in measurements that employ fluorescent dyes.

Ideally Polarizable Interface with Supporting Electrolytes.

Supporting electrolytes are important in potentiometric determinations. A LL system with supporting electrolytes B_1A_1 and B_2A_2 can be described by the cell



The salts chosen as supporting electrolytes must conform to certain rules. It is essential that the ions in water be very hydrophilic, which, in terms of the potentials of transport for the ions, means that

$$\Delta_{\beta}^{\alpha}\varphi_{B_1^+}^0 \gg 0 \quad \text{and} \quad \Delta_{\beta}^{\alpha}\varphi_{A_1^-}^0 \ll 0 \quad (12)$$

The salt in the nonaqueous phase must be very lipophilic:

$$\Delta_{\beta}^{\alpha}\varphi_{B_2^+}^0 \ll 0 \quad \text{and} \quad \Delta_{\beta}^{\alpha}\varphi_{A_2^-}^0 \gg 0 \quad (13)$$

Very little repartitioning of the supporting electrolyte salts is expected for such a system. These conditions are fulfilled for supporting electrolytes such

as LiCl in water and TBATPB in nitrobenzene. Under the described conditions, eq 1 can be solved explicitly for the interfacial potential:

$$\Delta_{\beta}^{\alpha}\varphi = \frac{RT}{2F} \ln \left\{ \frac{c^{\alpha} \exp \left[\frac{z_i F}{RT} (-\Delta_{\beta}^{\alpha} \varphi_{\Lambda_1}^0) \right] + c^{\beta} \exp \left[-\frac{z_i F}{RT} (-\Delta_{\beta}^{\alpha} \varphi_{B_2}^0) \right]}{c^{\alpha} \exp \left[-\frac{z_i F}{RT} (\Delta_{\beta}^{\alpha} \varphi_{B_1}^0) \right] + c^{\beta} \exp \left[\frac{z_i F}{RT} (\Delta_{\beta}^{\alpha} \varphi_{\Lambda_2}^0) \right]} \right\} \quad (14)$$

Potential of the Supporting Electrolyte. The actual equilibrium potential expressed by this equation is of little importance. Any imposition of extraneous potential will occur without much opposition because the change requires only minute ionic repartitioning. This case can be illustrated by the response of the interface that consists of 0.01-mol/L LiCl in water and 0.01-mol/L TBATPB in nitrobenzene.

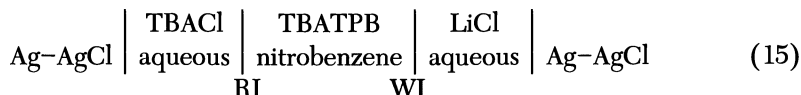
Repartitioning. When the two phases are brought into contact, repartitioning equal to 0.0017% of all ions present has to take place to establish equilibrium. The equilibrium potential will be 58.2 mV. When a 100-mV step is applied on the interface from an outside source, only 0.035% of the total ions will have to repartition to achieve the new equilibrium. This situation contrasts markedly with the reference interface, where only a 10-mV potential step requires a 20.5% concentration change.

The minimal repartitioning when a potential difference is applied on this interface is reflected by only negligible current flow. This behavior is observed within the limits of the standard potentials of transfer of the ions present in the potential window region of the system (cf., Figure 3). For the previously mentioned TBATPB–LiCl system, the potential window is limited on the positive end by TPB[−] ($\Delta_{\beta}^{\alpha} \varphi^0 = 372$ mV) and on the negative end by TBA⁺ ($\Delta_{\beta}^{\alpha} \varphi^0 = -248$ mV).

The potential described by eq 14 will become unimportant if an analyte ion that is capable of repartitioning is added to the system. Within the described potential window it is possible to observe voltammetric response due to the presence of ions whose potentials of transport are between those of the supporting electrolytes. Any ion that can partition within the potential window will take the function of the potential poisoning species. Therefore, a supporting electrolyte, which is necessary for potentiometry of partitioning ions, does not interfere with the measurement.

Experimental Procedure for Potentiometry. The two dyes described here, 3,3'-diethyloxadicyanone iodide [DiOC₂(5)] and 3,3'-dimethyloxadicyanone iodide [DiOC₁(3)], were obtained from Molecular

Probes, Inc. (Eugene, OR). Their fluorescent behavior is described elsewhere (21, 22). These two dyes were chosen because their potentials of transfer fall within the potential window of the supporting electrolytes being used. The apparatus used for the potential measurements is similar to that shown in Figure 2, but only the reference electrodes are used. The cell composition is



The supporting electrolytes (when used) were 0.01-mol/L lithium chloride in aqueous phase and 0.01-mol/L tetrabutylammonium tetraphenylborate (TBATPB) in nitrobenzene.

The interface of experimental interest, the working interface, is labeled WI; the constant potential or reference interface (*vide supra*) is labeled RI. The aqueous phase of the RI is 0.01-mol/L tetrabutylammonium chloride. The interfacial potential of the reference interface is poised by the concentration ratio of tetrabutylammonium, a constant concentration ion shared by both phases. The exact potential of the reference interface can be calculated using eq 1. The electrochemical cell is connected to an electric circuit via two Ag-AgCl electrodes immersed in an aqueous chloride solution.

Potentiometric Results. As shown earlier, a single salt concentration variation has no effect on the interfacial potential. Thus, to study the effect of the dye cation on the interfacial potential, other ions must be present. Supporting electrolytes, selected in such a way that an ideally polarizable interface is formed when the dye is absent, are conveniently used.

The function of sodium chloride as the aqueous supporting electrolyte is physiologically relevant to the experiment. Figure 4 shows the variation of interfacial potential as a function of dye concentration at selected concentrations of sodium chloride. The value 0.12 mol/L (7-g/L NaCl) corresponds to a physiological concentration.

Supplemental curves in Figure 5 give an insight into the effect of the supporting electrolyte concentration. To underscore the importance of the supporting electrolytes in the function of the dye separation, the result is also given for the iodide form of the dye in the absence of any supporting electrolytes (curve E). As expected, the potential established on the interface by the dye alone is constant regardless of the dye concentration. Calculated interfacial potential vs. dye concentration is shown for the following organic phase-supporting electrolyte cations: tetramethylammonium (TMA⁺), tetraethylammonium (TEA⁺), tetrabutylammonium (TBA⁺), tetraphenylarsonium

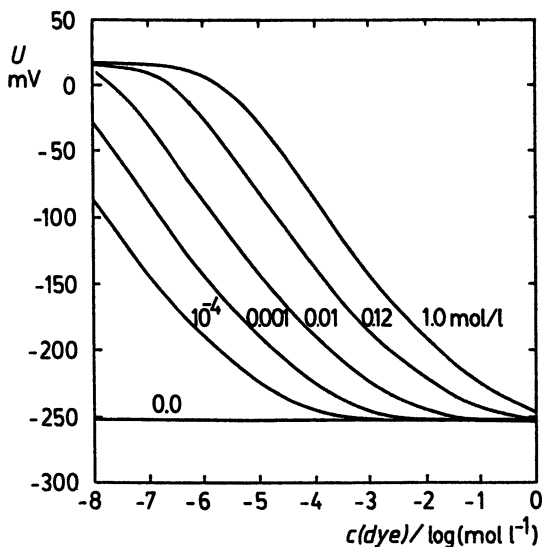


Figure 4. Calculated interfacial potential as a function of dye concentration for a system that contains aqueous sodium chloride in concentrations ranging from 0 to 1 mol/L as indicated at the curves. 0.12 mol/L is a physiological saline solution (7 g/L NaCl). The dye $\text{DiOC}_1(3)\text{I}$ was dissolved in the nitrobenzene phase.

(TPAs⁺), and crystal violet (CV⁺) with tetraphenylborate as the counterion. Lithium chloride is the aqueous phase supporting electrolyte.

Because numerical analysis reveals that it is the relative concentration, rather than its absolute value, that determines the interfacial potential, the results of these calculations are plotted in Figure 6 as the interfacial potential vs. the logarithm of base electrolyte to dye ratio. This graph shows a linear plot over the range of concentration ratios between 1:10 and 1:10⁻⁵. For dye concentrations from 10⁻³ to 10⁻⁵ mol/L, the supporting electrolyte concentration that allows the interfacial potential to work in the linear region is between 0.01 and 1.0 mol/L. A concentration of 0.01 mol/L was selected for this study.

Equation 1 shows that the ratio of the volumes of the two phases is related to the interfacial potential. Table II gives the slopes of the potential-concentration relationships for water to nitrobenzene volume ratios between 10⁻⁵ and 10⁵. These slopes show that to approach the ideal linear voltammetric slope of 55 mV/decade in the dye concentration range of 10⁻³-10⁻⁵ mol/L, the water to nitrobenzene volume ratio should be between 1:1 and 33:1. The broadest range of the dye concentration that has linear slope is 10⁻²-10⁻⁶ mol/L, at a volume ratio of 10:3. To simplify the calculations and experimental setup, equal volumes of water and nitroben-

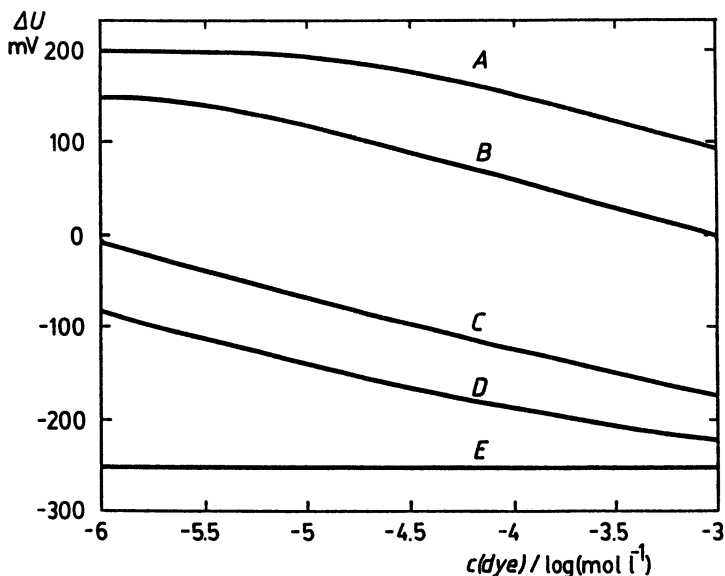


Figure 5. Effect of the supporting electrolyte cation in the nitrobenzene phase on the relationship between interfacial potential and dye iodide ($\text{DiOC}_1(3)\text{I}$) concentration. A, 0.01 mol/L tetramethylammonium tetraphenylborate; B, 0.01 mol/L tetraethylammonium tetraphenylborate; C, 0.01 mol/L tetrabutylammonium tetraphenylborate; D, two identical curves, 0.01 mol/L tetraphenylarsonium tetraphenylborate and 0.01 mol/L crystal violet tetraphenylborate. (The crystal violet has no supporting electrolyte in the nitrobenzene phase.) The supporting electrolyte in the water phase is always 0.01 mol/L LiCl, except for curve E, which has no supporting electrolytes.

zene are often used. If activation coefficients in both phases are also assumed to be equal, eq 1 becomes

$$\sum_{i=1}^j z_i c_i \left/ \left\{ 1 + \exp \left[\frac{z_i F}{RT} (\Delta_{\beta}^{\alpha} \varphi - \Delta_{\beta}^{\alpha} \varphi_i^0) \right] \right\} \right. = 0 \quad (16)$$

where c_i is the sum of the concentrations of the ion i in the two phases.

The plots of calculated interfacial potential as a function of $\text{DiOC}_1(3)$ concentration are shown in Figure 7 together with the experimental results for $\text{DiOC}_1(3)$ and $\text{DiOC}_2(5)$. In the range of dye concentration from 10^{-2} to 10^{-6} mol/L, the measured values agree with those predicted through calculations.

The 55-mV/decade theoretical slope of the ideal linear potentiometric response is different from the intuitively expected 59-mV slope. This difference is easy to understand qualitatively. A 10-fold increase in concentration in one phase will be followed by a subsequent repartitioning of all the ions

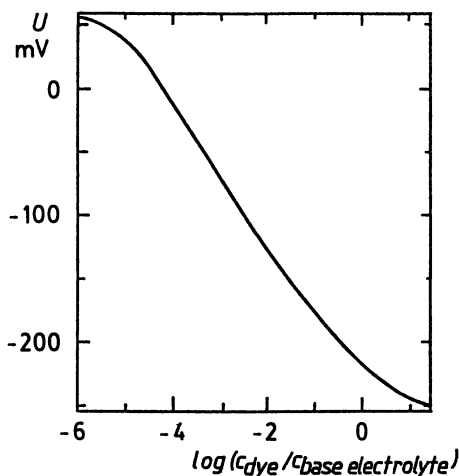


Figure 6. Calculated effect of supporting electrolyte concentration on the potential–dye concentration relationship. The calculated interfacial potential is plotted vs. the logarithm of the ratio of the $\text{DiOC}_1(3)\text{I}$ dye concentration to the supporting electrolyte concentration.

Table II. Slopes (millivolts per decade) of the Potential vs. Logarithm of Dye Concentration Plots at Various Dye Concentrations and Volume Ratios of Water to Nitrobenzene

V_α / V_β	Dye Concentration (mol/L)						
	10^{-7}	10^{-6}	10^{-5}	10^{-4}	10^{-3}	10^{-2}	10^{-1}
10^5	0	0	0	-2	-6	-70	-70
10^4	0	0	-0.5	-3	-29	-104	-72
10^3	0	0	-2	-26	-62	-106	-70
10^2	0	-2	-26	-57	-62	-106	-52
10	-3.2	-26	-58	-58	-62	-86	-20
1	-24	-56	-60	-58	-48	-38	-20
10^{-1}	-50	-56	-50	-38	-32	-34	-22
10^{-2}	-52	-46	-36	-34	-32	-34	-30
10^{-3}	-40	-34	-32	-32	-38	-46	-36
10^{-4}	-26	-32	-32	-38	-50	-54	-36
10^{-5}	-12	-27	-38	-50	-58	-54	-36

present. Because repartitioning aids the interfacial potential by maintaining the interfacial equilibrium, less than the 59-mV change is needed. The slope of the experimental curve is 52 ± 1 mV/decade.

Interfering Ions. Experimental points in Figure 7 show that at lower dye concentrations the potential attains a constant value whereas the calculation still predicts a change with the slope of 55 mV/decade. This disagree-

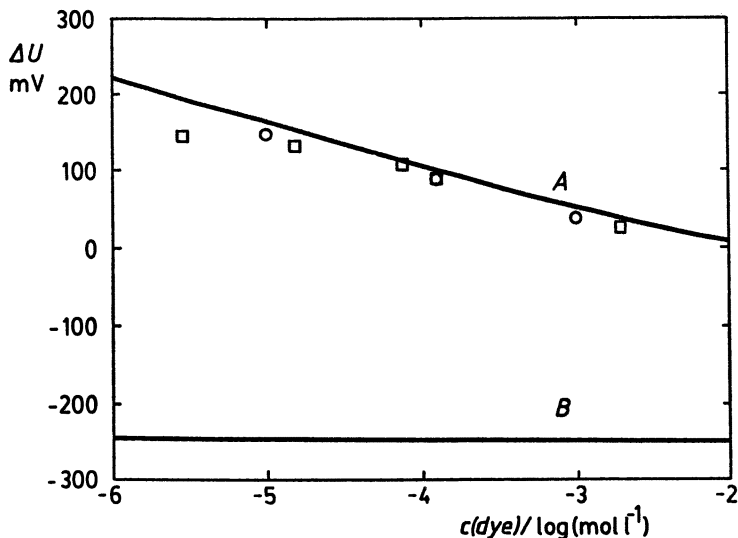


Figure 7. Relationship between interfacial potential and the logarithm of the initial $\text{DiOC}_1(3)$ concentration in the nitrobenzene phase. Curve A shows the calculated potential of the working interface between 0.01 mol/L LiCl in water and 0.01 mol/L TBATPB in the presence of $\text{DiOC}_1(3)$, with the reference interface potential subtracted. Curve B is the calculated potential of the reference interface between 0.01 mol/L TBACl in water and 0.01 mol/L TBATPB in nitrobenzene. The experimentally determined potential differences between the reference interface and the working interface are given for $\text{DiOC}_2(5)$ (○) and $\text{DiOC}_1(3)$ (□).

ment can be explained by the presence of an ionic impurity that poises the interfacial potential at low dye concentration. Figure 8 is a three-dimensional plot that illustrates the difference between the calculated interfacial potential with and without added interfering ion at 10^{-5} mol/L. The standard potential of transfer was chosen to be -100 mV for the cation and $+100$ mV for the anion of the interfering or impurity salt. The presence of this assumed species takes effect at dye concentrations below 10^{-5} mol/L at water to nitrobenzene volume ratios between 0.1 and 1.00. The flat region corresponds to composition in which the added salt (impurity) has no effect on the observed potential.

Further simulations, which are not shown here, were performed in which the impurity was assumed to be a lithium salt of an interfering anion present in aqueous solution. The impurity caused an increase in the slope of the potential-concentration relationship below 10^{-4} mol/L of dye. Conversely, a cationic impurity will cause the slope to decrease at dye concentrations below 10^{-5} mol/L when a chloride salt of the impurity is included in the calculations. The reason for the discrepancy between experimental and calculated

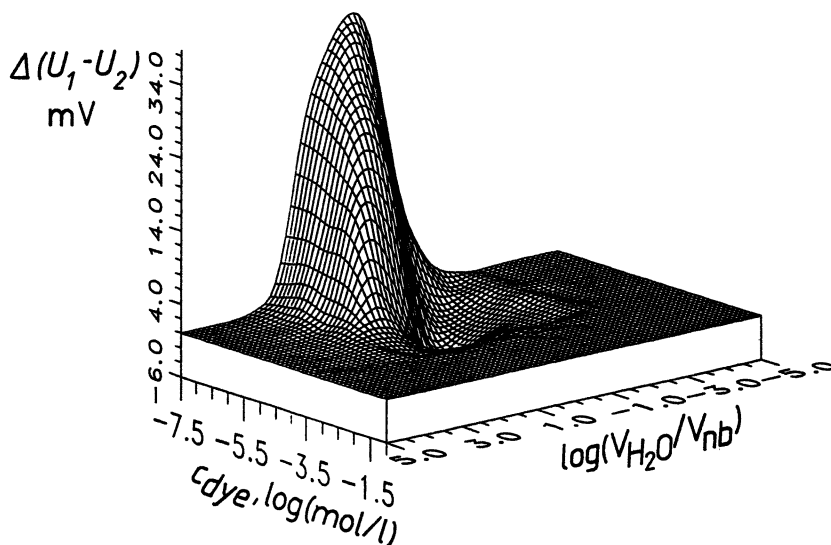


Figure 8. Influence of an electroactive impurity on the interfacial potential-dye concentration relationship. The x axis is the logarithm of the dye concentration, the y axis is the logarithm of the ratio of water volume to nitrobenzene volume, and the z axis is the difference between interfacial potential with and without the impurity. Standard potentials of transport for the impurity cation $\Delta_{\beta}^{\alpha}\phi_{+}^0 = -100$ mV and for the anion $\Delta_{\beta}^{\alpha}\phi_{-}^0 = +100$ mV; $c = 1 \times 10^{-5}$ mol/L.

data in Figure 7 must be some contamination in the system. The source of the contaminant is probably nitrobenzene itself, but it cannot be the typical nitrobenzene contaminant aniline because aniline is too hydrophilic; a higher, more lipophilic analog is a likely contaminant. It is important to realize that calculations show that protons (pH), at least at concentrations below 10^{-3} mol/L, have a negligible effect on the established interfacial potential.

Concluding Remarks on Potentiometry. Due to the unique characteristics of the liquid-liquid interface system, factors in addition to the concentration of analyte ion must be considered in potentiometric studies. These factors include the nature and concentration of the supporting electrolytes and the relative volume of the phases in contact. Numerical solutions of the theoretical relationship derived by Hung (15) are useful to predict the effect of such factors as volume of the phases and concentration of added ions. Experimental results with an oxacyanine dye in a water-nitrobenzene system show a linear response in the 10^{-3} - 10^{-5} -mol/L concentration range, which corresponds to a 120-mV dynamic range of these dyes for use as potential sensors. This response agrees with measurements on biological

membranes that show a linear range over 100 mV (23–25). Deviation from linear behavior at low dye concentrations appears to be caused by a cationic impurity in one of the phases. Similar limits on the linear range of dye–potential studies observed in biological systems are most likely due to the other ions present in the cellular fluid. Additional experiments using chelating agents to mask the effects of these interfering ions are necessary to determine the effect of chelation on the interfacial potential and, thus, to determine the feasibility of this approach.

Insensitivity to pH. Calculation and experiments show that pH will not affect the potential measurement if the pH is between 3 and 7. This is an important finding because any buffers in the liquid–liquid system complicate the system by increasing the number of ionic components. Acidity will, however, be important if the dissociation of the transported ion will be affected by pH. In our calculations, complete dissociation of all ions was assumed.

Protein Adsorption on the Water–Nitrobenzene Interface

Adsorption on the LL interface can be observed in voltammetric curves, but a more sensitive indication of adsorption can be obtained from impedance measurements. Voltammetric studies (26, 27) showed that the addition of proteins to a so-called blocked (i.e., ideally polarizable) aqueous–nitrobenzene interface resulted in narrowing of the potential window of the supporting electrolyte system. This observation implies that the difference in hydrophilic–hydrophobic properties of the two solvents decreased. This decrease can be explained by postulating the formation of a third phase between the original two. The third phase would allow mediated, easier transport of the supporting electrolyte ions.

Earlier studies of adsorption on LL interfaces involved phospholipids (28–31). To investigate possibilities for study of a less defined material (32), we chose a protein as the adsorbing material: bovine serum albumin (BSA) with a molar mass of 69,000 (CRG-7, Armour Pharmaceutical Company). The preparation is known to contain a certain amount of fatty acids. The same starting material was used throughout the measurement. The aqueous protein solutions were prepared fresh from a dry sample before each experiment. The effects of BSA on the imaginary and real impedance and interfacial capacitance of a water–nitrobenzene interface are discussed under varying BSA concentration, temperature, and pH.

Impedance Measurements. These experiments were carried out with a frequency analyzer (Solartron 1250) and a four electrode potentiostat (Solartron 1286). The cell, similar to that in Figure 2, was equipped with a

thermostated water jacket. In impedance studies it is desirable to keep the interfacial capacitance small so that the time constant of the system is also small and the pertinent impedance can be studied in the frequency range of 1–100 Hz. Larger capacitances shift the frequencies below 1 Hz, which poses experimental difficulties. Therefore, an interface of only 2-mm diameter was studied.

Figure 9 shows a complex impedance plane plot of the water–nitrobenzene interface that contains 0.01-mol/L LiCl in the aqueous phase and 0.01-mol/L tetrabutylammonium teraphenylborate (TBATPB) in the nitrobenzene phase as the supporting electrolytes (filled circles). Upon addition of 3-ppm BSA (open circles) dramatically changes the low-frequency values, which implies that addition of the protein to the system causes a change in the interfacial structure, especially in the capacitance of the interface.

The impedance response displays significant dependence on the applied interfacial potential (Figure 10). It can be deduced from the data analysis (32) that the protein adsorbs at the interface. At more negative potentials the aqueous side of the interface has a negative surface charge (anions) and at more positive potentials it has a positive surface charge (cations). It is an important result that the curves of imaginary impedance vs. interfacial

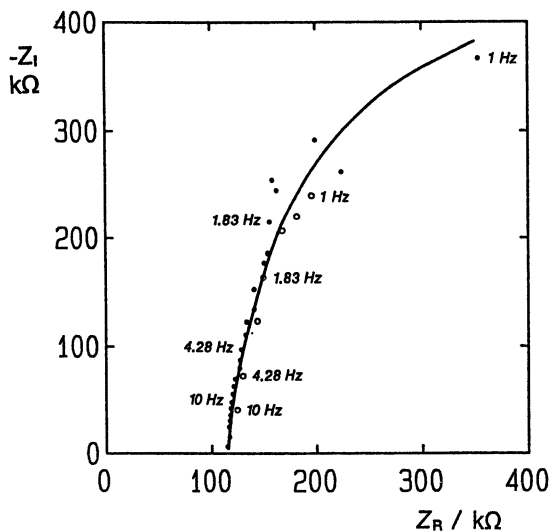


Figure 9. Complex plane impedance plots of the water–nitrobenzene interface (negative imaginary impedance vs. real impedance) with and without bovine serum albumin. The filled circles denote the supporting electrolyte only: 0.01 mol/L LiCl in water; 0.01 mol/L TBATPB in nitrobenzene. The open circles indicate addition of 3 ppm BSA in water. The applied interfacial potential is 0.30 V (vs. TBA⁺ ion selective electrode); $t = 25.0\text{ }^{\circ}\text{C}$. The frequency of the measurement for selected values is indicated at the data points. (Reproduced with permission from reference 32. Copyright 1990 Elsevier.)

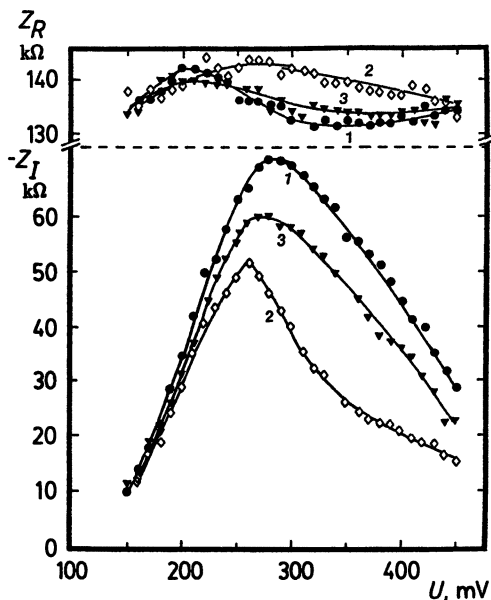


Figure 10. Real (in phase; top) and imaginary (out of phase; bottom) impedance as a function of applied interfacial potential at different BSA concentrations. Water: 0.01 mol/L LiCl, BSA concentrations (ppm) 0.0 (curve 1, ●); 0.5 (curve 2, ▼); 3.0 (curve 3, ◇). Nitrobenzene: 0.01 mol/L TBATPB; $f = 5$ Hz, $t = 25.0$ °C. (Reproduced with permission from reference 32. Copyright 1990 Elsevier.)

potential change and the curve maxima shift when BSA is added to the system. This suggests that the BSA is adsorbed at the interface and causes the distribution of the charging ions in the interface to be altered.

Calculation of Interfacial Capacitance. From the data it is possible to obtain approximate value for the potential of zero charge (PZC). If a simple Randles circuit is assumed (Figure 11), then the maximum of the curve $-Z_I$ vs. E corresponds to the PZC of the system. Figure 12 shows how the potential of zero charge changes in the presence of BSA. The gradual increase with increasing concentration from 1 to 6 ppm is due to the gradual formation of a monolayer of BSA on the interface. The decrease at higher concentrations is explained by the formation of a thick layer that has the character of a third interface. Figure 13 displays the curves of a real and imaginary impedance as a function of BSA concentration at constant interfacial potential, 0.35 V (vs. TBA⁺ ion selective reference interface). The dramatic change in the imaginary (out-of-phase) impedance as a function of the protein concentration is important.

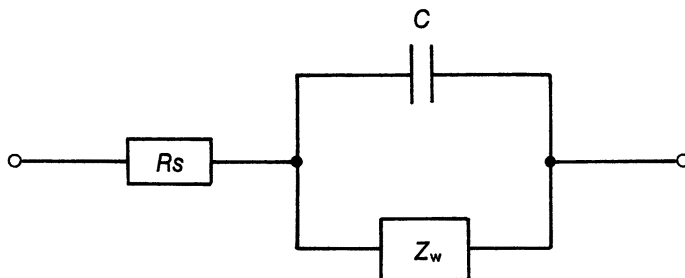


Figure 11. Randles equivalent circuit used in the calculation of the interfacial capacitance. C , interfacial capacitance, R_s , bulk solution resistance; Z_w , Warburg impedance.

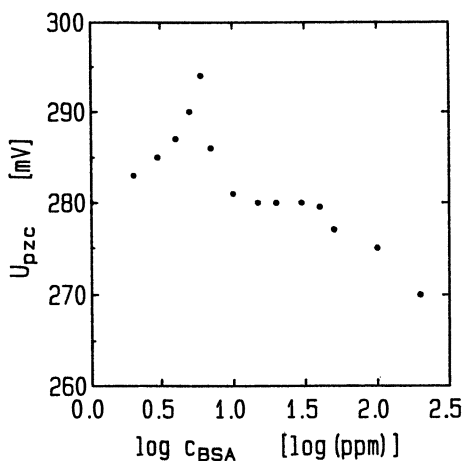


Figure 12. Potential of zero charge of the water–nitrobenzene interface as a function of varying concentration of BSA in log (ppm). Supporting electrolytes: 0.01 mol/L LiCl in water; 0.01 mol/L TBATPB in nitrobenzene.

The imaginary component of the impedance gives a qualitative picture of the changing interfacial capacitance, but the value has to be interpreted from a correctly devised equivalent circuit to obtain the capacitance value. Here we used the simple Randles circuit (Figure 11). The procedure was similar to that used by Wandlowski et al. (30, 31). The total impedance Z of the Randles circuit is

$$Z = R_s + 1/\left\{ (1/jX_C) + 1/\left[(Z_w/\sqrt{2}) - j(Z_w/\sqrt{2}) \right] \right\} \quad (17)$$

$X_C = -1/\omega C$ is the interfacial reactance, R_s is the bulk (solution) resistance, C is the capacitance of the interface, Z_w is the Warburg impedance, ω

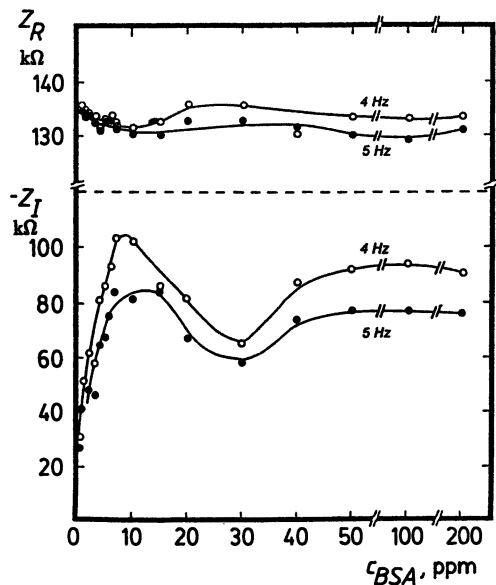


Figure 13. Real and imaginary impedance as a function of the concentration of BSA in aqueous phase at indicated frequencies. Water: 0.01 mol/L LiCl; nitrobenzene: 0.01 mol/L TBATPB. Applied interfacial potential $U = 0.35$ V vs. TBA^+ ion selective electrode; $t = 25$ °C. (Reproduced with permission from reference 32. Copyright 1990 Elsevier.)

is the circular frequency of the applied perturbing signal, and j is the imaginary unit. After separating the real and imaginary components, the following relationship for calculating the interfacial reactance is obtained:

$$X_C = \left(Z_I^2 + (Z_R - R_s)^2 \right) / (Z_I + Z_R - R_s) \quad (18)$$

The real and imaginary impedances Z_R and Z_I are directly accessible from the impedance measurement. R_s , the solution resistance, has to be obtained from examination of the complex plane impedance plot (cf., Figure 9). In the impedance plane plot, the imaginary value decreases with increasing frequency until the curve approaches the real impedance axis. The real impedance is equal at this point to the solution resistance R_s . The value is independent of applied interfacial potential, but it depends on the position of the reference electrodes (different uncompensated resistance). Because the calculated capacitance is very sensitive to the calculated R_s , the placement of the reference electrodes must be carefully controlled.

Once R_s is determined, capacitance can be calculated from eq 18 using only one set of impedances. However the recommended approach is to calculate C from all the frequencies obtained. This approach allows for

averaging measurement uncertainty and it also allows verification of the correctness of the calculation. In an ordinary system, the calculated capacitance should be independent of frequency. Any drift with frequency other than experimental noise indicates a possible problem. One cause for variation may be the use of an incorrect equivalent circuit for the evaluation.

Evaluated interfacial capacitance is shown in Figure 14 as a three-dimensional surface plot that charts the dependence of the capacitance on the BSA concentration and on the applied interfacial potential. The capacitance decreases with increasing concentration of the protein, until a plateau is reached.

Effect of pH on Adsorbed BSA. The capacitance measurement is very useful in the study of protein adsorptive properties as a function of pH. Figure 15 shows the capacitance change as the pH was varied using a Robinson–Britton buffer. The capacitance is essentially invariant in the absence of protein, but the addition of the protein has a pronounced effect. The change of the charge of the adsorbed zwitterionic protein with changing pH clearly shows the gradual ionization in both the cationic and anionic states. As expected, at the isoelectric point, where all the lines intercept, only a small change of capacitance with protein concentration is observed. This behavior positively demonstrates the adsorption of ionized functional groups of the protein.

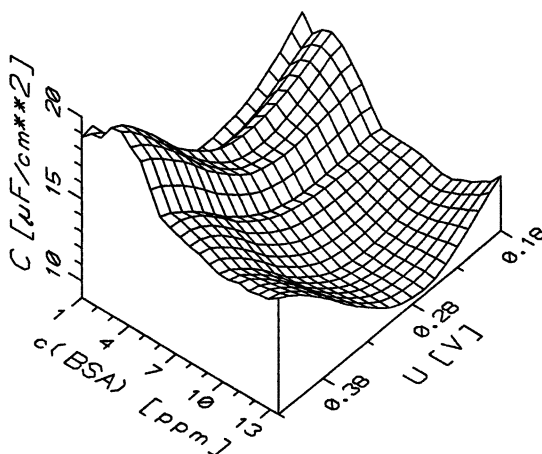


Figure 14. Three-dimensional surface plot of the interfacial capacitance as a function of BSA concentration and applied interfacial potential. Water: 0.01 mol/L LiCl; nitrobenzene: 0.01 mol/L TBATPB; $t = 25.0\text{ }^{\circ}\text{C}$. Interfacial potential U given vs. TBA^+ ion selective electrode. (Reproduced with permission from reference 32. Copyright 1990 Elsevier.)

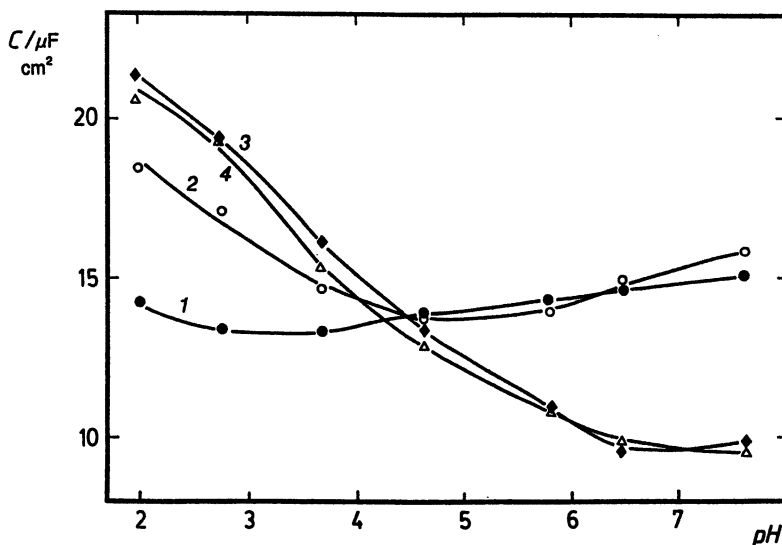


Figure 15. The capacitance of the interface as a function of pH in the presence of different concentrations of BSA, buffered with Robinson-Britton solution. Water: 0.01 mol/L LiCl; BSA concentration (ppm): 0.0 (curve 1); 0.5 (curve 2); 3.0 (curve 3); 15.0 (curve 4); nitrobenzene: 0.01 mol/L TBATPB. Applied interfacial potential 0.30 V vs. TBA⁺ ion selective electrode. (Reproduced with permission from reference 32. Copyright 1990 Elsevier.)

Application of the impedance methods in the described manner can be useful to the understanding of films of biochemical materials adsorbed at liquid-liquid interfaces and can provide some information for modeling ion transport across a biological membrane.

Microinterface between Two Immiscible Solutions

The cell in Figure 2 is a typical apparatus used in LL studies. However, recently small interfaces, called here microinterfaces, were shown to have some experimental advantage. The purpose of this modification was to use the same advantage that the ultramicroelectrodes have. Ultramicroelectrodes help to overcome solution resistance difficulties that originate from a potential shift due to an uncompensated iR drop. As the interfacial area becomes smaller, the diffusion geometry becomes a spherically symmetric process, which means that the ratio of charge transport current versus solution resistance increases and, ultimately, renders the iR drop minimal. In ITIES studies, restriction of the interfacial area and use of a current amplifier for voltammetric studies is a viable alternative to a four-electrode potentiostat.

Small LL interfaces have been used by Girault and co-workers (33–38) and by Senda et al. (39, 40). We have used a small hole formed in a thin glass wall (41–43). Figure 16 shows the voltammetric response of lauryl sulfate anion transport between water and nitrobenzene. Recent analytical applications of these microinterfaces have resulted in construction of gel-solidified probes. The advantage of such a modification is ease of handling (44–47). The immobilization can be extended further to studies of frozen interfaces, or even to solid electrolytes. Significantly, ITIES theory also applies to interfaces that are encountered in ion-doped, conductive, polymer-coated electrodes.

Fast scan voltammetry, in particular on microinterfaces, can be used for determination of charge-transfer rate constants. Impedance analysis can be used not only in analytical applications, but also to obtain a better understanding of surface phenomena (48) and adsorption (32). Microinterfaces, with their high own resistance, are well suited for impedance analysis derived from measurements of noise generated by electrochemical systems (49, 50). Understanding the phenomena peculiar to microinterfaces is essential to future studies of the electrochemistry of small domains.

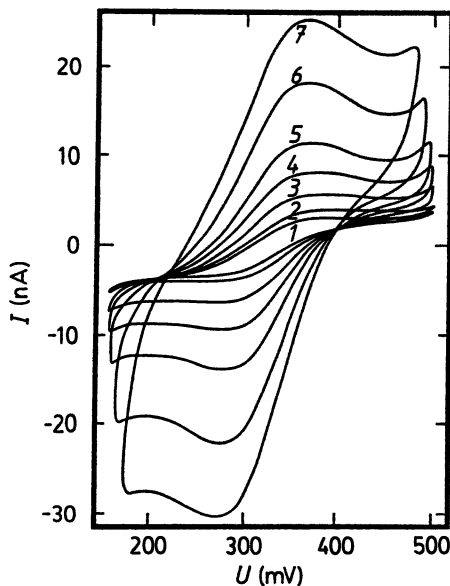


Figure 16. Voltammetric determination of lauryl sulfate (0.4 mmol/L) on a liquid-liquid microinterface. Scan rates (mV/s): 10 (curve 1); 20 (curve 2); 50 (curve 3); 100 (curve 4); 200 (curve 5); 500 (curve 6); 1000 (curve 7). Supporting electrolytes are 0.02 mol/L LiCl in water and 0.02 mol/L TBATPB in nitrobenzene. Diameter of the hole 130 μm . (Reproduced from reference 4. Copyright 1990 American Chemical Society.)

Acknowledgment

The research results described in this chapter and preparation of the manuscript have been supported by the Office of Naval Research.

References

1. Nernst, W. Z. *Phys. Chem.* **1888**, 2, 613–637.
2. Blank, M.; Feig, S. *Science (Washington, D.C.)* **1963**, 141, 1173–1174.
3. Koryta, J.; Vanýsek, P.; Březina, M. *J. Electroanal. Chem.* **1976**, 67, 263–266.
4. Vanýsek, P. *Anal. Chem.* **1990**, 62, 827A–835A.
5. Vanýsek, P. *Electrochemistry on Liquid/Liquid Interfaces*; Springer: Berlin, Germany, 1985.
6. Koryta, J. In *The Interface Structure and Electrochemical Processes at the Boundary between Two Immiscible Liquids*; Kazarinov, V. E., Ed.; Springer: Berlin, Germany, 1987.
7. Girault, H. H. J.; Schiffrin, D. J. In *Electroanalytical Chemistry*; Bard, A. J., Ed.; Marcel Dekker: New York, 1989; Vol. 15.
8. Samec, Z. *Chem. Rev.* **1988**, 88, 617–632.
9. Vanýsek, P.; Buck, R. P. *J. Electrochem. Soc.* **1984**, 131, 1792–1796.
10. Senda, M.; Kakiuchi, T.; Osakai, T. *Electrochim. Acta* **1991**, 36, 253–262.
11. Koryta, J. *Select. Electr. Rev.* **1991**, 13, 133–158.
12. Waggoner, A. S. *Annu. Rev. Biophys. Bioeng.* **1979**, 8, 47–68.
13. Bashford, C. L. *Biosci. Rep.* **1981**, 1, 183–196.
14. Wiegand, D. H. Ph.D. Thesis, Northern Illinois University, DeKalb, IL, 1990.
15. Hung, L. Q. *J. Electroanal. Chem.* **1980**, 115, 159–174.
16. Parker, A. J. *Electrochim. Acta* **1976**, 21, 671–679.
17. Rais, J. *Collect. Czech. Chem. Commun.* **1971**, 36, 3253–3262.
18. Vanýsek, P. *Electroanalysis* **1990**, 2, 409–413.
19. Buck, R. P.; Vanýsek, P. *J. Electroanal. Chem.* **1990**, 292, 73–91.
20. Vanýsek, P.; Buck, R. P. *J. Electroanal. Chem.* **1991**, 297, 19–35.
21. Wiegand, D. H.; Vanýsek, P. *J. Colloid Interface Sci.* **1990**, 135, 272–282.
22. Wiegand, D. H.; Vanýsek, P. *Appl. Spectrosc.* **1988**, 42, 958–961.
23. Ehrenberg, B.; Montana, V.; Wei, M.-D.; Wuskell, J. P.; Loew, L. M. *Biophys. J.* **1988**, 53, 785–794.
24. Gross, D.; Loew, L. M. In *Methods in Cell Biology*; Taylor, D. L.; Wang, Y.-L., Eds.; Academic: San Diego, CA, 1980; Vol. 30, Chapter 7.
25. Åkerman, K. E. O.; Scott, I. G.; Heikkilä, J. E.; Heinonen, E. *J. Neurochem.* **1987**, 48, 552–559.
26. Vanýsek, P. Ph.D. Thesis, Czechoslovak Academy of Sciences, J. Heyrovský Institute of Physical Chemistry and Electrochemistry, Prague, Czechoslovakia, 1982.
27. Vanýsek, P.; Reid, J. D.; Craven, M. A.; Buck, R. P. *J. Electrochem. Soc.* **1984**, 131, 1788–1791.
28. Kakiuchi, T.; Yamane, M.; Osakai, T.; Senda, M. *Bull. Chem. Soc. Jpn.* **1987**, 60, 4223–4228.
29. Yamane, M.; Kakiuchi, T.; Osakai, T.; Senda, M. *Rev. Polarogr. (Kyoto)* **1983**, 2A26.
30. Wandlowski, T.; Račinský, S.; Mareček, V.; Samec, Z. *J. Electroanal. Chem.* **1987**, 227, 281–285.

31. Wandlowski, T.; Mareček, V.; Samec, Z. *J. Electroanal. Chem.* **1988**, *242*, 277–290.
32. Vanýsek, P.; Sun, Z. *Bioelectrochem. Bioenerget.* **1990**, *23*, 177–194.
33. Taylor, G.; Girault, H. H. J. *J. Electroanal. Chem.* **1986**, *208*, 179–183.
34. Campbell, J. A.; Stewart, A. A.; Girault, H. H. J. *J. Chem. Soc., Faraday Trans. I* **1989**, *85*, 843–853.
35. Campbell, J. A.; Girault, H. H. J. *J. Electroanal. Chem.* **1989**, *266*, 465–469.
36. Taylor, G.; Girault, H. H.; McAleer, J. J. *J. Electroanal. Chem.* **1990**, *293*, 19–44.
37. Stewart, A. A.; Shao, Y.; Pereira, C. M.; Girault, H. H. J. *J. Electroanal. Chem.* **1991**, *305*, 135–139.
38. Shao, Y.; Osborne, M. D.; Girault, H. H. J. *J. Electroanal. Chem.* **1991**, *318*, 101–109.
39. Senda, M.; Kakutani, T.; Osakai, T.; Ohkouchi, T. *Proceedings of the 1st Bioelectrochemical Symposium, Mátrafüred, 1986; Akademiai Kiado: Budapest, Hungary, 1986; pp 353–364.*
40. Ohkouchi, T.; Kakutani, T.; Osakai, T.; Senda, M. *Anal. Sci.* **1991**, *7*, 371–376.
41. Vanýsek, P.; Hernandez, I. C. *Anal. Lett.* **1990**, *23*, 771–785.
42. Vanýsek, P.; Hernandez, I. C.; Xu, J. *Microchem. J.* **1990**, *41*, 327–329.
43. Vanýsek, P.; Hernandez, I. C. *J. Electrochem. Soc.* **1990**, *137*, 2763–2768.
44. Kakutani, T.; Ohkouchi, T.; Osakai, T.; Kakiuchi, T. *Anal. Sci.* **1985**, *1*, 219–225.
45. Mareček, V.; Jänchenová, H.; Colombini, M. P.; Papoff, P. *J. Electroanal. Chem.* **1987**, *217*, 213–219.
46. Baum, G. *Anal. Lett.* **1970**, *3*, 105–111.
47. Osakai, T.; Kakutani, T.; Senda, M. *Bunseki Kagaku* **1984**, *33*, E371–E377.
48. Buck, R. P. *Ion-Select. Electr. Rev.* **1982**, *4*, 3–74.
49. Bezegh, A.; Janata, J. *Anal. Chem.* **1987**, *59*, 494A–508A.
50. Mareček, V.; Gratzl, M.; Pungor, A.; Janata, A. *J. Electroanal. Chem.* **1989**, *266*, 239–252.
51. Koryta, J.; Vanýsek, P.; Březina, M. *J. Electroanal. Chem.* **1977**, *75*, 211–228.
52. Vanýsek, P. *J. Electroanal. Chem.* **1981**, *121*, 149–152.

RECEIVED for review March 5, 1991. ACCEPTED revised manuscript June 25, 1992.

Channel-Forming Peptides in Uniformly Aligned Multilayers of Membranes

Huey W. Huang

Physics Department, Rice University, Houston, TX 77251

We describe one new method of ultraviolet circular dichroism (CD) and one improved method of X-ray lamellar diffraction for obtaining structural data of membrane proteins. Both methods employ samples of uniformly aligned multilayers of membranes. It was proved earlier that a CD band of α -helices is polarized along the helix axis. Because membrane proteins often contain α -helical sections, measurement of CD at the normal and oblique incident angles relative to the plane of the membrane reveals the orientation of the protein molecules. This method of oriented CD is used to study a long-standing problem of alamethicin; that is, how does the amphipathic helical peptide associate with a membrane? Our investigation led to the discovery of a new phenomenon of cooperative peptide insertion in bilayer lipid membranes. We next describe a method of high-resolution lamellar diffraction that was used to reveal the location of the monovalent and divalent ion binding sites in the gramicidin channel.

TWO METHODS FOR OBTAINING STRUCTURAL INFORMATION on membrane proteins and applications of these methods to the structural problems of two channel-forming peptides are described in this chapter. Both methods use uniformly aligned multilayers of membranes, and alamethicin and gramicidin are the peptides that are investigated. We will show that two long-standing problems are resolved by these methods: the location of the ion binding sites in the gramicidin channel and the states of alamethicin associated with membranes.

0065-2393/94/0235-0083\$08.72/00
© 1994 American Chemical Society

Uniformly aligned multilayers of membranes (containing proteins) possess one-dimensional structural order perpendicular to the plane of the membrane and preserve the orientational order of proteins relative to the plane of the membrane. Both the one-dimensional structure and the orientation of proteins can be measured with the methods to be described. We stress that proteins in these samples are in the membrane active forms. With time-resolved measurement, our methods can be extended to study the structural dynamics of membrane proteins.

Orientational Information

Membrane proteins often contain α -helical sections. We have developed a method called oriented circular dichroism (OCD; *see* reference 1), which can be used to determine the orientation of α -helices with respect to the plane of the membrane. This method is simple and easy to use compared with, for example, the NMR method, which requires isotope labeled samples. Indeed, it is the ease of this method that allowed us to examine alamethicin in many different chemical conditions and that resolved a controversial question about the nonconducting state of alamethicin and subsequently led to the discovery of a new phenomenon of amphiphilic helical peptides (2).

One-Dimensional Structure

X-ray lamellar diffractions of bilayer membranes have been studied since the late 1960s. The samples used in most X-ray measurements were either powders (not aligned) or partially aligned multilayers. With uniformly aligned multilayers, we can perform lamellar diffraction using the θ - 2θ scanning geometry. In this way we have routinely obtained high-resolution diffraction data. From these measurements, the z coordinate (normal to the plane of the membrane) of a label atom can be obtained from difference electron density profiles. For example, the ion distribution in an ion channel can be obtained by subtracting the electron density profile of a sample that contains no ions from the electron density profile of a sample that does contain ions. In this way we directly measured the monovalent and divalent cation binding sites in the gramicidin channel (3). More recently, we also performed X-ray scattering with the momentum transfer confined in the xy plane (4). Such scattering curves describe the lateral organizations of proteins and peptides in membranes. The in-plane scattering will not be discussed here.

In the next section, uniformly aligned multilayers of membranes are described. The third section illustrates the theoretical basis and applications of the method of oriented circular dichroism (OCD). The OCD study of alamethicin is discussed in the fourth section and the last section is devoted

to lamellar diffraction of membrane multilayers and the resolution of the ion binding sites in the gramicidin channel.

Uniformly Aligned Multilayer Samples

Hydrated peptide–lipid mixtures can be manually aligned between two parallel, flat surfaces. The procedures are described in references 5 and 6. For OCD and neutron diffraction experiments, we used two silica plates. For X-ray diffraction experiments, we used a polished beryllium (Be) plate and a silica plate. The sample thickness (1–80 μm) was controlled by a spacer between two plates. A circular hole was made in the spacer to provide a cavity to hold the sample. The thicker the sample, the smaller the area of monodomain region will be. The desirable radius of the cavity is about 8 mm for thick ($\sim 80\text{-}\mu\text{m}$) samples. A sample was aligned between two plates by hand using the procedure of shearing and compression–dilation first described in reference 5.

The condition of a multilayer sample, that is, its degree of alignment (or mosaic) and its thermodynamic phase, can be rigorously determined by X-ray diffraction. Fortunately, for the purpose of aligning multilayers, the condition can also be determined qualitatively by visual inspection with a polarized microscope. This inspection is possible because the defect structures of the liquid crystalline L_α or smectic A phase of lipids have been classified and studied by polarization microscopy (5, 7–9). Indeed if a lipid sample is in the L_α phase, it is most conveniently ascertained by the appearance of smectic defects. The defects that are most disruptive to multilayer alignment are oily streaks. The most effective way to align a sample is to push (rather than dissolve) the oily streaks to the periphery. If polygonal array defects appear, either the heating and cooling process described in reference 4 can be used or the sample can simply be left at the L_α phase temperature for several days, in which case the defects usually anneal away.

For X-ray diffraction samples, the alignment is examined from the silica side by using a reflection polarizing microscope. X-ray diffraction was measured from the Be side. For electric field experiments, the silica plate is coated with indium tin oxide (ITO) to form a thin transparent electrode on the inside (10). For circular dichroism (CD) experiments, it is important to remove any possible stress in the silica plates. Stress removal can be accomplished by temperature annealing at 1150 $^\circ\text{C}$ for 6 h, followed by slow cooling at a rate of 10 $^\circ\text{C}/\text{h}$ down to 900 $^\circ\text{C}$ and subsequent cooling at a rate of 100 $^\circ\text{C}/\text{h}$ until room temperature is reached.

Thus far, we have aligned the following lipids: dilauroyl-, dimyristoyl-, dipalmitoyl-, diphytanoyl-, and dioleoylphosphatidylcholine (DLPC, DMPC, DPPC, DPhPC, and DOPC, respectively), dimyristoylphosphatidylglycerol (DMPG), dipalmitoylphosphatidylethanolamine (DPPE), L- α -phosphati-

dylcholine from bovine brain (BBPC), and DMPC-cholesterol mixtures. The peptides and proteins incorporated in multilayer samples include alamethicin, melittin, gramicidin, magainins, and their synthetic analogues.

It has been shown (2, 3, 11, 12) that both the bilayer structure and the state of a peptide in a multilayer preparation are the same as in a vesicle sample prepared from the same materials.

Method of Oriented Circular Dichroism

Theory. Ultraviolet circular dichroism (CD) spectroscopy has been used routinely in the analysis of the secondary structures of proteins. The principle of this diagnostic method is based on the experimental fact that the CD spectra (below 250 nm) of polypeptides and proteins are dominated by the electronic transitions of the peptide units and are relatively independent of side chains. The asymmetric and periodic arrangements of a polypeptide give rise to characteristic CD spectra. In particular, the α -helix conformation has a highly distinctive spectrum. According to the exciton theory of Moffitt (13) (*see* review of the theory in reference 6), the peptide π - π^* transition in an α -helix is split into components with polarization either perpendicular or parallel to the helix axis. This important theory is difficult to prove experimentally, because it is difficult to align a sample of α -helices. The use of long polypeptides in an electric field led to conflicting results (*see* review in reference 10), because the bending of long polypeptides was not taken into account. The theory was finally demonstrated experimentally by the use of membrane-spanning α -helices aligned in lipid multilayers. In particular, it was shown that the CD band of helices at 205 nm is polarized along the axis (6, 10). Thus we may summarize the ultraviolet CD spectra of α -helical peptides as follows (2, 14): Between 185 and 240 nm the peptide spectra are dominated by the π - π^* and n - π^* transitions. The n - π^* transition is characterized by a magnetic dipole transition moment directed along the carbonyl bond, which in a helix gives rise to a negative CD band near 224 nm that is approximately Gaussian. The π - π^* transition in a helix splits into three. One transition has its electric transition dipole polarized parallel to the helical axis and gives rise to a negative Gaussian band near 205 nm. The other two transitions have their electric transition dipoles polarized perpendicular to the helical axis, and their amplitudes strongly depend on the angle between the direction of the probing light and the helical axis. When the angle is 0° , these two transitions combine to have the shape of the derivative of a Gaussian centered near 190 nm with the positive amplitude on the long wavelength side, called the helix band (15). On the other hand, when the angle is 90° , the two transitions are degenerate, both positive Gaussians, and centered near 190 nm. Thus if the incident light is parallel to the helix axis,

its CD, G_{\parallel} , is given by two components (denoted by θ):

$$G_{\parallel} = \theta_{\pi \rightarrow \pi^*}(g_H, 190 \text{ nm}, \parallel) + \theta_{n \rightarrow \pi^*}(-g, 224 \text{ nm}, \parallel) \quad (1)$$

If the incident light is perpendicular to the helix axis, its CD, G_{\perp} is given by

$$G_{\perp} = \theta_{\pi \rightarrow \pi^*}(+g, 190 \text{ nm}, \perp) + \theta_{\pi \rightarrow \pi^*}(-g, 205 \text{ nm}, \perp) \\ + \theta_{n \rightarrow \pi^*}(-g, 224 \text{ nm}, \perp) \quad (2)$$

where, in the parentheses, the symbol g or g_H indicates that the band is a Gaussian or the helix form, respectively, and the sign in front of g stands for positive or negative amplitude; the second entry is the wavelength; and the third entry denotes whether the helix is parallel or perpendicular to the light.

The polarization of the 205-nm band (the Moffitt theory) can be used to determine the orientation of α -helices in a membrane. This determination is accomplished by the method of OCD; that is, the CD spectra of a multilayer sample are measured with light incident at various angles with respect to the normal of the membrane planes (1). Let the normal to the plane of the membrane be n (the sign of n is immaterial, as we will see), the direction of the probing light be k , and the angle between them be α . OCD is the CD spectrum as a function of α , $\theta(\alpha)$. The following equation is a general property of CD spectra (16):

$$\theta(\alpha) = \theta(0^\circ) \cos^2 \alpha + \theta(90^\circ) \sin^2 \alpha \quad (3)$$

Thus, $\theta(0^\circ)$ and $\theta(90^\circ)$ can be obtained by measuring $\theta(\alpha)$ at two different α angles. Suppose that helices are embedded in bilayers with their axes inclined at an angle ϕ with respect to the normal n and uniformly or randomly distributed in the azimuthal angles around n . Using the general property eq 3, we can show

$$\theta(0^\circ) = G_{\parallel} \cos^2 \phi + G_{\perp} \sin^2 \phi \quad (4)$$

$$\theta(90^\circ) = \frac{1}{2} G_{\parallel} \sin^2 \phi + G_{\perp} \left(1 - \frac{1}{2} \sin^2 \phi\right) \quad (5)$$

Equations 3–5 are the basis of OCD analysis.

Applications. We will discuss two possible applications of OCD.

Nonhelical Molecules. If there are no theoretical restrictions on G_{\parallel} and G_{\perp} , OCD can be used to distinguish a rotation of a molecule from a conformational change. (In this case G_{\parallel} and G_{\perp} are, respectively, the CD parallel and perpendicular to a molecular axis.) Suppose that the same protein molecules are prepared under two different conditions A and B, such

that the inclination angle ϕ is changed from ϕ_A to ϕ_B . The $\theta(0^\circ)$ and $\theta(90^\circ)$ for states A and B are given by

$$\theta_A(0^\circ) = G_{\parallel} \cos^2 \phi_A + G_{\perp} \sin^2 \phi_A \quad (6)$$

$$\theta_A(90^\circ) = \frac{1}{2} G_{\parallel} \sin^2 \phi_A + G_{\perp} \left(1 - \frac{1}{2} \sin^2 \phi_A\right) \quad (7)$$

$$\theta_B(0^\circ) = G_{\parallel} \cos^2 \phi_B + G_{\perp} \sin^2 \phi_B \quad (8)$$

$$\theta_B(90^\circ) = \frac{1}{2} G_{\parallel} \sin^2 \phi_B + G_{\perp} \left(1 - \frac{1}{2} \sin^2 \phi_B\right) \quad (9)$$

These four equations are not independent (even if one makes use of two or more CD bands at different wavelengths). The fourth equation is consistent with the other three. This is, of course, only true if the states A and B are related by a rotation. In other words, if states A and B represent two different conformations ($G_{\parallel A} \neq G_{\parallel B}$, etc.), the fourth equation will not be consistent with the other three. To test if states A and B are related by a rotation, one may assume an arbitrary value for ϕ_A and use three equations to solve for G_{\parallel} , G_{\perp} , and ϕ_B . Then the fourth equation is used to check for consistency. A positive result can be used as a proof that states A and B differ only by a rotation of the molecular axis. On the other hand, a negative result would indicate that a conformation change occurs between states A and B.

Another case of interest is that there are two (and only two) possible orientations for the molecular axis, and states A and B represent two different mixtures of the molecules in these two orientations. In this case, OCD will satisfy eqs 6–9. OCD cannot distinguish a two-orientation problem from a rotation problem (1).

Helices. Because the 205-nm band is polarized along the helix axis, OCD can be used to determine the orientation of helices. Assume that the 190- and 224-nm bands make negligible contributions to the CD amplitude at 205 nm. Then, from eqs 4 and 5, we obtain the approximate relation

$$\theta(0^\circ)_{205 \text{ nm}} / \theta(90^\circ)_{205 \text{ nm}} \approx \sin^2 \phi / \left(1 - \frac{1}{2} \sin^2 \phi\right) \quad (10)$$

from which the value for the inclination angle ϕ can be estimated. For a more exact analysis, decompose the spectra into the bands described in eqs 1 and 2. An example of such an analysis is given later for the channel-forming peptide, alamethicin.

CD of alamethicin associated with phospholipids shows a typical α -helical form. For example, CD of alamethicin with dilauroylphosphatidylcholine (DLPC) vesicles is shown in Figure 1 (1). If we assume that the mean residue ellipticity of α -helices is independent of the length of the peptide and compare the CD of alamethicin with that of a standard α -helix (e.g.,

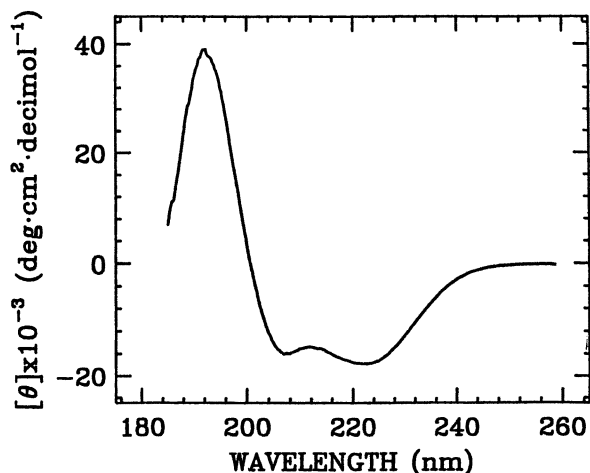


Figure 1. CD spectrum of alamethicin in DLPC vesicles. (Reproduced with permission from reference 6. Copyright 1988 American Institute of Physics.)

poly- γ -methyl-L-glutamate in hexafluoro-2-propanol; see reference 10), we conclude that about 40% of the residues of alamethicin are helical. However, the mean residue ellipticity depends on the length of the peptide when it is short. For example, synthetic α -helical peptides of 21 amino acids show a mean residue ellipticity of about -2×10^4 deg cm²/d at 224 nm (17), which is only about 60% of the standard value for long α helices. Therefore, in fact as much as 60–70% of alamethicin residues could be α helical. The nonhelical part of alamethicin apparently contributes little to the total CD (18). Thus the OCD of alamethicin in the membrane will reflect the orientation of its α -helical section.

Figure 2 shows two sets of OCD (I and S) for a multilayer sample of alamethicin in DPhPC with two different hydration conditions. (The technique of OCD measurement is described in reference 1.) Moffitt's theory predicts that the negative CD band near 205 nm consists of G_{\perp} components only; that is, $G_{\parallel} = 0$ for this band. Consequently, we expect the CD amplitude near 205 nm to obey the α -dependence

$$\theta(\alpha) = G_{\perp} \left[\sin^2 \phi + \left(1 - \frac{3}{2} \sin^2 \phi \right) \sin^2 \alpha \right] \quad (11)$$

In particular, for helices parallel to the membrane normal ($\phi = 0^\circ$), $\theta(\alpha)$ increases with $\sin^2 \alpha$, whereas for helices perpendicular to the membrane normal ($\phi = 90^\circ$), $\theta(\alpha)$ decreases with $\sin^2 \alpha$. Thus a visual inspection of the OCD (Figure 2) is sufficient to conclude that the inclination angle ϕ must be close to 0° for the spectra I and close to 90° for the spectra S.

A nonlinear least-squares program was written to fit the phenomenological expressions eqs 1 and 2 to the spectra of normal incidence ($\alpha = 0^\circ$) in

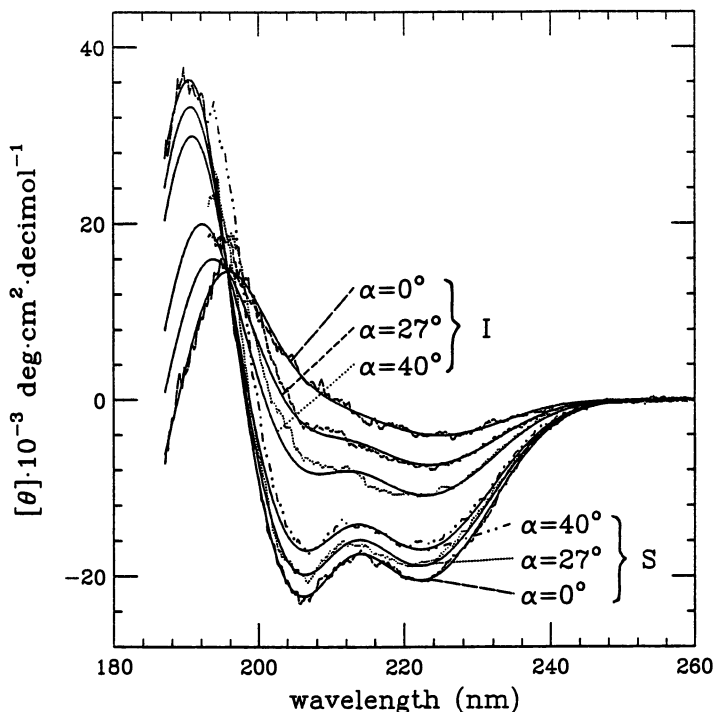


Figure 2. OCD of alamethicin in aligned multilayers of DPhPC ($L:P = 50:1$) when the sample is in equilibrium with 100% relative humidity (RH) (spectra I) and with 50% RH (spectra S). CD was measured with light incident at an angle α relative to the normal to the planes of bilayers. The α dependence of spectra I indicates that the helical parts of alamethicin molecules are perpendicular to the plane of the bilayer, whereas the α dependence of spectra S indicates that the helices are parallel to the plane of the bilayer. The solid lines for the $\alpha = 0^\circ$ spectra are the least-squares fits; the solid lines for the spectra of oblique angles are theoretical constructions from the $\alpha = 0^\circ$ spectra. (Reproduced with permission from reference 1. Copyright 1990.)

Figure 2. Each Gaussian band is assumed to have the form

$$g = A \exp \left[-(\lambda - \lambda_0)^2 / \Delta^2 \right] \quad (12)$$

with three parameters: amplitude A , peak position λ_0 , and bandwidth Δ . The helix band has the form (12)

$$g_H = A \left[2(\lambda - \lambda_0)(\lambda_0 / \Delta^2) + 1 \right] \exp \left[-(\lambda - \lambda_0)^2 / \Delta^2 \right] \quad (13)$$

also with three parameters. The 0° spectrum of the S state fits very well (see Figure 3) with three Gaussian bands as prescribed by the theory (eq 2) for helices perpendicular to the light. On the other hand, the 0° spectrum of the

I state would not fit well with a combination of Gaussian bands; instead it fits a combination of a Gaussian and a helix band (*see* Figure 4), exactly as predicted by the Moffitt theory (eq 1) for helices parallel to the light. The band parameters obtained from our fit (Table I) are in good agreement with the calculated values given by reference 19. Thus we showed that the spectrum I, 0° and spectrum S, 0° are indeed G_{\parallel} and G_{\perp} , respectively.

We completed the experimental proof for G_{\parallel} and G_{\perp} by constructing the right-hand side of eq 3 using eqs 4 and 5 with $\phi = 0^\circ$, $\alpha = 27^\circ$ and 40° , and comparing it with spectrum I, $\alpha = 27^\circ$ and 40° in Figure 2, respectively; similarly with $\phi = 90^\circ$, $\alpha = 27^\circ$ and 40° was compared with spectrum S, $\alpha = 27^\circ$ and 40° , respectively. We see that they are all in good agreement. Thus we have demonstrated the following two points:

1. The α -helical section is perpendicular to the plane of the membrane in state I and parallel to the plane of the membrane in state S.
2. There is no change in the secondary structure between states I and S because their spectra are related to each other by rotation.

Finally, we can also compare the OCD of a multilayer sample with the CD of a vesicle sample. Because the orientations of helices are isotropically

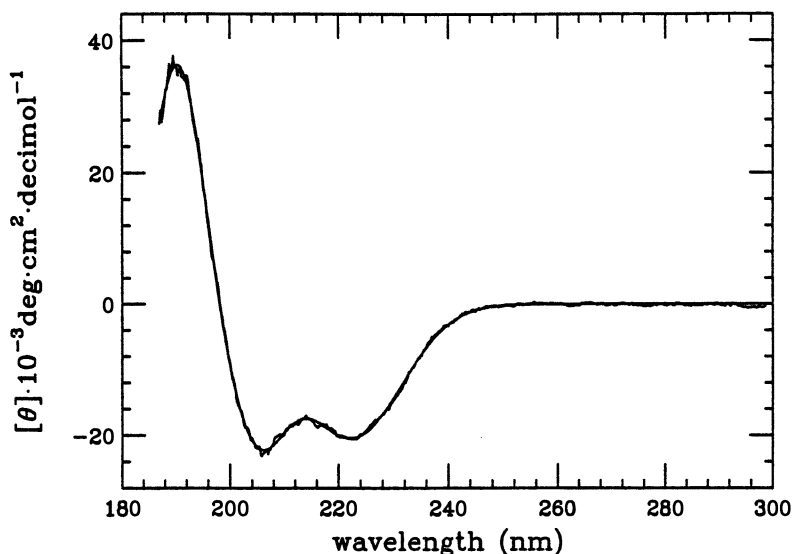


Figure 3. Spectrum S, $\alpha = 0^\circ$ of Figure 2 is fitted with eq 2. The band parameters are given in Table I. (Reproduced with permission from reference 1. Copyright 1990.)

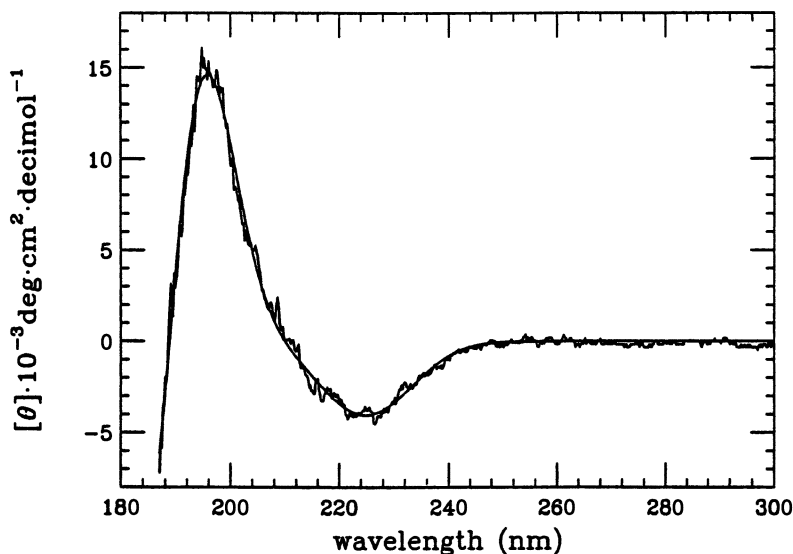


Figure 4. Spectrum I, $\alpha = 0^\circ$ of Figure 2 is fitted with eq 1. The band parameters are given in Table I. (Reproduced with permission from reference 1. Copyright 1990.)

Table I. Band Parameters for CD of α Helix

CD Band ^b	Band Center λ (nm)	Bandwidth Δ (nm)	Amplitude of Alamethicin A (10^{-3} deg cm ² /dmol)	Amplitude of α Helix ^a A (10^{-3} deg cm ² /dmol)
$n \rightarrow \pi^*$, helix $\perp k$ (g)	222.3	12.9	-20.37	-51
helix $\parallel k$ (g)	224.9	11.9	-4.04	-10
$\pi \rightarrow \pi^*$, helix $\perp k$ (g)	204.8	7.4	-18.65	-46
$\pi \rightarrow \pi^*$, helix $\perp k$ (g)	190.4	6.4	36.73	92
helix $\parallel k$ (g _H)	188.5	10.1	-0.95	-2.4

^a The mean residue ellipticity poly- γ -methyl-L-glutamate in hexafluoro-2-propanol solution is used as the standard CD for isotropically distributed α -helices. The CD of alamethicin in vesicles is compared to the standard, from which we estimate that 40% of the residues of alamethicin are helical. The numbers in the fifth column are the numbers in the fourth column divided by 40%.

^b g denotes a Gaussian band; g_H denotes a helix band.

SOURCE: Reproduced with permission from reference 1. Copyright 1990.

distributed in a vesicle sample, we can take, for example, $\phi = 0^\circ$ in eqs 4 and 5 (which give $\theta(0^\circ) = G_{\parallel}$ and $\theta(90^\circ) = G_{\perp}$) and average eq 3 over the solid angle $2\pi d(\cos \alpha)$ to obtain the CD for vesicles (θ_v):

$$\theta_v = \frac{1}{3}G_{\parallel} + \frac{2}{3}G_{\perp} \quad (14)$$

The spectrum constructed from G_{\parallel} and G_{\perp} agrees well with the measured vesicle spectrum (Figure 5) and proves that the secondary structure of alamethicin is essentially the same, whether the membranes are vesicles or multilayers.

How Does Alamethicin Associate with a Membrane?

Alamethicin is a natural peptide of 20 amino acids (produced by the fungus *Trichoderma viride*). Since the late 1960s, the channels formed by alamethicin in lipid bilayers have been studied as a model for voltage-gated ion channels (20; review in reference 21; see a fairly complete list of references in reference 2). Recently the alamethicin channels have been shown to be tension dependent (22). Although alamethicin is one of the best characterized channels, there is a long-standing controversy about which model best describes the experimental data.

Since the early 1970s, most investigators agree that alamethicin monomers form a water-filled conducting pore like the staves of a barrel, and this assumption is consistent with most ion conduction data (23–25). However, conduction experiments provided no clues for the nonconduction state, either

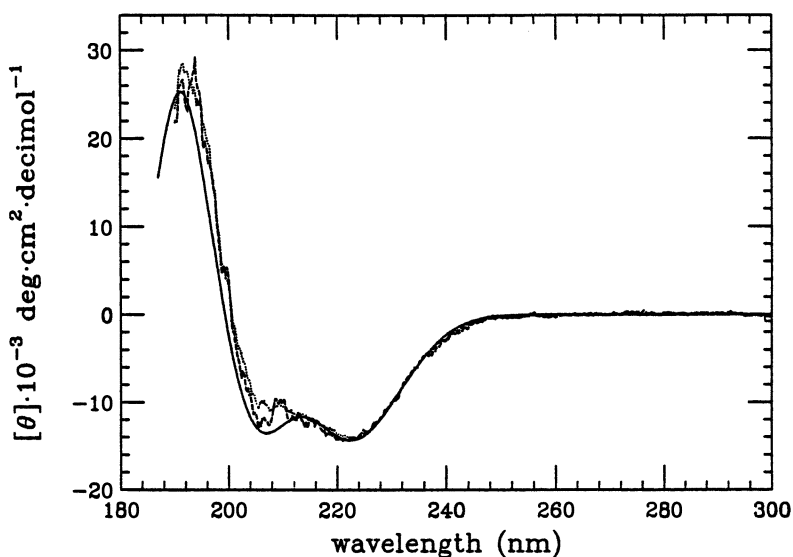


Figure 5. CD of alamethicin in DPhPC vesicles. The solid line is the construction (eq 14) from the OCD spectra of the multilayer sample (Figure 2). The dashed and dotted lines are the measured spectra of vesicles with 100:1 and 50:1 lipid-peptide ratios, respectively. (Reproduced with permission from reference 1. Copyright 1990.)

about the location of the molecule (relative to the membrane) or its configuration.

In the last 10 years, numerous spectroscopic and other methods have been used to study the nonconducting state. Such methods include Raman spectroscopy (26–28); ^1H , ^2H , and ^{31}P nuclear magnetic resonance (NMR) studies (27); infrared attenuated total reflection spectroscopy (29); alamethicin–phospholipid cross-linking studies (21); titration and stopped-flow analyses using circular dichroism (CD) and fluorescence to monitor the alamethicin–lipid interactions (30); capacitance studies (31); and studies of synthetic analogues (31–33). These studies led to many different conclusions. In particular, there are conflicting conclusions as to whether, in the absence of a transmembrane electric field, alamethicin partitions into the apolar region of a lipid bilayer or adsorbs to the lipid–water interface. Evidence for both interfacial interactions and alamethicin insertion into bilayers was found. Recent theoretical models (30, 32–35) have avoided the surface state of alamethicin.

We investigated this problem by OCD (2). Alamethicin–DPhPC multilayer samples at various peptide–lipid molar ratios (1:10–1:140) were prepared as previously described. The aligned multilayer samples were placed in a series of humidity chambers to be equilibrated at chosen relative humidities (RH) at room temperature. Samples obviously exchanged water with the environment through the gap between the two silica plates. Dependent on initial and final RH, the equilibration time for a sample varied from 4 to 20 days. The equilibrium states of the samples were examined by OCD. In most cases the samples exhibited spectra either like spectra I or like spectra S (Figure 2). Because spectra I represent helices perpendicular to the plane of the membrane, we call such a state the inserted (I) state. On the other hand, spectra S will be called the surface (S) state because they represent helices parallel to the plane of the membrane. Samples were either in the surface state or in the inserted state as shown in the RH versus L:P (the lipid–peptide molar ratio) phase diagram (Figure 6), unless a sample was near the phase boundary. Near the phase boundary the sample spectrum was a linear superposition of spectra I and S. Phase change reversibility was examined by exchanging two samples of the same L:P between difference humidity chambers across the phase boundary. During the transition, the spectra were linear superpositions of I and S, but once the samples reached equilibrium, the initial spectra were reversed. When a sample changed its state (i.e., underwent a phase transition), it took a longer time (up to 20 days) to reach equilibrium, if the final point was closer to the phase boundary. An equilibrium spectrum remained unchanged in time as long as the sample was kept in the same humidity chamber. The samples were examined under a polarized microscope each time a CD measurement was made. All the data points on the phase diagram are in the L_α phase of the lipid. Except for L:P less than 10:1, the lipid changes to the gel phase for RH below 89%.

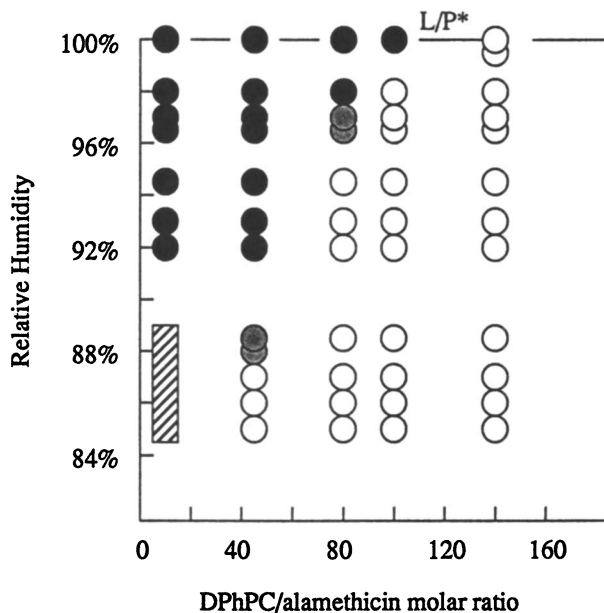


Figure 6. The phase diagram for alamethicin in DPhPC on the plane of relative humidity (RH) versus the lipid-peptide molar ratio (L:P). A multilayer sample of a certain L:P was in turn equilibrated in humidity chambers of various RH; in each equilibrium state, the OCD spectrum was measured. If the OCD spectrum is spectrum I (Figure 2), indicating that alamethicin is in the inserted state, a black circle is shown at the corresponding L:P and RH. If the OCD spectra are spectra S, indicating that alamethicin is in the surface state, an open circle is shown. A gray circle implies that the OCD spectra are linear superpositions of spectra I and S, which indicates that the state of alamethicin is a coexistent state. The shaded area for L:P = 10:1 indicates that the sample at RH below 89% turned into the gel phase. In all other data points, the samples were in the L_α phase. We define a critical L:P value L:P*. For L:P greater than L:P*, the majority of alamethicin molecules are in the surface state; for L:P smaller than L:P*, the majority of alamethicin molecules are in the inserted state if the sample is in equilibrium at 100% RH. (Reproduced with permission from reference 2. Copyright 1991.)

Thus we discovered a new phenomenon of phase transition for alamethicin in a membrane. The phase diagram (Figure 6) is characterized by a phase boundary that ends at a critical lipid:peptide molar ratio L:P* at 100% RH. If the lipid-peptide ratio is greater than L:P* (that is, at a low peptide concentration), alamethicin is always on the membrane surface in equilibrium. For L:P smaller than L:P*, alamethicin is always inserted in the membrane in equilibrium at 100% RH, but if RH is below the phase boundary, alamethicin is again on the membrane surface. Starting from the critical L:P*, the phase boundary decreases to lower RH for lower L:P.

This surprising property of alamethicin is not unique to the lipid DPhPC. Alamethicin behaves similarly in dioleoylphosphatidylcholine (DOPC) (Figure 7). Alamethicin in *L*- α -phosphatidylcholine from bovine brain (BBPC) at L:P \sim 50:1 also shows an I \leftrightarrow S transition as RH varies. Thus, these features appear to be the general characteristics of alamethicin in lipid membranes. In fact, our preliminary investigation indicates that amphipathic helical peptides may all have this property. Different combinations of peptide and lipid apparently have different values of critical L:P*.

Based on these observations, the conflicting reports about the state of alamethicin are understandable in terms of different investigators using different lipids, different lipid-peptide ratios, and different preparation procedures. (It is quite possible that some measurements were made before the samples reached equilibrium.)

In a typical conduction experiment, alamethicin molecules are partitioned between the aqueous phase and the lipid phase. In the lipid phase, the peptide-lipid ratio is usually several orders of magnitude smaller than the observed P:L*, so the majority of the membrane-associated alamethicin molecules are on the membrane surface, with perhaps a small fraction of them inserted in the bilayer. When a transmembrane potential is applied, the inserted molecules (and presumably the number of channels) increase because the free energy of the inserted state is decreased by the coupling of the

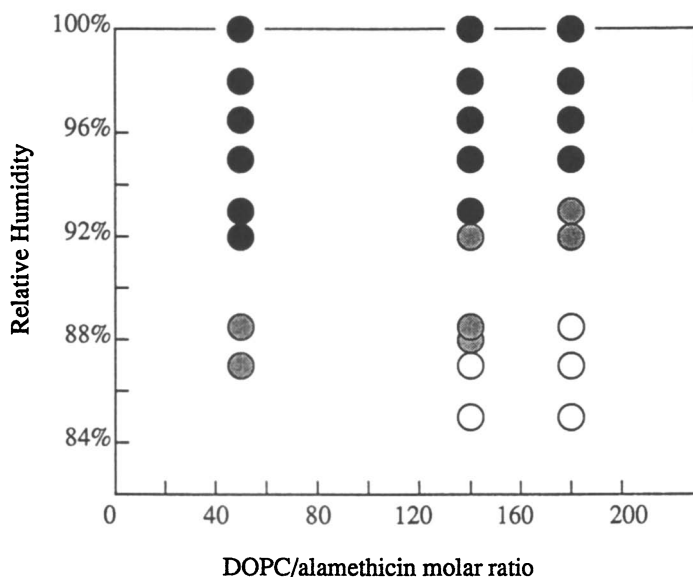


Figure 7. The phase diagram of alamethicin in DOPC. See Figure 6 for explanations. (Reproduced with permission from reference 2. Copyright 1991.)

peptide dipole with the electric field (2). This mechanism of voltage gating was in fact proposed a long time ago by Bauman, Mueller, and Boheim (21).

Location of Ion Binding Sites in the Gramicidin Channel by High-Resolution Lamellar Diffraction

There are two frequently used methods for X-ray diffraction of membrane systems. In one method, diffraction of an aligned, flat sample is performed with an oscillating camera. In another method, the membrane multilayers are aligned on a curved surface to produce powder patterns. The diffraction patterns obtained by these methods are sometimes intermediate between the pattern of a powder and that of a single crystal; consequently the Lorentz corrections for such patterns are ambiguous. Also, in the second method, it is difficult to make corrections for the sample absorption (this correction is necessary for the first two Bragg orders). We believe that an alternative method of single crystal diffraction (i.e., θ - 2θ scan) that uses well-aligned samples is advantageous for two reasons: (1) the above-mentioned difficulties are avoided and (2) high-resolution data are always produced. We used this single crystal diffraction method to solve a long-standing problem of the gramicidin channel (3), namely, where are its ion binding sites?

Gramicidin, a linear pentadecapeptide, is by far the most extensively studied membrane-active peptide that forms a transmembrane ion channel. The gramicidin channel is a cylindrical pore formed by two monomers, each a single-stranded $\beta^{6.3}$ helix, that are hydrogen-bonded head-to-head at their *N* termini (36, 37). The pore selectively facilitates the diffusion of monovalent cations across bilayer membranes, but does not transmit anions and divalent cations (38). Extensive kinetic data describe the effect on the channel conductivities of a great number of variables including amino acid variation, membrane variation, ion valence variation, and cation variation (38-40). The relatively simple structure and the wealth of experimental data on its ion conductions make gramicidin an ideal model system to study the principles governing ion transport across lipid membranes. Many molecular dynamics computations and simulations have been performed in an attempt to understand the detailed properties of the channel, such as the free energy profiles of ions, the hydrogen-bonding pattern of water, and the ion and water motions (41-43). Despite these extensive studies, there were no direct structural measurements on the gramicidin channel. It occurred to us that X-ray diffraction of well-aligned gramicidin-containing membrane multilayers might resolve the location of the ion binding sites in the channel (3).

That the channel has two monovalent cation binding sites is consistent with known experimental data (36, 38). Indeed, the binding constants for the first and second bindings of alkali metal cations have been estimated by TI^+ -205 chemical shift studies (44) and NMR relaxation methods (36). The

bindings of divalent cations were first inferred from the ability of the cations to reduce the fluxes of monovalent ions (38); further evidence was obtained from ^{13}C and ^{43}Ca NMR relaxation studies (36, 45). However, the locations of all these binding sites were unknown. An earlier study on ion-induced chemical shifts of carbonyl carbon NMR resonances by Urry and his collaborators concluded that two symmetric binding sites for monovalent cations are each localized between the Trp-11 and Trp-13 carbonyls of one monomer (36). However, this same evidence was also used to conclude that the gramicidin helix is left-handed—a conclusion contradicted by more recent NMR studies (37, 46).

The direct measurement of ion locations was performed by difference X-ray diffraction of gramicidin samples with various ions. Unlike the CD experiment, where the multilayer samples can be as thin as 1 μm or less, X-ray diffraction samples must be at least 10 μm . To align thick multilayers, it is essential to use two substrates. We know of no example of a thick ($>10 \mu\text{m}$) and large ($>10 \text{mm}^2$) single-domain multilayer preparation on one flat substrate without the help of a second surface. Furthermore, if multilayers are formed by evaporation or centrifugation of a vesicle solution (either method requires only one substrate surface), it would be difficult to control the ion concentration in the multilayers. On the other hand, finding a substrate suitable for alignment of multilayers as well as for X-ray transmission is not trivial either. The problem is accentuated by the fact that the first Bragg peak of membrane diffraction is about 1° , which means that the X-ray path length through the substrate will be 60 times the thickness. This problem shows why it is necessary to use a polished beryllium plate.

DLPC membranes were chosen for convenience because they are in the L_α phase at room temperature. Gramicidin–DLPC multilayer samples aligned between a polished Be plate and a silica plate produced high quality diffraction patterns. Typically eight Bragg orders were recorded (Figure 8), which is a very high resolution for DLPC membranes in the L_α liquid-crystalline phase. By the same method, 13 Bragg orders were recorded for dimyristoylphosphatidylcholine (DMPC)–cholesterol multilayers in the L_α phase (47), which represents the highest resolution ever recorded for such systems (11). Data reduction included (1) background subtraction; (2) corrections for polarization, the Lorentz factor, scattering volume, Be and specimen absorption, the second harmonic (which becomes significant due to the absorption by the Be plate) and the atomic scattering factors; and (3) the detector vertical slit correction for beam divergence and sample mosaic ($0.3\text{--}0.5^\circ$) (48).

The phases of Bragg reflections were determined by the swelling method. The reciprocal space is sampled by changing the lamellar spacing (or repeat distance) of the multilayers through the hydration variation. If the bilayer structure is unchanging or slowly changing with water content, the scattering amplitudes (whose phases are either 0 or π due to the centrosymmetry of

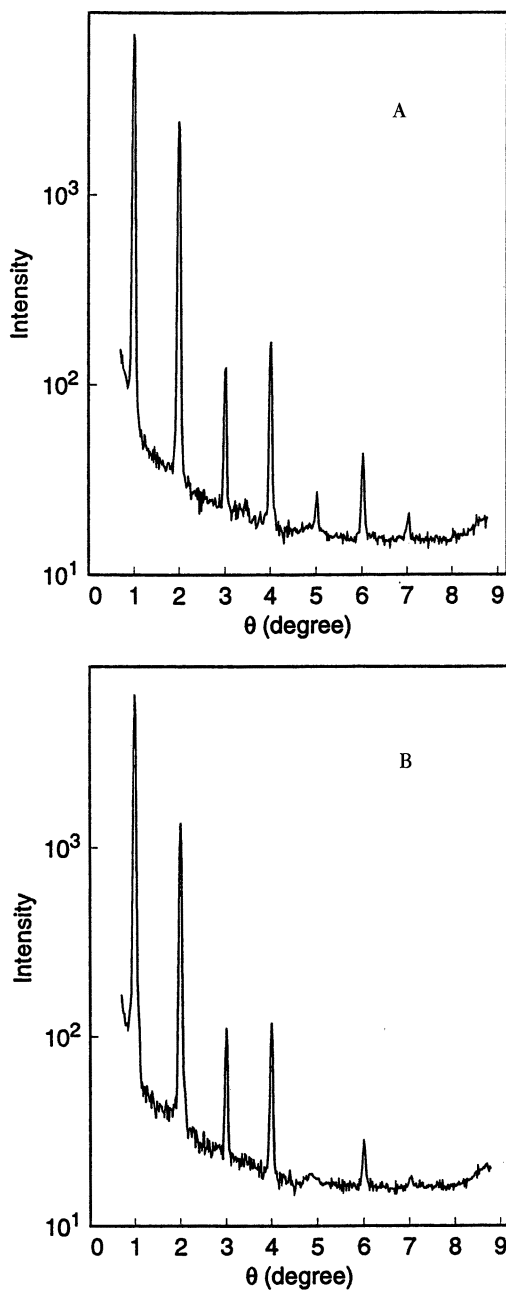


Figure 8. Our typical X-ray diffraction patterns of gramicidin-DLPC multilayers with thallium acetate, A, and without salt, B. Eight Bragg orders were recorded.

bilayer structures) will fall on a single smooth curve. Examples are given in Figure 9. Once the phases are determined, the structure factors are Fourier transformed to obtain the scattering density profiles. The scattering density profile can be normalized to the true electron density, ρ , if we know the composition of the sample and the molecular areas (along the plane of the membrane) of lipid and gramicidin (*see* the details in reference 3). Figure 10 shows the normalized electron density profiles of gramicidin-DLPC bilayers with Tl^+ (peptide-lipid-ion molar ratios 1:10:1), K^+ (1:10:1.5), and without salt (1:10:0).

A difference electron density profile is obtained from two ρ profiles that have the same lamellar spacing D . The top two curves in Figure 11 are two examples of the difference profile $\rho(\text{Tl}^+ \text{ sample}) - \rho(\text{salt-free sample})$ obtained from the data of 42.4- and 43.4-Å lamellar spacings. Each profile represents a measurement of the electron density distribution of Tl^+ . The distributions indicate that the majority of Tl^+ ions are bound inside the channels; each (dimeric) channel binds two Tl^+ ions according to the ion-gramicidin ratio. The peak positions indicate the locations of the Tl^+ binding sites; the width of the peak represents the resolution of diffraction, ~ 5 Å. We also calculated $\rho(\text{Tl}^+ \text{ sample}) - \rho(\text{K}^+ \text{ sample})$ which is shown as the bottom two curves in Figure 11. Because K^+ has a relatively small binding constant (44), excessive amounts of K^+ in the sample are considered necessary to ensure that the majority of the binding sites are occupied. As a result, about one-third or more of K^+ ions are outside the channel. Consequently the apparent peak positions of Tl^+ obtained from $\rho(\text{Tl}^+ \text{ sample}) - \rho(\text{K}^+ \text{ sample})$ are shifted slightly toward the center. Due to its unfavorable signal-to-noise ratio, the K^+ distribution profile was not analyzed further. The location of Tl^+ binding sites was determined solely from the difference profiles, $\rho(\text{Tl}^+ \text{ sample}) - \rho(\text{salt-free sample})$.

The locations of the two binding sites are symmetric with respect to the center. This is proven by the fact that, although both binding sites are occupied, there is only one sharp peak on each side of the center. (Because of the manner of sample preparation, if two sites were asymmetric, two peaks would appear on each side.) We measured the peak positions of the difference profiles $\rho(\text{Tl}^+ \text{ sample}) - \rho(\text{salt-free sample})$ obtained from using four different Tl^+ samples and three different salt-free samples, evaluated at various lamellar spacings. From the average, Tl^+ binding sites are determined to be at 9.6 ± 0.3 Å from the midpoint of the channel.

Figure 12 shows the profiles of the gramicidin-DLPC bilayers with Ba^{2+} (peptide-lipid-ion molar ratios 1:10:1) and Mg^{2+} (1:10:1) at 42.8-Å lamellar spacing. The central regions of the two profiles are essentially the same, but they are substantially different from the central regions of the monovalent cation samples and the salt-free sample, which are essentially the same in the central region (Figure 10). For this reason, we subtract the Mg^{2+} profile, but

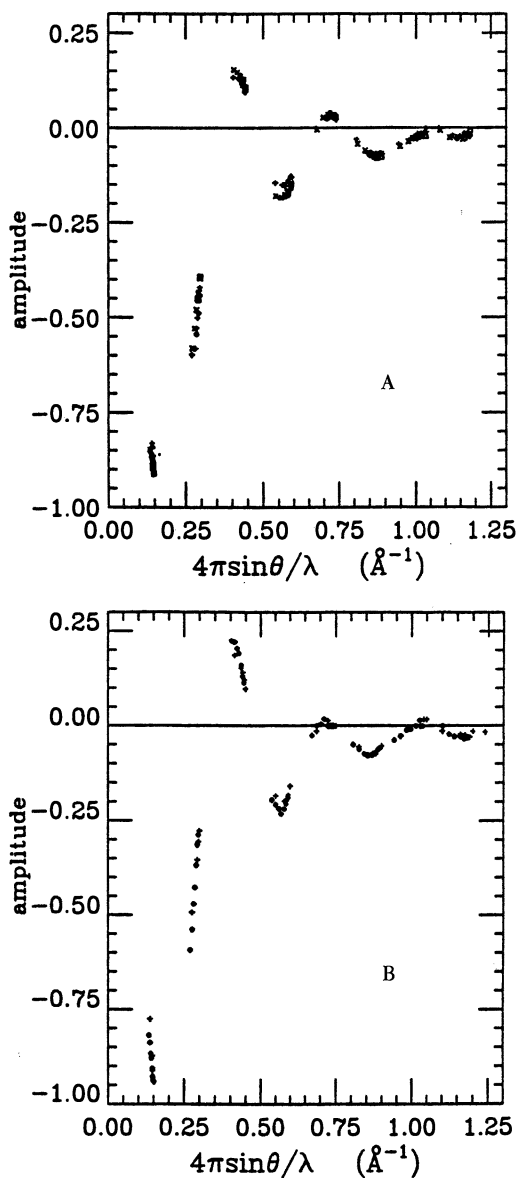


Figure 9. Structure factors obtained from H_2O swelling experiments for four different Tl^+ samples, A, and three different salt-free samples, B. Phases are chosen so that the data points fall on a single smooth curve. (Reproduced with permission from reference 3. Copyright 1991.)

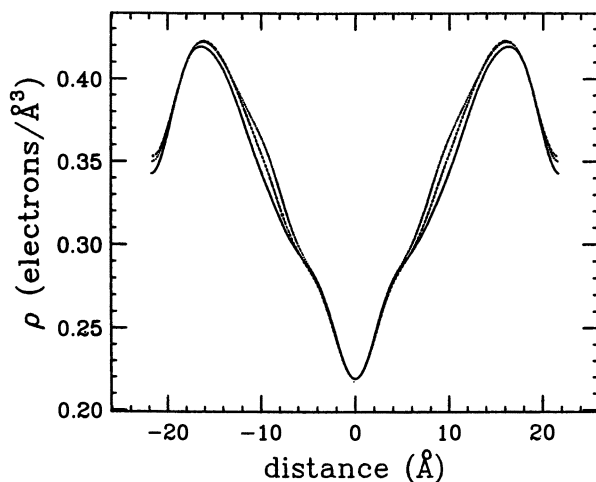


Figure 10. Normalized electron density profiles of gramicidin-DLPC bilayers with Tl^+ (dotted line), with K^+ (dashed line), and without salt (solid line), obtained from the structure factors of 43.4-Å lamellar spacing. (Reproduced with permission from reference 3. Copyright 1991.)

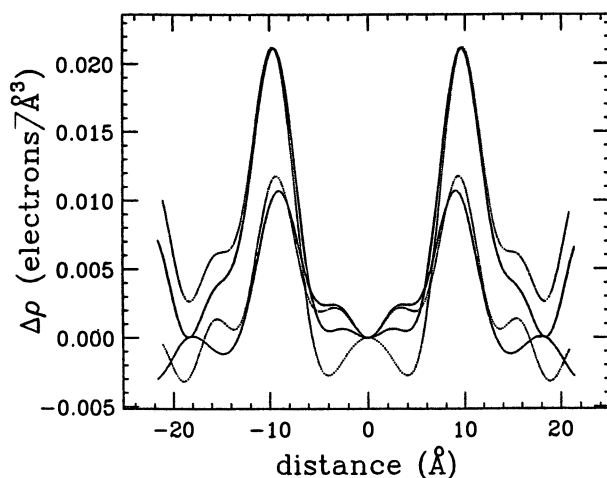


Figure 11. Difference electron density profiles. The top two curves are $\rho(\text{thallium sample}) - \rho(\text{salt-free sample})$. The bottom two curves are $\rho(\text{thallium sample}) - \rho(\text{potassium sample})$. Solid lines are obtained from the profiles of 43.4-Å lamellar spacing; dotted lines are obtained from 42.4-Å lamellar spacing. (Reproduced with permission from reference 3. Copyright 1991.)

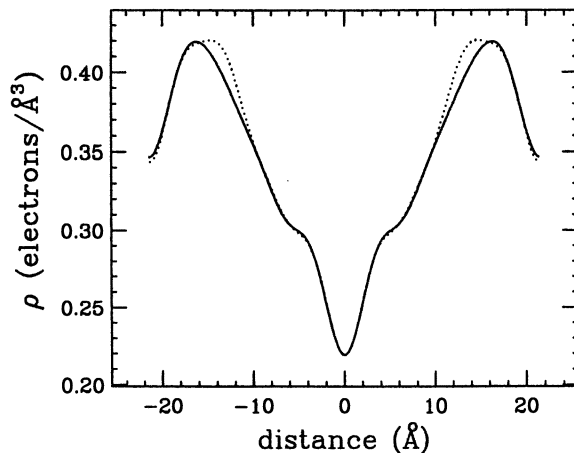


Figure 12. Normalized electron density profiles of gramicidin-DLPC bilayers with Ba^{2+} (dotted line) and with Mg^{2+} (solid line), obtained from the structure factors of 42.8-Å lamellar spacing. (Reproduced with permission from reference 3. Copyright 1991.)

not the salt-free profile, from the Ba^{2+} profile. However, unlike the case of $\rho(\text{Tl}^+ \text{ sample}) - \rho(\text{K}^+ \text{ sample})$, where there are excessive K^+ ions, we have equal numbers of Ba^{2+} and Mg^{2+} ions in the respective samples.

Figure 13 shows two examples of the difference profile $\rho(\text{Ba}^{2+} \text{ sample}) - \rho(\text{Mg}^{2+} \text{ sample})$ obtained from the data of 42.8- and 44.4-Å lamellar spacings. The sharp peaks indicate that Ba^{2+} ions are well localized. We measured the peak positions of the difference profiles $\rho(\text{Ba}^{2+} \text{ sample}) - \rho(\text{Mg}^{2+} \text{ sample})$ obtained from using four different Ba^{2+} samples and three different Mg^{2+} samples evaluated at various lamellar spacings. From the average, two symmetric Ba^{2+} binding sites are determined to be at 13.0 ± 0.2 Å from the channel midpoint.

Based on the $\beta^{6.3}$ helical structure of the gramicidin channel, it is quite natural to suggest that the ion binding site is on the first turn of the helix from the mouth (38). At the mouth of the channel, the last six carbonyls are hydrogen-bonded only to one neighbor. Three unbonded carbonyl oxygens are pointing toward the outside of the channel, as is the hydroxyl group of the ethanol amine tail. This cluster of negative charges seems to provide a binding site for cations. The surprising finding of our experiment is that the Tl^+ binding site, at 9.6 ± 0.3 Å from the channel midpoint, is either near the bottom of or below the first turn of the helix (49).

On the other hand, Ba^{2+} ions, at 13.0 ± 0.2 Å from the channel midpoint, apparently bind to the channel near the ends. This location is

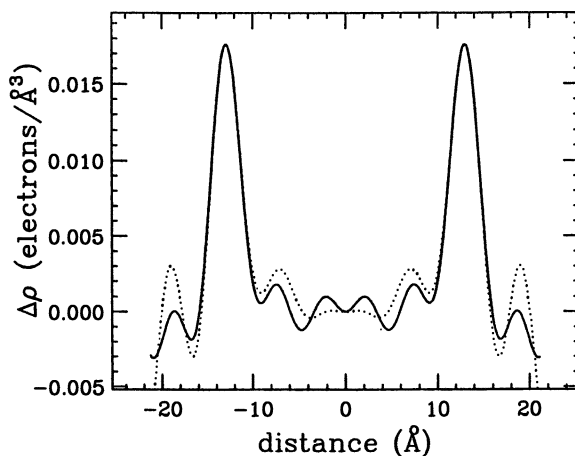


Figure 13. Difference electron density profiles $\rho(\text{barium sample}) - \rho(\text{magnesium sample})$ at 42.8- and 44.4-Å lamellar spacing. (Reproduced with permission from reference 3. Copyright 1991.)

consistent with the experimental observation that divalent cations do not permeate but block the channel (50). Thus we suggest that the separation between two opposite Ba^{2+} binding sites (i.e., 26.0 ± 0.4 Å) is a good measure for the length of the gramicidin channel. The molecular basis for the selectivity against divalent cations is probably straightforward. The gramicidin channel is a pore of 4 Å in diameter separated from the hydrophobic dielectric medium only by a single layer of polypeptide backbone. A cation entering the channel must overcome the channel dehydration energy (42) and encounters an image potential (51). Both the dehydration energy and the image potential are greater for divalent cations than for monovalent cations.

Our diffraction experiment revealed some other interesting properties of membrane-gramicidin interactions. It is well-known that a pure lipid bilayer changes its thickness with hydration (47). However, if the bilayers contain cholesterol at a sufficiently high concentration, this effect is absent (47 and references cited therein) and there is a tendency for the hydrocarbon thickness of the bilayer to match the thickness of a pair of cholesterol molecules (11). For this reason, cholesterol is called a membrane thickness buffer. Gramicidin is another membrane thickness buffer. In all our samples the phosphate peak-to-peak distances across the DLPC-gramicidin bilayers are virtually identical at 32.1 Å, irrespective of the degree of hydration. The assumption that the local hydrocarbon thickness of a lipid bilayer tends to match that of an embedded gramicidin channel was the basis of a previous study on the effect of membrane thickness on the gramicidin channel lifetime (38, 52, 53).

Acknowledgments

The research reported here was supported in part by the Office of Naval Research Grant N00014-90-J-1020, the Robert A. Welch Foundation, and the National Institutes of Health Biophysics Training Grant GM 08280.

References

1. Wu, Y.; Huang, H. W.; Olah, G. A. *Biophys. J.* **1990**, *57*, 797–806.
2. Huang, H. W.; Wu, Y. *Biophys. J.* **1991**, *60*, 1079–1087.
3. Olah, G. A.; Huang, H. W.; Liu, W.; Wu, Y. *J. Mol. Biol.* **1991**, *218*, 847–858.
4. He, K.; Ludtke, S. J.; Wu, Y.; Huang, H. W. *Biophys. J.* **1993**, *64*, 157–162.
5. Huang, H. W.; Olah, G. A. *Biophys. J.* **1987**, *51*, 989–992.
6. Olah, G. A.; Huang, H. W. *J. Chem. Phys.* **1988**, *89*, 2531–2537.
7. Asher, S. A.; Pershan, P. S. *J. Phys. (Paris)* **1979**, *40*, 161–173.
8. Asher, S. A.; Pershan, P. S. *Biophys. J.* **1979**, *27*, 393–422.
9. Schneider, M. B.; Webb, W. W. *J. Phys. (Paris)* **1984**, *45*, 273–281.
10. Olah, G. A.; Huang, H. W. *J. Chem. Phys.* **1988**, *89*, 6956–6962.
11. Franks, N. P.; Lieb, W. R. *J. Mol. Biol.* **1979**, *133*, 469–500.
12. Wilkins, M. H. F.; Blaurock, A. E.; Engelman, D. M. *Nature (London) New Biol.* **1971**, *230*, 72–76.
13. Moffitt, W. *J. Chem. Phys.* **1956**, *25*, 467–478.
14. Woody, R. W. In *The Peptides*; Udenfriend, S.; Meienhofer, J., Eds.; Academic: New York, 1985; pp 15–114.
15. Tinoco, I., Jr. *J. Am. Chem. Soc.* **1964**, *86*, 297–298.
16. Tinoco, I., Jr.; Hammerle, W. G. *Phys. Chem.* **1956**, *60*, 1619–1623.
17. Yang, J. T.; Wu, C.-S. C.; Martinez, H. M. *Methods in Enzymology* **1986**, *130*, 208–269; DeGrado, W. F.; Lear, J. D. *Biopolymers* **1990**, *29*, 205–213.
18. Nagaraj, R.; Balaram, P. *Biochemistry* **1981**, *20*, 2828–2835.
19. Woody, R. W. *J. Chem. Phys.* **1968**, *49*, 4797–4806.
20. Mueller, P.; Rudin, D. O. *Nature* **1968**, *217*, 713–719.
21. Latorre, R.; Alvarez, O. *Physiol. Rev.* **1981**, *61*, 77–150.
22. Opsahl, L. R.; Mak, D. D.; Webb, W. W. *Biophys. J.* **1990**, *57*, 321a.
23. Eisenberg, M.; Hall, J. E.; Mead, C. A. *J. Membr. Biol.* **1973**, *14*, 143–176.
24. Gordon, L. G. M.; Haydon, D. A. *Philos. Trans. R. Soc. London Ser. B* **1975**, *270*, 433–447.
25. Boheim, G.; Kolb, H. *J. Membr. Biol.* **1978**, *38*, 99–150.
26. Lis, L. J.; Kauffman, J. W.; Shriver, D. F. *Biochim. Biophys. Acta* **1976**, *436*, 513–522.
27. Banerjee, U.; Zidovetzki, R.; Birge, R. R.; Chan, S. I. *Biochemistry* **1985**, *24*, 7621–7627.
28. Knoll, W. *Biochim. Biophys. Acta* **1986**, *863*, 329–331.
29. Fringeli, U. P.; Fringeli, M. *Proc. Natl. Acad. Sci. U.S.A.* **1979**, *76*, 3852–3856.
30. Schwarz, G.; Gerke, H.; Rizzo, V.; Stankowski, S. *Biophys. J.* **1987**, *52*, 685–692.
31. Vodyanoy, I.; Hall, J. E.; Vodyanoy, V. *Biophys. J.* **1988**, *53*, 649–658.
32. Hall, J. E.; Vodyanov, I.; Balasubramanina, J. M.; Marshal, G. R. *Biophys. J.* **1984**, *45*, 233–247.
33. Menestrina, G.; Voges, K.; Jung, G.; Boheim, G. *J. Membr. Biol.* **1986**, *93*, 111–132.
34. Fox, R. O.; Richard, F. M. *Nature (London)* **1982**, *300*, 325–330.
35. Boheim, G.; Hanke, W.; Jung, G. *Biophys. Struct. Mech.* **1983**, *9*, 181–191.

36. Urry, D. W. In *The Enzymes of Biological Membranes*; Martonosi, A. N., Ed.; Plenum: New York, 1985; Vol. 1, pp 229–258.
37. Arseniev, A. S.; Barsukov, I. L.; Bystrov, V. F.; Lomize, A. L.; Ovchinnikov, Yu. A. *FEBS Lett.*, **1985**, *186*, 168–174.
38. Hladky, S. B.; Haydon, D. A. In *Current Topics in Membranes and Transport*; Stein, W. D., Ed.; Academic: New York, 1984; Vol. 21, pp 327–372.
39. Andersen, O. S.; Koeppe, R. E., II; Durkin, J. T.; Mazet, J.-L. in *Ion Transport through Membranes*; Yagi, K.; Pullman, B., Eds.; Academic: New York, 1987; pp 295–314.
40. Koeppe, R. E., II; Andersen, O. S. In *Proteins: Structure and Function*; (L'Italien, J. J., Ed.); Plenum: New York, 1987; pp 623–628.
41. Mackay, D. H. J.; Berens, P. H.; Wilson, K. R.; Hagler, A. T. *Biophys. J.* **1984**, *46*, 229–248.
42. Pullman, A. Q. *Rev. Biophys.* **1987**, *20*, 173–200.
43. Roux, B.; Karplus, M. *Biophys. J.* **1988**, *53*, 297–309.
44. Hinton, J. F.; Fernandez, J. Q.; Shungu, D. C.; Whaley, W. L.; Koeppe, R. E.; Millett, F. S. *Biophys. J.* **1988**, *54*, 527–533.
45. Urry, D. W.; Jing, N.; Trapane, T. L.; Luan, C.-H.; Waller, M. In *Current Topics in Membranes and Transport*; Hoffman, J. F.; Giebisch, G., Eds.; Academic: New York, 1988; Vol. 33, pp 51–90.
46. Nicholson, L. K.; Cross, T. A. *Biochemistry* **1989**, *28*, 9379–9385.
47. Olah, G. A. Ph.D. thesis, Rice University, 1990.
48. Saxena, A. M.; Schoenborn, B. P. *Acta Cryst.* **1977**, *A33*, 813–818.
49. Koeppe, R. E., II; Kimura, M. *Biopolymers* **1984**, *23*, 23–38.
50. Bamberg, E.; Läuger, P. J. *Membr. Biol.* **1977**, *35*, 351–375.
51. Parsegian, A. *Nature (London)* **1969**, *221*, 844–846.
52. Elliott, J. R.; Needham, D.; Dilger, J. P.; Haydon, D. A. *Biochem. Biophys. Acta* **1983**, *557*, 95–103.
53. Huang, H. W. *Biophys. J.* **1986**, *50*, 1061–1070.

RECEIVED for review January 29, 1991. ACCEPTED revised manuscript January 28, 1993.

Conformation and Mobility of Membrane Proteins in Electric Fields

I. R. Miller¹, V. Brumfeld¹, and R. Korenstein²

¹Membrane Department, The Weizmann Institute of Science, 76100 Rehovot, Israel

²Department of Physiology and Pharmacology, Tel Aviv University, Tel Aviv 69978, Israel

Electric fields affect the movement and the conformation of membrane proteins and channel forming polypeptides in the membrane. Diffusion potentials, created by a potassium concentration gradient across the membrane in the presence of valinomycin, affect the circular dichroism (CD) of bacteriorhodopsin reconstituted in lipid vesicles. The changes in CD indicate that the applied electric field, irrespective of its direction, decreases the helical fraction and increases the fractions of the random and β structures. Donnan potentials, created across the vesicular bilayer membrane by polyelectrolytes, are used to induce the conformational changes in alamethicin. The induced change of CD by the electric field across the membrane was not symmetrical with respect to the field direction. Tangential electric fields induce lateral movements of membrane components. The electrophoretic movement of photosystem I (PSI) along the membrane of hypotonically swollen thylakoid vesicles induced by low electric fields (40–80 V/cm) is studied by analyzing its electrophotoluminescence (EPL) from the different poles of the vesicle. The average apparent electric mobility, determined from the time course of the increase of EPL on the enriched hemisphere and of the decrease of EPL on the depleted hemisphere, was of the order of $3.10^{-5} \text{ cm}^2 / (\text{V s})$. The distribution of PSI reaches a steady state when the diffusional, electrostatic, and other counteracting forces balance the electrophoretic driving force. The electrophoretic mobility obtained from the steady state conditions

0065-2393/94/0235-0107\$08.54/0
© 1994 American Chemical Society

was only 5×10^{-7} cm²/s. The lateral diffusion coefficient was $\sim 5 \times 10^{-9}$ cm²/s, which was obtained from the diffusional relaxation after cessation of the electric field.

MEMBRANE PROTEINS ARE EXPOSED TO ELECTRIC FIELDS that are either normal or tangential with respect to the plane of the membrane. The fields perpendicular to the membrane plane, which are related to the membrane potentials, influence directly the biological activity of the membrane proteins including ion channel gating (1, 2) proton translocation (3), and enzymatic activity (4–6). The effect of membrane potential on the biological activity is assumed to be through its effect on the conformation of the membrane proteins. In spite of the plausibility of this assumption, only preliminary attempts have been made to demonstrate directly that the membrane potential does indeed affect the conformation of the membrane proteins (7, 8). In the case of voltage gating, the change in conformation is assumed to be minute; it consists of charge shifts within the channel formed by the protein (1, 2). Such a small conformational change hardly could be detected by spectral changes that involve the whole molecule. Despite these prevailing ideas, one has to be mindful that the very high fields of ~ 330 kV/cm or a membrane potential of 100 mV may affect membrane proteins with their large dipole moments. Transient conformational changes of charged (9) and noncharged polypeptides in solutions were induced by electric field pulses (10). The observed change was in the direction of the conformation with the higher effective dipole moment. The electric potential gradient across the membranes may affect the membrane protein either directly or by transferring sections of the membrane protein from the hydrophobic phase into the hydrophilic phase or vice versa.

The sporadic tangential electric fields that may originate along the surface of the membrane from surface reactions and result in local changes in charge are considerably weaker than the cross membrane fields; they may, however, suffice to mobilize other charged membrane components and serve as a means for lateral communication or signal transduction. In this respect, the protein complexes of the photosynthetic membrane are of special interest. The majority of thylakoid membrane proteins are organized in five integral membrane spanning complexes: photosystems I and II (PSI and PSII), light harvesting complex II, cytochrome b6-f complex, and adenosine triphosphate (ATP) synthetase complex (11). These proteins are responsible for coupled light harvesting, proton and electron transport, and ATP synthesis. Spatial segregation of PSI and PSII exists between the oppressed and the nonoppressed regions and, at the same time, PSI and PSII are functionally linked through the lateral mobility of plastoquinone and of plastocyanin.

However, under short-term environmental stresses (e.g., sudden increase in light intensity) there is a lateral redistribution of some of the complexes (12). The efficient conversion of light energy into electrochemical driving force by the multicomponent protein-complex system relies on the lateral interactions of the complexes. Thus, the understanding of the diffusional and the electrophoretic mobility of these components in the plane of the photosynthetic membrane is essential for the elucidation of the dynamic process and the mechanism of the photosynthetic process.

The lateral mobility of proteins and lipids in natural and artificial lipid bilayer membranes was determined by different methods. For long-range mobility, fluorescence recovery after photobleaching (13–15) and electrophoresis of membrane components (16) were employed. We employed the electrophoresis method for determination of the electrophoretic and diffusional mobilities of PSI in the plane of hypotonically inflated, spherical thylakoid vesicles. To monitor the redistribution of PSI particles, we made use of the spatial characteristics of the contribution of PSI particles to electrophotoluminescence (EPL) (17, 18). The contribution of PSII to EPL was eliminated by heat treatment of the chloroplasts (19). The EPL originates from the PSI particles at the hemisphere of the vesicles at which the induced electrical field destabilizes the photoinduced charge separation (18). The electrophoretic and diffusional mobilities were measured in vesicular suspensions to avoid immobilization for microscopic visualization (20). The photosynthetic membranes are devoid of cytoskeletal elements that might interfere with the lateral mobility.

Experimental Details

Reconstitution of Bacteriorhodopsin in Lipid Vesicles and Application of Diffusional Membrane Potential. Purple membrane fragments were obtained from *Halobacterium halobium* bacteria that were cultured according to Becher and Cassim (21) and then kept at -20°C . The purification of membrane fragments also was done according to the method of Becher and Cassim (21). The final absorption and circular dichroism (CD) spectra of the purified fragments were in good agreement with previous results (22, 23), which indicate a high degree of purity. The equivalent protein concentration of the stock suspension of purple membrane fragments was 1.8 mg/mL as determined from absorption data with an extinction coefficient corrected for scattering of $63,000\text{ cm}^{-1}\text{ M}^{-1}$ at 568 nm (24) and a molecular weight of 26,000 Da (25).

The purple membrane fragments that contained dark-adapted bacteriorhodopsin were used to form reconstituted vesicles with a mixture of phospholipids that contained 80% egg phosphatidyl choline and 20% bovine phosphatidylserine (Lipid Products, Nuttfield, England). The lipids in chloroform and methanol solutions were mixed to the desired composition, dried in a stream of nitrogen, placed in a 0.1-torr

vacuum for 3 h, and then vortexed in the buffer solution at a total concentration of 5 mg/mL. The lipid suspension was then sonicated in a circular bath sonicator (Laboratory Supplies Co.) until the suspension became clear.

The pure phospholipid dispersion was then mixed with purple membrane fragments to a final lipid concentration of 0.4 mg/mL and a protein concentration of about 0.045 mg/mL (a molar ratio of about 300 lipids per bacteriorhodopsin). The final mixture was frozen in liquid nitrogen and thawed. Large unilamellar vesicles ($\sim 0.12\text{--}0.3\ \mu\text{m}$) were obtained after a final short (1 min) sonication. The vesicle suspension was unaffected by centrifugation at speeds at which purple membrane fragments tend to precipitate.

The absorbance of bacteriorhodopsin at the experimental concentrations (40–50 mg/mL) varied between 0.6 and 0.8 in a 1-mm-thick cell at 198 nm, which allowed a correct CD measurement down to this wavelength. Transmembrane potentials were maintained by K^+ gradients across the membrane in buffer solutions (7) as follows.

Typical buffers were 2- or 20-mM phosphate (K_2HPO_4 and Na_2HPO_4) buffers with a 0.3-M K_2SO_4 (which will be called K buffer) or 0.3-M Na_2SO_4 (which will be called Na buffer). Some vesicles were prepared with K buffer (having inside 0.3-M K_2SO_4) and some with Na buffer (having inside 0.3-M Na_2SO_4). From each kind of vesicle, half were dialyzed against K buffer for 24 h at 4 °C and half against Na buffer under the same conditions. Finally, we obtained vesicle suspensions with high K^+ inside and Na^+ concentration outside, high Na^+ inside and high K^+ outside, and control suspensions having equal concentrations (either high Na^+ or high K^+) inside and outside. The diffusion potential was obtained by adding valinomycin ($10^{-7}\ \text{M}$) to both the samples. In the controls without ion gradient the CD was measured in the presence of 10^{-7}-M valinomycin.

Incorporation of Alamethicin into Lipid Vesicle Membranes and Generation of Donnan Potential Gradient across the Membrane. Alamethicin from *Trichoderma viride* was purchased from Sigma and used without further purification.

Small sonicated unilamellar vesicles were prepared from egg phosphatidyl choline (Lipid Products, Surrey, England) in a solution containing $2 \times 10^{-5}\text{-M}$ NaCl and 0.1-M glucose by sonication in a bath sonicator (Laboratory Supply Company, Hicksville, NY) until a clear dispersion was obtained. After vesicle preparation, small aliquots of alamethicin in methanol (10 mL) were added to $\sim 1.8\ \text{mL}$ of vesicle-containing solution. The final lipid concentration was 1 mg/mL and the final polypeptide concentration was 150 $\mu\text{g/mL}$. The polypeptide to lipid ratio was about 1:20. The Donnan potentials across the membrane were established as follows (8).

After 5 min, during which the alamethicin equilibrated with the lipid bilayer and its CD spectrum did not change, different amounts of 0.1 N (normality equals molarity in monomeric units) of degree of polymerization $\sim 100,000$, sodium polyacrylate (PA^-) solution were added. Free alamethicin in the presence of salt tends to interact with PA^- to form gels. Lack of gelation with added PA^- indicates that the alamethicin is incorporated into the membranes. The final polyacrylate concentrations were between 0 and 0.1 N. The concentrations of Na^+ and glucose added up to 0.1 M to maintain isotonicity. Due to the permeability of alamethicin channels to small ions, different polyacrylate concentrations resulted in different Donnan potentials across the membrane.

To reverse the field direction, we prepared big phosphatidyl choline (PC) vesicles by injection of PC solution in pentane into a solution containing 0.1-M sodium

polyacrylate. After vesicle formation, the polyacrylate from outside the vesicles was removed by treatment with excess (about 10 equivalent) anion exchange resin (Bio-Rad, Richmond, CA) for 4 h. The collected residue suspension was then centrifuged twice at 2500 g to remove the remaining resin. The final polyacrylate concentration outside the vesicles was measured by precipitation with CaCl_2 and by measurement of the light scattering at 350 nm of the resuspended precipitate. For calibration we used precipitates obtained from polyacrylate solutions at different concentrations.

CaCl_2 also induced a partial aggregation of the vesicles due to its interaction with lipids, which produced a background light scattering. To correct this background, we subtracted the scattering from vesicles in glucose solution without polyacrylate and with Ca^{2+} added. After the ion-exchange resin treatment, the vesicles were dialyzed for 12 h against solutions containing 2×10^{-5} M NaCl and 10^{-1} -M glucose or 0.03-M NaCl₂ and 0.04-M glucose. The alamethicin was added 10 min before any measurement. After the ion-exchange treatment, only 0.5-mg/mL phospholipid remained in the sample as determined by phosphate measurements. The remaining phospholipid was taken into account when alamethicin was added so that a 1/20 polypeptide to lipid ratio was obtained.

An alternative method to obtain a negative inside Donnan potential across the vesicular membrane involves preparation of the vesicles as in the first case (i.e., in glucose solution) and the addition of polyethylene imide (PEI^+) instead of sodium polyacrylate after incubation with alamethicin. The polyethylene imide concentrations, as well as the polypeptide to lipid ratio, were approximately equivalent to the polyacrylate.

The Donnan potential, $\Delta\psi$, was calculated from the Donnan equilibrium and fulfilled the requirement for electroneutrality where the anion and cation distribution between the inside and the outside of the vesicle is determined by the potential

$$\Delta\psi = \frac{RT}{zF} \ln \frac{a_{\text{out}}^+}{a_{\text{in}}^+} = \frac{RT}{F} \ln \frac{a_{\text{in}}^-}{a_{\text{out}}^-} \quad (1)$$

where a and z are the activity and charge of the permeable ionic species involved, R is the gas constant, T is temperature in kelvins, and F is the Faraday constant.

When we add different quantities of 0.1 N/ $\text{Na}_\nu\text{PA}^{\nu-}$ (where ν is the number of charges on the polyion) to the vesicular suspension prepared in salt concentration C (here $C = 2 \times 10^{-5}$ M) and 0.1-M glucose to maintain equal inside-outside osmotic pressure, the requirements of equilibration $[\text{Na}^+]_{\text{out}}[\text{Cl}^-]_{\text{out}} = [\text{Na}^+]_{\text{in}}[\text{Cl}^-]_{\text{in}}$ at electroneutrality demand a flux of neutral NaCl into the vesicles. The increase in osmotic pressure due to the increase in NaCl concentration in the vesicles is negligible and the vesicular volume remains constant. The Donnan potential at equilibrium then becomes

$$\Delta\psi = \frac{RT}{zF} \ln \frac{f[\text{PA}] + C - \Delta C}{C + (v_o/v_i) \Delta C} = \frac{RT}{zF} \ln \frac{C + (v_o/v_i) \Delta C}{C - \Delta C} \quad (2)$$

where $f = 0.2$, the PA^- counterion osmotic factor, or activity coefficient in the absence of salt, is taken to be the effective counterion contribution to the activity

(26–28) and $[PA^-]$ is the polymer concentration in monomeric units. ΔC is the decrease in salt concentration in the outer solution due to equilibrium after addition of the polyacrylate and it is calculated by equating the logarithmic terms. v_o/v_i is the outer to inner volume ratio (200) as determined from the measured internal volume and the lipid concentration. $\Delta\Psi$ was similarly calculated for PEI^+ outside the vesicles.

In the case when PA^- was inside the vesicles and the salt concentration was in the outer phase, C_o was obtained by equilibrium dialysis and the Donnan potential is given by

$$\Delta\Psi = \frac{RT}{zF} \ln \frac{f[PA^-] + \Delta C}{C} = \frac{RT}{F} \ln \frac{C}{\Delta C} \quad (3)$$

The equation of the membrane potential to the Donnan potential is an idealization that assumes that no segment of the polysalts penetrates the membrane.

Preparation of Thylakoid Vesicles. Broken (class C) chloroplasts from peas (*Pisum sativum*) and tobacco (*Nicotiana tabacum*) were prepared according to the method of Avron (29). The chloroplasts were resuspended in a medium containing 0.4-M sucrose and 10-mM tris(hydroxymethyl)aminomethane (Tris; pH 7.5), and stored at liquid nitrogen temperature in the same medium supplemented with 30% v/v of ethylene glycol (30). The chloroplasts (6-mg/mL chlorophyll) were heat inactivated for 3 min 51 °C and then diluted by 1:500 with a double-distilled water that was adjusted to pH 7.7 with Tris buffer. Large thylakoid vesicles were formed due to the swelling process under these hypotonic conditions. The size distribution of the thylakoid vesicles was determined as previously described (18).

Membrane Potential Determination by the Potential-Sensitive Fluorescent Dye 3,3'-Diethylthiadicarboxycyanine. The 3,3'-diethylthiadicarboxycyanine ($DisC_2$) dye (31) was obtained (from Molecular Probes Inc., Eugene OR) in methanol solution and was added to vesicle suspensions that contained ~ 0.2 -mg/mL lipid to a final concentration of 10^{-8} M. The fluorescence of the dye in the presence of lipids was about half that observed in the absence of lipids. The cationic dye is sensitive to potentials that are negative inside and it interacts with negatively charged surfaces and polymers; it was used only in compliance with these conditions. Moreover, because of these interactions the quantitative values of the results are in some doubt. It was very useful to follow the kinetics of the development of the potential across the membrane as the Donnan equilibrium was established. The negative potential inside the vesicles indicated by fluorescence quenching was maintained by the positive Donnan potential in the outer phase that contained the added PEI^+ (polyethylene imine). The rate of progress toward Donnan equilibrium and establishment of the membrane potential (increase in F_o/F) increases with increasing concentration of added alamethicin (Figure 1).

CD Measurement. The CD spectra were obtained with a spectropolarimeter (JASCO 500) using a 0.2-mm path length cylindrical cuvette. At least 16 scans between 190 and 200 nm at a scan speed of 20 nm/mm were performed during each

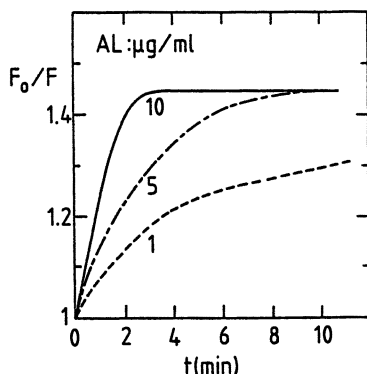


Figure 1. Time dependence of fluorescence quenching of the potential-sensitive dye DisC_2 in the presence of 0.1-mg/mL CD vesicles in $2 \times 10^{-5}\text{-M}$ NaCl upon addition of 0.1-M PEI⁺ and different amounts of alamethicin to the outer phase. The excitation wavelength was 620 nm and emission wavelength was 670 nm. (Reproduced with permission from reference 8. Copyright 1990 Elsevier.)

measurement. No scattering corrections were necessary because all measurements were performed on small vesicles, which do not distort the CD spectra of protein (32).

Electrophotoluminescence Measurements. Electrophotoluminescence (EPL) measurements were performed as described previously (15). Voltage pulses were applied by a pair of parallel stainless steel electrodes with an adjustable gap. The experimental protocol consisted of preillumination with a 120-ms light pulse filtered by a Corning 4-96 glass (approximate wavelength band 390–600 nm). After a dark time of 10 ms, the external electric field pulse was applied and the resulting luminescence, filtered by a cutoff filter (Schott RG 665), was monitored on a fast oscilloscope (Tektonix 2403A) interfaced to a compatible computer (IBM PC). In all cases the amplitude of a particular EPL signal was taken at its maximum.

Before opening the illumination shutter, we applied a long electric prepulse on the same electrodes that are used for the electric stimulation of luminescence. Thus, we were able to study the effect of an electric prepulse on the EPL signal. To avoid electrode polarization, the electrophoretic driving force consisted of a train of 1-ms-long electrical pulses at a relatively high frequency (usually 200 pulses/s). To detect possible polarization of the electrodes, we continuously monitored the current shape and amplitude produced during the prepulse.

The prepulse amplitudes generally used were 40, 60, and 80 V/cm. To determine the electrophoretic mobility, the vesicle suspension (0.8 mL) was inserted into a 1-cm path length spectrophotometric cell that contained the parallel electrodes spaced 2 mm apart and equilibrated at 10 °C, and the reference EPL of nonexposed vesicles to the prepulse was measured. After the exposed samples were allowed to equilibrate in the dark for 60 s, a train of 1-ms prepulses, 4 ms apart, was applied for time periods 1–8 s. Following the prepulse the new EPL amplitude was measured. The amplitude of the EPL in the direction of the prepulse and opposite to it, as shown in Figure 2, was studied as a function of the length of the prepulse and its amplitude.

The back diffusion from the enriched to the depleted hemisphere was determined by measuring the EPL from the two hemispheres at different times after prepolarization by 6–8-s prepulse trains. All the experiments were carried out in normal low-viscosity and high-viscosity media achieved by 4% 500-kDa dextran

(Sigma, St. Louis, MO) in the solution. The results were not affected by the higher viscosity, which indicates that the mobility is determined by the membrane viscosity only and that even for the low-viscosity medium the rotational diffusion of the whole vesicles is too slow to affect the results.

Results

Electric Field Effect on CD of Bacteriorhodopsin. Figure 3 shows the effect of valinomycin on the far UV CD spectra of the bacteriorhodopsin in lipid vesicles. In the presence of a potential gradient, irrespec-

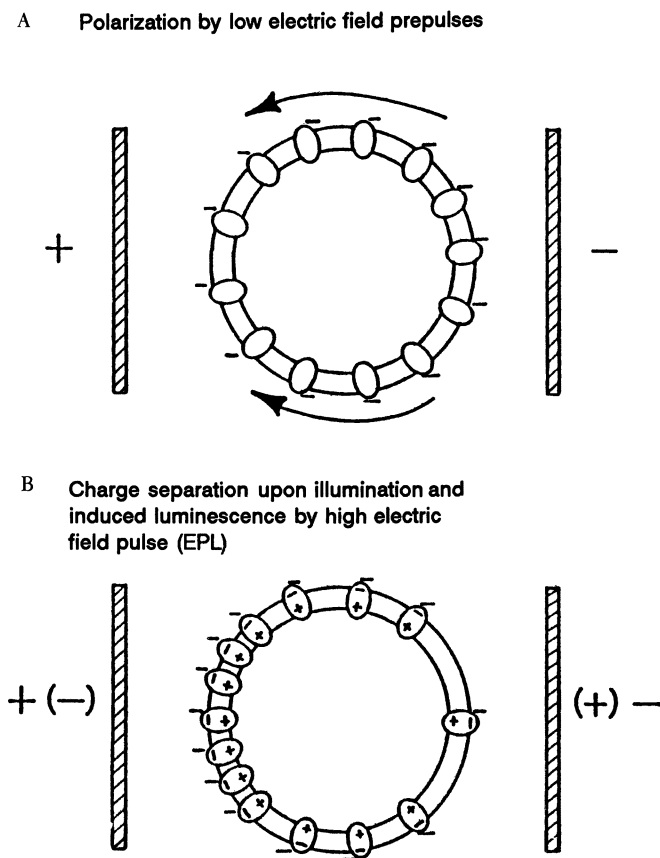


Figure 2. Scheme of the experimental procedure. A, Electrophoretic propagation of PSI particles along the surface of the vesicle that causes accumulation on one pole and depletion on the other one. B, EPL from the depleted or the enriched (electrode signs in brackets) hemispheres. (Reproduced with permission from reference 20. Copyright 1989 Biophysical Society.)

C EPL traces

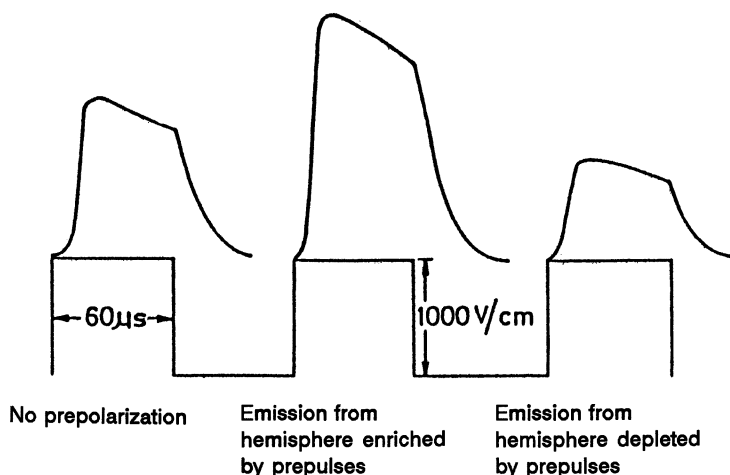


Figure 2. —Continued. C, EPL traces without prepulse (left), from the enriched hemisphere (middle), and from the depleted hemisphere (right).

tive of direction (with high K^+ inside and high Na^+ outside or with high Na^+ inside and high K^+ outside), the CD signal at ~ 210 nm is smaller in the presence of valinomycin than in its absence. The contribution of valinomycin at 10^{-7} M on the CD spectra is small and is taken into account by deducting the change in the CD spectra of the controls with equal ionic composition on both sides of the membrane, upon addition of 10^{-7} -M valinomycin.

Preparation and dialysis of the vesicles in buffers that contained 20-mM K_2HPO_4 and NaH_2PO_4 instead of 2 mM, which produced smaller concentration ratios of K^+ across the membrane yielded results that were similar, but the effects were smaller. Figure 4 shows the effect of the electrical potential on the CD intensity of bacteriorhodopsin reconstituted vesicles. The potentials on the abscissa are calculated assuming unity for K^+ transport number; the sign refers to the polarity of the interior of the vesicles.

The potentials inferred from fluorescence potential-induced quenching of 3,3'-diethylthiodicarbocyanine iodide are smaller than the potentials computed assuming the Nernst potential.

In Figure 3 the CD spectra in the presence and in the absence of valinomycin as well as the difference spectra are presented. The corrected difference spectra obtained by subtraction of the difference spectrum in the absence of an ion gradient (Figure 3b and d, curves $\Delta\theta$) from the difference spectrum in the presence of an ion gradient (Figure 3a and c, curves $\Delta\theta$) are also presented [Figure 3a and c, curves $\Delta(\Delta\theta)$]. Taking into account the accumulated error, the values of $\Delta(\Delta\theta)$ are reliable within 10–15% through

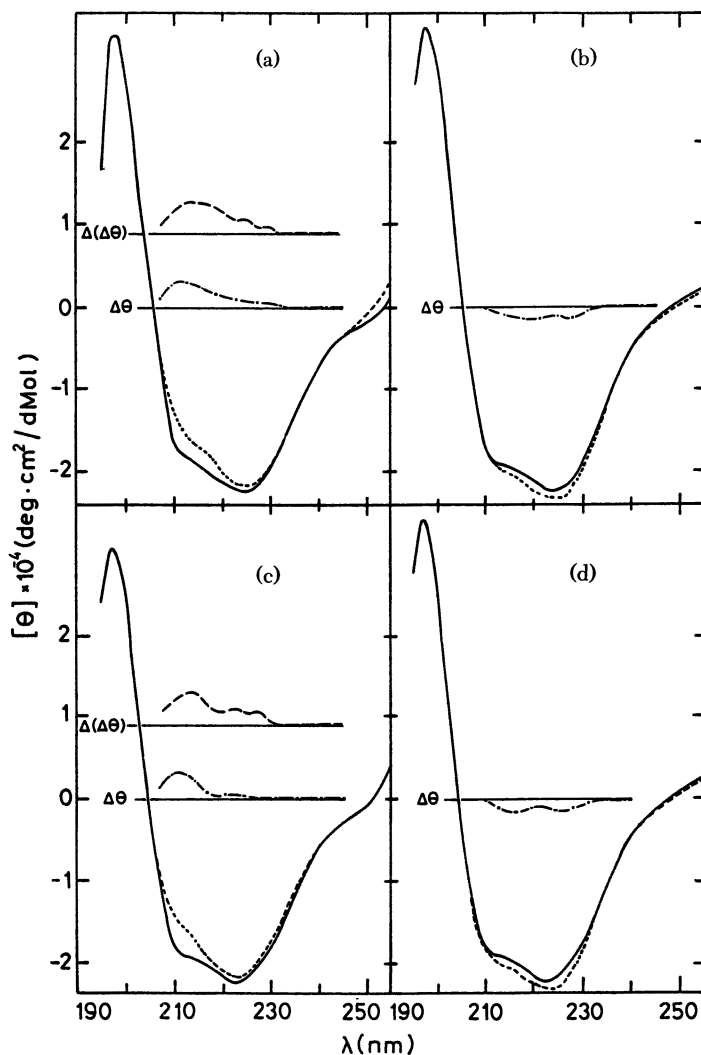


Figure 3. CD spectrum of bacteriorhodopsin reconstituted vesicles in the far UV region. The lipid protein weight ratio is $\sim 10:1$. a, Inside 0.6-M MK^+ ions and 2-mM Na^+ ions; outside 0.6-M Na^+ ions and 2-mM K^+ ions. b, 0.6-M K^+ ions outside and inside. c, Inside 0.6-M Na^+ ions and 2-mM K^+ ions; outside 0.6-M K^+ ions and 2-mM Na^+ ions. d, 0.6-M Na^+ ions outside and inside. Solid lines denote without valinomycin; dotted lines denote with valinomycin. Curve $\Delta\theta$ shows differences between valinomycin and valinomycin-free spectra. Curve $\Delta(\Delta\theta)$ shows differences between the difference spectra in a and b (respectively, in c and d) that show the total field effect. The combined error was < 500 (deg cm^2)/ dmol at 210 nm. (Reproduced with permission from reference 7. Copyright 1988 Biophysical Society.)

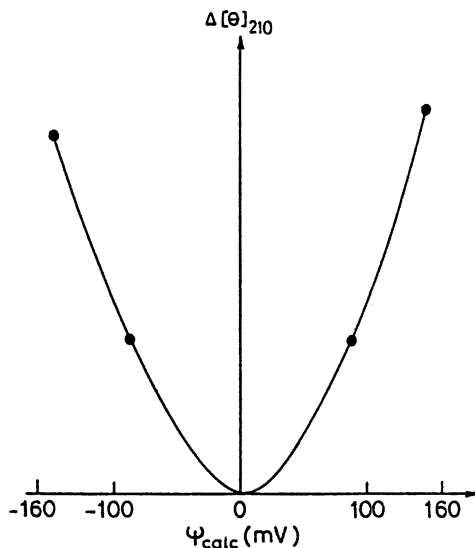


Figure 4. The dependence of the ellipticity of bacteriorhodopsin reconstituted in vesicles on the electric diffusion potentials. The ordinate is the decrease of the CD signal at 210 nm induced by 10^{-7} -M valinomycin. The abscissa is the electrical potentials calculated by the Nernst equation. The sign indicates the polarity inside the vesicle.

most of the range. The decrease of the negative ellipticity between 205 and 235 nm indicates that the applied membrane potential, irrespective of its direction, decreases the helicity of the protein. For this evaluation, we used fitting methods that employ the basis spectra for the α helix, random coils, and β forms presented either by Chen et al. (33) or by Chang et al. (34). The CD spectra of the bacteriorhodopsin reconstituted in vesicles without any diffusion potential nearly agreed with the published spectra of the protein reconstituted in dimyristoyl phosphatidylcholine (DMPC) (17). The spectra of bacteriorhodopsin embedded in lipid vesicles differ to some extent from those in purple membrane fragments because of the difference in the scattering and the consequent optical flattening (7). Using a nonlinear least squares technique with basis spectra from Chen et al. (33), we got 74% α helix and 17% random coil without any field and only 67% α helix and 26% random coil when the field, regardless of polarity, is applied. Using the basis spectra from Chang et al. (34), we obtained 68% α helix, 23% β sheets and β turns, and 9% random coil without applied electrical field. Analysis of the modified spectra with applied Nernst potential of 146 mV and irrespective of the field direction yielded 61% α helix, 24% random coil, and 15% β and β structure.

Electric Field Effect on CD Spectra of Alamethicin Added to PC Vesicles. The ellipticity of alamethicin at 208 nm in methanol is approximately twice that in aqueous solution (5). When lipid vesicle are added to the aqueous solution, a greater than twofold increase in ellipticity is observed at ~ 223 nm from 7×10^3 to about 17×10^3 (deg cm^2)/dmol. The ratio of the ellipticities at 222 and at 208 nm depends on the local alamethicin concentration or on the alamethicin to lipid ratio (35, 36). Sodium polyacrylate has a small effect on the CD spectrum in an aqueous solution but no effect at all in the presence of vesicles if there is no membrane potential (8).

Figure 5a shows the CD spectra of alamethicin for different electric potentials either positive inside the vesicles (polyacrylate added to vesicles with low salt content and with alamethicin embedded in the membrane) or positive outside (PA^- in the vesicles). When the polyacrylate concentration outside increases, we may notice the decrease in the absolute value of the CD signal at 220 nm and the appearance of a shoulder at shorter wavelengths. When the potential is positive outside of the vesicle, the effect is reversed; that is, the CD band at around 220 nm is increased. The effect does not

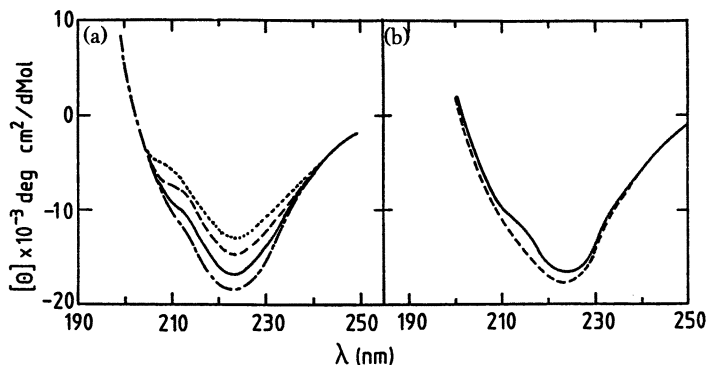


Figure 5. *a*, CD spectra of alamethicin embedded in PC vesicles prepared in 2×10^{-5} -M NaCl (alamethicin concentration $150 \mu\text{g}/\text{mL}$; lipid concentration $1 \text{ mg}/\text{mL}$; polypeptide to lipid molar ratio 1:20) in the presence of added or entrapped PA^- . The solid line indicates no PA^- (identical spectra were obtained with 0.1-M PA^- inside the vesicles and 0.1-M NaCl outside; Donnan potential $\approx 2 \text{ mV}$); the dashed line indicates 0.03-M PA^- outside the vesicle; the dotted line indicates 0.1-M PA^- outside the vesicles; the dash-dot line indicates 0.1 PA^- inside the vesicles. PA^- outside exchanged for Cl^- and dialyzed against 2×10^{-5} -M NaCl and 0.02-M glucose. *b*, CD spectra of polyethylene imide-affected alamethicin vesicles. The solid line indicates $150\text{-}\mu\text{g}/\text{mL}$ alamethicin embedded in PC vesicles prepared in 2×10^{-5} -M NaCl (lipid concentration $1 \mu\text{g}/\text{mL}$); the dashed line indicates the same vesicles with 0.1-M polyethylene imide added to the outer phase. (Reproduced with permission from reference 8. Copyright 1990 Elsevier.)

depend on the way the field is created, namely, by PA^- in the vesicles or polyethylene imide (PEI^+) in the outer phase, as shown in Figure 5b.

Figure 5b shows the PEI^+ effect on the CD spectra: increasing helicity at 222 nm with increasing concentration. Cascio and Wallace (35) showed that the CD spectra depend on the lipid to alamethicin ratio. The effect of potential on the CD spectrum remained practically the same when the lipid to alamethicin molar ratio was changed within an order of magnitude. The similarity of the results in Figure 5a and b indicates that the conformation of alamethicin is a function of membrane potential and its direction only, irrespective of the experimental condition under which the potential has been generated.

In Figure 6, the change in ellipticity, $\Delta\theta$, is presented under different experimental conditions as a function of the calculated transmembrane potential. The experimental points obtained under the different conditions are a continuous curve. Table I shows the secondary structure calculated from the ellipticity at different potential differences across the membrane. The evaluation of the alamethicin conformation was performed similarly to that of bacteriorhodopsin under the influence of electric field, namely, by fitting the basis spectra for a helix, random coil, and β forms presented either by Chen et al. (33) or by Chang et al. (34). There is a trend toward β structure as the positive inside potential increases and toward helicity at opposite polarity.

The quantitative estimates presented in Table I are to be taken with caution because the ellipticity-conformation relation derived for globular proteins is probably not fully applicable to alamethicin that contains 8 α -aminoisobutyric acids (aibs) out of 20 amino acids. The aib residues,

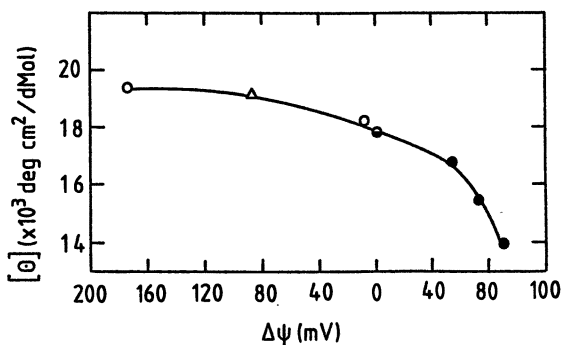


Figure 6. The molar ellipticity of alamethicin as a function of Donnan potential calculated from eq 2. The experimental points were obtained by PA^- addition outside the vesicles (\bullet), by preparing the vesicles with 0.1-M PA^- and then dialyzing against NaCl (\circ), or by adding PEI^+ outside the vesicles (Δ). See text for details about generating the electric field. (Reproduced with permission from reference 8. Copyright 1990 Elsevier.)

Table I. Alamethicin Conformation at Different Membrane Potentials

$\Delta\Psi$	θ (deg cm ²)/dmol	α helix	β structure	β turn	Unordered (%)
89	12,900	48	40	3	9
72	14,400	63	16	5	16
55	15,700	68	13	4	15
0	16,800	74	8	5	12
-89	18,100	79	10	6	5
-173	18,400	81	8	5	6

NOTE: The polarity corresponds to the inner phase of the vesicles.

particularly near the C terminal (35, 37) tend to form a less dichroic 3^{10} helix rather than a α -helix, and thus the helicity derived from the measured ellipticity may be underestimated. Moreover, depending on direction, the transmembrane electric field may help to insert the polypeptide into the lipid bilayer with concomitant aggregation and pore formation (38) or to extract it. Thus, it may modulate the environmental effect on polypeptide conformation. Enhanced insertion of alamethicin into the membrane is equivalent to an effective increase in the polypeptide to lipid ratio that brings about an increase in ellipticity around 223 nm.

Mobility of PSI in the Plane of the Vesicular Thylakoid Membrane. Figure 7 shows the relative change in EPL and their dependence on prepulse amplitude, duration, and polarity. The relative change in EPL is defined as the difference between the EPL in the presence of the prepulse (EPL) and in its absence (EPL₀), divided by EPL₀. For parallel polarization, (i.e., the same polarities of the prepulse and the luminescence stimulating pulse) we observe a decrease in the EPL, whereas the EPL increases with the prepulse when polarization is in the antiparallel direction. These effects increase with the prepulse duration until saturation is approached. The saturation time decreases as the field strength increases and varies from integrated polarization time of ~ 0.5 s at 60 V/cm to ~ 0.8 s at 40 V/cm. Taking into account that PSI has to move a distance of the order of 10^{-3} cm during this time (average particle diameter of 10^{-3} cm), we obtain values of the order of 3×10^{-5} cm²/(V s) for the electrophoretic mobility.

The EPL signal increases with the amplitude of the prepulse up to 60 V/cm. At ~ 80 V/cm a maximal effect is observed, after which increasing the prepulse amplitude causes decrease in the relative change of the EPL. This observation may suggest that at high fields the electrophoretic currents induce convective surface turbulence that abolishes the concentration gradients or that long exposure to these fields induces some electroporation. This phenomenon seems to start at approximately 80 V/cm. Figure 8 shows that a fivefold increase in the aqueous viscosity does not affect the electrophoretic

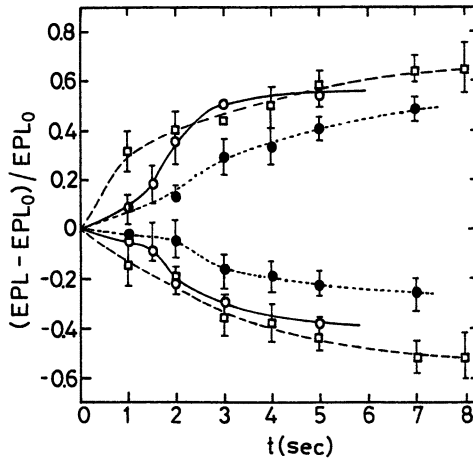


Figure 7. Accumulation of PSI on one pole (the relative change in EPL, $[EPL - EPL_0]/EPL_0$, obtains positive values when the EPL-stimulating pulse is in the opposite direction to prepulse) and its depletion on the other pole ($[EPL - EPL_0]/EPL_0$ obtains negative values when the EPL-stimulating pulse is in the parallel direction to the prepulse) as a function of pulse train duration time t . EPL_0 is the electric field-stimulated luminescence without prepulse train; EPL is the electric field-stimulated luminescence in the presence of the prepulse train. Prepulse amplitudes are 40 (●), 60 (○), and 80 (□) V/cm. Prepulse train characteristics: pulse length, 1 ms; pulse spacing, 4 ms (200 Hz). (Reproduced with permission from reference 20. Copyright 1989 Biophysical Society.)

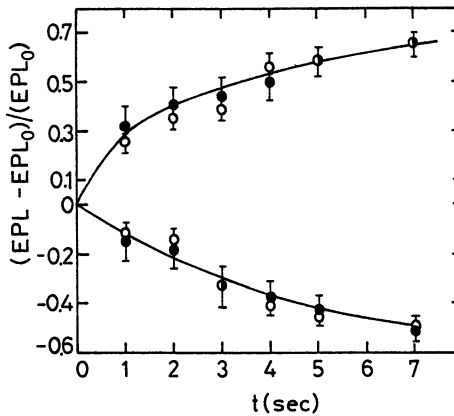


Figure 8. Accumulation of PSI on one pole (EPL inducing pulse and prepulse antiparallel) and its depletion on the other pole (EPL inducing pulse and prepulse parallel) as a function of prepulse train duration time. Prepulse field amplitude is 80 V/cm in the presence of 4% dextran (○) and in its absence (●). (Reproduced with permission from reference 20. Copyright 1989 Biophysical Society.)

mobility of the photosystem. The time dependence of EPL enhancement on one pole and its lowering on the other pole is the same in the presence and in the absence of dextran. Thus, one may conclude that the electrophoretic mobility is only a function of the hydrodynamic resistance of the membrane.

Figure 9 illustrates the relaxation of EPL after turning off the electrical field at 40 and 80 V/cm. The field free diffusional relaxation at 80 V/cm is also shown in the presence of dextran. The time dependence of the EPL after termination of the prepulse indicates that the diffusional recovery is independent of the polarizing field intensity or of the viscosity of the solution.

Quantitative Interpretation of the Electrophoretic Mobility and of the Back Diffusion Results. A uniform electric field E in a conducting fluid is distorted near the cell, and the tangential field at the cell surface, E_{θ} , that produces the electrophoretic driving force is

$$E_{\theta} = fE \sin \theta \quad (4)$$

where f is a numerical factor that represents the field distortion (1.5 for a nonconducting sphere) and θ is the polar angle. This electrophoretic driving force propels the negatively charged PSI complex along the membrane surface until opposing forces (e.g., diffusional, electrostatic, or elastic) stop the process. The native PSI complex corresponds to the 10–12-nm-diameter

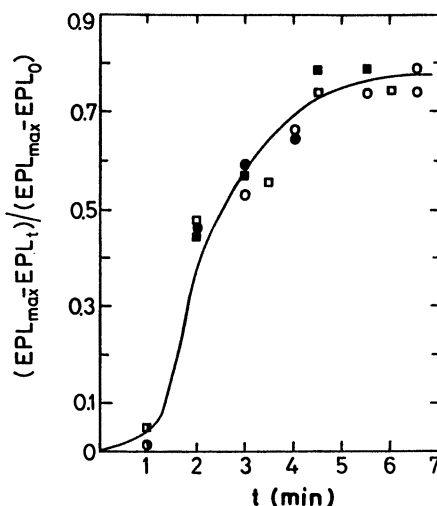


Figure 9. Diffusional relaxation of prepolarization. The time course of repopulation of the depleted poles by PSI. The depletion accomplished by prepulses of the amplitudes 40 (○), 60 (●), and 80 (□) V/cm in the absence of dextran and 80 (■) V/cm in the presence of 4% dextran. (Reproduced with permission from reference 20. Copyright 1989 Biophysical Society.)

particles observed on freeze-fracture micrographs of thylakoid membranes (39); it consists of a PSI complex of ~ 8 -nm diameter surrounded by associated light-harvesting pigment proteins. For the case where only back diffusion counteracts the electrophoretic mobility, the flux of these charged membrane components across a unit length of a circle at angle θ is (40)

$$\left(\frac{dN}{dt}\right)_{\theta} = m\Gamma_{\theta}fE \sin \theta - \frac{D}{r} \frac{d\Gamma_{\theta}}{d\theta} \quad (5)$$

where Γ_{θ} is the surface concentration of the components at angle θ , and m and D are the electrophoretic mobility and the diffusion coefficient of the moving components, respectively. At equilibrium, $dN/dt = 0$ and

$$mfE_{\theta} \sin \theta d\theta = \frac{D}{r} d \ln \Gamma_{\theta} \quad (6)$$

After integration, a simple expression for the ratio of the equilibrium concentrations at the two poles is obtained:

$$\left(\frac{\Gamma_{\pi}}{\Gamma_0}\right)_{\infty} = \exp\left(\frac{2fEmr}{D}\right) \quad (7)$$

However, EPL is not measured from the poles only, but from a large fraction of the two hemispheres. The ratio of the total number of PSI complexes in the enriched $\bar{\Gamma}_{\pi}$ to that in the depleted hemisphere $\bar{\Gamma}_0$ is

$$\frac{\bar{\Gamma}_{\pi}}{\bar{\Gamma}_0} = \frac{\int_{\pi/2}^{\pi} \Gamma_0 r^2 \sin \theta d\theta}{\int_0^{\pi/2} \Gamma_{\theta} r^2 \sin \theta d\theta}$$

Because from eq 5, $\Gamma_{\theta} = \Gamma_{1/2} \exp(-\alpha \cos \theta)$, where $\alpha = rmfE/D$, the ratio is

$$\frac{\bar{\Gamma}_{\pi}}{\bar{\Gamma}_0} = \frac{\exp(\alpha) - 1}{1 - \exp(-\alpha)} \quad (8)$$

Taking $D = 5 \times 10^{-9} \text{ cm}^2/\text{s}$ results in the electrophoretic mobility equal to $4 \times 10^{-7} \text{ cm}^2/(\text{V s})$ assuming that the measured EPL is from the poles only and is equal to $\sim 8 \times 10^{-7} \text{ cm}^2/(\text{V s})$ if the EPL is from the entire hemispheres. The real value should be between these two extreme values. In either case, the value is nearly 2 orders of magnitude smaller than estimated from the time required to yield saturation: $\sim 3 \times 10^{-5} \text{ cm}^2/(\text{V s})$. Equation 6 may be grossly incorrect if strong repulsive electrostatic forces become involved at saturating pulse.

The initial concentration distribution obtained from reference 11 for the different values of α can be obtained from eq 7 for different values of E . The equation for the diffusional relaxation is given by

$$\frac{\partial \Gamma(\theta, t)}{\partial t} = \frac{D}{r^2 \sin \theta} \frac{\partial}{\partial \theta} \left[\sin \theta \frac{\partial \Gamma(\theta, t)}{\partial \theta} \right] \quad (9)$$

Solving eq 9 according to Poo (16, 37) yields

$$\Gamma(\theta, t) = \sum_{-0}^{\infty} \frac{2\alpha \exp \alpha(1 - \cos \theta)}{\exp 2\alpha - 1} K_l P_l(\cos \theta) \exp - \left[\frac{Dl(l+1)t}{r^2} \right] \quad (10)$$

where $P_l(\cos \theta)$ is Legendre polynomial of order l and K_l s are constant coefficients. Solution of eq 9 with approximations similar to those adapted by Poo renders an exponential dependence of $(\Gamma_{\theta=0} - \Gamma_{E=0})$ on time that is depicted for different values of D in Figure 10. The 1-min lag period obtained experimentally is not reproduced by calculations carried out for different values of D and α . The curve that represents the experimental points is shifted by 1.2 min along the time coordinate as shown in Figure 10.

The lag period before back diffusion starts is just like the whole diffusion time course; it is practically identical for all the prepulse amplitudes. The lag period is also independent of the viscosity of the aqueous solution. It is possible that the photosystems aggregate when compressed under the influence of the electrical field, in which case the lag time could be identified with disaggregation time. Because contact between particles is a necessary condition for aggregation, elastic as well as electrostatic forces are probably invoked to stop electrophoretic motion.

Discussion

The experimental data presented in this chapter suggest that electric fields affect the conformation, the location, and the dynamic behavior of membrane proteins; thus the proteins may modulate their reactivity and their performance in carrying out specific functions. Local potential transients generated by electrochemical and photoelectrochemical processes may induce movement of membrane components to facilitate formation or cancellation of active centers. A charge generated in the membrane at a distance of 200 nm from a protein complex of an electrophoretic mobility of 10^{-6} cm²/(V s) will instantaneously accelerate the complex to a velocity on the order of $\sim 5 \times 10^{-3}$ cm/s. If the generated interaction is attractive, the collision between the complex and the charged site will occur within 2 ms. It may be proposed that the transient generation of charges serves as a means of communication between membrane components within the plane of the membrane.

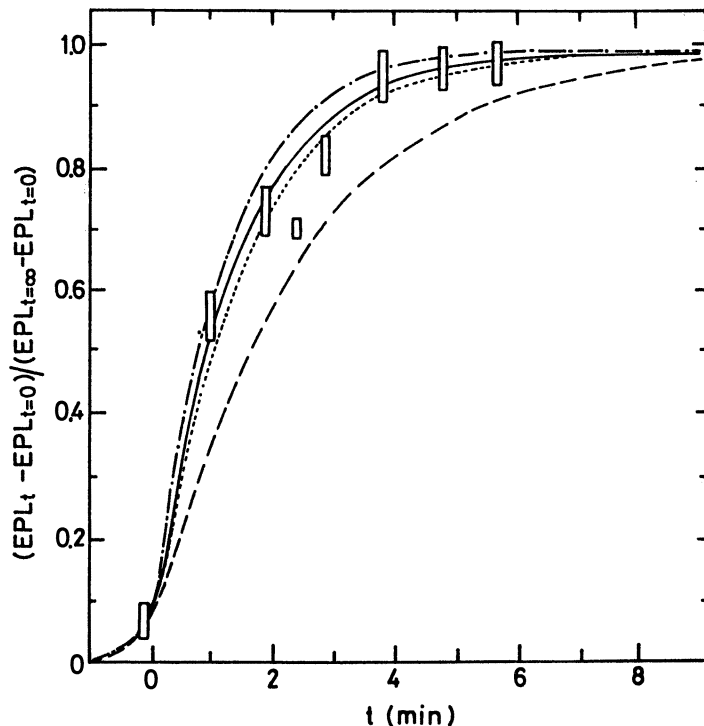


Figure 10. Diffusive relaxation calculated by eq 10 taking EPL_t proportional to $\Gamma_{\theta=0,t}$ (at the depleted poles of the vesicles) for the following values of D and α : $D = 3 \times 10^{-9}$, $\alpha = 0.375$, dashed line; $D = 5 \times 10^{-9}$, $\alpha = 0.8$, dotted line; $D = 5 \times 10^{-9}$, $\alpha = 0.375$, solid line; $D = 6 \times 10^{-9}$, $\alpha = 0.375$, dash-dot line. The rectangles encompass the experimental points from Figure 9 after multiplying the ordinate by 1.25 to account for the incomplete recovery by setting $EPL_{t=\infty} = EPL_0$ (without prepulse). (Reproduced with permission from reference 20. Copyright 1989 Biophysical Society.)

There is much more awareness of the possible effect of the electric fields normal to the plane of the membrane on the structure and on the function of membrane proteins. However, no such relation was experimentally documented. There is an appreciable amount of information on the potential dependence of channel conductance, which is assumed to be caused by shifts of charged groups within the channel (41). These shifts correspond to small changes in conformation that could not be detected by methods sensitive to the secondary structure of the proteins. In the present and in some previous reports (7, 8), we have shown that membrane potentials of comparable magnitude to the physiological membrane potentials are sufficient to modulate the secondary structure of membrane proteins. The effect may be direct or indirect. The indirect effect shifts part of the molecular fraction immersed

in the hydrophobic membrane layer to a more polar environment. Transient electric fields of comparable intensity to fields that occur in natural membranes were shown to affect the conformation of polypeptides in homogeneous solutions (9, 10). The fields in biological membranes are long lasting and equilibrium distribution of the protein fractions between the different phases with the corresponding equilibrium conformations are obtained. In the case of channel-forming polypeptides, the degree of polypeptide insertion into the lipid membrane with the corresponding channel formation also depends on the membrane potential and its sign (42, 43). The conformation of the polypeptide is expected to depend on the degree of insertion. In the present experiments with alamethicin adsorption from the aqueous solution into the outer side of the vesicle, the degree of helicity increases when the potential is negative inside and it decreases quite strongly when the potential is negative outside. It follows from this observation that the negative inside field across the membrane facilitates insertion of alamethicin whereas the field in the opposite direction prevents insertion and leaves a larger part of the alamethicin at the membrane-water interface. A larger degree of insertion corresponds to a higher effective polypeptide to lipid ratio, which yields a higher ellipticity around 223 nm and an increased degree of helicity.

References

1. Guy, H. R. In *Current Topics in Membranes and Transport 33: Molecular Biology of Ionic Channels*; Agnew, W. S.; Claudio, T.; Sigworte, F. Y., Eds.; Academic: New York, 1988; Chapter 15, p 299.
2. Armstrong, C. M. *Physiol. Rev.* **1981**, *61*, 644.
3. Tsuji, K.; Hess, B. *Eur. Biophys. J.* **1986**, *13*, 273.
4. Vinkler, C.; Korenstein, R. *Proc. Natl. Acad. Sci. U.S.A.* **1981**, *79*, 3183.
5. Sepersu, E. H.; Tsong, T. Y. *Biol. Chem.* **1985**, *259*, 7155.
6. Blank, M.; Soo, L. *Bioelectrochem. Bioenerg.* **1989**, *22*, 313.
7. Brumfeld, V.; Miller, I. R. *Biophys. J.* **1988**, *54*, 747.
8. Brumfeld, V.; Miller, I. R. *Biochim. Biophys. Acta* **1990**, *1024*, 49.
9. Schwartz, G.; Schrader, V. *Biopolymers* **1975**, *14*, 1181.
10. Kikuch, K.; Yoshka, K. *Biopolymers* **1976**, *15*, 1669.
11. Murphy, D. Y. *Biochim. Biophys. Acta* **1986**, *864*, 33.
12. Stachelin, L. A.; Arntzen, C. J. *J. Cell Biol.* **1983**, *97*, 1327.
13. Eddin, M.; Zagvansky, Y.; Lardner, T. J. *Science (Washington, D.C.)* **1976**, *197*, 466.
14. Schlesinger, J.; Koppel, D. E.; Azelrod, D.; Jacobson, K.; Webb, M. M.; Elson, E. L. *Proc. Natl. Acad. Sci. U.S.A.* **1976**, *73*, 2409.
15. Webb, W. W. In *Electrical Phenomena at the Biological Membrane Level*; Roux, E., Ed.; Elsevier: New York, 1977; p 119.
16. Poo, M. M. *Annu. Res. Biophys. Bioenerg.* **1981**, *10*, 245.
17. Ellenson, J. L.; Sauer, K. *Photochem. Photobiol.* **1976**, *23*, 113.
18. Farkas, D. L.; Korenstein, R.; Malkin, S. *Biophys. J.* **1984**, *45*, 363.
19. Symmons, M.; Korenstein, R.; Miller, I. R. *Biochem. Biophys. Acta* **1985**, *806*, 305.
20. Brumfeld, V.; Miller, I. R.; Korenstein, R. *Biophys. J.* **1989**, *56*, 607.

21. Becher, B.; Cassim, J. Y. *Prep. Biochem.* **1975**, *5*, 161.
22. Jap, B. K.; Maestrie, M. F.; Hayward, S. B.; Glaeser, R. M. *Biophys. J.* **1983**, *43*, 81.
23. Nabedoyk, E.; Bardin, A. M.; Breton, J. *Biophys. J.* **1985**, *48*, 873.
24. Rehorek, M.; Heyn, M. P. *Biochemistry* **1979**, *18*, 4977.
25. Reynolds, J. A.; Stoeckenius, W. *Proc. Natl. Acad. Sci. U.S.A.* **1977**, *74*, 2803.
26. Nagasawa, M.; Takahashi, A.; Yzumi, M. Kagawa, J. *J. Polym. Sci.* **1959**, *38*, 213.
27. Alexandrowicz, Z.; Katchalsky, A. *J. Polym. Sci.* **1963**, *A1*, 3231.
28. Katchalsky, A.; Alexandrowicz, Z.; Kedem, O. In *Chemical Physics of Ionic Solutions*; Conway, B. E.; Bonadas, R., Eds.; Wiley: New York, 1966; p 295.
29. Avron, M. *Biochem. Biophys. Acta* **1960**, *40*, 257.
30. Farkas, D. L.; Malkin, S. *Plant Physiol.* **1979**, *60*, 449.
31. Loew, L. M.; Rosenberg, I.; Bridge, M.; Gitler, C. *Biochemistry* **1983**, *22*, 837.
32. Mao, D.; Wallace, B. A. *Biochemistry* **1984**, *23*, 2667.
33. Chen, Y. H.; Yang, Y. T.; Chan, K. H. *Biochemistry* **1974**, *13*, 3350.
34. Chang, T. C.; Wu, C. S. C.; Yang, Y. T. *Anal. Biochem.* **1978**, *91*, 13.
35. Cascio, M.; and Wallace, B. A. *Proteins* **1988**, *4*, 89.
36. Vogel, H. *Biochemistry* **1987**, *26*, 4562.
37. Fox, R. O.; Richards, F. M. *Nature (London)* **1982**, *300*, 325.
38. Fringer, U. P.; Frogeli, M. *Proc. Natl. Acad. Sci. U.S.A.* **1979**, *76*, 3852.
39. Mullet, J. E.; Burke, J. J.; Arntzen, C. Y. *Plant Physiol.* **1980**, *65*, 814.
40. Poo, M. M.; Lam, J. W.; Orida, N.; Chao, N. *Biophys. J.* **1979**, *26*, 1.
41. Miller, C. *Science (Washington, D.C.)* **1991**, *252*, 1092.
42. Gordon, L. G. M.; Haydon, D. A. *Philos. Trans. R. Soc. London* **1975**, *270*, 433.
43. Boheim, G.; Kolb, H. A. *J. Membr. Biol.* **1978**, *38*, 99.

RECEIVED for review February 26, 1991. ACCEPTED revised manuscript July 6, 1992.

Coupling between Bilayer Curvature Elasticity and Membrane Protein Activity

Sol M. Gruner

Department of Physics, Princeton University, Princeton, NJ 08544

A summary is given of investigations that show that lipid-water mixtures near lamellar-nonlamellar phase boundaries are under an elastic curvature stress that may couple to conformational changes of imbedded membrane proteins. Lamellar-nonlamellar phase transitions are shown to be the result of geometrically frustrated competing free energies associated with a spontaneous tendency for lipid layers to bend and with the hydrocarbon packing configurations in the core of the lipid layers. Experimental procedures for measuring the magnitude of the curvature energy and for altering the competition between curvature and packing are described. Mechanisms whereby frustrated bilayer curvature elasticity may couple to membrane protein conformations are outlined, and experiments that indicate a correlation between elastic curvature stress and protein function are summarized.

THE STRUCTURE, MECHANISM OF OPERATION, AND LIPID INTERACTIONS of integral membrane proteins have not been thoroughly described. Even though membrane proteins represent a large fraction of all proteins, it is surprising that, with only a very few exceptions, little detailed information is available. This lack of information is not due to a lack of interest in membrane proteins; rather, it is a direct consequence of the experimental difficulties of manipulating large amphiphilic molecules, which generally require, at all times, the presence of both polar and nonpolar environments. Consider, for example, a comparison of what is known about the structure of aqueous versus integral membrane proteins. The detailed structures of many

0065-2393/94/0235-0129\$08.18/0
© 1994 American Chemical Society

water-soluble proteins are known because these proteins are relatively easy to crystallize and can, therefore, be subjected to X-ray crystallographic analysis. By contrast, membrane proteins are very difficult to crystallize. Only recently have membrane protein-detergent cocrystals suitable for X-ray analysis become available for a few proteins. As a result, membrane protein structures are only now appearing. The acquisition of detailed information about the structure and physical properties of the lipid bilayer matrix, which comprises roughly half the mass of a typical biomembrane, is limited due to the lack of either fully liquid or fully crystalline order and the difficulty of chemical manipulation of amphiphiles.

In the absence of essential information about membrane components, it is generally assumed that functional themes appropriate to aqueous proteins can be extended to membrane proteins. This extension is not necessarily valid because the lipid bilayer introduces an environmental anisotropy external to the proteins that has no simple analog in aqueous proteins. Another consequence of the lack of information is the simplistic view that the lipid bilayer consists simply of two sheets of head groups that sandwich a fluid, oily matrix. This view ignores the importance of the liquid crystalline nature of the bilayer that endows the bilayer with elastic properties that do not occur in a true liquid. The possible coupling of these elastic stresses to protein function has been largely ignored, again because of the lack of an analogous situation with the better known aqueous proteins.

The purpose of this chapter is to summarize some recent developments in the physics of lipid bilayers that demonstrate the existence of curvature-elastic stresses in bilayers and to review mechanisms whereby the resultant forces may couple to membrane protein conformations (*see also* references 1-3 for reviews). A consequence of these forces is that membrane proteins may have mechanistic themes that are qualitatively different from themes operative in aqueous proteins. Moreover, because these forces are directed generally parallel to the membrane surface, the actual conformational motions to which the forces couple may ultimately be simpler to understand than the complex conformations of aqueous proteins.

At first it might seem contradictory that the addition of another macromolecular component, namely, the lipid bilayer, could simplify understanding of the protein mechanism. Indeed, many membrane proteins have substantial mass that protrudes into the aqueous space and that is likely to be as complex in operation as soluble proteins. However, many integral membrane proteins share a common structural theme, namely, a core of almost parallel, bilayer-spanning helices or sheets. The structural order of these helices is a direct consequence of the amphiphilic environment introduced by the lipid bilayer. The discussion that follows will focus on mechanistic forces as they apply to this common core, and not to large aqueous protrusions. By contrast, aqueously soluble proteins are structurally more diverse and, in the absence of a common structural theme, cannot be approached in the same manner.

Another distinction between aqueous and membrane proteins is that the lipid bilayer introduces an anisotropy into the protein environment that results in a specific distribution of line tensions directed parallel to the membrane-water interface (4). These tensions may act against or with certain conformational motions of the protein core and, thereby, result in an exchange of free energy with the bilayer matrix during the protein conformational cycle (1, 5). The lipid bilayer matrix is, then, effectively an extension of the elastic cage provided by the bulk of the protein. The line tensions vary with depth through the bilayer in a manner that is controlled primarily by the lipid composition. By reconstituting the membrane protein in bilayers of varied composition, it should be possible to continuously alter the elastic response of the protein. This approach provides an important and, to date, little explored, experimental handle for the evaluation and testing of models of protein mechanisms. Aqueous proteins cannot be readily modulated in this way because, in contrast to bilayer lipid compositional variation, the essential properties of water are difficult to change perturbatively.

A detailed understanding of the modes of interaction of an integral membrane protein with the embedding lipid bilayer requires knowledge of the physical forces present within the bilayer matrix. A distinction must be made here between lipid effects that are chemically specific and localized to binding sites on the protein and distributed forces that are mediated by the extended physical properties of the lipid matrix. Many membrane proteins have chemically specific lipid requirements; indeed, this is the main concern of the bulk of the biochemical literature on lipid-protein interactions. Lipid interactions associated with a binding site will not be discussed here. Instead, a fundamentally physical approach will be taken whereby the lipid matrix will be described phenomenologically as an elastic continuum that is capable of distributed energy storage. It will be shown that lipid bilayers that are near lamellar-nonlamellar mesomorphic transitions on the phase diagrams are in a state of geometrically frustrated elastic stress and the mesomorphic transitions may be used to probe this stress. The magnitude of the stress may be sufficiently large to significantly alter the energetics of conformational changes of proteins imbedded in the bilayers.

Biomembrane Lipid Diversity

The biological importance of concepts derived from studies of lipid mesomorphism follows not from the relatively rare biological occurrence of nonlamellar phases, but from the prevalence of mesomorphically prone molecules in biomembrane bilayers. Scientists have long been puzzled by the large number of structurally similar but chemically distinct lipids—usually hundreds—in biomembranes. A typical biomembrane lipid consists of one of roughly a dozen polar head groups attached to two hydrocarbon chains. Each hydrocar-

bon chain is anywhere from a few to 24 or so carbons long. In addition to length, the hydrocarbon chains may vary in the degree of short side branches, in the extent and type of carbon-carbon double bonds, and in the chemical linkages whereby the chains are attached to the polar head groups. Altogether, different combinations of head groups, chains, and linkages encompass thousands of chemically distinct lipid species, many of which exhibit dramatically different mesomorphic behavior.

Although the lipid compositions of biomembranes are generally complex, they are hardly random. Membranes from a given organelle in a given type of cell have a characteristic lipid composition under a given set of environmental conditions (6). For example, all else being equal, the lipid compositions of the visual pigment disks of the retinal rod outer segment cells in the eyes of two people would be relatively similar. Likewise, the lipid compositions of the mitochondrial bilayers in those same cells will be similar for the two individuals. However, these characteristic membrane lipid compositions are organelle specific. For example, the lipid compositions of the disk and mitochondrial membranes are very different, even within the same cell.

The constraints of similarity are not absolute in that the lipid species present vary somewhat with factors such as diet, environmental conditions, and age. Experiments with bacteria (for which the range of available lipid precursors can be extensively altered) have shown that whole groups of lipids can be removed which results in characteristic readjustments of the ratios of the remaining lipids (7). A comparison of the range of biomembrane lipid variation with the very limited range of environmentally induced variability of protein or nucleic acid primary sequences encountered within a given individual is useful. In the cases of protein or nucleic acid, fundamental information is encoded in the primary sequences, which are preserved against environmental changes. By contrast, biomembrane lipid compositions conform to organelle-specific rules that are dominated by the adjustment of collective properties of the lipid mixture, as well as the specific lipid requirements of different membranes. It is the collective properties that are of interest here. The cellular mechanisms that control biomembrane lipid composition appear to operate to optimize poorly understood parameters of the lipid mixture within a substantial range of substitutional plasticity. The overlap of allowed ranges of physical parameters and of specific lipid requirements sets the limits of compositional variation that can be tolerated by a given membrane.

What physical parameters are adjusted by the organism? Experiments with bacteria suggest that the amount of charged lipid species, bilayer thickness, and degree of "fluidity" (i.e., the state of gel versus liquid crystallinity) of the lipid chains are controlled. However, this set is not likely to be exhaustive because there are many compositions within the resource range of the bacteria that are not observed but that would yield fluid membranes of a suitable charge and thickness.

Within the last decade, scientists have recognized that roughly 25–50% of the lipids in a typical biomembrane do not form stable bilayer phases when they are purified and hydrated under normal cellular conditions (8). The prevalence of “nonlamellar-prone” lipids in biomembranes has stimulated research on the phase behavior of lipids and has led to suggestions that nonlamellar-prone lipids participate in essential cellular functions (2, 8). This theory has been supported by experiments that suggest that at least some cells have metabolic mechanisms that act to regulate the nonlamellar-prone lipids in the bilayers (7, 9, 10).

Several explanations have been proposed for the prevalence of nonlamellar-prone lipid species in biomembranes. One possibility is that overt nonlamellar phases have functional importance. Although nonlamellar lipid phases have been observed in cells, their occurrence is sufficiently rare that it is unlikely that this is an explanation for the general prevalence of nonlamellar-prone lipid. Another suggestion is that nonlamellar-prone lipid promotes the transient, local destabilization of bilayers during cellular events, such as endocytosis and membrane fusion, where the topology of the bilayer necessarily changes. Although there is evidence that nonlamellar phases enhance fusion in pure lipid systems (11), biological fusion, which occurs under carefully controlled conditions, involves several proteins and proceeds via a poorly understood mechanism. It will be difficult to evaluate the role of nonlamellar-prone lipid until more is known about the biological process.

Another possibility is that nonlamellar-prone lipids modify the physical properties of bilayers in such a manner as to modulate the activities of important membrane proteins (1, 5, 12). Investigation of lamellar–nonlamellar phase transitions led to the conclusion that the addition of nonlamellar-prone lipid to stable bilayers creates a frustrated curvature stress within the bilayer leaflets. If sufficient nonlamellar-prone lipid is added, the curvature stress overwhelms competing positive free energy contributions present in the nonlamellar phases and the phase transition occurs. However, just short of the phase transition, the magnitude of the stress may be sufficiently large to have significant effects upon certain protein conformations. If this is, indeed, the case, then regulation of this stress would be important to optimal functioning of the organism and would provide a rationale for both the prevalence and regulation of the nonlamellar-prone lipid components. The experiments that led us to this conclusion are summarized in the next section.

Lipid Curvature Elasticity

The theory of mesomorphic phase transitions, developed at Princeton, has been extensively described in the literature (1, 3) and will only be briefly summarized here. (Charvolin and colleagues independently developed similar ideas at about the same time. *See* reference 13 for a summary.) The basic

idea is that lipid monolayers, which are the fundamental construction units for all liquid crystalline lipid mesomorphs (Figure 1), have a spontaneous tendency to bend to a well-defined curvature, C_0 . The use of interfacial curvature to classify lipid mesomorphs is an old idea (14), and the notion of an elastic curvature energy is inherent in several treatments of lipid mesomorphism (e.g., see reference 15). What was missing was an explanation for the sudden change in interfacial curvature that results when a system undergoes a lamellar–nonlamellar phase transition, such as the L_α – H_{II} transition (Figure 1). One possibility, of course, was to assume that in each phase the interfacial curvature is close to the spontaneous curvature (i.e., the monolayers are always elastically relaxed with respect to bend) and that the spontaneous curvature is a sensitive function of a transition variable, such as temperature. Transitions occur because of discontinuous changes in the spontaneous curvature. The difficulty with this approach is that consideration of the molecular interactions responsible for the spontaneous curvature does not reveal any obvious reason why C_0 should discontinuously change from a flat value to a highly curved value at the L_α – H_{II} transition temperature.

Some background phenomenology of the L_α – H_{II} phase transition would be useful here. The most common biomembrane lipids that undergo the L_α – H_{II} phase transition are unsaturated phosphatidylethanolamines (PEs) and monoglycosyldiacylglycerols (MGDGs). Each of these lipids has a structurally similar analog that is quite stable in bilayer form over a wide range of conditions. For example, MGDGs, which are probably the most common lipids found in plant cells, are usually found mixed with enough diglycosyldiacylglycerols (DGDGs) to form bilayers under growth conditions of the plant. A similar situation occurs in animal cells, where PEs and the structurally similar phosphatidylcholines (PCs) form the majority lipid constituents of most cell membranes. For this reason, we chose to study the phase behavior of PEs and PCs.

Because these lipids are electrically neutral, the dominant interactions between bilayers are algebraically decaying, attractive van der Waals forces and an exponentially decaying hydration repulsion. These interactions lead to

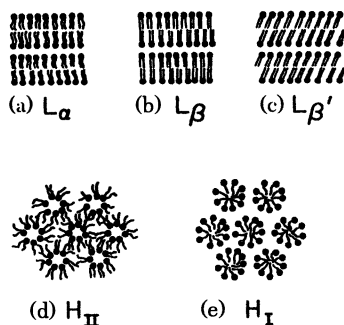


Figure 1. Cross section through a number of lipid–water phases. Frozen (gel) chain phases (b, c), lamellar phases (a, b, c), and hexagonal phases (d, e) are shown. The L_α (a) and H_{II} (d) phases are most relevant for this chapter.

a well-defined potential energy minimum at small ($< 20\text{-\AA}$) separations (16). The separations are renormalized to slightly larger lengths by undulation forces (17, 18), but this shift is small because lipid bilayers have a large rigidity compared to surfactant bilayers. An important consequence of the energy minimum with respect to bilayer separation is that multiple-bilayer assemblies of PEs and PCs will swell to a limited degree upon the addition of water; thereafter, additional water pools as a coexisting bulk water phase.

Whenever L_α - H_{II} transitions are observed thermotropically, the L_α phase is always the lower temperature phase. The fact that the H_{II} phase, which has two-dimensional symmetry, occurs at higher temperatures than the one-dimensional L_α phase indicates that the lattice entropy is not the dominant entropy contribution within the system. Instead, the dominant entropy sources are the large number of configurations available to the lipid hydrocarbon chains and (probably to a lesser extent) to the water. The shape of the mean molecular volume available to the lipid hydrocarbon chains changes dramatically at the transition, which suggests that the hydrocarbon entropy increases at the transition. This hypothesis is supported by recent deuterium NMR studies of the chain order parameter profile that indicate that the H_{II} chains are more disordered than the L_α chains (19, 20).

Changes in lattice dimensions provide important keys for understanding the L_α - H_{II} transition. As an L_α phase is heated, the mean molecular area at the lipid-water interface increases. This increase is due to the thermal thinning of the lipid hydrocarbon chain layer. Luzzati and co-workers demonstrated long ago (*see* reference 21) that long-chain liquid crystalline lyotropes have a negative coefficient of thermal expansion along a direction normal to the head-group surface. Excitation of a gauche rotamer about a carbon-carbon bond in the chains requires only about 0.02 eV, which is a bit less than thermal energy (kT) at room temperature. Increasing temperature excites gauche rotamers, which allows the chains to access a larger number of configurations (22) and results in a decrease in the mean length of the chains, very much as observed with normal polymers. The geometric constraints of the lamellar phase are that the molecular area times the layer thickness yields the molecular volume. Because thermal thinning occurs as a near-constant volume process, a progressive increase in the interfacial area with temperature results. This increase presumably is associated with an increased exposure of hydrophobic area to water and a concomitant free energy cost.

As the L_α - H_{II} transition proceeds, the mean interfacial molecular area drops and the mean area at the chain end of the molecule increases (2, 23). Effectively, the molecular volume has been subjected to a torque due to an expansive chain pressure relative to a net cohesive interaction near the head groups (4). This torque is conveniently described as a spontaneous curvature, C_0 (4, 17), to a specific radius of curvature, $R_0 = 1/C_0$, at which point the net torque is almost zero. All H_{II} phases swell only to a limited degree. In a transition in coexistence with excess water, there is generally a change in the

water concentration in the lipid phase. The change was formerly thought to be such that the H_{II} phase was less hydrated than the L_{α} phase, but counterexamples are now known. A more consistent picture is that the degree of hydration is dominated by relaxation of the curvature of the monolayers toward the spontaneous curvature; that is, most of the water is simply drawn in to fill an aqueous cavity of a specific radius. This notion is especially reasonable if we consider that the cavity may be 25 Å or more in radius. A head-group hydration interaction that could reach that far into a water volume and still be strong is difficult to envision. The energetics of removing this water will be discussed in succeeding text.

The hexagonal lattice basis length decreases rapidly with temperature (Figure 2). This decrease may be understood predominantly as a simple consequence of the geometry and the continued thermal thinning of the lipid monolayers with increasing temperatures (24). The L_{α} lattice is a one-dimensional phase, whereas the H_{II} lattice is two-dimensional. A consequence of the additional degree of dimensional freedom is that the interfacial molecular area and the hydrocarbon layer thickness may vary independently for a given molecular volume. Insofar as the interfacial area and molecular volume change only slightly with temperature, this means that the geometry acts as an amplifier that translates small changes in the hydrocarbon thickness

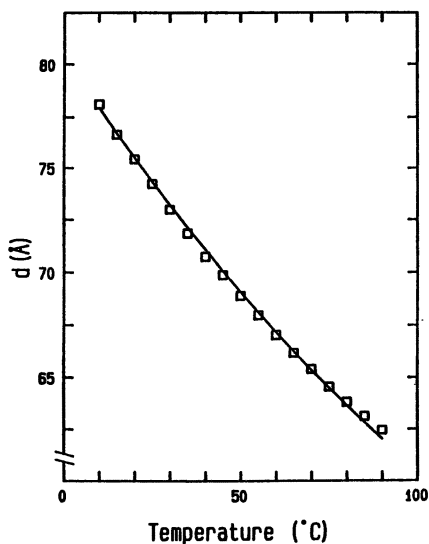


Figure 2. Temperature dependence of the basis vector length, d (see Figure 5), of the fully hydrated H_{II} phase of DOPE is shown by the open squares. The line is the fit to the data under the assumption of a linear dependence of the monolayer thickness with temperature. (Reproduced from reference 24. Copyright 1989 American Chemical Society.)

into large changes in the lattice dimension. This is illustrated by the simplified numerical example shown in Figure 3: Assume a molecular volume of $V = 1250 \text{ \AA}^3$ and a lipid thickness of $L = 20.0 \text{ \AA}$. Let L increase by 1% to 20.2 \AA , perhaps by lowering the temperature. This change of $\Delta L = 0.2 \text{ \AA}$ is difficult to measure by the limited resolution X-ray diffraction obtainable from lipid liquid crystals. Now consider the same change in a cylindrical

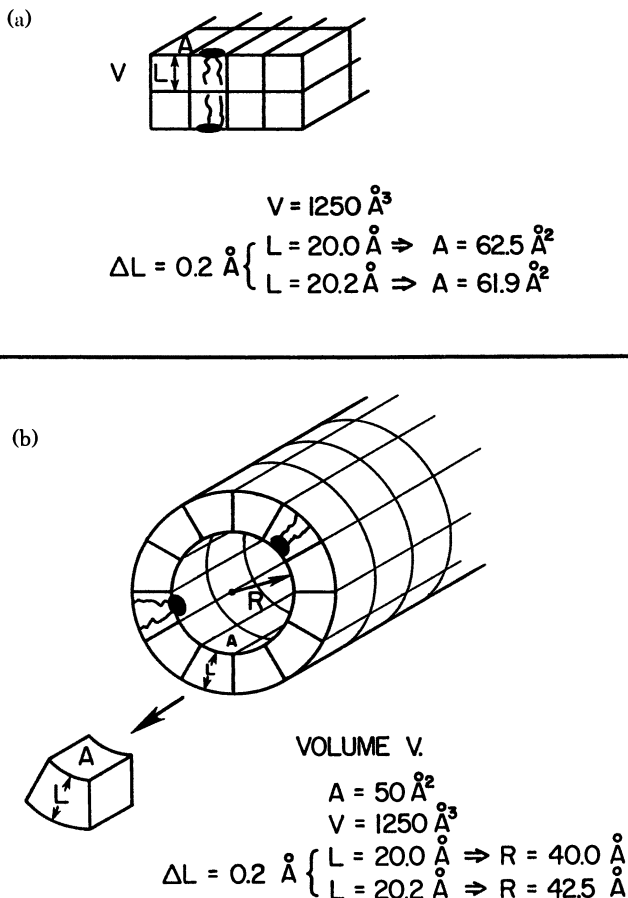


Figure 3. The cylindrical geometry of the H_{II} phase acts as a geometric amplifier for small changes in the thickness of the lipid monolayers. In the lamellar phase (a), a very small change of thickness, $\Delta L = 0.2 \text{ \AA}$, of the monolayers results in very small changes in the measurable dimensions, such as the mean molecular area A . By contrast, in a cylinder (b), the same change in monolayer thickness leads to a change in the radius of the water core, ΔR , of 2.5 \AA and a change in the lattice repeat of $d = 5 \text{ \AA}$. These large changes are very easily measured by X-ray diffraction.

geometry, as shown in Figure 3b. Here, the interfacial area, A , and volume are uncoupled, so we may change L without changing either V or A . Given A , V and L of the molecular volume tiling the cylindrical wall, it is trivial to show that the change in inner radius is of magnitude $\Delta R = |40.0 \text{ \AA} - 42.5 \text{ \AA}| = 2.5 \text{ \AA}$. The lattice basis change is about 5 \AA , which is 20 times the change in L and is easily measured by X-ray diffraction. Figure 2 shows the fit of a slightly more sophisticated version of this approach to the actual change in lattice basis for an excess water phase of an unsaturated phosphatidylethanolamine (PE) (24) under the assumption that the lipid layer thickness decreases linearly with a measured coefficient of $0.0139 \text{ \AA}/^\circ\text{C}$. This example illustrates that most of the water simply fills the cylindrical core volume and varies in response to a very small, nearly linear thermal thinning of the lipid wall.

The preceding example also illustrates that most of the water is probably not involved in chemical hydration of the lipid head groups; indeed, most of the water molecules are many water diameters removed from contact with a head group. Therefore, osmotic withdrawal of much of the water can be performed without chemically dehydrating the head groups. In this case, the energetic cost of water removal is primarily in bending the cylinder to a smaller radius; that is, a monolayer bending energy. If an H_{II} phase is put into osmotic equilibrium with a hydrophilic polymer solution, the lattice basis length falls as the osmotic pressure of the polymer solution increases. Here, chemical work is performed to extract water from the H_{II} cores. By measuring the change in core water volume per lipid molecule versus the osmotic pressure, the magnitude of the chemical work needed to achieve a given radius can be determined. Assume, for the moment, that the monolayer bending energy, ΔE , is given by (25)

$$\Delta E = (K_0/2)(1/R - 1/R_0)^2 \quad (1)$$

Here, K_0 is a rigidity of the monolayer, R is the radius of the cylinder, and R_0 is the spontaneous monolayer radius of curvature. If eq 1 describes the osmotic work of water extraction, then (23)

$$PR^2 = (2K_0/A)(1/R_0 - 1/R) \quad (2)$$

where P is the osmotic pressure required to achieve radius R and molecular area A . Now, if eq 1 is consistent with the bending energy, a graph of PR^2 versus the measured values of $1/R$ should be a straight line. This experiment was performed for H_{II} phases of dioleoylphosphatidylethanolamine (DOPE) and DOPE-dioleoylphosphatidylcholine (DOPC) mixtures (the prefix DO stands for dioleoyl chains, which are 18 carbon chains with a *cis* double bond in the middle); the results are shown in Figure 4 (23, 26). R was chosen near the middle of the chains where the molecular area changes little with changes

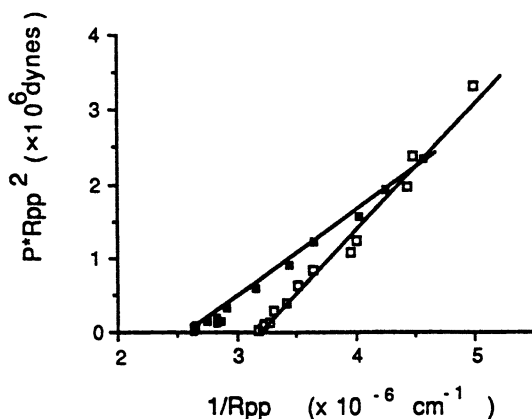


Figure 4. A test of the fit of eq 2 (lines) to data from osmotically dehydrated H_{II} phases. The open squares are for DOPE and the filled squares are for a mixture of roughly DOPE:DOPC = 3:1 in the presence of 12 wt% tetradecane. The fit yields $R_0 = 30.9 \text{ \AA}$ and $K_c = 1.7 \times 10^{-12} \text{ erg}$ for DOPE and $R_0 = 37.5 \text{ \AA}$ and $K_c = 1.2 \times 10^{-12} \text{ erg}$ for the DOPE-DOPC-tetradecane mixture. (Reproduced from reference 23. Copyright 1990 American Chemical Society.)

in the water content. With reference to eq 2, the intercept yielded R_0 and the slope yielded $2K_0/A$, which is just the bending modulus, K_c , of a bilayer with a freely sliding glide plane between the monolayers.

Several important conclusions may be drawn from this experiment. First, as seen in Figure 4, the data are consistent with an energy dependence such as given by eq 1. Higher osmotic pressures that correspond to removal of all but 80% or more of the water are not shown on Figure 4 because the points deviate significantly from the straight line fit. This deviation may represent the point at which true chemical dehydration of the head groups or steric factors comes into play. With reference to eq 2, the slope of the line yields $2K_0/A$, which is just the rigidity of a bilayer. The derived values of bilayer rigidities were in the range of $1\text{--}2 \times 10^{-12} \text{ erg}$, which compares favorably to values derived by other means on PC bilayers (27), especially given that ambiguity in the exact placement of R leads to rather large error bars on the rigidity. Equation 2 indicates that the osmotic pressure goes to zero at $1/R_0$, so the consistency of fit of Figure 4 suggests that the fully hydrated H_{II} phase is nearly elastically relaxed.

Equation 2 may now be extrapolated to fully flat ($1/R = 0$) to estimate the bending energy locked into the monolayers of a lamellar bilayer. Of course, this is just a crude estimate because there is no expectation that eq 2 is valid over such a large range of extrapolation. The result is an energy of about kT per lipid at room temperature. This value suggests that a protein

interacting with many lipid molecules at its periphery may have a potential energy store of several times kT to draw upon.

One important part of this experiment which I have not yet mentioned is that the DOPE–DOPC mixture contains a small amount of tetradecane, without which the system normally does not form H_{II} phases at room temperature. Kirk et al. (28) modeled the L_{α} – H_{II} transition as a set of geometrically frustrated free energies. Specifically, for electrically neutral systems, a phase-invariant spontaneous curvature was assumed to compete primarily with free energies associated with the optimal packing of the lipid chains. The hydrocarbon chain environment in a lamellar phase is invariant with respect to translation parallel to the lipid–water interface and is assumed to represent a low free-energy state. In the H_{II} phase, however, there is a six-fold periodic variation of environment (Figure 5) as one rotates axially about the lipid tubes. In particular, the strongest anisotropy, and a correspondingly large free-energy cost is assumed to associate with the existence of the stippled, triangular-like region between three adjacent lipid tubes (Figure 5). The ratio of volumes of this interstitial region to the total lipid hydrocarbon volume may be taken as a rough measure of the free-energy cost of packing the chains in the anisotropic environment.

The frustration that drives the L_{α} – H_{II} phase transition now becomes clear: In the L_{α} phase, just below the L_{α} – H_{II} transition temperature, the monolayers have a high free energy because they are strongly bent away from the desired value of curvature representative of the H_{II} phase, but the free energy of the chains of the lipid hydrocarbon is low. If the lipid were in an H_{II} phase of radius $R = R_0$, the curvature energy would be low, but the hydrocarbon chain energy, due to the chain anisotropy, would be high. As temperature increases, R_0 decreases, which increases the curvature cost of remaining flat as well as decreases the relative volume of the interstitial triangle; that is, the energetic cost of packing chains in the H_{II} geometry. At some sufficiently high temperature, the sum of the curvature and packing free energies in the lamellar geometry will exceed that in the H_{II} geometry and the phase transition will occur.

Several predictions follow from this transition energetics scenario. If the hydrocarbon packing energy could somehow be eliminated, the H_{II} phase would be expected to extend to low temperatures without appreciable discontinuities in the H_{II} tube radius. One way to remove most of the hydrocarbon packing energy would be to add an oil, such as dodecane or tetradecane. The oil, which is hydrophobic, would not be anchored to the lipid–water interface, and would be free to preferentially partition among the lipid chains so as to reduce chain stress; that is, in the interstitial triangle region. Kirk and Gruner (29) demonstrated that the addition of just 5-wt% dodecane reduced the L_{α} – H_{II} transition temperature of a 3:1 DOPE–DOPC mixture by about 55 °C. Moreover, comparison of the lattice sizes of the system with and without dodecane above the normal transition temperature, T_{bh} , shows that

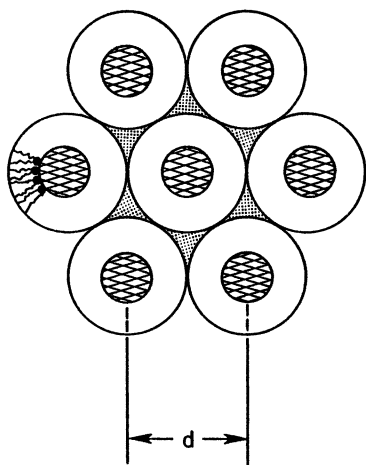


Figure 5. A cross section through a H_{II} phase that illustrates that the interstitial areas (stipled) break the axial symmetry of the H_{II} tubes. The water cores (hatched) are in the center. A few lipids are shown in the leftmost cylinder for orientation. Lipid hydrocarbon chains fill the interstitial as well as the annular regions. Deviations from the mean hydrocarbon chain-segment density or in the mean extended length of the chains correspond to an entropically expensive set of chain configurations.

dodecane has only very small effects on the size. Because the monolayer thickness changes by less than 1 Å in these experiments, the lattice size, to a good approximation, is proportional to the water core radius plus a constant. Also, a graph of the lattice size in the presence of dodecane versus temperature has no apparent discontinuities at T_{bh} , which indicates that T_{bh} has no special significance for the smoothness of the underlying spontaneous curvature of the system.

The ability of alkanes and other hydrophobic chains to reduce the L_{α} - H_{II} transition temperature has now been tested in many ways, which include the prediction that the addition of a few percent of extra-long chain lipids to a mixture that is otherwise chain homogeneous, would lower the transition temperature (30; *see also* references 5 and 23).

This picture of the transition also identifies a quantitative feature that distinguishes nonlamellar-prone lipids from chemically similar lamellar-prone lipids, namely, the relative magnitudes of the spontaneous curvatures. So, for example, whereas DOPE forms an H_{II} phase with tightly curled tubes at relatively low temperatures, DOPC forms lamellar phases, except at very high temperatures. The reason is that the H_{II} tubes that result at lower temperatures involve intolerably large chain packing energies. However, the underlying spontaneous curvatures becomes apparent when alkane is added, in which case DOPC will form an H_{II} phase at lower temperatures. The transition temperature in the absence of alkane correlates with both the size of the H_{II} tubes obtained with alkane and the amount of alkane required to include the H_{II} phase (the required amount of alkane is given roughly by the volume of the interstitial region). Even saturated chain PCs will form H_{II} phases with sufficient alkane (31, 32). These H_{II} phases may have radii of hundreds of angstroms (M. W. Tate and S. M. Gruner, unpublished results). For different lipids that have about the same chain length and that are well mixed within a

monolayer, the resultant spontaneous curvature, which arises from colligative interactions of the layer, is expected to vary systematically with the stoichiometry. For example, if DOPC and DOPE are mixed, the transition temperature and the size of the resultant H_{II} tubes at a given temperature both increase systematically with DOPC fraction. In fact, the curvature of the lipid-water interface varies linearly with the stoichiometry (M. W. Tate and S. M. Gruner, unpublished results).

In summary, the energetics of bending the monolayers of an H_{II} phase are well described as work done against a spontaneous curvature. The value of this curvature is a well-behaved, colligative property that is very sensitive to the stoichiometry of the components. The energy per lipid of a system near the L_{α} - H_{II} transition at room temperature (i.e., with a water core in the vicinity of 20-Å radius) that is naively extrapolated to a flat geometry is comparable to the thermal (kT) energy. This comparison suggests that the frustrated curvature energy in bilayer leaflets just below the transition is quite significant. A description of the L_{α} - H_{II} transition as primarily a competition between frustrated curvature and chain packing has been used successfully to qualitatively predict the effects of alkanes and long-chain lipids. The same description also has provided, incidentally, a coherent basis for understanding lipid cubic phases (1, 33). Finally, recent X-ray and neutron scattering results have directly demonstrated that the alkane in the H_{II} phase preferentially partitions into the interstitial region and that the magnitude of the difference of the interstitial chain density from the average density rises dramatically as the transition temperature is approached from above (34-36). These results confirm the essential features of the curvature versus packing model.

Before proteins are considered, it is important to explicitly state some limitations of the use of the spontaneous curvature. The spontaneous curvature is a result of the distribution of lateral tensions, $s(z)$, as a function of depth, z , through the monolayer. For a monolayer to remain flat, as in the case of a bilayer leaflet, one must have (17)

$$K_c C_0 = - \int z s(z) dz \quad (3)$$

where K_c is a monolayer bending modulus. Thus, the product $K_c C_0$ is given by the first integral moment of the lateral tension profile. Physically, the lateral tension profile (i.e., the stress-depth distribution) is expected to couple to protein conformations. We have chosen to speak in terms of the expressed curvature of the H_{II} phase because this is a quantity that can be readily measured and because the foregoing experiments indicate that the bilayer leaflets just below the phase transition have a substantial tendency to curl to this ultimate curvature. However, it is clear from eq 3 that specification of a given value of C_0 does not uniquely specify $s(z)$; there are, in fact, an infinite number of profiles for any given value of C_0 . Obviously, we ideally wish to

know $s(z)$. Unfortunately, an experimental method whereby $s(z)$ may be uniquely determined has yet to be developed (e.g., see reference 4).

The change in curvature that occurs during the L_{α} - H_{II} transition is large and typically results in radii of curvature comparable to the thickness of the monolayer. It is unlikely that the stress profile remains constant over this large change of curvatures. In addition, interactions that depend on the global geometry of the water cavity, such as van der Waals and electrostatic forces, have not yet been adequately taken into account. These interactions may very well contribute to the work required to change the size of the H_{II} tubes. Hence, we cannot confidently extrapolate to a quantitative value of the frustrated energy locked into the monolayer leaflets of a general bilayer just below the L_{α} - H_{II} phase transition temperature. The use of spontaneous curvature, especially in concert with measurements of the rigidity, is justified, but only as a qualitative indicator of trends. This problem should not, however, deter examination of the implications of various assumed values of the frustrated energy, especially given that experiments suggest significant effects on protein activities.

Effects on Proteins

For many decades, biochemists have sought to understand the interactions between intrinsic membrane proteins and the imbedding lipid bilayer. The most commonly considered interaction, for which there is strong evidence, is the site-specific binding of particular lipids. Another kind of interaction, which is still under debate, is a relatively nonspecific coupling between the protein and the "boundary lipid"; that is, the lipid molecules that are in immediate proximity to the protein. A third possibility relevant to the case considered here is interaction with the elastic stress field of the lipid matrix. This interaction differs from the other two types of interactions in that the stress field originates with the large-scale collective interactions of many lipids. Although the field is certainly communicated to the protein by nearest neighbor lipids, the field involves many lipids that are many nearest neighbor distances removed from the protein. An appropriate analogy would be to consider the forces exerted on an object imbedded in a copper sheet as the sheet is cooled. The compressive forces are communicated to the imbedded object by the immediately adjacent copper, but much of the force originates with contractions in the sheet as a whole.

It is straightforward to imagine protein conformational changes that couple to the stress of a frustrated monolayer elastic curvature. The experiments described in the preceding sections demonstrate that there is an energetically significant elastic stress locked into the leaflets of a lamellar bilayer near to a lamellar-nonlamellar phase transition. Experimentally, "bilayers near to a lamellar-nonlamellar transition" means that relatively

small shifts in temperature or composition in the lipid phase diagram would lead to a crossover to an inverted nonlamellar phase in which the curvature stress is relaxed.

Now, the ultimate source of the monolayer curvature stress is a mismatch between the lipid polar and nonpolar cross-sectional molecular areas. This mismatch leads to a tendency for the head groups to pull together and reduce their cross-sectional area and for the nonpolar regions to spread apart with larger cross-sectional areas. Any process that leads to a net reduction of the polar area of the monolayer relative to the nonpolar area relaxes the stress. Imagine a membrane protein that has, say, two conformational states that differ in their relative cross-sectional area in the polar and nonpolar parts of the monolayer. The conformation that involves an increase of the protein area in the polar region relative to the nonpolar region is acted upon by the curvature stress in that the net relative area left for the lipid head groups has decreased whereas the relative area of the nonpolar region has increased. In other words, the lipid matrix has done work on the protein. By contrast, the return to the other conformational state involves a net increase of the available lipid polar area relative to the nonpolar area, which means that the protein must do work on the lipid matrix.

There are many conformational geometries that may perform the required changes. For the sake of illustration, a suitable geometry is an axial rotation of an α -helical bundle that comprises, say, a channel or membrane pore. To visualize this concept, grab a bundle of pencils (which represent bilayer-spanning α -helices) in your left hand such that half the length of the pencils protrudes from the top of your hand and only an inch or so protrudes from the bottom of your hand. Now, wrap your right hand around the shorter protrusion and twist the bundle. The upper end of the bundle will splay apart. The net bundle area at the very top (i.e., in the upper monolayer polar region) has an increased area relative to the middle of the bundle in the nonpolar region. If the upper monolayer is curvature stressed so that it tends toward an H_{II} phase, then splaying the bundle amounts to moving with the force field applied to the protein. The reverse twist acts against the force field.

Convincing experimental tests of such a conformational mechanism have yet to be performed. Ideally, we would like to show that a suitable probe molecule, with two known conformational states with differing polar versus nonpolar areas, has an activation energy between the states that depends on the magnitude of the frustrated curvature stress. Although we are unaware of a suitable probe molecule, the required characteristics of the molecule are clear. A demonstration of a shift in activation energies of such a molecule would be a convincing plausibility argument for a similar mechanism in proteins.

Of course, a direct demonstration of the effects of lipid monolayer curvature on membrane proteins is desirable. Biochemists have long been

aware that the activity of many reconstituted integral membrane proteins varies with the composition of the lipid bilayer. In particular, many researchers have noted that behavior is different in protein reconstituted in PC relative to native lipid extracts (*see*, for example, reference 37), which tend to be rich in nonlamellar-prone lipids. The difficulty here, is performance of a clean experiment that isolates lipid curvature effects from other lipid-dependent effects, such as specific lipid binding, charge dependence, and requirements on the bilayer thickness. Typically, the focus of reconstitution studies is on a specific protein, in which case the concern of the investigators is to obtain a lipid mixture that promotes activity and not to study the systematics of lipid variation. In cases where lipid systematics have been studied, a specific lipid binding site is usually assumed and the relative efficacy of different head groups or lipid chains is investigated. Only a few studies have systematically examined the possibility of physical effects related to the mesomorphic behavior of the lipids.

Because of the difficulties involved in performing membrane protein reconstitutions, few studies that have investigated the physical effects of lipid composition have been subjected to critical, repeated evaluation by other groups. Little impetus exists to repeat difficult measurements simply to see if they are right or wrong, which is unfortunate because assays of the function of reconstituted membrane proteins are subject to many systematic errors of interpretation. For example, assays of channels or pumps typically involve measurement of leakage out of vesicles. This leakage may well correlate with the lipid composition. Another pitfall is that the membrane composition must be measured carefully, because, for mixed lipid systems, the actual lipid stoichiometry of the reconstituted vesicles frequently differs from the stoichiometry of the starting material: Vesicles of different sizes may also have different lipid stoichiometries; residual detergent may affect membrane leakage, protein function, and the degree of curvature stress; the fraction of proteins that survive the reconstitution procedure may be a function of the lipids used. The lack of critical reevaluation of reconstitution experiments must be borne in mind during consideration of the literature on the subject.

What studies have been performed? One of the more interesting of the few studies that exist was the examination of the activity of the Ca^{2+} adenosinetriphosphatase (ATPase) of sarcoplasmic reticulum membranes that were reconstituted into bilayer vesicles of different, defined lipid compositions (38). This survey found that the activity, which may be defined as the number of Ca^{2+} pumped across the bilayer per adenosine 5'-triphosphate (ATP) hydrolyzed, correlated strongly with the H_{II} tendencies of the imbedding lipid bilayer. For example, activities were high in compositions rich in either DOPE or MGDG, both of which readily form low-temperature H_{II} phases. By contrast, activities were low in DOPC or DGDG, as well as in other lipids that do not readily form H_{II} phases. Decreasing the amount of

H_{II} -tending lipid species in vesicles of mixed lipid composition decreased the activity in all cases.

The striking result of the foregoing study (38) was that the activity of the protein correlated with the phase tendency of the lipid and not with the chemical similarity of the lipid molecules. This result suggests that the effect was not due to specific binding interactions. For example, DOPE and DOPC are both dipolar phospholipids that differ only in that three head-group hydrogens in DOPE are replaced by methyl groups, yet these molecules had very different effects on the protein activity. These molecules are both very different from the chemically similar lipids MGDG and DGDG, both of which have head groups that consist of hexose sugars. However, only MGDG, the H_{II} -prone lipid of this pair, promoted high activities. Note, however, that this study (38) is subject to the criticism that the effects of residual detergent and composition-dependent ionic leakage were not fully evaluated, so the results do not provide unambiguous support for or against the lipid curvature model. Similar, but not identical, studies on the lipid dependence of the Ca^{2+} ATPase (39, 40) have also suggested that the protein function varies with the mesomorphic tendencies of the lipid (*see* references 12 and 41 for overviews).

Other proteins that have activities that correlate with the mesomorphic tendencies of the lipid bilayer include the vertebrate photoreceptor protein rhodopsin (42) and a dolichylphosphomannose synthase (43). The paucity of other examples reflects the lack of systematic studies. Membrane protein reconstitutions are generally difficult to perform, especially if the lipid composition is to be varied, and, therefore, are unlikely to be undertaken without good reason. Studies of correlations with lipid mesomorphic tendencies, stimulated by research such as that reported here, are now under consideration by several biochemical groups. Certainly, much more work is needed in this area.

The importance of lipid mesomorphic tendencies on cell membrane function has also been suggested by studies in which the lipid composition of cells has been varied. Such experiments are problematic because cells maintain regulatory apparatus that makes it difficult to alter the biomembrane lipid composition in a controlled manner. Furthermore, for eukaryotes, it is hard to obtain the pure membrane fractions of a single organelle membrane such as are required for meaningful determinations of the lipid compositions of particular membranes. In the case of bacteria, it is difficult to obtain pure plasma membrane fractions without cell wall contamination. However, mycoplasmas with only a single plasma membrane allow unambiguous determination of the overall plasma membrane composition.

The detailed studies performed by Lindblom, Wieslander, and co-workers on the lipid adjustments of the mycoplasma *Acholeplasma laidlawii* A are especially interesting (*see* references 44 and 7 for reviews of these and related experiments). *Acholeplasma laidlawii* A incorporates exogenous fatty

acids into its membrane lipids if it is grown in otherwise lipid-depleted media. This incorporation provides a mechanism for alteration of the membrane lipid composition. The organism still maintains the plasticity to choose the ratios of fatty acids incorporated from among the exogenously available acids and to attach the head groups of its choice. For example, Lindblom et al. (10) demonstrated that when two major membrane lipid head groups were grown on different ratios of exogenous oleic and palmitic acids, the ratios of the head groups and the ratios of the palmitic to oleic chains actually incorporated both varied by almost a factor of 10. Even so, the transition temperature from the lamellar–nonlamellar phases of the lipid extracts was approximately constant. In view of the discussion in earlier sections, this result strongly suggests that the cells compensate for fatty acid changes by head-group changes with the result that the membrane lipid spontaneous curvature is stabilized. The response of the B strain of the organism is quite different and does not conform to this picture (*see* reference 7).

Conclusion

Study of the phase behavior of lipid systems has led to the conclusion that the lipid bilayers of many biomembrane systems may be under significant curvature stress and that this stress may couple to conformational change in membrane proteins in a novel, energetically significant way. This conclusion has led to the suggestion of a number of concrete, although difficult, experiments to test if curvature stress modulation is active with respect to a well-defined class of conformational changes of membrane probes and membrane proteins. Clearly, more questions have been raised than have been answered, but at least the questions that have been raised are highly directed at specific physical mechanisms whereby lipid bilayers interact with membrane proteins. If experiment successfully proves that membrane elastic curvature modulates protein function, then we will not only have gained insight into the way proteins operate, but will also have a better understanding of the rationale behind the lipid compositional diversity of biological membranes.

Acknowledgments

I am fortunate to have had the pleasure to work with many talented colleagues and students; their names appear on publications describing our work. I thank them for the opportunity to have worked with them. In addition to the essential support of the Office of Naval Research, this research has benefited from the support of the Department of Energy and the National Institutes of Health.

References

1. Gruner, S. M. *J. Phys. Chem.* **1989**, *93*, 7562–7570.
2. Seddon, J. M. *Biochim. Biophys. Acta* **1990**, *10031*, 1–69.
3. Tate, M. W.; Eikenberry, E. F.; Turner, D. C.; Shyamsunder, E.; Gruner, S. M. *Chem. Phys. Lipids* **1991**, *57*, 147–164.
4. Petrov, A. G.; Bivas, I. *Prog. Surf. Sci.* **1984**, *16*, 389–512.
5. Gruner, S. M. *Proc. Natl. Acad. Sci. U.S.A.* **1985**, *82*, 3665–3669.
6. Quinn, P. J.; Chapman, D. *CRC Crit. Rev. Biochem.* **1980**, *8*, 1–117.
7. McElhaney, R. N. *CRC Crit. Rev. Microbiol.* **1989**, *17*, 1–32.
8. Cullis, P. R.; Hope, M. J.; de Kruijff, B.; Verkleij, A. J.; Tilcock, C. P. S. In *Phospholipids and Cellular Regulations*; Kuo, J. F., Ed.; CRC Press: Boca Raton, FL, 1985; Vol. 1.
9. Wieslander, A.; Rilfors, L.; Lindblom, G. *Biochemistry* **1986**, *25*, 7511–7517.
10. Lindblom, G.; Brentel, I.; Sjolund, M.; Wikander, G.; Wieslander, A. *Biochemistry* **1986**, *25*, 7502–7510.
11. Ellens, H.; Siegel, D. P.; Alford, D.; Yeagle, P. L.; Boni, L.; Lis, L. J.; Quinn, P. J.; Bentz, J. *Biochemistry* **1989**, *28*, 3692–3703.
12. Hui, S. W. *Comments Mol. Cell Biophys.* **1987**, *4*, 233–248.
13. Charvolin, J. *Contemp. Phys.* **1990**, *31*, 1–17.
14. Winsor, P. A. *Chem. Rev.* **1968**, *68*, 1.
15. Israelachvili, J. N.; Marcelja, S.; Horn, R. G. Q. *Rev. Biophys.* **1980**, *13*, 121–200.
16. Rand, R. P. *Annu. Rev. Biophys. Bioeng.* **1981**, *10*, 277–314.
17. Helfrich, W. In *Physics of Defects*; Poirier, J.-P., Ed.; North-Holland: Amsterdam, The Netherlands, 1980.
18. Evans, E. A.; Parsegian, V. A. *Proc. Natl. Acad. Sci. U.S.A.* **1986**, *83*, 7132–7136.
19. Sternin, E.; Fine, B.; Bloom, M.; Tilcock, C. P. S.; Wong, K. F.; Cullis, P. R. *Biophys. J.* **1988**, *5*, 689–694.
20. Laffeur, M.; Cullis, P. R.; Fine, B.; Bloom, M. *Biochemistry* **1990**, *29*, 8325–8333.
21. Luzzati, V. In *Biological Membranes*; Chapman, D., Ed.; Academic: New York, 1968; Vol. I, pp 71–123.
22. Day, J.; Willis, C. R. *J. Theor. Biol.* **1981**, *88*, 693–718.
23. Rand, R. P.; Fuller, N. L.; Gruner, S. M.; Parsegian, V. A. *Biochemistry* **1990**, *29*, 76–87.
24. Tate, M. W.; Gruner, S. M. *Biochemistry* **1989**, *28*, 4245–4253.
25. Helfrich, W. *Z. Naturforsch., C: Biosci.* **1973**, *28*, 693–1703.
26. Gruner, S. M.; Parsegian, V. A.; Rand, R. P. *Faraday Discuss.* **1986**, *81*, 29–37.
27. Bo, L.; Waugh, R. E. *Biophys. J.* **1989**, *55*, 509–517.
28. Kirk, G. L.; Gruner, S. M.; Stein, D. L. *Biochemistry* **1984**, *23*, 1093–1102.
29. Kirk, G. L.; Gruner, S. M. *J. Phys.* **1985**, *46*, 761–769.
30. Tate, M. W.; Gruner, S. M. *Biochemistry* **1987**, *26*, 231–236.
31. Sjolund, M.; Lindblom, G.; Rilfors, L.; Arvidson, G. *Biophys. J.* **1987**, *52*, 145–154.
32. Sjolund, M.; Rilfors, L.; Lindblom, G. *Biochemistry* **1989**, *28*, 1323–1329.
33. Anderson, D.; Gruner, S. M.; Leibler, S. *Proc. Natl. Acad. Sci. U.S.A.* **1988**, *85*, 5364–5368.
34. Turner, D. C. Ph.D. Thesis, Princeton University, Princeton, NJ, 1990.
35. Turner, D. C.; Gruner, S. M. *Biochemistry* **1992**, *31*, 1340–1355.
36. Turner, D. C.; Gruner, S. M.; Huang, J. S. *Biochemistry* **1992**, *31*, 1356–1363.

37. Tamkun, M. M.; Talvenheimo, J. A.; Catterall, W. A. *J. Biol. Chem.* **1984**, *259*, 1676–1688.
38. Navarro, J.; Toivio-Kinnucan, M.; Racker, E. *Biochemistry* **1984**, *23*, 130–135.
39. Cheng, K-H.; Lepock, J. R.; Hui, S. W.; Yeagle, P. L. *J. Biol. Chem.* **1986**, *261*, 5081–5087.
40. Cheng, K-H.; Hui, S. K. *Arch. Biochem. Biophys.* **1986**, *244*, 382–386.
41. Hui, S-K.; Sen, A. *Proc. Natl. Acad. Sci. U.S.A.* **1989**, *86*, 5825–5829.
42. Wiedman, T. S.; Pates, R. D.; Beach, J. M.; Salmon, A.; Brown, M. F. *Biochemistry* **1988**, *27*, 6469–6474.
43. Jensen, J. W.; Schutzbach, J. S. *Biochemistry* **1988**, *27*, 6315–6320.
44. Lindblom, G.; Rilfors, L. *Biochim. Biophys. Acta* **1989**, *988*, 221–256.

RECEIVED for review March 8, 1991. ACCEPTED revised manuscript October 13, 1992.

Characterization of Potentiometric Membrane Dyes

Leslie M. Loew

Department of Physiology, University of Connecticut Health Center,
Farmington, CT 06030

Dye indicators of membrane potential have been available for the past 20 years and have been employed in numerous studies of cell physiology. "Fast" dyes are able to follow changes in the millisecond range—fast enough to monitor individual electrical events in excitable cells and tissue. Fast dyes include compounds with styryl, oxonol, and merocyanine chromophores that are engineered to stain the plasma membrane. Generally fast dyes have small sensitivities to voltage changes but are very useful for detecting voltage transients or mapping voltage differences along the surface of a cell. "Slow" dyes can measure voltage changes that may accompany hormonal responses in nonexcitable cells or the level of activity in energy-transducing organelles. Slow dyes have delocalized charges, as in the cyanine or rhodamine chromophores, and usually operate via a potential-dependent redistribution between the extracellular medium and the cytosol. Techniques based on these indicators can be used to monitor both spatial and temporal variations in membrane potential with resolutions not possible with the more traditional electrode-based methodologies.

POTENTIOMETRIC MEMBRANE DYES are employed to study cell physiology. The pioneering work of Cohen and his co-workers (1–3) led to the availability of a large number of organic dyes whose spectral properties are sensitive to changes in membrane potential. The applications of these dyes to a variety of problems in cell biology and neuroscience were reviewed in a series of chapters in a recent book (4). The aim of this chapter is to review the characteristics of these dyes as determined in model and cell membranes.

0065-2393/94/0235-0151\$08.54/0
© 1994 American Chemical Society

The size of the voltage-dependent signal, although certainly important, is by no means the only factor to be considered in choosing a dye. The intent here is to identify the important parameters of dye chemistry that enable it to be a useful and practical indicator of potential. Some brief generalities about the structures and physical properties of the various dye chromophores that form the backbones of potentiometric dyes are also introduced. This information should provide a basis for better initial selection of suitable dyes for a given experimental application and help take some of the mystery out of the chemistry of potentiometric dyes.

Particular emphasis will be placed on electrochromic and Nernstian redistribution dyes developed in our laboratory. Several of the methods used to test and analyze dye response to changes in membrane potential will be detailed.

Dye Design

Initially, the primary method for finding good potentiometric dyes was trial and error. Large numbers of dyes were screened on the squid giant axon by Cohen and his colleagues (1–3). The resultant database revealed several broad rules that could be used to design new generations of probes. For example, the large class of azo dyes are not particularly suitable because of their photoinstability and their propensity for toxic and photodynamic damage to biological preparations. The azo dyes require some hydrophobic appendages to promote interaction with the membrane, but alkyl groups longer than about eight carbons impart too much insolubility for some applications. The database also indicated that several different molecular mechanisms are employed by different dyes to produce potential-dependent spectral changes. The varied chemistry underlying the activity of these dyes is intrinsically fascinating.

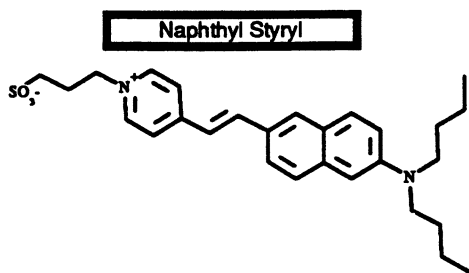
A simple yet extremely useful classification of potentiometric dyes that emerged from these studies (5) is based on the speed of their response to voltage changes. “Fast” dyes are able to follow changes in the millisecond range—fast enough to monitor individual electrical events in excitable cells and tissue. “Slow” dyes can measure voltage changes that may accompany hormonal responses in nonexcitable cells or the level of activity in energy-transducing organelles. Interestingly, in addition to identifying the range of applications accessible to potentiometric indicators, this classification also divides the existing potentiometric indicators into realms of mechanism and sensitivity.

Fast Dyes. Generally, the mechanisms underlying the fast dye responses involve potential-dependent intramolecular rearrangements or small movements of the dye from one chemical environment to another. These

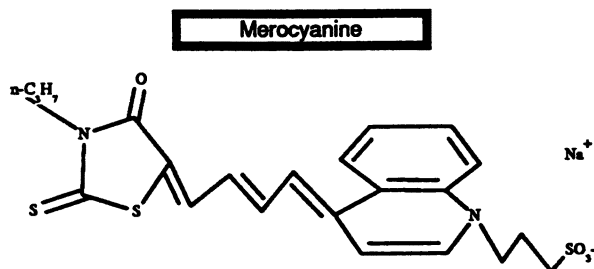
reactions have the requisite speed but usually do not produce very large changes in the spectra of the dye. The largest reported fluorescence response to an action potential was greater than 20% relative to the resting fluorescence level (6). Typically, however, good fast dyes respond with fluorescence changes of only 2–10% per 100 mV and transmittance changes of 0.02–0.1% per 100 mV. A sampling of some of the best fast dyes is included in Chart I, which will be referenced in the following discussion.

A great deal of effort has been invested to develop fast dyes that employ an electrochromic (7–9) mechanism. Briefly, electrochromism is possible if there is a large shift in electronic charge when a chromophore is excited from the ground to the first excited state; if the direction of charge movement lies parallel to an electric field, the energy of the transition will be sensitive to the field amplitude. Thus, if the chromophore is oriented so that the charge redistribution is perpendicular to the membrane surface, an electrochromic dye should be an indicator of membrane potential. These ideas are summarized in Figure 1. The reason this mechanism is attractive is that it lends itself to a theoretical molecular orbital treatment (9) that aids in the design of appropriate targets for organic synthesis. The aminostyrylpyridinium chromophore best fits the criterion of a large charge shift upon excitation and can easily be modified with sidechains that assure an appropriate orientation in the membrane. Variations on this chromophore have been the targets of synthetic efforts in our lab (10–12) and in Grinvald's lab (6, 13). Chart I includes two examples: di4-ANEPPS (10) and RH421 (6), which have been particularly successful in a variety of applications. Note that the potentiometric responses of these dyes in different biological preparations may be complex superpositions of several mechanisms with only a minor contribution from electrochromism (14). Nevertheless, the styryl dyes have emerged as the most popular fast fluorescent potentiometric indicators. Among their special attributes are relatively good photostability, a high fluorescence quantum yield for the membrane-bound dyes, and almost no fluorescence from aqueous dye.

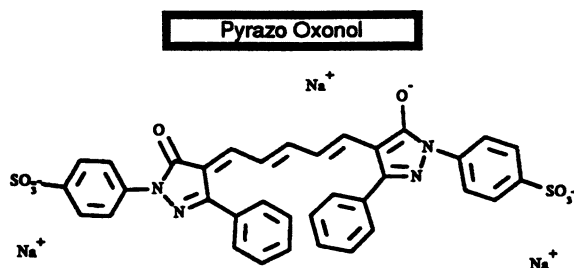
Absorbance measurements are often desirable, especially for complex preparations with nonexcitable satellite cells, because the large background fluorescence from the membranes of these uninvolved cells attenuates the relative fluorescence response with a corresponding degradation of the signal-to-noise ratio; a transmitted light signal is used in absorbance and is not significantly affected by background staining. The oxonol class of dyes now has emerged as the most sensitive for detecting fast potential-dependent absorbance changes, although some merocyanine dyes, the earliest class of successful fast indicators, are also still in use. The oxonol chromophore is defined by its delocalized negative charge. The mechanism for the potential-dependent response has been determined for several of these probes; it involves a movement between a binding site on the membrane surface and an aqueous region adjacent to the membrane (15, 16). The merocyanine chro-



DI-4-ANEPPS
JPW-211

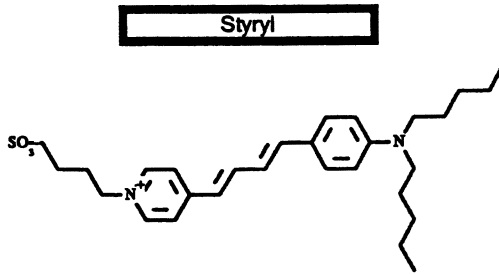


JPW-1120-2
WW-401

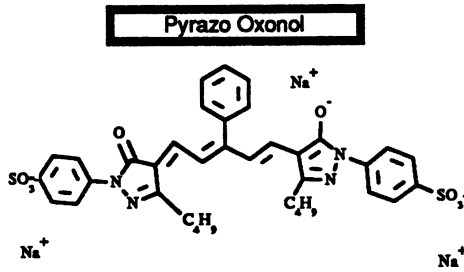


JPW-1034
RGA509

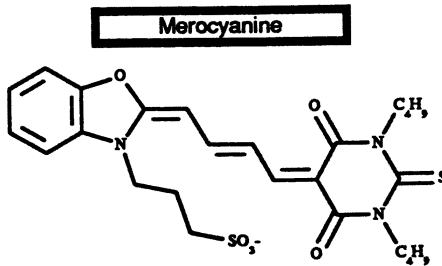
Chart I. A representative sampling of good fast dyes. The name of the general chromophore is given in the box above each structure. The common names of the dyes are listed under each structure.



RH-421



JPW-1150



M-540

Chart I.—Continued.

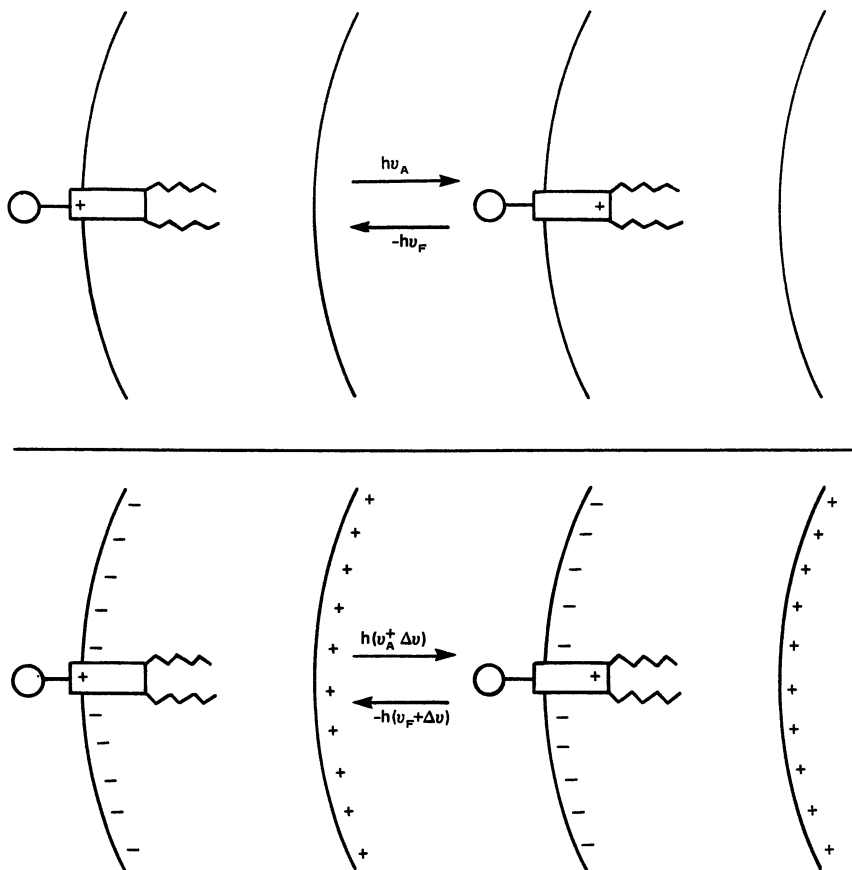


Figure 1. An electrochromic dye undergoes an internal charge migration upon excitation (top). In the presence of the electric field produced by a potential drop across the membrane, the energy required for the excitation is altered (bottom) resulting in a spectral shift.

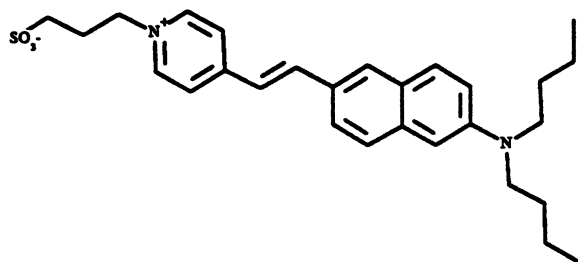
mophore is characterized by neutral and zwitterionic resonance structures. Merocyanines are often highly solvatochromic and can theoretically respond to membrane potential via electrochromism. However, the only thorough experimental investigations of merocyanine mechanisms performed to date have been with just one dye, M-540 (Chart I). These studies indicated that dye reorientation possibly coupled with aggregation at the membrane surface underlies the potentiometric response of this early member of the merocyanine family of potentiometric dyes (2, 17, 18).

Probes can be designed with variable overall charge and hydrophobicity as appropriate for different applications. The rationale for these ideas will be illustrated for the styryl dyes, of which Joe Wuskell in this laboratory has

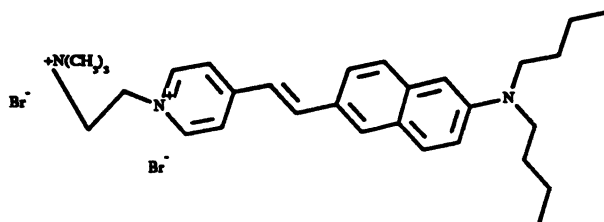
made many variants. Structures of some of these probes are shown in Chart II. Di-4-ANEPPS is a good general purpose fast probe that has several beneficial attributes (based on both published (10, 19–26) and unpublished results in this laboratory as well as those of L. B. Cohen, B. M. Salzberg, G. Salama, J. Pine, J. Dix, P. Schrager, W. Webb, D. Gross, D. Zecevic, J. Jalife, J. M. Davidenko, W. Müller, and H. Windisch). Di-4-ANEPPS is reasonably consistent in giving a relative fluorescence change of $\approx 10\%$ per 100 mV in a variety of different cell types and experimental protocols, and it can be used in a dual wavelength ratiometric excitation mode to normalize out artifacts due to uneven staining or photobleaching (27). As with other styryls, only the membrane-bound dye displays appreciable fluorescence. In several experimental protocols, it has been persistent for hours under continuous perfusion with dye-free medium. Decreasing the size of the chromophore as in di-4-ASPPS results in a blue shift of the spectral characteristics of the response of about 30 nm; unfortunately a 40% reduction in sensitivity also occurs. A decrease in the chain length of the hydrocarbon tails as in di-2-ANEPPS increases the water solubility of the dye. This is necessary for thick tissue preparations where the dye must penetrate through many cell layers; the more water-soluble dyes, of course, will give less persistent staining of the preparation. The opposite situation will pertain to a dye like di-8-ANEPPS, where low solubility requires a high molecular weight surfactant like Pluronic F127 (BASF Corporation) to promote staining (28, 29). In addition to persistence, we discovered that another attribute of di-8-ANEPPS is a very slow rate of internalization. In several cell types, di-4-ANEPPS was incorporated into intracellular organelles over times as short as 10 min; di-8-ANEPPS is retained exclusively on the plasma membrane over periods of hours. Di-4-ANEPEP and di-4-ANEPEQ represent dyes with varying head-group charges. These charges can subtly change the location of bound dye in the membrane with the effect of sometimes significant improvements in sensitivity. Generally it is true that positively charged dyes are especially well suited for experiments that require microinjection to localize dye to just one cell in a complex preparation (30, 31).

Slow Dyes. Slow dyes generally operate by a potential-dependent partitioning between the extracellular medium and either the membrane or the cytoplasm. This redistribution of dye molecules is effected via the interaction of the voltage with the ionic charge on the dye. Unlike fast potentiometric indicators, slow redistribution dyes must be charged. Three chromophore types have yielded useful slow dyes: cyanines, oxonols, and rhodamines. Each of these chromophores has special features that suit different kinds of experimental requirements. A set of important slow dyes is depicted in Chart III.

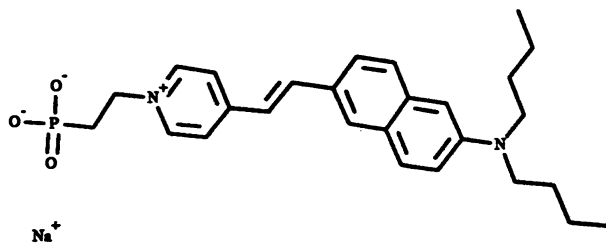
The cyanine class of symmetrical dyes with delocalized positive charges was originally introduced by Alan Waggoner and has provided extraordinarily



DI-4-ANEPPS
JPW-211

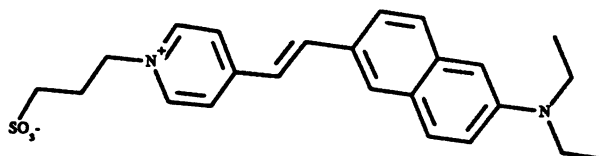


JPW-1063
Di-4-ANEPEQ

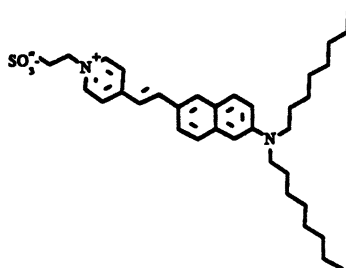


JPW-1064
Di-4-ANEPEP

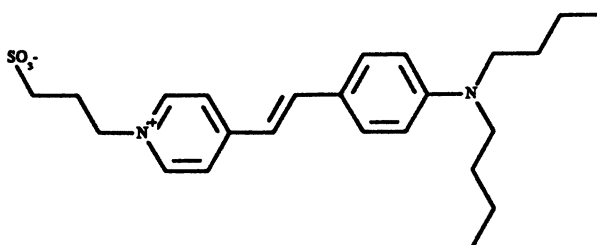
Chart II. A collection of styryl dyes engineered to meet specific experimental demands.



JPW-1113
DI-2-ANEPPS



JPW-1153
DI-8-ANEPPS



DI-4-ASPPS

Chart II.—Continued.

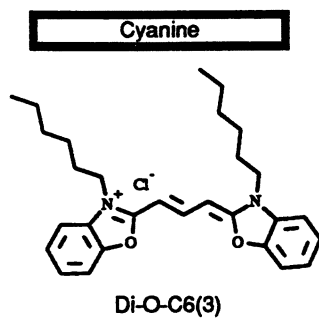
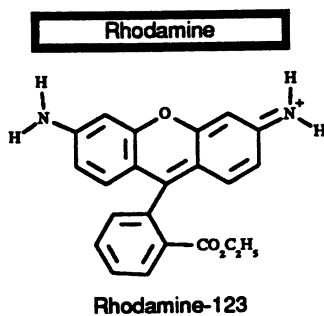
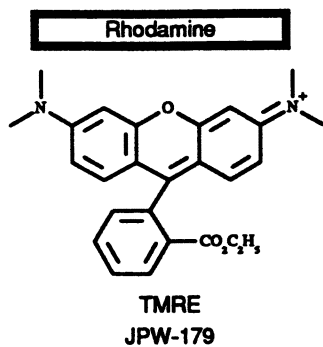
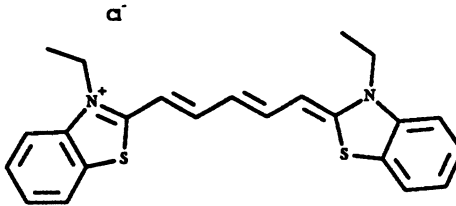


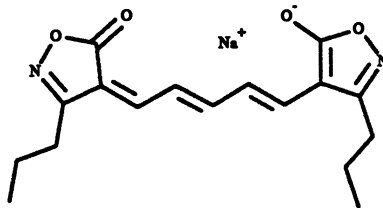
Chart III. A representative sampling of good slow dyes.

Cyanine



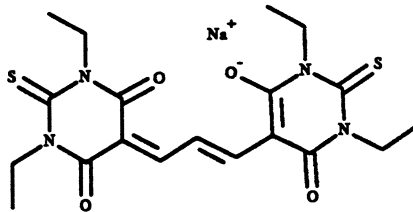
Di-S-C2(5)

Oxonol



Oxonol-VI

Oxonol



Bis-oxonol
DiS-BaC2(3)

Chart III.—Continued.

sensitive probes for potential changes in populations of nonexcitable cells (5, 32–34). A large number of these dyes with varying hydrocarbon chain lengths, numbers of methine groups in the bridging polyene, and heterocyclic nuclei are available. Depending on the nature of the dye and its concentration, potential-dependent uptake can effect either an increase or a decrease in fluorescence intensity. In general, the fluorescence of these dyes is enhanced upon membrane binding; thus accumulation of dye leads to fluorescence enhancement. However, at high dye:lipid ratios many of the dyes have a tendency to aggregate, which results in fluorescence self-quenching. Self-quenching occurs in the case of di-S-C2(5) (Chart III), which can lose 98% of its fluorescence when a cell or vesicle preparation is polarized to 100 mV (32, 35, 36). Di-O-C6(3) has less tendency to aggregate and displays an increased fluorescence quantum yield as it binds to the plasma and organelle membranes. The lipophilicity of di-O-C6(3) is responsible for its use as a stain for mitochondria and endoplasmic reticula (37). However, dye association with intracellular organelles can lead to cytotoxicity or misinterpreted fluorescence changes (38).

Anionic oxonols also show enhanced fluorescence upon binding to membranes, but, because of their negative charge, binding is promoted by depolarization. More importantly, the negative charge lessens intracellular uptake of oxonol dyes, which solves some of the difficulties encountered with the cyanines. Oxonols are, however, less sensitive than the cyanines. Oxonol VI, depicted in Chart III, is among several similar oxonols developed by Chance et al. (39, 40) for dual wavelength absorbance measurements on energy-transducing organelle suspensions. Bis-oxonol and its relatives with barbituric acid nuclei have been used in fluorescence experiments on cell suspensions (41–43).

The membrane potential of individual cells can be monitored with a fluorescence microscope. For this purpose, however, it is preferable to use a permeable redistribution dye with spectral characteristics that have minimal environmental sensitivity. Thus, the fluorescence intensity will reflect the degree of Nernstian accumulation of dye only and can, therefore, be readily interpreted. The plasma membrane potential can be distinguished from the organelle membrane by simply using the microscope to identify appropriate regions of the cell (44). Rhodamine-123 (Chart III) was introduced as a mitochondrial stain by Chen and co-workers (45–47); it has been used largely in qualitative studies of mitochondrial membrane potential and has been especially effective in flow cytometry applications.

Our laboratory (44) has synthesized two rhodamine dyes, TMRE (Chart III) and TMRM, that are very similar to rhodamine 123 except the free amino groups are substituted with methyl substituents. This substitution makes the dyes more permeable than rhodamine 123 and also blocks any poorly reversible hydrogen-bonding interactions with anionic sites in the mitochondrial inner membrane and matrix. These qualities combined with

the general environmental insensitivity of rhodamine fluorescence and the low tendency of TMRE and TMRM to aggregate, makes them good “Nernstian” indicators of membrane potential. That is to say, the ratio of fluorescence intensities measured in two compartments separated by a membrane (viz. F_1/F_2), when properly corrected for background dye binding, can be inserted into the Nernst equation to provide a direct measure of the potential difference between the compartments (ΔV_m):

$$\Delta V_m = - \frac{RT}{F} \ln \frac{F_1}{F_2} \quad (1)$$

R is the ideal gas constant, T is the absolute temperature, and F is Faraday's constant. This approach was successfully applied to the plasma membrane potential of several different cell types (44) and was used to follow changes in mitochondrial membrane potential via digital imaging microscopy (48). Although ordinary wide-field microscopy is successful in monitoring these kinetic events, the actual magnitude of mitochondrial membrane potential cannot be quantitated because it is not possible to obtain an accurate measure of fluorescence intensity that emanates from such a small compartment with the broad depth of field set by the microscope optics. This limitation can be overcome if confocal microscopy is employed with its very narrow depth of field. Although this approach has been successfully demonstrated (48–50), the high excitation light intensities necessitated by the technique (at least in the current generation of confocal microscopes) limits its usefulness for measurements on living cells. Thus, single measurements can be performed, but the accumulation of large image sets for either kinetics or three-dimensional reconstructions leads to fading of the dye or phototoxic effects on the cell.

Dye Characterization

To determine if a dye will be a useful potentiometric probe in biological applications, information on its chemical, physical, spectral, and toxicological properties must be gathered in addition to data on the sensitivity to membrane potential. A number of model membrane systems are employed to characterize dye properties as well as some simple biological preparations.

Lipid Vesicles. Lipid vesicles are composed of lipid bilayers that separate the bulk aqueous medium from an entrapped aqueous compartment. They are easily prepared by mixing phospholipid with the appropriate aqueous buffer. The vigor of the mixing operation determines the number and size distribution of bilayers that comprise each vesicle. For example, extensive sonication of egg phosphatidylcholine produces an optically clear suspension

of unilamellar vesicles with an average diameter of about 250 Å (51). This simple model system can be used to assess the spectral properties of membrane-bound dyes and their binding affinities. In addition, it is possible to generate well controlled membrane potentials across the vesicle membranes and thereby calibrate the spectral response of a potentiometric probe.

A fixed dye concentration can be titrated with aliquots of lipid vesicles and the fluorescence or absorption spectra can be monitored. Almost all dyes that are sensitive to membrane potential will display a significant difference in the spectra of membrane-bound versus free aqueous forms. (Notable exceptions are the Nernstian rhodamine dyes.) Along with the spectral characteristics of the membrane-bound dyes, these experiments provide information on the binding equilibria. A thorough analysis of such data (39) can be used to generate both binding constants and binding numbers (i.e., the number of binding sites per vesicle). We use the fluorescence of a 1- μ M dye solution titrated with lipid vesicles to determine the ratio of the dissociation constant to the binding number, K_d/n , to serve as a convenient quantitative measure of the relative affinities of potentiometric dyes:

$$F_C = \frac{(F_\infty - F_0)C}{C + K_d/n} + F_0 \quad (2)$$

F_C is the fluorescence of the dye in a lipid vesicle suspension with a lipid concentration of C ; F_0 and F_∞ are the limiting dye fluorescence readings in the absence of lipid and at very high lipid concentrations, respectively. The fluorescence as a function of lipid concentration is fitted to this equation via nonlinear regression. The results of such measurements for a series of styryl dyes (10), as well as the spectral characteristics of the dyes in several solvents, are given in Table I. As expected, the membrane affinity of the dyes increases with the length of the chromophore or the number of carbons in the appended hydrocarbon chains. Also noteworthy is the striking increase in fluorescence quantum yield for the membrane-bound dyes; this is probably due to the well-ordered immobile environment of the membrane, which inhibits nonradiative decay processes that require molecular motion in the excited state.

The kinetics of dye binding to the membrane is of practical importance. Contrary to expectation, the rate of association with the bilayer is not directly related to the binding affinity. Indeed, dyes with the longest hydrocarbon chains have the slowest binding kinetics (29), which is presumably due to the presence of stable oligomeric aggregates of the dye in aqueous solution. The rate of dissociation of a monomer from these aggregates is rate limiting when the hydrocarbon chains are longer than three or four carbons. A nonionic macromolecular detergent, Pluronic F127, can be used as a catalyst for staining cells with these sluggish dyes. Interestingly, dyes with long hydrocar-

bon tails flip across the lipid bilayer at slower rates than slower dyes and are required for many cell types to prevent rapid internalization.

The vesicle system can support a valinomycin-mediated K^+ diffusion potential, which affords a quick and simple means for calibrating a potentiometric dye response. The potential can be generated by adding valinomycin, a highly K^+ -selective ionophore, to a vesicle suspension in which the inner and outer potassium concentrations are unequal. This unequal concentration can be achieved most simply by preparing the vesicles in a solution at one $[K^+]$ and diluting the vesicles into a solution prepared with a different $[K^+]$. The membrane potential can be calculated directly from the Nernst equation (eq 1). This approach was originally applied to the cyanine dyes by Waggoner and Hoffman and their colleagues for both lipid vesicles and erythrocytes (32). In general, the effectiveness of a dye in a cell suspension can be assessed with a lipid vesicle experiment; however, possible complications (such as the accumulation of dye by mitochondria and other organelles) require that such comparisons be made with care.

Spherical Lipid Bilayer. Spherical or hemispherical 2–4-mm-diameter lipid bilayers can be prepared by applying hydrostatic pressure to a hydrocarbon solution of lipid that covers the tip of an electrolyte-filled tube suspended in the electrolyte (52). This model membrane is particularly convenient for determination of the response of a membrane-bound dye to a directly applied voltage (16, 17). A diagram of the implementation of this method for screening potentiometric dyes is shown in Figure 2 (21). In this latest version of an apparatus that has continuously evolved over the last 13 years, we induce a membrane potential by applying voltage to a pair of external parallel plate electrodes. Earlier versions applied the voltage directly to the membrane via a voltage-clamp circuit connected to an electrode inside the tube (53).

This apparatus can be used to determine the sensitivity of a dye as well as to gain insight into the dye mechanism. Dragsten and Webb (17) used polarized light and signal averaging of the fluorescence response to a voltage pulse to show that the mechanism of M-540 (Chart I) involved a voltage-driven reorientation of the molecule along the membrane surface coupled to an orientation-dependent dye aggregation. A series of fast oxonol dyes were examined and showed absorbance changes with magnitudes that were dependent on the offset applied to a train of voltage pulses (15, 54, 55). This observation was interpreted as evidence for the voltage-dependent occupation of two sites near the membrane surface (“on-off” mechanism). We used the spherical bilayer to investigate the mechanism of the styryl dyes (10, 12, 53, 56). A square wave voltage applied to the membrane provided the reference for a lock-in amplifier that was able to extract a small voltage-dependent optical signal from a large background. This signal permitted us to determine the complete wavelength dependence of the absorbance and fluorescence

response. An example of a fluorescence excitation response spectrum for di-4-ANEPPS is given in Figure 3. A detailed investigation of the wavelength, polarized light, voltage, and dye concentration dependences of the potentiometric response led us to conclude (35, 56) that many of the styryl dyes operated via an electrochromic mechanism (although this is not the dominant

Table I. Spectroscopic and Binding Properties of Charge-Shift Probes

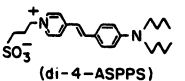
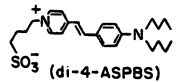
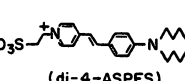
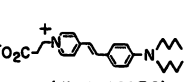
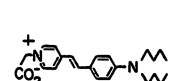
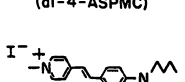
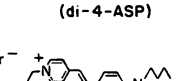
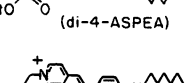
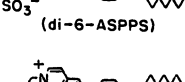
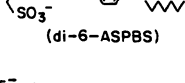
No.	Structure and Abbreviation	Solvent ^a	λ_{max}^{abs} (nm)	$\log \epsilon$	λ_{max}^{em} (nm)	ϕ	K_d/n (mg/mL)
1.	 (di-4-ASPSPS)	A	492	4.7	625	0.04	0.10
		B	525	4.8	595	0.3	
		C	482	4.6	635	0.003	
		D	467	4.6	595	0.3	
2.	 (di-4-ASPBS)	A	492	4.7	615	0.04	0.13
		B	517	4.7	600	0.3	
		C	478	4.5	635	0.005	
		D	465	4.5	597	0.3	
3.	 (di-4-ASPES)	A	490	4.7	620	0.03	0.09
		B	519	4.7	600	0.4	
		C	487	4.6			
		D	465	4.5	602	0.2	
4.	 (di-4-ASPPEC)	A	487	4.4	612	0.05	0.20
		B	511	4.3	578	0.15	
		C	480	4.3	630	0.003	
		D	468	4.2	602	0.2	
5.	 (di-4-ASPMC)	A	486	4.6	614	0.06	0.13
		B	509	4.5	580	0.5	
		C	484	4.4	630	0.004	
		D	467	4.4	602	0.3	
6.	 (di-4-ASP)	A	490	4.6	615	0.5	0.07
		B	518	4.7	600	0.02	
		C	476	4.5	625	0.002	
		D	467	4.4	595	0.3	
7.	 (di-4-ASPEA)	A	507	4.7	630	0.01	0.07
		B	523	4.8	605	0.07	
		C	498	4.6	640	0.001	
		D	482	4.6	607	0.1	
8.	 (di-6-ASPSPS)	A	496	4.8	624	0.04	0.015
		B	526	4.9	600	0.3	
		C	468	4.6	635	0.002	
		D	467	4.5	595	0.3	
9.	 (di-6-ASPBS)	A	495	4.8	622	0.05	0.010
		B	519	4.8	600	0.5	
		C	469	4.5	630	0.003	
		D	465	4.5	595	0.3	
10.	 (di-6-ASP)	A	490	4.7	615	0.03	0.012
		B	518	4.9	605	0.06	
		C	476	4.6	630	0.003	
		D	462	4.4	595	0.2	

Table I.—Continued

No.	Structure and Abbreviation	Solvent ^a	λ_{max}^{abs} (nm)	log ϵ	λ_{max}^{em} (nm)	ϕ	$K_d/3n$ (mg/mL)	
11.		A	565	4.7	692	0.2	0.06	
		B	587	4.8	665			
		C	500	4.4				
		D	533	4.5	665			
12.		A	475	4.5	610	0.003	0.3	
		B	507	4.5	605	0.003		
		C	460	4.3				
		D	450	4.1	584	0.04		
13.		A	498	4.7	625	0.05	0.08	
		B	524	4.7	545	0.5		
		C	485	4.5	640	0.004		
		D	471	4.4	605	0.3		
14.		A	485	4.6	715	0.04	0.04	
		B	521	4.5				
		C	467	4.4				
		D	463	4.2	690			
15.		A	482	4.6	~750	0.02	0.02	
		B	532	4.6				
		C						
		D	461	4.4				670
16.		A	493	4.5	745	0.03	0.03	
		B	542	4.4	675			
		C	470	4.1				
		D	468	4.3	640			
17.		A	495	4.6	745	0.04	0.04	
		B	542	4.6	675			
		C						
		D	467	4.5	640			
18.		A	427	4.5	600	0.002	1.9	
		B	423	4.1	587	0.04		
		C	410	4.4				
		D						
19.		A	440	4.5	588	0.3	0.3	
		B	462	4.5	560	0.1		
		C	422	4.5	599	0.02		
		D	421	4.3	566	0.3		
20.		A	523	4.5	640	0.03	No binding	
		B	553	4.7	620	0.5		
		C	496	4.4	655	0.003		
		D						

^a Solvent A, ethanol; B, chloroform; C, water; and D, lipid vesicles.

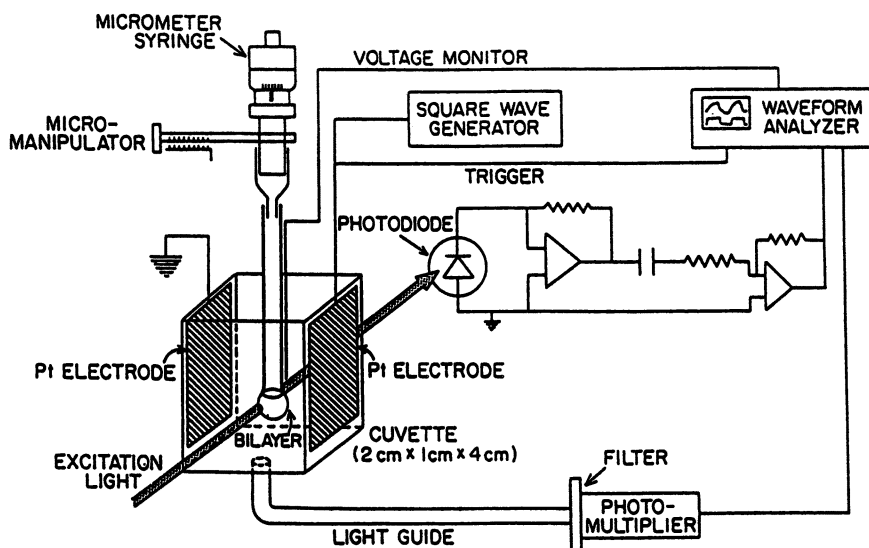


Figure 2. Apparatus for measuring potential-dependent spectral changes from a stained spherical lipid bilayer. (Reproduced with permission from reference 21. Copyright 1989 Biophysical Society.)

mechanism in some biological membranes that have been investigated; cf. reference 14).

Squid Axon and Other Excitable Cell Preparations. Over 1000 fast dyes have been screened on the voltage-clamped squid giant axon by Cohen and co-workers (1-3). A stabilized direct current (dc) light source is focussed onto the dye-stained axon and both fluorescence and transmittance changes in response to the voltage-clamp pulse are recorded via signal averaging. In addition to the tabulation of dye sensitivities, the axon system has been used for a more limited number of dyes to determine mechanistic information (2, 14). Many of the same experiments performed with the spherical bilayer can be repeated on the axon, thereby affording a direct comparison of dye behavior on a model and a natural membrane.

The size of the signal depends on a number of factors in addition to the sensitivity of the bound-dye spectra to membrane potential. A light-dependent toxicity, termed photodynamic damage, has been documented and tabulated in the axon (3) and can severely limit the usefulness of a dye. The efficiency with which a dye penetrates through the glial cells encasing the axon and then binds to the excitable membrane is clearly critical. The extinction coefficient and, for fluorescence, the emission quantum yield are

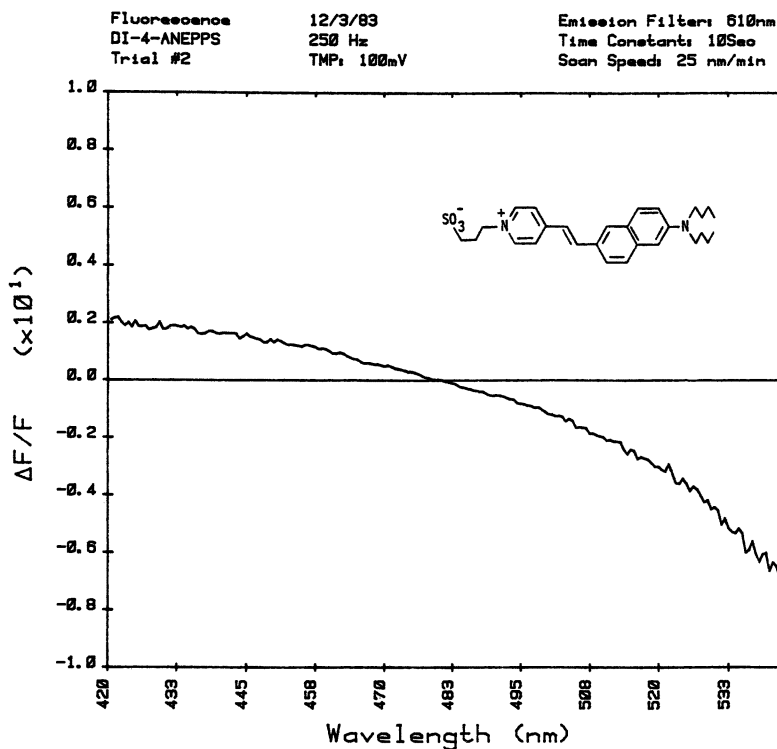


Figure 3. Relative fluorescence change as a function of excitation wavelength for a spherical bilayer stained with di-4-ANEPPS. (Reproduced from reference 10. Copyright 1985 American Chemical Society.)

other important factors. Recognition that these issues can be as significant as the relative spectral response prompted Cohen and his colleagues (1-3) to use the signal-to-noise ratio as the primary criterion for the merit of a dye on the squid axon. The signal-to-noise ratio incorporates all of the qualities that make a dye a useful potentiometric indicator, but also includes some of the idiosyncracies specific to the squid axon and its apparatus. Thus, neither the relative response obtained with the spherical bilayer model membrane nor the signal-to-noise ratio obtained with the squid axon are perfect measures of the general effectiveness of a dye. Furthermore, there is no guarantee that the mechanism of a dye response will be conserved from one preparation to another. Some very striking cases where the characteristics of a potentiometric response change in different species or cell types have been reported (14, 57). Still, in the majority of cases, the squid axon results do correlate well with the ability of a fast dye to monitor membrane potential changes in other excitable cell preparations.

Thus, although the tabulated squid axon data are extremely valuable for identifying a set of dyes that may prove suitable in a given experimental application, many investigators incorporate a testing and calibration phase into their research plans to find the optimal dye for their particular purpose. For example, Salama screened many dyes on his perfused heart preparation to find a dye with persistence and stability in addition to large potentiometric sensitivity (58–60). Grinvald screened a number of styryl dyes on neuroblastoma cells under the microscope and found some compounds with extraordinarily large sensitivities (6, 13) that have proven to be unique to that particular system. Grinvald et al. (30) found dyes that are optimized for intracellular injection of a single neuron within a network. A book edited by this author includes a series of chapters with other examples of preparation-specific dye optimization (4).

Quantitative Microscopy of Individual Nonexcitable Cells.

The slow dyes that change their spectral characteristics as a result of potential-dependent accumulation are well suited for cells in suspension. However, the complexity of these mechanisms makes it very difficult to interpret the change in dye fluorescence within a single cell. Accordingly, we set out to find dyes that display a rapid, reversible, potential-dependent intracellular accumulation with no accompanying spectral perturbation (44). As previously discussed, the dyes TMRE (Chart III) and TMRM emerged from this investigation and have proven useful in a wide variety of cultured cells.

Fast dyes often are directly sensitive to the local electric field, rather than the potential difference between the two compartments separated by the membrane. Therefore, fast dyes are capable of indicating differences in membrane potential along the surface of a single cell. Such membrane potential maps were first obtained (19, 61, 62) by using a digital video fluorescence microscope system to obtain and analyze images of cultured cells stained with di-4-ANEPPS (Chart II). A defined variation in membrane potential along the surface was generated by imposing a uniform external electric field across the cell. This field induces a membrane potential that, for spherical cells, varies according to a simple cosine dependence. This approach produces a predictable membrane potential based on a solution of Laplace's equation that is very convenient for screening fast dyes in a variety of cultured cells. The approach also has been used to calibrate the change in the ratio of di-4-ANEPPS fluorescence excited by two wavelengths (27). This technique overcomes problems associated with uneven dye staining and gradual fading of dye emission intensity. Most of the dyes in Chart II can be used to map membrane potential in this manner. The choice of appropriate dye usually depends on binding and solubility requirements for a given cell type and experimental protocol.

Summary

Potentiometric dyes have become widely accepted tools. Hundreds of papers in which such dyes are routinely used are published each year. However, the proper and optimal implementation of this technology requires an appreciation of the physical, chemical, and spectral properties of a dye, in addition to its voltage sensitivity. Some knowledge of the potentiometric mechanism also is needed for the intelligent use of a dye. This chapter has attempted to provide this information, but this knowledge can only help narrow the field to a manageable selection of candidates for a particular application. The final choice of the best dye will depend on appropriate experiments to test the candidates.

Acknowledgment

This work was supported by the U.S. Public Health Service Grant GM-35063.

References

1. Cohen, L. B.; Salzberg, B. M.; Davila, H. V.; Ross, W. N.; Landowne, D.; Waggoner, A. S.; Wang, C. H. *J. Membr. Biol.* **1974**, *19*, 1–36.
2. Ross, W. N.; Salzberg, B. M.; Cohen, L. B.; Grinvald, A.; Davila, H. V.; Waggoner, A. S.; Wang, C. H. *J. Membr. Biol.* **1977**, *33*, 141–183.
3. Gupta, R. K.; Salzberg, B. M.; Grinvald, A.; Cohen, L. B.; Kamino, K.; Leshner, S.; Boyle, M. B.; Waggoner, A. S.; Wang, C. H. *J. Membr. Biol.* **1981**, *58*, 123–137.
4. Loew, L. M. *Spectroscopic Membrane Probes*; CRC Press: Boca Raton, FL, 1988.
5. Cohen, L. B.; Salzberg, B. M. *Rev. Physiol. Biochem. Pharm.* **1978**, *83*, 35–88.
6. Grinvald, A.; Fine, A.; Farber, I. C.; Hildesheim, R. *Biophys. J.* **1983**, *42*, 195–198.
7. Platt, J. R. *J. Chem. Phys.* **1956**, *25*, 80–105.
8. Liptay, W. *Angew. Chem. Int. Ed. Engl.* **1969**, *8*, 177–188.
9. Loew, L. M.; Bonneville, G. W.; Surow, J. *Biochemistry* **1978**, *17*, 4065–4071.
10. Fluhler, E.; Burnham, V. G.; Loew, L. M. *Biochemistry* **1985**, *24*, 5749–5755.
11. Hassner, A.; Birnbaum, D.; Loew, L. M. *J. Org. Chem.* **1984**, *49*, 2546–2551.
12. Loew, L. M.; Simpson, L.; Hassner, A.; Alexanian, V. J. *Am. Chem. Soc.* **1979**, *101*, 5439–5440.
13. Grinvald, A. S.; Hildesheim, R.; Farber, I. C.; Arglistner, J. *Biophys. J.* **1982**, *39*, 301–308.
14. Loew, L. M.; Cohen, L. B.; Salzberg, B. M.; Obaid, A. L.; Bezanilla, F. *Biophys. J.* **1985**, *47*, 71–77.
15. George, E. B.; Nyirjesy, P.; Pratap, P. R.; Freedman, J. C.; Waggoner, A. S. *J. Membr. Biol.* **1988**, *105*, 55–64.
16. Waggoner, A. S.; Wang, C. H.; Tolles, R. L. *J. Membr. Biol.* **1977**, *33*, 109–140.
17. Dragsten, P. R.; Webb, W. W. *Biochemistry* **1978**, *17*, 5228–5240.
18. Verkman, A. S.; Frosch, M. P. *Biochemistry* **1985**, *24*, 7117–7122.
19. Gross, D.; Loew, L. M.; Webb, W. W. *Biophys. J.* **1986**, *50*, 339–348.
20. Ehrenberg, B.; Farkas, D. L.; Fluhler, E. N.; Lojewska, Z.; Loew, L. M. *Biophys. J.* **1987**, *51*, 833–837.

21. Lojewska, Z.; Farkas, D. L.; Ehrenberg, B.; Loew, L. M. *Biophys. J.* **1989**, *56*, 121–128.
22. Müller, W.; Windisch, H.; Tritthart, H. A. *Biophys. J.* **1989**, *56*, 623–629.
23. Loew, L. M.; Cohen, L. B.; Dix, J.; Fluhler, E. N.; Montana, V.; Salama, G.; Wu, J.-Y. *J. Membr. Biol.* **1992**, *130*, 1–10.
24. Davidenko, J. M.; Pertsov, A. V.; Salomonsz, R.; Baxter, W.; Jalife, J. *Nature (London)* **1992**, *355*, 349–351.
25. Rosenbaum, D. S.; Kaplan, D. T.; Kanai, A.; Jackson, L.; Garan, H.; Cohen, R. J.; Salama, G. *Circulation* **1991**, *84*, 1333–1345.
26. Chien, C.-B.; Pine, J. *Biophys. J.* **1991**, *60*, 697–711.
27. Montana, V.; Farkas, D. L.; Loew, L. M. *Biochemistry* **1989**, *28*, 4536–4539.
28. Davila, H. V.; Salzberg, B. M.; Cohen, L. B.; Waggoner, A. S. *Nature New Biol.* **1973**, *241*, 159–160.
29. Lojewska, Z.; Loew, L. M. *Biochim. Biophys. Acta* **1987**, *899*, 104–112.
30. Grinvald, A.; Salzberg, B. M.; Lev-Ram, V.; Hildesheim, R. *Biophys. J.* **1987**, *51*, 643–651.
31. Parsons, T. D.; Kleinfeld, D.; Raccuia-Behling, F.; Salzberg, B. M. *Biophys. J.* **1989**, *56*, 213–221.
32. Sims, P. J.; Waggoner, A. S.; Wang, C.-H.; Hoffman, J. F. *Biochemistry* **1974**, *13*, 3315–3330.
33. Waggoner, A. S. *Annu. Rev. Biophys. Bioeng.* **1979**, *8*, 847–868.
34. Waggoner, A. S. In *The Enzymes of Biological Membranes*; Martonosi, A. N., Ed.; Plenum: New York, 1985.
35. Loew, L. M.; Benson, L.; Lazarovici, P.; Rosenberg, I. *Biochemistry* **1985**, *24*, 2101–2104.
36. Loew, L. M.; Rosenberg, I.; Bridge, M.; Gitler, C. *Biochemistry* **1983**, *22*, 837–844.
37. Terasaki, M.; Song, J.; Wong, J. R.; Weiss, M. J.; Chen, L. B. *Cell* **1984**, *38*, 101–108.
38. Korchak, H. M.; Rich, A. M.; Wilkenfeld, C.; Rutherford, L. E.; Weissmann, G. *Biochem. Biophys. Res. Commun.* **1982**, *108*, 1495–1501.
39. Bashford, C. L.; Chance, B.; Smith, J. C.; Yoshida, T. *Biophys. J.* **1979**, *25*, 63–85.
40. Smith, J. C.; Chance, B. *J. Membr. Biol.* **1979**, *46*, 255.
41. Brauner, T.; Hulser, D. F.; Strasser, R. J. *Biochim. Biophys. Acta* **1984**, *771*, 208.
42. Labrecque, G. F.; Holowka, D.; Baird, B. *J. Immunol.* **1989**, *142*, 236–243.
43. Mohr, C. F.; Fewtrell, C. J. *J. Immunol.* **1987**, *138*, 1564–1570.
44. Ehrenberg, B.; Montana, V.; Wei, M.-d.; Wuskell, J. P.; Loew, L. M. *Biophys. J.* **1988**, *53*, 785–794.
45. Johnson, L. V.; Walsh, M. L.; Chen, L. B. *Proc. Natl. Acad. Sci. U.S.A.* **1980**, *77*, 990–994.
46. Johnson, L. V.; Walsh, M. L.; Bockus, B. J.; Chen, L. B. *J. Cell Biol.* **1981**, *88*, 526–535.
47. Chen, L. B. *Annu. Rev. Cell Biol.* **1988**, *4*, 155–181.
48. Farkas, D. L.; Wei, M.; Febroriello, P.; Carson, J. H.; Loew, L. M. *Biophys. J.* **1989**, *56*, 1053–1069.
49. Loew, L. M.; Farkas, D. L.; Wei, M.-D. In *Optical Microscopy for Biology*; Herman, B.; Jacobson, K., Eds.; Wiley-Liss: New York, 1990.
50. Loew, L. M. In *New Techniques of Optical Microscopy and Microspectrophotometry*; Cherry, R. J., Ed.; The Macmillan Press: London, 1991.
51. Huang, C. *Biochemistry* **1969**, *8*, 344–352.

52. Tien, H. T. *Bilayer Lipid Membranes*; Marcel Dekker: New York, 1974.
53. Loew, L. M.; Simpson, L. *Biophys. J.* **1981**, *34*, 353–365.
54. George, E. B.; Nyirjesy, P.; Basson, M.; Ernst, L. A.; Pratap, P. R.; Freedman, J. C.; Waggoner, A. S. *J. Membr. Biol.* **1988**, *103*, 245–253.
55. Nyirjesy, P.; George, E. B.; Gupta, R. K.; Basson, M.; Pratap, P. R.; Freedman, J. C.; Raman, K.; Waggoner, A. S. *J. Membr. Biol.* **1988**, *105*, 45–53.
56. Loew, L. M.; Scully, S.; Simpson, L.; Waggoner, A. S. *Nature (London)* **1979**, *281*, 497–499.
57. Ross, W. N.; Reichardt, L. F. *J. Membr. Biol.* **1979**, *48*, 343–356.
58. Morad, M.; Salama, G. *J. Physiol.* **1979**, *292*, 267–295.
59. Salama, G.; Johnson, R. G.; Scarpa, A. *J. Gen. Physiol.* **1980**, *75*, 109–140.
60. Salama, G.; Lombardi, R.; Elson, J. *Am. J. Physiol.* **1987**, *252*, H384–H394.
61. Gross, D.; Loew, L. M.; Ryan, T. A.; Webb, W. W. In *Ionic Currents in Development*; Nuccitelli, R., Ed.; Alan R. Liss: New York, 1986.
62. Gross, D.; Loew, L. M. In *Methods in Cell Biology*; Wang, Y.; Taylor, D. L., Eds.; Academic: New York, 1989; Vol. 30.

RECEIVED for review March 14, 1991. ACCEPTED revised manuscript September 1, 1992.

Water at the Macromolecular Surface

Solvation Energy and Functional Control

V. Adrian Parsegian¹, R. Peter Rand², Marcio Colombo^{3,4}, and Donald C. Rau³

¹Laboratory of Structural Biology, Division of Computer Research and Technology, National Institutes of Health, Bethesda, MD 20892

²Biological Sciences, Brock University, St. Catharines, Ontario L2S 3A1, Canada

³Laboratory of Biochemistry and Metabolism, National Institute of Diabetes, Digestive, and Kidney Disease National Institutes of Health, Bethesda, MD 20892

The contribution of hydration to the energetics of molecular conformation and assembly has been recognized for a long time, but has been difficult to measure. We use osmotic stress to measure the forces and energies in molecular assemblies. The same strategy can be used to measure the contribution of water to the chemical free energy change of individually functioning molecules. We describe, as examples, the contribution of water to the gating of membrane channels to the binding of oxygen to hemoglobin; and to the forces between bilayer membranes, within nonbilayer lipid assemblies, and on macromolecular surfaces. From the magnitude of their energies we conclude that hydration–dehydration reactions play an important but neglected role in molecular function.

THE MEASUREMENT OF INTERMOLECULAR FORCES and of the solvation of biomolecules can give new physical insight into the control of cellular processes. Our aim in this chapter is to illustrate the role of such measurements in molecular function. It has been known for some time that the forces encountered when macromolecules or membranes approach contact are

⁴ Current address: Department of Physics, IBILCE–UNESP, Sao Jose de Rio Preto, Sao Paulo, Brazil 15054

generally exponentially varying “hydration forces” coming from the energy needed to remove water from between membranes or between macromolecular surfaces. Quite recently, it became apparent that “allosterism”, changes in the functioning form of proteins, might entail substantial changes in the number of water molecules devoted to solvating the protein surface. If data from the systems examined so far are typical, that is, if molecular hydration–dehydration is a part of functional control, then measured hydration energies can be an important but neglected part of molecular function.

Our first task is linguistic: to present in tandem the mathematical forms that describe interaction forces together with the expressions for the chemical free energies acting to change macromolecular conformation. With this vocabulary we then review several examples of measured forces and conformation reactions. We conclude by comparing the magnitude of energies derived from forces with the energies needed to change properties of proteins or of lipid assemblies.

The Language of Hydration Forces

The hydration pressure, P (in dynes per centimeter squared or force per unit area), acts between parallel membranes and varies exponentially with a decay distance λ ($1-10$) so that one may write

$$P = P_0 \exp(-d_w/\lambda)$$

The base 10 logarithm of the fitted coefficient P_0 can be from 9 to 12 with P_0 in dynes per centimeter squared, λ can be from 1 to 2.5 Å (6), and d_w is membrane separation. When pressure P is integrated, it becomes an energy per unit area, E , and

$$E = \lambda P$$

with respect to infinite separation, an energy that can be on the order of 100 erg/cm² for polar surfaces brought to anhydrous contact.

It is instructive to convert these hydration energies of contact into chemical units. For example, over a 1×1 -nm patch of membrane the energy of 100 erg/cm² becomes

$$100 \text{ erg/cm}^2 \times 10^{-14} \text{ cm}^2 = 10^{-12} \text{ erg/nm}^2$$

If we divide by thermal energy units $kT = 4 \times 10^{-14}$ erg, this energy becomes

$$25kT/\text{nm}^2$$

Recalling that kT per particle is equivalent to 0.6 kcal/mol of particles, we have

$$15 \text{ kcal}/(\text{mol} \cdot \text{nm}^2 \text{ patch of membrane})$$

The area 1 nm^2 is on the order of the area occupied by one or two phospholipid molecules in membranes. The energy, 15 kcal/mol, is already on the order of the high-energy bonds involved in the production–utilization of adenosine triphosphate.

Between parallel linear molecules in well-defined arrays, exponential variation is again observed (11–13). The work of transfer of water from such an array is expressed in terms of a chemical potential of water or, equivalently, of an osmotic stress Π_{osm} on the lattice as a function of a lattice parameter such as lattice interaxial distance d_i :

$$\Pi_{\text{osm}} = \Pi_0 \exp(-d_i/\lambda)$$

When there is purely repulsive interaction between parallel linear molecules, the decay distance λ can range from 2.5 to 3.5 Å. Usually the molecules pack into a hexagonal array. The osmotic stress on the lattice can be converted to a force per unit length f between parallel molecules. Specifically (11),

$$f(d_i) = \Pi_{\text{osm}}(d_i)(d_i/\sqrt{3})$$

Because in most cases $\lambda \ll d_i$, both force per unit length and osmotic stress essentially vary exponentially.

For either the two- or the three-dimensional geometry of molecular arrays, the free energy of assembly, ΔG , is measured as the integral of osmotic stress versus solvent volume V :

$$\Delta G = \int \Pi_{\text{osm}} dV$$

Note that the temperature derivative of Π_{osm} gives the temperature derivative of free energy and is thus a measure of the entropy changes with molecular separation (14).

Chemical Free Energies

To derive the relation between the hydration energies of these structural arrays and the hydration energy of a single molecule undergoing a transition reaction between states, the free energy changes must be translated from force measurements into the terms of free energies that are inferred from

simple reactions. For the simplest possible case of Y being reversibly converted to Z,



we speak of an equilibrium constant K as

$$K = [Z]/[Y]$$

the ratio of the concentrations of the reactants, and a “standard free energy of reaction”

$$\Delta G = -RT \ln K$$

The reaction might be the allosteric switching of a protein between two states, which is often written



for the tense (T) and relaxed (R) states, or the opening (O) and closing (C) of a transmembrane ionic channel



If, for example, the transition between states incurs association with small molecules, L, the free energy of transition is changed by an amount equal to the number n of associated smaller molecules times the chemical potential of the small species:



$$K = [Z]/([Y][L]^n)$$

$$\Delta G = -RT \ln K = -RT \ln [Z]/[Y] + nRT \ln [L]$$

$$\Delta G = -RT \ln K_{Z/Y} + nRT \ln [L]$$

where we have explicitly written the Z/Y ratio in the equilibrium relation

$$K_{Z/Y} = [Z]/[Y]$$

More precisely, the function $RT \ln [L]$ should really be the variable part of the chemical potential of species L and the concentration [L] should be the activity, a_L , of substance L. The relation is then

$$\Delta G = -RT \ln K_{Z/Y} + nRT \ln a_L$$

Higher activity of L drives the molecule to state Z because the standard free energy ΔG is constant and independent of concentration.

This consideration of single molecules and their change in state in an Y/Z transformation can be combined with the idea of pressure volume work. It is immediately apparent that there can be an identifiable hydration part to a molecular transition; it will be felt by the protein as an osmotic sensitivity to the equilibrium balance of two states. Specifically, for

$$Y \rightleftharpoons Z$$

$$\Delta G = -RT \ln K$$

If the two states have different associated water volumes V_z and V_y , then there is a part of ΔG that is $\Pi_{\text{osm}}(V_z - V_y)$ and a change in equilibrium constant K that is

$$\exp(-\Pi_{\text{osm}}(V_z - V_y)/RT)$$

The associated volume change ($V_z - V_y$) can be measured directly through K as a function of system Π_{osm} . Both molecular arrays and individual molecules can be described in parallel language.

Force Measurements

We turn now to the actual measurement of swelling pressures and free energies, together with more specific enumeration of the biological systems that have now been characterized.

Because the swelling of any material in water is an osmotic process (i.e., a transfer of water between the system of interest and a reference phase of known water activity), it is most natural to study hydration by controlling water activity. The osmotic stress method, amply described elsewhere (15), was first used for direct force measurement between assembled molecules (1), but increasingly has been used to change the state of functioning proteins. It is now possible to observe the change in configurational motion of interacting molecules as a function of molecular separation wherein entropic forces of configuration couple with direct interactions to enhance the action of each (16). In brief, the system of interest is brought into thermodynamic equilibrium with a separate "reservoir" phase that has a volume in excess of the system under observation and that has water activity, pH, temperature, and small solute activities all strictly controlled. This thermodynamically equilibrated system can then also be observed further with every available experimental approach.

It should be obvious that measurements of forces between materials that are held onto rigid surfaces (17) are not equivalent to measurements of forces between free surfaces, or forces between free molecules, or of in-

tramolecular interactions. In comparison, the strategy of using osmotic stress allows the system to be measured in its spontaneously occurring form.

Osmotic stress measures forces corresponding to pressures over six decades, from 0.01 to 10,000 atm. With X-ray diffraction by ordered arrays, as shown in Figure 1, molecular dimensions and intermolecular spacings can be obtained with accuracies often better than 0.2 Å reproducibility. Alternatively, with probes of ionic channel conductance or of protein activity, the behavior of single molecules can be observed and the osmotically sensitive part of the underlying structural transformation can be extracted. Consequently, the change in the volume of associated water as the system goes between active and inactive forms can also be extracted.

Transmembrane Ion Transport Channels

We now describe some common features of swelling at different levels from osmotic stress measurements on several kinds of experimental systems.

Perhaps the most appealing example of a hydration–dehydration molecular system is that of an ionic channel across a low dielectric lipid bilayer or cell membrane. With reconstitution methods, it is possible to observe one molecular channel or conducting unit at a time; that is, to see the protein switching between open and closed states.

With osmotic stress, as illustrated in Figure 2, the opening of the channel takes place in the presence of neutral or charged molecules, particles so large as to be sterically excluded from channel entry and transport. It is as though there is a semipermeable membrane across the mouth of the channel. Excluded species then act osmotically against the aqueous space that is created when the channel is open. It should be obvious, but it is still necessary to emphasize, that the large-solute-excluding space need not be identical to the space through which ions move across the membrane.

In reaction–equilibrium language, there is work $\Pi_{\text{osm}} \Delta V$ required for the act of opening the channel. A measure of the ratio of times that the

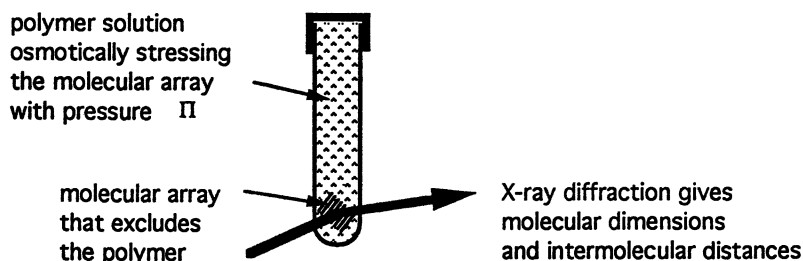


Figure 1. Schematic of the general method of using osmotic stress to measure the contribution of water to the energetics of a molecular array or of a molecular activity.

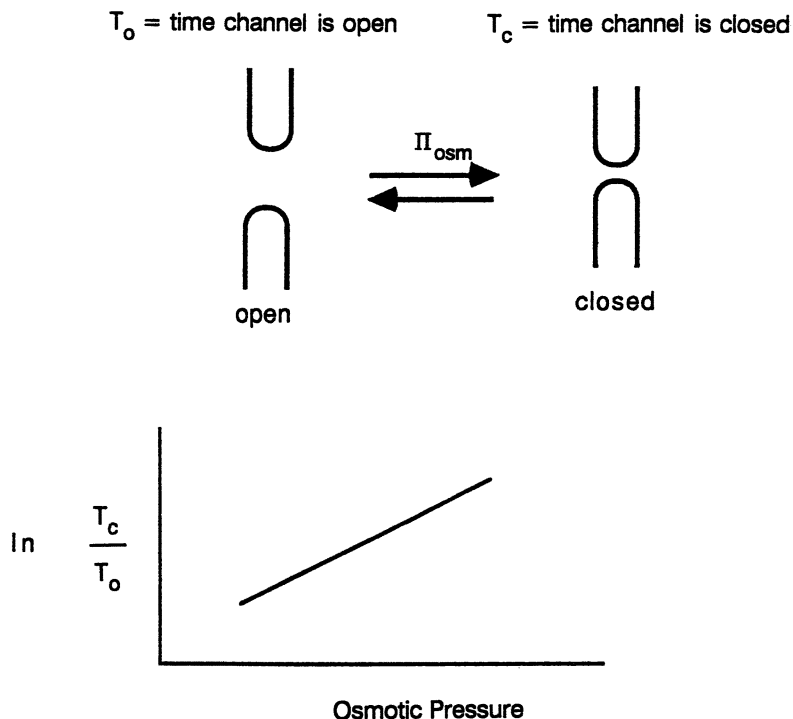


Figure 2. Illustration of how the osmotic stress method is used to measure the volume of water associated with the opening and closing of a membrane channel.

channel is open and closed is thus a measure of the equilibrium constant K and the osmotic work. Specifically,

$$K = [\text{open}]/[\text{closed}] = \text{constant} \times \exp(-\Pi_{\text{osm}} \Delta V/kT)$$

Measurement of how this ratio changes with the osmotic pressure of excluded solutes, in fact, measures ΔV :

$$d(\ln K)/d(\Pi_{\text{osm}}) = -\Delta V/kT$$

(Here we have used the molecular unit kT rather than the molar $RT = N_0 kT$, where N_0 is Avogadro's number, because we want to compute a volume change per single molecule.) ΔV is the actual volume of solute-excluding water that goes in and out of the channel on opening and closing.

The osmotic stress method was first applied to the large voltage dependent anion channel (VDAC), also known as "mitochondrial porin", from the outer membrane of mitochondria. The protein was placed in an artificial

bilayer membrane (BLM) and the conductance of a single molecule was observed between electrodes placed in adjoining chambers (18).

The volume of water associated with VDAC opening was $2-4 \times 10^4 \text{ \AA}^3$, a significant fraction of the total open channel volume of $2-8 \times 10^4 \text{ \AA}^3$ inferred earlier from the channel length and diameter. These dimensions were estimated from single channel conductivity (19) or from the size of excluded solutes or from reconstructed images (20). The qualitatively important result here is that channel "gating" seems to involve significant changes in channel structure. The act of opening and closing is not the result of inserting a plug or closing a turnstile that would show minimal osmotic sensitivity. The individual molecule seems to swell and shrink by some 700–1000 water molecules (18).

Another, more striking, feature is that even though the channel might stay in the open or closed state for minutes, the statistics gathered over very long observation times show that the occupation of these states follows the Boltzmann statistics implicit in the previously stated equations. That is to say, thermodynamics holds between and within states whose lifetimes are much longer than all characteristic molecular times of vibration, rotation, and even helix coil transition. From watching single-molecule kinetics, we are reassured that the statistics of protein conformation follow classical laws and that times of experiencing statistical averages fall into different domains. There is a good but neglected opportunity in these channels for protein physicists to think about kinetics.

Similar results have been seen in the four other osmotically stressed channels: the potassium channel from the squid giant axon (21), the sodium channel from the crayfish giant axon (22), alpha toxin from bacteria (23), and the peptide channel alamethicin (24). The volume of water that comes out seems to be a major part of the water volume inferred from open channel size. For example, the average K channel in squid giant axon, much smaller than VDAC, seems to expel 40–60 water molecules upon tightly closing (21).

Simultaneous recognition of the large volume of solute-excluding water that accompanies opening-closing and of the ion specificity of ion channels makes it clear that channels are always under osmotic stress from excluded species. This natural osmotic stress can be a significant factor in the control of those channels whose activity is sensitive to solution conditions.

Single Molecules in Solution

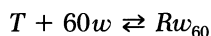
From proteins in membranes it is conceptually a small step to molecules in solution. Again, any change in molecular shape can incur changes in exposure of the protein area to the bathing solution as well as changes in the volume of aqueous cavities in proteins or between components of tetameric or oligomeric molecules. In principle, any of the seemingly ubiquitous allosteric transitions

of functioning proteins are susceptible to osmotic stress in the test tube or in the native cell.

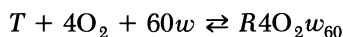
The first successful application of osmotic stress to a functioning protein was by Kornblatt and Hoa (25), who were working with cytochrome *c* oxidase. Equilibrium between the fully oxidized state and the first reduced state was found to be osmotically sensitive. The quantitative relation between osmotic pressure and redox equilibrium showed that about 10 water molecules must enter the protein during the entry of electrons undergoing transfer. Additionally, further intramolecular electron transport was shut down if these 10 water molecules were prevented from leaving. Consideration of the energy of moving a charge from highly polarizable water to poorly polarizable protein suggests that there should be no surprise that the electron needs water on its inbound journey. However, from the perspective of protein mechanism, it is news-worthy that the “apparently futile” water cycle must reflect a swelling and shrinking of the protein as it conducts charges through itself.

Hemoglobin seems to act like a molecular osmometer (26). Protein structure tells us that there is a 500–700-Å² increase in surface exposed to solution when the tetramer switches from the tense (*T*) deoxygenated form (with its tight bridges between polar groups on facing surfaces) to the relaxed (*R*) oxygenated form. The osmotic stress sensitivity of loading oxygen onto hemoglobin, Figure 3, shows that some 60 solute-excluding water molecules, *w*, are associated with the switching event.

In equilibrium-reaction language,



to emphasize the addition of water. Including the four oxygens,



In fact, for energetic purposes, these water molecules behave like a ligand whose transition-effecting action is analogous to that of ligands, such as oxygen, protons, and various anions, and controller molecules such as diphosphoglycerate (DPG). Because the sensitivity of a macromolecule to the activity of an associating ligand is directly proportional to the required number of molecules, the presence of 60 water molecules compared to 4 oxygen molecules or 1 DPG molecule should inspire reexamination of the importance of solvation in controlling oxygen uptake.

This reconsideration takes us into the purely phenomenological realm, to the fact that lowering the activity of water shifts the oxygen loading curve, O₂ bound versus O₂ pressure, *down*; fewer oxygen molecules bind at a given oxygen pressure. The existence of major solvation unexpectedly leads us to recognize a neglected factor in ligand binding, a new variable for allosteric control: water. The same molecules that bind to hemoglobin also can change

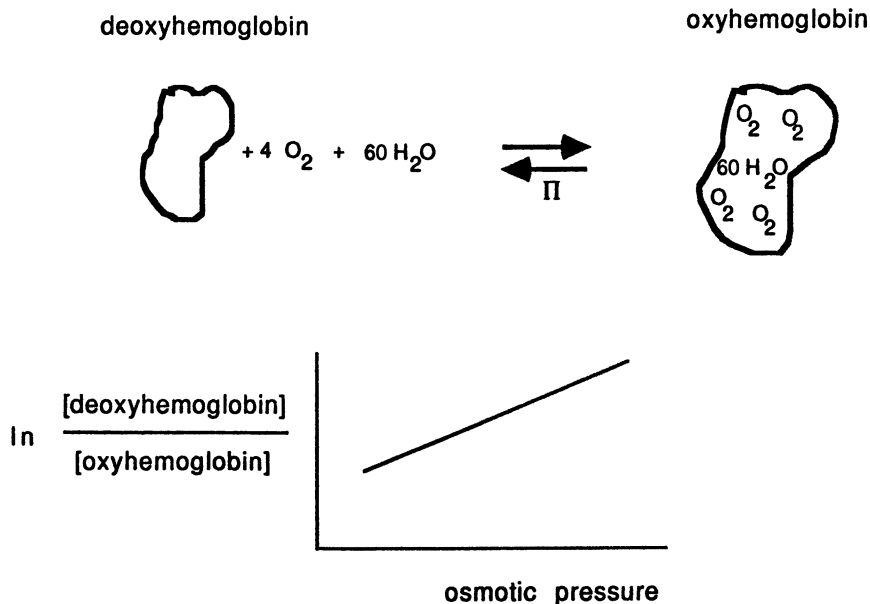


Figure 3. Illustration of how the osmotic stress method is used to measure the volume associated with the process of oxygen binding to hemoglobin.

the activity of water and, therefore, water binding. Both effects must be considered in dealing with conformational equilibrium. Molecular hydration can be a strong and neglected source of the energy that changes the oxygen affinity of heme groups when the molecule makes its deoxy \rightleftharpoons oxy switch. Potentially, this role of water would occur for most allosteric enzymes.

Ever since X-ray diffraction showed little difference in the two forms for the structure around the heme binding site, it has been a puzzle where the energy came in to change oxygen binding affinity. The best explanation is that the energy is delocalized over a large volume of protein (27). In fact, structural data also showed differences in protein-protein interaction between the two conformations: there are more protein-protein contacts in the deoxy than in the oxy form. Upon oxygenation, the large energy of hydrating the extra exposed surface, implicit in the 60 newly bound water molecules, may be the missing ingredient.

The most explicit recognition of macromolecular energies as surface energies of solvent excess or deficit is in the work of Blank (28, 29), who showed the essential equivalence of Gibbs adsorption isotherms and the changes in the energy of alternate protein states.

The attractive pulling forces of intramolecular bridging polar groups in the deoxy form might become repulsive spreading forces of hydration when

the same groups are exposed to water. The magnitude of energies involved might be gauged from the directly measured work of surface dehydration.

Forces Measured in Lipid Assemblies and between Large Molecules

Lipids. After 15 years of systematic measurement, interactions between amphiphilic assemblies, particularly between phospholipid bilayer membranes, are as well elaborated as for any class of materials (for a recent review, *see* reference 6). By their very nature, amphiphilic molecules self-assemble in water into structures that separate polar group-water compartments from hydrophobic compartments. Aqueous spaces in these assemblies swell and shrink under the combined influence of all the forces that stabilize the molecular assemblies as well as those that determine their association. Because the subject has been so thoroughly reviewed, we need mention only general points here.

Forces between Bilayers. For each of the several dozen systems examined, bilayer interactions are dominated at close range by exponential hydration repulsion, which can be described by the equations given earlier. Electrostatic repulsion and van der Waals attraction contribute little to the interaction energy when the surfaces are closer than about 20–30 Å. A number of specific differences have been observed, and the coefficients and decay lengths have all been documented. One of the largest differences is shown in Figure 4. The design and goal of these studies has been to understand the cause of hydration repulsion. Polar group identity, polar group methylation, the physical state of the hydrocarbon chain, chain heterogeneity, and mixing of lipid species all appear to affect hydration repulsion.

One general and large influence on the magnitude of hydration repulsion is methylation of the surface. The addition of a single methyl group or of a small fraction of methylated species to the surface molecules causes a disproportionate increase in hydration repulsion and bilayer swelling or separation. The ability of surface molecules to form intermolecular hydrogen bonds appears to diminish considerably the net repulsive forces. Correlation of the strength of hydration forces with surface dipole potentials (30) has raised the difficulty of separating the cause and effect of these two forces, because perturbed water is expected to contribute to both. The overall picture is one in which specific polar group-water interactions greatly influence the hydration forces, attractive and repulsive, at small separations.

Although hydration forces are dominant at short range, it is the equilibrium separations in excess water that really determine the degree of swelling in these systems. At this limit of swelling it is the other forces against which the shorter range hydration repulsion is balanced that determines the final

interbilayer separation measured using X-ray diffraction

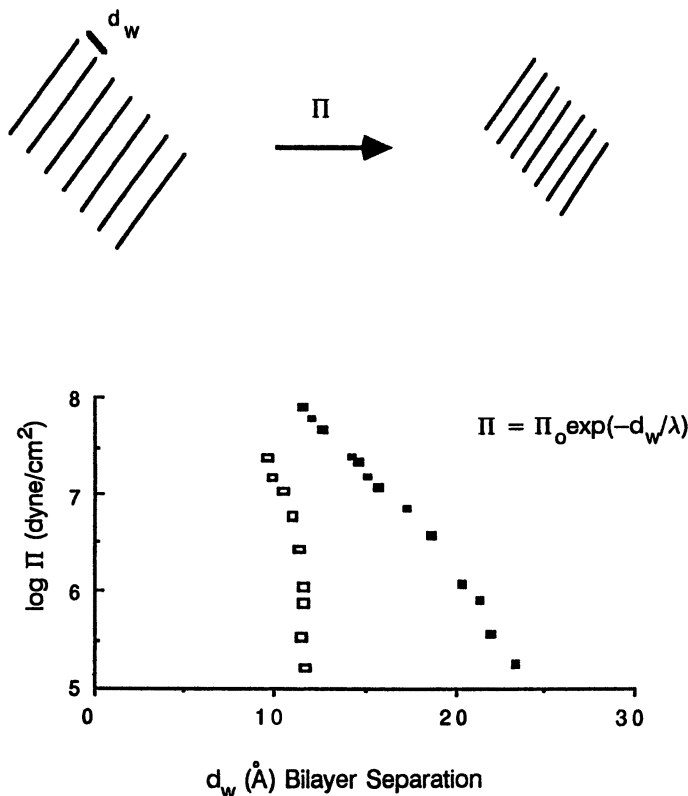


Figure 4. The osmotic stress method used to measure net repulsive pressure between membranes as it varies with membrane separation. Solid symbols represent stearyl-oleoylphosphatidylcholine; open symbols represent palmitoyl-oleoylphosphatidylethanolamine.

state. The van der Waals attraction is normally balanced by hydration repulsion to determine the equilibrium swelling of electrostatically neutral bilayers; it is capable of producing collapse to a fully dehydrated state only in those instances where hydration repulsion is apparently balanced by attractive intersurface correlations (31), for example, in the cases of divalent-cation-induced aggregation of acidic phospholipids (32, 33). Another force that has gained fuller appreciation in the past few years is that caused by thermal fluctuations of bilayers (34). When the net forces between bilayers are weak enough to allow bilayer thermal motion, the consequent steric forces of mutual collision enhance the separation of neutral bilayers (35). Through the interplay of these configurational forces and direct forces, decay rates of electrostatic repulsion are modified (36). Otherwise, electrostatic repulsion

alone results in indefinitely large swelling or separation of charged lipid bilayers.

Nonbilayer Assemblies. Osmotic stress has also been used to probe the energetics of nonbilayer assemblies of phospholipids, particularly the inverted H_{II} phase shown in Figure 5. In this structure parallel tubes of water, whose axes are arranged on a hexagonal net, are bounded by the polar groups of the phospholipids whose tails fill the intervening space. The monolayer of lipid has a spontaneous radius of curvature (37) that it assumes when excess water and alkane solvents together relax both hydration and hydrocarbon chain stresses. This radius, in the absence of solvent stress, defines the degree of swelling and it can be greatly increased by the addition of lipids with larger or more hydrated polar groups. The remarkable point is that the hexagonal phases of larger spontaneous radii of curvature take up much more water than does the equivalent lamellar phase (7). This extra drive for hydration, that previously required the polar groups to hydrate directly, is understood in terms of the monolayer curvature energy that creates large water cavities required by the large spontaneous radius.

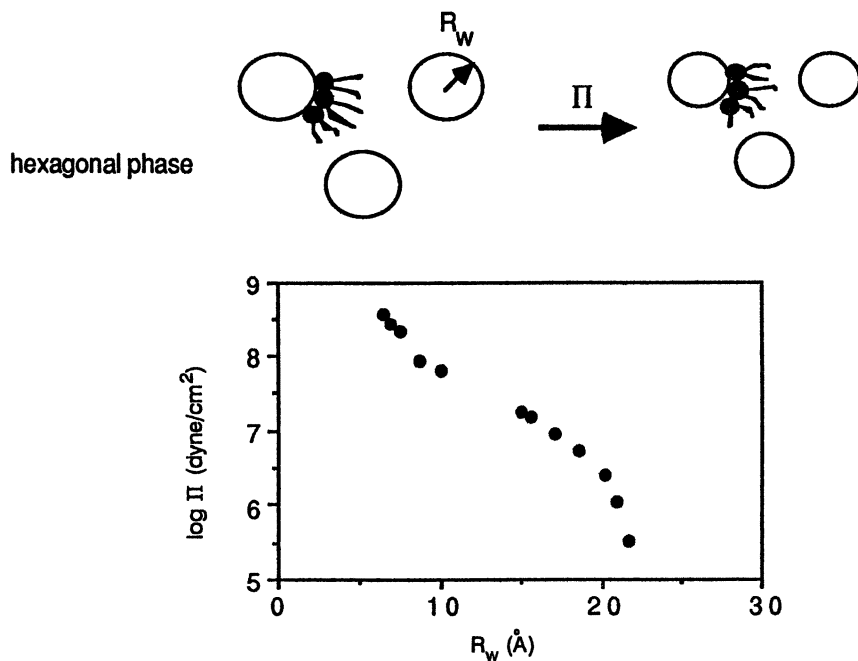


Figure 5. The osmotic stress method used to determine the relation between structural dimensions of the hexagonal phase and the applied stress.

Under osmotic stress, the aqueous compartment shrinks and the monolayer around the water cylinder bends. The osmotic work can be translated into monolayer- and bilayer-bending moduli (7) to yield a bilayer value of about 1.5×10^{-12} erg, which is in qualitative agreement with measurements from bilayer mechanics (38). It is possible to refine the analysis of H_{II} dehydration to include the change in area per lipid molecule and to extract both a bending modulus and a lateral compressibility moduli. This refinement gives moduli in close quantitative agreement with other measures of mechanical deformation (39).

Phase Transitions in Lipid Assemblies. The rich polymorphism of amphiphilic systems, of which the multilamellar and the H_{II} phases are only two structures, was made evident from the seminal work of Luzzati and co-workers. Since that early work, an immense variety of water-induced phase transitions have been observed and rationalized in terms of an apparently systematic connection between water content and polar group molecular area. Therefore, the recent observation of a double transition— H_{II} to lamellar back to H_{II} —from continual hydration of dioleoylphosphatidylethanolamine (40) was a surprise. Furthermore, an estimate of the cost of uncurling the monolayer in the formation of bilayers based on the previously described bending modulus far exceeds the osmotic work that actually produced the transition. Although this transition sequence can successfully be accounted for by simple thermodynamical principles, it, in fact, contains many geometry-dependent free energy contributions that we simply do not yet understand (41).

Interactions between Macromolecules. Polysaccharides. Consistent with other materials, stiff polysaccharides approaching contact repel with a force that varies exponentially with distance (Figure 6). The forces are essentially independent of ionic strength. A recent study (13) on xanthan polysaccharides, aligned into well defined arrays, showed a 3.3-Å decay distance regardless of whether the bathing medium contained 0.1–1-M NaCl or 0.05–0.1-M $MgCl_2$ or Ca rather than Mg ions. Independence of salt concentration and type is all the more striking when one recalls that xanthan bears charged pyruvate groups. The force versus distance curve shifts slightly to smaller separations with no effect on the spatial decay constant when pyruvates are removed from the molecular surface. Another polysaccharide, wholly uncharged schizophyllan, showed similar spatial variation but weaker forces.

Polysaccharides are found throughout the plant and animal kingdoms where they are essential for their ability to absorb water, to control viscosity, and to maintain the integrity of neighboring cells. In most cases these molecules are flexible; their swelling is a combination of polymer entropic, electrostatic, and hydration forces (42). The difficulty of simultaneously

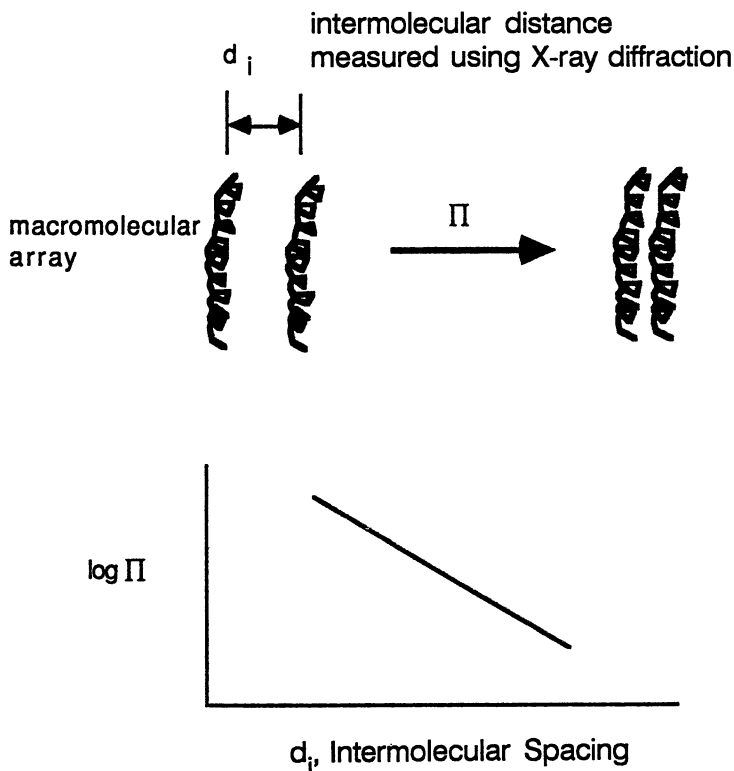


Figure 6. Osmotic stress used to measure the intermacromolecular force as it varies with molecular distance.

accounting for so many factors has made the identification of each factor difficult. Now, with the results of forces measured between stiff molecules in various ionic solutions, it is possible to separate the contribution of direct solvation from the entropic and electrostatic contributions.

Forces between DNA Double Helices. The repulsion and attraction of DNA is the molecular interaction most studied to date. In simple salts, repulsion is again exponential with decay rates of 2.8–3.3 Å (11). Unlike forces between polysaccharides, the coefficient of the force depends on the type of cationic counterion, even though electrostatic double layer repulsion is low enough to suggest that the helix is largely neutralized by ion association.

The fact that DNA is tightly packaged in cells or in viruses suggests the action of condensing species that seem to hold the double helices together. In vitro experiments with these condensing agents show the DNA precipitating into well-defined arrays with equilibrium separations of 5–15 Å between

molecular surfaces. By measuring the forces encountered to bring the molecules closer together than the 5–15-Å spontaneous separations, we have realized that the operative attractive force is also a force of hydration or, rather, also a structural force with its origin possibly in the perturbation of the arrangement of water around the DNA helix (43).

The measured strength of this attractive hydration force, especially its sensitivity to the identity and activity of the condensing agent, makes it a likely candidate for explaining the strong fit of complementary surfaces. The old lock-and-key idea is revitalized by the quantitative idea of the nature of the attractive force that radically differs from the much weaker van der Waals forces usually invoked to explain the formation of molecular arrays.

The temperature dependence of measured forces has allowed us to separate the entropic and enthalpic parts of the free energy of interaction. Because the force between two molecules is a derivative of the free energy of bringing them together and because the temperature derivative of a free energy is an entropy, the temperature derivative of a force is entropy versus separation (43). Remarkably, both of these components show exponential variation with separation. For the best-studied case, Mn–DNA, the entropy of water release from between two helices as they are brought together is *positive*, which is evidence for the idea that water is to some extent immobilized in the vicinity of the molecular surface relative to its condition upon release into the bathing water solution.

Since the theories of Kauzmann (44) were published, entropically inspired forces have been recognized as a key factor in macromolecular organization. This concept is usually thought of in terms of hydrophobic forces around nonpolar surfaces, although Kauzmann recognized both polar and nonpolar surfaces in his original work. The results of the DNA force measurements show that water entropy is also important in considering the interaction of polar molecules. In fact, the possibilities of specifying and modifying polar surfaces are so great that we now believe that entropic forces that involve hydration are a key factor in molecular assembly.

Discussion and Conclusions

The origin of life in aqueous milieu and the necessity of the internal aqueous environment in living systems leads us to expect the hydration and swelling of biomolecules to be a central feature of their organization and function. Direct measurement of intermolecular forces in aqueous solutions now shows us new ways in which nature achieves the controlled swelling essential to living matter.

Even single molecules go between well-defined states with different degrees of hydration. How might this theme of hydration be an organizing principle for thinking about biological processes? How might the exquisitely

controlled physical and chemical properties of a single hemoglobin molecule or an ionic channel be related with the general forces observed between less-specific surfaces, such as lipid bilayers or DNA double helices?

We have investigated two ideas:

- Biological materials, such as allosteric proteins, appear to control hydration through the molecular design of interacting surfaces and by the adsorption of specifically designed molecular ligands.
- Hydration energies of interaction are large.

We stated before that it takes about 100 erg/cm^2 to push phosphatidylcholine (PC) bilayers together to anhydrous contact. Per 100 \AA^2 , this is about the energy of two high-energy phosphate bonds in ATP hydrolysis. (It is worth noting here our unpublished observation that phosphate-backbone DNA in a $\text{N}^+(\text{CH}_3)_4$ counterion salt solution shows approximately the same repulsion as egg phosphatidylcholine when one corrects for curvature and for area per polar group. The phosphorylcholine polar group of PC is a phosphate linked to a $\text{N}^+(\text{CH}_3)_4$ by a $-\text{CH}_2-$ bond. There seems to be a simple way to go between planar membrane and cylindrical molecular geometry.)

How might one think about this energy as it is felt in the transition between the forms of hemoglobin with a difference of 60 associated water molecules and a 550-\AA difference in solvent exposed area? Even if hydration energy of the exposed protein surface were only one-tenth of that for PC or DNA, the expected contribution would be

$$550 \text{ \AA}^2 \times 1.5 \text{ kcal/mol}/100 \text{ \AA}^2 = 8 \text{ kcal/mol hemoglobin}$$

Is it only a coincidence that this is of the same magnitude as the difference in the energy of oxygen binding when the binding constant changes by a factor of 1000? Specifically,

$$RT \ln 1000 = 0.6 \text{ kcal/mol} \times 6.9 = 4 \text{ kcal/mol}$$

The solvation-desolvation of the protein surface might be considered as a means of storing or spending energy in a way that can be shifted to other parts of the molecule, such as the oxygen-binding heme groups, when molecular transitions occur.

Hydration is only one part of the ligand-binding and conformation-changing event. At the midpoint of a transition, the condition where the molecule is equally likely to be in one or the other form, the *total* free energy difference is *zero*. However, this zero is a balance of energies on the scale of the energies computed before. The proverbial small difference between large

numbers is the reason why the transition will be exquisitely sensitive to changes in solution condition or to changes thorough mutation.

It is worth noting that the free energy consequence of water removal, the osmotic pressure times the volume of water removed, need not be that great. The 0.15 ionic molarity of mammalian blood translates into an osmotic pressure on the order of 5–10 atm or $5\text{--}10 \times 10^6$ erg/cm³. One way to comprehend the meaning of this is to say that removal of a 5000-Å³ volume of solute-inaccessible water will “cost” one kT per molecule or one RT per mole of protein. On this scale the osmotic work of removing 60 water molecules with a volume of $\Delta V = 30 \times 60 = 1800$ Å³ is not so great.

Put another way, for this volume there is a corresponding work,

$$\begin{aligned}\Pi_{\text{osm}} \Delta V &= 10^{(7)} \text{ erg/cm}^3 \times 1800 \times 10^{(-24)} \text{ cm}^3 \\ &= 1.8 \times 10^{(-14)} \text{ erg} = (1.8/4.2)kT \\ &= 0.43kT/\text{molecule} = 0.43RT/\text{mol}\end{aligned}$$

This value is about what one needs to change a 50–50 distribution between two states to a 60–40 distribution; that is,

$$\Pi_{\text{osm}} \Delta V = RT \ln(60/40) = 0.4RT$$

The important part of the energy of hydration is that which is seen through the reversible process of bringing two surfaces together from infinite separation—the 100 erg/cm² used in the foregoing illustration. These hydration energies, then, can translate into large stresses on solvent-exposed surfaces.

How might these energies of interaction couple with the energies of protein deformation that effect changes in function? In a set of highly original papers, Blank (28, 29) has elaborated the connection between surface energies, adsorption isotherms, and hemoglobin function. For a specific suggestion of this kind of connection in terms of the energies described here, we close with a speculation. It has been known for some time that hydration forces between surfaces couple with forces of lateral deformation within each surface (3). For a functioning protein, exposure of new surface to water does not only mean a large energy of solvation; it also means a significant energy for stressing the protein surface. Groups that are pinned down by peptide contact in the unsolvated state experience a reversal of lateral tension as they spread out in solvent. The energies available and the reversal of sign of lateral tension might provide a key to illumination of the connection between allostery, hydration, and changes in molecular activities.

Acknowledgments

R. P. Rand acknowledges the financial support of the Natural Sciences and Engineering Research Council of Canada. V. A. Parsegian thanks the Office of Naval Research for the award of Grant No. N00014-93-F-0201.

References

1. LeNeveu, D. M.; Rand, R. P.; Parsegian, V. A. *Nature (London)* **1976**, *259*, 601-603.
2. LeNeveu, D. M.; Rand, R. P.; Parsegian, V. A.; Gingell, D. *Biophys. J.* **1977**, *18*, 209-230.
3. Parsegian, V. A.; Fuller, N. L.; Rand, R. P. *Proc. Natl. Acad. Sci. U.S.A.* **1979**, *76*, 2750-2754.
4. Lis, L. J.; McAlister, M.; Fuller, N. L.; Rand, R. P.; Parsegian, V. A.; *Biophys. J.* **1982**, *37*, 657-666.
5. Rand, R. P. *Annu. Rev. Biophys. Bioeng.* **1981**, *10*, 277-314.
6. Rand, R. P.; Parsegian, V. A. *Biochim. Biophys. Acta* **1989**, *988*, 351-376.
7. Rand, R. P.; Fuller, N. L.; Gruner, S. M.; Parsegian, V. A. *Biochemistry* **1990**, *29*, 76-87.
8. McIntosh, T. J.; Simon, S. A. *Biochemistry* **1986**, *25*, 4058-4066.
9. McIntosh, T. J.; Simon, S. A. *Biochemistry* **1986**, *25*, 4948-4952.
10. McIntosh, T. J.; Magid, A. D.; Simon, S. A. *Biochemistry* **1988**, *26*, 7325-7332.
11. Rau, D. C.; Lee, B. K.; Parsegian, V. A. *Proc. Natl. Acad. Sci. U.S.A.* **1984**, *81*, 2621-2625.
12. Rau, D. C.; Parsegian, V. A. *Biophys. J.* **1987**, *51*, 503.
13. Rau, D. C.; Parsegian, V. A. *Science (Washington, D.C.)* **1990**, *249*, 1278-1281.
14. Prouty, M. S.; Schechter, A. N.; Parsegian, V. A. *J. Mol. Biol.* **1985**, *184*, 517.
15. Parsegian, V. A.; Rand, R. P.; Fuller, N. L.; Rau, D. C. In *Methods in Enzymology, Biomembranes, Protons and Water: Structure and Translocation*; Packer, L., Ed.; Academic: New York, 1986; Vol. 127, pp 400-416.
16. Podgornik, R.; Rau, D. C.; Parsegian, V. A. *Macromolecules* **1989**, *22*, 1780-1786.
17. Israelachvili, J. N.; Marra, J. In *Methods in Enzymology, Biomembranes, Protons and Water: Structure and Translocation*; Packer, L., Ed.; Academic: New York, 1986; Vol. 127, pp 353-360.
18. Zimmerberg, J.; Parsegian, V. A. *Nature (London)* **1986**, *323*, 36-39.
19. Benz, R.; Ludwig, O.; de Pinto, V.; Palmieri, F. In *Achievements and Perspectives of Mitochondrial Research*; Quagliariello, E.; Slater, E. C.; Saccone, C.; Palmieri, F.; Kroon, A. M., Eds.; Elsevier: New York, 1985; Vol. 1, pp 317-327.
20. Manella, C. A.; Radermacher, M.; Frank, F. *Proc. 42nd Electron Micros. Soc. Am.* **1984**;664.
21. Zimmerberg, J.; Benzanilla, F.; Parsegian, V. A. *Biophys. J.* **1990**, *57*, 1049-1064.
22. Starkus, J. G.; Rayner, M. D.; Ruben, P. C.; Alicata, D. A. *Biophys. J.* **1991**, *59*, 71a.
23. Kasianowicz, J. J.; Moore, C. R.; Zimmerberg, J.; Pasternak, C.; Bashford, C. L.; Parsegian, V. A. *Biophys. J.* **1991**, *59*, 458a.
24. Bezrukov, S. M.; Vodyanoy, I. *Biophys. J.* **1991**, *59*, 457a.
25. Kornblatt, J. A.; Hoa, G. H. B. *Biochemistry* **1990**, *29*, 9370-9376.
26. Colombo, M. F.; Rau, D. C.; Parsegian, V. A. *Biophys. J.* **1991**, *59*, 611a.
27. Hopfield, J. J. *J. Mol. Biol.* **1973**, *77*, 207-222.

28. Blank, M. In *Bioelectrochemistry: Ions, Surfaces, Membranes*; Advances in Chemistry Series 188; Blank, M., Ed.; American Chemical Society: Washington, DC, 1980; pp 187–192.
29. Blank, M. *Colloids Surf.* **1980**, *1*, 139–149.
30. Simon, S. A.; McIntosh, T. J. *Proc. Natl. Acad. Sci. U.S.A.* **1989**, *86*, 9263–9267.
31. Rand, R. P.; Fuller, N. L.; Parsegian, V. A.; Rau, D. C. *Biochemistry* **1988**, *27*, 7711–7722.
32. Kachar, B.; Fuller, N. L.; Rand, R. P. *Biophys. J.* **1986**, *50*, 779–788.
33. Coorssen, J.; Rand, R. P. *Stud. Biophys.* **1988**, *127*, 53–60.
34. Helfrich, W. *Z. Naturforsch.* **1978**, *33a*, 305–315.
35. Safinya, C. R.; Smith, E. B.; Roux, D.; Smith, G. S. *Phys. Rev. Lett.* **1989**, *62*, 1134–1137.
36. Evans, E.; Parsegian, V. A. *Proc. Natl. Acad. Sci. U.S.A.* **1986**, *83*, 7132–7136.
37. Kirk, G. L.; Gruner, S. M. *J. Phys. (Les Ulis, Fr.)* **1985**, *46*, 761–769.
38. Bo, L.; Waugh, R. E. *Biophys. J.* **1989**, *55*, 509–517.
39. Kozlov, M. M.; Winterhalter, M. *J. Phys. II France* **1991**, *1*, 1085–1100.
40. Gawrisch, K.; Parsegian, V. A.; Hajduk, D. A.; Tate, M. W.; Gruner, S. M.; Fuller, N. L.; Rand, R. P. *Biophys. J.* **1991**, *59*, 548a.
41. Gawrisch, K.; Parsegian, V. A.; Hajduk, D. A.; Tate, M. W.; Gruner, S. M.; Fuller, N. L.; Rand, R. P. *Biochemistry* **1992**, *31*, 2856–2864.
42. Peitsch, R., Reed, W. *Biopolymers* **1992**, *32*, 219–238.
43. Leikin, S.; Rau, D. C.; Parsegian, V. A. *Phys. Rev. A* **1991**, *44*, 5272–5278.
44. Kauzmann, W. *Adv. Protein Chem.* **1959**, *14*, 1–63.

RECEIVED for review August 12, 1991. ACCEPTED revised manuscript August 17, 1992.

Connexin-32: A Protein That Forms Channels through One or Two Membranes

Andrew L. Harris

Thomas C. Jenkins Department of Biophysics, The Johns Hopkins University, 3400 North Charles Street, Baltimore, MD 21218

Connexin protein, which forms gated channels through closely apposed cell membranes ("gap junction channels"), also forms channels in single membranes. The mechanisms by which single- and double-membrane connexin channels are formed, gated, and regulated are of biophysical interest, yet are largely unknown. Biophysical studies have been hindered by inaccessibility of cellular connexin channels and by the unique problems of connexin reconstitution. Connexin-32 from isolated gap junctions and from monoclonal immunoaffinity purification from plasma membrane forms large, dynamically gated channels in liposomes and planar bilayers. These connexin channels may be single hemichannels—the subunits that span a single membrane in situ—and are accessible for detailed biophysical study. Implications and possibilities for future studies of permeation, gating, and modulation are discussed.

THE STUDY OF PROTEIN FUNCTION is increasingly focused on the interactions between protein structure, electrochemical potentials, and molecular motion. For membrane proteins, insertion through a phospholipid bilayer imparts a defined orientation to the protein and a specified relation between the macroscopic electrical field and the axis of the molecule normal to the membrane. These constraints can be exploited to obtain detailed information about membrane protein function and dynamics, particularly for proteins that form aqueous pores through membranes. The ability to record currents that

0065-2393/94/0235-0197\$09.26/0
© 1994 American Chemical Society

flow through individual channel molecules [in cell membranes (1) and in planar phospholipid bilayers (2, 3)] and so to observe directly transitions between conductance states provides precise functional information that is unavailable for other proteins. Membrane ion channels, therefore, afford a unique opportunity to explore how physical and electrochemical forces interact with the structure–function of proteins, particularly when amino acid sequence and transmembrane topology are known.

This chapter reviews some of the molecular biophysical questions that are raised by the properties of one class of channel-forming proteins, *connexin*, and that may be addressed through the study of connexin in reconstituted membrane systems. The first section introduces issues of biophysical interest and provides background information about connexin. The second section discusses the prospects for utilizing reconstituted systems to study the key questions, followed by a brief review of data from our laboratory. The final sections evaluate the findings and discuss future studies.

The Gap Junction Channel, Connexin Protein, and Their Importance for Electrochemical Studies

In tissues, connexin protein composes structures called *gap junction channels*. Each junctional channel forms a wide, dynamically gated aqueous pore through two closely apposed cell membranes (Figure 1) (4–6). Solutes up to ~ 14 Å across can diffuse from cell to cell through the pores without leakage to the extracellular environment. The junctional channel is formed by two end-to-end subunits (called *hemichannels* or *connexons*) that each span a single cell membrane. The hemichannel is composed of six connexin monomers arranged around a central aqueous pore. Each connexin monomer spans the plasma membrane four times, with C- and N-termini in the cytoplasm and two extracellular loops (7–9; reviewed in reference 10). Connexins are a family of closely related proteins of which a steadily increasing number have been cloned and sequenced (11, 12). The amino acid sequences of connexins are highly homologous to one another in transmembrane and extracellular domains, but highly variable in cytoplasmic domains (11).

Gap junction channels provide pathways for direct current flow between cells and for regulated intercellular movement of important cellular signaling molecules, including cyclic nucleotides (5, 13–17). Consequently, gap junction channels are thought to play crucial regulatory roles in cell biology, development, and physiology (18–22).

Connexin protein is unique in forming a gated pore through two membranes. Two questions particular to this structure are (1) how is the junctional channel assembled (e.g., how do the two hemichannels find each other and interact to form a stable structure) and (2) what is the interaction between

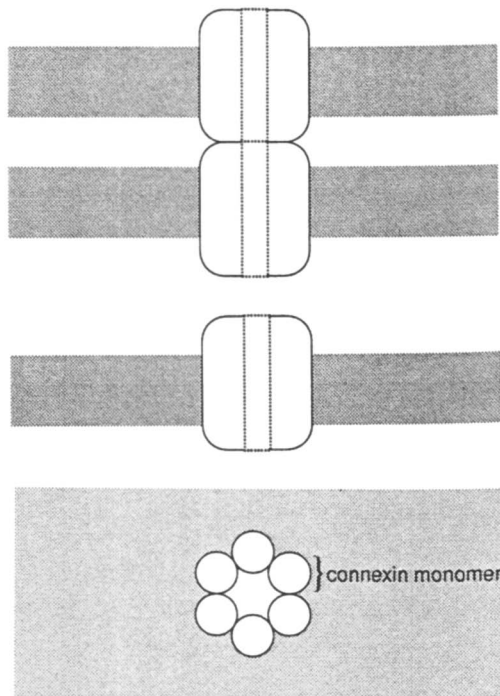


Figure 1. Schematic drawings of connexin channels. The upper figure is an edge-on view of the junctional channel in situ that spans two plasma membranes (gray areas) across extracellular space. The middle figure shows a single hemichannel, the subunit of the junctional channel that spans each membrane. The lower figure is an end-on view of a hemichannel that shows the arrangement of six connexin monomers around a central, water-filled pore.

the two hemichannels during gating transitions and regulatory processes? Analogous questions apply to other protein complexes that mediate signaling across double-membrane structures, such as the ryanodine receptor–dihydropyridine receptor complex in muscle (23). These questions, and others that pertain specifically to ion channels, are introduced in succeeding text.

Junctional Channel Structure(s). At regions of cell contact, junctional channels are found in two-dimensional arrays that can contain thousands of channels. The arrays vary from loose collections of channels to pseudocrystalline two-dimensional lattices. A portion of the most regular arrays can be isolated by techniques that select for membrane structures that are resistant to severe chaotropic treatments such as ionic detergents or prolonged exposure to highly alkaline conditions (pH 12.5) (24–27). The highly regular arrays of channels obtained have been studied in detail with electron and X-ray diffraction techniques (reviewed in reference 28), and

recently by atomic force microscopy (29), to reveal structural features. These studies established the hexameric structure of the hemichannel and provided two possible structural correlates of gating. In one view, the pore is occluded at each cytoplasmic end by a protein mass that can lift away from the pore—a trap door system (30). Another view is that the connexin monomers are rigid rods that undergo a torsional tilt, sliding against each other and twisting to close the lumen of the pore at the cytoplasmic end—somewhat analogous to an iris diaphragm (31, 32).

Functional Hemichannels in Cells. A growing body of circumstantial evidence indicates that single hemichannels are functional channels in plasma membranes. There is indirect evidence for the existence of large channels formed by connexin in the plasma membrane of a macrophage cell line (33). Physiological data strongly suggest that hemichannels mediate a gated plasma membrane conductance in teleost horizontal cells (34). When *Xenopus* oocytes are injected with mRNA coding for connexin-46 (but not other connexins), a voltage-gated conductance and a permeability to the dye Lucifer Yellow are induced in the plasma membrane (35, 36). These findings indicate that plasma membrane connexin channels have normal physiological functions, and they also may afford access to hemichannels for certain types of electrophysiological studies.

Permeability. Permeation through most ion channels is described by barrier models based on Eyring rate theory (37). Permeation through the junctional pore, however, might be more accurately described by electrodiffusion (38) because the junctional pore is sufficiently wide that atomic ions may pass one another. Larger permeants may interact with the walls of the pore (39, 40) and their deviation from electrodiffusive fluxes may reveal details about the structure of the pore. Voltage-clamp studies of coupled cells typically show a broad distribution of unitary channel conductances, ranging from ~ 20 pS to several hundred picosiemens (cf. references 41–44; for review, see reference 45). Some of this variability is undoubtedly due to the presence of varying and multiple connexins, but even in junction-incompetent cells transfected with cDNA for a single connexin, more than one size can be observed (46). Unitary conductance might be modulated by factors in the cellular milieu including protein kinases (47). A relation between differences in unitary conductance and selectivity among large permeants has yet to be established.

Transjunctional Voltage Sensitivity. In most tissues where junctional conductance has been examined, it is sensitive to transjunctional voltage, membrane potential, or both. Furthermore, in a single junction there can be more than one kinetically distinct process for a given type of voltage sensitivity (6, 45). In general, for transjunctional voltage sensitivity, junctional

conductance is highest when the transjunctional voltage is zero and decreases with transjunctional voltage of either sign (48, 49; but *see* reference 50). In a well-characterized case of steep transjunctional voltage sensitivity, when the polarity of the transjunctional voltage was reversed, the junctional channels opened transiently (51). The kinetics of the transient were modeled as if the channel was gated by two oppositely oriented voltage sensors and the gate that was closed by the initial voltage polarity had to open before the other gate could sense the new voltage. A proposed mechanism for this "contingent gating" located the voltage-sensing moieties within the lumen of the pore. For this mechanism, when the lumen is occluded by one gating structure, the bulk of the membrane field drops across it, leaving little of the field to be sensed by the voltage-sensing moiety in series. This mechanism is a specific example of a state-dependent alteration of field across a protein (52). An alternative explanation is that the interaction between the gating mechanisms is mediated not by changes in the field, but by allosteric interactions between the two hemichannels. Recent studies that utilized molecular genetic techniques showed that domain swaps involving the extracellular domains of differing connexins can affect transjunctional voltage sensitivity (45, 53–55) [there is no obvious analog of the S-4 region thought to be crucial for voltage sensitivity in other channels (56)]. These studies also indicate that the end-to-end interactions of hemichannels can dramatically affect voltage-dependent behavior. Indirect evidence implies that in one cell type, such end-to-end modulatory interactions do not take place (34). Studies of the voltage dependence are further complicated by observations of differing voltage sensitivities for the same connexin expressed in different cells (*see* reference 45). The study of hemichannel voltage sensitivity under simple and defined conditions would be useful.

Ligand Sensitivity. Rigorous identification of cellular ligands that act directly on junctional channels has been difficult because access to the physiological modulatory sites of the junctional channel is only via cytoplasm (and it has been difficult to identify junctional channels in patch-clamp studies even where they are likely to exist; *see* reference 57). Experiments in which junctional coupling is modulated by exposure of cells to various agents can be informative with regard to aspects of cellular regulation of junctional channels, but cannot precisely define which cytoplasmic factors act on the channel protein itself to effect a change.

Connexins and Channel Composition. The molecular diversity among connexins is likely to produce differences in the properties of the channels they form (cf. reference 58). The presence of naturally occurring connexin variants may be useful in elucidating the role of specific domains of the protein. The physiology of junctional channels *in situ* varies dramatically from tissue to tissue (*see* reference 6), and some of the variability is no doubt

due to the fact that different combinations of connexins are found in each tissue. In at least one tissue, one connexin predominates sufficiently that it must be capable of forming homo-oligomeric hemichannels (59–61). In tissues where there are comparable amounts of different connexins, two different connexins can be found in the same array of junctional channels (62), and recent biochemical data indicate that hemichannel structures can be formed of more than one connexin (63). Experiments in which mRNAs that code for different connexins are expressed in *Xenopus* oocytes show that junctional channels can be formed by two hemichannels, each of which is wholly formed by different connexins (cf. references 53, 54, 64, 65). These experiments and others (48, 66, 67) indicate that each hemichannel contains discrete gating mechanisms (that may interact strongly with those of the hemichannel with which it is in series). Thus, properties of junctional channels may be determined by the variable composition of each hemichannel (hemichannel-specific properties) as well as the variable effects of end-to-end hemichannel cooperative interactions. The ability to define hemichannel properties independently of the effects of their interactions with each other would be of value.

Lateral Interactions between Hemichannels. Connexin channels display a profound tendency to aggregate laterally, which gives rise to the large arrays of channels previously mentioned. No “helper” protein or cytoskeletal organizing influence has been identified. Although the functional role of this aggregation is unclear, it could favor the formation of junctional channels by accumulation of precursors to localized membrane domains, or perhaps it facilitates cooperative gating interactions between adjacent junctional channels [as some researchers have reported (68, 69)], even though adjacent hemichannels in tightly packed arrays are separated by lipid (30, 31). When hemichannels are isolated from junctional membranes by biochemical techniques, they can form linear structures, regular two-dimensional arrays, and three-dimensional stacks (70, 71). A model of the interchannel spacing in the arrays in cell membranes led to the proposal that the interactions between the channels are inherently repulsive, and that they aggregate to minimize repulsive force between the apposed membranes (72). This mechanism may not operate in the previously mentioned example of in vitro aggregation of purified hemichannels.

Junctional Channel Formation. The mechanism of formation of junctional channels is not known. Although direct data are lacking, by analogy with other oligomeric membrane proteins, connexin is thought to be organized into oligomeric (probably hemichannel) structures in intracellular membrane compartments (73, 74). Two extreme views are (1) that hemichannels are inserted into the plasma membrane solely at sites of junction formation and (2) that hemichannels are already present in the membrane and nucleate at

the time of junction formation (75). The reality may involve both processes. Early immunofluorescence studies failed to reveal nonjunctional connexin in plasma membrane (59, 76), but dispersed protein would have been difficult to detect. More recent data argue strongly that in normal cells, connexin precursors (presumably hemichannels) are present nonjunctionally in the plasma membrane and, furthermore, their assembly into plaques of junctional channels is associated with a phosphorylation (77). For a connexin expressed in oocytes, indirect data argue that connexin precursors are accessible to extracellular reagents prior to formation of junctional channels (78).

The formation of junctional channels requires end-to-end association between the extracellular domains of hemichannels. This interaction is not likely to be covalent because junctional channels can be split into hemichannels by alkaline urea treatments (7, 79). However, the formation of junctional channels between mRNA-injected oocytes is critically dependent on the presence of the three cysteines in each connexin extracellular loop (78). These cysteines apparently do not form interhemichannel disulfide bonds (80–82), but may serve to stabilize the extracellular domains during the homophilic binding reaction with the apposing hemichannel.

Hemichannels in apposing membranes must be brought sufficiently close for them to interact. Each hemichannel protrudes extracellularly only $\sim 10 \text{ \AA}$ from the plasma membrane (30, 31), which is a very short distance compared with usual intercellular separation. The typical membrane–membrane separation within a gap junction is $\sim 20 \text{ \AA}$ (19) [intriguingly close to the equilibrium distance between uncharged phospholipid surface (83)]. Strong evidence indicates that cell adhesion molecules play a crucial role in bringing cell membranes close enough for the hemichannels to interact (84, 85).

There are significant physiological, structural, and biochemical data with regard to the junctional channel. This body of knowledge provides a basis for exploration of certain issues with respect to the physics of channel-forming proteins and of molecular dynamics specific to junctional channels that may have implications for other macromolecular structures. These issues include the location of voltage-sensing charges, the roles of specific protein domains, testing of specific mechanisms of channel closure, interactions between conductance state and electric field, cooperative effects between hemichannels, mechanism of permeation, and the forces involved in formation of double-membrane protein structures.

Prospects for Biophysical Study of Channels Formed by Connexin

What are the possibilities for addressing these issues? In most cases, the required data are difficult to obtain due to (1) the inaccessibility of the

junctional channel in situ or (2) the complications of the presence of two functional hemichannels in series, which furthermore interact in unknown ways, or a combination of both. For example, it is difficult to obtain a selectivity sequence when the ionic environment at neither end of the pore can be changed with impunity. Changes in the connexin amino acid sequence can affect the nature of the hemichannel–hemichannel interactions simultaneously with the gating, kinetic, and permeability properties that are of primary interest. These factors might be deconvoluted by parametric studies of oocytes that express hemichannels formed by differing connexins (cf. reference 54), but straightforward studies of the properties of single hemichannels would be of clear value.

The *Xenopus* oocyte expression system can be used to study macroscopic junctional conductances, but not to make single-channel measurements. Dual voltage clamp of coupled cells under conditions of reduced junctional conductance can reveal single-channel transitions (41, 46), but the problems of accessibility and series hemichannels remain.

A well-defined accessible system is required. Reconstitution into liposomes and planar phospholipid bilayers can provide the accessibility and has been used to great advantage for many ion channels (86). The disadvantages of reconstitution are that the protein may be damaged and that it may lack chemical factors required for physiological function. In addition, several unique problems arise for reconstitution of connexin channels (87).

The gap junction channel spans two membranes. Although it is desirable to reconstitute double-membrane connexin channels at the interface of two closely apposed bilayers, at present a well-characterized and reliable system of this type does not exist (but *see* reference 88). On the other hand, the junctional channel is composed of discrete single-membrane structures that, as previously mentioned, may function normally as channels in nonjunctional plasma membrane. Therefore, it may be possible to study single hemichannels with standard reconstitution techniques. Data from structural studies and from cellular physiology indicate that each hemichannel has a full complement of gating structures and sensitivities (e.g., each can respond to voltage, pH, etc.) (31, 48, 64–67, 89). Even though some aspects of junctional channel operation are likely to involve end-to-end hemichannel–hemichannel interactions, it would be a major step to fully characterize the biophysics of a single hemichannel. In fact, this must be achieved in order to determine how the cooperative end-to-end interactions affect the function of each hemichannel.

A second problem is the identification of a bilayer channel as a relevant connexin channel. Most channels in bilayers are identified by defining physiology (e.g., ionic selectivity, toxin effects). For the junctional channel, the only certain defining properties are permeability to large molecules and, in most cases, voltage sensitivity. Other factors that affect junctional conduc-

tance between cells (e.g., pH, calcium, octanol) may not act on the channel molecule itself. Because bilayers report the activity of a very small number of molecules (typically < 5 for single-channel recordings), standard biochemical criteria alone cannot be used to identify a connexin channel in a bilayer because the sampling error is too great. For example, $10 \mu\text{g}$ of protein added to a bilayer chamber corresponds to approximately 3×10^{13} channels of the molecular weight of a hemichannel; even an extremely minor contaminant could produce significant and misleading channel activity, especially if consideration is given to (1) differences in efficiency of incorporation into the bilayer and (2) lack of certainty that an incorporated connexin channel will function under a given set of conditions. For the same reason, the use of antisera to identify bilayer channels places exceedingly stringent requirements on antisera purity, because only a few antibody molecules with undesired specificity could misidentify the small number of channel molecules active in a bilayer.

A related problem is how to obtain connexin suitable for reconstitution. Purity would not be necessary if there were an easy way to specifically activate or select for reconstituted connexin channels. The preparations of isolated junctional membrane described previously yield condensed junctional membranes and involve denaturing conditions known to affect connexin secondary structure (90). The preparations also contain nonconnexin protein, because it is the junctional membrane structure that is purified, not specifically the channel-forming protein. Several studies report channel activity from such preparations, or from detergent-solubilized material from these preparations, comparing the channel activity with physiology, pharmacology, and antisera effects inferred from cellular coupling studies (91–96). Our own early work with this material selected specifically for reconstituted channels that were permeable to large molecules (97).

Recently, preparations for connexin that may provide more suitable material for reconstitution have been reported. Immunoaffinity purification of two different connexins, under nondenaturing conditions, from membranes solubilized with nonionic detergent has been reported: one purification used a monoclonal antibody against a specific connexin (98 and Rhee, S. K.; Harris, A. L., unpublished) and the other used a sequence-specific polyclonal antibody (99). A technique that combined alkaline conditions, nonionic detergent, and chromatography yielded morphologically pure hemichannels (e.g., not junctional membranes) from liver (70). Detergent solubilization of lens fiber cell membranes yielded single hemichannels, though this preparation contains nonconnexin protein (71). Functional reconstitution of channels from the hemichannels purified from liver has been reported (100). Our studies with junctional membranes and connexin purified with monoclonal antibody (87, 101–103, and Rhee, S. K.; Harris, A. L., unpublished) are briefly summarized in the following section.

Development of a Reconstitution System for Study of Channels Formed by Connexin-32

The studies outlined in this section describe the ways we have addressed the foregoing problems of connexin reconstitution by utilizing connexin-32, the predominant form of connexin in rat liver. Our goals were to establish unambiguously that connexin-32 formed channels in liposome membranes, to identify connexin channels in planar bilayers, and to study their properties. Two methods were used to identify reconstituted channels formed by connexin-32. In one method, protein was solubilized from preparations of junctional membrane and incorporated into unilamellar liposomes. Connexin-32 was identified as a channel-forming protein by its specific enrichment in liposomes that were permeable to sucrose. In the other method, connexin-32 was affinity-purified (with a monoclonal antibody directed specifically against connexin-32) directly from octylglucoside-solubilized plasma membranes. Liposomes formed with such material were permeable to sucrose and Lucifer Yellow. Sucrose-permeable liposomes from each method were fused with planar bilayers to study the properties of connexin channels.

Connexin from Isolated Junctions Forms Large Channels in Liposomes (87, 101, 102). Protein solubilized in octylglucoside from preparations of junctional membranes was incorporated into unilamellar phospholipid liposomes by gel filtration (104). Liposomes that contained large open channels were separated from those that did not using a permeability-specific liposome fractionation protocol (105). In brief, the liposomes were formed in a solution that contained several hundred millimolar urea and were spun on an isoosmotic density gradient formed from the urea buffer and a buffer in which the urea was osmotically replaced by sucrose (sucrose is more dense than urea). Liposomes that are impermeable to sucrose and urea move a short distance into the gradient to a steady-state position. Liposomes that contain large open pores exchange urea for sucrose and move to a characteristic lower position (higher density) in the gradient (Figure 2A-C). In calibration studies using VDAC (voltage-dependent anion channel) (106), the movement of the liposomes to the lower (sucrose-permeable) position was correlated with a loss of a large intraliposomal marker (calcein; molecular weight MW = 660 Da) (105). This method is reliable for separation of liposomes that are permeable to large molecules from liposomes that are not. Sucrose can permeate gap junction channels, but not most other membrane channels.

A significant fraction of the liposomes that contain junctional protein were sucrose-permeable (Figure 2D and E). This result shows a correlation between protein from junctional membrane and sucrose permeability, but does not, by itself, permit the conclusion that connexin-32 forms the sucrose-permeable pathway.

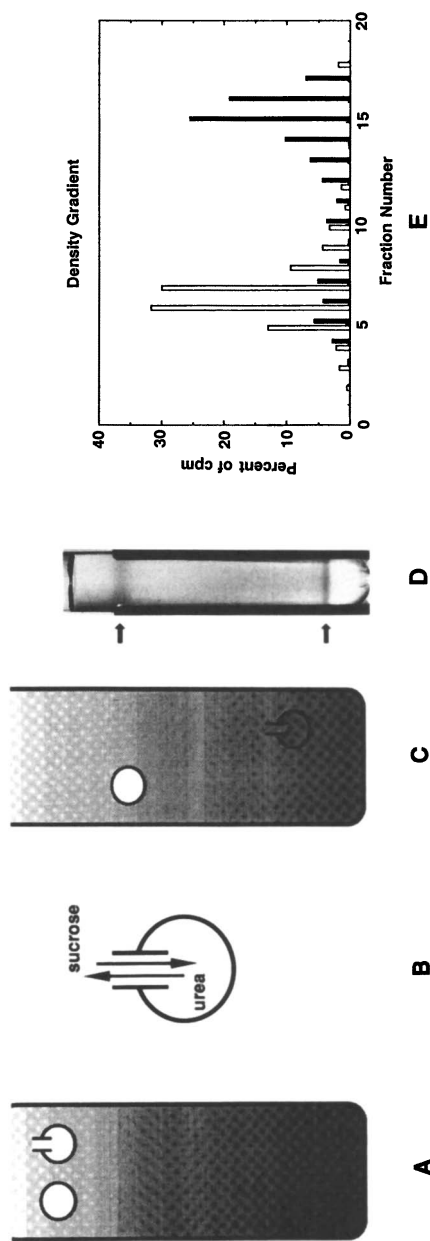


Figure 2. Sucrose permeability in liposomes induced by protein from isolated gap junctions. Unilamellar liposomes are separated on the basis of permeability to urea and sucrose on iso-osmotic density gradients as described in the text and in reference 107. Liposomes containing large open channels exchange urea for sucrose and increase in density (move to a lower position in the gradient), whereas those that are not remain at a lighter density nearer the top of the gradient. A-C, Diagram of the transport-specific liposome fractionation technique. D, Sucrose permeability induced by protein from isolated gap junctions. Liposomes containing junctional protein segregated into two characteristic populations. A fluorescently labeled lipid (rhodamine-PE) was a marker for the liposomes in this experiment. The upper arrow indicates the band formed by the sucrose-impermeable liposomes, and the lower arrow indicates the band formed by the sucrose-permeable liposomes. Liposomes formed without junctional protein or with control proteins remained in a single band at the position of the upper arrow (see E). E, Graph of liposome fractionation. Liposomes without protein (open bars) and with junctional protein (filled bars) were separated as in D (in this experiment, a radioactive lipid was used to follow liposome position). The tops of the gradients are at the left. Liposomes formed without protein were in a single band at fractions 6 and 7. Liposomes formed with junctional protein separated into two bands: one at the upper position defined by the sucrose-impermeable liposomes and one approximately threefold larger at the higher density sucrose-permeable position (fractions 15 and 16). The lower relative position of the sucrose-impermeable liposomes compared with those in D results from a longer centrifuge spin (8 h vs. 3 h); with longer spins the upper band tends to drift slowly to lower positions, a possible reflection of nonspecific liposome permeability (105). (Reproduced with permission from reference 102. Copyright 1992 Elsevier.)

To identify the protein responsible for the permeability, proteins in the liposomes were separated by standard denaturing electrophoresis, blotted, and stained for total protein and for connexin-32. Western blots of unfractionated liposomes formed in the presence of protein solubilized from isolated gap junctions are shown in Figure 3A. The blots show the monomeric, dimeric, and trimeric forms of connexin-32 commonly observed in sodium dodecyl sulfate (SDS) gels of isolated junctions (59–61, 107). They also show the presence of a commonly seen proteolytic fragment of connexin-32 (59, 61, 107) (better seen in Figure 3B), which contributes to the broadness of the staining below the monomer and dimer bands. The liposomes typically contained no detectable nonconnexin protein.

Western blots of transport-selected liposomes (Figure 3B) show specific selection for full-length connexin-32 by sucrose permeability: the ratios of connexin-32 to its proteolytic fragment were very different in the sucrose-permeable and sucrose-impermeable liposomes. The ratio was much greater in the sucrose-permeable liposomes than in the sucrose-impermeable liposomes. Digital integration of lanes 5 and 6 (areas under the peaks in the tracings) show that the ratio of full-length connexin-32 peak to its fragment was 1.6 for the sucrose-permeable liposomes and 0.52 for the sucrose-impermeable liposomes. Thus, the sucrose permeability essentially enriched for full-length connexin-32, and sucrose impermeability selected for the connexin-32 fragment. Full-length connexin-32 was almost totally absent from the sucrose-impermeable liposomes. A simple explanation is that full-length connexin-32 can form a sucrose-permeable pore (and the fragment cannot).

The argument against sucrose permeability being due to a nonconnexin protein is as follows: If the sucrose permeability was due to a hypothetical nonconnexin protein, and the proteins were distributed independently of one another in the liposomes, then connexin-32 and its fragment would be present in the same ratio in the two liposome populations, each distributed independently of sucrose permeability. Because they are not, it is reasonable to conclude that connexin-32 causes a permeability to sucrose. The presence of some fragment in the sucrose-permeable liposomes is accounted for by its presence in liposomes that also contained full-length (functional) connexin. The conclusion that connexin-32 forms a pore does not require that all nonconnexin protein be excluded from the sucrose-permeable liposomes or that connexin-32 account for all of the sucrose permeability. It relies on the positive and specific correlation between sucrose permeability and enrichment for full-length connexin-32.

Affinity-Purified Connexin-32 Forms a Large Pore in Liposomes (103). Connexin-32 solubilized in octylglucoside from crude plasma membrane was affinity-purified under nondenaturing conditions using a monoclonal antibody specific for connexin-32 (7) that was attached to a bead matrix (98 and Rhee, S. K.; Harris, A. L., unpublished). Overloaded denatur-

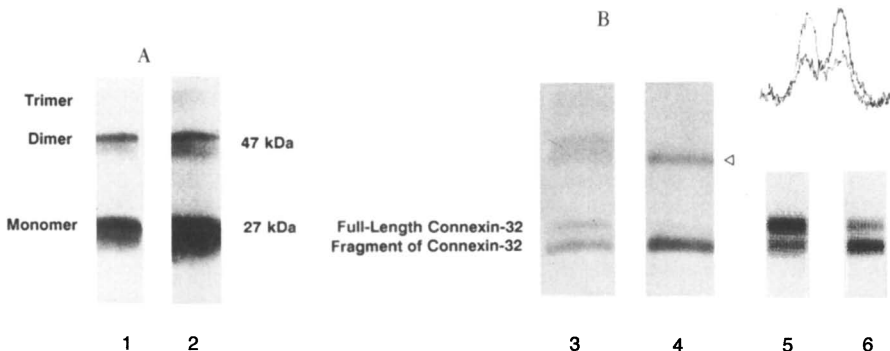


Figure 3. *Sucrose permeability selects for liposomes containing full-length connexin-32.* **A,** Western blots of liposomes containing protein solubilized from isolated gap junctions. Left lane: stained for protein with colloidal gold. Right lane: stained with monoclonal antibody against connexin-32 (7), visualized with an alkaline phosphatase conjugated secondary antibody. (Connexin-32 is a 32-kD protein that runs anomalously at the 27-kD position in these 13% acrylamide gels (126). Gels were intentionally overloaded so the positions of multimeric and proteolytic connexin-32 could be identified.) **B,** Western blots of transport-selected liposomes show specific selection for full-length connexin-32 by sucrose permeability. Lanes 3 and 5 are blots of sucrose-permeable liposomes, and lanes 4 and 6 are of sucrose-impermeable liposomes. The left pair (lanes 3 and 4) are stained with monoclonal antibody against connexin-32 as in part A. The right pair (lanes 5 and 6) are digital reconstructions of blots stained for protein with colloidal gold. Tracings are integrations of blots stained for protein with colloidal gold in the monomer region; right to left on the tracings correspond to moving down the lanes of the blots. The lighter and darker tracing lines correspond to the sucrose-permeable and sucrose-impermeable lanes, respectively, and the right and left peaks correspond to the full-length and proteolytic fragment positions, respectively. Each pair of blots (3 and 4; 5 and 6) shows that sucrose permeability selects for a liposome population containing more full-length connexin-32, relative to its fragment, than do sucrose-impermeable liposomes. Sucrose impermeability strongly selects against the full-length form, as it is almost absent in the sucrose-impermeable liposomes. The proteolyzed fragment contributes to the dimeric connexin-32, producing a lower molecular weight form of the dimer (open arrowhead). (All four lanes are from the same starting population of liposomes and the same density gradient spin. To demonstrate the difference in distribution of the two bands in the transport-selected populations, the liposome population used in this example contained more of the connexin-32 fragment than the full-length monomer. Absorbance of gold-stained blots was digitized and background absorbance subtracted. Staining density of the full lane width was integrated along its length. Peaks were approximated by overlapping Gaussian curves, represented at densities in lanes 5 and 6. Differences in staining between the left and right pairs of lanes occur because the antibody method (lanes 3 and 4) stains the connexin-32 fragment darker than the full-length form and stains the multimeric forms with decreasing intensity, perhaps because of increasing inaccessibility of the antigenic site.) (Reproduced with permission from reference 102. Copyright 1992 Elsevier.)

ing gels showed no detectable contaminants. The yield of connexin-32 was considerably greater than that obtained by junctional membrane isolation, and the connexin-32 was in a soluble form. Gel filtration of the material indicated that the connexin-32 was predominantly of a size consistent with hexameric connexin.

The affinity-purified connexin-32 was incorporated into unilamellar liposomes as before. The connexin-32 induced a sucrose permeability in liposomes, as assayed by the density-shift technique, and gave results essentially identical to those in Figure 2. Liposomes that were sucrose-permeable did not retain the dye Lucifer Yellow (retained by the sucrose-impermeable liposomes), which is near the upper size-permeability limit for gap junction channels (19, 108, 109). The fraction of the liposomes that were permeable to sucrose decreased by a factor of 4 when the pH in the gradients was changed from 7.5 to 6.0. This effect was partially reversible.

Taken together, the two preceding liposome studies provide a robust demonstration that connexin-32 can be successfully reconstituted into unilamellar phospholipid membranes, where it forms pores with permeability similar to that of junctional channels. The data are consistent with the conducting unit being the hemichannel.

Bilayer Channels from Sucrose-Permeable Liposomes (87, 101, 102). Sucrose-permeable liposomes from the foregoing studies were fused with planar phospholipid bilayers (110, 111). The data from the liposomes that contain connexin from isolated junctions differed in some respects from the data obtained with the affinity-purified connexin. At the present time, the data from the affinity-purified material is not fully characterized. Therefore, most of the data described in the following text are from liposomes that contain connexin-32 from isolated junctions; exceptions are noted.

Fusion into the bilayer of sucrose-permeable liposomes resulted in three unitary conductance levels, two of which could be attributed to connexin-32. Figure 4A shows typical channel bilayer activity at ± 100 mV. At +100 mV, one 130-pS channel and at least two 20-pS channels undergo gating transitions. At -100 mV, three 45-pS channels are seen. The channel activity is more fully characterized by the voltage ramp shown in Figure 4B. The membrane conductance is high and linear, without channel gating activity from -25 to +25 mV. At more negative voltages, four 45-pS channels tended to close. At more positive voltages, a 130-pS channel tended to close and a 20-pS channel tended to open. In this bilayer, the entire membrane conductance was accounted for by the sum of the observed unitary conductance transitions. The 20-pS channel was also seen in sucrose-impermeable liposomes and was closed at 0 mV (i.e., it was not likely to mediate a liposome density shift), so it cannot be assigned an identity based on the density shift studies.

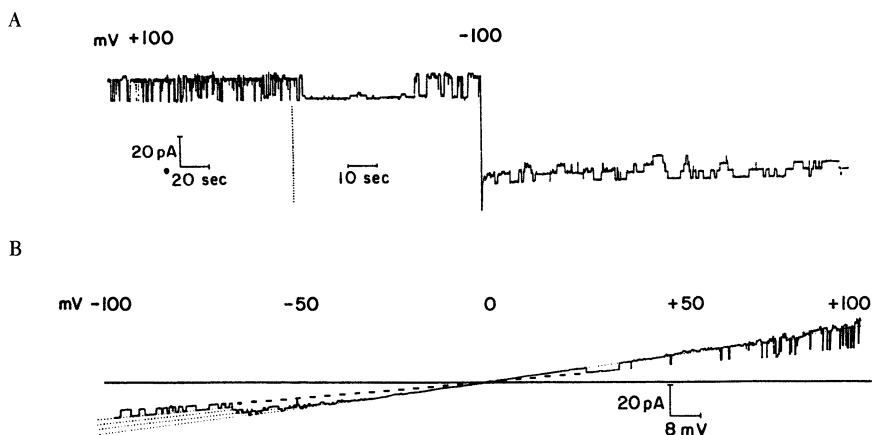


Figure 4. Channel activity following fusion of transport-selected (sucrose-permeable) connexin-32 containing liposomes with planar bilayers. A, Record showing the three channel sizes observed. Sucrose-permeable liposomes were added to one side of a bilayer chamber and fused with a planar phospholipid bilayer (1:1, PS:PE) by an osmotic stress technique (110, 111). Positive bilayer voltages correspond to inside-liposome positive potentials. B, Voltage ramp showing character of the channel activity. A slow voltage ramp from -100 to $+100$ mV over 8.5 min was delivered to the same membrane as in part A. At positive voltages, a 130-pS channel tends to close and a 20-pS channel tends to open. At negative voltages, several 45-pS channels tend to close. (Adapted with permission from reference 87. Copyright 1991 CRC Press.)

The two larger channel transitions (those at 45–55 pS and at 120–140 pS), on the other hand, were found only with sucrose-permeable liposomes and therefore can be attributed to connexin. The two conductance levels could indicate either two distinct channels or the presence of a subconductance state. The former interpretation is favored because the two levels were not found in constant ratio in different membranes, and because (as in Figure 4B) the entire conductance of the bilayer could often be accounted for by the summed conductances of the transitions, as if each contributed independently to the bilayer conductance. The key properties of the connexin channels were that they were open at zero bilayer voltage and exhibited profoundly asymmetric sensitivity to voltage. The larger channel tended to close at positive voltages and remain open at negative voltages. The smaller one had a voltage sensitivity of opposite sign, tending to close only at negative potentials.

The voltage sensitivity of the reconstituted channels was well characterized by a form of the Boltzmann relation that contained a voltage-dependent energy term, indicating that the voltage-sensitive transitions are first order and that the energy difference between the open and closed states is a linear function of voltage (49, 112). The number of equivalent gating charges for

the larger channel ranged from 1.5 to 2.5, and the voltage at which the open probability is one-half (V_0) is ~ 110 mV. Overall, the smaller channel had approximately one-half the voltage sensitivity of the larger channel and a similar V_0 . A description of a possible pitfall in determination of voltage sensitivity follows.

A common method to determine voltage sensitivity is shown in Figure 5A, in which the data for the larger channel from one experiment are fitted to a form of the Boltzmann relation that can be plotted as a linear function of

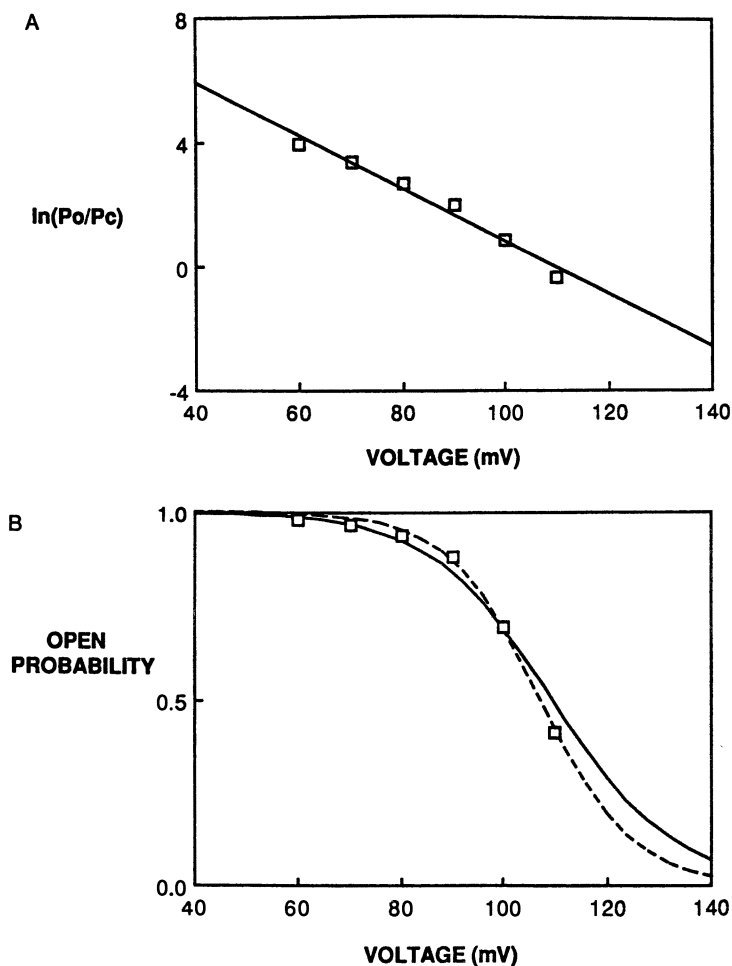


Figure 5. Voltage dependence of P_o for the larger (130-pS) connexin-32 channels. A, Fit to $\ln(P_o/P_c)$ as a function of voltage. B, Fit to P_o as a function of voltage. The solid line is calculated with the Boltzmann relation (SSE = 0.007) and the dashed line is an independent fit (SSE = 0.001).

voltage: $\ln(P_o/P_c) = nqV/kT$, where P_o is the open probability, P_c is the closed probability calculated as $1 - P_o$, q is the electronic charge, n is the number of charges that move through the bilayer voltage V , k is Boltzmann's constant, and T is temperature (49, 106, 113). The fit appears reasonable ($r = 0.99$) and evaluates n as 2.1, which corresponds to an e -fold change in the open-closed ratio for every ~ 12 mV. The V_o is 109 mV.

When these parameters are used to predict the P_o versus V relation and the exponential form of the Boltzmann relation ($P_o = 1/\{1 + \exp[nq(V - V_o)/kT]\}$) is used, a reasonable fit to the data is also seen (solid line in Figure 5B). However, fitting this form of the Boltzmann relation directly to the P_o versus V data (dashed line in Figure 5B) gives a statistically improved fit (F -test; $P < 0.05$) and particularly well describes the region of the greatest slope. The independent fit gives a greater voltage sensitivity ($n = 2.8$, which corresponds to an e -fold change for ~ 9 mV) and approximately the same V_o (107 mV). The reason for the difference in the results from the two fitting procedures is that, due to the mathematical transformation from P_o to $\ln(P_o/P_c)$, the uncertainty for values derived from P_o s that approach 1 is greater than the uncertainty derived from smaller P_o s [e.g., a ± 0.01 uncertainty in a P_o of 0.95 gives deviations of +0.234 and -0.192 in $\ln(P_o/P_c)$, whereas the same ± 0.01 deviation in a P_o of 0.5 gives a deviation of ± 0.04]. Because of this difference, the lower values of $\ln(P_o/P_c)$ should be weighted more than the higher values during the curve fitting. This weighting can be achieved by use of a well-defined mathematical technique (114). When the values are appropriately weighted, the curves generated by fitting to the logarithmic form and the exponential form of the Boltzmann relation are statistically indistinguishable and give similar values of n and V_o ($n = 2.6$ and $V_o = 107$ mV for the weighted logarithmic fit). This observation is of some interest because curve fitting to $\ln(P_o/P_c)$ is a long-standing technique. Failure to appropriately weight the data in the fitting procedure may contribute to some of the variability in voltage sensitivity reported for many conductances and channels, including junctional conductances and connexins.

The channels had dwell times that ranged from several hundred milliseconds to several seconds. Channels that responded to positive and negative voltages in a symmetric manner were rarely seen. At voltages near V_o , the larger channel had an exponential distribution of open times, which indicates a single open state (Figure 6A). At lower voltages, the fit to a single exponential was not as good, though reasonable, suggesting the contribution of a minor, slower second exponential, which could indicate closures from a second open state. The primary component of the mean open times had an exponential relation to voltage (Figure 6B). The apparent voltage sensitivity of the closing rate corresponds to the movement of ~ 1.6 charges through the bilayer field. This suggests that most of the voltage sensitivity of the steady-state P_o arises from the closing rate.

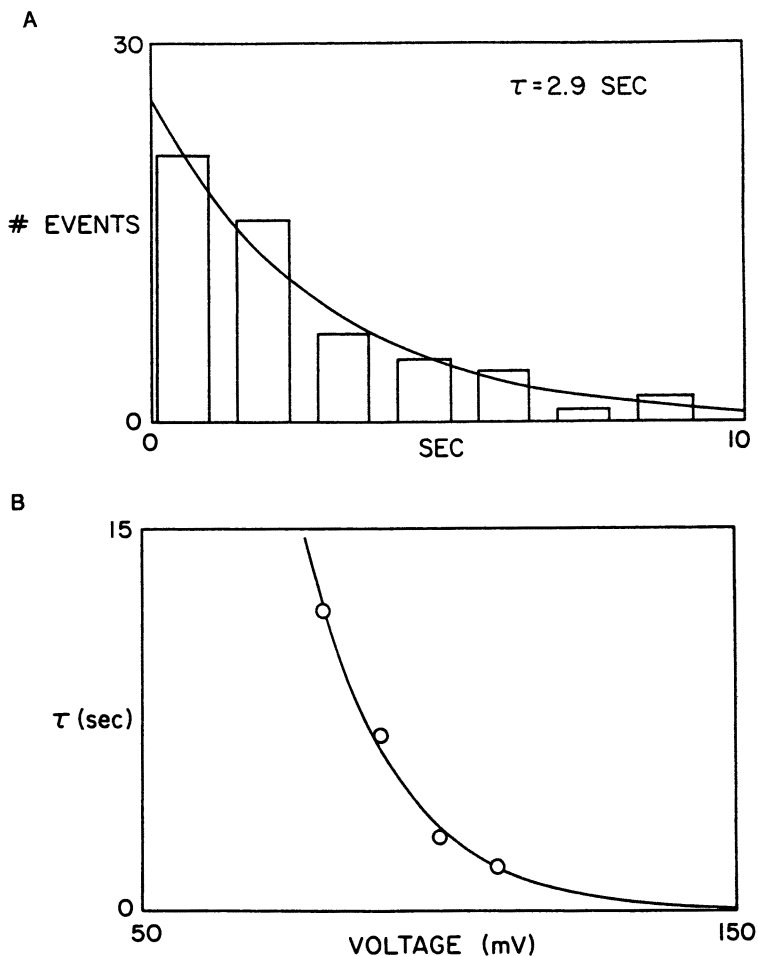


Figure 6. Voltage-dependent kinetics of the larger connexin-32 channels. A, Open time histogram of the larger channel. The open dwell times at 100 mV (near V_0) were well-fit by a single exponential, suggesting that the channel closes from a single open state. Bin width is 1.4 s. (Reproduced with permission from reference 87. Copyright 1991 CRC Press). B, Open time versus voltage for the larger channel. The mean open times for the channel are plotted as a function of voltage, and well-fit by an exponential. The voltage sensitivity of the apparent closing rate corresponds to the movement of ~ 1.6 charges through the bilayer field.

The reversal potentials for bilayers containing the channels were measured under asymmetric KCl and NaCl conditions, and polarity was confirmed in the KCl experiments by addition of the potassium-selective ionophore valinomycin. The reversal potentials indicated approximately a three-fold selectivity for chloride over either potassium or sodium ions.

A 20-pS channel was occasionally observed along with these channels, but because it was closed at zero membrane voltage, it was unlikely to mediate the density shift. Because it was also found in sucrose-impermeable liposomes, the 20-pS channel could not be assigned an identity based on sucrose permeability. This channel may be a minor contaminant or a partially denatured form of connexin-32.

Liposomes that contained immunopurified connexin-32 produced macroscopic bilayer conductances that were highly asymmetric with regard to voltage. However, clean single-channel transitions were only occasionally observed, even at low (100–200-pS) macroscopic membrane conductance, because the bilayer currents were noisy and unsteady. Such recordings often characterize “dirty” bilayers or detergent-induced conductances, but without the profound asymmetry with respect to voltage observed here. Addition of control liposomes made under the same conditions without protein produced no detectable conductances, and addition of octylglucoside eventually produced only symmetric increases in conductance noise (the liposome membranes should not contain appreciable detergent in any case).

When these records are filtered extensively, the transitions are seen to cluster at intervals of ~ 125 pS (Figure 7A). Although these currents are difficult to interpret, the findings might be accounted for by high conductance channels that fluctuate rapidly between many subconductance levels. Preliminary higher resolution bilayer experiments (in collaboration with S. M. Bezrukov; Figure 7B) revealed discrete conductance transitions with large-magnitude current fluctuations during the open states, supporting this idea, but further studies are required.

Discussion of the Major Findings

What do these liposome and bilayer data imply about connexin-32 channels?

Structural Form of the Reconstituted Channels. The experiments with connexin-32 from isolated junctions do not directly address the issue of structural form. However, the asymmetry of the voltage dependence of channels formed by connexin-32 from both sources suggests an asymmetric structure, which rules out a normally configured junctional channel. The sizing data suggest that the purified connexin is isolated predominantly as single hemichannels. Also, the Lucifer Yellow permeability suggests that the aqueous pore is not significantly narrower than the pores of connexin channels in situ. These considerations, plus the fact that the channels exist in what are macroscopically single membranes, place the weight of the evidence on the reconstituted connexin-32 being in the form of single hemichannels. This conclusion is consistent with voltage-clamp studies of cells, which suggest that each hemichannel contains a gating mechanism sensitive to a single voltage polarity (35, 48, 51, 54).

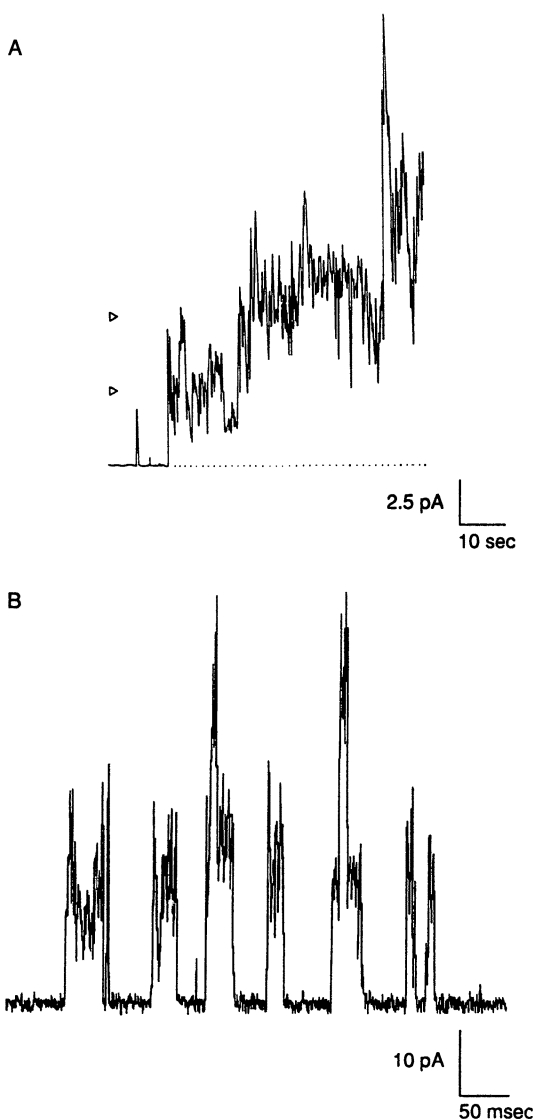


Figure 7. Bilayer conductance induced by affinity-purified connexin-32. A, Sucrose-permeable liposomes formed with affinity-purified connexin-32 were fused with planar phospholipid bilayers as described. Highly filtered (5-Hz corner frequency) currents show unstable conductances, but large, rapid fluctuations that cluster around multiples of about 125 pS may be discerned (arrowheads). The bilayer voltage was 50 mV. B, Higher resolution recording of channels from affinity-purified connexin-32. Records show discrete gating conductance transitions, but with a high rate and amplitude of current fluctuations through the open channels. Unitary conductance is difficult to determine, but is near 200 pS. The bilayer voltage was 100 mV.

Effects of the Two Methods of Obtaining Connexin-32. The pH sensitivity of the sucrose permeability of liposomes that contain affinity-purified connexin suggests that pH can act directly on connexin channels. This contrasts with the lack of pH sensitivity of the connexin-32 channels obtained from isolated junctional membranes [our own studies (102) and references 93 and 94]. The apparent difference in single channel behavior between the two preparations may also be a function of the different isolation procedures. These differences could result from harsher conditions involved in junction isolation [known to alter secondary structure of connexin (90)], in which case the physiology of the affinity-purified material may more accurately reflect the physiology of the native form of the protein. In addition, the two isolation methods could select for connexin that originated in differing populations of junctional structures. This is almost certainly the case because the affinity-purified preparation consists only of readily soluble plasma membrane connexin (not obtained in junctional membrane preparations).

Open Channels in Single Membranes. For future reconstitution studies, the most significant finding is simply that connexin-32 can form large, open, regulated channels in single phospholipid membranes. Several factors argue that these channels represent functionally relevant channels and not structures that are overly denatured, damaged, or in other ways artifactual. The aqueous pathway through the molecule is as wide as that of junctional channels, and the channels are regulated by voltage in an asymmetric manner that is consistent with them being single hemichannels. The pH effect on permeability of the channels formed by affinity-purified connexin-32 is also supportive, as are the data with regard to the size of the purified structures and the finding of asymmetric voltage dependence.

From a biological perspective, the finding of functioning hemichannels seems counterintuitive. There is an understandable bias that such large channels, if they were open, would rapidly kill cells by destruction of the selective permeability of the plasma membrane. However, the plasma membrane of macrophages and mast cells can become permeable to Lucifer Yellow [possibly through connexin channels (33)] for many minutes without lethal effect (115, 116).

The finding of open connexin channels in single membranes suggests that either single hemichannels do not exist in plasma membranes (for very long) or that if they exist, they are kept closed most of the time by cytoplasmic, extracellular, or membrane factors not present in the reconstituted system [as may occur in the teleost horizontal cells (34) and does not occur in oocytes that express connexin-46 (35, 36)]. In the former case, when intercellular channels are formed, the hemichannels may be inserted in apposing membranes in a coordinated fashion, so that there is only a very brief opening to the outside during channel formation. In the latter case, the reconstituted

system offers a way to precisely identify the factors that modulate hemichannel gating.

Interactions between Hemichannels. What does the isolation of single hemichannels imply about the end-to-end interactions of hemichannels? This is an important consideration for possible reconstitution of junctional channels from individual hemichannels. Unfortunately, the data summarized above are not informative on this point. Harsh conditions are required to “split” apart isolated junctional membranes (7, 79). However, any junctional structures that were easily solubilized, as in the affinity-purified preparation, would not have been recovered as isolated junctional membranes and so might not require such harsh conditions for splitting.

The starting material for the affinity purification was predominantly plasma membrane from presumably well-coupled cells; therefore, the connexin that is isolated is most likely from junctional structures. Because the purified connexin-32 is predominantly in structures the size of single hemichannels, a simple conclusion is that octylglucoside can disrupt the end-to-end interactions of junctional channels. However, there is the caveat that the junctions may split *prior* to solubilization, that is, in the preparation of the crude plasma membrane fraction. Junctions can split when a tissue is perfused with hyperosmotic solutions (117), so a “cellular” splitting could precede disruption of junctional channels by octylglucoside.

Future Studies

The fundamental problems regarding reconstitution of connexin channels have been overcome: connexin forms channels in unilamellar liposomes and planar bilayers. Size, permeability, and gating behavior are consistent with conducting units that are single hemichannels—the structures that span a single cell membrane and form one-half of the junctional channel. Connexin can be obtained by affinity purification under nondenaturing conditions. Thus, channels formed by a single connexin can be studied in a well-defined and accessible system.

What are some of the important biophysical questions that can be addressed? The permeability and selectivity of the channel can be characterized in detail. The selectivity to large, charged molecules can be assessed. Also the nature of permeation (electrodiffusive versus barrier models) can be assessed for various permeants. The voltage sensitivity can be explored, particularly with regard to the location of the dipoles or charges involved. In the single-membrane channels, the voltage sensitivity can be explored without the confounding presence of another gate in series, as in the junctional channel (*see* reference 51). It may be possible to determine the change in volume in the lumen of the pore during gating transitions (118, 119), and so

to distinguish the two models of gating proposed from structural data (30, 31).

Modulation of the channels can be studied by exposing the bilayer channels to agents that regulate junctional channels (e.g., kinases, cyclic nucleotides) and other agents that elucidate the function of specific domains or regulatory sites (e.g., specific peptidases, sequence-specific antibodies, group-specific reagents). It will be important for biophysical and biological studies to establish in the bilayer system precisely which cellular components or covalent modifications alter the rapidly fluctuating transitions produced by the affinity-purified connexin.

Presumably other connexins can be similarly purified and studied in bilayers to provide a solid basis of data on the relation between specific amino acid sequences and single-channel physiology. Variants of the connexins produced by the techniques of molecular biology can also be reconstituted, and careful comparison of the channel behavior in bilayers with that seen in cellular expression systems will be fruitful.

It is hoped that such studies of single hemichannels will be complemented by studies of reconstituted junctional channels: the double-membrane form. Development of a stable, well-characterized, and well-controlled double-membrane system is a challenging prospect. The literature on osmotic control of fusion of apposed bulged bilayers may be helpful in this regard (120, 121). Such a system would permit exploration of the forces involved in the assembly of junctional channels, which would be of interest from biophysical and cellular perspectives. For example, does the space between two membranes need to be dehydrated for hemichannels to interact (122)? Do the hemichannels find each other by random interactions or does dielectric attraction (123–125) play a role? Once junctional channels are formed, how reversible is the interaction between them and what forces tend to stabilize it? Most important, how are the permeability, gating, and modulation of single hemichannels altered by interactions with each other in the double-membrane form? These and other considerations make the exploration of connexin channels in reconstituted systems of profound interest and promising prospects.

Acknowledgments

The various experiments summarized here were carried out over the last few years in collaboration with Carville Bevans, Sergei Bezrukov, Daniel Goodenough (National Institutes of Health Grant GM18974), David Paul (National Institutes of Health Grant GM37751), Seung K. Rhee (American Liver Foundation Student Research Fellowship), Anne Walter, and Joshua Zimmerberg. Their experimental and intellectual contributions are most gratefully appreciated. The author expresses appreciation to V. A. Parsegian for his

unwavering support and his contagious spirit of inquiry and exploration. Research was supported by Office of Naval Research Grant N00014-90-J-1960 and National Institutes of Health Grant GM36044 to the author and National Institutes of Health Biomedical Research Support Grant S07RR07041 to Johns Hopkins University. Research was performed with equipment and supplies provided, in part, by the Millipore Corporation.

References

1. Neher, E.; Sakmann, B. *Nature (London)* **1976**, *260*, 799–802.
2. Mueller, P.; Rudin, D. O. *J. Theor. Biol.* **1968**, *18*, 222–258.
3. Bean, R. C.; Shepherd, W. C.; Chan, H.; Eichner, J. J. *Gen. Physiol.* **1969**, *53*, 741–757.
4. Spray, D. C.; Bennett, M. V. L. *Annu. Rev. Physiol.* **1985**, *47*, 281–303.
5. *Gap Junctions*; Hertzberg, E. L.; Johnson, R. G., Eds.; Alan R. Liss: New York, 1988.
6. *Biophysics of Gap Junction Channels*, Peracchia, C., Ed.; CRC Press: Boca Raton, FL, 1991.
7. Goodenough, D. A.; Paul, D. L.; Jesaitis, L. *J. Cell Biol.* **1988**, *107*, 1817–1824.
8. Milks, L. C.; Kumar, N. M.; Houghton, R.; Unwin, N.; Gilula, N. B. *EMBO J.* **1988**, *7*, 2967–2975.
9. Yeager, M.; Gilula, N. B. *J. Mol. Biol.* **1992**, *223*, 929–948.
10. Stauffer, K. A.; Unwin, N. *Semin. Cell Biol.* **1992**, *3*, 17–20.
11. Beyer, E. C.; Paul, D. L.; Goodenough, D. A. *J. Membr. Biol.* **1990**, *116*, 187–194.
12. Kumar, N. M.; Gilula, N. B. *Semin. Cell Biol.* **1992**, *3*, 3–16.
13. Lawrence, T. S.; Beers, W. H.; Gilula, N. B. *Nature (London)* **1978**, *272*, 501–506.
14. Bennett, M. V. L. In *Handbook of Physiology: The Nervous System*; Kandel, E., Ed.; Williams and Wilkins: Baltimore, MD, 1977; Vol. 1, Sec. I, pp 357–416.
15. Lasater, E. M.; Dowling, J. E. *Proc. Natl. Acad. Sci. U.S.A.* **1985**, *82*, 3025–3029.
16. Fraser, S. E.; Green, C. R.; Bode, H. R.; Gilula, N. B. *Science (Washington, D.C.)* **1987**, *237*, 49–55.
17. Saez, J. C.; Connor, J. A.; Spray, D. C.; Bennett, M. V. L. *Proc. Natl. Acad. Sci. U.S.A.* **1989**, *86*, 2708–2712.
18. Pitts, J. D. In *Intercellular Junctions and Synapses. Receptors and Recognition*; Feldman, J.; Gilula, N. B.; Pitts, J. D., Eds.; Chapman and Hall: London, 1978; Series B, Vol. 2, pp 63–79.
19. Bennett, M. V. L.; Goodenough, D. A., Eds. *Neurosci. Res. Prog. Bull.* **1978**, *16*, 373–486.
20. Bennett, M. V. L.; Spray, D. C.; Harris, A. L. In *Perspectives in Differentiation and Hypertrophy*; Anderson, W. A.; Sadler, W., Eds.; Elsevier: New York, 1982; pp 103–119.
21. Loewenstein, W. R.; Rose, B. *Semin. Cell Biol.* **1992**, *3*, 59–79.
22. Warner, A. *Semin. Cell Biol.* **1992**, *3*, 81–91.
23. Tanabe, T.; Beam, K. G.; Adams, B. A.; Niidome, T.; Numa, S. *Nature (London)* **1990**, *346*, 567–569.
24. Goodenough, D. A.; Stoeckenius, W. *J. Cell Biol.* **1972**, *54*, 646–656.
25. Hertzberg, E. L.; Gilula, N. B. *J. Biol. Chem.* **1979**, *254*, 2138–2147.

26. Hertzberg, E. L. *J. Biol. Chem.* **1984**, *259*, 9936–9943.
27. Baker, T. S.; Caspar, D. L. D.; Hollingshead, C. J.; Goodenough, D. A. *J. Cell Biol.* **1983**, *96*, 204–216.
28. Sosinsky, G. E. *Electr. Microsc. Rev.* **1992**, *5*, 59–76.
29. Hoh, J. H.; Lal, R.; John, S. A.; Revel, J.-P.; Arnsdorf, M. F. *Science (Washington, D.C.)* **1991**, *253*, 1405–1408.
30. Makowski, L.; Caspar, D. L. D.; Phillips, W. C.; Goodenough, D. A. *J. Mol. Biol.* **1984**, *174*, 449–481.
31. Unwin, P. N. T.; Zampighi, G. *Nature (London)* **1980**, *283*, 545–549.
32. Unwin, P. N. T.; Ennis, P. D. *J. Cell Biol.* **1984**, *97*, 1459–1466.
33. Beyer, E. C.; Steinberg, T. H. *J. Biol. Chem.* **1991**, *266*, 7971–7974.
34. DeVries, S. H.; Schwartz, E. A. *J. Physiol.* **1992**, *445*, 201–230.
35. Paul, D. L.; Ebihara, L.; Takemoto, L. J.; Swenson, K. I.; Goodenough, D. A. *J. Cell Biol.* **1991**, *115*, 1077–1089.
36. Ebihara, L.; Steiner, E. *Biophys. J.* **1992**, *61*, A408.
37. Lauger, P. *Biochim. Biophys. Acta* **1973**, *311*, 423–441.
38. Lauger, P. *Biochim. Biophys. Acta* **1976**, *445*, 493–509.
39. Flagg-Newton, J. L.; Loewenstein, W. R. *J. Membr. Biol.* **1979**, *50*, 65–100.
40. Brink, P. R.; Dewey, M. M. *Nature (London)* **1980**, *285*, 101–102.
41. Neyton, J.; Trautmann, A. *Nature (London)* **1985**, *317*, 331–335.
42. Veenstra, R. D.; DeHaan, R. L. *Science (Washington, D.C.)* **1986**, *233*, 972–974.
43. Burt, J. M.; Spray, D. C. *Proc. Natl. Acad. Sci. U.S.A.* **1988**, *85*, 3431–3434.
44. Somogyi, R.; Kolb, H.-A. *Pflugers Arch.* **1988**, *412*, 54–65.
45. Bennett, M. V. L.; Verselis, V. K. *Semin. Cell Biol.* **1992**, *3*, 29–47.
46. Eghbali, B.; Kessler, J. A.; Spray, D. C. *Proc. Natl. Acad. Sci. U.S.A.* **1990**, *87*, 1328–1331.
47. Moreno, A. P.; Fishman, G. I.; Spray, D. C. *Biophys. J.* **1992**, *62*, 51–53.
48. Bennett, M. V. L.; Verselis, V.; White, R. L.; Spray, D. C. In *Modern Cell Biology*; Hertzberg, E. L.; Johnson, R. G., Eds.; Alan R. Liss: New York, 1988; Vol. 7, pp 287–304.
49. Spray, D. C.; Harris, A. L.; Bennett, M. V. L. *J. Gen. Physiol.* **1981**, *77*, 75–94.
50. Jaslove, S. W. In *Biophysics of Gap Junction Channels*; Peracchia, C., Ed.; CRC Press: Boca Raton, FL, 1991; pp 145–162.
51. Harris, A. L.; Spray, D. C.; Bennett, M. V. L. *J. Gen. Physiol.* **1981**, *77*, 95–120.
52. Finkelstein, A.; Peskin, C. S. *Biophys. J.* **1984**, *46*, 549–558.
53. Barrio, L. C.; Suchyna, T.; Bargiello, T. A.; Xu, L. X.; Roginski, R. S.; Bennett, M. V. L.; Nicholson, B. J. *Proc. Natl. Acad. Sci. U.S.A.* **1991**, *88*, 8410–8414.
54. Rubin, J. B.; Verselis, V. K.; Bennett, M. V. L.; Bargiello, T. A. *Biophys. J.* **1992**, *62*, 183–195.
55. Rubin, J. B.; Verselis, V. K.; Bennett, M. V. L.; Bargiello, T. A. *Proc. Natl. Acad. Sci. U.S.A.* **1992**, *89*, 3820–3824.
56. Catterall, W. A. *Science (Washington, D.C.)* **1988**, *242*, 50–61.
57. Brink, P. R.; Fan, S. *Biophys. J.* **1990**, *56*, 579–593.
58. Veenstra, R. D.; Wang, H. Z.; Westphale, E. M.; Beyer, E. C. *Circ. Res.* **1992**, *71*, 1277–1283.
59. Paul, D. L. *J. Cell Biol.* **1986**, *103*, 123–134.
60. Kumar, N. M.; Gilula, N. B. *J. Cell Biol.* **1986**, *103*, 767–776.
61. Nicholson, B. J.; Zhang, J. In *Modern Cell Biology*; Hertzberg, E. L.; Johnson, R. G., Eds.; Alan R. Liss: New York, 1988; Vol. 7, pp 207–218.
62. Traub, O.; Look, J.; Dermietzel, R.; Brummer, F.; Hulser, D.; Willecke, K. *J. Cell Biol.* **1989**, *108*, 1039–1051.
63. Kordel, M.; Nicholson, B. J.; Harris, A. L. *Biophys. J.* **1993**, *64*, A192.

64. Werner, R.; Levine, E.; Rabadan-Diehl, C.; Dahl, G. *Proc. Natl. Acad. Sci. U.S.A.* **1989**, *86*, 5380–5384.
65. Swenson, K. I.; Jordan, J. R.; Beyer, E. C.; Paul, D. L. *Cell* **1989**, *57*, 145–155.
66. Spray, D. C.; Bennett, M. V. L.; Campos de Carvalho, A.; Eghbali, B.; Moreno, A. P.; Verselis, V. In *Biophysics of Gap Junction Channels*; Peracchia, C., Ed.; CRC Press: Boca Raton, FL, 1991; pp 97–116.
67. Verselis, V. K.; White, R. L.; Spray, D. C.; ZwiLOWITZ, J.; Bennett, M. V. L. *J. Cell Biol.* **1987**, *105*, 307a.
68. Chen, Y. H.; DeHaan, R. L. *J. Membr. Biol.* **1992**, *127*, 95–111.
69. Manivannan, K.; Ramanan, S. V.; Mathias, R. T.; Brink, P. R. *Biophys. J.* **1992**, *61*, 216–227.
70. Stauffer, K. A.; Kumar, N. M.; Gilula, N. B.; Unwin, N. *J. Cell Biol.* **1992**, *115*, 141–150.
71. Lampe, P. D.; Kistler, J.; Hefti, A.; Bond, J.; Muller, S.; Johnson, R. G.; Engel, A. *J. Struct. Biol.* **1991**, *107*, 281–290.
72. Abney, J. R.; Braun, J.; Owicki, J. C. *Biophys. J.* **1987**, *52*, 441–454.
73. Ceriotti, A.; Coleman, A. *J. Cell Biol.* **1990**, *111*, 409–420.
74. Paulson, H. L.; Ross, A. F.; Green, W. N.; Claudio, T. *J. Cell Biol.* **1991**, *113*, 1371–1384.
75. Loewenstein, W. R. *Physiol. Rev.* **1981**, *61*, 829–912.
76. Beyer, E. C.; Kistler, J.; Paul, D. L.; Goodenough, D. A. *J. Cell Biol.* **1989**, *108*, 595–605.
77. Musil, L. S.; Goodenough, D. A. *J. Cell Biol.* **1991**, *115*, 1357–1374.
78. Dahl, G.; Werner, R.; Levine, E.; Rabadan-Diehl, C. *Biophys. J.* **1992**, *62*, 172–182.
79. Manjunath, C. K.; Goings, G. E.; Page, E. *J. Membr. Biol.* **1984**, *78*, 147–155.
80. Dupont, E.; el Aoumari, A.; Briand, J. P.; Fromaget, C.; Gros, D. *J. Membr. Biol.* **1989**, *108*, 247–252.
81. John, S. A.; Revel, J.-P. *Biochem. Biophys. Res. Commun.* **1991**, *178*, 1312–1318.
82. Rahman, S.; Evans, W. H. *J. Cell Sci.* **1991**, *100*, 567–578.
83. Lis, L. J.; McAlister, M.; Fuller, N.; Rand, R. P.; Parsegian, V. A. *Biophys. J.* **1982**, *37*, 657–666.
84. Mege, R. M.; Matsuzaki, F.; Gallin, W. E.; Goldberg, J. I.; Cunningham, B. A.; Edelman, G. M. *Proc. Natl. Acad. Sci. U.S.A.* **1988**, *85*, 7274–7278.
85. Musil, L. S.; Cunningham, B. A.; Edelman, G. M.; Goodenough, D. A. *J. Cell Biol.* **1990**, *111*, 2077–2088.
86. Miller, C., Ed. *Ion Channel Reconstitution*; Plenum: New York, 1986.
87. Harris, A. L. In *Biophysics of Gap Junction Channels*; Peracchia, C., Ed.; CRC Press: Boca Raton, FL, 1991; pp 373–389.
88. Brewer, G. J. In *Biophysics of Gap Junction Channels*; Peracchia, C., Ed.; CRC Press: Boca Raton, FL, 1991; pp 301–316.
89. Makowski, L.; Caspar, D. L. D.; Phillips, W. C.; Goodenough, D. A. *J. Cell Biol.* **1977**, *74*, 629–645.
90. Cascio, M.; Gogol, E.; Wallace, B. A. *J. Biol. Chem.* **1990**, *265*, 2358–2364.
91. Lynch, E.; Harris, A. L.; Paul, D. *Biophys. J.* **1984**, *45*, 61a.
92. Spray, D. C.; Saez, J. C.; Brosius, D.; Bennett, M. V. L.; Hertzberg, E. L. *Proc. Natl. Acad. Sci. U.S.A.* **1986**, *83*, 5494–5497.
93. Young, J. D.; Cohn, Z. A.; Gilula, N. B. *Cell* **1987**, *48*, 733–743.
94. Campos de Carvalho, A. C.; Eiras, L. A.; Waltzman, M.; Hertzberg, E. L.; Spray, D. C. *Braz. J. Med. Biol. Res.* **1992**, *25*, 81–92.
95. Donaldson, P.; Kistler, J. *J. Membr. Biol.* **1992**, *129*, 155–165.

96. Mazet, J. L.; Jarry, T.; Gros, D.; Mazet, F. *Eur. J. Biochem.* **1992**, *210*, 249–256.
97. Walter, A.; Zimmerberg, J.; Paul, D.; Harris, A. L. *Soc. Neurosci. Abstr.* **1988**, *12*, 1191.
98. Rhee, S. K.; Paul, D. L.; Harris, A. L. *FASEB J.* **1989**, *3*, A602.
99. Dupont, E.; el Aoumari, A.; Fromaget, C.; Briand, J.-P.; Gros, D. *Eur. J. Biochem.* **1991**, *200*, 263–270.
100. Ehring, G. R.; Kumar, N. M.; Stauffer, K. A.; Unwin, P. N. T.; Gilula, N. B.; Hall, J. E. *Biophys. J.* **1992**, *61*, A409.
101. Harris, A. L.; Park, J.; Balakrishnan, K.; Bevans, C.; Rhee, S.; Paul, D. *Biophys. J.* **1988**, *53*, 507a.
102. Harris, A. L.; Walter, A.; Paul, D.; Goodenough, D. A.; Zimmerberg, J. *J. Mol. Brain Res.* **1992**, *15*, 269–290.
103. Rhee, S. K.; Harris, A. L. *Biophys. J.* **1991**, *59*, 439a.
104. Mimms, L. T.; Zampighi, G.; Nozaki, Y.; Tanford, C.; Reynolds, J. A. *Biochemistry* **1981**, *20*, 833–840.
105. Harris, A. L.; Walter, A.; Zimmerberg, J. *J. Membr. Biol.* **1989**, *109*, 243–250.
106. Schein, S. J.; Colombini, M.; Finkelstein, A. *J. Membr. Biol.* **1976**, *30*, 99–120.
107. Hertzberg, E. L.; Skibbens, R. V. *Cell* **1984**, *39*, 61–69.
108. Stewart, W. W. *Cell* **1978**, *14*, 741–759.
109. Bennett, M. V. L.; Spira, M. E.; Spray, D. C. *Dev. Biol.* **1978**, *65*, 114–125.
110. Cohen, F. S.; Zimmerberg, J.; Finkelstein, A. *J. Gen. Physiol.* **1980**, *75*, 251–270.
111. Zimmerberg, J.; Cohen, F.C.; Finkelstein, A. *J. Gen. Physiol.* **1980**, *75*, 241–250.
112. Ehrenstein, G.; Lecar, H. *Q. Rev. Biophys.* **1977**, *10*, 1–34.
113. Labarca, P.; Coronado, R.; Miller, C. *J. Gen. Physiol.* **1980**, *76*, 397–424.
114. Bevington, P. R. *Data Reduction and Error Analysis for the Physical Sciences*; McGraw-Hill: New York, 1969; pp 180–182.
115. Buisman, H. P.; Steinberg, T. H.; Fischbarg, J.; Silverstein, S. C.; Vogelzang, S. A.; Ince, C.; Ypey, D. L.; Leijh, P. C. J. *Proc. Natl. Acad. Sci. U.S.A.* **1988**, *85*, 7988–7992.
116. Tatham, P. E. R.; Lindau, M. *J. Gen. Physiol.* **1990**, *95*, 459–476.
117. Goodenough, D. A.; Gilula, N. B. *J. Cell Biol.* **1974**, *61*, 575–590.
118. Zimmerberg, J.; Parsegian, V. A. *Nature (London)* **1986**, *323*, 36–39.
119. Zimmerberg, J. A.; Bezanilla, F.; Parsegian, V. A. *Biophys. J.* **1990**, *57*, 1049–1064.
120. Fisher, L. R.; Parker, N. S. *Biophys. J.* **1984**, *46*, 253–258.
121. Lucy, J. A.; Ahkong, Q. F. *FEBS Lett.* **1986**, *199*, 1–11.
122. Rand, R. P.; Parsegian, V. A. *Biochim. Biophys. Acta.* **1989**, *988*, 351–376.
123. Lifshitz, E. M. *Sov. Phys.* **1956**, *2*, 73–83.
124. Parsegian, V. A.; Ninham, B. W. *Nature (London)* **1969**, *224*, 1197–1198.
125. Ninham, B. W.; Parsegian, V. A. *Biophys. J.* **1970**, *10*, 646–663.
126. Green, C. R.; Harfist, E.; Gourdie, R. G.; Severs, N. J. *Proc. R. Soc. Lond. Ser. B* **1988**, *233*, 165–174.

RECEIVED for review February 20, 1991. ACCEPTED revised manuscript January 26, 1993.

Structure and Function of Gap Junctions in the Photoreceptor Axon Terminals of the Fly

Michael J. Wilcox

Department of Anatomy, School of Medicine, University of New Mexico, Albuquerque, NM 87131-5211

The structure of the compound eye of dipteran insects provides a unique preparation for investigation of functional coupling by gap junctions in photoreceptor axon terminals in an intact animal. Axon terminals of individual photoreceptors converge and synapse onto a pair of cells that form a visual element. These terminals are electrically coupled by gap junctions. Characterization of the nature of the photoreceptor input at this synapse is a prerequisite to understanding how the stimulus is encoded by a visual element. Control of coupling is imperative to isolate individual photoreceptor cells and preserve their optical disparity. An anatomical substrate that possibly underlies hyperacuity in this animal is shown by optically staining the photoreceptor mosaic in the retina. Although photoreceptor axon terminals are electrically coupled, their gap junctions do not allow dye coupling of the cells. The hypothesis that the gap junctions are voltage sensitive was tested by adaptation of the animal to light or darkness and by injection of depolarizing and hyperpolarizing current directly into the recorded axon terminal after dye injection. Control of the gap junctions by calcium concentration or pH in the terminal was tested by injection of buffers into the terminal. Ongoing experiments will better define these differences and dissect the control mechanism of electrical coupling of photoreceptor axon terminals in a complex but highly structured region of the nervous system.

0065-2393/94/0235-0225\$08.00/0
© 1994 American Chemical Society

Information Processing in the Retina

The retina provides a good model for the study of information processing in the nervous system because it is an accessible extension of the brain, located behind a clear window of cornea and lens; it has a well-defined structure; and its input elements can be modulated by an easily controlled stimulus—light. To emphasize the problem of dendritic integration at the first synapse, we will drastically oversimplify the organization of the more familiar vertebrate retina. Photoreceptors make synaptic contact with horizontal cells, which spread lateral interactions among neighboring synaptic terminals, and with bipolar cells, which in turn contact the ganglion cells, the output of the retina. Characterization of interaction at the first synapse is the goal of our research. Control of the gap junctions coupling these terminals is essential to that understanding. There is apparent convergence of many photoreceptor synapses onto the dendrites of two types of bipolar cell: “on center” with antagonistic surround and “off center” with antagonistic surround (1). The dendritic fields of the two cell types have considerable overlap. When several inputs synapse onto a dendrite, the general assumption is that they simply sum in a linear fashion, as shown in the classical case of motor neuron dendrites in the central nervous system. This assumption may not accurately represent dendritic integration by the bipolar. However, to test interaction between these convergent synaptic inputs, it is necessary to stimulate individual photoreceptor cells and record dendritic integration by the bipolar cell. This procedure is difficult in the vertebrate retina because physiological stimuli enter the retina through intervening blood vessels, ganglion and bipolar cell layers, and the photoreceptor layer, which is enshrouded by pigmented epithelium, and a clear view of the receptor matrix is obstructed. The usual approach is to remove the retina from the pigment epithelium, which allows visualization of the photoreceptors. Unfortunately, this procedure disrupts the matrix that maintains axial orientation of the outer segment of the photoreceptor that houses the visual pigment. Moreover, lack of pigment epithelium increases scatter of the light stimulus. The foregoing problems can be offset by use of an intact animal with a simplified retina.

Unlike humans, most animals view the world through compound eyes. However, the cellular architecture in the retina is parallel in animals as evolutionarily different as mollusks, insects, and vertebrates (2, 3). This commonality suggests that there are only a few good ways to process visual information and that far back in evolution, these processing tricks were adapted and adopted. A compound eye consists of many individual retinas, each of which looks at a different point in space (Figure 1). Consideration of only one facet of the compound eye of a fly reveals that it is a “simplified retina” in that it has a lens that images a small part of the world onto a miniretina that consists of only eight photoreceptor cells, which are called an ommatidium (Figure 2). A basement membrane separates the retina from its

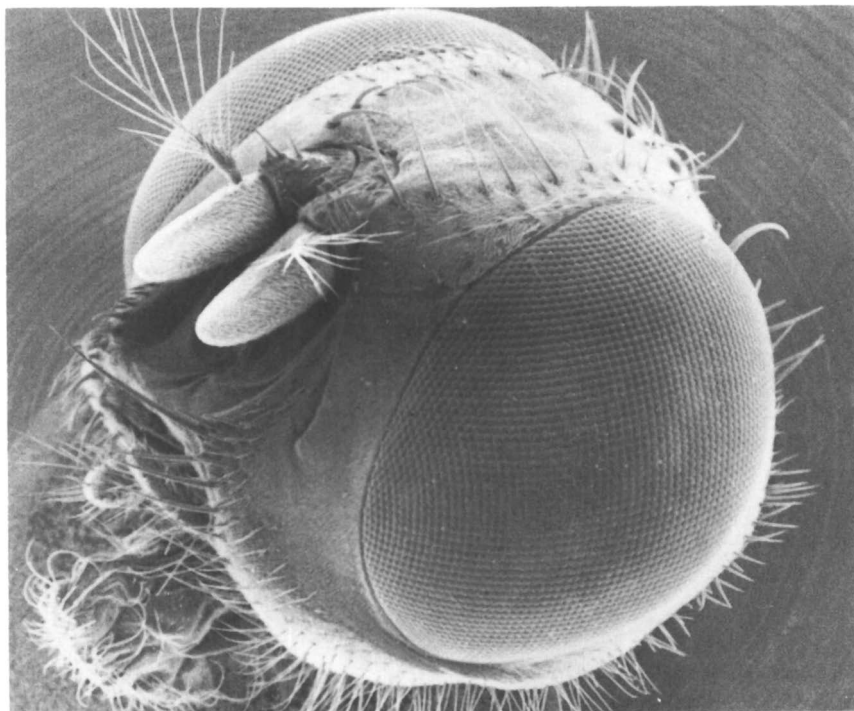


Figure 1. Scanning electron micrograph of the compound eyes of a female housefly, *Musca domestica*.

underlying compartment, which is called the *lamina*. Photoreceptor axons leave the ommatidia and form bundles that penetrate the basement membrane and distribute themselves so that the photoreceptors that share a common visual axis form synapses with the underlying structure, which is called a *cartridge* (Figure 3). Three thousand ommatidia and their processing subunits make up the compound eye of a fly and provide a nearly panoramic view of the fly's world. In addition to the broad field of view, this retina enables a male fly to pursue a female in flight, using relatively few facets, and to follow her with amazing accuracy (4) despite his coarse visual acuity, which is only about 2° (5)—the extent of the entire human macula. Even with such coarse acuity, the animal can detect small displacements of a stimulus far better than the resolution dictated by the spacing of retinal photoreceptors (6); this is contradictory to the channeling assumptions made in information

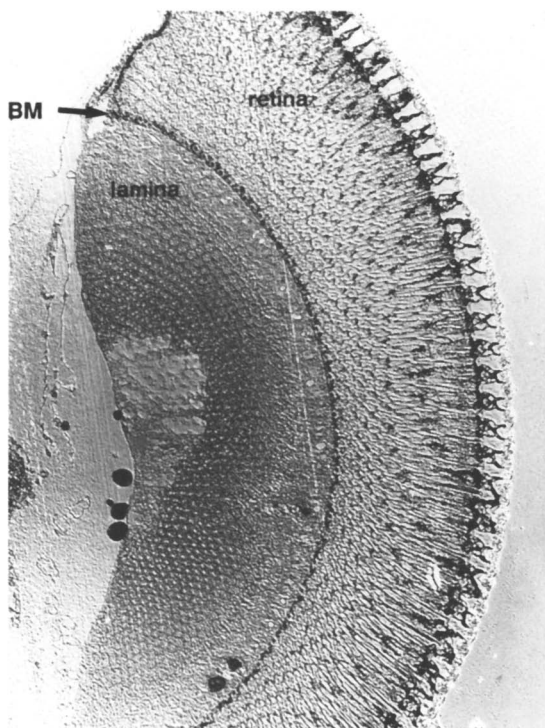


Figure 2. Interference contrast micrograph of a frontal section of the compound eye that shows the retina and lamina compartments separated by a basement membrane (BM). Lateral facet lenses are present on the outer edge of the section. Each lens in the eye images light onto a single ommatidium. Peripheral photoreceptors in each diamond-shaped ommatidium project axons across the basement membrane with 1:1 retinotopy onto the lamina cartridges.

processing theory (7). Such enhanced resolution, beyond the limit imposed by the spacing of receptors in the matrix, is called hyperacuity (8–10). Presently, machine vision does not have this capability, but many animals do. If the neural basis for hyperacuity can be determined, machines can be endowed with the same ability.

How hyperacuity works in any visual system is not understood. From experiments with human subjects, time delay and adaptational constraints suggest that hyperacuity occurs at an early (possibly retinal) level of visual processing (9). With this in mind, how the disparity of individual photoreceptor cells can be maintained when all the receptors appear to be electrically coupled to one another is even more puzzling. Electrical coupling possibly raises retinal sensitivity to light by “pooling” receptor inputs at the first synapse, which effectively increases the presynaptic surface area of an indi-

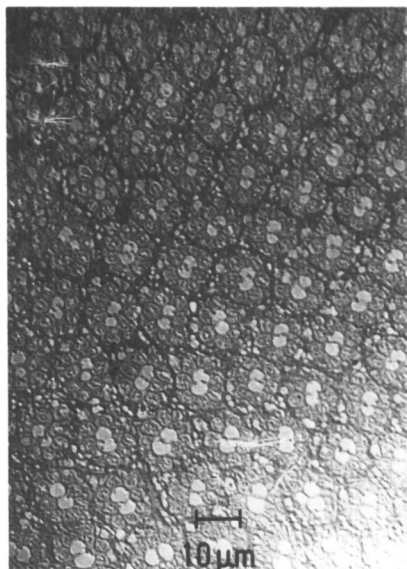


Figure 3. Interference contrast micrograph of a 1- μm -thick section of the lamina that shows photoreceptor axon terminals surrounding the paired monopolar neurons in each cartridge.

vidual receptor. Tight coupling along with an increase in synaptic surface would guarantee transmission of small signals in the presence of noise and, at the same time, reduce the effects of noise by shunting current to neighboring terminals. However, this same coupling should destroy the acuity gained by the disparity of individual cells that look at different points in space. Electrical coupling of neural elements is an important issue because of its apparent ubiquity, not only in the retina (1, 11), but also in the rest of the nervous system (12). Moreover, control mechanisms of gap junctions offer many possibilities to vary the nature of functional circuitry.

The function of coupling is difficult to assess in a vertebrate retina due to the numbers of cells coupled by gap junctions that form a large syncytium with neighboring cells. Fortunately, a similar arrangement exists in the fly eye, but the arrangement is simplified by limited coupling and the optical simplicity of the compound eye. Electrical coupling is limited to six photoreceptors that look at the same point in space (13, 14). Optics of the compound eye aids visualization of individual cells. Each photoreceptor cell has a specialized organelle called a rhabdomere that houses the visual pigment. This highly refractile organelle is an optical waveguide that contains and transmits light along its length until the energy is absorbed by the visual pigment. The distal tip of this waveguide is located in the focal plane of the facet lens, and light reaches the organelle without passing through intervening tissue. For an experimenter, this optical arrangement provides a tool for direct observation of individual organelles via transmitted, reflected, or fluorescent illumination through the animal's own corneal lens. Thus, the

rhabdomere becomes an *in vivo cuvette* that is 1 μm in diameter and 100 μm long, viewed end-on through a lens with a photographic *f* number of about 2.0. Alternatively, diffraction of the lens can be neutralized with water (15) and the organelles can be viewed directly by focusing the microscope on the tips of the organelles (Figure 4). Because the refractive index of the rhabdomere is higher than the surrounding tissue, light that passes through the cell body is effectively captured and piped up the organelle (16). The animal's own lens images the light along a well-defined axis to be captured by the microscope objective. Due to this end-on geometry, detection of injected

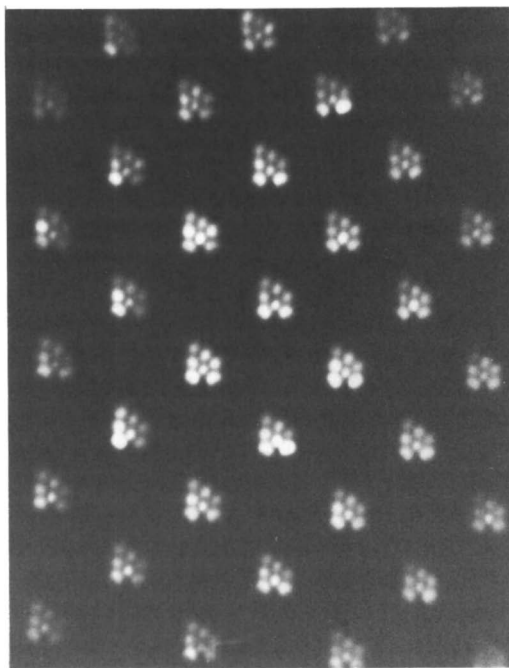


Figure 4. Micrograph of the rhabdomere tips in a living animal. Because the rhabdomeres act as waveguides, they can trap transmitted, reflected, or fluorescent light. A drop of water placed between the microscope objective and the fly's eye effectively neutralizes diffraction of the cornea and allows the microscope to focus on the distal tips of the rhabdomeres, which are physically and optically isolated from their neighbors. In this animal, the fluorescent dye rhodamine B was introduced to the retinal extracellular space. Epiillumination was used to excite the dye. Fluorescent light is piped up the organelle into the objective lens. The pattern of organelles shows the ommatidial arrangement, which consists of eight photoreceptor cells: six peripheral cells (R1–R6) that surround two central cells (R7 and R8) whose rhabdomeres are arranged in tandem (R8 below R7, to form a continuous waveguide). Independent stimuli can be selectively imaged onto individual rhabdomeres in this asymmetric pattern of seven optically isolated waveguides.

dyes at low concentration is enhanced. In all other animals that have compound eyes, the rhabdoms of the photoreceptors in each ommatidium are fused together into a single waveguide. Thus, illumination excites all cells in the ommatidium at once. Only in diptera are the rhabdomeres of each cell optically isolated, and, as a consequence, each rhabdomere can be seen and independent stimuli can be projected onto each one. This situation allows initiation of cellular interactions between neighboring cells by independent stimulation of preselected photoreceptors in the retinal matrix and simultaneous recording from one of those cells via a microelectrode.

Photoreceptor Matrix in the Retina of *Musca domestica*

Each ommatidium consists of six peripheral photoreceptor cells (R1–R6) that surround a pair of tandemly oriented central cells (R7 distal to R8). The two central cells bypass the lamina and form synapses in the underlying neuropil of the medulla. Therefore, the present discussion will ignore effects of central cell contribution and also feedback from the medulla and lateral interactions from neighboring cartridges. Axons of six peripheral cells, one from each of six adjacent ommatidia, join in the underlying layer, which is called the lamina, to form a structure called a *neuroommatidium* (17) (Figure 5). The photoreceptors that contribute their axons to a neuroommatidium share the same visual axis, that is, they look at the same point in space (18), as depicted in Figure 6a. This anatomical and optical relationship is called the principle of neurosuperposition.

Anatomical Substrate for Hyperacuity

Illumination of the animal's head from behind and use of the animal's own facet lens as an objective to image the rhabdomeres onto the far-field radiation allowed Pick (19) to project each rhabdomere in a single neuroommatidium onto the visual world. Pick showed that the photoreceptors in neuroommatidia of living animals do not share precisely the same visual axis; they are "misaligned" and show divergence when their rhabdomeres are imaged at infinity (effectively 10 mm in front of the animal). Slight divergence of the optical axes of the six photoreceptors results in an overlapped sampling of a point in the visual space. Compare Figure 6a and b. Such an overlap could provide a better sampling of the distant point in space, but independent axes could also form a substrate for hyperacuity. We performed an experiment that was the reverse of Pick's and used a photosensitization technique to stain photoreceptor cells illuminated by a high contrast stimulus (20, 21). A spot of light subtending 8° to the fly's eye illuminated a small portion of the retinal far field (depicted by the large circle in Figure 6a and b). Photoreceptors oriented on axis to the stimulus incorporated a fluorescent

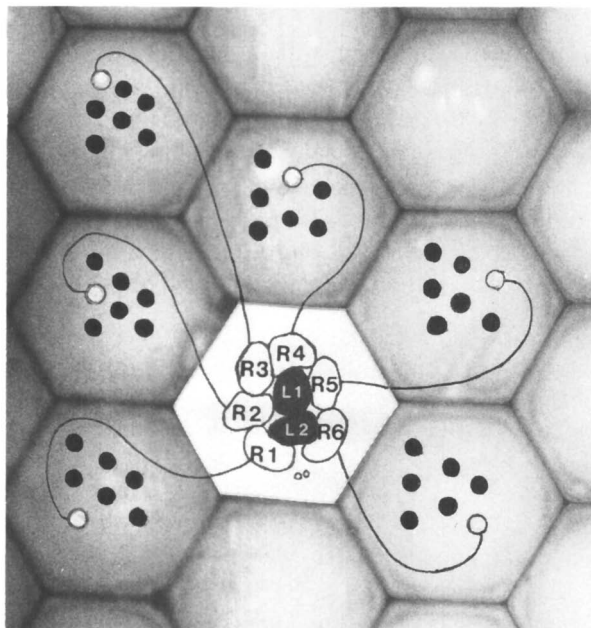


Figure 5. Light micrograph of a few facets of a fly's compound eye. Dark spots that represent the rhabdomeres of the photoreceptors have been superimposed onto each corneal lens to demonstrate the principle of neuro-superposition. The central corneal facet has been removed from the photograph to depict the underlying lamina cartridge. Anatomically, six peripheral photoreceptor axon terminals (R1–R6) synapse with two second-order cells (L1 and L2) in the underlying neuropil that is called the lamina. Each of these six photoreceptors is illuminated by a different lens, but optically they share the same visual axis; that is, they look at the same point in space. This lamina subunit is known as neuroommatidium. Axons of the central receptor cells (R7 and R8) from the overlying ommatidium pass close to this cartridge, but simply bypass the lamina and do not contribute synapses at this neural level.

dye. If all the receptors in a single neuroommatidium looked at precisely the same point in space and that point was illuminated, the receptors would all take up the dye and all the photoreceptor axon terminals in a single cartridge would be stained as depicted in Figure 6a and c. However, if the axes of the receptors were different, only the illuminated photoreceptors would be stained, while the nonilluminated photoreceptors in the same neuroommatidium would not be stained; the pattern shown in Figure 6b and d would be produced. Compared with the in situ view of Figure 4, the asymmetric array of rhabdomeres in Figure 6b appears upside down. However, recalling that the animal's own facet lens is being used to project an image of the rhabdomeres at infinity, this inversion is expected. Each rhabdomere was mapped from the far-field radiation (Figure 6b) onto its target in the lamina

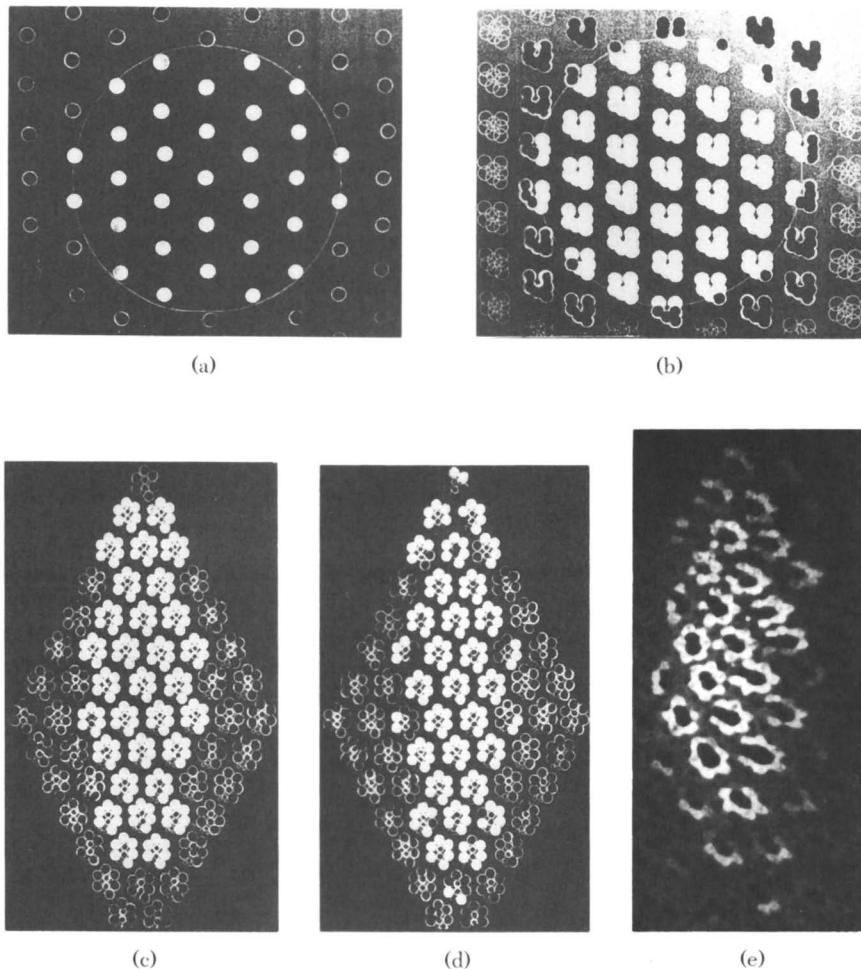


Figure 6. The staining pattern of photoreceptor somas (a and b) and axon terminals in the lamina (c and d) predicted by the principle of neurosuperposition (c) and the pattern predicted using the “misaligned” optical axes of the photoreceptors discovered by Pick (d). If every photoreceptor in the neuroommatidium looked at the same point in space (depicted as a dot in a), illumination of that point in space by a spot of light (as depicted by the circle in a) should induce all of those cells to incorporate dye and stain all photoreceptor axons in a cartridge. Uniform staining of each neuroommatidium would occur (as depicted in c). However, if the optical axes of the photoreceptors in a neuroommatidium are different, some of the cells would look at the bright light while others would not (d). Photoreceptors stained in b would produce a pattern like the one shown in d. The pattern in e was produced by staining a portion of the retina with an 8° spot of light. This pattern closely resembles the predicted pattern shown in d.

(Figure 6d). Results show that the axon terminals in the neuroommatidia were not uniformly stained (Figure 6e), contrary to the principle of neurosuperposition, where photoreceptor images are perfectly superimposed. This means that the disparate visual axis of each receptor in a single neuroommatidium is maintained and that those cells can be selectively stained by use of a high contrast stimulus imaged in the animal's field of view. We think that the animal would not maintain such precise alignment of individual receptors within a neuroommatidium if the eye could not make use of the advantage gained by disparate photoreceptor axes. Moreover, if the disparate input is not maintained and encoded by the monopolar cells, it is difficult to imagine how hyperacuity could be recovered by a downstream circuit.

Electrical Coupling of Axon Terminals in a Single Neuroommatidium

We hypothesized that optically disparate photoreceptor inputs that form an overlapped sampling of a distant point could form the substrate for hyperacuity in the fly eye. How lamina cartridges use this disparity to increase acuity without proper neural circuitry is hard to imagine. Recall that gap junctions are present between the six photoreceptor axon terminals in each lamina cartridge (13, 14). Electrical coupling should pool the information of all six terminals and smear the individual inputs. Scholes (22) first suggested that tight coupling by the gap junctions was functional. Shaw (23) refined the measurement by use of a fiber optic to stimulate cells in a single ommatidium while recording from photoreceptors. Because he stimulated all cells under the lens, equivalent to seven sampling points in space, many lateral interactions were induced, which complicated the analysis. Van Hateren (24) avoided this problem by stimulating only the cells that contributed axons to a cartridge, via the technique of corneal neutralization (25), and recorded from photoreceptors. Van Hateren showed that the six terminals in a single neuroommatidium are electrically coupled. The soma is separated from the axon terminal by a long, narrow axon. Signals that originate in a fellow neuroommatidial photoreceptor must traverse its own axon, cross from terminal to terminal through the gap junctions, and invade the soma of the recorded cell through its own narrow axon. The signal is attenuated when it invades the larger soma. Therefore, significant coupling measured at the distant soma suggests that the terminals are indeed tightly coupled. Gating of these gap junctions could be pivotal for information processing at the first synapse, between photoreceptors and interneurons. Opening and closing gap junctions, as a function of either adaptation or neural feedback, would be one way to effectively couple and decouple individual cells in the neuroommatidium.

Gap junctions can be opened either by lowering the intracellular free calcium concentration or by raising the cytoplasmic pH (26). Light-adapted photoreceptors have a higher intracellular calcium concentration than dark-adapted photoreceptors. Therefore, a simple solution to the problem would be that the junctions could open and close with respect to the state of adaptation of the receptor cell. Thus, sensitivity could be elevated by pooling receptor inputs when the cell is dark-adapted and acuity could be elevated by isolating disparate inputs when the cell is light-adapted. However, this does not appear to be the case in the excised vertebrate retina, where cell coupling is resistant to extracellular perfusion (11) that would decouple epithelial cells. In that study, the cell body was recorded. Cytoplasmic calcium concentration was not controlled from inside the cell, near the site of the gap junctions. The axon terminal, viewed as a structured process with all the necessary machinery for intercellular communication firmly in place, becomes another *in vivo* *cuvette*, isolated from the soma of the cell by a narrow axon that crosses the basement membrane between retina and lamina. A long axon effectively compartmentalizes the soma of the terminal, and impairs diffusion. Moreover, each cartridge is electrically insulated from its neighbors by a sheath of glial cells (27). Therefore, the terminal is appropriately handled as an independent entity. The intracellular calcium concentration of the soma, known to be affected by light adaptation, may not be controlled in the same way in the terminal. The basement membrane also provides an effective barrier for the diffusion of dyes added to the retina. Thus, two separate extracellular compartments are accessible for perfusion of the soma and the axon terminal. Furthermore, we can pharmacologically manipulate this isolated corner of the cell by a combination of pressure and electrophoretic injection into the terminal near the site of the gap junctions, while continuing electrical recording, and then recover the terminal for histological examination (Figure 7). Thus, control of coupling in the receptor axon terminals seems pivotal, not only for mechanisms of hyperacuity but also for characterization of gap junctions in this highly developed nervous system.

Dye Coupling between Photoreceptors

Classical approaches to verification of functional gap junctions include conductance measurement, pharmacological manipulation, and demonstration of dye coupling (28). Dye coupling is a straightforward method for demonstrating gap junctional function. Injection experiments are simple and results are easily interpreted. The outcome is assessed immediately with an *in vivo* preparation. A lower dye concentration is necessary for detection because dye lost during fixation and tissue processing is avoided.

In the fly, when the recording electrode crosses the basement membrane, the polarity of the extracellular potential in response to light, which is

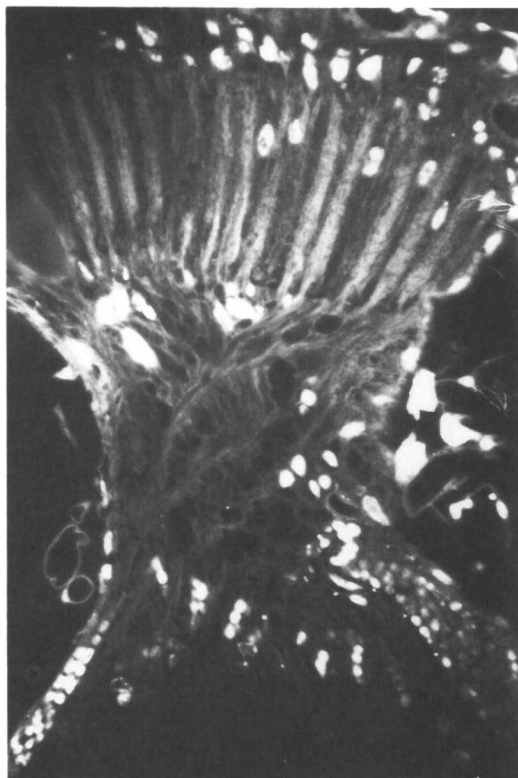


Figure 7. Fluorescence micrograph of a 1- μm -thick section of the lamina of a male fly that shows stained photoreceptor axon terminals cut parallel to their long axis. Gap junctions between the six peripheral cells occur in the outer 10 μm of the axon terminal, just below the somas of the monopolar neurons. Because recorded cells are located in reference to the corneal facet matrix, the location and orientation of that cell in the underlying neuropil is predetermined, so it can be sectioned in any given plane and recovered for histological and histochemical examination.

called the electroretinogram, inverts. Thus, the electrode position in the eye can be verified. Once an axon terminal is penetrated, the cell is brought on axis to the stimulus by moving the animal through orthogonal arcs until the cell responds to stimulation with a localized maximum. Furthermore, the facet lens that illuminates the cell can be localized by imaging a field diaphragm onto the corneal surface. Figure 8 shows the result of an experiment in which the axon terminal of a photoreceptor was coinjected with 6-carboxyfluorescein and the calcium chelator, ethyleneglycoltetraacetic acid (EGTA). The steady-state response of the receptor potential was augmented after injection, whereas the transient response remained unchanged, which



Figure 8. Fluorescence micrograph of the surface of the fly eye with a single facet lit. Although only one photoreceptor under that lens is stained (confirmed by examination of the ommatidium via corneal neutralization), the whole facet is illuminated like the lens of an oncoming car. If dye had spread to its neuroommatidial neighbors, adjacent facets would light up in response to fluorescent excitation.

indicates that EGTA had lowered the free calcium ion concentration within the terminal (29). EGTA chelation of cytosolic calcium near the site of coupling should have opened gap junctions and permitted dye coupling. The same experiment has been performed with Lucifer yellow, fluorescein, 6-carboxyfluorescein, fluorescein isothiocyanate, coumarin 175, Lissamine rhodamine B, and rhodamine 123, all of which have low molecular weight, either neutral, positive, or negative charge, and differing partial solubilities in lipid. Attempts also have been made to raise the cytoplasmic pH in the terminal by coinjection of alkaline dye solutions and buffers with dye. Each experiment has failed to show dye coupling, even though there was clear evidence of dye filling the injected cell and we used the end-on enhanced sensitivity of illumination, which was sensitive to dye filling of the impaled cell by diffusion alone. Although the results were negative, these experiments suggest either that control of gap junctional permeability is not a simple function of the cytosolic free calcium concentration or pH or that some other process interferes with dye coupling through this protein. Although Shaw and Stowe (14) reported that Lucifer yellow did not cross gap junctions of these

cells, they neither injected dye directly into the terminal nor tried to manipulate the permeability of the junction to induce coupling. Because we used dyes of various lipid solubility and charge, if the channel was open, dye solubility, resident charge in the channel, or charge of the molecule did not exclude passage of the tracer. The simplest explanation of our negative result is either that the channel in the gap junction is too small to accommodate the dyes used or that some other molecule obstructs the entrance to the channel.

Many insect tissues are coupled by gap junctions. In salivary glands (30), cuticular epithelia (31, 32), and the segmental partition of imaginal discs (33), dye coupling via gap junctions occurs readily. However, during development, the extent of dye coupling diminishes as compartmentalization of the tissue proceeds, whereas electrical coupling remains. The process involved in sealing off these compartments may be similar to the process seen in photoreceptor axon terminals. In our future research, dissection of the control mechanism will focus on manipulation of the membrane and gap junction proteins themselves in the intact preparation. Coupling effects on synaptic transmission can be assessed by recording from these interneurons. The combined approach of pharmacology, electrophysiology, and histochemistry of the same tissue will lead to a better understanding of not only function of neuronal gap junctions in their native membranes, but also information processing at the first synaptic layer of the retina.

Conductance of gap junctions between salivary gland cells of another dipteran, *Drosophila*, is voltage sensitive both to the intracellular voltage as well as the transjunctional voltage (34). If gap junctions in the photoreceptor terminals of our preparation were open, dye should have entered the coupled cell. If gating the junctions were a function of adaptation, light or dark adaptation of the cells should have opened the junctions and allowed dye coupling. Even though we obtained stable recordings from the terminals, we saw no dye coupling, perhaps because the impaled terminal was damaged by the electrode and the resting potential was no longer physiological. Based on this premise, we injected current from 0.5 to 30 nA of both polarities to modulate transjunctional as well as intracellular voltage of the terminal. Still, no dye coupling was seen.

Voltage Coupling across Gap Junctions in Axon Terminals

The strength of electrical coupling between adjacent terminals was measured by intracellular recording directly from the axon terminal. A spatially filtered and expanded laser beam illuminated two diaphragms that were imaged at the back focal plane of a 25-mm achromat lens used as an objective. This apparatus produced a small luminous spot that subtended a solid angle of 3.4 arcmin to the fly eye. Two other, moveable diaphragms were placed in the image plane of the same objective to form field diaphragms that allowed

illumination of any two facet lenses in the field. Once a photoreceptor axon terminal was recorded, the cell was brought on axis to the stimulus by moving the animal in orthogonal arcs until a local maximum response was recorded. The animal was moved in planar coordinates until the facet that contained the photoreceptor entered the illuminated field. Both field diaphragms were imaged onto the same facet. Both beam intensities were adjusted to give a criterion response in the recorded photoreceptor axon terminal. Then the field diaphragms were used to selectively illuminate photoreceptors whose coupled axon terminals formed synapses in the same cartridge as the recorded cell. Experiments show that neighboring terminals are tightly coupled at all intensities from the photon range to near saturation. The coupling ratio can be defined as the voltage recorded when the adjacent terminal is stimulated divided by the voltage recorded in response to stimulation of the cell whose terminal is impaled by the electrode. In this case, the ratio is between 0.7 and 0.9, which indicates tight coupling (Figure 9a). Imaging stimuli onto cells that do not contribute to the same cartridge resulted in either an unrecordable response or a response from the impaled terminal with less than 10% of the amplitude of a response from coupled cells. Therefore, 10% is considered the maximum contribution due to light scatter in our imaging system. This coupling factor compares with 0.5 for Van Hateren's measurements via corneal neutralization.

Both stimuli were brought closer together until they overlapped in time. The two signals summed unexpectedly (Figure 9b). Because stimulus intensity was the same for both photoreceptors, voltage in each terminal should have been the same, which would cancel any coupling current. This summation suggested that our original assumption—that all inputs to the monopolar dendrites are equal—may not be correct. If so, the nonlinear interaction should be integrated by the monopolar nonlinearly. To verify this, we performed the same experiment while recording from a monopolar cell. When both receptors were illuminated together, the amplitude of the monopolar response was actually less than the amplitude when either receptor was illuminated (Figure 9c). Such an interaction suggests an inhibitory process. Perhaps the encoding of the monopolar dendrite is a differential process rather than a summatory process. The observed nonlinear behavior may be due to feedback synapses or other lateral interactions, which for this discussion we have ignored. Optical isolation of the stimulus to photoreceptors that contribute synapses only to the cartridge that contains the recorded monopolar cell suggests that lateral interactions are minimized. If lateral interactions are present at all, they must be due to light scatter of the stimulus to neighboring ommatidia, which we measured at less than 10% of the response to stimulation of cells directly synapsing with the recorded monopolar cell.

An inhibitory process is consistent with lateral current shunting through the gap junctions to neighboring terminals. A mechanism of electrotonic

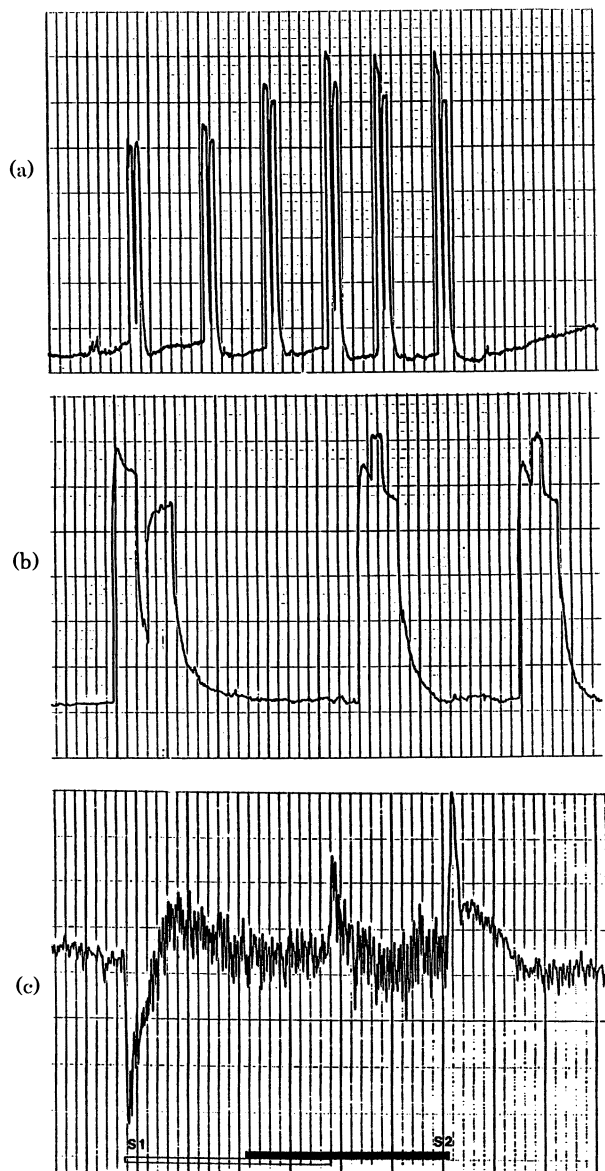


Figure 9. Traces of intracellular recordings from photoreceptor axon terminals (a and b) while the soma of the cell and the soma of a coupled cell were stimulated by a laser and from a monopolar cell (c) while two coupled photoreceptors were stimulated. Half-second stimuli were used in all three cases. In a and b the photoreceptor that contributes its axon terminal to the same cartridge was stimulated by a laser with increasing intensity, and the voltage was recorded from the impaled terminal. The recordings show that coupling is strong between adjacent axon terminals and also that disparate information is retained and encoded by the monopolar cell.

inhibition, which involves voltage in a restricted extracellular space, was first proposed for the well-known Mauthner cell (35, 36). A modification of that model can be used to explain our experimental results. Glial isolation of each cartridge (27) together with high ohmic resistance across the basement membrane imparts high input impedance for the photoreceptor input to the lamina. High impedance prevents voltage degradation and improves fidelity. Somas of nonstimulated photoreceptors within the same cartridge would provide a virtual ground for current that would be drawn through the gap junction and back to nonstimulated somas. The distal position of gap junctions (13) prevents passage of current through the main body of a nonstimulated photoreceptor terminal; however, current is directed antidromically through its axon. Therefore, current would not contribute to transmitter release from that terminal and input would be inhibited functionally. Maintenance of extracellular voltage could explain the apparent voltage summation in the terminals. In this case, depolarization of the extracellular space would induce current flow back toward the retina through the unstimulated photoreceptors. At low luminance, extracellular voltage does not saturate and shunting of small currents could actually sum in the electrically coupled terminals. A similar model was proposed by Shaw (23) as a nonsynaptic basis for lateral inhibition with neighboring cartridges. This mechanism, which operates between cartridges, may be responsible for an antagonistic surround. If a similar mechanism operates within a single neuroommatidium, it could form a substrate for hyperacuity in the compound eye and functional units in the vertebrate retina as well.

By use of a high-contrast stimulus to differentially stain the cells in the neuroommatidium, we have shown that optical disparity of individual photoreceptors that form the input to lamina cartridges in the fly eye is maintained. Electrical coupling of these same axon terminals is high at low and moderate luminance. Even though evidence shows that coupling is structurally mediated by gap junctions, these junctions do not allow dye coupling and dye coupling is insensitive to treatment that would open closed junctions in other cells.

Quantification of electrical coupling remains to be determined by conductance measurement. These experiments are in progress. However, at low and moderate luminance, it is sufficient that the gap junctions remain in a conducting state to accomplish both goals of this system: elevated sensitivity at low luminance by allowing lateral spread of current to coupled photoreceptor terminals and contrast enhancement of individual inputs from optically disparate receptors; both functions use current shunted through gap junctions. Therefore, the original postulate that gap junctions open and close with respect to light adaptation is not even necessary. Moreover, the use of constitutively open gap junctions that enables the transition from summation at low intensity to inhibition at moderate intensity could be a continuous function of stimulus contrast. The morphological and physiological evidence

presented here does not prove that the proposed mechanism underlies hyperacuity. However, it is a plausible explanation that functions well in a computer simulation (37) and shows that, at least at the level of the monopolar dendrites, disparate information is maintained and encoded by the monopolar cells. The advantage of this system is that information about the absolute position of a point source of light is preserved in an analog signal and yields high resolution that is not limited by spacing of retinal detectors.

References

1. Kaneko, A. *Trends Neurosci.* **1983**, *6*, 219–223.
2. Cajal, S. R.; Sanchez, D. *Trab. Lab. Invest. Biol. Univ. Madrid* **1915**, *13*, 1–168.
3. Zawarzin, A. *Z. Wiss. Zool. Leipzig* **1925**, *124*, 118–212.
4. Wehrhahn, C. *Biol. Cybern.* **1979**, *32*, 239–241.
5. Wehrhahn, C.; Poggio, T.; Bülthoff, H. *Biol. Cybern.* **1982**, *45*, 123–130.
6. Coombe, P. E.; Srinivasan, M. V.; Guy, R. G. *J. Comp. Physiol. A* **1989**, *166*, 23–35.
7. Shannon, C. *Proc. IRE* **1949**, *37*, 10–21.
8. Thibos, L.; Walsh, D.; Cheney, F. *Vision Res.* **1987**, *27*, 2193–2197.
9. Nakayama, K. *Vision Res.* **1985**, *25*, 625–660.
10. Bischof, W.; Groner, M. *Vision Res.* **1985**, *25*, 839–847.
11. Griff, E. R.; Pinto, L. H. *Vision Res.* **1984**, *24*, 149–157.
12. Jaslove, S. W.; Brink, P. R. In *Cell-to-Cell Communication*; De Mello, W. C., Ed.; Plenum: New York, 1987; pp 103–148.
13. Ribí, W. *Cell Tissue Res.* **1978**, *195*, 299–308.
14. Shaw, S. R.; Stowe, S. J. *Cell Sci.* **1982**, *53*, 115–141.
15. Franceschini, N. In *Photoreceptor Optics*; Snyder, A. W.; Menzel, R., Eds.; Springer: Berlin, Germany, 1975; pp 98–125.
16. Snyder, A. In *Photoreceptor Optics*; Snyder, A. W.; Menzel, R., Eds.; Springer: Berlin, Germany, 1975; pp 38–55.
17. Braitenberg, V. *Exp. Brain Res.* **1967**, *3*, 271–247.
18. Kirschfeld, K. *Exp. Brain Res.* **1967**, *3*, 248–270.
19. Pick, B. *Biol. Cybern.* **1977**, *26*, 215–224.
20. Wilcox, M. J.; Franceschini, N. J. *Science (Washington, D.C.)* **1984**, *225*, 851–854.
21. Wilcox, M. J.; Franceschini, N. J. *Neurosci. Lett.* **1984**, *50*, 187–192.
22. Scholes, J. *Kybernetik* **1969**, *6*, 149–162.
23. Shaw, S. R. *J. Exp. Biol.* **1984**, *112*, 225–251.
24. Van Hateren, J. *J. Comp. Physiol.* **1986**, *158*, 795–811.
25. Franceschini, N.; Kirschfeld, K. *Kybernetik* **1971**, *8*, 1–13.
26. Rose, B.; Rick, R. *J. Membr. Biol.* **1978**, *44*, 377–415.
27. Sainte-Marie, R. L.; Carlson, S. D. *J. Neurocytol.* **1983**, *12*, 243–275.
28. Larsen, W. J. In *Cell Interactions and Gap Junctions*; Sperelakis, N.; Cole, W. C., Eds.; CRC Press: Boca Raton, FL, 1989; pp 3–28.
29. Brown, J. E.; Pinto, L. H. *J. Physiol.* **1974**, *236*, 575–595.
30. Zimmerman, A. L.; Rose, B. *J. Membr. Biol.* **1985**, *84*, 269–283.
31. Caveney, S.; Safranyos, R. G. A. In *Cell Interactions and Gap Junctions*; Sperelakis, N.; Cole, W. C., Eds.; CRC Press: Boca Raton, FL, 1989; pp 107–123.
32. Safranyos, R. G. A.; Caveney, S. *J. Cell Biol.* **1985**, *100*, 736–747.

33. Lo, C. W. In *Cell Interactions and Gap Junctions*; Sperelakis, N.; Cole, W. C., Eds.; CRC Press: Boca Raton, FL, 1989; pp 85–96.
34. Verselis, V. K.; Bennett, M. V. L.; Bargiello, T. A. *Biophys. J.* **1991**, *59*, 114–126.
35. Furshpan, E. J.; Potter, D. D. *J. Neurophysiol.* **1963**, *26*, 140–176.
36. Korn, H.; Faber, D. S. *J. Neurophysiol.* **1975**, *38*, 452–471.
37. Moya, J.; Wilcox, M. J.; Donohoe, G. W. *Proc. 14th Int. Conf. IEEE-EMB* **1992**, *4*, 1574–1575.

RECEIVED for review January 29, 1991. ACCEPTED revised manuscript January 26, 1993.

The Mitochondrial Voltage-Dependent Anion-Selective Channel

Marco Colombini

Laboratories of Cell Biology, Department of Zoology, University of Maryland,
College Park, MD 20742

The mitochondrial outer membrane contains a 30-kDa protein called voltage-dependent anion-selective channel (VDAC) that forms channels with 3-nm pores through which metabolites travel between the cytoplasm and the mitochondrial spaces. Electron micrographs of two-dimensional crystals of these channels after freeze-drying, shadowing, and computer processing reveal detailed surface images of the channels. Both surfaces look very similar: most of the protein appears to be embedded in the membrane. The ion selectivity of the channel and changes in it induced by site-directed mutations fit quite well to the fixed-charge theory of Teorell. The voltage-dependent closure of VDAC at both positive and negative potentials can be modulated by polyanions, osmotic pressure, aluminum hydroxide, and a soluble mitochondrial protein called the VDAC modulator. VDAC acts as a binding site for proteins perhaps through a domain located on the membrane surface.

MITOCHONDRIA CONTAIN TWO AQUEOUS COMPARTMENTS, one impermeable to sucrose and the other permeable to sucrose but impermeable to high-molecular-weight polysaccharides. This description was proposed by Werkheiser and Bartley (1) in 1956. Their conclusion that mitochondria consist of two membrane-enclosed compartments, one inside the other, is universally accepted today. Translocation across the inner membrane is performed by a host of specific transport systems whereas movement across the outer membrane occurs via a protein, called voltage-dependent anion-

0065-2393/94/0235-0245\$08.00/0
© 1994 American Chemical Society

selective channel (VDAC), that forms large aqueous pores. The size selectivity for nonelectrolytes observed by early investigators for the sucrose-permeable compartment (now known as the intermembrane space) can be readily understood by the presence of these channels (2–4).

VDAC channels with virtually the same properties have been isolated from mitochondria representing all the eukaryotic kingdoms (5). The only source of mitochondria lacking VDAC channels is a yeast strain whose VDAC gene was skillfully deleted (6, 7).

A major function of mitochondria—to provide cells with adenosine 5'-triphosphate (ATP) produced by oxidative phosphorylation—requires that ATP, adenosine 5'-diphosphate (ADP), inorganic phosphate (Pi), and metabolic substrates cross the outer membrane. The discovery (8) that VDAC channels are voltage-gated raises possibilities for regulation with far-reaching consequences. If the outer membrane were to become impermeable to critical metabolites, important functions such as mitochondrial ATP production would cease.

Structure of the VDAC Channel

High-resolution images of VDAC channels have been obtained by taking advantage of the fact that VDAC channels in the *Neurospora crassa* mitochondrial outer membranes can be induced to form large two-dimensional crystals (9, 10). Electron micrographs of these crystals can be converted into high-resolution averaged images through the use of computer averaging and filtration techniques. Negatively stained crystals allow the aqueous pore formed by the channel to be visualized (Figure 1D). Frozen-hydrated methods have visualized the protein regions forming the pore (11). More recently, a freeze-drying-shadowing procedure was used to visualize the surface topography of each side of the channel (Figure 1A and B). The results clearly show that VDAC forms a large aqueous pore with a small amount of protein; most of the protein is embedded in the membrane (Figure 2A and B).

The proteins that form VDAC channels have been sequenced for three species, *N. crassa*, *S. cerevisiae*, and *H. sapiens*. All these species are probably composed of 282 amino acids and have molecular weights of 29,848, 29,752, and 30,641, respectively (12–14). The closeness of the molecular weights and amino acid content between proteins from fungi to mammals is in harmony with the high degree of similarity in the properties of VDAC from many different sources (5). The degree of amino acid identity between the fungal sequences and the human is only 24–29% (14), but the degree of conservation is underestimated.

Probes into the secondary structures of the three channel-forming proteins reveal a high degree of conservation. The nature of the channel and its location within the membrane greatly limit the possible secondary structures. A cylinder formed primarily of a beta-sheet wall was proposed (6, 15) and

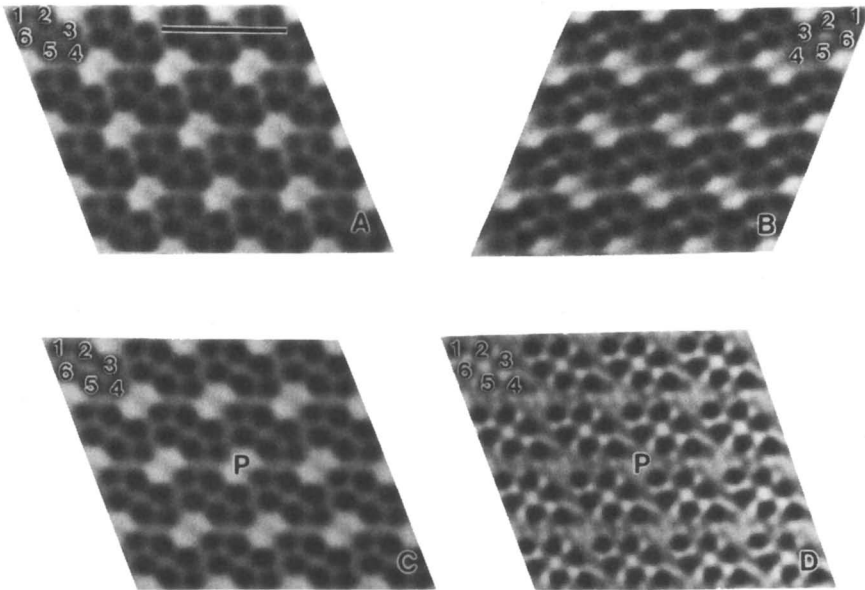


*Figure 1. Two-dimensional crystals of VDAC from *N. crassa* were freeze-dried and shadowed with platinum. The electron micrographs were digitized, and averaged and filtered images were obtained by computer processing. A, The average reconstructed image of filtered, freeze-dried-shadowed (45°) VDAC crystals as seen from one membrane surface. The dark areas are depressions, presumably the openings of the channels. The same crystal was viewed from the other surface of the membrane, B. The image in B was flipped about the axis of mirror symmetry and aligned with that in A by cross-correlation, and then averaged. C, This image represents eight crystals with different shadowing directions. D, The Fourier-filtered image of a negatively stained VDAC crystal. The dark areas are the location of stain accumulation, presumably the pores of the channels. All images are at the same magnification. The bar marker = 20 nm. (Reproduced with permission from reference 19. Copyright 1991 Academic.)*

supported by site-directed mutagenesis of VDAC from yeast (16). Such a beta-sheet wall, which separates the polar environment within the channel from the nonpolar environment of the bilayer, would have to be composed of beta strands with amino acid side chains that alternate between polar and nonpolar residues. This would form a “sided” strand that is well suited to form the interface between these two different phases. A computer search (6) for such alternating patterns in 10-amino-acid stretches (3.5 nm long; enough to span the nonpolar portion of the membrane) of the protein sequence revealed many locations (Figure 3). These locations were used to generate a model for the open state of VDAC that was tested by site-directed mutations and found to be largely correct (16). The location of the amino acid stretches appropriate to form the “sided” beta strands is well conserved

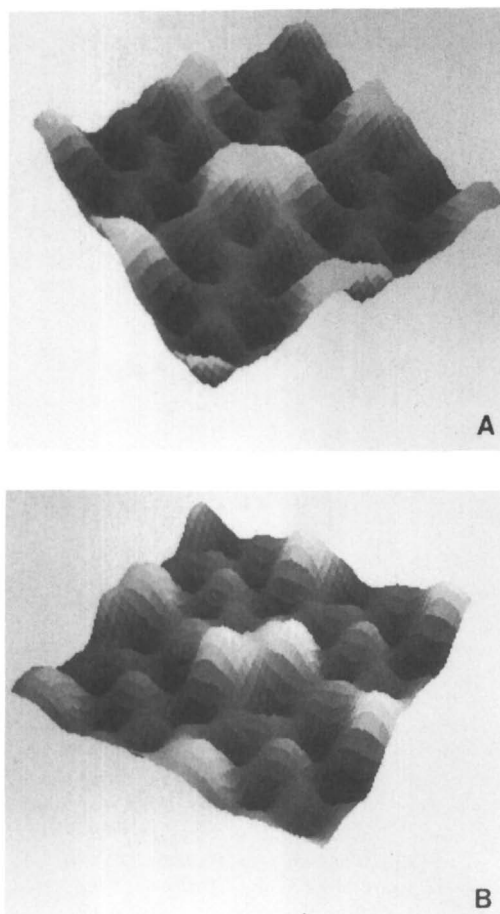


Figure 2. Three-dimensional representation of the averaged surface reconstructions. A and B correspond to Figure 1A and B, respectively. Dark areas are regions of lowest elevation and white areas are those of highest elevation. (Reproduced with permission from reference 19. Copyright 1991 Academic.)

among the species (Figure 3), which indicates a very similar secondary structure (17).

Despite earlier indications that VDAC is a dimer, recent evidence strongly favors a monomer. Early attempts to quantitate the amount of protein mass in the two-dimensional crystals of VDAC indicated that there may not be enough mass to form a dimer (11, 18). More recently, the use of scanning transmission electron microscopy on the VDAC crystals allowed precise estimates of mass per channel (19). These scans showed a 1:1 relation between channels and 30-kDa polypeptide chains if the crystal also contained 32% lipid. Results (20) of attempts to make hybrid channels by growing cells

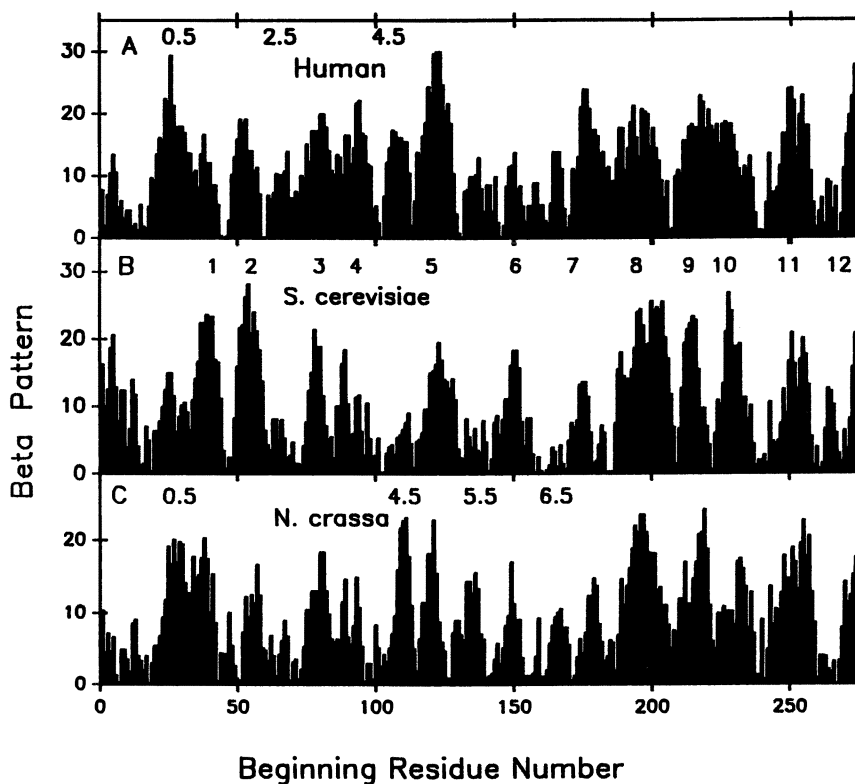


Figure 3. An evaluation of the potential of stretches of amino acids in the VDAC sequences from *S. cerevisiae* and *N. crassa* and of a homologous human sequence to form beta strands lining the walls of a water-filled pore. The hydrophathy values of each group of 10 adjacent amino acids were combined as follows: $\sum_{i=1}^{10} (-1)^{i+1} v(i)$, where $v(i)$ is the hydrophathy value of the i th amino acid. The absolute value of these sums was plotted against the number of the first amino acid in the summation. The numbers in panel B represent the locations of the major peaks in this panel. The numbers in panels A and C refer to major peaks found in these panels that were minor or absent in panel B. (Reproduced with permission from reference 17. Copyright 1991 Academic.)

containing two different VDAC genes (one wild and one mutant) are supportive of a monomeric channel. Channels isolated from the mitochondria of such cells were either wild or entirely mutant in their properties. No channels were observed with properties intermediate between the wild and mutant phenotypes. Thus it is likely that only one 30-kDa polypeptide, which is capable of two separate voltage-gating processes, forms a cylindrical channel that results in a 3-nm (in diameter) aqueous pore through the membrane.

From the hydrodynamic properties of VDAC isolated from rat liver, Lindén and Gellerfors (21) deduced that VDAC exists as a dimer in deter-

gent solution. This finding, and the observation that the rate of channel insertion into planar membranes is linearly dependent on the amount of detergent-solubilized protein added to the aqueous phase, led early on to the conclusion that VDAC was a dimer. A reexamination of the hydrodynamic data shows that no correction was made for the large aqueous pore of VDAC. The measured sedimentation coefficient, Stokes radius, and partial specific volume were used to determine the effective molecular weight of detergent-solubilized VDAC. The calculated value of 171,000 for the molecular weight was corrected for detergent binding and resulted in a net value of 61,000. A further correction for water in the aqueous pore (3 nm in diameter and 5 nm long) would yield a net value of 40,000. Tightly bound water and lipids could account for the difference between 40,000 and the actual molecular weight of 30,000. Thus the hydrodynamic data are consistent with a monomeric channel.

Channel Selectivity

The charge selectivity of channels that form a large aqueous pore is likely to be dominated by the electrostatic environment within the pore rather than the binding of the passing ions to the wall of the pore. Therefore, charged residues on the wall should have strong effects. This expectation was verified for VDAC by using site-directed mutations to change residues at specific locations (16). Indeed, identification of residues lining the wall of the pore was possible by determining whether a charge change at that location resulted in the appropriate change in selectivity as measured by determining the reversal potential in the presence of a KCl salt gradient.

Greater insight into the molecular basis for selectivity in VDAC was obtained (22) by comparing the observed reversal potentials as a function of the engineered charge change with that expected from the fixed-charge membrane theory of Teorell (23). Figure 4 reveals a remarkably good fit between reversal potential changes due to charge changes at residues thought to be in the pore (triangles and circles) and the theory (solid curve). Charge changes at locations thought to be outside the pore (squares) had no significant effect on the reversal potential. The data plotted as circles all contained the mutation K19E (the lysine at position 19 converted to glutamate) that displays a stronger than expected effect on the selectivity. Overall, the theory and experimental observations agree very well, which indicates that the molecular basis for ion selectivity in VDAC can be understood using a fairly simple theory.

Voltage Dependence

Each VDAC channel can close at both positive and negative potentials (Figure 5), which indicates the presence of two gating processes within the

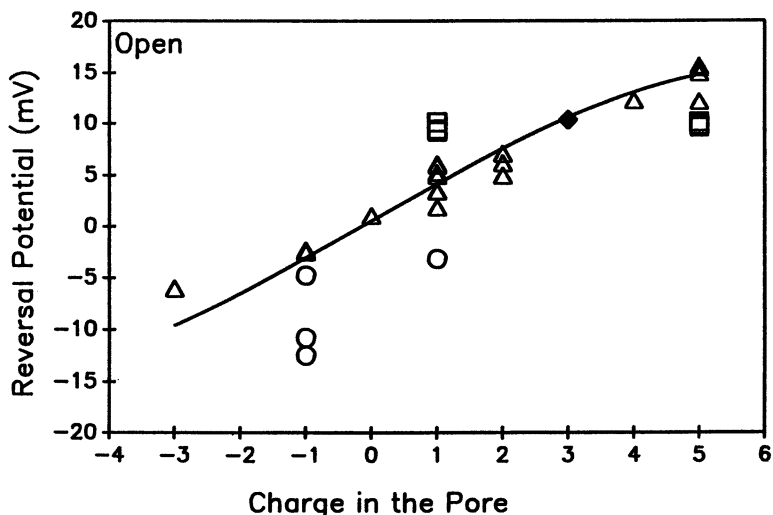


Figure 4. The change on the reversal potential of the VDAC channels with change in the charge within the pore was calculated by applying the theory of Teorell to the VDAC channel (solid line). The charge within the pore for the wild-type channel (solid diamond) was chosen to lie close to the theoretical curve. All other points were plotted according to the measured reversal potentials and the charge change induced by the mutation. Mutations at sites determined to be within the pore by other criteria were plotted as triangles or circles; those mutations determined to be outside the pore were plotted as squares. The salt concentration gradient and sign of the potential are indicated in Table I. Taken from the data of Peng et al. (22).

protein. The most conductive ("open") state is the preferred conformation at low or zero membrane potential. At high fields, low-conducting ("closed") states are occupied. In KCl solutions, the conductance of the most frequently observed closed state is 40–50% of the conductance of the open state. However, there is evidence (24–26) to indicate that the closed states are impermeable to the biologically important ions (ATP and ADP). The fact that these closed states can still conduct KCl has allowed researchers to study the properties of these states.

The process of channel closure in VDAC must involve rather extensive structural changes. The effective pore diameter is reduced from 3 to 1.8 nm (27, 28). The volume of aqueous solution within the pore is reduced by about 30 nm³ (29). The selectivity of the channel, as measured by the reversal potential for a 10-fold KCl gradient, reverses (4, 30) from a mild preference for anions to a preference for cations (a change of over 30 mV in reversal potential). The slow rate of channel closure [from milliseconds to seconds, depending on the applied voltage (2, 8)] is consistent with an extensive conformation change. Surprisingly, the rate of channel opening is

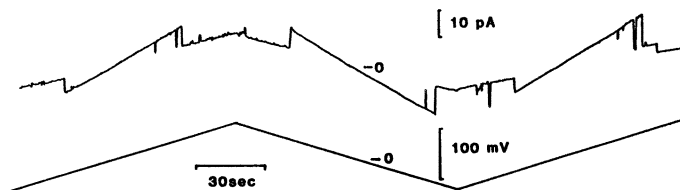


Figure 5. The voltage dependence of VDAC as illustrated by the behavior of a single VDAC channel from *P. aurelia*. The upper trace shows the current trace recorded under voltage-clamp conditions. The lower trace is the applied voltage. The zero current and voltage levels are indicated. A steep slope in the current indicates a high conductance; thus, the channel was in the open state. Transitions to a shallower slope are channel closures (the reverse is an opening). Time proceeded from left to right. The channel was open at low potentials and closed at both positive and negative potentials. (Reproduced with permission from reference 5. Copyright 1989 Springer-Verlag.)

fast (microseconds) if the channels have not been allowed to adapt to the closed state (2, 8).

The high sensitivity that can be achieved when current flowing through a planar phospholipid membrane is recorded allows the properties of individual channels to be studied. In this way, variability in properties from channel to channel can be examined and multiplicities in the number of states that the channel can achieve can be observed. By raising and lowering the applied voltage, a VDAC channel can be induced to open and close. In principle, the channel may sample many different conformations, and these conformations could be distinguished by their properties such as conductance and ion selectivity. In practice, for VDAC the properties of the open state are quite constant whereas the properties of the closed state are much more variable, which demonstrates a multiplicity of closed states (30). There are wide variations in both the size and selectivity of the closed states. The variability is somewhat greater between channels than for the same channel, but not by very much. The variability can be dramatically reduced by adding agents that increase the voltage dependence (*see* Table I; note change in standard deviation). These agents seem to favor a particular closed-state conformation.

Modulation of Voltage Dependence of VDAC

The voltage-gating process of a channel can be influenced in two ways:

1. The switching region (i.e. the voltage range over which channels go from predominantly open to predominantly closed) can be moved along the voltage axis.
2. The voltage dependence can be increased or decreased to yield a narrower or wider switching region.

Table I. Single-Channel Properties with and without König's Polyanion

<i>Property</i>	<i>Control</i>	<i>Plus 0.5 $\mu\text{g}/\text{mL}$ Polyanion</i>
Open channel		
Conductance (nS)	1.8 \pm 0.1 (11)	1.9 \pm 0.1 (3)
Reversal potential (mV)	10.0 \pm 1.1 (11)	10.5 \pm 0.6 (3)
Closed channel		
Conductance (nS)	0.81 \pm 0.17 (7)	1.2 \pm 0.07 (3)
Reversal potential (mV)	-8.6 \pm 1.4 (7)	-22.6 \pm 1.0 (5)

NOTE: Measurements made in 1 M KCl vs. 0.1 M KCl with 5 mM CaCl_2 , 1 mM 2-(*N*-morpholine)ethanesulfonic acid, pH 5.8, on each side (sign refers to high-salt side). Values are means plus or minus standard deviation, and the number of estimates is given in parentheses.

Movement of the switching region is quantitated by measuring V_0 , the voltage at which the channels have an equal probability of being either open or closed (8). Alteration of the voltage dependence is quantitated by determining the parameter n —the number of charges that would have to move through the entire membrane potential to account for the observed voltage dependence. Both of these mechanisms and a combination of the two were observed in VDAC.

A variety of highly negatively charged polymers from synthetic polyanions (such as dextran sulfate) to highly negatively charged proteins (such as pepsin) can increase the voltage dependence of VDAC and result in both an increase in n and a decrease in V_0 (31, 32). Voltage-dependence can increase more than 20-fold (P. Mangan and M. Colombini, unpublished results) and result in large conductance changes for a fraction of a millivolt change in membrane potential. Because asymmetric addition effects only one gating process (31), the polyanion must be added to both sides of the membrane to influence both gating processes. This exquisite sensitivity can be exploited easily by cells to detect very small changes in membrane potential. The voltage dependence can be modulated in this way by regulation of the charge on a polymer such as the degree of phosphorylation of a protein.

A particularly potent polyanion that was produced by König et al. (33) had potent effects (27) at less than 1 $\mu\text{g}/\text{mL}$. In addition to increasing the voltage dependence of VDAC (as was the case for the other polyanions), this polyanion also caused channels to remain closed even in the absence of a membrane potential. Addition of this polyanion to the solution on both sides of the membrane resulted in a marked effect on both gating processes, whereas addition to only one side of the membrane resulted in selective stimulation of the gating process in response to negative potentials on the polyanion side (22). This polyanion also reduces the size of negatively stained pores of two-dimensional crystals of VDAC channels, which results in a

reduction in observed pore diameter to 1.7 nm (28) that is very consistent with estimates from nonelectrolyte fluxes (1.8 nm; 27). This polyanion also is an effective inhibitor of ADP and ATP flux across mitochondrial outer membranes (24–26).

The switching region can be moved along the voltage axis without affecting the steepness of the VDAC voltage dependence by changing the colloidal osmotic pressure of the medium (29). The effect may be enhanced by higher molecular weight polymers (P. S. Mangan and M. Colombini, unpublished) or charged polymers. In addition, there is a synergistic effect of polyanions and osmotic pressure that can result in enormous effects (P. S. Mangan and M. Colombini, unpublished). Zimmerberg and Parsegian proposed (29) that a cell could use VDAC to monitor and regulate the concentration of intracellular polymers.

A water-soluble protein that increases the rate and extent of VDAC channel closure has been identified (34) and localized to the mitochondrial intermembrane space (M. Holden and M. Colombini, unpublished observations). This protein, called the VDAC modulator, may be the natural substance that the polyanions mimic, but its high potency (operating in the nanomolar range; 34) indicates a much more specific and directed action than simply acting as a polyanion. Like König's polyanion, it binds to VDAC and induces more complex effects. The importance of the VDAC modulator is indicated by the remarkable degree of conservation of the protein. Not only can it be isolated from the mitochondria of species as diverse as rat, potato, and fungi, but the modulators isolated from each species act on VDAC isolated from any of the species (35).

Micromolar amounts of aluminum hydroxide profoundly reduce the voltage dependence of VDAC (36, 37). Although initial results were consistent with a direct neutralization of the voltage sensor (36), further work (30) indicates that an indirect effect is more likely. The presence of aluminum hydroxide in the compartment on one side of a membrane inhibits channel closure when that side is made negative. Positive potentials on the aluminum side result in VDAC closure, but channel reopening is inhibited. This phenomenon can be explained in terms of an aluminum hydroxide binding site that is translocated across the membrane (30).

VDAC as a Site for Protein Attachment

The images of the freeze-dried VDAC crystals (Figure 2A and B) reveal that VDAC channels do not protrude into the bulk aqueous phase. Indeed, the protein that forms the rim of the pore seems to be at or below the level of the membrane surface (19). This lack of protrusion was also observed in negatively stained membranes (9) and may account for the observation that

VDAC is quite resistant to the action of proteases (9). If VDAC lacks domains extending into the bulk phase, how can proteins like the VDAC modulator (34), hexokinase (38–40), and microtubule associated proteins (41) bind to the channel without obstructing the ion flow?

A number of laboratories have reported strong evidence that hexokinase (38–40) and other kinases (42) bind to mitochondria by attaching to VDAC. Attempts to observe the effects of hexokinase on channel behavior have been unsuccessful (P. S. Mangan and M. Colombini, unpublished results). Thus, it is possible that hexokinase binds but does not affect channel conductance or behavior.

Other binding agents seem to have no effect on channel behavior. Concanavalin A binds to rat liver VDAC in the triton X100-solubilized form (4, 43). Antibodies against *N. crassa* VDAC inhibit VDAC insertion into planar membranes and bind to VDAC crystals in membranes, but do not affect channel behavior (44). These agents may interact with a surface domain on VDAC that does not respond to membrane potentials.

Blachly-Dyson and co-workers mapped out regions of the VDAC protein that form the walls of the pore (16). Many of the protein loops attributed to the surface are rather short. However, there is a much longer region that extends from amino acid 186 to 227 that, based on the fact that amino acid substitutions in this region do not effect channel selectivity (16, 22), is on the surface. This region is a good candidate for a surface domain that proteins might bind to.

Structural evidence for this surface domain may be the elevated regions in the freeze-dried images (Figure 2A and B). Although these regions are likely to contain lipids, protein may also be present. Freeze-fracture images (Figure 6) show elevations in the same location as the elevations seen in the freeze-dried images. One interpretation of the lower resolution freeze-fracture images is that the channels form the depressions between the raised areas. If the raised areas were just lipid, the fracturing process should have removed the top layer of lipid, resulting in a depression. The presence of an elevation may indicate that the lipids are covered by a protein domain that links the six channels into one visible particle and also forms a binding site for proteins. Frozen-hydrated specimens indicate the presence of protein in this region (11) and there is evidence that cytochrome *c* binds to this region (45).

Summary and Conclusion

The VDAC channel has a rather simple structure and yet performs a variety of interesting tasks. The simple cylindrical channel has selectivity, two voltage-gating processes, and a binding site (or sites) for enzymes and modulating proteins. The high degree of conservation of structure and properties indi-

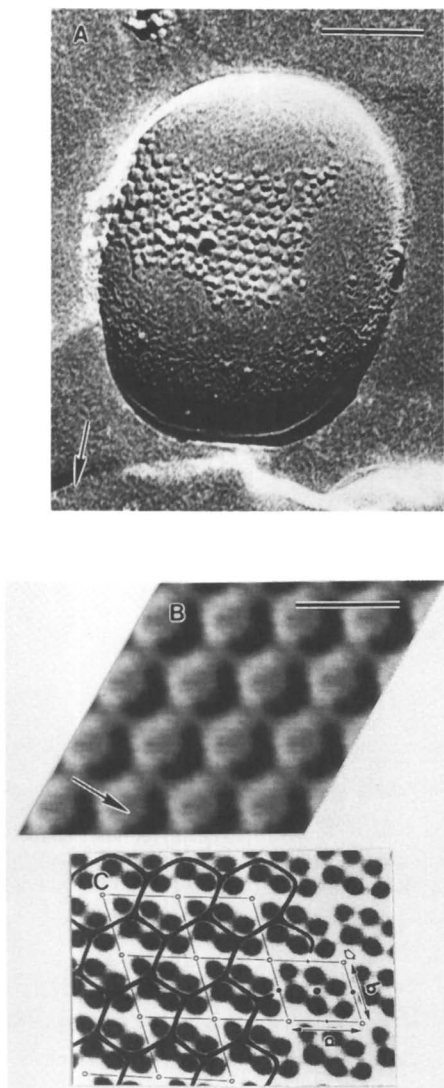


Figure 6. A, Freeze-fracture electron micrograph ($\times 200,000$) of a mitochondrial outer membrane vesicle of *N. crassa*. The micrograph is printed with black shadows. The arrow indicates the direction of shadowing. Bar marker = 100 nm. B, Averaged image of the freeze-fractured array. Defects in the lattice of the array were corrected for by cross-correlation between unit cells and a reference alignment of the unit cells. The arrow indicates the direction of shadowing. Bar marker = 20 nm. This is unpublished data from L. Thomas and M. Colombini. C, Interpretation of the particles viewed in the freeze-fracture image as suggested by Carmen Mannella, who also provided the image. This image is an averaged projected image of a negatively stained crystalline array of channels from *N. crassa*. A dark line drawn around each six-channel unit may correspond to one quasihexagonal particle observed in the freeze-fractured image.

cates the existence of important physical or physiological constraints. An understanding of how this channel works and the physiological roles it serves is likely to be achieved in the near future.

References

1. Werkheiser, W. C.; Bartley, W. *Biochem. J.* **1957**, *66*, 79–91.
2. Colombini, M. *Nature (London)* **1979**, *279*, 643–645.
3. Zalman, L.; Nikaido, S. H.; Kagawa, Y. *J. Biol. Chem.* **1980**, *255*, 1771–1774.
4. Colombini, M. *Ann. N. Y. Acad. Sci.* **1980**, *341*, 552–563.
5. Colombini, M. *J. Membr. Biol.* **1989**, *11*, 103–111.
6. Dihanich, M.; Suda, K.; Schatz, G. *EMBO J.* **1987**, *6*, 723–728.
7. Blachly-Dyson, E.; Peng, S. Z.; Colombini, M.; Forte, M. *J. Bioenerg. Biomembr.* **1989**, *21*, 471–483.
8. Schein, S. J.; Colombini, M.; Finkelstein, A. *J. Membr. Biol.* **1976**, *30*, 99–120.
9. Mannella, C. A. *J. Cell Biol.* **1982**, *94*, 680–687.
10. Mannella, C. A. *Science (Washington, D.C.)* **1984**, *224*, 165–166.
11. Mannella, C. A.; Guo, X.-W.; Cognon, B. *FEBS Lett.* **1989**, *253*, 231–234.
12. Kleene, R.; Pfanner, N.; Pfaller, R.; Link, T. A.; Sebald, W.; Neupert, W.; Tropschug, M. *EMBO J.* **1987**, *6*, 2627–2633.
13. Mihara, K.; Sato, R. *EMBO J.* **1985**, *4*, 769–774.
14. Thinnes, F. P.; Gotz, H.; Kayser, H.; Benz, R.; Schmidt, W. E.; Kratzin, H. D.; Hilschmann, N. *Biol. Chem. Hoppe-Seyler* **1989**, *370*, 1253–1264.
15. Forte, M.; Guy, H. R.; Mannella, C. A. *J. Bioenerg. Biomembr.* **1987**, *19*, 341–350.
16. Blachly-Dyson, E.; Peng, S. Z.; Colombini, M.; Forte, M. *Science (Washington, D.C.)* **1990**, *247*, 1233–1236.
17. Colombini, M.; Peng, S. Z.; Blachly-Dyson, E.; Forte, M. In *Ion Channels*; Rudy, B.; Iverson, L. E., Eds.; Methods in Enzymology 207; Academic: Orlando, FL, 1991; Chapter 29, pp 432–444.
18. Mannella, C. A. *J. Bioenerg. Biomembr.* **1987**, *19*, 329–340.
19. Thomas, L.; Kocsis, E.; Colombini, M.; Erbe, E.; Trus, B. L.; Steven, A. C. *J. Struct. Biol.* **1991**, *106*, 161–171.
20. Peng, S.; Blachly-Dyson, E.; Colombini, M.; Forte, M. *J. Bioenerg. Biomembr.* **1992**, *24*, 27–31.
21. Lindén, M.; Gellerfors, P. *Biochim. Biophys. Acta* **1983**, *736*, 125–129.
22. Peng, S.; Blachly-Dyson, E.; Colombini, M.; Forte, M. *Biophys. J.* **1992**, *62*, 123–135.
23. Teorell, T. *Prog. Biophys.* **1953**, *3*, 305–369.
24. Benz, R.; Wojtczak, L.; Bosch, W.; Brdiczka, D. *FEBS Lett.* **1988**, *231*, 75–80.
25. Benz, R.; Kottke, M.; Brdiczka, D. *Biochim. Biophys. Acta* **1990**, *1022*, 311–318.
26. Liu, M. Y.; Colombini, M. *Biochim. Biophys. Acta* **1992**, *1098*, 255–260.
27. Colombini, M.; Yeung, C. L.; Tung, J.; König, T. *Biochim. Biophys. Acta* **1987**, *905*, 279–286.
28. Mannella, C. A.; Guo, X.-W. *Biophys. J.* **1990**, *57*, 23–31.
29. Zimmerberg, J.; Parsegian, V. A. *Nature (London)* **1986**, *323*, 36–39.
30. Zhang, D.-W.; Colombini, M. *Biochim. Biophys. Acta* **1990**, *1025*, 127–134.
31. Mangan, P. S.; Colombini, M. *Proc. Natl. Acad. Sci. U.S.A.* **1987**, *84*, 4896–4900.

32. Colombini, M.; Holden, M. J.; Mangan, P. S. In *Anion Carriers of Mitochondrial Membranes*; Azzi, A.; Nalecz, K. A.; Nalecz, M. J.; Wojtczak, L., Eds.; Springer: Berlin, Germany, 1989; pp 215–224.
33. König, T.; Kocsis, B.; Meszaros, L.; Nahm, K.; Zoltan, S.; Horvath, I. *Biochim. Biophys. Acta* **1977**, *462*, 380–389.
34. Holden, M. J.; Colombini, M. *FEBS Lett.* **1988**, *241*, 105–109.
35. Liu, M.; Colombini, M. *Am. J. Physiol.* **1990**, *260*, C371–C374.
36. Dill, E. T.; Holden, M. J.; Colombini, M. *J. Membr. Biol.* **1987**, *99*, 187–196.
37. Zhang, D.-W.; Colombini, M. *Biochim. Biophys. Acta* **1989**, *991*, 68–78.
38. Linden, M.; Gellerfors, P.; Nelson, B. D. *FEBS Lett.* **1982**, *141*, 189–192.
39. Fiek, C.; Benz, R.; Roos, N.; Brdiczka, D. *Biochim. Biophys. Acta* **1982**, *688*, 429–440.
40. Nakashima, R. A.; Mangan, P. S.; Colombini, M.; Pedersen, P. L. *Biochemistry* **1986**, *25*, 1015–1021.
41. Lindén, M.; Nelson, B. D.; Leterrier, J.-F. *Biochem. J.* **1989**, *261*, 167–173.
42. Östlund, A. K.; Göhring, U.; Krause, J.; Brdiczka, D. *Biochem. Med.* **1983**, *30*, 231–245.
43. Colombini, M. *J. Membr. Biol.* **1983**, *74*, 115–121.
44. Mannella, C. A.; Colombini, M. *Biochim. Biophys. Acta* **1984**, *774*, 206–214.
45. Mannella, C. A.; Ribeiro, A. J.; Frank, J. *Biophys. J.* **1987**, *51*, 221–226.

RECEIVED for review January 29, 1991. ACCEPTED revised manuscript June 9, 1992.

The Structural Basis of Peptide Channel Formation

Garland R. Marshall and Denise D. Beusen

Center for Molecular Design, Washington University, St. Louis, MO 63130

The increased interest in peptide ion channels as model systems for larger, physiological channels coincides with improvements in experimental techniques that make peptides more accessible and enable the determination of their structures. This chapter surveys peptides from natural sources of less than 50 residues that are known to function as ion channels and for which three-dimensional structural information is available. Although the helix was initially recognized as a structural motif that made insertion of a peptide into the lipid bilayer energetically feasible, this survey suggests it is not unique. While the magainins, the peptaibols, and the cecropins are examples of helical structures, the role of beta-sheet structures is apparent in tachyplestin and the defensins. Other peptides, such as the lantibiotics, are as yet structurally unclassifiable. A number of structural themes emerge from this analysis that help to explain how such small chemical entities can form pores that enable the transit of ions across the lipid bilayer.

THE ABILITY OF PEPTIDES TO FORM CHANNELS (1) in membranes has been an active area of investigation since the seminal observations on alamethicin by Mueller and Rudin (2) in 1968. In recent years, the number of peptides known to act on membranes has increased dramatically. The motivations to study these molecules are diverse and include the development of antibacterial and antiviral agents and the possibility that those peptides that form voltage-gated channels can act as simple model systems for naturally occurring ion channels in nerve membranes (3, 4). The lure of a small, chemically defined system for the study of ion selectivity (5) and the role of the electric field in triggering changes in conduction have been strong. Numerous bio-

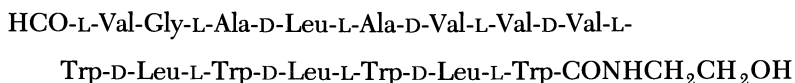
0065-2393/94/0235-0259\$14.48/0
© 1994 American Chemical Society

physical techniques have been exploited to probe the channel-forming activity of peptides. Although significant progress has been made in understanding the details of some systems, in no case has a general mechanism evolved to explain all the observations. The perspectives of these studies have been many and varied: characterization of the peptide-membrane interaction, the effect of the peptide on the lipid phase, and elucidation of the structures of the peptides involved in ion channel formation. Because a comprehensive survey of all of these efforts for every known peptide ion channel would be enormous and because interactions of peptides with membranes have been reviewed previously (6, 7), we have focused our efforts on the structural aspects of channel-forming peptides that consist of 50 residues or less. The synergy between the molecular architecture (8) of pore-forming peptides (9) and mechanistic theory has heightened in recent years as structure-determination techniques and access to peptides have improved. Information attainable includes the three-dimensional structure of peptides, both in solution and bound to the membrane, orientation of peptides in membranes in the open or closed state of the channel, degree of aggregation in solution or in the membrane, and the aggregation number and tertiary structure of the aggregate. Although the amphipathic helix (Figure 1) (10) is a recurring motif in many of the peptides that show pore formation, it is by no means unique. An examination of the structural data on the wide variety of peptides that form ion channels in membranes reveals other themes, many of which are sufficiently new that their real significance is to provide fertile ground for future investigation.

Peptide Antibiotics

Numerous examples exist in which compounds isolated as antibiotics form channels in lipid bilayers (7). Certainly, the most highly refined channel structure is that of gramicidin A, and many of the experimental paradigms used to elucidate its structure and function are being applied to other systems.

Gramicidin A. Gramicidin A is a hydrophobic, linear peptide of 15 residues arranged in alternating chirality (11, 12) and toxic to Gram-positive bacteria. Produced by *Bacillus brevis* (13), the biological function of gramicidin A in transcriptional regulation (14, 15) appears to be unrelated to its most interesting biophysical activity: It acts as a channel for monovalent cations in lipid membranes (16, 17). An impressive arsenal of chemical and



Gramicidin A

biophysical techniques has been directed to the study of gramicidin A over the last 20 years, and the resulting literature is covered in several review articles (18–21).

Initial structural models of the gramicidin channel (22, 23) based on experimental results that implicated a dimer (24, 25) have persisted (Figure 2). These models consist of helical dimers (Figure 2A and B) and double-stranded helices (Figure 2C and D), all of which are helically wound beta-sheet structures in which the peptide dipoles alternate in orientation and result in no net dipole. The absence of a net dipole and any charged amino acids may explain the lack of voltage dependence in gramicidin. Qualitatively, the two classes of structural models are similar in pore size and length. Both classes have side chains oriented to the lipid and polar carbonyl groups lining the central pore that presumably act to solvate the ion.

The helical dimers characterized by Urry et al. (22) consist of single-stranded helices stacked end-to-end (Figure 2A and B). Of the theoretically possible forms, the $\beta^{6.3}$ dimer best fits expectations of length (25–30 Å) and pore size (4 Å) needed for channel activity and ion selectivity. The head-to-head dimer (Figure 2A) is currently favored as the active form based on NMR (26) and other biophysical techniques as well as the activity of cross-linked dimer analogues (22, 27). Recent solid-state NMR studies (28) are consistent with a right-handed helical dimer, a conformation also seen in sodium dodecyl sulfate micelles (29). Ion-binding sites of gramicidin incorporated into phospholipids have been characterized by ^{13}C NMR and are located at residues 11–14 (30–32), approximately 20 Å apart.

The double-stranded helical (Figure 2C and D) models of gramicidin were proposed by Veatch et al. (23) to explain the presence of four interconverting conformations in dioxane. These structures are unlikely to be the conducting species, but they have been difficult to dismiss because of their frequent occurrence in organic solvents. Many of the possible conformational perturbations due to chain orientation (parallel vs. antiparallel), residues per turn, helical handedness, and chain stagger have been observed in solution (for a recent review, *see* reference 21). X-ray analyses of gramicidin A crystallized from ethanol (33, 34) (Figure 3) and from methanol–CsCl (35) reveal structures of this class. The observation of potential ion-binding sites in the first case and the actual presence of Cs ions in the pore in the second study suggest that these types of structures are capable of ion binding and raise additional questions about their biological significance.

Several studies suggest that the conformation (double-stranded helix or helical monomer) of gramicidin inserted into the membrane is that found in solution (36–39). Upon heating, the membrane-bound, antiparallel, double-stranded helix converts to a helical dimer (37). Subsequent studies have suggested that the initially inserted double-stranded helical forms are unlikely to have any conductance capabilities (40).

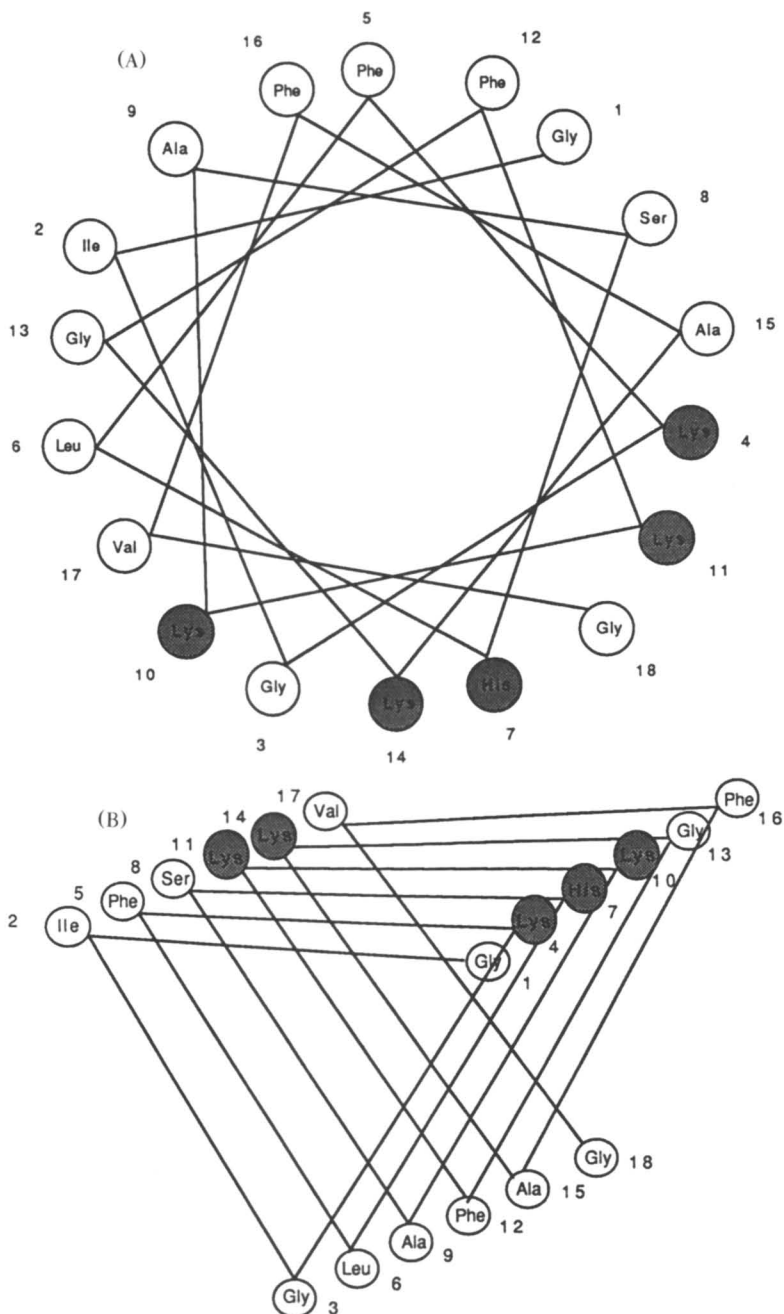


Figure 1. Amphipathic helices cluster hydrophilic residues on one face, which results in a cylinder that has one hydrophobic and one hydrophilic surface. The first 18 amino acid residues of magainin II are arranged on an α -helical wheel diagram (A) and 3_{10} -helical wheel diagram (B).

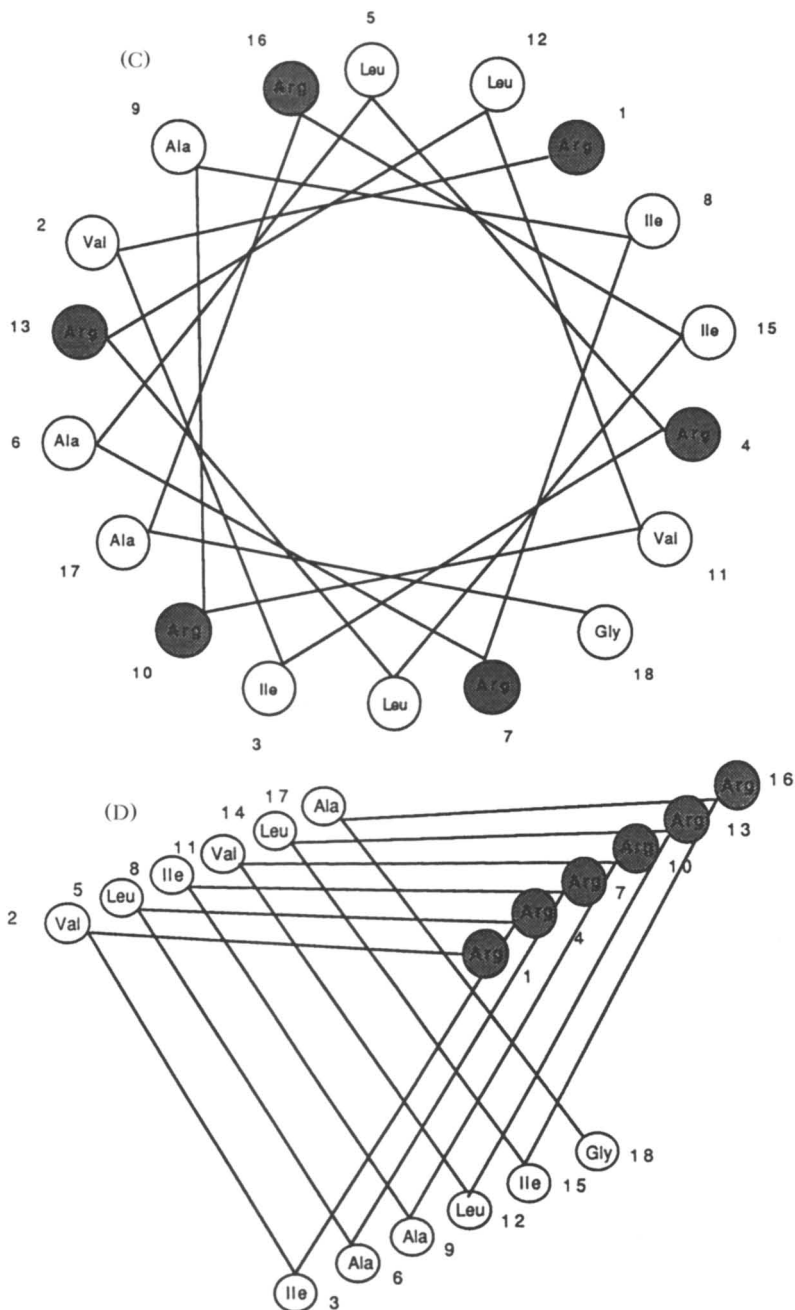


Figure 1.—Continued. In the α -helical conformation, the amphipathicity is evident. In an even more striking comparison, the first 18 residues of the S4 segment of the sodium ion channel are plotted in the same two ways (C and D). Here the 3_{10} -helical conformation (D) clearly segregates the positively charged Arg residues on the same face, whereas an α -helical conformation (C) results in a uniform arrangement of the charged residues.

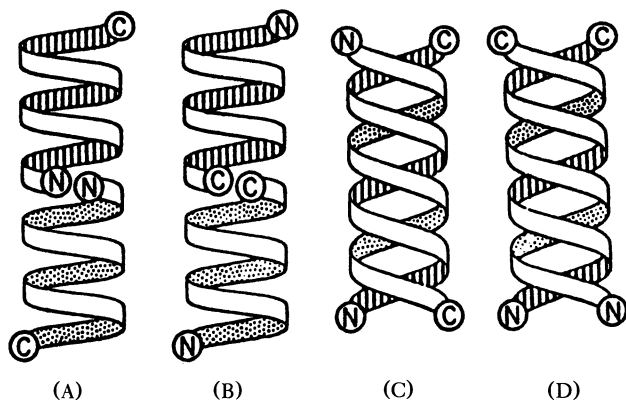


Figure 2. Schematic models of gramicidin A dimers: (A) head-to-head helical dimer; (B) tail-to-tail helical dimer; (C) antiparallel double-stranded helix; (D) parallel double-stranded helix. (Reproduced with permission from reference 301. Copyright 1986 Biophysical Society.)

Peptaibols. Alamethicin is the best known member of the class of fungal antibiotics known as peptaibols (Table I). The name arises from shared structural features: the presence of several α -methylalanine (MeA) or aminoisobutyric acid (Aib) residues and a C-terminal amino acid alcohol such as phenylalaninol (Phol). The voltage-dependent conductance of peptaibols in black lipid membranes was first demonstrated by Mueller and Rudin (2), who suggested that alamethicin provided a site that bridged the bilayer through self-aggregation. A wide variety of naturally occurring variants and analogues of the peptaibol antibiotics exhibit voltage dependence and form single-channel, multilevel conductance states in planar lipid bilayers (Figure 4) (41). These are attributed to differing numbers of helical monomers that aggregate to form the pore (42). A recent study suggests that rather than increase the pore (or "barrel") size by increasing the number of monomers (or "staves"), these conductance states represent clusters of "pipes" in which differing numbers of pipes with different diameters are present (43). Strong aggregation of alamethicin in the lipid bilayer is observed spectroscopically above a critical concentration, and the onset of pores can be characterized by a critical voltage. Modulation of these two parameters by the addition of NaCl to the medium or cholesterol to the bilayer are highly correlated, which suggests that voltage dependence is due to the electric field effect on the partition between the aqueous and membrane phases (44). Ion channels have been observed and characterized for alamethicin (2, 41), emerimicin (I. Vodyanoy, personal communication), paracelsin (45), trichorzianin (46), and the zervamicins (47).

Other neutral peptide sequences in addition to peptaibols are capable of voltage-dependent conductance changes in lipid bilayers. Molle et al. (56)

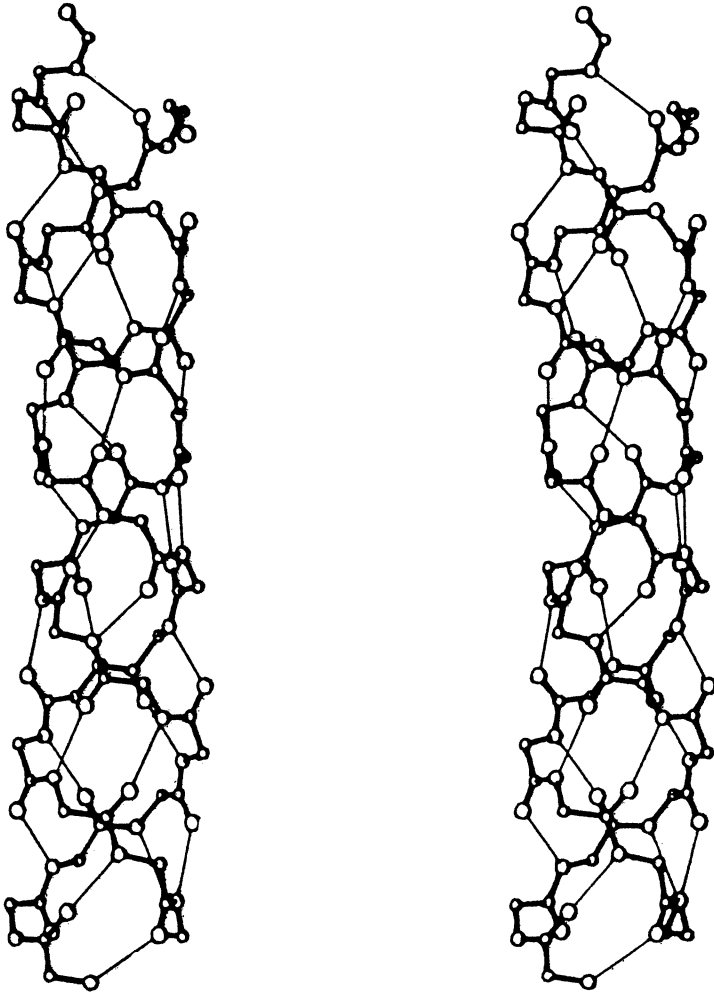


Figure 3. Stereoview (backbone atoms only) of the gramicidin A antiparallel double-stranded $\beta^{5,6}$ -helix crystallized from ethanol. Narrow lines indicate hydrogen bonds. (Reproduced with permission from reference 33. Copyright 1988 AAAS.)

showed that an analogue of alamethicin in which all MeA residues were replaced by Leu and C-terminal Pheol was replaced by Phe-NH₂ retained its conductance properties, but with a higher threshold voltage and with mean open lifetimes 5–10 times smaller. Peptides such as oligoAla that have sufficient length (15–20 residues depending on composition) and are composed of normal amino acids also show channel formation in lipid bilayers (57). One advantage of peptaibol study, however, relates to the structural

Table I. Amino Acid Sequences of Several Peptaibols

<i>Peptaibol</i>	<i>Sequence</i>
Alamethicin (48)	Ac-MeA-Pro-MeA-Ala-MeA-Ala-Gln-MeA-Val-MeA ¹⁰ -Cly-Leu-MeA-Pro-Val-MeA ¹⁵ -MeA-MeA-Glu-Gln-Phol ²⁰
Trichotoxin A-40 (49)	Ac-MeA-Gly-MeA-Leu-MeA-Gln-MeA-MeA-Ala-MeA-Pro-Leu-MeA-(R)Eta-Gln-Valol ¹⁵
Emerimicin IV (50)	Ac-Phe-MeA-MeA-MeA-Val-Gly-Leu-MeA-MeA-Hyp-Gln-(R)Eta-Hyp-MeA-Phol ¹⁵
Antiamoebin I (51)	Ac-Phe-MeA-MeA-MeA-(R)Eta-Gly-Leu-MeA-MeA-Hyp-Gln-(R)Eta-Hyp-MeA-Pro-Phol ¹⁵
[Leu ¹]Zervamicin (52)	Ac-Leu-Ile-Gln-Iva-Ile-Thr-MeA-Leu-MeA-Hyp-Gln-MeA-Hyp-MeA-Pro-Phol ¹⁵
Paracelsin A (49)	Ac-MeA-Ala-MeA-Ala-MeA-Ala-Gln-MeA-Val-MeA-Gly-MeA-MeA-Pro-Val-MeA-MeA-Gln-Gln-Phol ²⁰
Suzukacillin A (53, 54)	Ac-MeA-Ala-MeA-Ala-MeA-(Ala) ⁵ -Cln-MeA-(MeA) ¹⁰ -Leu ¹⁰ -MeA ¹⁵ -Cly-Leu-MeA-Pro-Val-MeA-(MeA) ²⁰ -Gln-Gln-Phol
Trichorzianine IIIc (55)	Ac-MeA-Ala-Ala-MeA-MeA-Gln-MeA-MeA-MeA-Ser-Leu-MeA-Pro-Val-MeA-Ile-Gln-Gln-Trpol ¹⁵

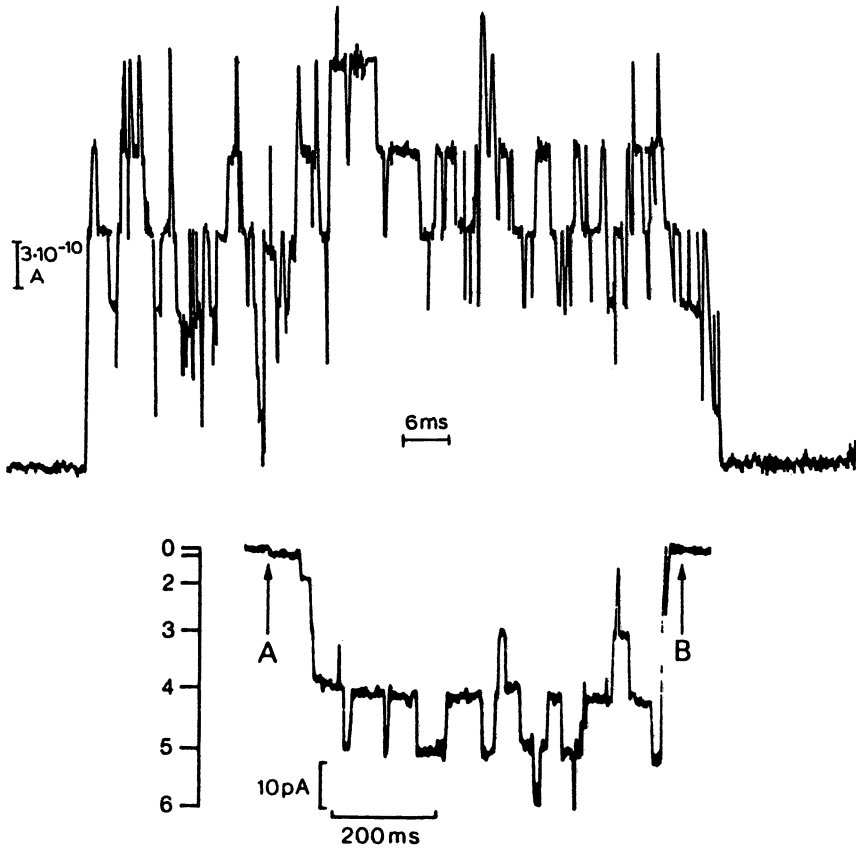


Figure 4. Multistate conductance shown by alamethicin on a planar bilayer membrane with applied potential of 210 mV (top) and on frog sarcolemmal membrane with -110 -mV resting potential (bottom). Current bursts begin at A and continue until B. The different levels observed are not integral multiples of unit current conductance, which implies different states of the pore. (Upper figure reproduced with permission from reference 41. Copyright 1972 Elsevier. Lower figure reproduced with permission from reference 302. Copyright 1979 Macmillan Magazines.)

roles of the unusual amino acids that characterize their sequences. The conformational constraints imposed by the α,α -dialkyl amino acids, such as MeA (Aib) and α -ethylalanine (EtA or Iva), dramatically limit the conformations that must be considered in any mechanism. α,α -Dialkyl amino acids have been shown theoretically by Marshall and Bosshard (58) and later by others (59–62) to favor Φ , Ψ torsional values associated with either 3_{10} - or α -helix (Figure 5). The large number of crystal structures for peptides that contain MeA (63–65) confirm the propensity of this residue to direct the

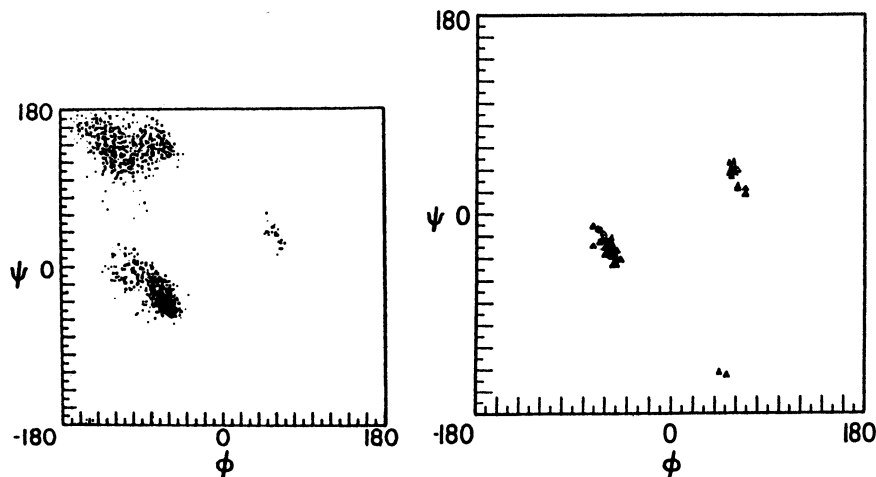


Figure 5. Experimentally observed values for torsional angles Φ and Ψ observed for alaninyl-type residues (left) and α -methylalanine in high-resolution crystal structures (right). (Reproduced with permission from reference 64. Copyright 1987 Wiley-Liss.)

conformation to be helical: either the α -helix, the 3_{10} -helix, or some combination of the two is seen predominantly. In the case of Aib (MeA) oligomers, Bavoso et al. (66) suggested that the 3_{10} -helix is preferred. Karle et al. (67) suggested that the 3_{10} -helix is promoted by MeA in short peptides or in longer peptides (> 7 residues) if MeA comprises 50% or more of the peptide, but the α -helix is preferred when the MeA residues comprise one-third of the longer peptides. Comparison of the crystal structure of emerimicin 2-9, which is a 3_{10} -helix (68), with that of emerimicin 1-9, which is an α -helix (69), suggests instead that the energy difference between the two forms is small and selection of a conformer is dependent on environmental factors. A qualitative explanation of the balance of forces that determine α - or 3_{10} -helix preference has been presented (69), and Zimm-Bragg theory has been modified to explain the composition and sequence dependence of helix preference (70, 71). Although the difference between α - and 3_{10} -helices stabilized by the multiple MeA residues is minimal in terms of torsional angles (Φ , Ψ), the consequences in terms of relative side-chain position and helix length are dramatic. A comparison of the characteristic parameters for the two helix types is given in Table II and shown in Figure 6. Recent investigation of the relative stabilities of these two helical forms for MeA and Ala oligomers has refined our understanding of the forces that determine their occurrence under a given set of experimental conditions (72, 73). Furthermore, molecular dynamics simulations have been used to construct an energy surface for the transition between the two helical forms and to

Table II. Comparison of Properties of α -Helix with 3_{10} -Helix

Property	α -Helix	3_{10} -Helix
Residues per turn	3.6	3.0
Atoms in H-bonding ring	13	10
Rise per residue (Å)	1.5	2.0
Number of H bonds for N residues	N-4	N-3
Average torsional angles ($^{\circ}$)		
Φ	-55	-50
Ψ	-52	-31

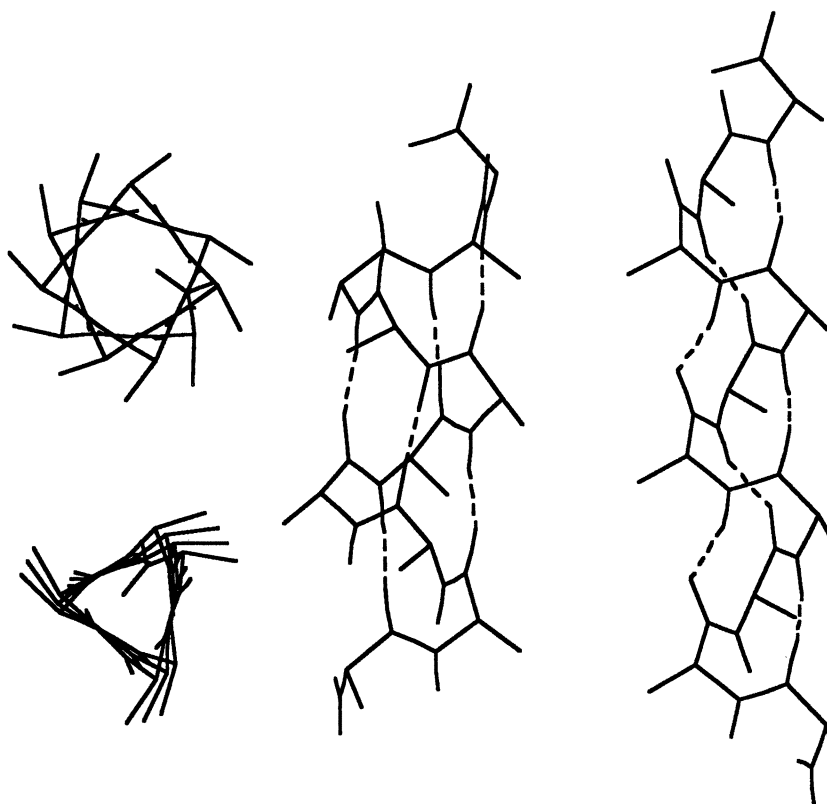


Figure 6. Comparison of structures for the α -helix (upper left and middle) and 3_{10} -helix (lower left and far right). The increased length of the 3_{10} -helix for the same number of residues is evident, as is the difference in hydrogen-bonding pattern: $1 \leftarrow 4$ for the 3_{10} -helix $1 \leftarrow 5$ for the α -helix. The side chains of the 3_{10} -helix pack in an eclipsed fashion, whereas the side chains of the α -helix are staggered.

estimate a free energy of activation (74). These calculations indicate that mechanisms involving transitions between the two helical forms, either upon insertion into the membrane or during voltage gating, are feasible. This facile transition may explain transmembrane signaling (75) in the case of the insulin receptor whose ligand-binding domain is extracellular with a single transmembrane helix connected to the intracellular tyrosine kinase. Simple modification of the hydrogen-bonding network at the extracellular terminus of the transmembrane helix by ligand occupancy could trigger the helix transition, resulting in displacement of the tyrosine kinase relative to the membrane and the subsequent activation of the enzyme.

Several proposed models of the alamethicin pore differ primarily in the role of aggregation, conformational change, and reorientation within the membrane as elements of the switch controlling the transition between closed and open states. None of the models satisfactorily explains the plethora of biophysical measurements reported, which may simply reflect a variety of mechanisms that depend on the peptaibol and the membrane system under study. Models proposed by Boheim (42), Baumann and Mueller (76), Fox and Richards (77), and Hall et al. (78) involve insertion of the peptide into the membrane as part of the gating mechanism. In the first two cases, alamethicin is monomeric and lies on the surface of the membrane in the absence of an electric field, but with an applied field, the alamethicin inserts and subsequently aggregates to form the open pore. Experimentally, the association of alamethicin with lipid bilayers depends on the conditions of the study. Vogel (79) has shown that alamethicin orients in an aggregated state with the helix axis parallel to the membrane normal, but it can associate with the helix axis aligned with the plane of the membrane under different experimental conditions. Wille et al. (80) concluded that spin-labeled analogues of alamethicin are bound to the membrane essentially in the monomeric state and that a transmembrane potential caused a change in the conformation of the peptide as well as a deeper insertion of the α -helix into the membrane.

The mechanism of Fox and Richards (Figure 7) is based on the crystal structure of alamethicin (77), which shows the molecule to be primarily α -helical with a bend in the helical axis at Gly¹¹-Leu¹²-MeA¹³-Pro¹⁴. This model suggests that only the N-terminus of the aggregated peptide is inserted into the membrane while the C-terminal helical residues lie on the membrane surface. Under the influence of an electric field, the ensemble inserts further to span the membrane and create the open channel. This conformational change is driven by the alignment of the dipole for each helical segment with the applied field (77). The model of Hall et al. (78), which is similar but invokes a parallel beta-sheet structure for residues 15–20, was based on the methanol NMR data of Banerjee and Chan (81). A similar structural and mechanistic model for anti-amoebein (82) resulted from a semiempirical energy analysis of minimum energy conformers. Each of these

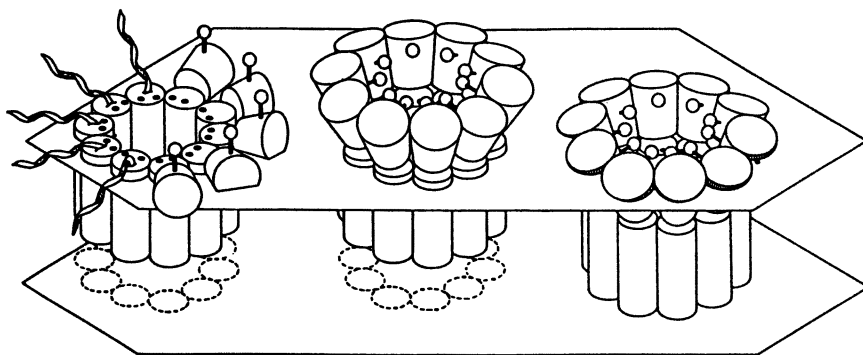


Figure 7. Voltage-gating channel model of alamethicin proposed by Fox and Richards (77). On the left is the structure for the helical bundle partially inserted in the absence of an applied voltage. The C-terminal residues are shown as helical ribbons that indicate extended random coil structures, or as cork-shaped α -helical structures partially buried on the surface of the membrane. The middle structure is an intermediate produced by application of voltage, and the right panel represents the open state that traverses the membrane. (Reproduced with permission from reference 77. Copyright 1982 Macmillan Magazines.)

mechanisms depends on defects in secondary structure regularity—either a change from helix to sheet or a helix kink induced by proline. Solution NMR studies in methanol and dimethyl sulfoxide (DMSO) (83, 84) indicate agreement between the solution and solid-state conformation, but because the NMR data were not used to generate a three-dimensional model, it is difficult to assess how well the solution structure of alamethicin is defined. Molecular dynamics simulations of alamethicin in vacuo (85) suggest a fairly rigid N-terminal helix (residues 1–9), a flexible hinge region, and a very flexible C-terminus (residues 12–20). These results are consistent with a recent NMR study in methanol, although the NMR data were not sufficient to exclude other interpretations (86). A model-free analysis of ^{13}C spin-lattice relaxation rates at two field strengths (87) suggests that alamethicin is a rigid molecule, which is consistent with a gating mechanism that involves reorientation of the entire helix (discussed later) and not a segmental motion (42, 76).

An alternate mechanism could be envisioned (Figure 8) for the peptaibols and other neutral hydrophobic helical bundles in which estimates of charge movement across membranes (78) are linked to voltage-dependent opening of the channel via movement of a segment of the helix dipole in response to the electric field. Most peptaibols have a Gly-Leu hinge region followed by a $(\text{MeA})_n\text{-Pro}$ sequence where $n = 1$ or 2. This would be compatible with a bent helix–turn–helix motif, similar to that seen in DNA-binding proteins (88) and suggested to be important for spontaneous

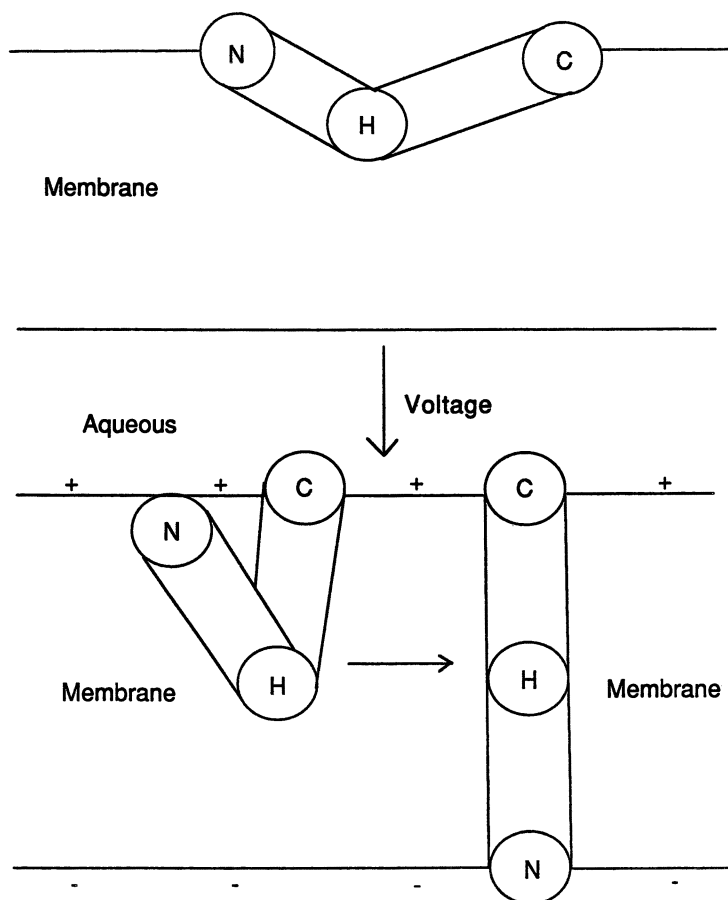


Figure 8. Schematic of the alamethicin mechanism in which the hinge region, H, provides a flexible linkage to allow alamethicin N-terminal (N) and C-terminal (C) helical segments to optimize their solvent and dipole interactions with the membrane in the presence and absence of a transmembrane potential. In the absence of a potential, helical segments could bury an optimal amount of hydrophobic surface in the bilayer while maintaining contact of the hydrophilic helix termini with the aqueous layer. A transmembrane potential could align helix dipoles with the field and facilitate movement of hydrophilic helix termini through the membrane. It is probable that a concerted mechanism of several aggregated alamethicin molecules that undergo simultaneous transitions could reduce the transition barrier.

insertion of proteins into membranes (89). The turn region of the peptide would be buried in the hydrophobic core of the membrane with the hydrophilic helix termini exposed to solvent, allowing aggregation of the monomer in bent rafts of peptides that are half-buried in the membrane. Any hydrophilic side chains would be exposed to solvent or, by virtue of in-

tramolecular interactions, be cryptic as far as the solvent is concerned. Exposure to the aqueous medium of the terminal amide and carbonyl hydrogen-bonding groups, which are not satisfied by intramolecular hydrogen bonds, should be energetically favorable (90). The voltage-dependent step would be the reorientation of the helix by elimination of the turn and extension across the membrane with the helix ends on opposite sides of the membrane. In effect, the response of the helix dipole to the applied field provides a driving force for the movement of a segment of the peptide and results in reorganization into a helical rod. In the process of aligning all the helical dipoles with the transmembrane field, the cluster would open like an umbrella, which would pull the hydrophilic surfaces apart and suck a tube of water into the channel that is formed. Recent studies (91, 92) in which a proline was introduced into a model helical peptide are supportive of this model in that the small deformation due to the proline insertion is associated with a defined pore that has a small voltage dependence.

Conformational switches of a different type arise from the X-ray structure of [Leu¹]zervamicin (93). This molecule is a sharply bent amphipathic helix with a kink angle of 30–45°, which depends on the crystal form. The solution NMR structure of emerimicin IV (94), another peptaibol that possesses the Hyp-Xxx-Xxx-Hyp motif, also shows a sharp bend in the helix and shares many features with the [Leu¹]zervamicin structure. In the crystal, [Leu¹]zervamicin aggregates with its polar faces packed together to form an hourglass-shaped channel. The side chain of Glu¹¹ is folded such that it blocks the opening, but extension of the side chain could allow the transit of cations. An alternative gating mechanism relies on flexibility induced by proline (95). Proline and hydroxyproline effectively increase the local helix pitch, which enables this short peptide (16 residues) to span the lipid bilayer. A constricted, hourglass-shaped pore formed by an aggregate of bent helices could open by twisting and bending of the helices.

Rigid reorientation of helices within the lipid bilayer in response to an electrical potential forms the basis of models proposed by Boheim et al. (96) and Mathew and Balaram (97). In the flip-flop gating mechanism (96), an aggregate of antiparallel helix rods is formed in the membrane (Figure 9). Application of the transmembrane potential is postulated to induce the rods to reorient (flip-flop) so that they become parallel and all of their helix dipoles are aligned with the electric field. The resultant dipolar repulsion between parallel monomers is reduced by an interior of higher dielectric (i.e., water). Although this idea is appealing for neutral peptaibols, the behavior of analogues of alamethicin prepared by Hall et al. (98) casts serious doubt on this mechanism. If alamethicin is added to one side of a lipid bilayer such as bacterial phosphatidylethanolamine, which does not allow alamethicin to cross the membrane readily, an asymmetric current–voltage curve usually is seen (Figure 10A). In alamethicin itself, this asymmetry is thought to be due to the ionic charge on the free carboxylate that anchors the C-terminus on

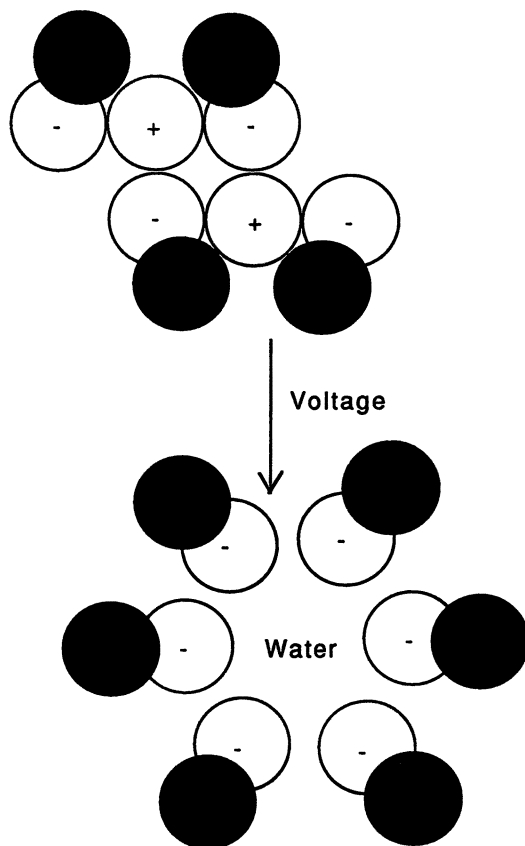


Figure 9. Adaptation of the schematic diagram of the dipole flip-flop gating mechanism of Boheim et al. (96). The perspective is from one side of the membrane looking at the ends of oriented α -helix dipoles. Closed circles represent the C-terminal nonhelical portion of alamethicin. Open circles with a + sign indicate the N-terminal helical portion of the peptide, and circles with a - sign are the C-terminal ends of the helix. At the top, two N-terminally oriented helices are aggregated in antiparallel alignment with four C-terminally oriented helices prior to gating. Upon application of a transmembrane potential, the two N-terminally oriented helices flip-flop to reorient in parallel fashion, and the realignment of dipoles results in monomer repulsion and opening of the channel.

one side of the membrane and prevents positive gating, because esterification of the carboxyl group gives symmetric curves (Figure 10B). An analogue with only a free amino group showed voltage-current curves of opposite asymmetry (only positive gating), which implied that the charged N-terminus remained on the side of the membrane to which it was added (Figure 10C). The channel properties were otherwise very similar to alamethicin itself. It is hard to reconcile the flip-flop model of pore formation with the observation

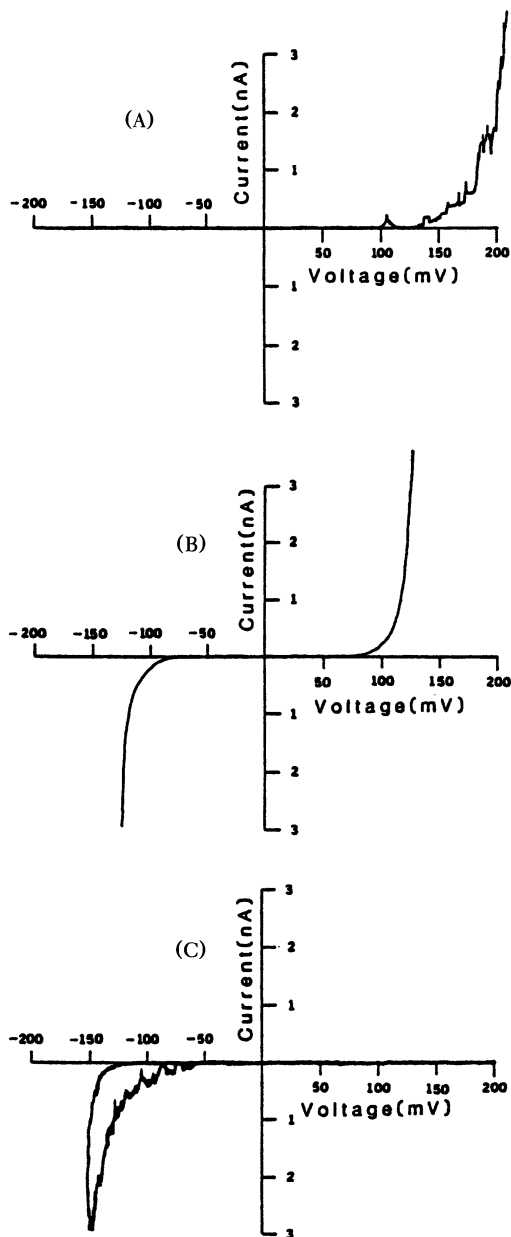
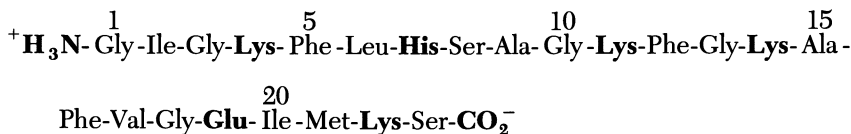


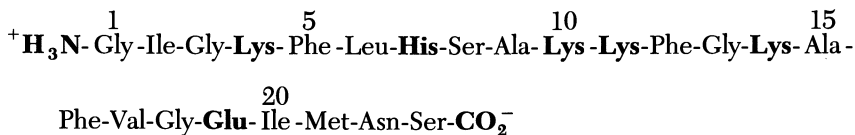
Figure 10. Current-voltage curves induced by alamethicin and analogues with different charged groups added to the *cis* side of membrane (bacterial phosphatidylethanolamine-squalene in 1 M KCl; pH 5.5; room temperature). (A) Major component of natural alamethicin (free carboxyl group at Glu¹⁸); (B) Boc-[des-Ac-MeA¹, Glu(OBzl)¹⁸]-alamethicin (no charged groups); (C) [des-Ac-MeA¹, Glu(OBzl)¹⁸]-alamethicin (free N-terminal amino group). (Reproduced with permission from reference 98. Copyright 1984 Biophysical Society).

of asymmetric current-voltage curves and the behavior of synthetic pores based on alamethicin. Similar arguments (1) have been used with charged gramicidin A analogues to support the head-to-head dimer model. The alamethicin model of Mathew and Balaram (97) is also based on an aggregate of antiparallel helical rods, but the gating mechanism is the removal of a central helical monomer with subsequent replacement by water to form the channel (Figure 11). Mechanisms of gating that do not require segmental motion of alamethicin are consistent with the foregoing solution NMR results, although circular dichroism studies of alamethicin (99) in phospholipid vesicles suggest that translation directly from solution structure to bilayers is not justified.

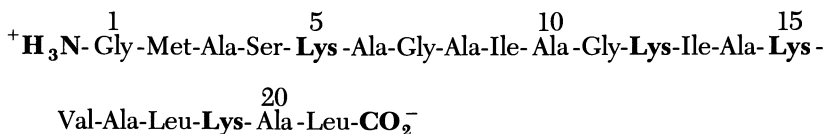
Magainins. Based on the resistance to infection shown by the African clawed frog, *Xenopus laevis*, these peptides were initially isolated from frog skin (102, 103). The magainins dissipate membrane potentials (104), and the bactericidal activity of all-D-magainin-2 (105, 106) is consistent with intrinsic peptide activity, which does not require interaction with a chiral receptor. Magainin 1 and 2 form voltage-dependent channels in lipid bilayers (107, 108), and the effects of magainin 1 on lipid bilayers (107) have been compared to those of alamethicin. A weakly voltage-dependent, anion-selective conductance was observed with large concentrations of magainin under high voltage. In contrast with the multistate behavior of alamethicin, separate single-channel experiments showed two main levels. Circular dichroic (CD)



Magainin I (100)



Magainin II (100)



pGLa (101)

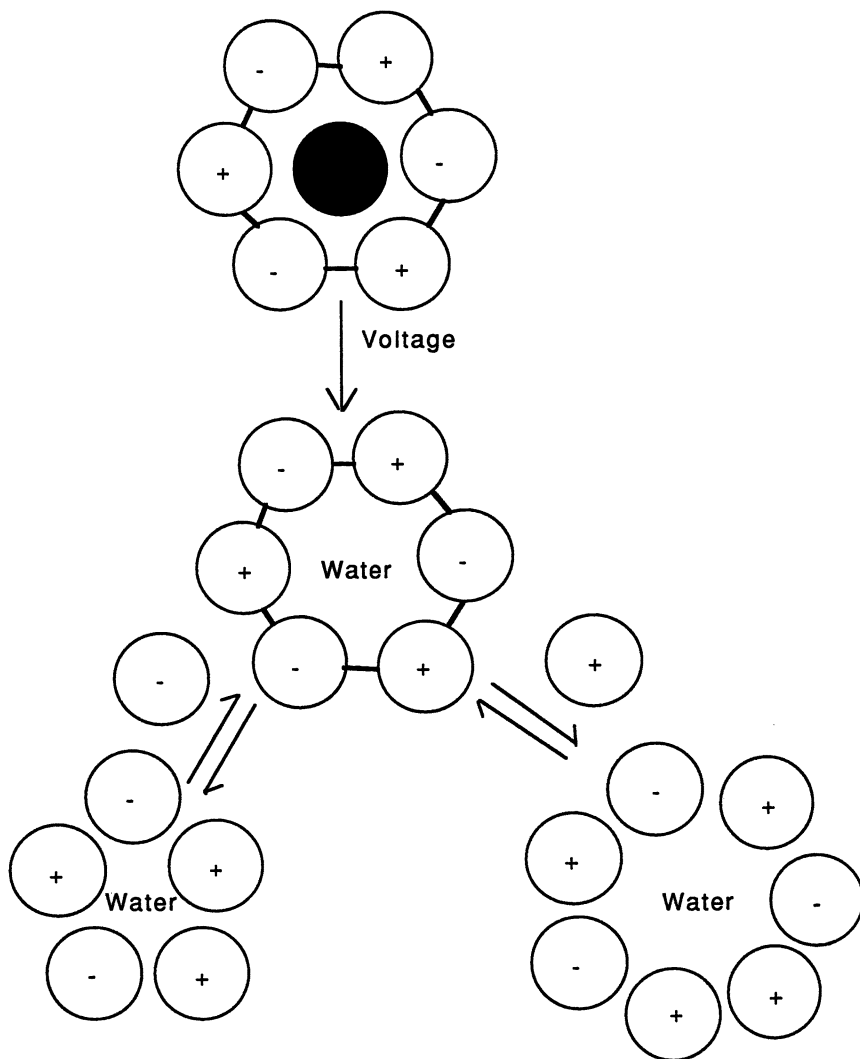
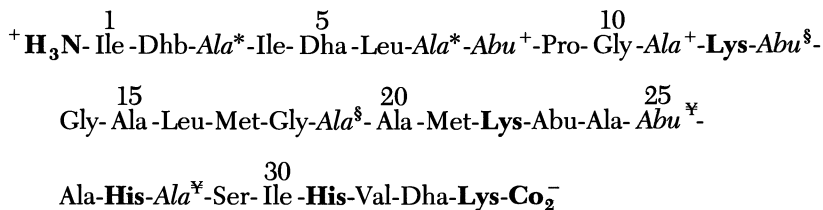


Figure 11. Adaptation of the schematic diagram of the alamethicin helix dipole model of Mathew and Balaram (97). A top view of the alamethicin aggregate is shown. The + and - signify opposite orientation of helix dipoles in the lipid bilayer. Bars that connect helices represent hydrogen bonding of polar side chains. The central core helix (shown as a filled circle) is not hydrogen-bonded to the aggregate and is ejected in response to an applied voltage to form the open channel. Conductance of the channels is modulated by changes in aggregation number.

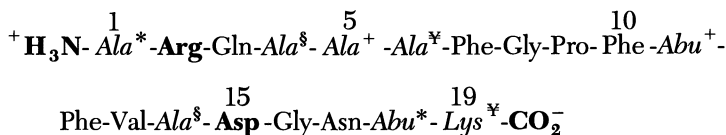
spectra in liposomes suggested a smaller relative proportion of the α -helical conformation for magainin 1 than for alamethicin, however. The conformation of magainin 2 in water is random, but an amphipathic helix is induced throughout the sequence as trifluoroethanol is added (109). Raman (110) and Fourier transform infrared spectroscopy (111) results are consistent with formation of an α -helix upon binding to liposomes, as long as the lipids are negatively charged. Other studies concur that the binding of magainin to membranes is primarily electrostatic (112) and the formation of the helix is dependent on the presence of a negative lipid surface (113). Analogues in which individual N-terminal amino acids are deleted lack antibacterial activity (114), which is consistent with a disruption of periodicity in the charge and an expected reduction in helical content. Solid-state NMR of oriented bilayers reveals that magainin associates with the lipid bilayer in an orientation parallel to its surface (115). Numerous analogues of magainin have been characterized with respect to microbial and membrane-perturbing activities (116) as a result of the search for compounds with more desirable therapeutic properties (e.g., lysis of tumor cells (117) and spermicides (118)). Several other sequences from frog skin such as pGLa have been characterized and found to have similar properties (101).

Lantibiotics. The class of antibiotics that contains the food preservative nisin (119) is generically termed lantibiotic (122, 123) because of the presence of the cross-linking dimeric amino acid lanthionine. In addition to the pentacyclic 34-residue nisin, this class of highly cross-linked peptides includes subtilin (124), epidermin (125), gallidermin (122), actagardine (126), duramycin-leucopeptin (127), Ro 09-0198, cinnamycin lanthiopeptin (128, 129), and Pep 5 (130), among others (131). Sahl et al. (132) showed that nisin forms voltage-dependent, transient, multistate pores in lipid bilayers similar to those seen with melittin. Further studies (133) of nisin, Pep 5, and subtilin (all of which form ion channels) suggest that the peptides do not span the bilayer of liposomes in the absence of a membrane potential. A threshold potential of -90 mV was essential for subtilin to lyse cells. This requirement is similar to observations in activity studies on planar bilayers (134). The symmetric current-voltage curve may reflect the symmetric distribution of charge. Multistate pores with lifetimes of several hundred milliseconds and conductances that correspond to pore diameters of 1.2, 1.9, and 2.2 nm were found. For Pep 5, a threshold voltage of -90 mV was required in lipid bilayers for the induction of multilevel, voltage-dependent pores (135). Ancovenin (136, 137), a smaller peptide that has only three thioether rings, was isolated from a culture broth of *Streptomyces* on the basis of its ability to inhibit angiotensin-converting enzyme. Another lantibiotic, lanthiopeptin (120), shows antiviral activity and structural similarity to ancovenin. Lanthiopeptin is thought to be identical to Ro 09-0198 (138), which is an immune stimulator. No data on the ability of ancovenin or



Nisin (119)

where residues 3* and 7* are connected by a side-chain thioether bridge (lanthionine); residues 8⁺ and 11⁺, 13[§] and 19[§], and 25^X and 28^X are each connected by a different thioether bridge (3-methylanthionine); Dha is dehydroalanine; and Dhb is dehydrobutyrine.



Ro 09-0198, cinnamycin, lanthiopeptin (120, 121)

where residues 1* and 18* and 5⁺ and 11⁺ are 3-methylanthionine bridges, residues 4[§] and 14[§] form a lanthionine bridge, and the side chains of residues 6^X and 19^X are linked by an aza-ether.

lanthiopeptin to form ion channels has been presented. Ro 09-0198 interacts specifically with phosphatidylethanolamine (139, 140), forms a specific complex with lysophosphatidylcholine, and enhances permeability in vesicles. Duramycin, which differs from cinnamycin by only a Lys for Arg exchange at position 2, forms ion channels in lipid bilayers (141).

NMR determination of the conformation of nisin (142–144) and subtilin (145) in DMSO or water suggests high flexibility and no dominant single conformation. In general, the only identifiable structural elements are in the cycles formed by the lanthionine bridges, many of which do not contain regular elements of beta-turns. An extended, screwlike model of gallidermin (146) based on NMR data in 95% trifluoroethanol seems unlikely to span the membrane either as a monomer or as part of an aggregate. The larger cycles in Ro 09-0198 are undoubtedly responsible for its compact shape (121) in which hydrophobic and hydrophilic side chains are segregated (Figure 12).

Immune Peptides. In response to microbial infection, mammalian macrophages and neutrophils release peptides that lead to oxygen-independent death of the invading organism. In recent years, the capability of other species to mount a similar defense has become apparent. The known immune peptides now include defensins, cecropins, dipterocins (147), attacins (148),

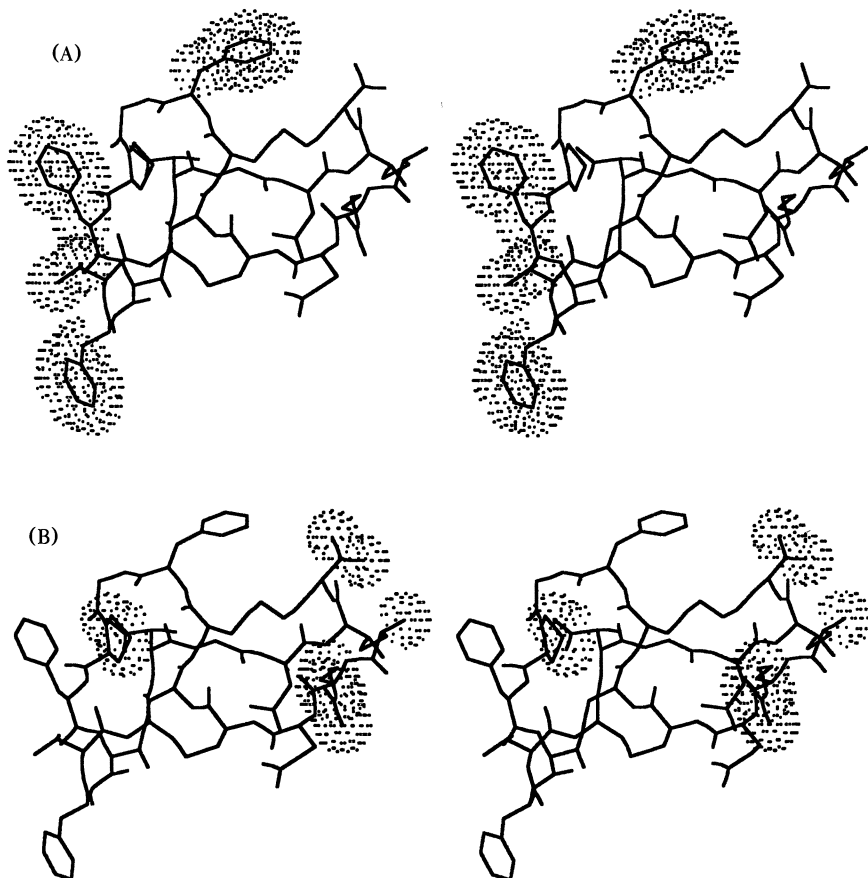


Figure 12. Stereoviews of the solution NMR structure of Ro 09-0198 (coordinates courtesy of H. Kessler (121)) that show (A) van der Waals surfaces of the Phe and Val side chains and (B) van der Waals surfaces of the charged amino, carboxy, and guanido groups.

tachyplesins, and bactenecin (148–151). Although the mechanism of action is not known in all cases, some of these peptides clearly possess the ability to permeabilize the membrane of the invading cell, and this ability is linked to their bactericidal activity.

Defensins. Defensins are small cationic peptides isolated from granules of mammalian phagocytic cells that share a conserved sequence motif (Figure 13) that includes three disulfide bridges, two arginines, one glycine, and one glutamate (152, 153). Similar sequences recently found in murine intestine (154, 155) were named cryptdins (Table III). Defensin NP-1 and HNP-1 form voltage-dependent, anion-selective channels in bilayer membranes (156) with a concentration dependence that varies from 2 to 4. The channel activity



Figure 13. Consensus sequence of the mammalian defensins that shows the positions of conserved residues and disulfide bridges.

may be relevant to the mechanism of bactericidal activity, in that HNP-1 sequentially permeabilizes the outer and inner membrane of *E. coli* (157). The solution structures of human (HNP-1) and rabbit defensins (NP-2 and NP-5) were determined by NMR (158, 159), and a recent crystal structure at 1.9-Å resolution for the human peptide HNP-3 was reported (160). All of the structures are similar: Three disulfide bridges constrain the sequences to a highly folded beta-hairpin structure (Figure 14) devoid of helix. The residues from the conserved Glu-Arg pair to the end form a twisted antiparallel beta-sheet, a portion of which is involved in a triple-stranded beta-sheet with residues that immediately follow the first Cys in the sequence. The remainder of the sequence forms a loop structure that is fixed with respect to the sheet in the crystal structure but in NMR studies shows a great deal of orientational variation. HNP-3 unexpectedly crystallized as a basket-shaped dimer (160). Subsequent NMR analysis found that NP-2 and HNP-1 are likely to exist in solution as aggregates whose number and geometry could not be determined (158, 159). Hydrophobic side chains dominate the base of the basket with a ring of six Arg residues above (Figure 14). This minimally amphipathic structure is difficult to reconcile with the activity on planar lipid bilayers and suggests that some alternative structure may be stabilized upon interaction with the bilayer. Reduced and carboxymethylated defensins with broken disulfide bridges, which are nontoxic to cells, have no bilayer activity.

Insect defensins (161) are small, highly disulfide-bridged peptides that are effective against Gram-positive bacteria and were thought, at one point, to be homologous to mammalian defensins (162). Members of this family include royalisin from the honeybee *Apis mellifera* L. (163), sapecin (164) from the flesh fly *Sarcophaga peregrina*, and phormicin (162) from *Phormia terranova*. The mechanism of action of these peptides is unknown but is assumed to involve membrane permeabilization. Sapecin shows high affinity for cardiolipin (164), which is a major phospholipid of *S. aureus*. A mutant of *E. coli* deficient in this lipid was more resistant to sapecin than wild type, and permeability of liposomes composed of various lipids supported the special affinity of sapecin for cardiolipin. The insect and mammalian defensins are now regarded as distinct classes of peptides because identical residues in the homologous regions of phormicin A (residues 15–34) and rabbit NP-1 (residues 4–24) are not conserved among the known sequences and because the two groups are structurally quite different. Two-dimensional NMR studies (165) reveal that the tertiary structure of sapecin is entirely different from

Table III. Selected Sequences of the Defensins

<i>Defensin</i>	<i>Sequence</i>									
Mammalian										
Human HNP-1	A	CY	CRIPA	CIAG	ERRY	GT	CIYQ	GRLWAF	CC	
Human HNP-3	D	CY	CRIPA	CIAG	ERRY	GT	CIYQ	GRLWAF	CC	
Rabbit NP-1	VV	CA	CRRAL	CLPR	ERRA	GF	CRIR	GRIHPL	CCRR	
Rabbit NP-2	VV	CA	CRRAL	CLPL	ERRA	GF	CRIR	GRIHPL	CCRR	
Rabbit NP-5	VF	CT	CRGFL	CGSC	ERAS	GS	CTIN	GVRHHL	CCRR	
Cryptdin 1	LRDLV	CY	CRSRG	CKGR	ERMN	GT	CRK	GHLLYTL	CCR	
Insect										
Phormicin A	AT	CDLLS	GTG	INHSA	CAAH	CLLRGNR	GGY	CNGKGV	CV	CRN
Sapecin	AT	CDLLS	GTG	INHSA	CAAH	CLLRGNR	GGY	CNGKAV	CV	CRN
Royalisin	VT	CDLLS	FKGQ	VNDSA	CAAN	CLSLGKA	GGH	CEKGV	CI	CRKTSFKDLWDKVF

NOTE: Charged residues are shown in bold. Because all sequences have free amino and carboxy groups, the terminal residues are also in bold. Sequences within each group are aligned to show the consensus cysteine locations.

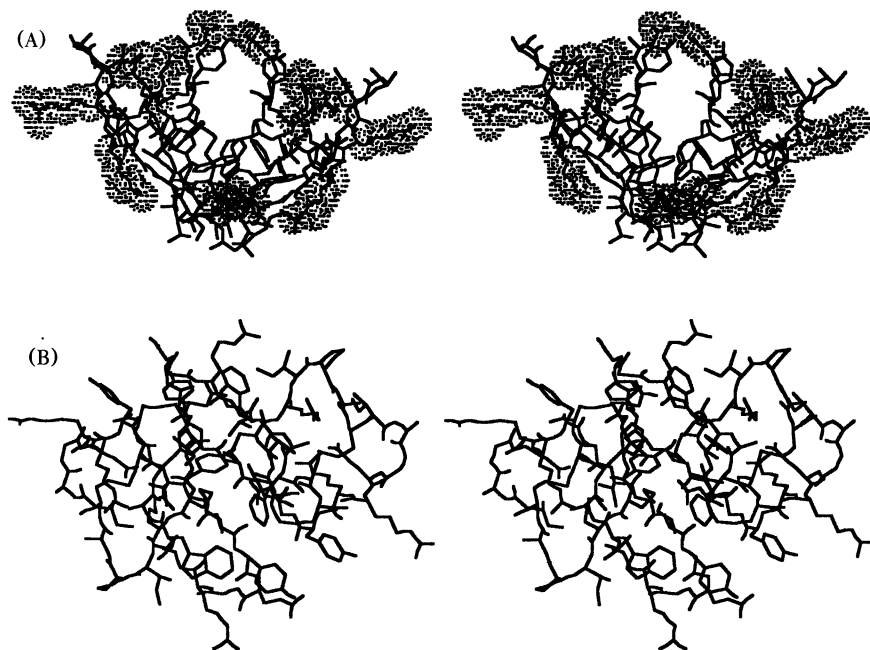
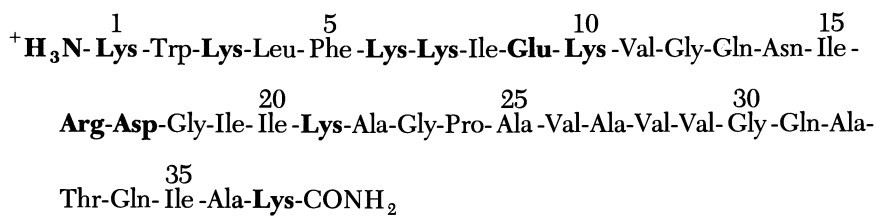


Figure 14. Stereoviews of the defensin dimer crystal structure [coordinates courtesy of D. Eisenberg (160)]. (A) Perspective that shows the basket shape of the molecule and the van der Waals surfaces of the charged side chains. In some cases, side-chain atom positions are not defined and have been placed in a low-energy conformation. (B) Perspective that shows the beta-sheets within each dimer and the subunit interaction.

NP-5 and that a different disulfide bridging (3/30, 16/36, and 20/38) exists (166). The molecule is amphipathic with one flexible loop between residues 4 and 12, a helix from residues 15 to 23, and an antiparallel sheet (residues 24–31 and 34–40). The insect defensins are structurally similar to peptides such as charybdotoxin that contain an α -helix stabilized by cysteine bridges (167). The amino acid sequences of sapecin and phormicin A differ only at position 35 and, as one would expect, their structures are very similar (168).

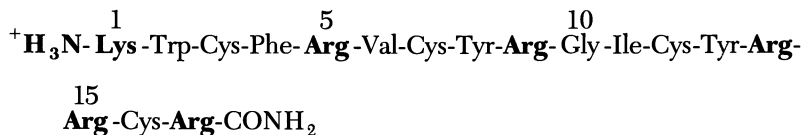
Cecropins. Cecropins (169) were isolated from the larval hemolymph of the giant silkworm moth, *Hyalophora cecropia*, on the basis of their antibacterial activity subsequent to bacterial injection. Cecropins are also produced by *Drosophila* (170) and the larva of the tobacco hornworm, *Manduca sexta* (110). Similar compounds called sarcotoxins (171) are produced by the flesh fly, *Sarcophaga*. Cecropins (169) are specific for prokaryotic cell lysis in contrast to melittin, which lyses eukaryotic cell membranes as well. Cecropins are characterized structurally by a concentration of basic



Cecropin A

residues in the N-terminal decapeptide in contrast to the magainins, where the charged residues are more evenly distributed, or melittin, where the basic residues cluster near the C-terminus. Bilayer activity and anion selectivity (2:1 Cl⁻:Na⁺) were demonstrated for cecropin and for several analogues by Christensen et al. (172). Voltage-dependent gating as well as antibacterial activity (173) were associated with the presence of the flexible sequence Gly-Pro between the N-terminal cationic amphipathic fragment and the C-terminal hydrophilic sequence. Shorter fragments (9–37 or 1–11 amide) were inactive. Bilayers with increased positive surface charge or with cholesterol incorporated show decreased sensitivity to cecropin, and this correlates with the lesser sensitivity of eukaryotic cells. The all-D enantiomer prepared by Wade et al. (106) retained the biological activity of the native material, suggesting that the cecropins exert their effect by direct action on the membrane without intervention by chiral receptors or enzymes. Activity against *E. coli* was retained when the helix-breaking amino acid Pro was substituted into either position 4 or 8 (174); however, the significant decrease in activity against three other bacteria implies different mechanisms at work. The structure of cecropin A in 15% hexafluoroisopropanol (175) consists of two well-defined amphipathic helical segments that extend from residues 5–21 and 24–37. The orientation of these helices with respect to one another could not be defined precisely, although the angle between the planes in which they lie was constrained to a range of 70–100°. This determination supports the role of a flexible hinge region suggested by structure–activity studies. The solution structure of a porcine cecropin (176) is helical and is somewhat different in that it has a well-defined helix in the center of the molecule. This structure may be a consequence of replacement of the Gly-Pro linkage with Gly-Ile and may correlate with the reduced range of antibacterial activity for this peptide.

Tachypleisin. Another cationic peptide with 17 residues, tachypleisin, was isolated from the hemolymph of the horseshoe crab, *Tachypleus tridentatus*, by Nakamura et al. (177) on the basis of antibiotic activity. Tachypleisin is active against both Gram-positive and Gram-negative bacteria and forms complexes with bacterial lipopolysaccharides. NMR data (178) suggest a beta-sheet structure stabilized by two disulfide bridges at 3–16 and 7–12.



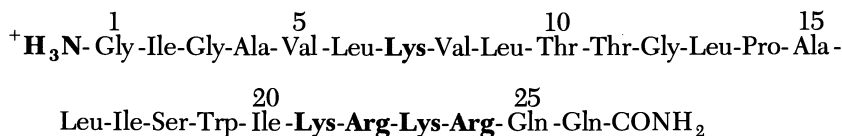
Tachyplesin

The resultant model of tachyplesin shows an antiparallel beta-sheet conformation (3–8 and 11–16) with a type I beta-turn (8–11). Side chains of Phe⁴, Val⁶, Tyr⁸, Ile¹¹, Tyr¹³, and Arg¹⁵ extend on one face of the beta-sheet. The side chains of Arg⁵ and Arg¹⁴ and two disulfides are on the other side; Arg⁹ is in the plane, which creates an amphipathic structure. Similar to the defensins in its mechanism of action (179), tachyplesin depolarizes inverted inner-membrane vesicles of *E. coli*. Leakage from vesicles prepared from phosphatidylglycerol was induced by tachyplesin (180), and fluorescence studies revealed that Trp² is located in a hydrophobic environment near the surface of the bilayers.

Natural Products (Venoms and Toxins)

A variety of peptides that evolved for use in defense or aggression possess the ability to modify membrane permeability. Although many of these compounds form channels in lipid bilayers, a major complication in the interpretation of their biological effects is their ability to interact with other proteins such as calmodulin, G proteins, and ion channels. Melittin is the most extensively studied member of this family of cationic peptides, although mastoparan and mast cell degranulating peptide also act independently as channel formers. The five homologous bombolitins isolated from bumblebee venom are members of this class (181) and share biological activities (erythrocyte lysis, histamine release, and phospholypase A₂ activation) with melittin and mastoparan. No evidence of channel formation by the bombolitins has been presented, although bombolitin I and III form amphipathic helices in association with micelles (182, 183).

Melittin. Melittin, the main toxin of bee venom, has a diverse biological spectrum and can lyse cells. Although it is tempting to associate its activities with channel formation, melittin activates G proteins (145) and also binds to calmodulin. The melittin sequence reveals a hydrophobic N-terminus



Melittin

and a highly charged C-terminal fragment with four basic amino acids in one stretch. In 1981, Tosteson and Tosteson (184) first demonstrated the ability of this peptide to form anion-selective channels in lecithin bilayers. The peptide shows an asymmetric current-voltage curve, presumably because of the inability of the highly charged C-terminal segment to cross the membrane. A concentration dependence of the fourth power suggested that four melittin monomers aggregate to form the channel. The opening of the pore is associated with the movement of one electronic charge early in activation followed by movement of four electronic charges during peak activation (185).

X-ray analysis (186, 187) reveals melittin to be a dimer of dimers (Figure 15): The apolar portion of each helix is buried in the center of the aggregate. All four helices are bent, and the helices within each dimer pair are in an antiparallel orientation. In water, melittin is a monomer, except at high concentration or high ionic strength, when it exists as a tetramer. The monomer has a random structure, and the tetramer has hidden hydrophobic surfaces that preclude effective interaction with the membrane. Solution NMR in methanol (188) reveals melittin to be helical from residues 2-11 and 13-26, with a hinge linking the two. Subsequent extended molecular dynamics simulations, both unrestrained and under NMR restraints (189), suggest a great deal of mobility in the two helices with respect to each other. NMR studies of melittin bound to sodium dodecyl sulfate (SDS) micelles (190, 191) reveal a bent helix, similar to the helix in the crystal structure and in methanol, and are consistent with orientation of the melittin monomer parallel to the plane of the lipid bilayer.

The variety of techniques used to study melittin association in phospholipid bilayers was reviewed by Dempsey (192). In studies on model mem-

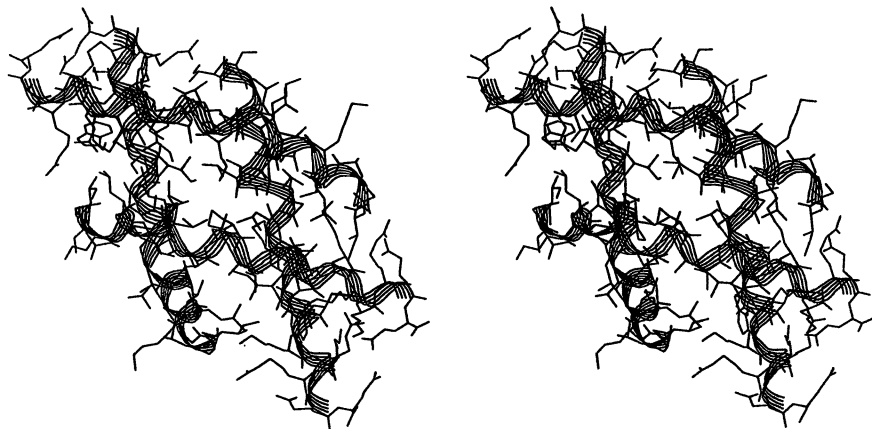


Figure 15. Stereoview of the melittin tetramer crystal structure (186, 187) with ribbon overlay that shows the bend in each helix and the hydrophobic contacts between monomers.

brane systems, melittin binds parallel to the surface in a conformation very similar to the conformation in the tetrameric crystal (Figure 15) (186, 187) and in methanolic solution. Data on spin-labeled analogues suggest that helical melittin binds to the bilayer as a monomer (193) and that it is oriented parallel to it, with the hydrophobic face of the helix buried (194). Several studies in oriented bilayers suggest that melittin can assume an orientation with the helical peptide perpendicular to the plane of the membrane, either as a transbilayer orientation or a helix-turn-helix motif, depending on experimental conditions (*see* Vogel (79), Frey and Tamm (195), and the review by Dempsey (192)). Kaiser and Kezdy (6) cite experimental data that suggest that the active hemolytic component of melittin is the dimer. Hemolytic activity does not necessarily parallel voltage-dependent pore formation, because [Ala¹⁴]melittin shows enhanced hemolytic activity and markedly reduced channel activity (196). This replacement of Pro¹⁴, which is responsible for the bending of the helix and the flexibility of the two adjacent helical segments with respect to each other, suggests that different mechanisms may be at work for the two processes. Talbot et al. (197) demonstrated oligomeric species in bilayers whose properties varied depending on the composition and physical state of the lipid. Vogel and Jahnig (198) studied melittin in lipid membranes and concluded that a bent α -helix (residues 1–21) with a nonhelical hydrophilic segment (22–26) was consistent with Raman spectra. Furthermore, the carboxy termini were found by fluorescence quenching to be located on the side of the membrane to which the peptide was added. These observations led to a proposal for a tetrameric structure of melittin in membranes that invoked a bilayer-spanning polar pore formed by orientation of the apolar faces to the lipid. IR studies (199) indicate that melittin adopts primarily an α -helical conformation oriented perpendicular to the lipid bilayer. A rigid, bent-rod model was postulated to account for the lytic properties by perturbation of the lipid structure.

Although both melittin and the cecropins share a structural motif that consists of two helices linked by a hinge region, the polarity of the helices is reversed in that melittin has a hydrophobic N-terminus and an amphipathic C-terminus; the converse is true for the cecropins. The relationship of structural difference to the different activities of these two peptides was probed by preparation of shortened cecropin–melittin hybrids (200, 201) that show enhanced antibacterial activity and decreased hemolytic effects.

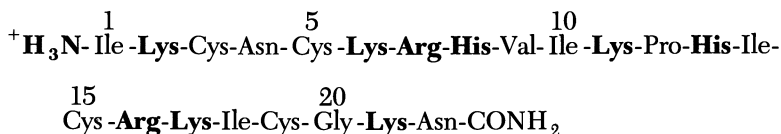
Mastoparan. Wasps produce a wide variety of toxic peptides (202) that includes mastoparan, a 14-residue peptide isolated from the venom of *Paravespula lewisii*. Mastoparan stimulates the degranulation of mast cells,



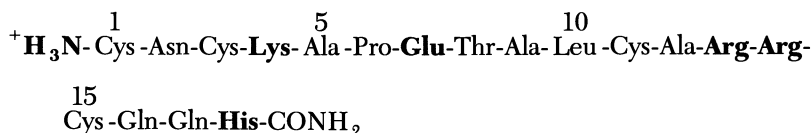
Mastoparan

which results in histamine release, and binds with high affinity to both calmodulin (203) and G proteins (145). Mastoparan forms weakly cation-selective channels in bilayers, and two types of voltage-dependent conductance are observed (204): The first behavior is characterized by discrete channel openings with multiple states between 15 and 700 pS and is also seen with a shortened analogue, [des-Ile¹-Asn²]mastoparan (MP3). The other behavior is characterized by transient increases in conductance to a level of 650 pS. Fluorescence experiments reveal that a membrane potential enhances the binding of mastoparan to cardiolipin vesicles (205). Channels are formed from mastoparan in a fashion that correlates with ionic strength, which in turn correlates with helical content (204). The membrane-bound conformation of mastoparan is an amphipathic α -helix as determined by NMR (206). Although the binding of mastoparan to G-proteins is well characterized, there is evidence that its ability to enhance membrane permeability in cells is, in part, due to a mechanism independent of G-protein activation (207).

Mast Cell Degranulating Peptide (MCD) and Apamin. Mast cell degranulating peptide (MCD) (208, 209) is a cationic peptide isolated from the venom of bees (*Apis mellifera*). The primary structure of MCD is related to another bee venom peptide, apamin. Two other peptides, tertiapin and secapin, are homologous and also found in bee venom. Although MCD and apamin are both neurotoxins that bind to K⁺ channels, only MCD forms voltage-dependent channels in bilayers (210). These multilevel channels exhibited a permeability ratio P_K/P_{Cl} of approximately 4, with a minimum size of 3.8 pS. Both MCD and apamin are highly basic throughout their length and are bridged by two similarly positioned disulfide linkages (MCD: Cys³/Cys¹⁵ and Cys⁵/Cys¹⁹; apamin: Cys¹/Cys¹¹ and Cys³/Cys¹⁵). The solution NMR structure of MCD (211) was found to resemble that of apamin (212–214) (Figure 16). The MCD structure consists of an extended N-terminus (residues 1–5) and an α -helical segment (residues 13–22) that are



MCD



Apamin

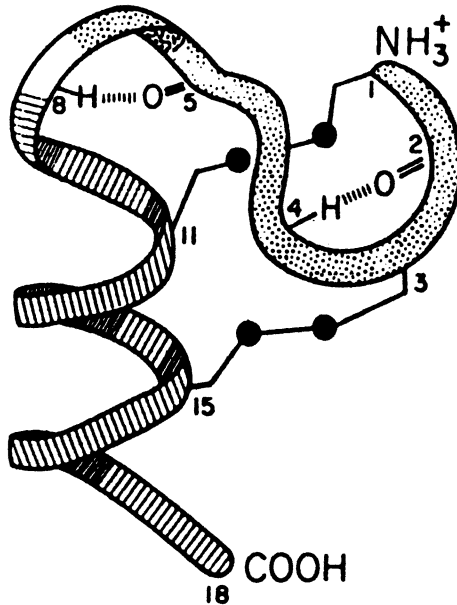
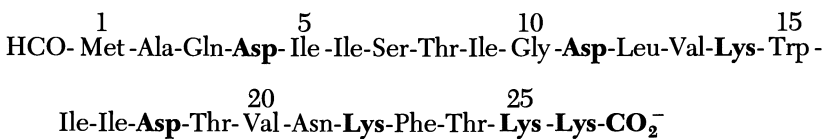


Figure 16. Schematic of the solution NMR structure of apamin that shows the C-terminal helix and two beta-turns centered at residues 3–5 and 6–8. (Reproduced from reference 214. Copyright 1983 American Chemical Society.)

connected by two tight beta-turns (residues 6 and 7 and 13 and 14) and cross-linked by two disulfide bridges. The toxic effects of MCD on the central nervous system may be due to inhibition of potassium channels rather than formation of ion channels in the membrane. A receptor site for MCD has been identified (215) on the K^+ channel, but it has a negative allosteric interaction with two other potassium channel blockers, dendrotoxin and charybdotoxin.

δ -Hemolysin from *S. aureus*. A 26-residue cytolytic peptide is secreted by pathogenic strains of *Staphylococcus aureus*; its interactions with lipid bilayers have been well characterized (216). A dose–response curve with a slope of 7 suggests that aggregates of the toxin form channels. Two substates were observed: one with conductances of 70 and 100 pS; the other with 420- and 470-pS levels. NMR in methanol indicates (217) a well-ordered



δ -Hemolysin

helical structure between residues 2 and 20 with a flexible C-terminus, similar to that seen when the peptide is bound to micelles. The charged residues align on one face of the helix. IR studies indicate that hemolysin penetrates the bilayer but is oriented much less than melittin. Preliminary crystallographic studies were reported (218) and used in the construction of a model for its mode of action (219). Hemolysin, like melittin, binds (220) to calmodulin, which may explain some of its biological spectrum.

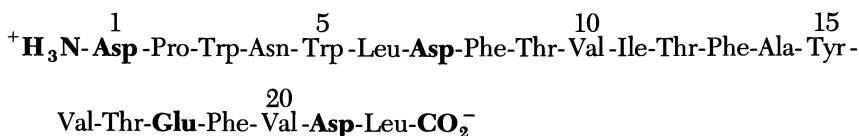
Fragments of Integral Membrane Proteins and Other Membrane-Active Proteins

Several examples now exist in the literature where fragments of proteins that interact with membranes exhibit ion channel activity. For some of these fragments, such as the sodium and calcium channels, the intact protein normally functions as a channel. Identification of likely transmembrane sequences has led to postulates about sequences that form the lining of the pore that have been tested by synthesis and evaluation of those fragments. When these short peptide fragments (22–23 residues) are assayed in planar lipid bilayers, they show many of the properties associated with the parent structures. Such simplified structures hold the promise of chemical modification and computational studies leading to a model that can be extrapolated to the larger assembly. However, the relevance of any conclusions based on these simple model systems is unknown until further knowledge of the integral transmembrane parent structures becomes available. As is apparent in this review, many peptides have the capacity to induce changes in ion permeability in membranes, and the modulating effect of nearby sequences should not be ignored.

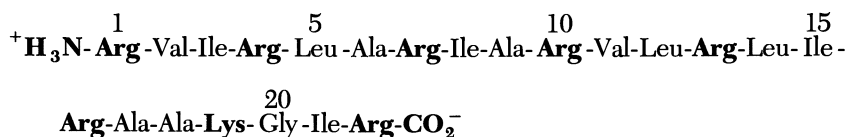
In other cases, the larger protein does not function as a channel but has other functions that require interaction with the membrane. Signal peptides, viral fusion factors, and phage lytic factors are included in this group. Fragments and analogues of the N-terminus of the influenza virus hemagglutinin HA-2 component increase the conductance of lipid bilayers and assume an α -helical conformation when bound to lipid membranes as judged by CD spectra (221, 222). The C-terminal 25 residues of RNA phage MS2 lytic protein, which has lytic activity, also increases liposome permeability and induces size-restricted hydrophilic pores in lipid bilayers (223). Signal peptides, which are N-terminal segments of protein precursors, determine the final location of the protein by directed transport across a cellular membrane. Gierasch (224) reviewed signal sequences and biophysical studies (225) aimed at elucidating their properties. Tosteson et al. (226) showed that a synthetic signal sequence and pro-region, the pre-pro fragment from parathyroid hormone, forms voltage-dependent ion channels with some cation selec-

tivity and a concentration dependence that varies between 2 and 3, depending on salt concentration. The signal sequences of mitochondrial protein precursors were used to guide design of a series of model peptides (227) in which basic amino acids were distributed between short stretches of hydrophobic residues in a fashion that resembles cationic peptide antibiotics. The bactericidal potency of the peptides correlated with helicity as measured by CD spectra when bound to liposomes.

Sodium Channel. The most exciting work of this class has focused on the sodium channel. Analysis of the amino acid sequence for the *Electrophorus electricus* and rat brain channels (230, 231) led to the identification of four homologous repeats, each of which encompassed several putative transmembrane helices. Several proposed models (230, 232–235) for the structure of the channel vary, among other things, in the number of transmembrane helices (designated S1 to S6 (230) or Sa to Sh (233)) and their orientation with respect to the actual pore. The Montal group postulated a schematic model (233) in which each of the four repeats contained eight transmembrane helices, of which one was an amphipathic helix that lined the channel with its hydrophilic residues. Four peptides of 22 residues that correspond to the four amphipathic helices from the homologous repeats were synthesized and examined on planar lipid bilayers (236). The peptide Sc 1 (S3) forms transmembrane ionic channels that mimic many of the properties of the authentic brain sodium channel. For example, the conductance γ is 20 pS for the synthetic peptide and 25 pS for the native protein. The kinetics for transition between open and closed states are almost identical to the native protein. The synthetic peptide, however, does not discriminate between sodium and potassium and shows no voltage dependence. A postulated hydrophobic transmembrane segment, Sh 1, with the sequence IF-FVLVIFLGSFYLINLILAVV, was also synthesized as a control and did not form channels in lipid bilayers (236). Molecular modeling of the amphipathic



Sc 1 segment of rat brain sodium channel (228)



S4 segment of *Electrophorus electricus* sodium channel (229)

only are a great variety of lipids employed, but conformational studies with planar bilayers are mixed with those of micelles and liposomes in which packing differences can change affinities (244, 245) and, perhaps, modes of interaction. There is little doubt that the observations are dependent on the experimental conditions used for many, if not most, of the peptides under discussion (246). Any efforts to generalize and reach a consensus view must be regarded skeptically, because of the lack of common experimental observations. This deficiency is exemplified in the polyene antibiotic amphotericin B (247), where multiple mechanisms are operative depending on experimental conditions and the selectivity seen with many of the antibiotic peptides. Some mechanisms are equally effective in eukaryotic cells, and some mechanisms are rather specific for prokaryotic membranes. Often one peptide can distinguish between Gram-negative and Gram-positive bacteria. If the composition of the membrane were immaterial, then pore formation would be expected to be equally effective against all membranes. Obviously, other factors can enter into determination of the lethal effects of channel formation on a given cell. For example, the transmembrane potential in prokaryotic cells, mitochondria, and chloroplasts is considerably greater than the potential seen across the plasma membrane of eukaryotic cells (248). Recently, Groisman (249) established a series of mutants of *Salmonella typhimurium* that varied in relative susceptibility to cecropin, mastoparan, melittin, defensin, and magainin. This variation implies that multiple mechanisms of resistance have evolved. The role of lipid composition in pore formation has been explored for a very few systems and then only in a limited fashion. A comprehensive review of the effects of lipid composition, transmembrane potential, and physical state on the electrostatics of the membrane was presented recently by Cevc (248).

The mechanism whereby a peptide first associates with the membrane and then undergoes a transition to become a transmembrane component is largely unknown. The membrane is a nonhomogeneous environment with a high density of polar head groups, often positively charged, at the interface between the thin hydrocarbon core and the aqueous solvent. This unusual environment imposes strong constraints on the possible conformations that can favorably interact with the membrane. Normally, hydrophobic residues cluster in the interior while charged and hydrophilic residues are fully solvated in the aqueous media. Hydrogen bond donors and acceptors are generally in equilibrium between internal hydrogen bonding and interaction with water, and many small peptides reflect this equilibrium in an ensemble of conformers with the average conformation dependent on experimental conditions. This equilibrium is perturbed upon association with a membrane, with the result that the peptide effectively turns itself inside out. Structure-activity studies (250) on peptides that interact with lipids indicate that the strength of interaction is related to the hydrophobic surface area, and transfer

of this surface from the aqueous to the nonpolar lipid phase must be energetically sufficient to overcome the increase in free energy associated with restriction of the peptide to the two-dimensional world of the lipid membrane.

The profound impact of the environment on the three-dimensional structure of peptides has made it difficult to define conformations relevant to the processes involved in the functioning of ion channels. Often a more nonpolar solvent is assumed to mimic the conditions seen at the lipid-water interface. Conformational studies in these solvents often induce helices in peptides of the size active in bilayers, by decreasing the availability of intermolecular hydrogen-bonding partners and by stabilizing the exposure of hydrophobic side chains. Because relatively stable conformations can be induced in organic solvents, many NMR studies of peptides are performed under these conditions. In certain respects, studies in these solvents are certainly more representative of the lipid interior of bilayers than studies in water. Studies in organic solvents may correlate with studies of peptides bound to lipids, depending on the conformational mobility of the molecule. The structural heterogeneity of gramicidin A is no doubt a consequence of its conformational freedom. In contrast, solution structures of the defensins may be relevant simply because of their extensive covalent constraints. In many ways, the attractiveness of peptaibols for study is their limited conformational freedom. Even studies in lipid environments are often difficult to interpret because of structural changes in liposomal lipids versus planar bilayers (245), differences in lipid composition, and structural changes dependent on the relative concentrations of the components. Nevertheless, information derived from studies of peptides associated with lipids are clearly relevant, at least as far as association and even insertion are concerned. The relevance of these structural studies to gating and pore formation is more problematic, as these events often require a transmembrane potential and may only involve a small percentage of the peptide present.

One issue that complicates efforts to develop a model for the mechanism by which peptide ion channels work is the width of the bilayer that must be spanned by the transmembrane helix. Vodyanoy and Hall (251) measured the dielectric thickness of monoglyceride bilayers and found it to vary from 3.1 to 2.0 nm as the fatty acid chain length went from C₂₂ to C₁₄. The crystal structure (252) of the photosynthetic reaction center indicates a 3.0–3.1-nm hydrophobic zone perpendicular to the membrane that is smaller than might be expected for C₁₈ lipids but is in accord with estimates of dielectric thickness as well as recent physical studies (253). With the assumption that a transmembrane segment must span this thickness to give a stable pore structure, a rise per residue of 1.5 Å can be estimated for an α -helix, and 20 amino acid residues would be required. Peptides shorter than 20 residues, such as mastoparan and emerimicin, are capable of ion channel formation,

and the concept of local membrane deformation is often invoked (204) to rationalize this discrepancy. The head-to-head dimerization of gramicidin A in the membrane insinuates that end-on interactions must be considered, especially with peptides as short as the membrane-active octapeptides of Menestrina et al. (91). This argument is supported by crystallographic studies of peptaibols that show head-to-tail hydrogen-bonding patterns, effectively making them continuous helical rods (65, 69). Only further experimental study will elucidate the mechanism by which shortened segments manage to form transmembrane channels. One complication is the effect of the transmembrane potential on membrane thickness (248) and on the rate of pore production (254), both due to thermal fluctuations. Conceivably, spontaneously formed thin patches or pores might allow channel formation by short segments, which in turn stabilize the local deformation of the membrane.

Mutational analysis was implemented to investigate the length requirements for transmembrane segments. Adam and Rose (255) showed that deletion of 6 residues of a 20-residue transmembrane-spanning domain did not prevent normal expression on the cell surface. Davis et al. (256) studied the anchor domain of an integral membrane protein by deletion analysis. Shortening the domain from 23 to 17 residues did not affect function. However, shortening to four residues led to secretion and loss of anchoring. One mutant protein with only 12 residues in this domain was found predominantly in the membrane fraction. Three suggestions were offered to explain the data: (1) the transmembrane domain is not α -helical, (2) charged residues are buried in the membrane, or (3) the membrane is locally deformed to accommodate a shortened transmembrane segment. The means by which the hydrophobic mismatch is accommodated is most likely determined by the relative energetics of nonideal peptide versus nonideal lipid configurations. Experimental (257) and theoretical (258) studies of this issue are in their infancy. Mutagenic techniques will, no doubt, continue to be invaluable in the definition of lipid-embedded regions of proteins and sequences important in interaction with head groups. Altenbach et al. (259) recently devised an experimental paradigm in which a series of spin-labeled mutants were probed with paramagnetic species that had differing affinities for the lipid phase. Periodicity in the relaxation behavior of the spin labels and differential response to paramagnetics favoring the aqueous phase yielded information about secondary structure elements and embedded sequences.

Several structural themes are apparent from the foregoing survey of pore-forming peptides. Certainly the most common theme is a propensity for a sequence to form a hydrophobic or amphipathic helix that inserts into the membrane and aggregates to form a pore. The limited number of examples to the contrary suggest that helices may, in general, be important in the larger issue of protein-membrane interactions and have spawned extensive investigations with regard to signal peptides (224) and integral membrane proteins

(260). The basic conclusions for transmembrane helices in integral membrane proteins are as follows:

1. Hydrophobic helices in lipid bilayers are highly stabilized structures.
2. Helix association in both parallel and antiparallel arrangements is favored by several possible mechanisms.
3. Insertion of a hydrophobic helix into a membrane is favored thermodynamically.

Jahnig (261) calculated that the transfer of a hydrophobic α -helix to the membrane would result in 15 kcal/mol of stabilization. With regard to signal peptides, the sequence specificity is very low as about one-fifth of random mutations in such a peptide function efficiently (262) in protein export. Functional signal peptides share a propensity to adopt α -helical conformations and associate with organized lipid assemblies, such as monolayers or vesicles. Conformational studies on signal peptides show considerable dependence on environment, but helix stability in a crucial hydrophobic core region correlates with signal peptide activity (225). Signal peptides do have a characteristic sequence pattern (224) that is different from transmembrane helices. A core hydrophobic region of 10 ± 3 residues is flanked by a less hydrophobic C-terminal region of five to seven residues preceding the signal peptidase cleavage site. On the N-terminal side of the hydrophobic core, there is a positively charged region of variable length and composition. These results suggest that a hydrophobic helix with little sequence specificity may be sufficient, although there is considerable evidence to suggest a role for beta-structure in signal peptides (224, 225). Under conditions that preclude insertion, the LamB signal peptide adopts a beta-structure parallel to the surface of a phospholipid monolayer, but when insertion is allowed, the C-terminus becomes α -helical and spans the monolayer (263). These results are consistent with membrane association of beta-structures such as the defensins but do not provide any insight into how they may associate to form pores, unless reorganization of the structure is involved.

The structural role of proline in the activity of membrane-active peptides appears to be significant. Proline can be accommodated (264, 265) in a helical structure with a concomitant bend of approximately 26° in the helix axis, and has been suggested to have a role in membrane-buried transport proteins (266). The flexible-hinge region of the peptaibols, often associated with the presence of a glycine and a proline, and observable in the alamethicin crystal structure (77), has served as a stimulus for the development of several of the mechanisms discussed earlier. These models, which are based on a bent helix that gates by segmental helical movement, all have the helix-dipole moment as their voltage-sensor, which was first suggested by

Urry (267). Although proline is not obligatory in the action of the peptides reviewed here, it is obvious that its role is important, for example, in cases such as the cecropins and melittin. A helical hinge region centered about proline is essential in a mechanism recently suggested by Karlake et al. (268) for the translocation of a mitochondrial signal peptide across a membrane barrier without the need for auxiliary membrane proteins. In the case of this 19-residue peptide, NMR showed two α -helical amphipathic helical segments separated by a hinge region when bound to micelles. The resultant model is essentially identical to the helix-hairpin model of membrane protein insertion suggested by Engelman and Steitz (89), which, in turn, was anticipated by von Heijne and Blomberg (269) and by Inouye and Halegoua (270) in their study of prokaryotic signal peptides. The two-domain structure appears to be a common motif in mitochondrial targeting peptides (271). More recently, Jacobs and White (272) considered the thermodynamics of peptide insertion into bilayers and found support for the present models.

In contrast to gating and membrane insertion of helices by segmental motion, Marshall (unpublished) envisioned a helix-hairpin model (Figure 17) in which the location of the turn is not static but dynamic. By switching between the α -helix and the 3_{10} -helix, hydrogen bond donors and acceptors can be exposed at the helix termini. From an initial helix-hairpin with both hydrophilic ends on the same side of the membrane, an intervening turn could migrate dynamically through the sequence and lead to a single helix that spans the membrane. This process could be driven by the transmembrane potential, and minimal changes in the number of unsatisfied hydrogen bond donors and acceptors exposed to the hydrophobic interior make this an energetically attractive mechanism of insertion. An α -helix has eight unsatisfied hydrogen-bonding groups in the peptide backbone: four amide hydrogens at the N-terminus and four carbonyl oxygens at the C-terminus. Exposure of these ends to the aqueous medium is energetically desirable. Because the 3_{10} -helix has one additional hydrogen bond for the same length of helix, its ends are less hydrophilic and more likely to translocate across the membrane than those of the α -helix. Proteins have an unusual distribution of amino acids at the ends of α -helices (273, 274) whose side chains can hydrogen bond to the initial four amide NH groups and final four carbonyl oxygens. Serrano and Fersht (275) showed by mutational studies that an adjacent side-chain residue satisfying one of these hydrogen-bonding sites at the helix N-terminus can stabilize the α -helix by up to 2.5 kcal/mol. Although helix-helix transitions are energetically feasible (74), the energetics of helix-turn transitions are not yet thoroughly characterized.

The cationic peptides possess two predominant themes: either a hydrophobic core (often helical) with an adjacent cluster of Lys and Arg residues (e.g., melittin and cecropins) or an amphipathic helix with basic side chains aligned along one helical face (e.g., magainins and the S4 segment of the sodium channel). The basic residues promote association with the acidic

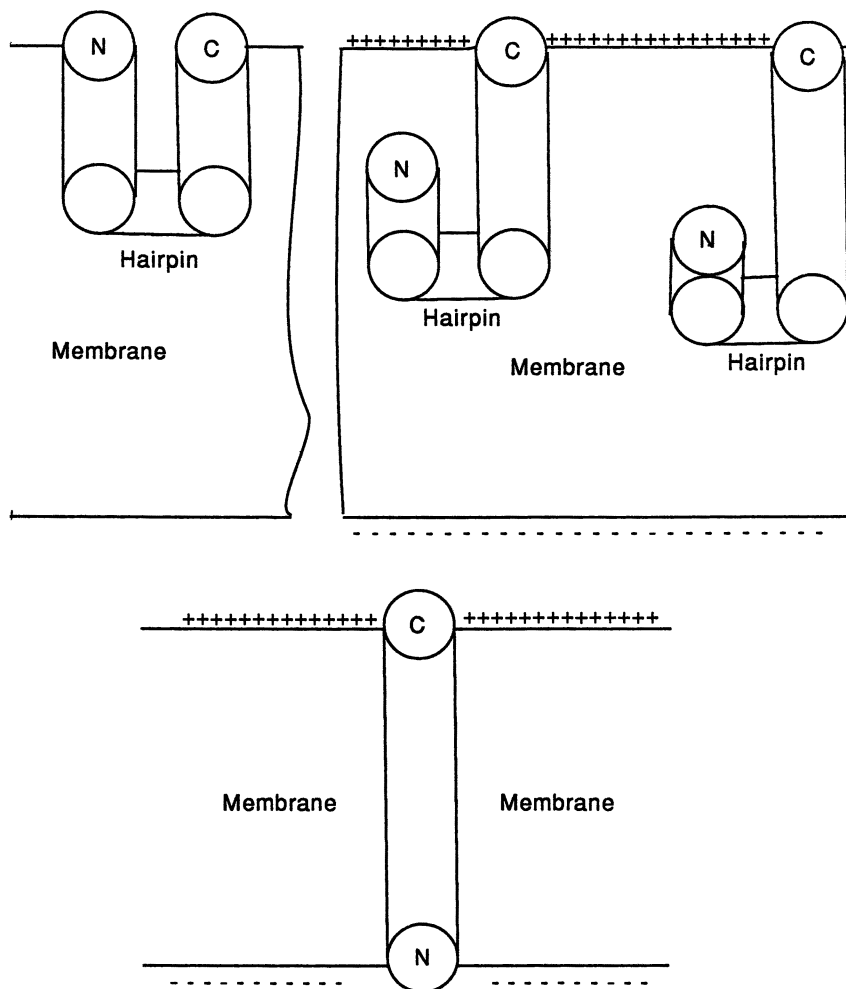


Figure 17. Schematic diagram of the dynamic helix-hairpin mechanism for gating and insertion of peptides. In response to an imposed transmembrane potential (indicated by + and -), the hairpin migrates in the sequence to transform the partially inserted helix-hairpin into a transmembrane helix.

head groups of the phospholipids. A common feature (276) of cytolytic peptides is the presence of a cationic site adjacent to a hydrophobic surface. In these cases, the hydrophobic helical segment governs association with the bilayer and a transmembrane potential provides the driving force to move the charged segment through the membrane. As might be expected, these cationic peptides interact more strongly with negatively charged lipids (192). The absence of peptides with acidic side chains that function as ion channels

stands in marked contrast to the class of cationic peptides. There are calcium-dependent membrane proteins such as synexin (277) that have a high percentage of Asp and Glu residues and form calcium channels in lipid bilayers. No localization of this property to a smaller peptide segment has been reported.

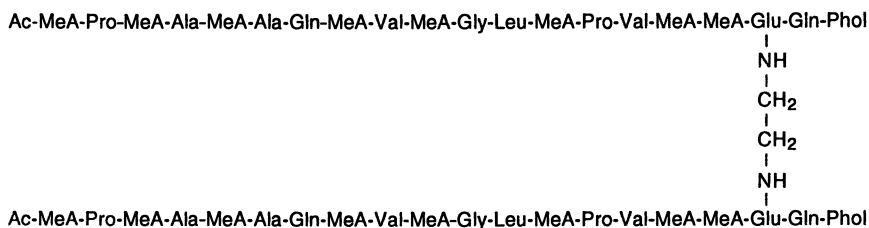
The beta-sheet as a structural motif in peptide ion channels is less recognized, primarily because there are so few examples. The defensins fall into this class, as does tachyplesin. The beta-barrel is recognized as a viable transmembrane structure (278) that has all possible hydrogen-bonding sites satisfied and is known to exist in large proteins such as the bacterial outer-membrane porins (279). Because a single beta-strand is unlikely to insert into a membrane, any beta-barrel peptide channel would have to insert as a preformed complex (280). The energetic requirements of such pre-organization of monomers makes this structural motif unlikely in the absence of covalent constraints such as the disulfide bridges of the defensins. Efforts to identify channel regions of large proteins by characterization of the properties of short segments may lead to erroneous inferences, because in the absence of constraints imposed by the large protein, these sequences may form transmembrane helices even if their normal structural motif is that of a sheet. As noted earlier, mutational analysis suggests that the Shaker potassium channel is lined with a beta-strand (239, 240), and a recent model of the voltage-dependent anion-selective channel, also based on mutational studies, invokes both beta-strands and α -helices in the formation of the channel (281).

Although helices dominate peptide ion channels structurally and sheets are exceedingly rare, one unifying theme is amphipathicity. Most of the peptides considered here are hybrids with segregation of hydrophobic segments from hydrophilic and charged segments, whether that segregation be through secondary structure periodicity or through clustering within the amino acid sequence. Amphipathicity is likely for all active peptides for at least one of the accessible conformations, even if the crystal structure or solution structure did not exhibit this characteristic.

A final structural theme that runs through this survey is the need to assemble large aggregates, such as helical barrels or bundles, to form pores. The aggregation state of the peptide prior to membrane penetration is not sufficiently characterized in most systems. If the peptide is present as an aggregate, either in solution or at the membrane surface, a simple interpretation of the concentration dependence of pore formation could be incorrect. In other words, if preformed tetramers are the active solution species, then formation of an octameric pore could show a concentration dependence of the second power over the concentration range studied. One persistent question is whether the peptides are pre-associated prior to insertion or whether the association to form channels occurs from individual monomers already inserted into the membrane. The energetics of insertion of a charge

into the lipid bilayer (282) suggest that all charged peptides insert as aggregates. The numerous observations of multistate conductance levels suggest that the number of monomers in a given pore varies with time and that monomers or aggregates too small to function as pores are readily exchanged between or in equilibrium with existing pores.

Attempts to control the aggregation state of the peptide drive the design and synthesis of covalently linked aggregates that generally consist of a template molecule to which channel-forming peptide chains are linked (283). One such molecule, tetramethicin (Chart I), is a tetrameric aggregate of alamethicin. The concentration dependence of alamethicin suggests six to eight monomers per pore. Dimerization of the molecule through the Glu¹⁸ side chains (Chart I) (284) results in a species that is dramatically more active than alamethicin itself. An alamethicin oligomer with the first 17 residues of alamethicin linked to the ϵ -amino group of oligoglycine was synthesized to create a pore with an amide backbone mouth at the C-terminus. The purified Ac-(Lys(Alamethicin 1-17))₄-NH₂, tetramethicin, shows channels of basic unitary conductance (~ 2.5 pS) on planar bilayers (Figure 18) (285) with longer stability than alamethicin. Tetramethicin shows an effective concentration 2.7 times that of alamethicin, which is dramatically different from the



Alamethicin dimer



Tetramethicin

Chart I. Oligomers of alamethicin synthesized to control the aggregation state of the peptide ion channel.

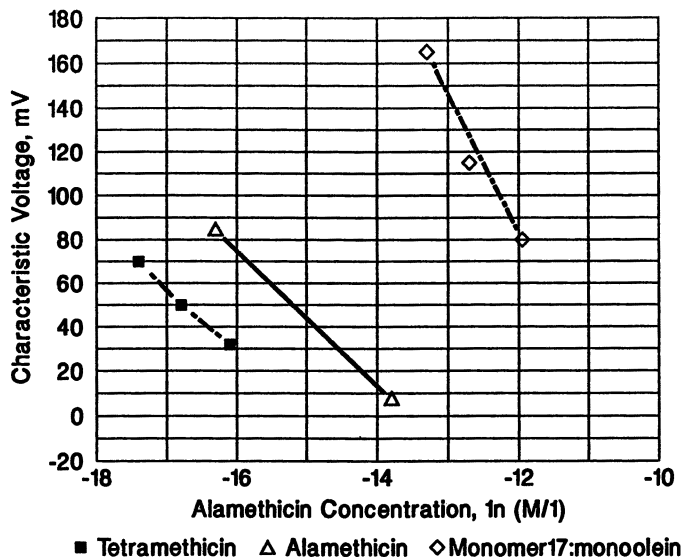


Figure 18. Conductance of tetramethicin, alamethicin, and the 1-17 fragment of alamethicin used to construct tetramethicin.

control monomeric alamethicin 1-17 benzyl ester but not equal to the expected value of 4. The characteristic voltage for tetramethicin is 5.78 mV, which is similar to that reported for alamethicin (4-5 mV). One interpretation of these results is that the linkage of monomers only slightly hinders the channel formation and that the voltage-dependent step is not affected by aggregation through a covalent linkage of the C-terminal residues. This mechanism makes the flip-flop mechanism discussed earlier (96) difficult to reconcile unless an antiparallel dimer of tetramethicin forms the pores and a complete tetramer is reoriented during gating.

A similar approach to the preparation of peptide aggregates has been reported in the preparation of a tetrameric form of the 23-residue M2 δ segment of the acetylcholine receptor (286). A nonapeptide backbone with four lysine side-chain attachment sites was used as a template, and the resulting 101-residue protein formed channels in planar bilayers. This "synporin" exhibited properties similar to those displayed by authentic acetylcholine receptor channels, such as single-channel conductance, cation selectivity, channel-gating kinetics, and sensitivity to local anesthetic (QX222) channel blockers. An analogue in which Ser⁸ in each of the four monomeric units was replaced with alanine showed a reduction in single-channel conductance similar to the reduction seen with mutant acetylcholine receptor having the same modification. A control synporin with M1 δ monomers (discussed earlier) substituted for the M2 δ units was inactive. These data support the

contention that the M2 δ unit forms the lining of the acetylcholine receptor channel and suggest that the strategy of preparing covalent aggregates will be useful in understanding fundamental properties of ion channels. A similar approach was implemented for the IVS3 segment of the dihydropyridine-sensitive calcium channel (287).

Although many parallels are drawn between large membranous channels and their peptide counterparts, a better reference point may be the colicins (288–290). These soluble proteins spontaneously insert into lipid bilayers and form voltage-gated monovalent ion channels. The initial interaction with the bilayer is driven by electrostatic interaction with phospholipid head groups (291), which results in the sequestering of some of the protein in the bilayer. When the channel opens, trypsin sensitivity of the protein is altered in a fashion consistent with additional insertion of protein into the lipid (292). An X-ray structure of a 204-residue C-terminal fragment from the channel-forming domain of colicin A (293) reveals an aggregate of 10 helices arranged in layers, with two hydrophobic helices linked by a turn at the core. This structure has some similarity to the aqueous NMR structure of a C-terminal fragment (294) from colicin E1. A model of the mechanism of action of the pore-forming fragment of colicin A (295) reconciles the structure with other experimental observations. The protein first associates with the membrane through a ring of eight basic residues around the terminus of the core hydrophobic hairpin loop. The spontaneous penetration of the two-helical segment leaves the outside helices parallel to the plane of the membrane, somewhat like the arms of an open umbrella. The membrane potential then drives the additional helical segments into the membrane to complete the pore. In this model, once the protein associates with the membrane, the association between helices is loosened and the ensemble can be thought of as a molten globule. Reorganization of the tertiary structure at both the association and insertion stages occurs with retention of secondary structural elements. In the case of channel-forming peptides, the aggregate present in the membrane prior to insertion or gating may involve a molten globule type of ensemble.

If the peptide aggregate is envisioned as a molten globule, one plausible mechanism (Marshall, unpublished; Figure 19) for gating of a pore formed by a helical bundle embedded in the membrane is a simple reorientation of helices. α -Helices have orientations of side chains that favor nonparallel association with an angle of approximately 25° between helix axes to pack optimally (*see* discussion and references cited in Chou et al. (296)) as seen in the transmembrane helices of the photosynthetic reaction center (252) and of bacteriorhodopsin (297). The surface tension of the membrane tends to minimize the volume of the helical bundle. The gating potential could simply be sufficient to force the helical elements to align with the potential field with a concomitant separation of helices due to the increased steric interaction

between side chains. This mechanism increases the separation between the helical cylinders with a resultant increase in the diameter of the pore between them, as shown diagrammatically in Figure 19. The α -helix to 3_{10} -helix transition allows local segments to optimize side-chain interactions by formation of mixed helical structures, as seen in many crystal structures of peptaibols and in molecular dynamics simulations (74). In several cases such as alamethicin the gating current has been estimated and is larger than predicted by such a simple adjustment. In other cases, however, small gating currents are consistent with experimental observation (92) and this mechanism becomes attractive. The helical bundle peptides of Lear et al. (298) show voltage dependence that is consistent with this gating model or may simply reflect the force necessary for insertion of the amphipathic helices preformed on the surface.

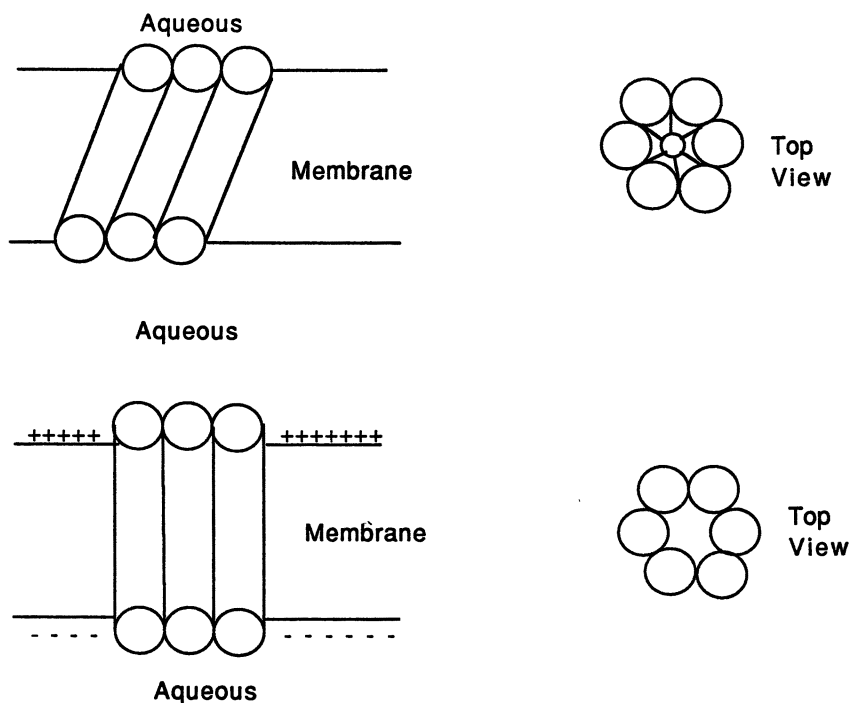


Figure 19. Schematic diagram of the helix realignment mechanism for gating. The closed state of the channel (top) shows the normal nonparallel alignment of helices that optimizes packing of side chains, shown from the side and from above. The application of a transmembrane potential (bottom; indicated by + and -) aligns helix dipoles with the field and increases the diameter of the channel interior due to steric repulsion between monomers.

Summary and Conclusions

Although an amphipathic molecule of adequate length may be essential for pore formation in membranes, the likelihood of a variety of modes of interaction between the lipid, the membrane potential, and other peptide molecules during the association, insertion, and gating phases of ion channel formation is clear. In addition to the helix–turn–helix or helix–hairpin motif, which may play a role in peptaibol and melittin voltage-gating, other mechanisms such as that proposed for the colicins, and the dipole flip-flop may be operative, depending on the peptide and the experimental conditions under study. Experimentally distinguishing between these alternatives provides a challenge for future investigation. One useful approach might be comparison of different peptides under a variety of identical experimental conditions to help define which properties have a specific structural basis. Characterization of the structure of the channel itself when activated by the transmembrane potential requires further development of appropriate experimental techniques, such as spin-labeled electron spin resonance or solid-state NMR (299, 300) approaches.

Acknowledgments

The authors acknowledge the support of a grant (N00014–90–J–1393) from the Office of Naval Research that made preparation of this review possible. In addition, we also thank M. T. Leplawy (Politechnika, Łódź, Poland) and Eduardo Groisman (Washington University) for supplying some of the reference materials, John D. Clark (BIOSYM Technologies, Inc.) for assistance in preparation of figures, David Eisenberg (UCLA) for the coordinates of the defensin dimer, and Horst Kessler (Munich) for the coordinates of Ro-0198.

References

1. Lauger, P. *Angew. Chem. Int. Ed. Engl.* **1985**, *24*, 905–923.
2. Mueller, P.; Rudin, D. O. *Nature (London)* **1968**, *217*, 713–719.
3. Catterall, W. A. *Science (Washington, D.C.)* **1988**, *242*, 50–61.
4. Jan, L. Y.; Jan, Y. N. *Cell* **1989**, *56*, 13–25.
5. Eisenman, G.; Dani, J. A. *Annu. Rev. Biophys. Biophys. Chem.* **1987**, *16*, 205–226.
6. Kaiser, E. T.; Kezdy, F. J. *Annu. Rev. Biophys. Biophys. Chem.* **1987**, *16*, 561–581.
7. Bernheimer, A. W.; Rudy, B. *Biochim. Biophys. Acta* **1986**, *864*, 123–141.
8. Urry, D. W. In *Proteins in the Nervous System: Structure and Function*; Haber, B.; Coulter, J. D.; Perez-Polo, J. R., Eds.; Alan R. Liss, Inc.: New York, 1982; pp 87–111.
9. Spach, G.; Duclouhier, H.; Molle, G.; Valleton, J.-M. *Biochimie* **1989**, *71*, 11–21.
10. Segrest, J. P.; De Loof, H.; Dohlman, J. G.; Brouillette, C. G.; Anantharamaiah, G. M. *Proteins* **1990**, *8*, 103–117.

11. Sarges, R.; Witkop, B. *J. Am. Chem. Soc.* **1964**, *86*, 1861–1862.
12. Sarges, R.; Witkop, B. *J. Am. Chem. Soc.* **1965**, *87*, 2011–2020.
13. Hotchkiss, R. D.; Dubois, R. J. *J. Biol. Chem.* **1940**, *132*, 791–792.
14. Sarkar, N.; Langley, D.; Paulus, H. *Biochemistry* **1979**, *18*, 4536–4541.
15. Fisher, R.; Blumenthal, T. *Proc. Natl. Acad. Sci. U.S.A.* **1982**, *79*, 1045–1048.
16. Mueller, P.; Rudin, D. O. *Biochem. Biophys. Res. Commun.* **1967**, *26*, 398–404.
17. Hladky, S. B.; Haydon, D. A. *Biochim. Biophys. Acta* **1972**, *274*, 294–312.
18. Woolley, G. A.; Wallace, B. A. *J. Membr. Biol.* **1992**, *129*, 109–136.
19. Andersen, O. S. *Annu. Rev. Physiol.* **1984**, *46*, 531–548.
20. Hladky, S. B.; Haydon, D. A. *Curr. Top. Membr. Trans.* **1984**, *21*, 327–372.
21. Wallace, B. A. *Annu. Rev. Biophys. Chem.* **1990**, *19*, 127–157.
22. Urry, D. W.; Goodall, M. C.; Glickson, J. D.; Mayers, D. F. *Proc. Natl. Acad. Sci. U.S.A.* **1971**, *68*, 1907–1911.
23. Veatch, W. T.; Fossel, E. T.; Blout, E. R. *Biochemistry* **1974**, *13*, 5249–5256.
24. Goodall, M. C. *Biochim. Biophys. Acta* **1970**, *219*, 471–478.
25. Tosteson, D. C.; Andreoli, T. E.; Tieffenberg, M.; Cook, P. J. *Gen. Physiol.* **1968**, *51*, 373S–384S.
26. Weinstein, S.; Durkin, J. T.; Veatch, W. R.; Blout, E. R. *Biochemistry* **1985**, *24*, 4374–4382.
27. Stankovic, C. J.; Heinemann, S. H.; Delfino, J. M.; Sigworth, F. J.; Schreiber, S. L. *Science (Washington, D.C.)* **1989**, *244*, 813–817.
28. Nicholson, L. K.; Cross, T. A. *Biochemistry* **1989**, *28*, 9379–9385.
29. Arseniev, A. S.; Barsukov, I. L.; Bystrov, V. F.; Lomize, A. L.; Ovchinnikov, Y. A. *FEBS Lett.* **1985**, *186*, 168–174.
30. Urry, D. W.; Walker, J. T.; Trapane, T. L. *J. Membr. Biol.* **1982**, *69*, 225–231.
31. Urry, D. W.; Long, M. M.; Jacobs, M.; Trapane, T. L. *Proc. Natl. Acad. Sci. U.S.A.* **1982**, *79*, 390–394.
32. Urry, D. W.; Trapane, T. L.; Prasad, K. U. *Science (Washington, D.C.)* **1983**, *221*, 1064–1067.
33. Langs, D. A. *Science (Washington, D.C.)* **1988**, *241*, 188–191.
34. Langs, D. A. *Biopolymers* **1989**, *28*, 259–266.
35. Wallace, B. A.; Ravikumar, K. *Science (Washington, D.C.)* **1988**, *241*, 182–187.
36. Tournois, H.; Killian, J. A.; Urry, D. W.; Bokking, O. R.; de Gier, J.; de Kruijff, B. *Biochim. Biophys. Acta* **1987**, *905*, 222–226.
37. Killian, J. A.; Prasad, K. U.; Hains, D.; Urry, D. W. *Biochemistry* **1988**, *27*, 4848–4855.
38. LoGrasso, P. V.; Mole, F., III; Cross, T. A. *Biophys. J.* **1988**, *54*, 259–267.
39. Bano, M. C.; Braco, L.; Abad, C. *Biochemistry* **1991**, *30*, 886–894.
40. Sawyer, D. B.; Koeppe, R. E., II; Andersen, O. S. *Biophys. J.* **1990**, *57*, 515–523.
41. Gordon, L. G. M.; Haydon, D. A. *Biochim. Biophys. Acta* **1972**, *255*, 1014–1018.
42. Boheim, G. *J. Membr. Biol.* **1974**, *19*, 277–303.
43. Vodyanoy, I.; Bezrukov, S. M. *Biophys. J.* **1992**, *62*, 10–11.
44. Stankowski, S.; Schwarz, U. D.; Schwarz, G. *Biochim. Biophys. Acta* **1988**, *941*, 11–18.
45. Bruckner, H.; Graf, H. *Experientia* **1983**, *39*, 528–530.
46. Duclohier, H.; Molle, G.; Spach, G. *Biochim. Biophys. Acta* **1989**, *987*, 133–136.
47. Balaram, P.; Krishna, K.; Sukumar, M.; Mellor, I. R.; Sansom, M. S. P. *Eur. Biophys. J.* **1992**, *21*, 117–128.

48. Pandey, R. C.; Cook, J. C., Jr.; Rinehart, K. L., Jr. *J. Am. Chem. Soc.* **1977**, *99*, 8469–8483.
49. Przybylski, M.; Dietrich, I.; Manz, I.; Bruckner, H. *Experientia* **1984**, *40*, 1189–1197.
50. Pandey, R. C.; Cook, J. C., Jr.; Rinehart, K. L., Jr. *J. Am. Chem. Soc.* **1977**, *99*, 5205–5206.
51. Pandey, R. C.; Meng, H.; Cook, J. C., Jr.; Rinehart, K. L., Jr. *J. Am. Chem. Soc.* **1977**, *99*, 5203–5205.
52. Argoudelis, A. D.; Johnson, L. E. *J. Antibiot.* **1974**, *27*, 274–282.
53. Jung, G.; Konig, W. A.; Leibfritz, D.; Ooka, T.; Janko, K.; Boheim, G. *Biochim. Biophys. Acta* **1976**, *433*, 164–181.
54. Katz, E.; Aydin, M.; Lucht, N.; Konig, W. A.; Ooka, T.; Jung, G. *Liebigs Ann. Chem.* **1985**, *1985*, 1041–1062.
55. Rebuffat, S.; El Hajji, M.; Hennig, P.; Davoust, D.; Bodo, B. *Int. J. Pept. Protein Res.* **1989**, *34*, 200–210.
56. Molle, G.; Dugast, J.-Y.; Duclohier, H.; Spach, G. *Biochim. Biophys. Acta* **1988**, *938*, 310–314.
57. Spach, G.; Trudelle, Y.; Heitz, F. *Biopolymers* **1983**, *22*, 403–407.
58. Marshall, G. R.; Bosshard, H. E. *Circ. Res.* **1972**, *31* (Suppl. 2), II-143–II-150.
59. Pletnev, V. Z.; Gromov, E. P.; Popov, E. M. *Khim. Prir. Soedin.* **1973**, *9*, 224–229.
60. Burgess, A. W.; Leach, S. J. *Biopolymers* **1973**, *12*, 2599.
61. Prasad, B. V. V.; Sasisekharan, V. *Macromolecules* **1979**, *12*, 1107–1110.
62. Paterson, Y.; Rumsey, S. M.; Benedetti, E.; Nemethy, G.; Scheraga, H. A. *J. Am. Chem. Soc.* **1981**, *103*, 2947–2955.
63. Prasad, B. V. V.; Balaram, P. *Crit. Rev. Biochem.* **1984**, *16*, 307–348.
64. Iijima, H.; Dunbar, J. B., Jr.; Marshall, G. R. *Proteins* **1987**, *2*, 330–339.
65. Karle, I. L.; Balaram, P. *Biochemistry* **1990**, *29*, 6747–6756.
66. Bavoso, A.; Benedetti, E.; Di Blasio, B.; Pavone, V.; Pedone, C.; Toniolo, C.; Bonora, G. M. *Proc. Natl. Acad. Sci. U.S.A.* **1986**, *83*, 1988–1992.
67. Karle, I. L.; Flippen-Anderson, J.; Uma, K.; Balaram, P. *Proc. Natl. Acad. Sci. U.S.A.* **1988**, *85*, 299–303.
68. Toniolo, C.; Bonora, G. M.; Bavoso, A.; Benedetti, E.; Di Blasio, B.; Pavone, V.; Pedone, C. *J. Biomol. Struct. Dyn.* **1985**, *3*, 585–598.
69. Marshall, G. R.; Hodgkin, E. E.; Langs, D. A.; Smith, G. D.; Zabrocki, J.; Leplawy, M. R. *Proc. Natl. Acad. Sci. U.S.A.* **1990**, *87*, 487–491.
70. Basu, G.; Bagchi, K.; Kuki, A. *Biopolymers* **1991**, *31*, 1763–1774.
71. Basu, G.; Kuki, A. *Biopolymers* **1992**, *32*, 61–71.
72. Aleman, C.; Subirana, J. A.; Perez, J. J. *Biopolymers* **1992**, *32*, 621–631.
73. Hodgkin, E. E.; Clark, J. D.; Miller, K. R.; Marshall, G. R. *Biopolymers* **1990**, *30*, 533–546.
74. Clark, J. D.; Hodgkin, E. E.; Marshall, G. R. In *Molecular Conformation and Biological Interactions* (Prof. G. N. Ramachandran Festschrift); Balaram, P.; Ramaseshan, S., Eds.; Indian Academy of Sciences: Bangalore, India, 1991; pp 503–510.
75. Hollenberg, M. *J. Med. Chem.* **1990**, *33*, 1275–1281.
76. Baumann, G.; Mueller, P. *J. Supramol. Struct.* **1974**, *2*, 538–557.
77. Fox, R. O.; Richards, F. M. *Nature (London)* **1982**, *300*, 325–330.
78. Hall, J. E.; Vodyanoy, I.; Balasubramanian, T. M.; Marshall, G. R. *Biophys. J.* **1984**, *45*, 233–247.
79. Vogel, H. *Biochemistry* **1987**, *26*, 4056–4062.
80. Wille, B.; Franz, B.; Jung, G. *Biochim. Biophys. Acta* **1989**, *986*, 47–60.

81. Banerjee, U.; Chan, S. I. *Biochemistry* **1983**, *22*, 3709–3713.
82. Krishnaswamy, S.; Patabhi, V.; *Indian J. Biochem. Biophys.* **1987**, *24*, 1–5.
83. Chandrasekhar, K.; Das, M. K.; Kumar, A.; Balaram, P. *Int. J. Peptide Protein Res.* **1988**, *32*, 167–174.
84. Esposito, G.; Carver, J. A.; Boyd, J.; Campbell, I. D. *Biochemistry* **1987**, *26*, 1043–1050.
85. Fraternali, F. *Biopolymers* **1990**, *30*, 1083–1099.
86. Yee, A. A.; O'Neil, J. D. *Biochemistry* **1992**, *31*, 3135–3143.
87. Kelsh, L. P.; Ellena, J. F.; Cafiso, D. S. *Biochemistry* **1992**, *31*, 5136–5144.
88. Brennan, R. G.; Matthews, B. W. *J. Biol. Chem.* **1989**, *264*, 1903–1906.
89. Engelman, D. M.; Steitz, T. A. *Cell* **1981**, *23*, 411–422.
90. Edmonds, D. T. *Eur. Biophys. J.* **1985**, *13*, 31–35.
91. Menestrina, G.; Voges, K.-P.; Jung, G.; Boheim, G. *J. Membr. Biol.* **1986**, *93*, 111–132.
92. Boheim, G.; Helbig, I.; Meder, S.; Vogel, H.; Nilsson, L.; Rigler, R.; Franz, B.; Jung G. In *Peptides: Chemistry, Structure and Biology*; Rivier, J.; Marshall, G. R., Eds.; ESCOM Scientific Publishers: Leiden, Netherlands, 1990; pp 658–660.
93. Karle, I. L.; Flippen-Anderson, J. L.; Agarwalla, S.; Balaram, P. *Proc. Natl. Acad. Sci. U.S.A.* **1991**, *88*, 5307–5311.
94. Beusen, D. D.; Head, R. D.; Clark, J. D.; Hutton, W. C.; Slomczynska, U.; Zabrocki, J.; Leplawy, M. T.; Marshall, G. R. In *Peptides 1992*; Schneider, C. H., Ed.; ESCOM Scientific Publishers: Leiden, Netherlands; pp 79–80.
95. Ballesteros, J. A.; Weinstein, H. *Biophys. J.* **1992**, *62*, 110–111.
96. Boheim, G.; Hanke, W.; Jung, G. *Biophys. Struct. Mech.* **1983**, *9*, 181–191.
97. Mathew, M. K.; Balaram, P. *FEBS Lett.* **1983**, *157*, 1–5.
98. Hall, J. E.; Vodyanoy, I.; Balasubramanian, T. M.; Marshall, G. R. *Biophys. J.* **1984**, *45*, 39a.
99. Cascio, M.; Wallace, B. A. *Proteins* **1988**, *4*, 89–98.
100. Zasloff, M. *Proc. Natl. Acad. Sci. U.S.A.* **1987**, *84*, 5449–5453.
101. Giovannini, M. G.; Poulter, L.; Gibson, B. W.; Williams, D. H. *Biochem. J.* **1987**, *243*, 113–120.
102. Bevins, C. L.; Zasloff, M. *Annu. Rev. Biochem.* **1990**, *59*, 395–414.
103. Berkowitz, B. A.; Bevins, C. L.; Zasloff, M. A. *Biochem. Pharmacol.* **1990**, *39*, 625–629.
104. Westerhoff, H. V.; Juretic, D.; Hendler, R. W.; Zasloff, M. *Proc. Natl. Acad. Sci. U.S.A.* **1989**, *86*, 6597–6601.
105. Bessalle, R.; Kapitkovsky, A.; Gorea, A.; Shalit, I.; Fridkin, M.; *FEBS Lett.* **1990**, *274*, 151–155.
106. Wade, D.; Boman, A.; Wahlin, B.; Drain, C. M.; Andreu, D.; Boman, H. G.; Merrifield, R. B. *Proc. Natl. Acad. Sci. U.S.A.* **1990**, *87*, 4761–4765.
107. Duclouhier, H.; Molle, G.; Spach, G. *Biophys. J.* **1989**, *56*, 1017–1021.
108. Cruciani, R. A.; Barker, J. L.; Durell, S. R.; Raghunathan, G.; Guy, H. R.; Zasloff, M.; Stanley, E. F. *Eur. J. Pharmacol.* **1992**, *226*, 287–296.
109. Marion, D.; Zasloff, M.; Bax, A. *FEBS Lett.* **1988**, *227*, 21–26.
110. Dickinson, L.; Russell, V.; Dunn, P. E. *J. Biol. Chem.* **1988**, *263*, 19424–19429.
111. Jackson, M.; Mantsch, H. H.; Spencer, J. H. *Biochemistry* **1992**, *31*, 7289–7293.
112. Bessalle, R.; Haas, H.; Gorla, A.; Shalit, I.; Fridkin, M. *Antimicrob. Agents Chemother.* **1992**, *36*, 313–317.
113. Matsuzaki, K.; Harada, M.; Funakoshi, S.; Fujii, N.; Miyajima, K. *Biochim. Biophys. Acta* **1991**, *1063*, 162–170.
114. Easton, P. L.; Hinton, J. F.; Newkirk, D. K. *Biophys. J.* **1990**, *57*, 63–69.
115. Bechinger, B.; Zasloff, M.; Opella, S. J. *Biophys. J.* **1992**, *62*, 12–14.

116. Cuervo, J. H.; Rodriguez, B.; Houghten, R. A. *Peptide Res.* **1988**, *1*, 81–86.
117. Cruciani, R. A.; Barker, J. L.; Zasloff, M.; Chen, H. C.; Colamonici, O. *Proc. Natl. Acad. Sci. U.S.A.* **1991**, *88*, 3792–3796.
118. Edelstein, M. C.; Gretz, J. E.; Bauer, T. J.; Fulgham, D. L.; Alexander, N. J.; Archer, D. F. *Fertil. Steril.* **1991**, *55*, 647–649.
119. Gross, E.; Morell, J. L. *J. Am. Chem. Soc.* **1971**, *93*, 4634–4635.
120. Wakamiya, T.; Fukase, K.; Naruse, N.; Konishi, M.; Shiba, T. *Tetrahedron Lett.* **1988**, *29*, 4771–4772.
121. Kessler, H.; Steuernagel, S.; Will, M.; Jung, G.; Kellner, R.; Gillessen, D.; Kamiyama, T. *Helv. Chim. Acta* **1988**, *71*, 1924–1929.
122. Kellner, R.; Jung, G.; Horner, T.; Zahner, H.; Schnell, N.; Entian, K.; Gotz, F. *Eur. J. Biochem.* **1988**, *177*, 53–59.
123. Schnell, N.; Entian, K.-D.; Schneider, U.; Gotz, F.; Zahner, H.; Kellner, R.; Jung, G. *Nature (London)* **1988**, *333*, 276–278.
124. Gross, E.; Kiltz, H. H.; Craig, L. C. *Hoppe-Seyler's Z. Physiol. Chem.* **1973**, *354*, 799–801.
125. Allgaier, H.; Jung, G.; Werner, R. G.; Schneider, U.; Zahner, H. *Angew. Chem. Int. Ed. Engl.* **1985**, *24*, 1051–1053.
126. Kettenring, J. K.; Malabarba, A.; Vekey, K.; Cavalleri, B. *J. Antibiot.* **1990**, *18*, 1082–1088.
127. Fredenhagen, A.; Fendrich, G.; Marki, F.; Marki, W.; Gruner, J.; Raschdorf, F.; Peter, H. H. *J. Antibiot. (Tokyo)* **1990**, *43*, 1403–1412.
128. Naruse, N.; Tenmyo, O.; Tomita, K.; Konishi, M.; Miyaki, T.; Kawaguchi, H.; Fukase, K.; Wakamiya, T.; Shiba, T. *J. Antibiot. (Tokyo)* **1989**, *42*, 837–845.
129. Hayashi, F.; Nagashima, K.; Terui, Y.; Kawamura, Y.; Matsumoto, K.; Itazaki, H. *J. Antibiot. (Tokyo)* **1990**, *43*, 1421–1430.
130. Sahl, H.-G.; Grossgarten, M.; Widger, W. R.; Cramer, W. A.; Brandis, H. *Antimicrob. Agents Chemother.* **1985**, *27*, 836–840.
131. Chatterjee, S.; Chatterjee, S.; Lad, S. J.; Phansalkar, M. S.; Rupp, R. H.; Ganguli, B. N.; Fehlhaber, H. W.; Kogler, H. *J. Antibiot. (Tokyo)* **1992**, *45*, 832–838.
132. Sahl, H.-G.; Kordel, M.; Benz, R. *Arch. Microbiol.* **1987**, *149*, 120–124.
133. Kordel, M.; Schuller, F.; Sahl, H.-G. *FEBS Lett.* **1989**, *244*, 99–102.
134. Schuller, F.; Benz, R.; Sahl, H.-G. *Eur. J. Biochem.* **1989**, *182*, 181–186.
135. Kordel, M.; Benz, R.; Sahl, H.-G. *J. Bacteriol.* **1988**, *170*, 84–88.
136. Wakamiya, T.; Ueki, Y.; Shiba, T.; Kido, Y.; Motoki, Y. *Tetrahedron Lett.* **1985**, *26*, 665–668.
137. Wakamiya, T.; Ueki, Y.; Shiba, T.; Kido, Y.; Motoki, Y. *Bull. Chem. Soc. Jpn.* **1990**, *63*, 1032–1038.
138. Kessler, H.; Steuernagel, S.; Gillessen, D.; Kamiyama, T. *Helv. Chim. Acta* **1987**, *70*, 726–740.
139. Choung, S. Y.; Kobayashi, T.; Takemoto, K.; Ishitsuka, H.; Inoue, K.; *Biochim. Biophys. Acta* **1988**, *940*, 180–187.
140. Wakamatsu, K.; Choung, S.-Y.; Kobayashi, T.; Inoue, K.; Higashijima, T.; Miyazawa, T. *Biochemistry* **1990**, *29*, 113–118.
141. Sheth, T. R.; Henderson, R. M.; Hladky, S. B.; Cuthbert, A. W. *Biochim. Biophys. Acta* **1992**, *1107*, 179–185.
142. Lian, L. Y.; Chan, W. C.; Morley, S. D.; Roberts, G. C.; Bycroft, B. W.; Jackson, D. *Biochem. J.* **1992**, *283*, 2.
143. Palmer, D. E.; Goodman, M. *Biophys. J.* **1990**, *57*, 406.
144. Van de Ven, F. J.; Van den Hooven, H. W.; Konings, R. N.; Hilbers, C. W. *Eur. J. Biochem.* **1991**, *202*, 1181–1188.

145. Higashijima, T.; Burnier, J.; Ross, E. M. *J. Biol. Chem.* **1990**, *265*, 14176–14186.
146. Freund, S.; Jung, G.; Gutbrod, O.; Folkers, G.; Gibbons, W. A.; Allgaier, H.; Werner, R. *Biopolymers* **1991**, *31*, 803–811.
147. Dimarcq, J.-L.; Keppi, E.; Dunbar, B.; Lambert, J.; Reichhart, J.-M.; Hoffman, D.; Rankine, S. M.; Fothergill, J. F.; Hoffman, J. A. *Eur. J. Biochem.* **1988**, *171*, 17–22.
148. Carlsson, A.; Engstrom, P.; Palva, E. T.; Bennich, H. *Infect. Immun.* **1991**, *59*, 3040–3045.
149. Skerlavaj, B.; Romeo, D.; Gennaro, R. *Infect. Immun.* **1990**, *58*, 3724–3730.
150. Romeo, D.; Skerlavaj, B.; Bolognesi, M.; Gennaro, R. *J. Biol. Chem.* **1988**, *263*, 9573–9575.
151. Gennaro, R.; Skerlavaj, B.; Romeo, D. *Infect. Immun.* **1989**, *57*, 3142–3146.
152. Ganz, T.; Selsted, M. E.; Lehrer, R. I. *Eur. J. Haematol.* **1990**, *44*, 1–8.
153. Lehrer, R. I.; Ganz, T.; Selsted, M. E. *Cell* **1991**, *64*, 229–230.
154. Selsted, M. E.; Miller, S. I.; Henschen, A. H.; Ouellette, A. J. *J. Cell Biol.* **1992**, *118*, 929–936.
155. Eisenhauer, P. B.; Harwig, S. S. S. L.; Lehrer, R. I. *Infect. Immun.* **1992**, *60*, 3556–3565.
156. Kagan, B. L.; Selsted, M. E.; Ganz, T.; Lehrer, R. I. *Proc. Natl. Acad. Sci. U.S.A.* **1990**, *87*, 210–214.
157. Lehrer, R. I.; Barton, A.; Daher, K. A.; Harwig, S. S.; Ganz, T.; Selsted, M. E. *J. Clin. Invest.* **1989**, *84*, 553–561.
158. Zhang, X.-L.; Selsted, M. E.; Pardi, A. *Biochemistry* **1992**, *31*, 11357–11364.
159. Pardi, A.; Hare, D. R.; Selsted, M. E.; Morrison, R. D.; Bassolino, D. A.; Bach, A. C., III *J. Mol. Biol.* **1988**, *201*, 625–636.
160. Hill, C. P.; Yee, J.; Selsted, M. E.; Eisenberg, D. *Science (Washington, D.C.)* **1991**, *251*, 1481–1485.
161. Hoffmann, J. A.; Hetru, C. *Immun. Today* **1992**, *13*, 411–415.
162. Lambert, J.; Keppi, E.; Dimarcq, J.-L.; Wicker, C.; Reichhart, J.-M.; Dunbar, B.; Lepage, P.; Van Dorsselaer, A.; Hoffman, J.; Fothergill, J. F.; Hoffman, D. *Proc. Natl. Acad. Sci. U.S.A.* **1989**, *86*, 262–266.
163. Fujiwara, S.; Imai, J.; Fujiwara, M.; Yaeshima, T.; Kawashima, T.; Kobayashi, K. *J. Biol. Chem.* **1990**, *265*, 11333–11337.
164. Matsuyama, K.; Natori, S. *J. Biochem.* **1990**, *108*, 128–132.
165. Hanzawa, H.; Shimada, I.; Kuzuhara, T.; Komano, H.; Kohda, D.; Inagaki, S.; Arata, Y. *FEBS Lett.* **1990**, *269*, 413–420.
166. Kuzuhara, T.; Nakajima, Y.; Matsuyama, K.; Natori, S. *J. Biochem.* **1990**, *107*, 514–518.
167. Bontems, F.; Roumestand, C.; Gilquin, B.; Menez, A.; Toma, F. *Science (Washington, D.C.)* **1991**, *254*, 1521–1523.
168. Bonmatin, J. M.; Bonnat, J. L.; Gallet, X. *J. Biomol. NMR* **1992**, *2*, 235–256.
169. Boman, H.; Hultmark, K. *Annu. Rev. Microbiol.* **1987**, *41*, 103–126.
170. Samakovlis, C.; Kimbrell, D. A.; Kylsten, P.; Engstrom, A.; Hultmark, D. *EMBO J.* **1990**, *9*, 2969–2976.
171. Okada, M.; Natori, S. *Biochem. J.* **1985**, *229*, 453–458.
172. Christensen, B.; Fink, J.; Merrifield, R. B.; Mauzerall, D. *Proc. Natl. Acad. Sci. U.S.A.* **1988**, *85*, 5072–5076.
173. Fink, J.; Boman, A.; Boman, H. G.; Merrifield, R. B. *Int. J. Peptide Protein Res.* **1989**, *33*, 412–421.
174. Andreu, D.; Merrifield, R. B.; Steiner, H.; Boman, H. G. *Biochemistry* **1985**, *24*, 1683–1688.

175. Holak, T. A.; Engstrom, A.; Kraulis, P. J.; Lindeberg, G.; Bennich, H.; Jones, T. A.; Gronenborn, A. M.; Clore, G. M. *Biochemistry* **1988**, *27*, 7620–7629.
176. Sipos, D.; Andersson, M.; Ehrenberg, A. *Eur. J. Biochemistry* **1992**, *209*, 163–169.
177. Nakamura, T.; Furunaka, H.; Miyata, T.; Tokunaga, F.; Muta, T.; Iwanaga, S.; Niwa, M.; Takao, T.; Shimonishi, Y. *J. Biol. Chem.* **1988**, *263*, 16709–16713.
178. Kawano, K.; Yoneya, T.; Miyata, T.; Tokunaga, F.; Terada, Y.; Iwanaga, S. *J. Biol. Chem.* **1990**, *265*, 15365–15367.
179. Ohta, M.; Ito, H.; Masuda, K.; Tanaka, S.; Arakawa, Y.; Wacharotayankun, R.; Kato, N. *Antimicrob. Agents Chemother.* **1992**, *36*, 1460–1465.
180. Matsuzaki, K.; Fukui, M.; Fujii, N.; Miyajima, K. *Biochim. Biophys. Acta* **1991**, *1070*, 259–264.
181. Argiolas, A.; Pisano, J. J. *J. Biol. Chem.* **1985**, *260*, 1437–1444.
182. Bairaktari, E.; Mierke, D. F.; Mammi, S.; Peggion, E. *Biochemistry* **1990**, *29*, 10097–10102.
183. Bairaktari, E.; Mierke, D. F.; Mammi, S.; Peggion, E. *Biochemistry* **1990**, *29*, 10090–10096.
184. Tosteson, M. T.; Tosteson, D. C. *Biophys. J.* **1981**, *36*, 109–116.
185. Tosteson, M. T.; Levy, J. J.; Caporale, L. H.; Rosenblatt, M.; Tosteson, D. C. *Biochemistry* **1987**, *26*, 6627–6631.
186. Terwilliger, T. C.; Eisenberg, D. *J. Biol. Chem.* **1982**, *257*, 6016–6022.
187. Terwilliger, T. C.; Eisenberg, D. *J. Biol. Chem.* **1982**, *257*, 6010–6015.
188. Bazzo, R.; Tappin, M. J.; Pastore, A.; Harvey, T. S.; Carver, J. A.; Campbell, I. D. *Eur. J. Biochem.* **1988**, *173*, 139–146.
189. Pastore, A.; Harvey, T. S.; Dempsey, C. E.; Campbell, I. D. *Eur. Biophys. J.* **1989**, *16*, 363–367.
190. Ikura, T.; Go, N.; Inagaki, F. *Proteins* **1991**, *9*, 81–89.
191. Inagaki, F.; Shimada, I.; Kawaguchi, K.; Hirano, M.; Terasawa, I.; Ikura, T.; Go, N. *Biochemistry* **1989**, *28*, 5985–5991.
192. Dempsey, C. E. *Biochim. Biophys. Acta* **1990**, *1031*, 143–161.
193. Altenbach, C.; Hubbell, W. L. *Proteins: Struct. Funct. Genet.* **1988**, *3*, 230–242.
194. Altenbach, C.; Froncisz, W.; Hyde, J. S.; Hubbell, W. L. *Biophys. J.* **1989**, *56*, 1183–1191.
195. Frey, S.; Tamm, L. K. *Biophys. J.* **1991**, *60*, 922–930.
196. Dempsey, C. E.; Bazzo, R.; Harvey, T. S.; Syperek, I.; Boheim, G.; Campbell, I. D. *FEBS Lett.* **1991**, *281*, 240–244.
197. Talbot, J. C.; Faucon, J. F.; Dufourcq, J. *Eur. Biophys. J.* **1987**, *15*, 147–157.
198. Vogel, H.; Jahnig, F. *Biophys. J.* **1986**, *50*, 573–582.
199. Brauner, J. W.; Mendelson, R.; Prendergast, F. G. *Biochemistry* **1987**, *26*, 8151–8158.
200. Andreu, D.; Ubach, J.; Boman, A.; Wahlin, B.; Wade, D.; Merrifield, R. B.; Boman, H. G. *FEBS Lett.* **1992**, *296*, 190–194.
201. Boman, H. G.; Wade, D.; Boman, I. A.; Wahlin, B.; Merrifield, R. B. *FEBS Lett.* **1989**, *259*, 103–106.
202. Nakajima, T.; Yasuhara, T.; Uzu, S.; Wakamatsu, K.; Miyazawa, T.; Fukuda, K.; Tsukamoto, Y. *Peptides* **1985**, *6*, 425–430.
203. Malencik, D. A.; Anderson, S. R. *Biochem. Biophys. Res. Comm.* **1986**, *135*, 1050–1057.
204. Mellor, I. R.; Sansom, M. S. P. *Proc. R. Soc. London B* **1990**, *239*, 383–400.
205. de Kroon, A. I.; de Gier, J.; de Kruijff, B. *Biochim. Biophys. Acta* **1991**, *1068*, 111–124.

206. Wakamatsu, K.; Okada, A.; Miyazawa, T.; Ohya, M.; Higashijima, T. *Biochemistry* **1992**, *31*, 5654–5660.
207. Tanimura, A.; Matsumoto, Y.; Tojyo, Y. *Biochem. Biophys. Res. Commun.* **1991**, *177*, 802–808.
208. Haberman, E. *Science (Washington, D.C.)* **1972**, *177*, 314–322.
209. Ziai, M. R.; Russek, S.; Wang, H. C.; Beer, B.; Blume, A. J. *J. Pharm. Pharmacol.* **1990**, *42*, 457–461.
210. Ide, T.; Taguchi, T.; Morita, T.; Sato, M.; Ikenaka, K.; Aimoto, S.; Kondo, T.; Hojo, H.; Kasai, M.; Mikoshiba, K. *Biochem. Biophys. Res. Comm.* **1989**, *163*, 155–160.
211. Kumar, N. V.; Wemmer, D. E.; Kallenbach, N. R. *Biophys. Chem.* **1988**, *31*, 113–119.
212. Bystrov, V. F.; Okhanov, V. V.; Miroshnikov, A. I.; Ovchinnikov, Y. A. *FEBS Lett.* **1980**, *119*, 113–117.
213. Pease, J. H.; Wemmer, D. E. *Biochemistry* **1988**, *27*, 8491–8498.
214. Wemmer, D.; Kallenbach, N. R. *Biochemistry* **1983**, *22*, 1901–1906.
215. Schweitz, H.; Bidard, J.-N.; Maes, P.; Lazdunski, M. *Biochemistry* **1989**, *28*, 9708–9714.
216. Mellor, I. R.; Thomas, D. H.; Sansom, M. S. P. *Biochim. Biophys. Acta* **1988**, *942*, 280–294.
217. Tappin, M. J.; Pastore, A.; Norton, R. S.; Freer, J. H.; Campbell, I. D. *Biochemistry* **1988**, *27*, 1643–1647.
218. Thomas, D. H.; Rice, D. W.; Fitton, J. E. *J. Mol. Biol.* **1986**, *192*, 675–676.
219. Raghunathan, G.; Seetharamulu, P.; Brooks, B. R.; Guy, H. R. *Proteins* **1990**, *8*, 213–225.
220. Garone, L.; Fitton, J. F.; Steiner, R. F. *Biophys. Chem.* **1988**, *31*, 231–245.
221. Takahashi, S. *Biochemistry* **1990**, *29*, 6257–6264.
222. Duzgunes, N.; Gambale, F. *FEBS Lett.* **1988**, *227*, 110–114.
223. Goessens, W. H. F.; Driessen, A. J. M.; Wilschut, J.; van Druijn, J. *EMBO J.* **1988**, *7*, 867–873.
224. Gierasch, L. M. *Biochemistry* **1989**, *28*, 923–930.
225. Jones, J. D.; McKnight, C. J.; Gierasch, L. M. *J. Bioenerg. Biomembr.* **1990**, *22*, 213–232.
226. Tosteson, M. T.; Caulfield, M. P.; Levy, J. J.; Rosenblatt, M.; Tosteson, D. C. *BioScience Rep.* **1988**, *8*, 173–183.
227. Lee, S.; Mihara, H.; Aoyagi, H.; Kato, T.; Izumiya, N.; Yamasaki, N. *Biochim. Biophys. Acta* **1986**, *862*, 211–219.
228. Oiki, S.; Danho, W.; Montal, M. *Proc. Natl. Acad. Sci. U.S.A.* **1988**, *85*, 2393–2397.
229. Tosteson, M. T.; Auld, D. S.; Tosteson, D. C. *Proc. Natl. Acad. Sci. U.S.A.* **1989**, *86*, 707–710.
230. Noda, M.; Shimizu, S.; Tanabe, T.; Takai, T.; Kayano, T.; Kurasaki, M.; Takahashi, H.; Numa, S. *Nature (London)* **1984**, *312*, 121–127.
231. Noda, M.; Ikeda, T.; Kayano, T.; Suzuki, H.; Takeshima, H.; Ikeda, T.; Takahashi, H.; Nakayama, H.; Kanaoka, Y.; Minamino, N.; Kangawa, K.; Matsuo, H.; Raftery, M.; Hirose, T.; Inayama, S.; Hayashida, H.; Miyata, T.; Numa, S. *Nature (London)* **1986**, *320*, 188–192.
232. Kosower, E. M. *FEBS Lett.* **1985**, *182*, 234–242.
233. Greenblatt, R. E.; Blatt, Y.; Montal, M. *FEBS Lett.* **1985**, *193*, 125–134.
234. Guy, H. R.; Seetharamulu, P. *Proc. Natl. Acad. Sci. U.S.A.* **1986**, *83*, 508–512.
235. Guy, H. R. In *Monovalent Cations in Biological Systems*; Pasternak, C. A., Ed.; CRC Press: Boca Raton, FL, 1990; pp 31–58.

236. Montal, M. In *Ion Channels*; Narahashi, T., Ed.; Plenum: New York, 1990; pp 1–31.
237. Oiki, S.; Madison, V.; Montal, M. *Proteins: Struct., Funct., Genet.* **1990**, *8*, 226–236.
238. Montal, M. *J. Membr. Biol.* **1972**, *7*, 245–266.
239. Yellin, G.; Jurman, M. E.; Abramson, T.; MacKinnon, R. *Science (Washington, D.C.)*, **1991**, *251*, 939–942.
240. Hartmann, H. A.; Kirsch, G. E.; Drewe, J. A.; Tagliatela, M.; Joho, R. H.; Brown, A. M. *Science (Washington, D.C.)* **1991**, *251*, 9942–9944.
241. Oiki, S.; Danho, W.; Madison, V.; Montal, M. *Proc. Natl. Acad. Sci. U.S.A.* **1988**, *85*, 8703–8707.
242. Kersh, G. J.; Tomich, J. C.; Montal, M. *Biochem. Biophys. Res. Commun.* **1989**, *162*, 352–356.
243. Molle, G.; Dugast, J.-Y.; Duclohier, H.; Daumas, P.; Heitz, F.; Spach, G. *Biophys. J.* **1988**, *53*, 193–203.
244. Kuchinka, E.; Seelig, J. *Biochemistry* **1989**, *28*, 4216–4221.
245. Beschiaschvili, G.; Seelig, J. *Biochemistry* **1990**, *29*, 52–58.
246. Portlock, S. H.; Clague, M. J.; Cherry, R. J. *Biochim. Biophys. Acta* **1990**, *1030*, 1–10.
247. Hartsel, S. C.; Benz, S. K.; Peterson, R. P.; Whyte, B. S. *Biochemistry* **1991**, *30*, 77–82.
248. Cevc, G. *Biochim. Biophys. Acta* **1990**, *1031*, 311–382.
249. Groisman, E. A. *Proc. Natl. Acad. Sci. U.S.A.* **1992**, *89*, 11939–11943.
250. McLean, L. R.; Hagaman, K. A.; Owen, T. J.; Krstenansky, J. L. *Biochemistry* **1991**, *30*, 31–37.
251. Vodyanoy, I.; Hall, J. E. *Biophys. J.* **1984**, *46*, 187–194.
252. Deisenhofer, J.; Michel, H. *Science (Washington, D.C.)* **1989**, *245*, 1463–1473.
253. Wiener, M. C.; White, S. H. *Biophys. J.* **1992**, *61*, 434–447.
254. Weaver, J. C.; Mintzer, R. A. *Phys. Lett.* **1981**, *86A*, 57–59.
255. Adams, G. A.; Rose, J. K. *Cell* **1985**, *41*, 1007–1015.
256. Davis, N. G.; Boeke, J. D.; Model, P. *J. Mol. Biol.* **1985**, *181*, 111–121.
257. Watnick, P. I.; Chan, S. I. *Biochemistry* **1990**, *29*, 6215–6221.
258. Helfrich, P.; Jakobsson, E. *Biophys. J.* **1990**, *57*, 1075–1084.
259. Altenbach, C.; Marti, T.; Khorana, H. G.; Hubbell, W. L. *Science (Washington, D.C.)* **1990**, *248*, 1088–1092.
260. Popot, J.-L.; Engelman, D. M. *Biochemistry* **1990**, *29*, 4031–4037.
261. Jahnig, F. *Proc. Natl. Acad. Sci. U.S.A.* **1983**, *80*, 3691–3695.
262. Kaiser, C. A.; Preuss, D.; Grisafi, P.; Botstein, D. *Science (Washington, D.C.)* **1987**, *235*, 312–317.
263. Cornell, D. G.; Dluhy, R. A.; Briggs, M. S.; McKnight, C. J.; Gierasch, L. M. *Biochemistry* **1989**, *28*, 2789–2797.
264. Sankararmakrishnan, R.; Vishveshwara, S. *Biopolymers* **1990**, *30*, 287–298.
265. Woolfson, D. N.; Williams, D. H. *FEBS Lett.* **1990**, *277*, 185–188.
266. Brandl, C. J.; Deber, C. M. *Proc. Natl. Acad. Sci. U.S.A.* **1986**, *83*, 917–921.
267. Urry, D. W. *Int. J. Quantum. Chem.: Quantum. Biol. Symp.* **1975**, *2*, 221–235.
268. Karlake, C.; Piotto, M. E.; Pak, Y. K.; Weiner, H.; Gorenstein, D. G. *Biochemistry* **1990**, *29*, 9872–9878.
269. von Heijne, G.; Blomberg, C. *Eur. J. Biochem.* **1979**, *97*, 175–181.
270. Inouye, M.; Haleboua, S. *CRC Crit. Rev. Biochem.* **1980**, *7*, 339–371.
271. von Heijne, G.; Steppuhn, J.; Herrman, R. G. *Eur. J. Biochem.* **1989**, *180*, 535–545.
272. Jacobs, R. E.; White, S. H. *Biochemistry* **1989**, *28*, 3421–3437.

273. Presta, L. G.; Rose, G. D. *Science (Washington, D.C.)* **1988**, *240*, 1632–1641.
274. Richardson, J. S.; Richardson, D. C. *Science (Washington, D.C.)* **1988**, *240*, 1648–1652.
275. Serrano, L.; Fersht, A. R. *Nature (London)* **1989**, *342*, 296–299.
276. Kini, R. M.; Evans, H. J. *Int. J. Peptide Protein Chem.* **1989**, *34*, 277–286.
277. Pollard, H. B.; Burns, A. L.; Rojas, E. J. *Membr. Biol.* **1990**, *117*, 101–112.
278. Kennedy, S. J. *J. Membr. Biol.* **1978**, *42*, 265–279.
279. Jap, B. K.; Walian, P. J.; Gehring, K. *Nature (London)* **1991**, *350*, 167–170.
280. von Heijne, G.; Manoil, C. *Protein Eng.* **1990**, *4*, 109–112.
281. Blachly-Dyson, E.; Peng, S.; Colombini, M.; Forte, M. *Science (Washington, D.C.)* **1990**, *247*, 1233–1236.
282. Singer, S. J. *Annu. Rev. Cell Biol.* **1990**, *6*, 247–296.
283. Mutter, M.; Vuilleumier, S. *Angew. Chem. Int. Ed. Engl.* **1989**, *28*, 535–54.
284. Hall, J. E.; Balasubramanian, T. M.; Hing, A.; Marshall, G. R. In *Peptides: Structure and Function*; Hruby, V. J.; Rich, D. H., Eds.; Pierce Chemical Company: Rockford, IL, 1983; pp 487–490.
285. Vodyanoy, I.; Marshall, G. R.; Chiu, F. *Biophys. J.* **1989**, *55*, 333a.
286. Montal, M.; Montal, M. S.; Tomich, J. M. *Proc. Natl. Acad. Sci. U.S.A.* **1990**, *87*, 6929–6933.
287. Grove, A.; Tomich, J. M.; Montal, M. *Proc. Natl. Acad. Sci. U.S.A.* **1991**, *88*, 6418–6422.
288. Lakey, J. H.; Gonzalez-Manas, J. M.; van der Goot, F. G.; Pattus, F. *FEBS Lett.* **1992**, *307*, 26–29.
289. Cramer, W. A.; Cohen, F. S.; Merrill, A. R.; Song, H. Y. *Mol. Microbiol.* **1990**, *4*, 519–526.
290. Lazdunski, C. J.; Baty, D.; Geli, V.; Cavard, D.; Morlon, J.; Llobes, R.; Howard, S. P.; Knibiehler, M.; Chartier, M.; Varenne, S.; Frenette, M.; Dasseux, J.-L.; Pattus, F. *Biochim. Biophys. Acta* **1988**, *947*, 445–464.
291. Massotte, D.; Dasseux, J.-L.; Sauve, P.; Cyrkclaff, M.; Leonard, K.; Pattus, F. *Biochemistry* **1989**, *28*, 7713–7719.
292. Slatin, S. L.; Raymond, L.; Finkelstein, A. J. *Membr. Biol.* **1986**, *92*, 247–254.
293. Parker, M. W.; Postma, J. P.; Pattus, F.; Tucker, A. D.; Tsernoglou, D. J. *Mol. Biol.* **1992**, *224*, 639–657.
294. Wormald, M. R.; Merrill, A. R.; Cramer, W. A.; Williams, R. J. P. *Eur. J. Biochem.* **1990**, *191*, 155–161.
295. Parker, M. W.; Tucker, A. D.; Tsernoglou, D.; Pattus, F. *Trends Biochem. Sci.* **1990**, *15*, 126–129.
296. Chou, K.-C.; Nemethy, G.; Scheraga, H. A. *Acc. Chem. Res.* **1990**, *23*, 134–141.
297. Henderson, R.; Baldwin, J. M.; Ceska, T. A.; Zemlin, F.; Beckmann, E.; Downing, K. H. *J. Mol. Biol.* **1990**, *213*, 899–929.
298. Lear, J. D.; Wasserman, Z. R.; DeGrado, W. F. *Science (Washington, D.C.)* **1988**, *240*, 1177–1181.
299. Marshall, G. R.; Beusen, D. D.; Kocielek, K.; Redlinski, A. S.; Leplawy, M. T.; Pan, Y.; Schaefer, J. *J. Am. Chem. Soc.* **1990**, *112*, 963–966.
300. Creuzet, F.; McDermott, A.; Gebhard, R.; van der Hoef, K.; Spijker-Assink, M. B.; Herzfeld, J.; Lugtenburg, J.; Levitt, M. H.; Griffin, R. G. *Science (Washington, D.C.)* **1991**, *251*, 783–786.
301. Wallace, B. A. *Biophys. J.* **1986**, *49*, 295–306.
302. Sakmann, B.; Boheim, G. *Nature (London)* **1979**, *282*, 336–339.

RECEIVED for review April 10, 1991. ACCEPTED revised manuscript February 11, 1993.

Genetic Approaches to Electrogenic Proton Transport by a Yeast H⁺-ATPase

D. S. Perlin¹, D. Seto-Young¹, B. C. Monk¹, S. L. Harris², S. Na²,
and J. E. Haber²

¹Department of Biochemistry, The Public Health Research Institute,
New York, NY 10016

²Department of Biology, Brandeis University, Waltham, MA 02254

A genetic approach is used to probe electrogenic proton transport by the Saccharomyces cerevisiae plasma membrane H⁺-ATPase (PMA1). Mutations in PMA1, selected by growth resistance to hygromycin B, cause a depolarization of cellular membrane potential. Enzyme from one mutant, pma1-105 (Ser368 → Phe), is largely insensitive to imposed membrane voltage and appears to catalyze electroneutral H⁺ transport. A countercurrent of K⁺ may provide charge compensation in this enzyme. Second-site mutations that partially revert the pma1-105 phenotype were identified within the membrane sector and provide strong evidence for coupling between cytoplasmic and membrane domains. Mutations conferring hygromycin B resistance have been identified in both cytoplasmic and membrane domains, and multiple transmembrane segments are presumed to be important for electrogenic H⁺ transport. However, a special emphasis is placed on the role of transmembrane segments 1 and 2, which provide the starting point for a more inclusive structural model of the membrane sector.

Approaching a Proton Transport Mechanism

Enzyme-linked proton transport systems have recently become the focus of intense molecular scrutiny. Such studies have established some of the ground work necessary to investigate long-standing mechanistic questions: (1) Can a translocation mechanism that moves H⁺ be defined at the molecular level? (2) Can such a mechanism accommodate the transport of other ions like Na⁺,

0065-2393/94/0235-0315\$08.00/0
© 1994 American Chemical Society

K^+ , and Ca^{2+} ? To address these questions properly requires a better understanding of the three-dimensional structure of transport enzymes, the identification of principal amino acids that participate in the translocation reaction, and an appreciation of the protein molecular dynamics that contribute to ion binding (and release) and movement in the translocation domain.

Few examples exist where the molecular architecture of a transport protein can be described at high resolution (1, 2). Difficulties arise because of the amphipathic character and preference of membrane proteins for a hydrophobic environment. These properties make the growth of suitably diffracting three-dimensional crystals difficult (3). The difficulties inherent in visualizing these structures at high resolution have prompted most investigators to rely on theoretical predictions for membrane protein disposition (4) and structure (5). Models derived from theoretical considerations are generally two-dimensional topographic maps that readily predict the sequences of hydrophobic amino acids that lie within the membrane but fail to predict the spatial relationships of individual amino acids or protein structure elements. Nonetheless, this modeling approach can be an extremely valuable tool in targeting putative amino acids that may participate in the transport reaction.

The application of site-directed mutagenesis for investigating amino acid functionality has provided a significant advance in attempts to probe the molecular basis of proton translocation. Numerous studies that encompass diverse proton transport systems have provided evidence for the role of membrane-embedded charged amino acids in the transport reaction. These amino acids include Glu, Asp, Lys, Arg, and other residues capable of acid-base reactions such as His and Tyr. In several systems, models to describe localized proton binding and release have emerged (2, 6, 7), but a generalized transport scheme has not been forthcoming.

The essential role of protein structure dynamics as a mechanistic consideration in proton transport has focused attention on amino acids such as proline (8, 9), which can confer localized flexibility within and between helical segments. Except for the unique case of bacteriorhodopsin, which is amenable to spectroscopic examination (10), little is known about the nature of molecular dynamics in transport enzymes.

The Yeast H^+ -ATPase as a Model System

The plasma membrane H^+ -ATPase from *Saccharomyces cerevisiae* is a highly electrogenic proton pump that maintains cellular membrane potentials in excess of -200 mV. This enzyme is used as a model system to probe the mechanism of electrogenic proton transport because it is readily amenable to genetic, biochemical, and biophysical analysis. The H^+ -ATPase plays an essential role in intracellular pH regulation and maintenance of electrochemi-

cal proton gradients across the plasma membrane (11); it belongs to the P-type family of ion-translocating ATPases that form acyl phosphate intermediates during catalysis and are sensitive to inhibition by vanadate (12). The gene encoding the H⁺-ATPase, *PMA1*, has been cloned and sequenced (13) and subjected to extensive mutagenesis for the purpose of functional mapping (14, 15). A high degree of amino acid sequence and structural homology has been observed with H⁺-ATPases from other fungi and plants, as well as for more distantly related enzymes like the Na⁺-K⁺-ATPase and Ca²⁺-ATPase (13, 16). The H⁺-ATPase can be purified and reconstituted in liposomes, and its electrogenic transport properties characterized in vitro (17). These features make the yeast H⁺-ATPase an attractive enzyme for the study of charge-transfer reactions.

The isolation of *pmal* mutants that are resistant to the aminoglycoside antibiotic hygromycin B (18) has provided the opportunity to probe the charge-transfer process in the H⁺-ATPase. These hygromycin B resistant cells have a defect in the H⁺-ATPase that causes a generalized depolarization of cellular membrane potential (19). This chapter will discuss how random mutations in *PMA1* may help identify putative transmembrane structures participating in electrogenic proton transport.

Genetic Probing of Electrogenic Proton Transport

Genetic approaches to analysis of molecular structure and function can be divided into two types. Nonrandom site-directed mutagenesis targets specific amino acids and is most successfully applied when elements of structure are reasonably well understood. The more classical, random mutagenesis approach does not require assumptions to be made about essential residues. Random mutagenesis has the advantage that numerous and diverse functionally defective mutants can be isolated. This latter approach was selected for initial probe studies of *PMA1*. Random mutagenesis required a special selection procedure to address the problem that the H⁺-ATPase is essential for cell growth and gross perturbation of enzyme function is lethal to the cell. A positive selection method for isolating *pmal* mutants was developed based on growth resistance of cells to the aminoglycoside antibiotic hygromycin B. The initial screen generated a collection of 53 *pmal* mutants with a wide range of cellular phenotypes including sensitivity to low external pH, weak acid loading (0.1-M acetate, pH 5.0), and NH₄⁺ (18). All of the mutant enzymes characterized were found to have kinetic defects that decreased the maximum initial velocity (V_{\max}) or the Michaelis-Menten constant (K_m) for ATP hydrolysis, and several mutant enzymes were insensitive to vanadate-induced inhibition (15). The cellular basis for growth resistance to hygromycin B was experimentally determined to be a deficiency in the maintenance of the normal hyperpolarized membrane potential in yeast (19). This potential

has been estimated to exceed -200 mV (20). Because direct electrophysiological examination of yeast is not possible, the lipophilic distribution probe tetraphenylphosphonium (TPP) was used as a representative measure of cellular membrane potential. Figure 1 illustrates that mutant cells metabolizing glucose take up 2.5–10-fold less TPP than wild-type cells, which suggests that *pma1* mutant enzymes were defective in maintaining the normally high level of membrane potential.

A Proton Transport Dilemma

The membrane potential depolarization in *pma1* mutants could be explained if the mutant enzymes were less active in pumping protons across the membrane. This notion was supported by kinetic studies on ATP hydrolysis by these enzymes that showed small but significant decreases in V_{\max} (15). However, a dilemma arose when whole cell medium acidification experiments were performed, which reflect the action of the H^+ -ATPase *in vivo*. The rate of glucose-induced proton efflux by *pma1* mutant cells was found to be considerably better than that of wild-type cells (Figure 2). Only when high external K^+ was included in the medium to minimize differences in membrane potential between mutant and wild-type cells did the activity of the

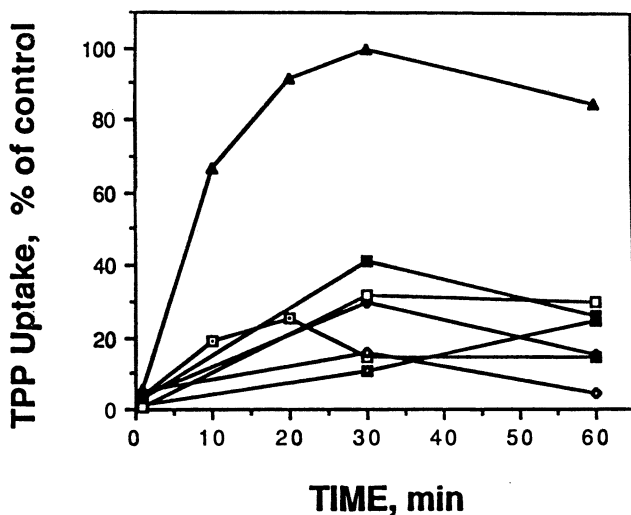


Figure 1. Uptake of $[^{14}C]$ TPP by *pma1* mutants. The uptake of $[^{14}C]$ TPP in the presence of glucose was determined for wild-type (▲), *pma1*-101 (◆), *pma1*-105 (□), *pma1*-114 (■), *pma1*-141 (◻), *pma1*-147 (◻), and *pma1*-155 (◇) cells. The reaction was initiated by the addition of $[^{14}C]$ TPP to the cell suspensions. (Reproduced with permission from reference 19. Copyright 1988 American Society of Biochemistry and Molecular Biology.)

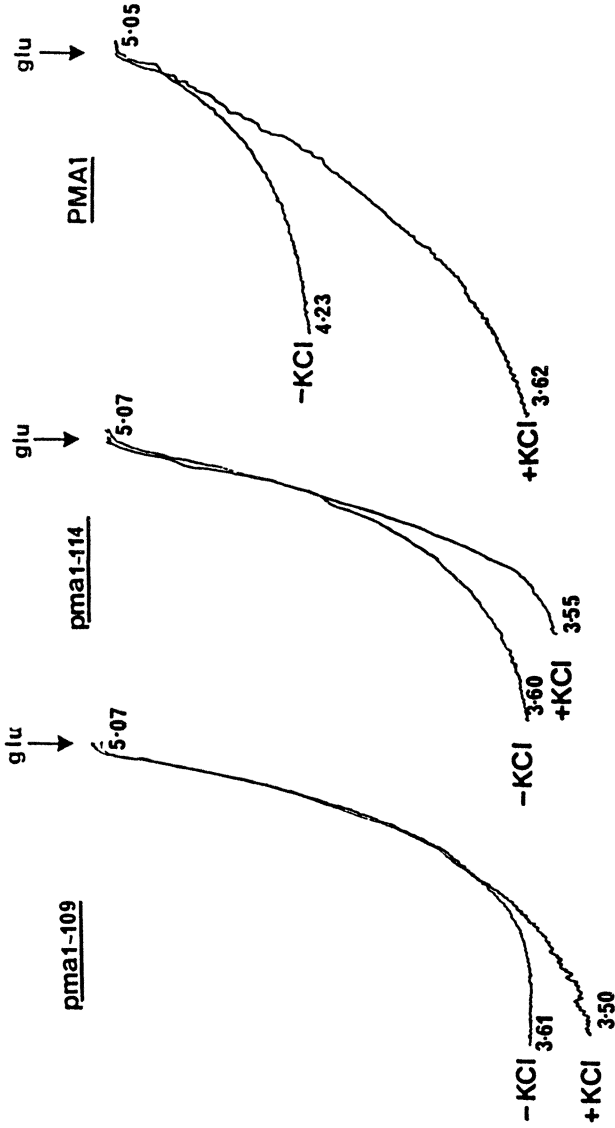


Figure 2. Effect of KCl on medium acidification. Wild-type (PMA1) and pma1 mutant cells (pma1-109 and pma1-114) were analyzed for glucose-induced medium acidification. (Reproduced with permission from reference 19. Copyright 1988, American Society for Biochemistry and Molecular Biology.)

wild-type approach that of the mutants (Figure 2). These results suggest that a simple kinetic explanation is inadequate to account for the membrane potential defect in *pma1* mutants. Clearly, some other fundamental property of electrogenic proton transport by the *pma1* mutant H^+ -ATPase had been altered.

Electrogenicity by the H^+ -ATPase

To assess more directly whether the electrogenicity of the H^+ -ATPase was altered, an in vitro assay was developed to examine the activity of the enzyme as a function of applied voltage. This approach was necessary because previously it has not been possible to use conventional electrophysiology or patch-clamp techniques to study the current-voltage behavior of the H^+ -ATPase in yeast. A simple system was used to examine the effects of interior positive membrane potential formation on the catalytic properties of purified H^+ -ATPase reconstituted into proteoliposomes. In this system, electron flow from vesicle-entrapped ascorbate to external $K_3Fe(CN)_6$ is mediated by the lipophilic electron carrier tetracyanoquinodimethane (TCNQ) (Figure 3). Interior positive membrane potential formation was readily followed using the optical probe oxonol V (Figure 3) and could be collapsed either by the addition of permeant anions like SCN^- or by the addition of valinomycin to K^+ -loaded vesicles (Figure 3). Potentials were calibrated by a null-point titration assay utilizing K^+ and valinomycin-induced diffusion potentials (17). A maximum membrane potential of approximately 254 mV was found to reduce ATP hydrolysis by wild-type enzymes up to 46%. The sensitivity of the enzyme to inhibition by vanadate was also modified under these conditions (17). The relationship between ATP hydrolysis and membrane voltage is shown in Figure 4. The wild-type enzyme is relatively insensitive to voltage over approximately 100 mV, but then shows voltage-sensitive behavior. A simple nonlinear extrapolation of the data in Figure 4 yields a predicted reversal potential of approximately 375 mV, which is consistent with electrophysiological studies of the closely related *Neurospora* H^+ -ATPase (21) and a stoichiometry of $1H^+$ transported per ATP hydrolyzed (22). In contrast to the behavior of the wild-type enzyme, a typical *pma1* mutant enzyme from strain *pma1-105* was found to be nearly insensitive to voltage, even at a maximum potential of 254 mV (17). This observation suggests that mutant enzyme *pma1-105* is insensitive to physiological levels of voltage. These data further suggest that other enzymes from hygromycin B resistant *pma1* mutants may be defective in electrogenic proton transport.

Evidence for Ion Counterflow by Mutant H^+ -ATPase

Electroneutrality by the mutant *pma1-105* H^+ -ATPase most likely results from a compensating charge movement following electrogenic proton trans-

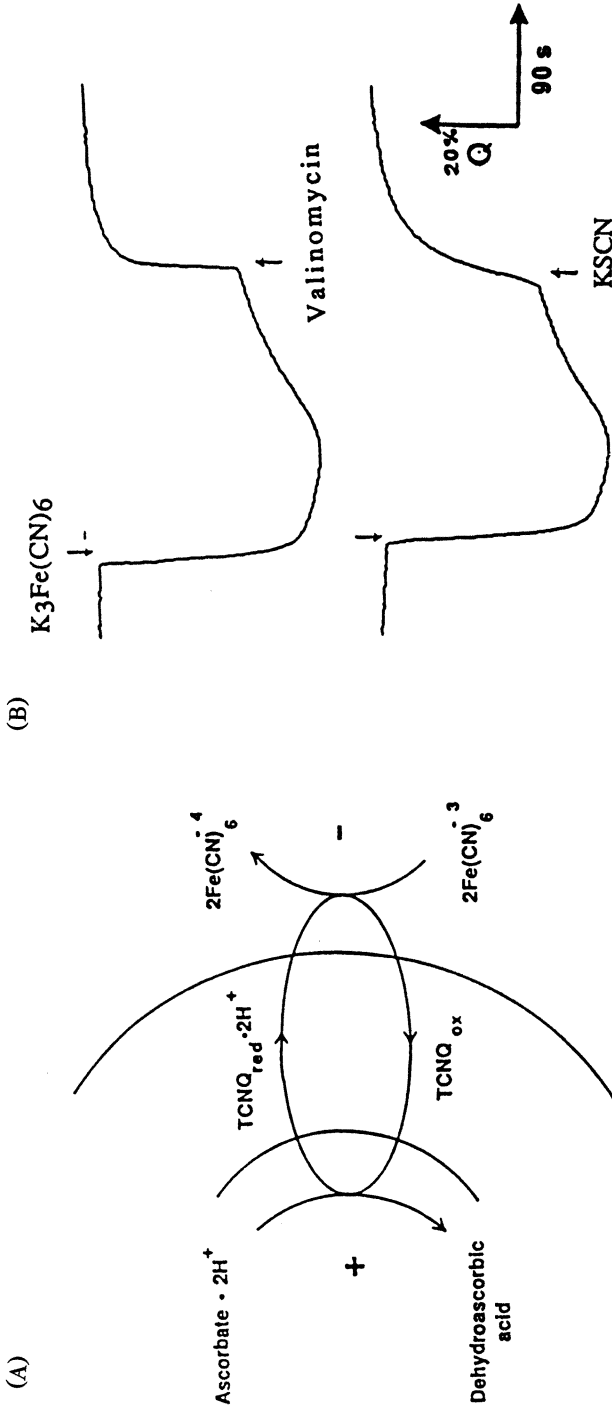


Figure 3. Description of systems used to generate and measure interior positive membrane potentials. (A) A schematic diagram for the ascorbate-TCNQ- $K_3Fe(CN)_6$ reaction. The interior positive membrane potential formation is catalyzed by the lipophilic electron carrier $TCNQ_{red}$, which mediates the flow of electrons from ascorbate inside the vesicle to $K_3Fe(CN)_6$ outside. (B) Membrane potential formation in reconstituted proteoliposomes was followed by the fluorescent probe oxonol V. (Reproduced with permission from reference 17. Copyright 1991 American Society for Biochemistry and Molecular Biology.)

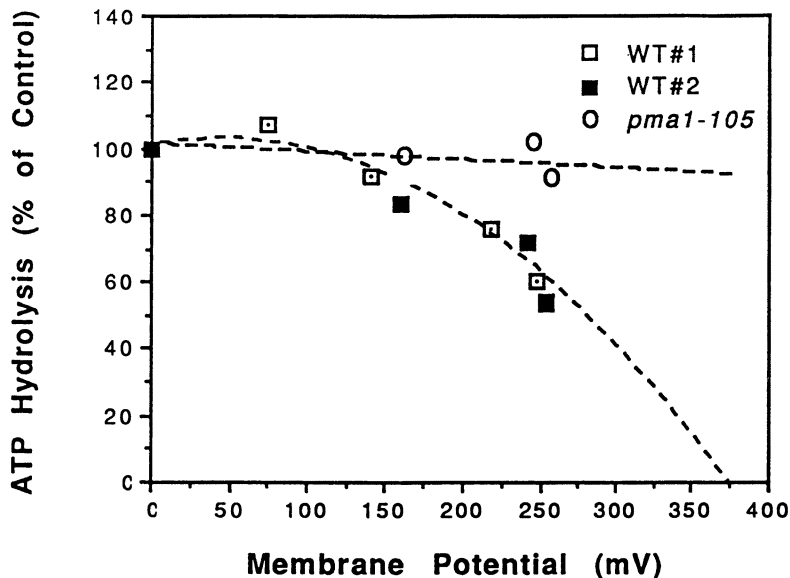


Figure 4. The relationship between ATP hydrolysis and membrane potential. ATP hydrolysis by purified and reconstituted H^+ -ATPase from wild-type and *pma1-105* was determined as a function of imposed membrane potential. ATP hydrolysis assays were performed for only 60 s to maintain a stable level of membrane potential. A nonlinear curve-fit routine was used to derive the extrapolated line drawn for the wild-type sample data. (Reproduced with permission from reference 17. Copyright 1991, American Society for Biochemistry and Molecular Biology.)

port, and there is strong precedent for this behavior in other P-type ATPases. In the gastric enzyme, an electrogenic H^+ current can be balanced by an equal and opposite K^+ current (23). In the Na^+-K^+ -ATPase, "uncoupled" Na^+ flux, which is electroneutral at pH 6.5, may require H^+ as a counterion (24). Finally, the apparent electroneutrality observed for the Ca^{2+} -ATPase from cardiac sarcolemma may also involve a counterflow of H^+ (25). The fungal H^+ -ATPase has no apparent catalytic requirement for any ion other than H^+ , although it has been shown that purified and reconstituted enzyme from *S. pombe* transports K^+ in an ATP-dependent manner (26). Recently, a patch-clamp analysis of hygromycin B resistant *pma1-105* mutant membranes identified an ATPase-dependent K^+ channel conductance in a physiological voltage range (60–120 mV). A K^+ conductance was also present in wild-type membranes, but it was not ATP activated and required higher gating voltages (>140 mV) (27). This work raised the possibility that K^+ transport is induced in mutant enzymes like *pma1-105* and may provide the electrical countercharge necessary for apparent electroneutrality.

Preliminary evidence suggests that the new K^+ conductance is directly mediated via the H^+ -ATPase, and two mechanistic schemes can be envisioned to account for this conductance (Figure 5). K^+ transport could involve the same translocation pathway as H^+ (but move in the opposite direction to H^+) or require an independent antiparallel translocation pathway. There are no data to distinguish between these two alternatives. Nonetheless, a common translocation mechanism that could accommodate H^+ and K^+ may be the most attractive because ion selectivity could be most easily accomplished by a single specialized gating mechanism.

Mapping *pma1* Mutations

Genetic mapping of hygromycin B resistant mutants was performed to identify specific amino acids and domains of protein structure that influence the electrogenic behavior of the H^+ -ATPase. Mutations within the coding region of *PMA1* map to either the membrane region or a large hydrophilic region containing the catalytic center (15). Figure 6A shows a schematic topography map of the H^+ -ATPase and the relative position of three prominent mutations. It can be seen that Gly158 \rightarrow Asp, which partially uncouples H^+ transport from ATP hydrolysis (15), is expected to lie within the bilayer. The other two mutations, Ser368 \rightarrow Phe and Pro640 \rightarrow Leu, are expected to be within the catalytic domain. This analysis is consistent with the finding that these latter mutations alter the kinetics for ATP hydrolysis and confer relative insensitivity to the mechanistic inhibitor vanadate (15). The fact that a mutation in the cytoplasmic ATP hydrolysis domain can alter the mechanistic nature of proton transport within the membrane strongly supports the notion of coupling between these disparate domains. Recently, we provided more

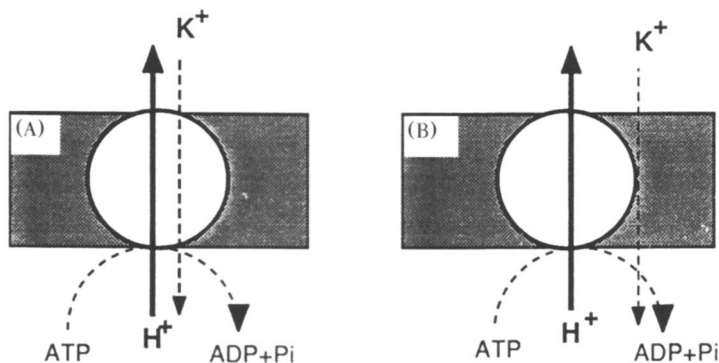


Figure 5. Schematic models for ATPase-mediated K^+ conductance. (A) K^+ transport occurs through the same pathway as H^+ . (B) K^+ transport occurs through a separate pathway from H^+ but is still mediated by the enzyme.

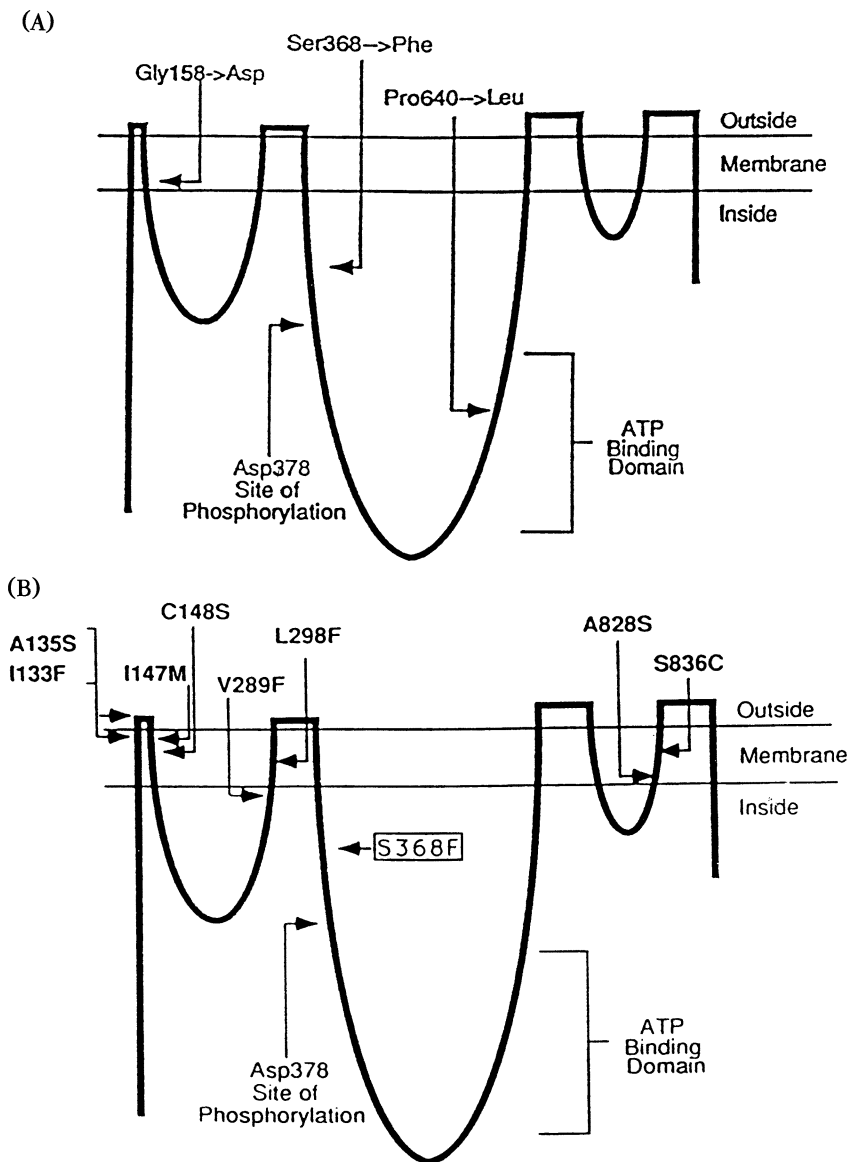


Figure 6. Diagram illustrating the membrane topography of the H^+ -ATPase. (A) The topography of the H^+ -ATPase was determined from analysis of hydrophathy profiles (16). Amino acid substitutions representing pmal-114, pmal-105, and pmal-147 mutant enzymes are indicated with respect to previously assigned functional domains. (Reproduced with permission from reference 15. Copyright 1989, American Society for Biochemistry and Molecular Biology.) (B) Topography map showing membrane locations of second-site mutations that suppress the NH_4^+ and low-pH sensitive phenotypes of a pmal-105 mutant (Ser368 → Phe). (Adapted from reference 28. Copyright 1991, American Society for Biochemistry and Molecular Biology.)

direct evidence (28) for such coupling by showing that second-site mutations expected to lie within the membrane bilayer can suppress the low pH and NH_4^+ sensitive phenotype induced by the Ser368 \rightarrow Phe mutation within the cytoplasmic catalytic domain (Figure 6B).

Table I summarizes the existing set of genetically mapped mutations, isolated from assorted mutagenesis schemes, that are believed to lie within the bilayer and result in hygromycin B resistance. An important outcome of the genetic mapping studies is that mutations conferring cellular hygromycin B resistance and, by inference, a depolarized cellular membrane potential are broadly distributed within transmembrane segments 1, 2, 3, 4, and 7 of the enzyme. These data suggest that multiple transmembrane elements participate in electrogenic proton transport and coupling to ATP hydrolysis.

Role of Membrane-Embedded Helices 1 and 2 in Electrogenic H^+ Transport

A detailed characterization of hygromycin B resistant mutants suggests that transmembrane segments 1 and 2 participate in electrogenic H^+ transport and coupling to ATP hydrolysis (28). These two segments and the connecting turn represent a template for the development of a three-dimensional model for the membrane sector of the enzyme and have been modeled as a hairpin loop structure that is dominated by a pair of antiparallel α helices (Figure 7). The hydrophobic helical elements are joined by a short (3–4 residues) turn region, which includes a polar serine residue and a highly charged Asp residue. The transmembrane loop is constrained into a single tightly packed configuration with the two helices pitched at an angle of about 15° to form an

Table I. Hygromycin B Resistant Mutants Mapping within the Bilayer

<i>Mutation</i>	<i>Helix</i>	<i>Mutation</i>	<i>Helix</i>
Ala135 \rightarrow Val	1	Leu298 \rightarrow Phe ^a	3
Ile133 \rightarrow Phe ^{a, b}		Leu327 \rightarrow Val ^{a, c}	3
Ala135 \rightarrow Ser	1	Met346 \rightarrow Val	4
Ile147 \rightarrow Met ^a	2	Met346 \rightarrow Thr	4
Cys148 \rightarrow Ser ^a	2	Ala828 \rightarrow Ser ^{a, c}	7
Val157 \rightarrow Phe ^{a, c}	2	Ser836 \rightarrow Cys ^{a, c}	7
Gly158 \rightarrow Asp	2		

^a These mutations were selected as second-site suppressors of either the low pH or NH_4^+ sensitive phenotype of *pmal-105* (Ser368 \rightarrow Phe). They confer hygromycin B resistance when separated from the primary-site (Phe368) mutation (28).

^b Ile133 \rightarrow Phe and Ala135 \rightarrow Ser comprise a double mutant.

^c These mutations were selected as in footnote *a*. They are hygromycin B resistant when present with the Phe368 mutation, but it is not known whether they confer hygromycin B resistance when separated from Phe368.

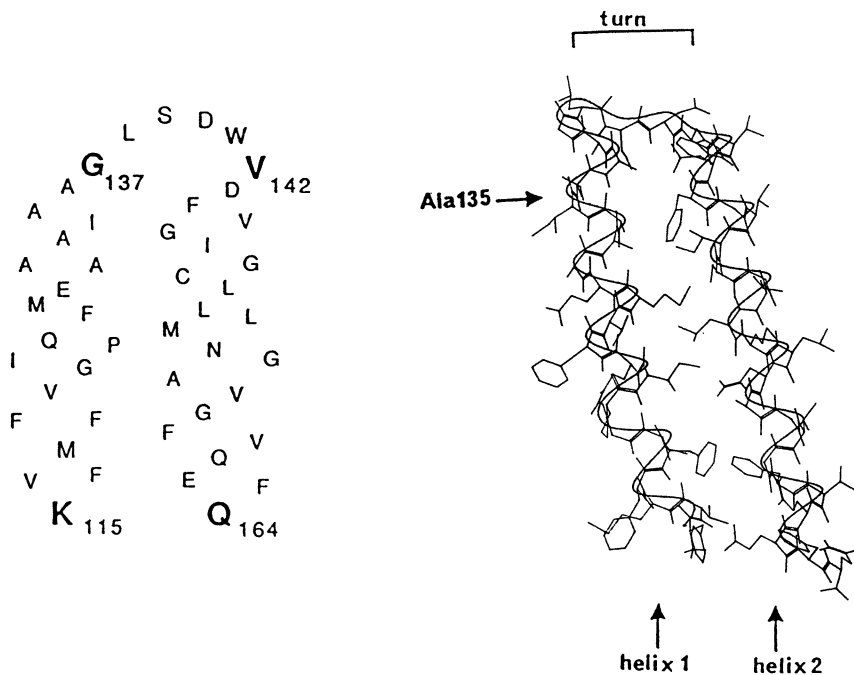


Figure 7. Amino acid sequence and molecular model for transmembrane helices 1 and 2. A molecular model generated with the program Quanta (Polygen, Inc.) that represents transmembrane helices 1 and 2 is shown next to its corresponding amino acid sequence.

inverted V-type structure that resembles the first two helices of a four-helix bundle (29). Several of the mutations identified in this region are predicted to alter the disposition of α helices relative to each other by sterically influencing the close packing of adjacent amino acid side chains. The close packing of amino acid side chains near the loop region suggests that mutations in this region would be poorly tolerated. In keeping with this notion, it was found that a relatively modest change, Ala135 \rightarrow Val, produced a dramatic perturbation in the enzyme function. This V-structure is highly conformationally active as indicated by the finding that site-directed mutations in the loop region, Leu138 \rightarrow Tyr and Asp140 \rightarrow Glu, both confer growth resistance to hygromycin B. If the hydrophilic domain extending from transmembrane segment 2 is rigid and in contact with the central hydrophilic domain containing the catalytic center, then it is possible to explain how a small perturbation in a distant portion of a transmembrane segment can influence the catalytic behavior of the enzyme. The role of transmembrane segments 1 and 2 in H^+ (and possibly K^+) transport is currently being investigated by a comprehensive mutagenesis approach.

Summary and Conclusions

Mutations in the *Saccharomyces cerevisiae* H⁺-ATPase gene, *PMA1*, that confer cellular growth resistance to hygromycin B cause a generalized depolarization of cellular membrane potential. The normal hyperpolarized membrane potential in yeast is maintained by the H⁺-ATPase, and it is believed that the *pma1* mutations alter electrogenic proton transport by the enzyme. Electroneutral H⁺ transport by the mutant enzymes may involve the counter-transport of K⁺, but other ions including H⁺ could participate. More direct evidence is needed to confirm the role of K⁺ as a counterion and to probe its putative transport mechanism. It will be important to determine whether H⁺ and K⁺ use the same mechanistic pathway for transport.

A significant outcome from the mutant mapping studies was the finding that amino acid substitutions within either the membrane domain or cytoplasmic catalytic domain render the enzyme defective in electrogenic proton transport. The disparate environments represented by these two domains provide indirect evidence for coupling between ATP hydrolysis and proton transport. More direct evidence for coupling was provided by the identification of second-site mutations within the membrane sector that partially suppress the phenotype of a primary-site mutation, Ser368 → Phe, located near the site of phosphorylation in the large central cytoplasmic domain. Multiple transmembrane segments have been implicated in electrogenic proton transport and coupling to ATP hydrolysis. A special emphasis was placed on transmembrane segments 1 and 2. Molecular model building suggests that these segments form a pair of antiparallel α helices that are both tightly compacted and highly conformationally active. It is believed that this structure can serve as a template for building a model of the entire transmembrane domain. Such a model will provide an important experimental tool for more detailed and direct genetic probing of the H⁺ transport mechanism.

Acknowledgments

This work was supported by the Office of Naval Research Grant N00014-89-J-1792 (to D. S. Perlin), National Institutes of Health grants GM38225 (to D. S. Perlin) and GM39737 (to J. E. Haber), and National Science Foundation Grant DCB8409086 (to J. E. Haber).

References

1. Deisenhofer, J.; Michel, H. *Science (Washington, D.C.)* **1989**, *245*, 1463–1473.
2. Henderson, R.; Baldwin, J. M.; Ceska, T. A.; Zemlin, F.; Beckman, E.; Downing, K. H. *J. Mol. Biol.* **1990**, *213*, 899–929.
3. Kühlbrandt, W. *Q. Rev. Biophys.* **1988**, *21*, 429–477.

4. Engelman, D. M.; Steitz, T. A.; Goldman, A. *Annu. Rev. Biophys. Biophys. Chem.* **1986**, *15*, 321–353.
5. Jähnig, F. *Trends Biochem. Sci.* **1990**, *15*, 93–95.
6. Kaback, H. R.; Bibi, E.; Roepe, P. D. *Trends Biochem. Sci.* **1990**, *15*, 309–314.
7. Cox, G. B.; Fimmel, A. L.; Gibson, F.; Hatch, L. *Biochim. Biophys. Acta* **1986**, *849*, 62–69.
8. Mogi, T.; Stern, L. J.; Chao, B. H.; Khorana, H. G. *J. Biol. Chem.* **1989**, *264*, 14192–14196.
9. Lolkema, J. S.; Püttner, I. B.; Kaback, H. R. *Biochemistry* **1988**, *27*, 8307–8310.
10. Braiman, M. S.; Rothschild, K. J. *Annu. Rev. Biophys. Biophys. Chem.* **1988**, *17*, 541–570.
11. Vallejo, C. G.; Serrano, R. *Yeast* **1989**, *5*, 307–319.
12. Perlin, D. S.; Brown, C. L. *J. Biol. Chem.* **1987**, *262*, 6788–6794.
13. Serrano, R.; Kielland-Brandt, M. C.; Fink, G. R. *Nature (London)* **1986**, *319*, 689–693.
14. Serrano, R.; Portillo, F. *Biochim. Biophys. Acta* **1990**, *1018*, 195–199.
15. Perlin, D. S.; Harris, S. L.; Seto-Young, D.; Haber, J. E. *J. Biol. Chem.* **1989**, *264*, 21857–21864.
16. Serrano, R. *Biochim. Biophys. Acta* **1988**, *947*, 1–28.
17. Seto-Young, D.; Perlin, D. S. *J. Biol. Chem.* **1991**, *266*, 1383–1389.
18. McCusker, J. H.; Perlin, D. S.; Haber, J. E. *Mol. Cell. Biol.* **1987**, *7*, 4082–4088.
19. Perlin, D. S.; Brown, C. L.; Haber, J. E. *J. Biol. Chem.* **1988**, *263*, 18118–18122.
20. van de Mortel, J. B. J.; Mulders, D.; Korthout, H.; Theuvenet, A. P. R.; Borst-Pauwels, G. W. F. H. *Biochim. Biophys. Acta* **1988**, *936*, 421–428.
21. Gradmann, D.; Hansen, U.-P.; Slayman, C. L. *Curr. Top. Membr. Transp.* **1982**, *16*, 257–276.
22. Warncke, J.; Slayman, C. L. *Biochim. Biophys. Acta* **1980**, *591*, 224–233.
23. Lorentzon, P.; Sachs, G.; Wallmark, B. *J. Biol. Chem.* **1988**, *263*, 10705–10710.
24. Goldshleger, R.; Shahak, Y.; Karlsh, S. J. D. *J. Membr. Biol.* **1990**, *113*, 139–154.
25. Dixon, D. A.; Haynes, D. H. *J. Membr. Biol.* **1989**, *112*, 169–183.
26. Villalobo, A. *J. Biol. Chem.* **1982**, *257*, 1824–1828.
27. Ramirez, J. A.; Vacata, V.; McCusker, J. H.; Haber, J. E.; Mortimer, R. K.; Owen, W. G.; Lecar, H. *Proc. Natl. Acad. Sci. U.S.A.* **1989**, *86*, 7866–7870.
28. Harris, S. L.; Perlin, D. S.; Seto-Young, D.; Haber, J. E. *J. Biol. Chem.* **1991**, *266*, 24439–24445.
29. Oiki, S.; Madison, V.; Montal, M. *Proteins* **1990**, *8*, 226–236.

RECEIVED for review January 29, 1991. ACCEPTED revised manuscript September 4, 1992.

Design Principles and Chemical Synthesis of Oligomeric Channel Proteins

John M. Tomich^{1,3}, Anne Grove², Takeo Iwamoto^{1,3}, Stephan Marrer^{2,4}, Myrta S. Montal², and Mauricio Montal^{2,5}

¹Department of Biochemistry, University of Southern California Medical School and Children's Hospital, Los Angeles, CA 90054-0700

²Department of Biology, University of California, San Diego, La Jolla, CA 92093-0319

Proteins that emulate pore properties of the dihydropyridine-sensitive calcium channel or the nicotinic acetylcholine receptor have been designed and synthesized. The designed proteins consist of bundles of amphipathic α -helices with sequences that correspond to specific segments of authentic proteins and are arranged such that charged or polar residues line an aqueous pore. Molecular models suggest that such structures satisfy geometric and functional requirements to constitute the pore-forming element of channel proteins. The designed proteins are synthesized by solid-phase methods and purified. The single-channel conductance properties of designed proteins are studied in lipid bilayers. The synthetic proteins mimic the ionic conductance, selectivity, and pharmacological properties of authentic channel proteins. Synthetic proteins that represent segments of the authentic proteins that are not predicted to line an aqueous pore do not mimic the targeted biological activity.

³ Current address: Department of Biochemistry, Kansas State University, Manhattan, KS 66506-3702

⁴ Current address: F. Hoffman-LaRoche Ltd., PSQA-2, Ch-4002 Basel, Switzerland

⁵ Corresponding author

NEUROTRANSMITTER RECEPTORS AND IONIC CHANNELS are responsible for two fundamental properties of the brain: electrical excitability and synaptic transmission. Neuronal signaling occurs through synaptic junctions between the nerve endings and the body of the nerve cell or other effector cells. Conduction and propagation of nerve signals through nerve cells and axons are mediated by voltage-gated channels (1). In neurons, as in other excitable cells, the influx of Ca^{2+} via voltage-sensitive calcium channels generates both electrical and chemical signals. Calcium influx carries depolarizing charge that contributes to electrical activity and also leads to a rise in intracellular calcium concentration from extracellular fluid or by release from intracellular stores. Changes in calcium concentration constitute a chemical message for calcium-sensitive mechanisms that control, for example, ion channel gating and transmitter release (1, 2).

Transfer of incoming signals at the chemical synapses present at nerve terminals occurs by releasing neurotransmitters from their presynaptic terminal and effecting a change in ion permeability of the postsynaptic cells. The channels in the postsynaptic membrane are often chemically gated; that is, they open or close in response to transmitter binding. Acetylcholine (ACh) is released by the presynaptic neuron. The binding of ACh to ACh receptors found on postsynaptic membranes of nerve terminals and neuromuscular endplates results in the transient opening of cation-selective channels that are responsible for depolarizing the postsynaptic cell (1).

Pre- and postsynaptic elements, therefore, play a key role in excitation of the brain. We focus here on prototypes of a presynaptic and a postsynaptic element. As an example of a presynaptic element, we selected the dihydropyridine-sensitive calcium channel, a member of the superfamily of voltage-gated channel proteins. The most extensively studied membrane protein, the nicotinic cholinergic receptor, which belongs to the family of ligand-gated channels, is present in the postsynaptic membrane. These two examples are used to describe a strategy that aims to identify sequence-specific motifs that are responsible for the performance of unique functions and to outline an experimental approach to evaluate identified structural motifs.

Inferences about Channel Protein Structure

Key functional elements of voltage- and ligand-gated ionic channels are the mechanisms by which their conformation changes in response to ligand binding or variations in membrane electric field; the sensor that detects a stimulus and couples it to the opening and closing of the channel; the permeation pathway, specifically pore size and ionic selectivity of the open channel; and the sites of action of drugs and toxins that specifically modify properties of the channel (1). Molecular cloning and sequencing led to the elucidation of primary structures of several superfamilies of voltage- and

ligand-gated channels (3). However, no high-resolution structural information is yet available. The challenge is, therefore, to try to identify from the primary sequences the structural elements that may determine the functional properties of channel proteins (4, 5).

A search for sequences that are compatible with a given function, such as the pore-forming structure of channel proteins, originated with the wealth of sequence information available on voltage- and ligand-gated channel proteins (3). Extensive sequence homology among members of these families of proteins is evident; characteristic structural features include the occurrence of homologous subunits oriented across the membrane and organized as a symmetric or pseudosymmetric array around a central aqueous channel and the presence of segments capable of adopting α -helical transmembrane structures. It is plausible, therefore, that a unifying structural motif in the biological design of ion channels is a cluster of amphipathic α -helices arranged such that charged or polar residues line the central hydrophilic pore and nonpolar residues face the hydrophobic environment of the protein and the bilayer interior (4, 5). Such a structure may account for geometric requirements, determine ionic specificity, and explain the diversity of channel proteins based on sequence specificity and oligomer size.

Identification of Possible Pore-Lining Segments

Identification of presumed pore-lining segments is based on the primary structure of the channel protein and knowledge of the physiology of the molecule. Amphipathic α -helical segments greater than 20 residues in length—sufficient to span the width of the bilayer core—are identified by the use of empirical secondary structure predictors; specific residues allow for appropriate ionic selectivity (6–8).

The dihydropyridine- (DHP)-sensitive calcium channel purified from skeletal muscle is composed of five subunits: α_1 , α_2 , β , γ , and δ (9–12). The α_1 subunit (molecular weight $M_r \approx 170$ kD) forms a functional voltage-gated calcium channel (9, 13–15) and contains the binding sites for the three classes of calcium channel modulators: 1,4-dihydropyridines (16), phenylalkylamines, and benzothiazepines (17). The primary structure of the α_1 subunit was first elucidated from skeletal muscle (18); highly homologous sequences have since been cloned from cardiac muscle (13, 19, 20) and brain (21), aorta (22), and lung (23) tissue.

Extensive sequence homology is evident between calcium (13, 18–23), sodium (24–29), and potassium channel proteins (30–34). The primary structure of sodium and calcium channel proteins suggests the occurrence of four homologous domains with the four repeats organized as pseudosubunits around a central pore (4, 24), whereas potassium channels are considered to be constructed of a cluster of four subunits (35, 36), each of which corre-

sponds to a single repeat of sodium or calcium channels. Each repeat contains six segments (S1–S6) that are predicted to form α -helical transmembrane structures.

A common function of S3 segments from calcium, sodium, and potassium channel proteins is suggested by the extensive sequence homology, particularly with respect to the position of negatively charged or polar residues that may be involved in lining a cation-selective channel. Four S3 segments may form a bundle of α -helices that create the transmembrane pore (4, 5, 37–39).

The ACh receptor (AChR) from *Torpedo californica* ($M_r \approx 250$ kD) is composed of four glycoprotein subunits with a stoichiometry of $\alpha_2\beta\gamma\delta$ that are assembled as a pentamer with the ion channel in the center (40–42). Gating of currents through these channels depends on binding of ligands such as ACh to specific sites on the α subunits. Analysis of the primary structure led to the assignment in each subunit of four hydrophobic transmembrane segments, M1–M4 (3, 42). The AChR channel is an aqueous pore that selects against anions but passes cations and many nonelectrolytes < 7 Å diameter (1). Theoretical and permeation studies suggest that the vestibules contain a net negative charge that attracts cations into the pore, which is presumed to be lined with polar uncharged residues (43). Labeling of the channel by noncompetitive inhibitors such as chlorpromazine (44) and triphenylmethylphosphonium (45, 46) has identified serine-262 in M2 of the δ subunit as part of a high-affinity site. Homologous regions from the different subunits contribute to the unique high-affinity site (47). Consequently, the M2 segment of the δ subunit is thought to be involved in forming the AChR channel (5, 48–51).

Design of Pore-Forming Proteins

To demonstrate the existence of functional elements responsible for pore properties of channel proteins, peptides with sequences that represent such functional segments are synthesized and their ability to mimic the targeted biological activity is tested by incorporation of the peptides into lipid bilayers. This approach allows rapid determination of which presumed transmembrane helices may form functional channels. The peptides self-assemble in the membrane to generate conductive oligomers, presumably with hydrophobic surfaces that face the phospholipid and hydrophilic residues that line the pore. Channels of different sizes (oligomeric number) result (37, 48).

The occurrence of a cluster of amphipathic α -helical peptides that forms the inner bundle of channel proteins and the determination of oligomeric number may be addressed through the design and synthesis of larger polypeptides that will pack in a predictable manner to yield a protein with predetermined conformational properties. Considerable effort has been de-

voted to the design and chemical synthesis of large polypeptides that assume tertiary structures. These approaches include *de novo* design of a four-helix bundle protein (52) and a mimic of the serine protease catalytic triad (53). A promising strategy for the construction of proteins with predetermined structure involves the covalent attachment of peptide segments with a high potential for secondary structure to a multifunctional carrier molecule (template) to generate nonlinear protein molecules that exhibit template-induced secondary structure; the product of attachment is the template-assembled synthetic protein (TASP) (54–56). A linear assembly of peptide blocks necessitates a specific folding process to achieve the proposed conformation, whereas the template molecules direct the attached peptide segments into the required conformation. The template molecule may be any multifunctional molecule with proper spatial arrangement of attachment sites and limited conformational flexibility. For example, spatial constraints induced by attaching amphiphilic α -helix-forming peptides to a template enhance peptide interactions and act as the major driving force to fold the template-assembled peptides into the predetermined conformation (57).

Proteins that mimic the presumed pore-forming structure of the DHP-sensitive calcium channel and the nicotinic AChR were designed using the TASP strategy. A nine amino acid template molecule (KKKPGKEKG) (54–56) that allows for attachment of peptides at the ϵ -amino groups of four lysines was used to generate four-helix bundle structures (49) by the assembly of four identical peptides. (Note that the standard one-letter amino acid code is used.) Each peptide represents the sequence of the S3 segment from the fourth internal repeat of the DHP-sensitive calcium channel (T_4 CaIVS3) (13, 18, 21) or the M2 δ segment of the nicotinic AChR (T_4 M2 δ ; Figure 1A) (58). This approach has generated a novel class of membrane associating, pore-forming molecules (synporins) (49). The devised nomenclature specifies a template with four attachment sites (T_4), followed by the conventional designation of individual transmembrane segments.

A homotetramer of IVS3 (T_4 CaIVS3) is a plausible model of the proposed heterotetramer that forms the pore of the authentic DHP-sensitive calcium channel. The sequence of IVS3 is conserved between skeletal muscle and isoforms of cardiac muscle, brain, and aorta, and empirical secondary structure predictors (6–8) suggest that the peptide forms an amphipathic α -helix (hydrophobic moment $\langle \mu \rangle = 0.19$) with a length sufficient to traverse the hydrocarbon core of the membrane. Such features are also characteristic of the other three S3 segments because of extensive sequence homology. Further, a synthetic peptide with the sequence of a homologous S3 segment of the brain sodium channel forms cation-selective channels in lipid bilayers (37).

M2 exhibits high homology both between subunits of the *Torpedo* AChR $\alpha_2\beta\gamma\delta$ complex and between species (3). Secondary structure predictors suggest that M2 δ segments could form amphipathic α -helices ($\langle \mu \rangle = 0.25$).

Similarly, a synthetic peptide with a sequence that represents the M2 δ segment of the *Torpedo* AChR forms discrete ionic channels in lipid bilayers with conductance properties comparable to those of the authentic AChR channel (48).

Four-Helix Bundles: A Plausible Model for the Pore Structure of Channel Proteins

For the construction of a four-helix bundle, the spatial orientation of template amino acids is considered. The conformational characteristics of the side chains of lysine predict a direction perpendicular to the plane of the template, and all attachment sites for peptide modules may be oriented *cis* relative to the plane of the template backbone.

Energetic considerations confirm that a bundle of four α -helices is a reasonable model for the pore structure of channel proteins. Models were generated using existent coordinates for the sodium channel S3 homotetramer (39) by specific residue replacements. The INSIGHT and DISCOVER program packages (Biosym Technologies, Inc., San Diego, CA) were used. Optimized helical structures for the homotetramers of T₄CaIVS3 and T₄M2 δ are shown in Figure 1B and C. The template portion of the molecules is modeled as a β hairpin with attachment sites for the channel-forming peptides all *cis* to the plane of the template (Figure 1B). The attached α -helical modules are parallel and aligned with the coupling sites at

(A)

Template:		K[*]K[*]K[*]P[*]G[*]K[*]E[*]K[*]G
IVS3	:	DPWNVFDFLIVIGSIIDVILSE
IVS5	:	YVALLIVMLFFIYAVIGMQMFGK
M2δ	:	EKMSTAISVLLAQA[*]VFL[*]LL[*]TSQR
M1δ	:	LFYVIN[*]FI[*]TPCVL[*]ISFLASLAFY

Figure 1. (A) Amino acid sequences of template and oligopeptides used to generate the proteins studied, pore-forming molecules T₄CaIVS3 and T₄M2 δ , and proteins designed using hydrophobic sequences, T₄CaIVS5 and T₄M1 δ . IVS3 corresponds to amino acids 1180–1201, IVS5 corresponds to residues 1269–1291 (18), and M2 δ and M1 δ correspond to amino acids 255–277 and 226–248, respectively (58). Peptides are attached to template lysines indicated with an asterisk (*). Standard one-letter amino acid code is used.

(B)

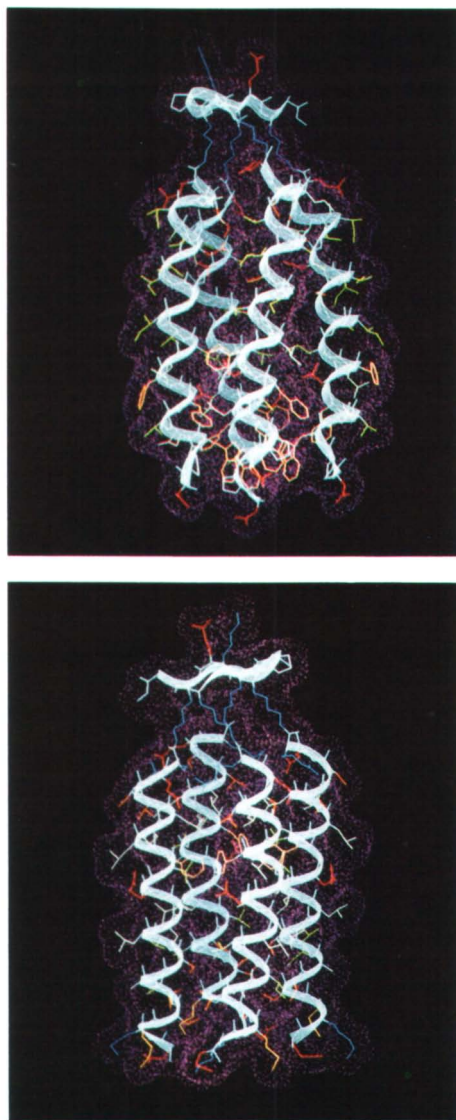


Figure 1.—Continued. Computer-generated molecular model of synthetic pore proteins. (B) Energy-optimized parallel tetramers of $T_4CaIVS3$ (upper) and $T_4M2\delta$ (lower). B is a side view with the nonapeptide template at the top and the N terminus at the bottom of the two α -helical bundles (Marrer, S.; Montal, M., unpublished). Residues are colored according to hydrophobicity: red, acidic residues; blue, basic residues; orange, serine and threonine; bright yellow, methionine; yellow, tryptophane and phenylalanine; pink, asparagine and glutamine; white, glycine and proline; green, lipophilic residues; light blue, α -carbon backbone and its ribbon representation; magenta, solvent-accessible surface (dotted). Continued on next page.

(C)

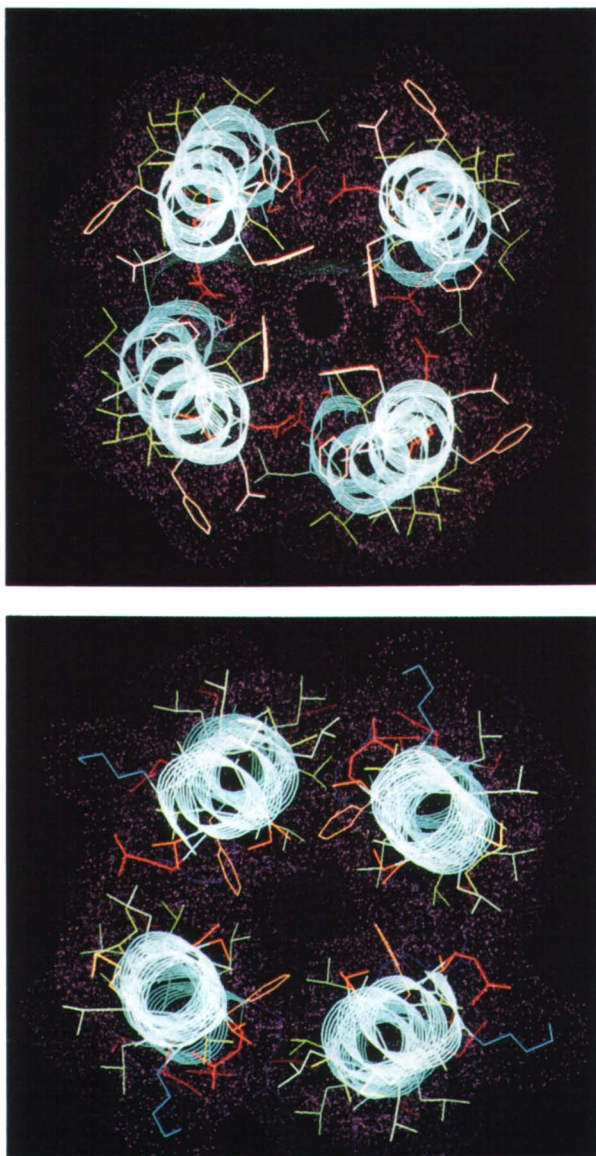


Figure 1.—Continued. Computer-generated molecular model of synthetic pore proteins. (C) Energy-optimized parallel tetramers of $T_2CaIVS3$ (upper) and $T_4M2\delta$ (lower). C is the end view with the N terminus in front (89). Residues are colored according to hydrophobicity; see previous page.

the ϵ -amino groups of template lysines providing the spatial organization for the four-helix bundles. The orientation of the template relative to the bundle is dependent on the conformational properties of attached helices. The N-terminal residues correspond to the untethered end of the helical modules and are assigned to the intracellular face of the membrane (1, 18). The length of the bundles is sufficient to span the lipid bilayer (32 Å) (39). The bundles show a left-handed twist with an interhelical angle of $\approx 15^\circ$.

Figure 1C shows an end view of the bundles; the N terminus is in front. Hydrophobic and hydrophilic residues occur on opposite faces of the helical cylinders. The solvent-accessible surface (dotted) discloses the symmetric nature of the $T_4CaIVS3$ pore (ring of overlapping surface density). The square vestibule at the entry of the pore of $T_4CaIVS3$ is formed by indole nitrogens of tryptophanes (W-3) that hydrogen bond with aspartates (D-1). The cross section is 7.9 Å, which corresponds to a distance between solvent-accessible surfaces of 4.5 Å. The lumen of the pore is lined with polar-neutral residues and two sequential clusters of acidic residues, D-7 and D-17. The narrowest section of the pore occurs at D-7; the distance between opposing carboxylates is 7.4 Å with 4.2 Å delimited by the boundaries of solvent-accessible surfaces. This cluster of negatively charged residues may provide a high-affinity binding site for permeant cations (59, 60).

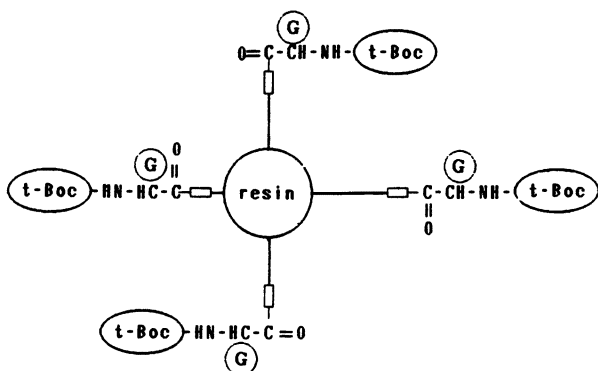
The lumen of the $T_4M2\delta$ pore is lined with polar-neutral residues. S-8 corresponds to serine-262 in the actual protein sequence and faces the lumen of the pore. Serine-262 is considered exposed to the lumen of the pore and may participate in the conduction of ions through the AChR channel (39, 44–46, 49–51). The cross section is 9.5 Å. F-16, which corresponds to phenylalanine-270 in the protein sequence, is exposed to the luminal surface and forms the narrowest section of the pore (8.3 Å). E-1, which corresponds to glutamate-255 of the δ subunit sequence, hydrogen-bonds with K-2 of each helix, and generates a ring of charged residues. E-1 corresponds to the postulated intracellular end of the receptor channel, considered to be negatively charged (39, 42, 43, 49, 61).

Hence, bundles of four amphipathic α -helices fulfill the structural and energetic requirements for the inner bundle that forms the pore of the DHP-sensitive calcium channel and the nicotinic AChR channel.

Synthesis and Purification

Synthesis of the four-helix bundles was accomplished by a two-step procedure (outlined as a flow chart in Figure 2). Proteins were synthesized by solid phase methods in accordance with general principles (62–64) using a peptide synthesizer (model 431, Applied Biosystems (ABI), Foster City, CA). *L*-configuration amino acid derivatives were used (The Peptide Institute, Osaka, Japan). The acid-labile *tert*-butyloxycarbonyl- (*t*-Boc)-protecting groups were

(A)



- ↓
1. t-Boc deprotection
 2. DCC coupling with 0.25 eq. t-Boc-fmoc-Lys
 3. capping of remaining sites

(B)

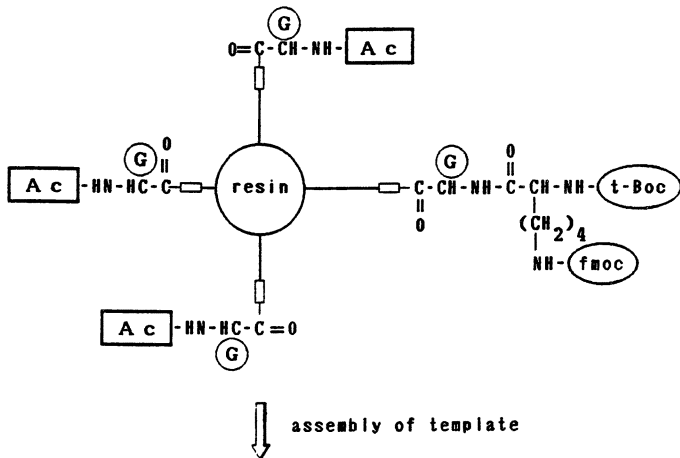
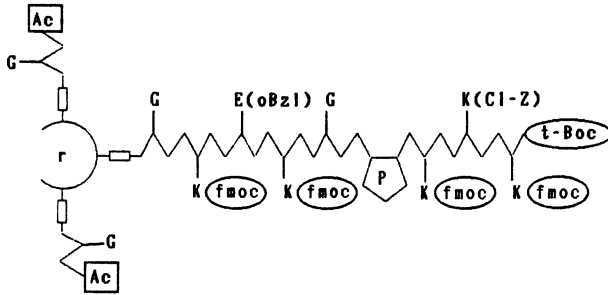
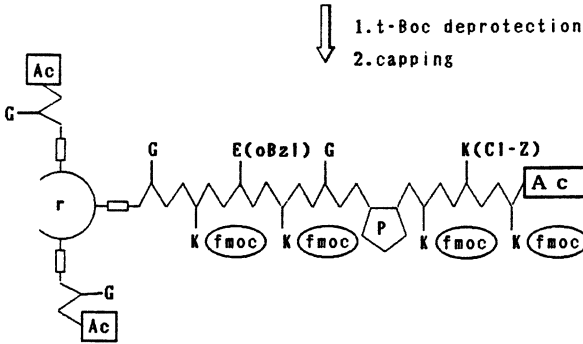


Figure 2. Flow chart of the protocol used to synthesize tetrameric bundles of defined amino acid sequence. (A) The highly substituted polystyrene resin, 0.75 mmol/g, that contains t-Boc glycine (G) attached through a PAM linker (open box). (B) The most accessible sites are selected by coupling with only 0.25 equivalents of the t-Boc-fmoc lysine. The remaining unreacted sites are blocked using an excess of acetic anhydride (Ac).

(C)



(D)



(E)

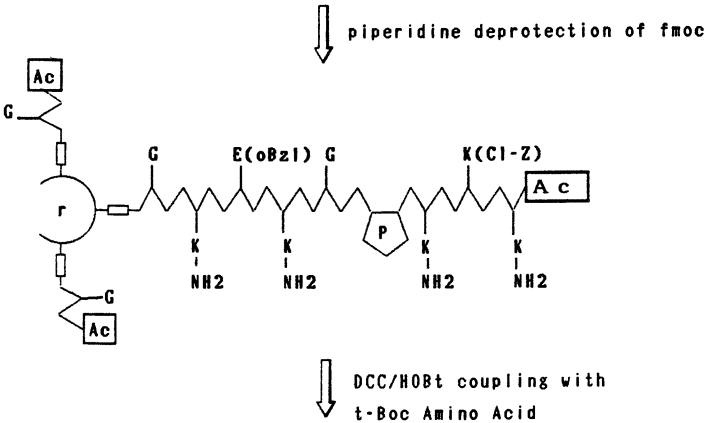
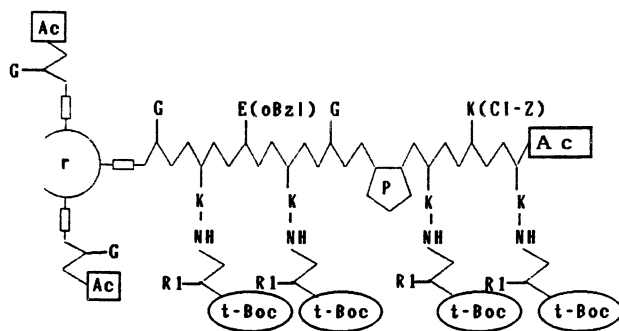


Figure 2.—Continued. Flow chart of the protocol used to synthesize tetrameric bundles of defined amino acid sequence. (C) The completed template KKKPGKEKG. (D) The free N terminus of the template is blocked with excess acetic anhydride. (E) The fmoc groups are removed by treatment with 20% piperidine in DMF. Continued on next page.

(F)



(G)

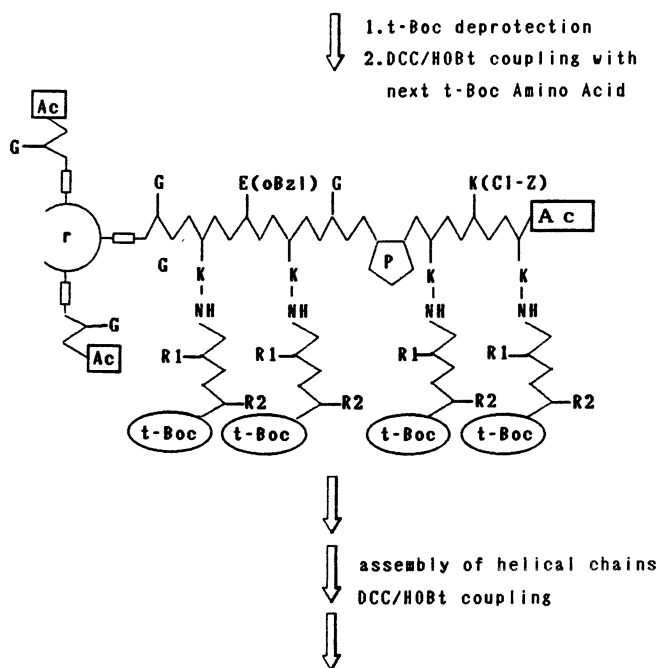


Figure 2.—Continued. Flow chart of the protocol used to synthesize tetrameric bundles of defined amino acid sequence. (F), (G) Single amino acids are added to sequentially assemble the peptide modules of the synthetic proteins. Continued on next page.

used for N^α protection. All coupling steps were performed in *N*-methylpyrrolidone (NMP) containing dimethyl sulfoxide (DMSO) for at least 30 min using a 10-fold excess of preformed 1-hydroxybenzotriazole (HOBT) esters. Coupling efficiencies at each step were monitored by the quantitative ninhydrin test (65).

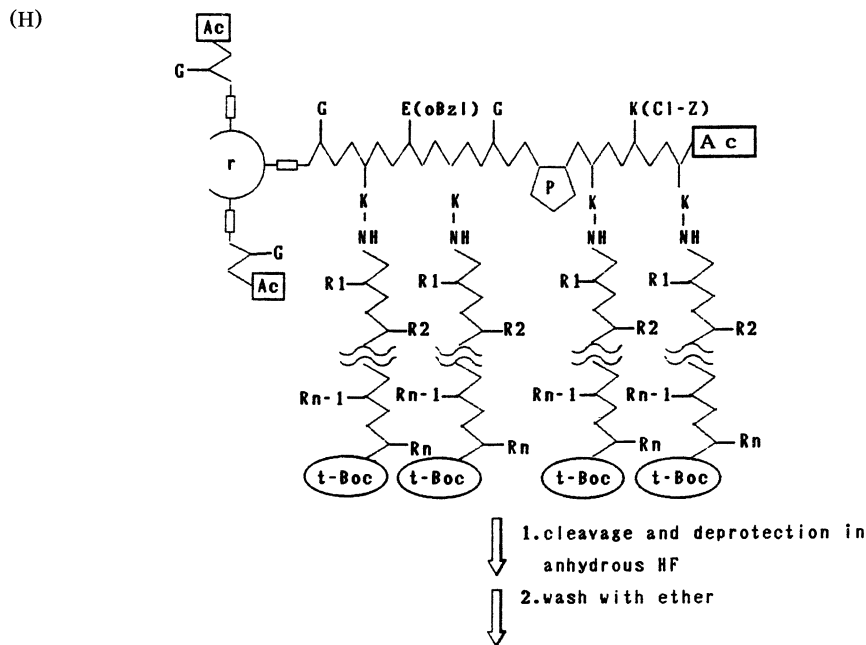


Figure 2.—Continued. Flow chart of the protocol used to synthesize tetrameric bundles of defined amino acid sequence. (H) Single amino acid added to sequentially assemble the peptide modules of the synthetic proteins. Continued on next page.

Steric constraints of the four-helix bundle proteins require the use of low-substitution resins for optimal synthetic yield. Reduced loading capacity of the preloaded *t*-Boc-glycine-PAM (4-oxymethylphenylacetamidomethyl) resin (0.76-mmol/g capacity; ABI) was accomplished during coupling of the first amino acid: a reduced amount of N^{α} -*t*-Boc- N^{ϵ} -fmoc (9-fluorenylmethoxycarbonyl)lysine (0.25 equivalent) was allowed to react with the resin for 1 h (Figure 2A). The remaining sites were capped with acetic anhydride. This strategy was designed to allow coupling to only the most accessible sites on the resin. By use of this lower substitution (0.1–0.3 mmol/g), the number of recouplings required to attain > 99.5% coupling efficiencies was reduced and increased weight gains were obtained.

A common nine amino acid template Ac-K(N^{ϵ} -fmoc)-K(N^{ϵ} -Cl-Z)-K(N^{ϵ} -fmoc)-P-G-K(N^{ϵ} -fmoc)-E(γ -OBzl)-K(N^{ϵ} -fmoc)-G-PAM resin (where Ac is acetyl, Cl-Z is 2-chlorobenzoyloxycarbonyl, and OBzl is benzyl ester) was synthesized. Failed sequences during synthesis of the template were capped using acetic anhydride (Figure 2B and C). The sequence was confirmed by automated Edman degradation on a peptide sequencer (ABI

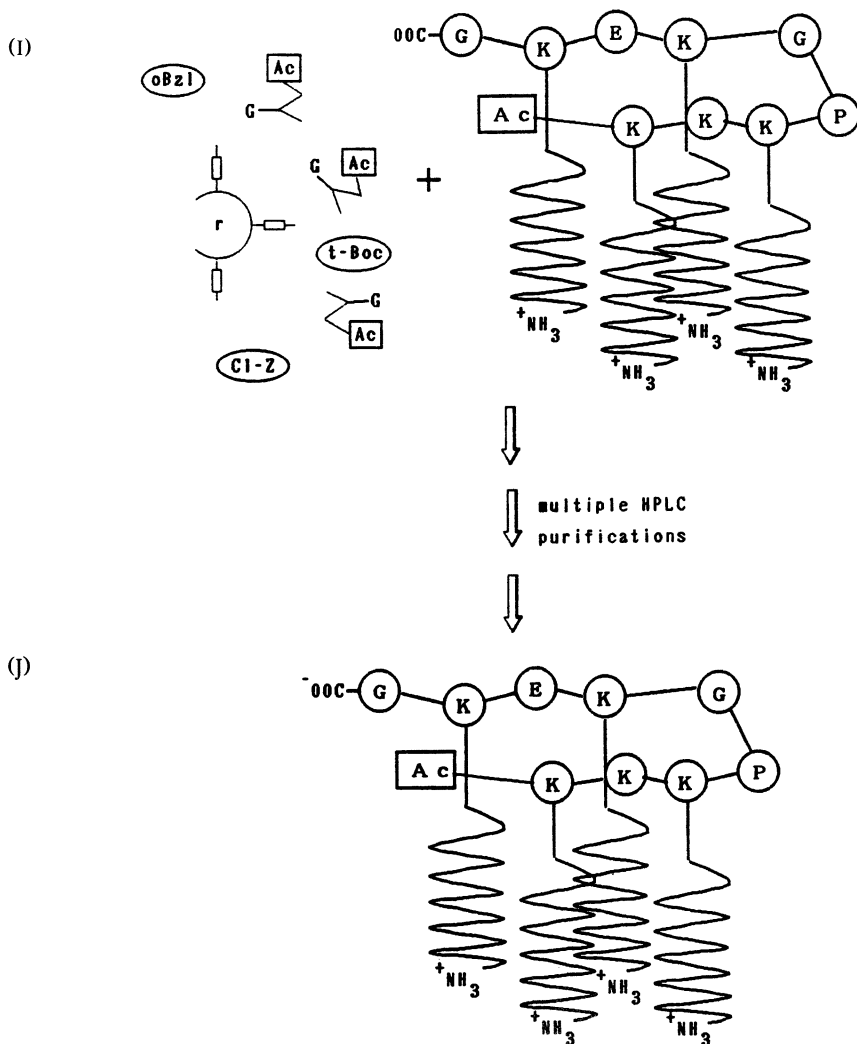


Figure 2.—Continued. Flow chart of the protocol used to synthesize tetrameric bundles of defined amino acid sequence. (I) HF cleavage releases the synthetic protein from the support and deprotects the amino acid sidechains. (J) Chromatography using HPLC generates the purified channel proteins.

model 477A), and the N-terminal lysine was blocked by treatment with 17% acetic anhydride and 7% diisopropylethylamine in NMP for 10 min.

Assembly of peptide blocks typically starts with 0.05 mol of template resin. The base-labile N^ϵ -fmoc-protecting groups were removed by incubation with 20% piperidine (v/v) in dimethylformamide for 20 min (Figure 2D). The four peptide blocks were assembled simultaneously (Figure 2E–G)

by stepwise synthesis using HOBt-activated esters of N^α-*t*-Boc amino acid derivatives on a synthesizer (ABI model 431). The side chains of trifunctional amino acids were protected as follows: E(OBzl), D(OBzl) or D(cyclohexyl ester) (Oc-Hex), S(benzyl ether) (Bzl), T(Bzl), R(tosyl), and W(CHO). Multiple couplings (3–5 per residue) were performed to ensure coupling efficiencies > 99.5% for each step. Capping of failed sequences with acetic anhydride was included in some syntheses. Tracer amounts of [³H] *t*-Boc-leucine were added to quantitate concentrations. N termini were not capped. Weight gains of > 80% were typically obtained for the channel proteins. Seven separate syntheses were performed for T₄M2δ, whereas five syntheses were completed for T₄CaIVS3.

Different cleavage protocols were used (Figure 2H and I): for T₄M2δ, cleavage and deprotection were performed in anhydrous HF for 30 min at -10 °C and for 90 min at 0 °C in the presence of *p*-cresol and *p*-thiocresol, 1.4 mL/g of resin. After HF was removed, the resulting peptide-resin mixture was washed with anhydrous diethylether and dried overnight under vacuum over KOH pellets. T₄CaIVS3 was cleaved from the solid-phase support using a low-high HF protocol (66) that considered the presence of tryptophane residues in the peptide segments. The low HF step was carried out in the presence of dimethylsulfide and *p*-cresol for 2 h at 0 °C. HF was removed and the resin was washed extensively, first with diethylether and then with chloroform. A standard HF protocol was then employed for 60 min at 0 °C. Cleaved protein-resin mixtures are stored under vacuum in the dark at room temperature.

Peptide composition and sequences were confirmed by amino acid analysis on a phenylthiocarbonyl (PTC) derivatizer-analyzer (ABI model 420) as well as automated Edman degradation on a peptide sequencer (ABI model 477A). Crude proteins were purified by reversed-phase high-performance liquid chromatography (HPLC) as shown in Figure 3. Both T₄CaIVS3 and T₄M2δ elute from the column as well-resolved peaks. Homogeneity of the preparation was confirmed by capillary zone electrophoresis (67) and sodium dodecylphosphate (SDS) gel electrophoresis (68) on 16% tricine gels (Novex, Encinitas, CA). Molecular weights (*M_r*) were determined using low-range molecular weight markers (Diversified Biotech, Newton Centre, MA). The molecular weight of T₄M2δ ≈ 11,000 and T₄CaIVS3 ≈ 9000. Yields are low—≤ 1% of the cleaved protein-resin mixture.

Reconstitution in Planar Lipid Bilayers and Single-Channel Assay

Proteins were incorporated into planar lipid bilayers from mixed lipid-protein monolayers. Purified protein was extracted with lipid (Avanti Biochemicals, Alabaster, AL): PC [1,2-diphytanoyl-*sn*-glycero-3-phosphocholine] or

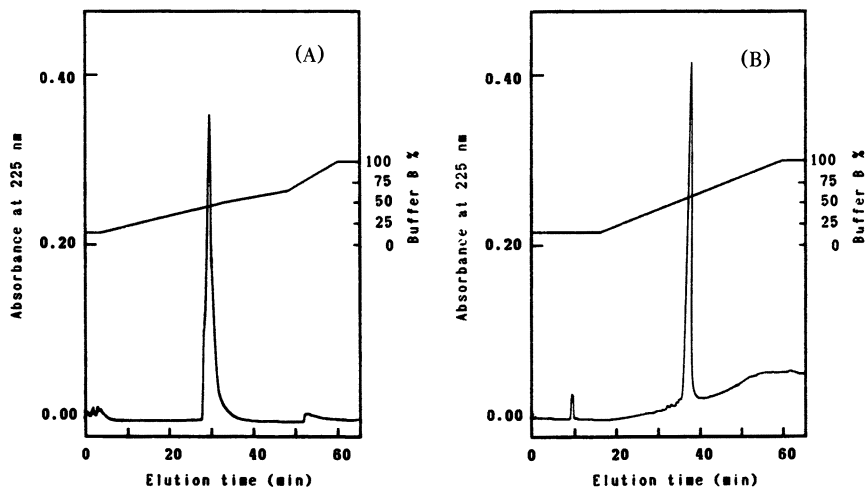


Figure 3. Reversed-phase HPLC of synthetic channel proteins. (A) $T_4CaIVS3$ was purified by repeated reversed-phase (RP) HPLC ($4\times$) with a base-stable $4.6\text{-mm} \times 150\text{-mm}$ PLRP-S- 8μ , 300-\AA C-18 column (Polymer Laboratories Ltd.) equilibrated in deionized-distilled water (pH 6.5) that contained 15% B (B = 90% 2-propanol in water, pH 9.0). Ammonium hydroxide was used to adjust pH. The crude cleaved peptide-resin mixture was dissolved in trifluoroethanol (TFE, 99 + %; Aldrich) and filtered through glass wool. The TFE solution was adjusted to pH 7.0 with dilute NH_4OH . Dissolved protein was injected onto the column. Protein was eluted using the previously described gradient. Fractions were analyzed by SDS polyacrylamide gel electrophoresis (PAGE) (16% tricine; Novex). Fractions that contained the correct molecular weight species were pooled and rechromatographed as before except that the TFE solution was diluted with 10 M guanidinium-HCl followed by 2 min of sonication and 5 min of centrifugation in a microfuge. This procedure was followed for the subsequent two HPLC runs. Further HPLC (beyond $4\times$) did not yield improved separation. The small peak that elutes at 52 min is also present in blank runs. (B) $T_4M2\delta$ was purified by multiple HPLC runs on a Vydac C_4 (semiprep) 214 TP 1010 RP column equilibrated in 75% solvent A (deionized-distilled water containing 0.1% HPLC grade trifluoroacetic acid; Pierce) and 25% solvent B (80% v/v HPLC grade acetonitrile and water containing 0.1% trifluoroacetic acid). Protein was purified through a series of gradient steps followed by 30-min isocratic periods at 55, 62, and 75% of solvent B. Fractions were collected and analyzed by SDS PAGE. Purified protein was reinjected onto a narrow-bore Vydac C_4 RP column TP 214 54 equilibrated as previously described. Protein was eluted using the gradient shown.

POPE-POPC [1-palmitoyl-2-oleoyl-*sn*-glycero-3-phosphoethanolamine (POPE) and 1-palmitoyl-2-oleoyl-*sn*-glycero-3-phosphocholine (POPC)] in a 4:1 ratio, 5 mg/mL in hexane (49). Bilayers were formed at the tip of patch pipets by apposition of monolayers initially formed at the air-water interface (69). Bilayer experiments were performed at $24 \pm 2^\circ\text{C}$. Electrical recordings

and data processing were carried out as described in the literature (49, 69). Conductance values were calculated from Gaussian fits to current histograms. Channel open and closed lifetimes were determined by probability density analysis (69).

Figure 4 shows single-channel current records obtained with T₄CaIVS3. The single-channel conductance in symmetric 50-mM CaCl₂ is 7 pS. The channel is cation-selective and conducts both divalent and monovalent cations with an apparent selectivity ratio inferred from conductance ratios of Ba²⁺ > Ca²⁺ > Sr²⁺ > Na⁺ > K⁺ ≫ Cl⁻ (70, 71). Channel conductance and selectivity are in agreement with known values for the authentic DHP-sensitive calcium channel (59).

The DHP-sensitive calcium channel exhibits nanomolar affinity for many DHP derivatives (16). In addition, enantiomers that act as activators (agonists) or blockers (antagonists) of calcium channels have been described (17). The synthetic pore protein T₄CaIVS3 emulates pharmacological properties of the authentic channel. Figure 4 shows the effect of addition of the agonist BayK 8644 (Figure 4B). Addition of the drug results in an increased channel mean open time as well as an increased open-channel probability. Channels are blocked by the DHP derivative nifedipine, as well as the phenylalkylamine verapamil, the local anesthetic derivative QX-222, and by Cd²⁺ and Ca²⁺. The remarkable stereospecific action of DHP enantiomers on authentic calcium channels by the agonist and antagonist effects of (-)BayK 8644 and (+)BayK 8644, respectively, is closely matched by the action exerted on T₄CaIVS3 (71).

T₄M2δ forms ionic channels in lipid bilayers (Figure 5). Conductance events are homogeneous, and openings that last several seconds are frequent. The channel is cation-selective. The single-channel conductance in PC bilayers and symmetric 0.5-M KCl is 24 pS. The channel is blocked by micromolar concentration of the local anesthetic channel blocker, QX-222 (49). These channel properties match properties characteristic of the authentic *Torpedo* AChR (Table I).

Sequence Specificity

The involvement of specific residues in the determination of conductance properties of the protein is readily addressed by use of the synthetic proteins. Accordingly, a tethered tetramer of M2δ segments in which serine-8 is replaced with alanine was synthesized. This analog, T₄M2δ(S → A), also forms channels in PC membranes with a single-channel conductance in symmetric 0.5-M KCl of 20 pS (49), lower than the 24 pS observed with T₄M2δ. These results are in accord with observations obtained with site-directed mutagenesis of rodent acetylcholine receptors (72).

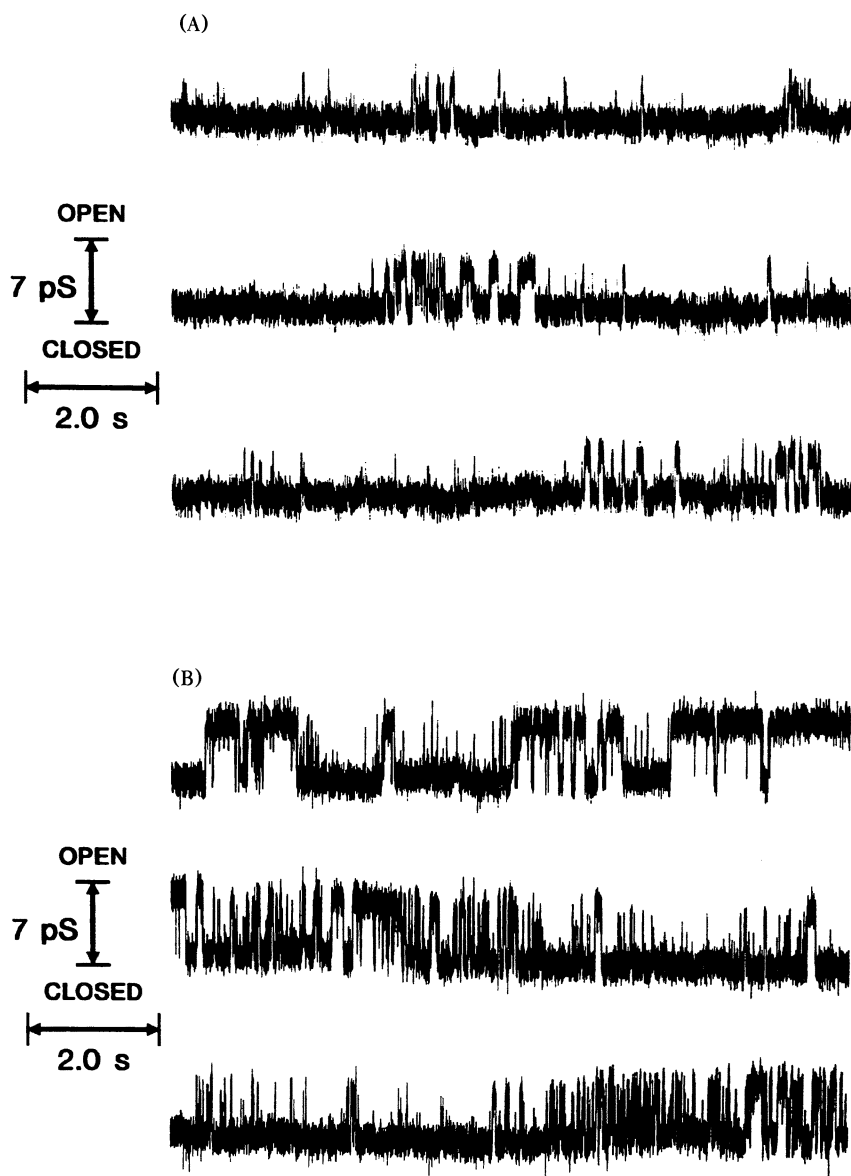


Figure 4. Single-channel recordings from a lipid bilayer containing $T_4CaIVS3$ in symmetric 50-mM $CaCl_2$. Currents were recorded at 100 mV from POPE-POPC membrane before (A) and after (B) addition of 100-nM racemic BayK 8644. Addition of BayK 8644 results in an increase in the open-channel probability from 5% to 35% and the concurrent prolongation of the channel mean open time.

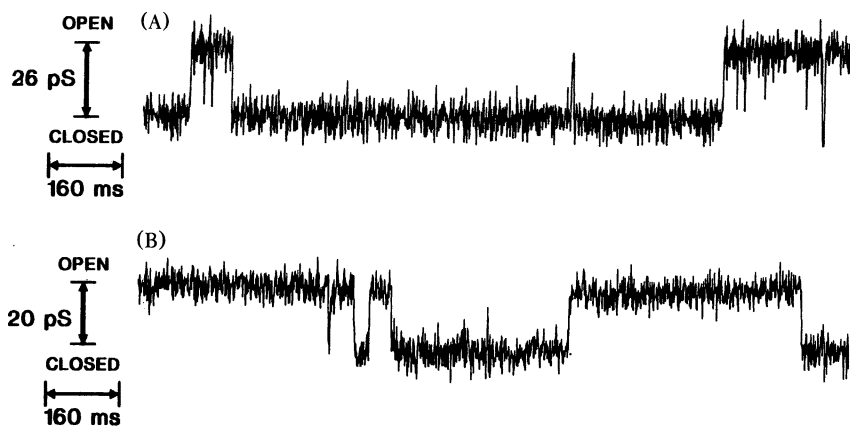


Figure 5. Single-channel currents from lipid bilayers containing the synthetic $T_4M2\delta$ and $T_4M2\delta(S \rightarrow A)$ proteins. Currents were recorded at 100 mV in symmetric 0.5-M KCl from PC membranes containing $T_4M2\delta$ (A) and $T_4M2\delta(S \rightarrow A)$ (B). Calculated single-channel conductances are 26 and 20 pS, respectively. For other details, see reference 49.

Table I. Ionic Conduction Characteristics of Authentic Muscle and Neuronal AChR and of the Synthetic Protein $T_4M2\delta$

Property	AChR (Muscle) ^a	AChR (Neuronal) ^b	M2 δ Peptide ^c	$T_4M2\delta$ Tetramer ^d
γK^+ (pS)	50	25–48	48	24
$\gamma K^+/\gamma Na^+$	1.1	≈ 1	1.2	1.33
$\gamma Cl^-/\gamma Na^+$	≤ 0.01	Cation selective	≤ 0.03	≤ 0.03

^a Determined in symmetric 0.5-M NaCl and KCl and from reversal potential measurements of *Torpedo* AChR (77).

^b Determined in 0.14-M KCl or CsCl and from reversal potential measurements on rat retinal ganglion cells (88) and chick ciliary ganglia (78).

^c Refers to the most frequent event determined in symmetric 0.5-M NaCl and KCl and from reversal potential measurements (48).

^d Determined in symmetric 0.5-M NaCl and KCl and from reversal potential measurements (49).

Other hydrophobic sequences postulated to form transmembrane segments in these two channel proteins were also considered. M1 δ of the AChR and IVS5 of the DHP-sensitive calcium channel were selected (Figure 1A); these sequences are also highly conserved but are not considered to line an aqueous channel (4–7). Tetramers of M1 δ and IVS5 are predicted to form clusters of α -helices and are of sufficient length to span the lipid bilayer. Accordingly, tethered tetramers $T_4M1\delta$ and $T_4CaIVS5$ were synthesized.

When these proteins are incorporated in lipid bilayers, they do not form distinct unitary conductance events characteristic of channel proteins (49, 71). Therefore, a requirement for sequence specificity in the design is apparent.

Oligomer Size as a Plausible Determinant of Single-Channel Conductance

Single-channel current records from membranes containing $T_4CaIVS3$ (Figure 4) or $T_4M2\delta$ (Figure 5) show increases in membrane conductance that occur as discrete steps—integral multiples of the elementary conductances—that indicate that a tethered tetramer, and not a self-assembled oligomer, is the conductive species. Therefore, the four-helix bundle proteins (Figure 1) are plausible structures that underlie the conductance events.

The *Torpedo* AChR, a muscle-type AChR, is a pentameric protein whereas the $T_4M2\delta$ pore-forming protein described is a four-helix bundle. The five-helix bundle ($T_5M2\delta$) has not yet been characterized; therefore, a detailed comparison of the single-channel conductance of *Torpedo* AChR with a $T_5M2\delta$ is not possible. However, information about the channel properties of other members of the superfamily of nicotinic AChRs is available.

Neuronal AChRs purified from avian, rodent, or bovine brains are composed of two classes of subunits: an α -like subunit that contains two adjacent cysteines that are homologous to the C-192,193 of the *Torpedo* AChR α subunit, and a β -like subunit (73). It was suggested that a tetrameric $\alpha_2\beta_2$ array could account for the known biochemical properties of neuronal AChRs. This contrasts with the $\alpha_2\beta\gamma\delta$ subunit structure of pentameric muscle AChRs. The single-channel conductance (with Na^+ as the permeant ion; Table I) of avian (20 pS) (74) and rodent (13 pS) (75) neuronal nicotinic AChRs expressed in *Xenopus* oocytes after cDNA or cRNA injection are remarkably lower than those of bovine muscle (50 pS) (76) or *Torpedo* (60 pS) (77) AChRs expressed and recorded under comparable conditions. Single-channel recordings from native neuronal AChRs in chick ciliary ganglia (78) have documented the occurrence of events with single-channel conductance for monovalent cations ≈ 20 pS. Sequences of the M2 segments of these AChR subunits are ostensibly homologous, which suggests that the distinct conductances may not arise from sequence specificity. It is likely that oligomeric size is a factor that underlies the conductance disparity. The similarity of single-channel conductances measured with $T_4M2\delta$ to that of the neuronal AChRs suggests that a tetrameric structure may underlie the conductance events of neuronal AChRs in contrast to the pentameric structure identified for muscle AChRs.

Concluding Remarks and Perspectives

The results summarized in Figures 4 and 5 and in Table I show that the designed pore-forming proteins contain a functional ion-conducting pore, an ion selectivity filter, channel blocker binding sites, and stereospecific drug-binding sites, and exhibit transitions between the closed and open states in the millisecond time range. The fact that these functional elements of the pore-forming structure of authentic channel proteins (1) are contained within the bundles of α -helices with specific amino acid sequence (Figure 1) demonstrates that the design mimics the key features of the inner bundle that forms the pore of voltage- and ligand-gated channel proteins.

A plethora of peptides aggregate in lipid bilayers, either to form well-defined single-channel events or to produce more erratic membrane-disruptive effects, as recently reviewed (79). Amphipathic peptides that aggregate as ordered aligned arrays that are parallel to the bilayer normal may expose charged or polar residues toward a central pore and thus form discrete conductance events. Aggregates of different oligomeric number and hence distinct conductances are expected to occur (5, 48, 79). However, dependent on the specific sequence, amphipathic peptides may preferentially orient themselves perpendicular to the membrane normal or form transient micelles that produce sporadic changes in conductance that resemble single-channel events (80). Consequently, it is of paramount importance that the channel-forming ability of peptides be thoroughly documented, including a careful selection of suitable controls, because otherwise erroneous conclusions are likely to be drawn.

Recently, a study was published on an amphipathic peptide, MA- β , that approximates the sequence of a segment of the nicotinic AChR (81). The amino acid sequence of the synthetic MA- β peptide included the substitution of the C-terminal glutamic acid for lysine. This change may profoundly influence potential channel properties of the peptide. The conclusion that synthetic peptides do not serve as a reliable model system for the pore structure of channel proteins is thus based on results obtained with a single peptide that does not exactly represent the sequence of the target protein. Further, the MA segments of the AChR are otherwise not considered to be involved in pore lining (5, 39, 42, 44–47, 49, 61). No efforts to evaluate the potential significance of the results obtained with the MA- β peptide with respect to the pore-forming structure of the AChR are apparent (81). MA- β is reported to form heterogeneous conductance events of diverse open-channel lifetime. Ionic selectivity of observed channels was not addressed. Recordings with MA- β were obtained with concentrations of peptide up to 50 $\mu\text{g}/\text{mL}$, a large excess for detection of single molecular events. Recordings were displayed at time resolution too low to validate the occurrence of discrete single-channel events, and very few events were analyzed; about 200

events were used to establish conductance levels. In addition, no control peptides of similar length or amino acid composition were investigated; neither were peptides that represent other segments of the authentic AChR or peptides with site-specific substitutions of the MA- β sequence. The very limited characterization of MA- β only demonstrates that the peptide indeed interacts with the bilayer but does not substantiate its channel-forming ability. Thus, these results do not warrant any deductions with regard to the relevance of synthetic peptides in emulating the structure of the authentic AChR channel.

Positively charged residues of a peptide interact with negatively charged lipids and cause channel activity (82). This limitation is associated with the study of the MA- β peptide (81) as well as a study of a positively charged peptide that represents an S4 segment of the voltage-dependent sodium channel (83); both peptides were studied in a negatively charged bilayer. The lack of appropriate controls further weakens the conclusions of such studies. Unfortunately, such superficial studies that lack rigor in design and characterization (81, 83, 84) are not infrequent and hamper the development of sound model systems for pore proteins.

The comprehensive strategy described here aims to identify in the primary structure of voltage- and ligand-gated channel proteins sequence-specific motifs that define the pore-forming properties. Particular emphasis is on pore size and ionic selectivity of the open channel. The validity of this approach is supported by

- the ability of both synthetic monomeric peptides that represent a single presumed transmembrane segment to self-assemble in lipid bilayers to form conductive oligomers
- the pore-forming capability of larger nonlinear synthetic proteins with sequences that represent suggested transmembrane segments, designed to adopt a predetermined conformation. Synthetic monomeric peptides with sequences of the M2 δ segment of the acetylcholine receptor or an S3 segment of the brain sodium channel form cation-selective channels in lipid bilayers (37, 48), and four-helix bundle proteins that represent the presumed pore structure of the AChR channel and the DHP-sensitive calcium channel mimic the activity of the target channel proteins (49, 71). Work in progress indicates that this strategy is also valuable for identification of pore-lining elements of a voltage-gated potassium channel and of the glycine receptor (85).

Synthetic peptides 21–23 amino acids in length, which represent the sequence of one transmembrane segment, provide a tool to readily assay the

involvement of such segments and the participation of specific residues in lining the pore. In addition, short peptides are quite accessible to chemical synthesis and purification. A salient advantage inherent in the design of branched molecules that favor the formation of α -helical bundles is the control of oligomeric number. At present, tethered tetramers of identical peptide blocks have been shown to mimic key pore properties of the target protein. An immediate goal is to design and synthesize proteins that more closely match the sequence of the authentic channel: The realization of heterooligomers as well as pentameric or hexameric structures would greatly enhance the power of this approach in investigations of the structure and functional properties of the pore-forming element.

The extensive sequence conservation and the occurrence of homologous domains within the superfamilies of voltage- and ligand-gated channel proteins suggests the existence of a common motif for the pore-forming element of these proteins. A tightly packed, ordered structure of proteins gives rise to regular structural motifs, such as the α -helix. Amphipathic segments of sufficient length to traverse the hydrocarbon core of a lipid bilayer and with a propensity for α -helical conformation are identifiable in all primary structures of channel proteins (5). Membrane-spanning helices 20–22 residues in length have been identified in the high-resolution structure of two membrane proteins, bacteriorhodopsin (86) and the photosynthetic reaction center (87). Consequently, a bundle of amphipathic α -helices that form an aqueous pore is a plausible unifying structure for this key functional element of channel proteins.

Acknowledgments

This research was supported by grants from the U.S. Public Health Service (GM-42340 and MH-44638 to M. Montal and GM-43617 to J. M. Tomich), the Office of Naval Research (N00014-89-J-1469 to M. Montal), the Department of the Army Medical Research (DAMD17-89-C-9032 to M. Montal), and by a Research Scientist Award to M. Montal from the Alcohol, Drug Abuse and Mental Health Administration's National Institute of Mental Health (MH-00778).

Literature survey was completed in February 1991.

References

1. Hille, B. *Ionic Channels of Excitable Membranes*; Sinauer: Sunderland, MA, 1984.
2. Hess, P. *Annu. Rev. Neurosci.* **1990**, *13*, 337–356.
3. Numa, S. *Harvey Lectures* **1989**, *83*, 121–165.
4. Greenblatt, R. E.; Blatt, Y.; Montal, M. *FEBS Lett.* **1985**, *193*, 125–134.
5. Montal, M. *FASEB J.* **1990**, *4*, 2623–2635.
6. Eisenberg, D.; Weiss, R. M.; Terwilliger, T. C.; Wilcox, W. *Faraday Symp. Chem. Soc.* **1982**, *17*, 109–120.

7. Eisenberg, D. *Annu. Rev. Biochem.* **1984**, *53*, 595–623.
8. Finer-Moore, J.; Bazan, J. F.; Rubin, J.; Stroud, R. M. In *Prediction of Protein Structure and the Principles of Protein Conformation*; Fasman, G. D., Ed.; Plenum: New York, 1989; pp 719–759.
9. Ellis, S. B.; Williams, M. E.; Ways, N. R.; Brenner, R.; Sharp, A. H.; Leung, A. T.; Campbell, K. P.; McKenna, E.; Koch, W. J.; Hui, A.; Schwartz, A.; Harpold, M. M. *Science (Washington, D.C.)* **1988**, *241*, 1661–1664.
10. Ruth, P.; Röhrkasten, A.; Biel, M.; Bosse, E.; Regulla, S.; Meyer, H. E.; Flockerzi, V.; Hofmann, F. *Science (Washington, D.C.)* **1989**, *245*, 1115–1118.
11. Jay, S. D.; Ellis, S. B.; McCue, A. F.; Williams, M. E.; Vedvick, T. S.; Harpold, M. M.; Campbell, K. P. *Science (Washington, D.C.)* **1990**, *248*, 490–492.
12. Catterall, W. A.; Seagar, M. J.; Takahashi, M. *J. Biol. Chem.* **1988**, *263*, 3535–3538.
13. Mikami, A.; Imoto, K.; Tanabe, T.; Niidome, T.; Mori, Y.; Takeshima, H.; Narumiya, S.; Numa, S. *Nature (London)* **1989**, *340*, 230–233.
14. Tanabe, T.; Beam, K. G.; Powell, J. A.; Numa, S. *Nature (London)* **1988**, *326*, 134–139.
15. Perez-Reyes, E.; Kim, H. S.; Lacerdan, A. E.; Horney, W.; Wei, X.; Rampe, D.; Campbell, K. P.; Brown, A. M.; Birnbaumer, L. *Nature (London)* **1989**, *340*, 233–236.
16. Triggle, D. J.; Langs, D. A.; Janis, R. A. *Med. Res. Rev.* **1989**, *9*, 123–180.
17. Vaghy, P. L.; Williams, J. S.; Schwartz, A. *Am. J. Cardiol.* **1987**, *59*, 9A–17A.
18. Tanabe, T.; Takeshima, H.; Mikami, A.; Flockerzi, V.; Takahashi, H.; Kangawa, K.; Kojima, M.; Matsuo, H.; Hirose, T.; Numa, S. *Nature (London)* **1987**, *328*, 313–318.
19. Shish, D. F.; Engle, D. B.; Varadi, G.; Lotan, I.; Singer, D.; Dascal, N.; Schwartz, A. *FEBS Lett.* **1989**, *250*, 509–514.
20. Perez-Reyes, E.; Wei, X.; Castellano, A.; Birnbaumer, L. *J. Biol. Chem.* **1990**, *265*, 20430–20436.
21. Snutch, T.; Leonard, J. P.; Gilbert, M. M.; Lester, H. A.; Davidson, N. *Proc. Natl. Acad. Sci. U.S.A.* **1990**, *87*, 3391–3395.
22. Koch, W. J.; Hui, A.; Shull, G. E.; Ellinor, P.; Schwartz, A. *FEBS Lett.* **1989**, *250*, 386–388.
23. Biel, M.; Ruth, P.; Bosse, E.; Hullin, R.; Stühmer, W.; Flockerzi, V.; Hofmann, F. *FEBS Lett.* **1990**, *269*(2), 409–412.
24. Noda, M.; Ikeda, T.; Kayano, T.; Suzuki, H.; Takashima, H.; Kurasaki, M.; Takahashi, H.; Numa, S. *Nature (London)* **1986**, *320*, 188–192.
25. Noda, M.; Shimizu, S.; Tanabe, T.; Takai, T.; Kayano, T.; Ikeda, T.; Takahashi, H.; Nakayama, H.; Kanaoka, Y.; Minamino, N.; Kangawa, K.; Matsuo, M. H.; Raftery, M. A.; Hirose, T.; Inayama, S.; Hayashida, H.; Miyata, T.; Numa, S. *Nature (London)* **1984**, *312*, 121–127.
26. Kayano, T.; Noda, M.; Flockerzi, V.; Takahashi, H.; Numa, S. *FEBS Lett.* **1988**, *228*, 187–194.
27. Bogart, R. B.; Cribbs, L. L.; Muglia, L. K.; Kephart, D. D.; Kaiser, M. W. *Proc. Natl. Acad. Sci. U.S.A.* **1989**, *86*, 8170–8174.
28. Trimmer, J. S.; Cooperman, S. S.; Tomiko, S. A.; Zhou, J.; Crean, S. M.; Boyle, M. B.; Kallen, R. G.; Sheng, Z.; Barchi, R. L.; Sigworth, F. J.; Goodman, R. H.; Agnew, W. S.; Mandel, G. M. *Neuron* **1989**, *3*, 33–49.
29. Salkoff, L.; Butler, A.; Wei, A.; Scavardi, N.; Giffen, K.; Ifune, C.; Goodman, R.; Mandel, G. *Science (Washington, D.C.)* **1987**, *237*, 744–749.
30. Tempel, B. L.; Papazian, D. M.; Schwarz, T. L.; Jan, Y. N.; Jan, L. Y. *Science (Washington, D.C.)* **1987**, *237*, 770–775.

31. Butler, A.; Wei, A.; Baker, K.; Salkoff, L. *Science (Washington, D.C.)* **1989**, *243*, 943–947.
32. Tempel, B. L.; Jan, Y. N.; Jan, L. Y. *Nature (London)* **1988**, *332*, 837–839.
33. Frech, G. C.; Van Dongen, A. M. J.; Schuster, G.; Brown, A. M.; Joho, R. H. *Nature (London)* **1989**, *340*, 642–645.
34. Baumann, A.; Grupe, A.; Ackermann, A.; Pongs, O. *EMBO J.* **1988**, *7*(8), 2457–2463.
35. Isacoff, E. Y.; Jan, Y. N.; Jan, L. Y. *Nature (London)* **1990**, *345*, 530–534.
36. Ruppertsberg, J. P.; Schröter, K. H.; Sakmann, B.; Stocker, M.; Sewing, S.; Pongs, O. *Nature* **1990**, *345*, 535–537.
37. Oiki, S.; Danho, W.; Montal, M. *Proc. Natl. Acad. Sci. U.S.A.* **1988**, *85*, 2393–2397.
38. Montal, M. In *Ion Channels*; Narahashi, T, Ed.; Plenum: New York, 1990; Vol. 2, pp 1–31.
39. Oiki, S.; Madison, V.; Montal, M. *Proteins: Struct. Function, Genet.* **1990**, *8*, 226–236.
40. Reynolds, J.; Karlin, A. *Biochemistry* **1978**, *17*, 2035–2038.
41. Toyoshima, C.; Unwin, N. *J. Cell Biol.* **1990**, *111*, 2623–2635.
42. Changeux, J. P. In *1988–1989 Fidia Research Foundation; Rita Levi-Montalcini Neuroscience Award Lecture*; Raven: New York, 1990; Vol. 4, pp 22–168.
43. Eisenman, G.; Dani, J. A. *Annu. Rev. Biophys. Biophys. Chem.* **1987**, *16*, 205–226.
44. Giraudat, J.; Dennis, M.; Heidmann, T.; Chang, J.-Y.; Changeux, J.-P. *Proc. Natl. Acad. Sci. U.S.A.* **1986**, *83*, 2719–2723.
45. Oberthür, W.; Hucho, F. *J. Protein Chem.* **1988**, *7*, 141–150.
46. Hucho, F.; Oberthür, W.; Lottspeich, F. *FEBS Lett.* **1986**, *205*, 137–142.
47. Revah, F.; Galzi, J.-L.; Giraudat, J.; Haumont, P.-Y.; Lederer, F.; Changeux, J.-P. *Proc. Natl. Acad. Sci. U.S.A.* **1990**, *87*, 4675–4679.
48. Oiki, S.; Danho, W.; Madison, V.; Montal, M. *Proc. Natl. Acad. Sci. U.S.A.* **1988**, *85*, 8703–8707.
49. Montal, M.; Montal, M. S.; Tomich, J. M. *Proc. Natl. Acad. Sci. U.S.A.* **1990**, *87*, 6929–6933.
50. Eisenman, G.; Villarroel, A.; Montal, M.; Alvarez, O. *Prog. Cell Res.* **1990**, *1*, 195–211.
51. Furois-Corbin, S.; Pullman, A. *Biochim. Biophys. Acta* **1989**, *984*, 339–350.
52. Regan, L.; DeGrado, W. F. *Science (Washington, D.C.)* **1988**, *24*, 976–978.
53. Hahn, K. W.; Klis, W. A.; Stewart, J. M. *Science (Washington, D.C.)* **1990**, *248*, 1544–1547.
54. Mutter, M.; Altmann, E.; Altmann, K.-H.; Hersperger, R.; Koziej, P.; Nebel, K.; Tuchscherer, G.; Vuilleumier, S.; Gremlich, H.-U.; Müller, K. *Helv. Chim. Acta* **1988**, *71*, 835–847.
55. Mutter, M.; Altmann, K.-H.; Tuchscherer, G.; Vuilleumier, S. *Tetrahedron* **1988**, *44*, 771–785.
56. Mutter, M.; Hersperger, R.; Gubernator, K.; Müller, K. *Proteins: Struct., Function, Genet.* **1989**, *5*, 13–21.
57. Rivier, J.; Miller, C.; Spicer, M.; Andrews, J.; Porter, J.; Tuchscherer, G.; Mutter, M. *Proceedings of the International Symposium on Solid Phase Synthesis*; 1991; pp 39–50.
58. Noda, M.; Takahashi, H.; Tanabe, T.; Toyosato, M.; Kikuyotani, S.; Hirose, T.; Asai, M.; Takashima, H.; Inayama, S.; Miyata, T.; Numa, S. *Nature (London)* **1983**, *301*, 251–255.

59. Tsien, R. W.; Hess, P.; McCleskey, E. W.; Rosenberg, R. L. *Annu. Rev. Biophys. Biophys. Chem.* **1987**, *16*, 265–290.
60. Palade, P. T.; Almers, W. *Pflügers Arch.* **1985**, *405*, 91–101.
61. Imoto, K.; Busch, C.; Sakmann, B.; Mishina, M.; Konno, T.; Nakai, J.; Bujo, H.; Mori, Y.; Fukuda, K.; Numa, S. *Nature (London)* **1988**, *335*, 645–648.
62. Merrifield, R. B. *J. Am. Chem. Soc.* **1963**, *85*, 2149–2154.
63. Merrifield, R. B. *Biosci. Rep.* **1985**, *5*, 353–376.
64. Kent, S. B. H. *Annu. Rev. Biochem.* **1988**, *57*, 957–989.
65. Sarin, V. K.; Kent, S. B. H.; Tam, J. P.; Merrifield, R. B. *Anal. Biochem.* **1981**, *117*, 147–157.
66. Tam, J. P.; Heath, W. F.; Merrifield, R. B. *J. Am. Chem. Soc.* **1983**, *105*, 6442–6455.
67. Firestone, M. A.; Michaud, J. F.; Carter, R. H.; Thormann, W. J. *Chromatogr.* **1987**, *407*, 363–368.
68. Laemmli, U. K. *Nature (London)* **1970**, *227*, 680–685.
69. Suarez-Isla, B. A.; Wan, K.; Lindstrom, J.; Montal, M. *Biochemistry* **1983**, *22*, 2319–2323.
70. Grove, A.; Tomich, J. M.; Montal, M. *Soc. Neurosci. Abstr.* **1990**, *16*(2), 957.
71. Grove, A.; Tomich, J. M.; Montal, M. *Proc. Natl. Acad. Sci. U.S.A.* **1991**, *88*, 6418–6422.
72. Leonard, R. J.; Labarca, C. G.; Charnet, P.; Davidson, N.; Lester, H. A. *Science (Washington, D.C.)* **1988**, *242*, 1578–1581.
73. Deneris, E. S.; Boulter, J.; Connolly, J.; Wada, K.; Goldman, D.; Swanson, L. W.; Patrick, J.; Heinemann, S. *Clin. Chem.* **1989**, *35*, 731–737.
74. Ballivet, M.; Nef, P.; Couturier, S.; Rungger, D.; Bader, C. R.; Bertrand, D.; Cooper, E. *Neuron* **1988**, *1*, 847–852.
75. Papke, R. L.; Boulter, J.; Patrick, J.; Heinemann, S. *Neuron* **1989**, *3*, 589–596.
76. Sakmann, B.; Methfessel, C.; Mishina, M.; Takahashi, T.; Takai, T.; Kurasaki, M.; Fukuda, K.; Numa, S. *Nature (London)* **1985**, *318*, 538–543.
77. Montal, M.; Anholt, R.; Labarca, P. In *Ion Channel Reconstitution*; Miller, C., Ed.; Plenum: New York, 1986; pp 157–204.
78. Margiotta, J. F.; Gurantz, D. *Dev. Biol.* **1989**, *135*, 326–339.
79. Sansom, M. *Prog. Biophys. Molec. Biol.* **1991**, *55*, 139–235.
80. Montal, M. *Annu. Rev. Biophys. Bioeng.* **1976**, *5*, 119–175.
81. Ghosh, P.; Stroud, R. M. *Biochemistry* **1991**, *30*, 3551–3557.
82. Montal, M. *J. Membr. Biol.* **1972**, *7*, 245–266.
83. Tosteson, M. T.; Auld, D. S.; Tosteson, D. C. *Proc. Natl. Acad. Sci. U.S.A.* **1989**, *86*, 707–710.
84. Anzai, K.; Hamasuna, M.; Kadono, H.; Lee, S.; Aoyagi, H.; Kirino, Y. *Biochim. Biophys. Acta* **1991**, *1064*, 256–266.
85. Grove, A.; Iwamoto, T.; Montal, M. S.; Reddy, G. L.; Marrer, S.; Tomich, J. M.; Montal, M. In *Biotechnology of Cell Regulation*; Verma, R., Ed.; Serono Symposia Publications; Raven: New York, 1991; pp 89–102.
86. Henderson, R.; Baldwin, J. M.; Ceska, T. A.; Zemlin, F.; Beckmann, E.; Downing, K. H. *J. Molec. Biol.* **1990**, *213*, 899–929.
87. Deisenhofer, J.; Michel, H. *Science (Washington, D.C.)* **1989**, *245*, 1463–1473.
88. Lipton, S. A.; Aizenman, E.; Loring, R. *Pflügers Arch.* **1987**, *410*, 37–43.

RECEIVED for review February 26, 1991. ACCEPTED revised manuscript July 20, 1992.

Fractal Analysis of Channel Mechanisms

Larry S. Liebovitch

Department of Ophthalmology, Columbia College of Physicians and Surgeons,
Columbia University, 630 West 168th Street, New York, NY 10032

The sequence of open and closed states measured from individual ion channels is fractal; namely, the pattern of openings and closings at one temporal resolution is similar to that viewed at other temporal resolutions. This phenomenon suggests that ion channel proteins have (1) many states that are shallow energy minima, (2) different physical processes that cooperate to open and close the channel, (3) activation energy barriers between states that vary in time, and (4) a set of processes that have different widths in their distribution of activation energy barriers. If the switching between different conformational states is deterministic chaos rather than a stochastic process, then channels may be able to organize structure fluctuations into coherent patterns of motion.

Ion Channels

As already described in detail in the previous chapters, ion channels are proteins that consist of a few thousand amino acid residues and a few hundred carbohydrate residues that span the lipid cell membrane (1, 2). These channel proteins can have several different three-dimensional structures called conformational states. Some conformational states have a central hole, so that the channel is open to the flow of ions into or out of the cell. Other conformational states are closed to the flow of ions. Because these conformational states differ by energies that are less than the thermal fluctuations, a channel is always spontaneously switching between different open and closed states.

0065-2393/94/0235-0357\$08.00/0
© 1994 American Chemical Society

The sequence of open and closed states of an individual ion channel can be revealed by the patch clamp technique developed by Neher, Sakmann, Sigworth, Hamill, and others (1, 2). A small piece of cell membrane, which may contain one ion channel, is sealed in the tip of a micropipette. The picoampere currents when the channel is open can be resolved. Thus, as shown in Figure 1, the durations of the times spent in the open and closed states can be measured. Because this measurement is performed on a single protein molecule, it is a much more sensitive probe of protein kinetics than other biochemical or biophysical techniques that average their signals over many molecules in different states.

The switching between different conformational states results from physical processes in the channel protein. Thus, the patch clamp data is an important probe of the mechanisms that cause the channel protein to change its conformational state. We will review how the changing interpretations of the patch clamp data led to a new understanding of the mechanisms that open and close the ion channel.

Hodgkin–Huxley Model

In 1952 Hodgkin and Huxley (3) proposed a mathematical form that could represent the currents measured across cell membranes. They noted (3) that “these equations can be given a physical basis if we assume that potassium can only cross the membrane when four similar particles occupy a certain region of the membrane . . . and if the sodium conductance is assumed to be proportional to the number of sites on the inside of the membrane which are

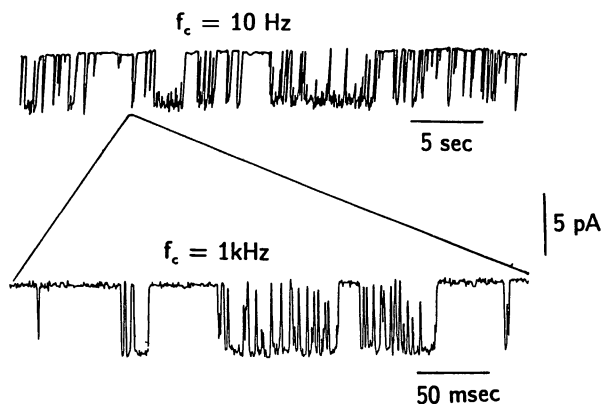


Figure 1. The current through an individual ATP-sensitive potassium channel of rat pancreatic B cells recorded by K. Gillis, L. Falke, and S. Mislser. At the bottom, one opening is shown at finer time resolution to illustrate that it has self-similar fractal properties. (Reproduced with permission from reference 38. Copyright 1990 New York Academy of Sciences.)

occupied simultaneously by three activating molecules but are not blocked by an inactivating molecule.” Although it is now known that channels function as fixed units rather than transitorily assembled forms, the central idea of this model that channels have only a few discrete states has remained. It is assumed that the switching between these different states is random; that is, there is a constant probability per second of switching from one state to another. This mathematical formulation is called a Markov model. The physical interpretation of these mathematical assumptions is that the channel protein has a few distinct, independent conformational states, which are separated by significant activation energy barriers, that are constant in time.

Fractals

The psychologist Maslow wrote that “if the only tool you have is a hammer, you tend to treat everything as if it were a nail” (4). Markov processes based on the Hodgkin–Huxley model had been widely used to describe ionic currents measured in many different experiments. However, in 1986, we began to use a new tool to analyze the patch clamp data. The insight gained from this new analysis has changed our ideas about the processes that open and close the ion channel. The new tool is based on fractals.

Fractals have fascinating properties that are present in many natural objects and had not been incorporated in previous models of nature (5, 6). If any small piece of a fractal is magnified, it appears similar to a larger piece. This property is called self-similarity and is illustrated by the fractal in Figure 2. Self-similarity can occur only if structures at a small scale are related to structures at a larger scale. Fractal objects include the repeated bifurcations of the airways in the lung (7), the distribution of blood flow in the ever-smaller vessels in the heart (8), and the ever-finer infoldings of cellular membranes (9).

Quantitatively, self-similarity means that a property L measured at scale x is proportional to the same property measured at scale ax ; namely,

$$L(x) = kL(ax) \quad (1)$$

where k is a constant. Such self-similarity means that a property L measured at resolution scale x will be a power law function of the scale x :

$$L(x) = Ax^{1-d} \quad (2)$$

where A is a constant and d , which is between 1 and 2, is called the fractal dimension. The scaling relation of eq 2 can be verified by substituting eq 2 into eq 1.

Fractals have some mathematical properties that many scientists may find surprising. For example, the moment of a set of measurements, such as the

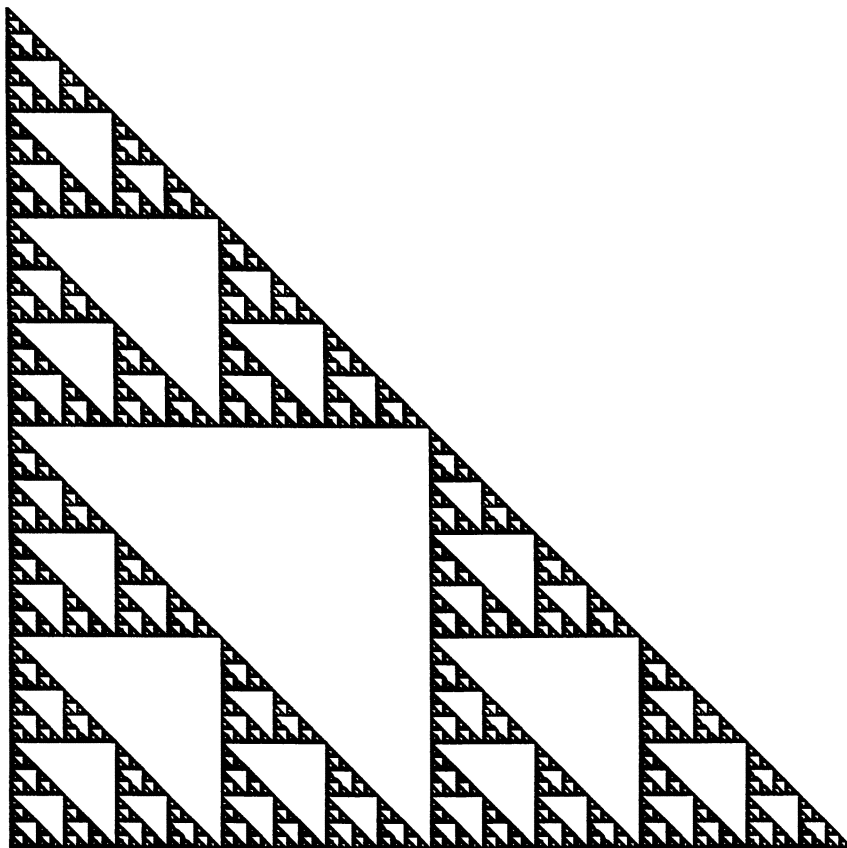


Figure 2. The Sierpinski triangle is an example of a fractal object. It is self-similar, that is, small pieces are similar to the whole object. (Reproduced with permission from reference 38. Copyright 1990 New York Academy of Sciences.)

mean or variance, exists when it approaches a finite limiting value as additional data are analyzed. However, in a fractal, a moment may not exist because as more data are analyzed, the value of the moment may continually increase or decrease rather than approach a finite limiting value (6). This changing moment value is due to the fact that self-similarity means that the small scale deviations are repeated as ever-larger deviations at larger scales. For example, examination of Figure 2 at ever-finer spatial resolution reveals ever more holes, and thus the average density approaches zero rather than a finite value. In a fractal time series, there will be ever-larger deviations that have the self-similar shape of the smaller deviations, and thus the variance will approach infinity. The value of the signal averaged over short times can thus fluctuate widely.

Single Channel Recordings Have Fractal Properties

Researchers who do patch clamp experiments (including us) often find that the activity of channel openings and closings fluctuates in time and changes suddenly from periods of great activity to periods of little activity. These changes are interpreted as reflections of sudden physical changes in the channel protein. However, to us these alternations resemble the fluctuations produced by a fractal process, with infinite variance, where the underlying physical process remains absolutely constant.

This interpretation is supported by the self-similar nature of the data shown in Figure 1. There are bursts within bursts within bursts of openings and closings. Channel data collected within the upper hierarchies of bursts will have high channel activity, whereas data collected between the hierarchies will have little channel activity.

These impressions were suggestive but only qualitative. Thus, we needed new quantitative methods to test if the channel data were fractal. Previously, people had assumed various kinetic schemes and fit these schemes to the data to determine the parameters of these models. Our approach was very different. We developed new methods to analyze and display the data (10, 11). On these new plots, fractal and other models obviously have different forms. Thus, we can plot the data and let the form of the plots reveal the characteristics of the channel kinetics.

We recorded the current through potassium channels in the corneal endothelium in analog form on a frequency modulation (FM) tape recorder. We sampled the data with an analog-to-digital (A/D) converter and then determined the distributions of closed times on our computer. To sample the same data at different time scales we repeated the analysis at different A/D sampling rates. These results are shown in Figure 3. Each histogram has a very different time scale. When the data are sampled very rapidly, the analysis concentrates on the short closings; when the data are sampled very slowly, the analysis concentrates on the long closings. Yet, as seen in Figure 3, the shape of each distribution is similar. This is self-similarity in time. That is, the form of the distribution is the same when the data are sampled at different time scales. This observation implies that there exists a fractal scaling relationship that describes how the brief closings are related to the long closings. When the data are not fractal, the histograms sampled this way do not have this form (10).

The self-similarity of the data suggests another new quantitative measure of the channel kinetics. The most frequently used kinetic measure is the kinetic rate constant, which is the probability per second that the channel switches from one state to another. However, the channel must remain in a state long enough to be detected in that state. Thus, what we really want to measure is the conditional probability (per second) that if the channel remains in a state for at least a certain time t_{eff} that it would switch to

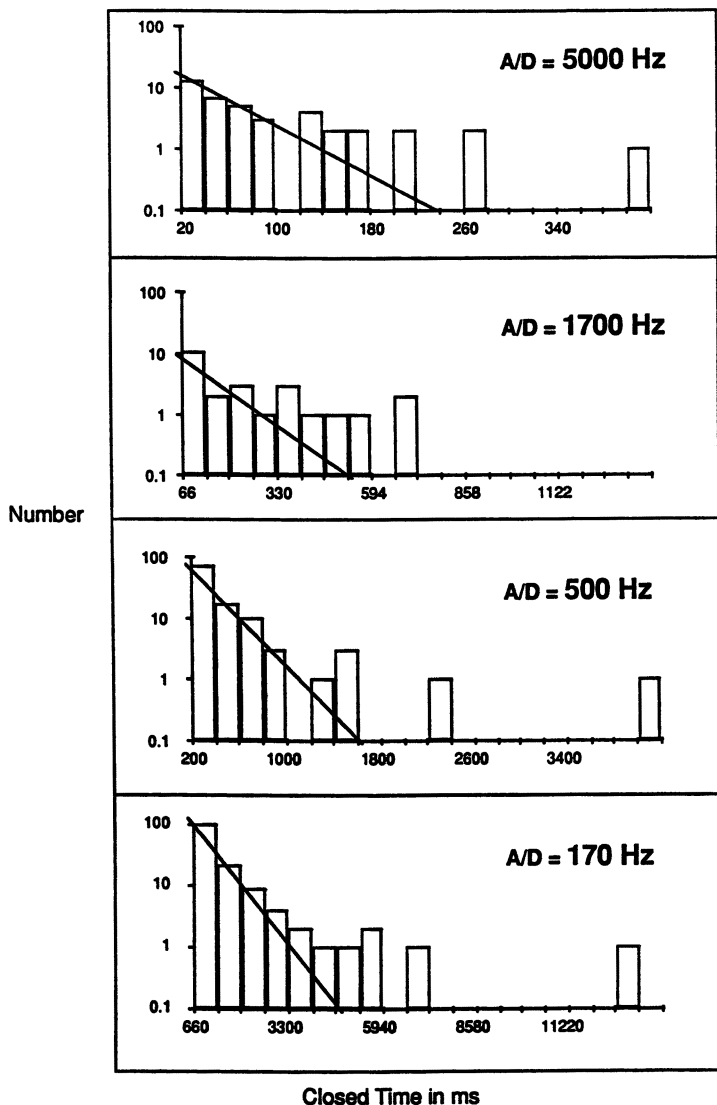


Figure 3. To determine if the current through a potassium channel in the corneal endothelium has fractal properties, we sampled the same analog recording of the current at four different analog-to-digital (A/D) conversion rates. The histogram of closed times determined from each A/D rate are shown. The time axis of each histogram is quite different because the fast A/D sampling rates preferentially sample the brief closings, whereas the slow A/D sampling rates preferentially sample the long closings. Note that the form of each distribution is similar. That is, the form of the closed-time histogram is the same when the data are sampled at different rates, indicating that these data are fractal in time. Thus there exists a fractal scaling relationship that describes how the brief closings are related to the long closings. (Reproduced with permission from reference 38. Copyright 1990 New York Academy of Sciences.)

another state. We called this measure the effective kinetic rate constant, k_{eff} (10, 11). The time t_{eff} required for detecting the state of the channel is the effective time resolution at which we measure the data.

The nature of the channel data can be determined by evaluating how the effective kinetic rate constant k_{eff} varies as a function of the effective time scale t_{eff} at which it is measured. We developed several different methods to determine this function from the experimental data (10, 11), and subsequently our methods have been improved by others (12, 13).

If the channel openings and closings are fractal, then in analogy to eq 2, we find that

$$k_{\text{eff}}(t_{\text{eff}}) = At_{\text{eff}}^{1-d} \quad (3)$$

The effective kinetic rate constant k_{eff} is the probability for changing states when we observe the data at temporal resolution t_{eff} . Note that because $1 \leq d < 2$, k_{eff} increases when we observe the channel at finer temporal resolution t_{eff} . That is, the faster we can look, the faster we see the channel open and close. If $\log k_{\text{eff}}$ is plotted versus $\log t_{\text{eff}}$, then eq 3 is a straight line. When the data are not fractal, this plot has other forms. For example, when there are only a few discrete states, such as those predicted by the Markov model, then there are a few well separated plateaus on this plot (10). Thus, without making any a priori assumptions about the data, we determine the function $k_{\text{eff}}(t_{\text{eff}})$ and thus plot $\log k_{\text{eff}}$ versus $\log t_{\text{eff}}$. The form of this plot can thus tell us the characteristics of the channel kinetics.

As shown in Figure 4, for the channel in the corneal endothelium, we found (10) that the logarithm of the effective kinetic rate constant k_{eff} as a function of the logarithm of the effective time scale t_{eff} is a straight line, which is consistent with eq 3. Thus, this channel has fractal kinetics. We also found a similar form for the currents recorded through channels in cultured hippocampal neurons (11).

If $P(t)$ is the cumulative probability that a channel remains in a state for a time t or longer, then it can be shown (10, 11) that

$$k_{\text{eff}}(t_{\text{eff}}) = -\{d[\ln P(t)]/dt\}_{t=t_{\text{eff}}} \quad (4)$$

Thus, for a channel with fractal kinetics, equations 3 and 4 imply that the cumulative dwell time distribution has the form

$$P(t) = \exp\{[-A/(2-d)]t^{2-d}\} \quad (5)$$

which is a form found in many fractals and is known by many different names, including stretched exponential, Weibull distribution, and Williams-Watts law (14). When $d \approx 2$, then eq 5 is approximately

$$P(t) = Bt^{-\alpha} \quad (6)$$

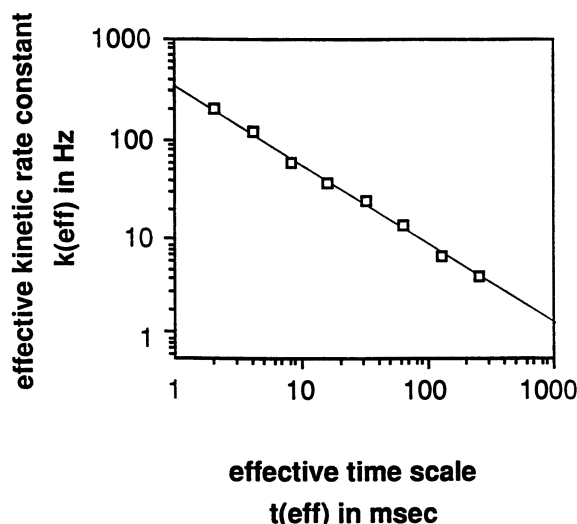


Figure 4. The effective kinetic rate constant k_{eff} is the probability that the channel changes state when the current through the channel is measured at an effective time resolution t_{eff} . The data shown were measured from a potassium channel in the corneal endothelium and have the power law form of eq 3, which is indicative of self-similar fractal behavior. (Reproduced with permission from reference 38. Copyright 1990 New York Academy of Sciences.)

where α and B are constant. The data from many different channels have this power law form (15, 16).

The data from some channels are more complex than the forms of equations 5 or 6. French and Stockbridge (12, 13) found a surprising and interesting form on their plots of $\log k_{\text{eff}}$ versus $\log t_{\text{eff}}$ from potassium channels in fibroblasts. These plots were power laws at short times with a plateau at long times. Thus, the kinetics were fractal at short time scales and had a single well-defined discrete Markov state at long time scales. The kinetics of the channel changed when the voltage across the membrane or the calcium concentration in the solution was changed. When French and Stockbridge fitted their data with a Markov model with three closed and two open states, the many kinetic rate constants of that model showed no consistent trends with voltage or calcium concentration. However, plots of $\log k_{\text{eff}}$ versus $\log t_{\text{eff}}$ revealed that the kinetics changes could be characterized by a change only in the value of the plateau of the Markov state. This discovery of unanticipated forms shows the value of using these plots. Moreover, because this description can characterize the changes in the kinetics in such a simple way, it may lead us to a better understanding of the underlying mechanisms.

Inspection of a large amount of published data suggests that some channels are best described by fractal scalings, some channels are best described by discrete single Markov states, and other channels show fractal behavior at some time scales and discrete-state Markov behavior at other time scales.

Protein Properties Suggested by the Fractal Interpretation

The Markov description of ion channel kinetics, originally derived from the Hodgkin–Huxley model, implies that the ion channel protein has certain physical properties.

1. The Markov model assumes that the channel protein can have only a few conformational states. The structure of a protein can be represented by a potential energy function. Stable conformational states correspond to local minima in that potential function. Thus, the well-defined discrete states of this model suggest that there are a *few deep local minima* in the potential that are well separated from other local minima.
2. The fact that the kinetic rates that connect different states are determined as independent parameters from the data suggests that the physical processes that cause these transitions are *independent*.
3. Because the probability to switch from one state to another is assumed to be constant in time, this model also suggests that the *energy structure remains constant*.

The discovery of the fractal properties of the single-channel recordings now suggests a different picture of the physical properties of the ion channel protein than the foregoing three properties that were suggested by the Markov model.

1. The continuous nature of the effective kinetic rate constant function $k_{\text{eff}}(t_{\text{eff}})$ suggests that there is actually a broad continuum of many channel states. That is, the energy structure of the channel must have a *very large number of shallow local minima*, rather than the few deep minima suggested by the Markov model.
2. The fractal nature of the single-channel data means that there is a relationship between short and long dwell times in a state. That is, rapid processes are *related* to slow processes, rather than being independent. Rapid processes are transitions over

small activation energy barriers, whereas slow processes are transitions over large activation energy barriers. Thus, the small activation energy barriers are related to the large activation energy barriers within the channel protein. Each transition over an activation energy barrier can be represented by a kinetic rate constant. Hence, the kinetic rate constants that connect the states are related, rather than being independent of each other. Thus, even though there are very many kinetic rate constants, we do not need a model with very many adjustable parameters, because the kinetics can be described by a fractal scaling with a small number of parameters. This fractal scaling determines the relationship between the kinetic rate constants. Because different processes are interrelated, the opening or closing of the channel depends on the coordinated interaction of these many different physical processes; that is, they function cooperatively. This mechanism is a very different physical picture from that suggested by the Markov model in which the different physical processes, represented by the different kinetic rate constants, are assumed to be completely independent. Both the fractal and Markov interpretations can have many states. The difference in the physical pictures suggested by these models is that the fractal model implies that the transition rates between these states are causally related because of the physical structure and dynamics in the channel protein. The relationships between the kinetic rate constants that are needed to result in kinetics with fractal properties were derived by Liebovitch (17), Millhauser et al. (18), Levitt (19), and Kienker (20).

3. Each change in channel conformation can be described as the transition across an activation energy barrier. The sequence of such barriers that are crossed thus describes the kinetics. A sequence of different barriers can be equivalently thought of as a single barrier whose value is different at different times. Thus, the cooperativeness of the different physical processes in the channel protein, suggested by the fractal properties, can also be equivalently described as transitions across an activation energy barrier that varies in time. This interpretation suggests that the *energy structure of the channel protein is changing*, rather than constant in time. Such transitions can be described by a time-dependent rate constant. The time dependence of such kinetic rates that are needed to result in kinetics with fractal properties was derived by Liebovitch et al. (10, 11, 17) and Lauser (21).

The different physical properties of the ion channel protein suggested by the Markov model and fractal properties of the data can also be described another way. The channel kinetics can be described as transitions between open and closed substates separated by activation energy barriers (22, 23). What distribution of activation energy barriers is needed to explain the statistical properties of the single-channel data? The Markov model assumes that this distribution is a small set of Dirac delta functions, as shown in Figure 5. That is, there are a few such activation energy barriers and each occurs only at one discrete energy rather than being spread over a distribution of energies. This set of energy barriers is assumed to remain constant in time. The Markov model, a priori, imposes a distribution of this form. This distribution is specified by its parameters, which are the number of activation energy barriers, their activation energies, and their relative strengths. To fit the data, only the parameters of this distribution are adjusted. This form of the distribution of activation energy barriers implies (23) that the cumulative probability distribution $P(t)$ that the channel remains in a state for a time t or longer has the form

$$P(t) = a_1 e^{-b_1 t} + a_2 e^{-b_2 t} + \dots + a_n e^{-b_n t} \quad (7)$$

where n is the number of discrete activation energy barriers, b_n are the time constants of the exponential terms, and a_n are the relative weights of the exponential terms.

On the other hand, rather than impose a functional form, we can determine the distribution of activation energy barriers from the observed channel kinetics. Liebovitch and Tóth showed (23) that when the channel data have fractal properties, this distribution has a broad peak. The broader this peak, the more fractal the data; the narrower the peak, the more the data resemble that of a single Markov state. Rubinson (24) and Croxton (25) have also derived distributions of activation energy barriers that result in kinetics with fractal properties. As noted in the previous section, many channels seem to have fractal properties at some time scales and yet single-state Markov properties at other time scales. Fractal kinetics result from physical processes that span large ranges of time scales and thus have very broad distributions of activation energy barriers. Single-state Markov processes result from physical processes with sharply defined time scales and thus very narrow distributions of activation energy barriers.

The fractal scaling arises when a continuous distribution of activation energy barriers spans a large range in energy. A similar scaling will occur if there are a large number of discrete activation barriers that nearly uniformly span a large range in energy. Thus, fractal scalings can also be constructed from discrete Markov-type models with appropriately chosen energy barriers; namely, when there are many states that have enough activation energy barriers to nearly uniformly cover a large range in energy (18, 19). This new type of Markov model, however, is qualitatively different and has a very

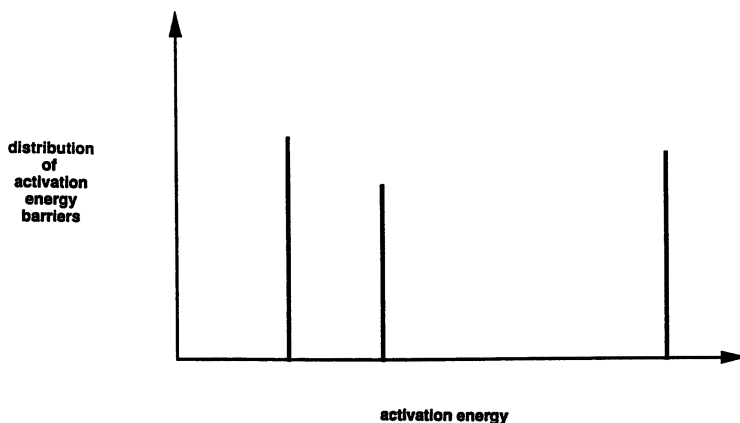
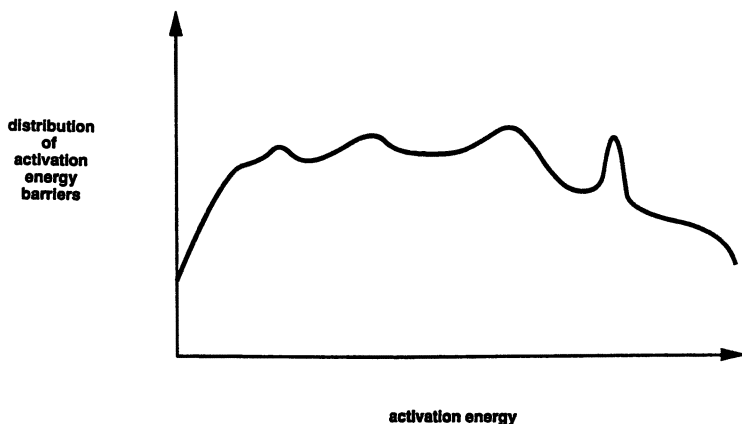
Markov**Fractal**

Figure 5. The kinetics of the channel switching between different states can be described by the distribution of activation energy barriers that connect the different states. Top: The Markov model assumes that this distribution is a small set of Dirac delta functions at discrete activation energies. That is, each activation energy barrier is sharply defined at only one unique value. Bottom: The published data from many channels suggest that the distribution of activation energy barriers consists of sets of activation energy barriers, each of which is a distribution with a finite width. At time scales corresponding to activation energies that have wide distributions, the kinetics have very strong fractal properties, which correspond to physical processes extending over many time scales. At time scales that correspond to activation energies that have narrow distributions, the kinetics are more like that of a single Markov state, which corresponds to physical processes that occur only over a small range of time scales.

different interpretation than the traditional Markov model, which has only a few states whose rate constants are independent of each other. Both the continuous fractal distribution and the new type of Markov model with many states with dependent rate constants imply that there are many states and that the form of the distribution of energy barriers arises from some physical mechanism within the channel protein.

The published data suggest that most channels have different processes that span different ranges of time scales. Some processes extend only over a limited range of time scales, have relatively narrow distributions of activation energy barriers, and thus are more Markov-like. Other processes extend over a very wide range of time scales, have very broad distributions of activation energy barriers, and thus are more fractal-like. Channel proteins display a collection of different types of physical processes with these different characteristics. Hence, the distribution of activation energy barriers that would fit the channel data is the distribution schematically shown in Figure 5.

Fractal Interpretation Consistent with Known Properties of Globular Proteins

The biophysical properties of membrane-bound proteins, such as ion channels, are much more difficult to determine than the properties of globular proteins because the structure and function of membrane proteins depend on their unique location: partially embedded in the hydrophobic lipid membrane, yet reaching into the hydrophilic aqueous solution. The structure of membrane-bound proteins significantly changes when they are removed from the lipid membrane. Thus, few membrane proteins have been crystallized for analysis by X-ray diffraction to determine their three-dimensional structure. Lack of this structural information also has limited theoretical simulation techniques, such as molecular dynamics, which require such experimental information as a starting point. Hence, the detailed biophysical properties of ion channels are not yet known. However, we expect that ion channel proteins share many properties with their cousins the globular proteins. Thus, we will briefly review the properties of globular proteins and compare them to the properties suggested by the Markov and fractal interpretations of the single-channel data.

Calculations of the potential energy function of a large number of different globular proteins demonstrate that these proteins all have a very large number of shallow local energy minima (26). This analysis is consistent with the physical properties of ion channel proteins suggested by the fractal properties of the channel data and inconsistent with the few deep minima predicted by the Markov model.

The time course of the binding of CO to myoglobin is determined by the distribution of activation energy barriers that the CO must cross to reach its binding site. Thus, experiments that measure the number of myoglobin molecules that have bound CO after a given time can be used to calculate the

distribution of activation energy barriers (22). The time course of the flipping of a tryptophan ring, as reported by fluorescence, can also be used to determine the distribution of activation energy barriers through which the ring moves (27). These examples, and many other experiments, demonstrate that globular proteins have a broad continuous distribution of activation energy barriers. Such distributions are consistent with the physical properties of ion channel proteins suggested by the fractal properties of the channel data and inconsistent with the set of a few Dirac delta functions predicted by the Markov model.

Molecular dynamic simulations of the fluctuations in proteins show that the energy structure varies in time and that such variations in the activation energy barriers are crucial in the functioning of enzymes. For example, the energy barrier determined from the static crystallographic structure of myoglobin is so large that oxygen would never be expected to reach the binding site in the protein. However, as time goes by, small fluctuations in the structure open up a passageway for oxygen to reach the binding site (28). The time dependence of the energy structure is consistent with the physical properties of ion channel proteins suggested by the fractal properties of the channel data and is inconsistent with the static structure predicted by the Markov model.

Thus, the biophysical studies demonstrate that globular proteins have (1) a very large number of conformational states corresponding to many shallow local minima in the potential energy function, (2) very broad continuous distributions of activation energies, and (3) time-dependent activation energy barriers. All these properties are consistent with the physical properties of ion channels derived from the fractal properties observed in the channel data and are inconsistent with the physical properties derived from the Markov model.

Controversy

The physical properties of the ion channel protein suggested by the Markov model differ from the properties suggested by the fractal properties of the single-channel data. The Markov model suggests that (1) there are a few discrete conformational states corresponding to well-defined energy minima, (2) the processes that cause transitions between these states are independent, (3) the energy structure of the channel remains constant in time, and (4) the distribution of activation energy barriers that separate these states are a few Dirac delta functions at discrete activation energies. The fractal properties of the single-channel data suggest that (1) there is a broad continuum of conformational states corresponding to a large number of shallow energy minima, (2) the processes that cause transitions between states are related, (3) the energy structures, such as the activation energy barriers, vary in time, and (4) the distribution of activation energy barriers consists of some distributions that are very broad and some that are narrow.

There is still some question as to whether the ion channel protein has the physical properties suggested by the Markov model or the fractal properties of the single-channel data. For example, note the lively exchange of views in the letters in the *Biophysical Journal* by Liebovitch (29), Horn and Korn (30), and McManus et al. (31). The Markov models can fit the single-channel data with great accuracy. However, this does not prove the validity of these models because the Markov models have a very large number of adjustable parameters; sometimes as many as 16. With such a large number of adjustable parameters, even an invalid model is likely to fit any data. Arguments have been made that some Markov models are a statistically better fit to the single-channel data than some fractal models (32–34). However, the mathematical justification that is the basis for this statistical comparison has been shown to be invalid (35). The extensive experimental and theoretical studies of globular proteins support the physical properties suggested by the fractal interpretation. However, it is not yet known if there are important differences between the properties of globular proteins and membrane proteins such as ion channels.

We think that ion channels have the physical properties suggested by the fractal interpretation because the fractal properties are so clearly present in the experimental data, and these properties are consistent with the extensive experimental and theoretical studies of globular proteins. However, this issue can only be resolved by future work that includes X-ray diffraction and NMR, which are needed to determine the three-dimensional structure of the channel protein at high resolution; molecular dynamic simulations, which are needed to determine the dynamics of the motions within the channel; and molecular biology, which can test our ideas of channel structure and dynamics by purposeful alterations of the channel.

Chaos

The entire previous discussion assumed that the switching of the ion channel from one conformational state to another is an inherently stochastic or random process. The kinetic rate constant, or the effective kinetic rate constant, tells us the probability per second that the channel will switch from one state to another, but it does not tell us exactly when this switch will occur. Are these transitions from one state to another really stochastic?

We now know that there are processes, which are not stochastic, whose output mimics stochastic behavior. This phenomenon is now called *chaos*. Chaos is a jargon word that means that a system has certain mathematical properties. It should not be confused with its nontechnical homonym that means confusion or disorder. A chaotic system can be described by a set of nonlinear difference or differential equations that have a small number of independent variables. Because these equations can be integrated in time, the future values of the variables are completely determined by their past values.

That is, the system is completely deterministic; there is no randomness at all. However, the evolution of the values of the variables is exquisitely sensitive to their exact initial values. That is, very slightly different initial values of the variables will soon evolve in very different ways. Because these initial conditions can only be specified with finite accuracy, the exact long-term behavior of the system is unpredictable, although its statistical properties can often be determined. Thus, chaotic systems are deterministic, yet unpredictable in the long run.

We have shown that chaotic models can describe the qualitative features and statistical properties of the single-channel data (36, 37). In these models the switching between different conformational states is a completely deterministic rather than a stochastic process. The ion channel is a mechanical structure of masses and springs, called atoms and bonds. These chaotic models suggest that such a mechanical structure can function as a nonlinear oscillator to amplify its own motions, to force itself from one conformational state to another. Alternatively, one could say that the channel is organizing the nonperiodic thermal fluctuations of its structure into coherent patterns of motion. Thus, the motions within channels that change the conformational state may be more organized than the stochastic switching models (previously described) suggest. These ideas are still in their infancy, but they may ultimately change the way that we view and understand channel structure and dynamics.

Summary

The patch clamp technique can measure the sequence of open and closed times in a single ion channel. This allows us the unprecedented opportunity to study how an individual protein switches between different conformational states. This single-channel data has fractal properties and is self-similar; that is, the statistical properties of the switching between open and closed states, viewed at one-time resolution, are similar to the properties viewed at finer time resolution. Thus, the short dwell times in a state are related to the long dwell times. These fractal properties suggest that the ion channel protein has certain physical properties:

1. There is a broad continuum of conformational states corresponding to a large number of shallow energy minima.
2. The processes that cause transitions between states are related.
3. The energy structure, such as the activation energy barriers, varies in time.
4. The distribution of activation energy barriers consists of distributions that are very broad and distributions that are narrow.

It had always been assumed that the changes in conformational state are inherently stochastic processes. However, new chaotic models suggest that channel proteins may organize fluctuations in structure into coherent patterns of motion, so that the switching between conformational states may be deterministic rather than stochastic.

Acknowledgments

This work was done during the tenure of an Established Investigatorship from the American Heart Association and was also supported in part by grants from the Whitaker Foundation and from the National Institutes of Health (EY6234).

References

1. *Single-Channel Recording*; Neher, E.; Sakmann, B., Eds.; Plenum: New York, 1981.
2. Hille, B. *Ionic Channels of Excitable Membranes*; Sinauer Associates: Sunderland, MA, 1984.
3. Hodgkin, A. L.; Huxley, A. F. *J. Physiol. (London)* **1952**, *117*, 500–544.
4. Maslow, A. H. *The Psychology of Science: A Reconnaissance*; Harper & Row: New York, 1966.
5. Mandelbrot, B. B. *The Fractal Geometry of Nature*; W. H. Freeman: San Francisco, CA, 1983.
6. Liebovitch, L. S. In *Advanced Methods of Physiological Systems Modeling*; Marmarelis, V. Z., Ed.; Plenum: New York, 1989; Vol. 2, pp 225–239.
7. West, B. J.; Bhargava, V.; Goldberger, A. L. *J. Appl. Physiol.* **1986**, *60*, 1089–1097.
8. Bassingthwaight, J. B.; van Beek, J. H. G. M. *Proc. IEEE* **1988**, *76*, 693–699.
9. Paumgartner, D.; Losa, G.; Weibel, E. R. *J. Microsc.* **1981**, *121*, 51–63.
10. Liebovitch, L. S.; Fischbarg, J.; Koniarek, J. P. *Math. Biosci.* **1987**, *84*, 37–68.
11. Liebovitch, L. S.; Sullivan, J. M. *Biophys. J.* **1987**, *52*, 979–988.
12. French, A. S.; Stockbridge, L. L. *Can. J. Physiol. Pharmacol.* **1988**, *66*, 967–970.
13. Stockbridge, L. L.; French, A. S. *Can. J. Physiol. Pharmacol.* **1989**, *67*, 1300–1307.
14. Klafter, J.; Shlesinger, M. F. *Proc. Natl. Acad. Sci. U.S.A.* **1986**, *83*, 848–851.
15. Blatz, A. L.; Magleby, K. L. *J. Physiol. (London)* **1986**, *378*, 141–174.
16. McGee, R., Jr.; Sansom, M. S. P.; Usherwood, P. N. R. *J. Membr. Biol.* **1988**, *102*, 21–34.
17. Liebovitch, L. S. *Math. Biosci.* **1989**, *93*, 97–115.
18. Millhauser, G. L.; Salepter, E. E.; Oswald, R. E. *Proc. Natl. Acad. Sci. U.S.A.* **1988**, *85*, 1503–1507.
19. Levitt D. G. *Biophys. J.* **1989**, *55*, 489–498.
20. Kienker, P. *Matching Fractal Ion Channel Gating Models with Markov Models*; Preprint, 1989.
21. Lauser, P. *Biophys. J.* **1988**, *53*, 877–884.
22. Austin, R. H.; Beeson, K. W.; Eisenstein, L.; Frauenfelder, H.; Gunsalus, I. C. *Biochemistry* **1975**, *14*, 5355–5373.

23. Liebovitch, L. S.; Toth, T. I. *Bull. Math. Biol.* **1991**, *53*, 443–455.
24. Rubinson, K. A. *Biophys. Chem.* **1986**, *25*, 43–55.
25. Croxton, T. L. *Biochim. Biophys. Acta* **1988**, *946*, 19–24.
26. McCammon, J. A.; Harvey, S. C. *Dynamics of Proteins and Nucleic Acids*; Cambridge University Press: New York, 1987.
27. Alcalá, J. R.; Gratton, E.; Predergast, F. G. *Biophys. J.* **1987**, *51*, 925–936.
28. Karplus, M.; McCammon, J. A. *CRC Crit. Rev. Biochem.* **1981**, *9*, 293–349.
29. Liebovitch, L. S. *Biophys. J.* **1989**, *55*, 373–377.
30. Horn, R., Korn, S. J. *Biophys. J.* **1989**, *55*, 379–381.
31. McManus, O. B.; Spivak, C. E.; Blatz, A. L.; Weiss, D. S.; Magleby, K. L. *Biophys. J.* **1989**, *55*, 383–385.
32. McManus, O. B.; Weiss, D. S.; Spivak, C. E.; Blatz, A. L.; Magleby, K. L. *Biophys. J.* **1988**, *54*, 859–870.
33. Korn, S. J.; Horn, R. *Biophys. J.* **1988**, *54*, 871–877.
34. Sansom, M. S. P.; Ball, F. G.; Kerry, C. J.; McGee, R.; Ramsey, R. L.; Usherwood, P. N. R. *Biophys. J.* **1989**, *56*, 1229–1243.
35. Liebovitch, L. S.; Tóth, T. I. *Synapse* **1990**, *5*, 134–138.
36. Liebovitch, L. S.; Tóth, T. I. *J. Theor. Biol.* **1991**, *148*, 243–267.
37. Liebovitch, L. S.; Czeglédy, F. P. *Ann. Biomed. Engr.*, **1992**, *20*, 517–531.
38. Liebovitch, L. S.; Tóth, T. I. In *Mathematical Approaches to Cardiac Arrhythmias*; Jalife, J., Ed.; *Ann. N. Y. Acad. Sci.* **1990**, *591*, 375–391.

RECEIVED for review January 29, 1991. ACCEPTED revised manuscript June 18, 1992.

Noise in Biological Membranes and Relevant Ionic Systems

S. M. Bezrukov^{1,3} and Igor Vodyanoy^{2,4}

¹University of Maryland, College Park, MD 20742

²Code 1141SB, Office of Naval Research, 800 North Quincy Street, Arlington, VA 22217

We review progress in understanding electric noise sources and their physical mechanisms in biological membranes and relevant ionic systems. Specifically, attention is given to noise components whose origin is different from the channel switching between conductance states. Nyquist's formula applications and limitations in model and biological membranes and electrolyte solutions are discussed in view of current experimental data. New experiments on conductance noise in electrolyte solutions, molecule number fluctuations in ion pores, and reversible protonation of the channel-forming molecule residues are presented. Several empirical and model approaches in studies of 1/f noise are critically reviewed. A simple analytical consideration of one-dimensional diffusion noise generation is presented to highlight the potential capacity of diffusion-induced kinetics in noise phenomena description.

ELECTRIC NOISE MEASUREMENTS IN IONIC SYSTEMS were first reported in 1928 by Johnson, who included several second-order conductors in his classical study of equilibrium noise (*I*). Since then a great deal of experimental and theoretical work has been performed. Ever-growing interest in electric noise measurements is motivated by two primary concerns. First, to acquire, process, and transduce information, living organisms use many ionic

³ On leave from the St. Petersburg Nuclear Physics Institute of the Russian Academy of Sciences, Gatchina, 188350 Russia

⁴ Corresponding author

systems. Most popular examples include sensory (such as visual, olfactory, and auditory) signal transduction and nerve impulse propagation along the axonal membrane of neuron cells. Fluctuation phenomena and noise in these biological systems set limits on the sensitivity and reliability of their function. Second, an electric noise is a source of information about the system under study. A classical example is the determination of the value of the electronic charge from the shot noise in vacuum tubes. During the last two decades correlation and spectral analysis of noise in biological and model membranes have provided novel insight into the molecular mechanisms of ionic conduction through these structures.

Use of classification long established in experimental physics enables identification of several sources that contribute to the total noise level in biological membranes. In application to membrane ionic transport, such a classification was first introduced by Stevens (2). Although these noise sources are not always distinctly different by physical mechanism of noise generation or by spectral features, they can be listed as follows:

1. Johnson noise (equilibrium voltage or current noise)
2. Shot noise (charge transport noise)
3. Conductance noise (impedance modulation noise)
4. $1/f$ noise (flicker noise)

Most review papers on the subject of biological membrane noise have been devoted primarily to conductance noise that arises from channel switching between different conductance states. Several excellent reviews that vary in volume and in mathematical level of presentation of material are available (3–9).

The aim of this chapter is to review progress in the field with particular attention to the area that is still developing and is far from complete. Specifically, we discuss noise components that have a different origin from or, at least, are not soundly established as channel switching between conductance states. A number of studies performed with electrolyte solutions and other relevant ionic systems are considered.

Johnson Noise

Ionic systems, such as water solutions of NaCl, CuSO₄, K₂CrO₄, and Ca(NO₃)₂ and solutions of sulfuric acid in ethyl alcohol, were among the objects of Johnson's experiments (1) that led him to conclude that there exists equilibrium electrical noise of a universal nature that manifests thermal motion of charged particles in conductors on a macroscopic level. Independently of a particular conductivity mechanism, the voltage spectral density, $S_V(f)$, of this noise can be calculated from the real part of the system

impedance, $\text{Re } Z(f)$, by the relation

$$S_v(f) = 4kT \text{Re } Z(f) \quad (1)$$

where k is the Boltzmann constant and T is the absolute temperature of the system. The spectral density of current noise can be obtained by dividing both sides of this relation by $|Z(f)|^2$, which gives the real part of system admittance on the right-hand side of eq 1.

This relation was proved by Nyquist (10) to be a consequence of basic thermodynamics laws and, except for quantum corrections, was never really challenged. Studies performed with glass microelectrodes (11) and heterogeneous ionic systems (12) showed that for zero ionic gradients and zero applied currents, the measured levels of noise were in agreement with noise levels calculated from the impedance according to eq 1. Hence, a study of electrical noise of a system under equilibrium conditions can be initiated for only two reasons. First, if there is some a priori information that the system is in equilibrium, then measurements of the system impedance or temperature can be performed without external perturbations (quantum effects are not considered here). Second, if impedance and temperature are measured independently by some other techniques, noise measurements can verify that the system under study is in an equilibrium state.

Initial measurements on valinomycin-doped membranes (13, 14) showed that lipid bilayers, which provide cells with an effective permeability barrier, are equilibrium objects by this criterion. Within an accuracy of several percent, the experimentally obtained values of the spectral density of voltage noise showed agreement with those calculated from relation 1. Figure 1 illustrates this agreement for three valinomycin concentrations. For the valinomycin- K^+ system chosen for these experiments and for the frequency range used in measurements, the dispersion in membrane impedance was caused only by geometrical capacitance of the bilayer; the characteristic times of the transport process itself were too small to influence impedance in this range.

Similar results that show complete correspondence between noise and impedance (or admittance) in equilibrium conditions were independently reported for lipid bilayers in the presence of hydrophobic ions (15-17) and for the valinomycin- Rb^+ transport system (18).

Indeed, even nonequilibrium systems do not necessarily show measurable excess noise and, thus, deviate from relation 1. An appropriate example that is relevant to the subject is a capillary channel that contains a stream of electrolyte maintained by an external pressure difference. Measurements on several aqueous polymer solutions with added electrolytes performed at up to 5000 dyn/cm^2 shear stresses and zero external voltage showed that measurable excess noise can be observed only for non-Newtonian solutions exhibiting elasticity (19, 20). Similar results were obtained for colloid suspensions

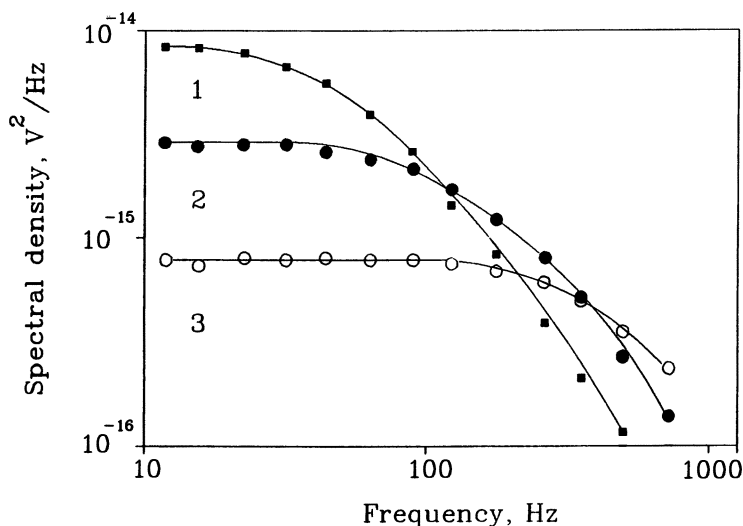


Figure 1. The agreement of the spectral density of voltage fluctuations from valinomycin-modified phospholipid bilayers at equilibrium conditions (13, 14) with the Nyquist relation 1. An aqueous 0.01-M KCl solution at 33 °C was used in the experiments. Bilayer direct current resistances and valinomycin solution concentrations were 0.52-M Ω and 1.5×10^{-8} M (1), 0.19 M Ω and 5×10^{-8} M (2), and 0.055 M Ω and 1.5×10^{-7} M (3). Solid lines are drawn in accordance with relation 1 for the impedance of a parallel resistance–capacitance (RC) circuit using foregoing resistance values and a value of membrane geometrical capacitance.

(21) and micellar solutions (22). In these experiments the differences in noise spectral densities of “unperturbed” electrolyte-filled capillaries and capillaries with maintained flow were below experimental accuracy of several percent.

Transport Noise

The Nyquist relation is no longer valid for nonequilibrium systems. When a nonzero mean electrical current flows through the system, the spectral density of electrical current fluctuations may differ by orders of magnitude from the fluctuations calculated from eq 1.

The first source of nonequilibrium noise, described as early as 1918 (23) (in fact 10 years earlier than Johnson noise), was shot noise that stems from the discrete nature of charge transfer. The current spectral density, $S_1(f)$, of this noise is white (independent of frequency f) up to frequencies of the order of the inverse time of elementary charge transfer and is given by

Schottky's formula:

$$S_I(f) = 2q\langle I \rangle \quad (2)$$

where $\langle I \rangle$ is the mean current through the system and q is the charge of flowing particles. This result holds for any system, independent of its complexity, if the transport of charge is unidirectional and charge-transfer events are uncorrelated.

Indeed, for a current pulse $i(t)$ produced as a result of the passage of a single charge-carrying particle, we can write

$$\int_{-\infty}^{\infty} i(t) dt = q \quad (3)$$

where q is the charge of the particle. The one-sided spectral density of current noise produced by the uncorrelated sum (i.e., by the Poisson wave) of such pulses is

$$S_I(f) = 2\nu|G(f)|^2 \quad (4)$$

where ν is the average number of pulses per second and

$$G(f) = \int_{-\infty}^{\infty} i(t)\exp(-2\pi jft) dt \quad (5)$$

Because of condition 3 the value of $G(f)$ at $f \rightarrow 0$ approaches the value of the particle charge. Then we have

$$S_I(f)|_{f \rightarrow 0} \rightarrow 2\nu q^2 \quad (6)$$

Use of the evident equality $\nu q = \langle I \rangle$ leads to relation 2, which implies that the low-frequency spectral limit of noise produced by unidirectional flow of noninteracting charge carriers is always described by the Schottky formula.

A persistent misconception that multistep charge transfer lowers shot noise exists in the current literature. Several papers devoted to superconductivity problems (24–26) make a misleading conclusion about the ability of intermediate stops of vortices at pinning centers to lower the zero-frequency level of magnetic shot noise. Similar statements about transport in ion channels are found in biophysical literature, as evidenced by a direct quote from reference 27: "If ions pass through a channel in multiple steps, each moving the ion through only a fraction of the width of the membrane, the result will be less transport noise than in the simple shot process." This statement can be true only for very high frequencies that are comparable to the inverse time of ion passage through a channel.

Only correlations between elementary steps of different charge carriers can change the low-frequency shot noise amplitude. The simplest example of such a system, which is shown in Figure 2, is a series arrangement of macroscopic shot noise generators, where each generator for a given mean current $\langle I \rangle$ can be represented by an equivalent circuit that consists of an "ideal" noise generator $2q\langle I \rangle$ in parallel with an "ideal" (noiseless) resistor R . Because the expression $2q\langle I \rangle$ stands for the spectral density and not for the current itself, the noise of the whole arrangement, which is voltage-clamped at terminals A and B, is described by $2q\langle I \rangle/N$. This is clear for the case $N = 2$ and, as a consequence, for any N that is an integral power of 2. Here, the decrease of shot noise amplitude is attributable to "anticorrelations" in transport events that arise from voltage fluctuations in connectors between generators. This simple example illustrates one of the reasons why shot noise is rarely seen in linear macroscopic conductors.

Some useful theoretical approaches have been developed to describe the noise of many special transport mechanisms, such as ion channels, carriers, and electrogenic pumps (28–33). Unfortunately, there are few experimental studies of transport noise in biological membranes and lipid bilayers.

A significant contribution was made by Heinemann and Sigworth, who studied noise in open gramicidin channels (27, 34). Remarkably, these authors minimized all other noise sources in the complex reconstitution system so that measurements of transport noise of a single ion channel became possible. In the case of NH_4^+ and Na^+ the measured noise was lower than the noise predicted by the Schottky formula. Heinemann and Sigworth explained this result using a four-state channel model. The model introduces an interaction between ions in such a way that certain anticorrelations arise between moments of successive ion passages through the channel. This anticorrelation results in lowered noise intensity at the frequencies used for spectral measurements.

For K^+ , Rb^+ , and Cs^+ the level of noise was larger than anticipated for transport noise and could not be described by the model. This noise level

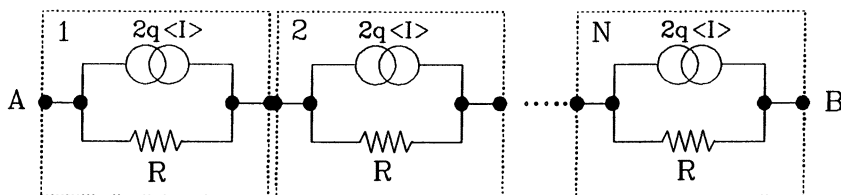


Figure 2. Shot noise damping in a simple model circuit demonstrates why macroscopic linear conductors are usually free from this type of noise. The circuit is a series connection of N "ideal" current noise generators paralleled by "ideal" resistors. Anticorrelations in elementary transport events arise from the voltage fluctuations in connectors between generators.

increase was attributed to conformational fluctuations in the channel structure.

Open-channel noise levels in excess of the Schottky formula were also reported in several papers on the same subject (35–39). Eisenberg et al. (39) obtained a $1/f$ type spectrum for a cation channel of frog lens epithelium. The intensity of the spectrum is orders of magnitude higher than expected for corresponding shot noise. An approximately flat noise spectrum of about $3 \times 10^{-30} \text{ A}^2/\text{Hz}$ from a potassium channel of lobster sarcoplasmic reticulum was reported by Eisenberg et al. (40), who claimed that it was close to the level of the channel Johnson noise.

Nonequilibrium noise generated by carrier-mediated ion transport was studied in lipid bilayers modified by tetranactin (41). As expected, deviations of measured spectral density from the values calculated from the Nyquist formula 1 were found. The instantaneous membrane current was described as the superposition of a steady-state current and a fluctuating current, and for the complex admittance in the Nyquist formula only a small-signal part of the total admittance was taken. The justification of this procedure is occasionally discussed in the literature (*see*, for example, Tyagai (42) and references cited therein), but is unclear.

A generalization of the Nyquist formula, eq 1, was proposed by Grafov and Levich (43) to describe fluctuations in a nonlinear steady state. This approach is based on the fluctuation–dissipation thermodynamics of irreversible nonlinear systems and introduces the so-called dissipative resistance (42), which differs from small-signal resistance in a general case. This result indicates that separation of equilibrium and transport noise is not a well-defined procedure.

Conductance Noise

A noise that has a clearly distinct origin from noise discussed in previous sections is the electric noise that originates in modulation of ion transport by fluctuations in system conductance. These temporal fluctuations can be measured, at least in principle, even in systems at equilibrium. Such a measurement was conducted by Voss and Clark in continuous metal films (44). The idea of the Voss and Clark experiment was to measure low-frequency fluctuations of the mean-square Johnson noise of the object. In accordance with the Nyquist formula, fluctuations in the system conductance result in fluctuations in the spectral density of its equilibrium noise. Measurement of these fluctuations (that is, measurement of the noise of noise) yields information on conductance fluctuations of the system without the application of any external perturbations. The samples used in these experiments require rather large amplitude conductance fluctuations to be distinguished from Johnson noise fluctuations because of the intrinsic limitation of statistics. Voss and

Clark (44) reported successful measurements for a InSb bridge with relative fluctuations as large as $S_G(f)/\langle G \rangle^2 = 10^{-1} \text{ Hz}^{-1}$ at 10^{-2} -Hz frequency. Here G is conductance of the sample and $S_G(f)$ is spectral density of conductance fluctuations.

In biological ionic systems, conductance noise is induced by membrane structures such as ion channels and fluctuations in electrolyte conductance. Noise that originates from the switching of ion channels between different conductance states has been reviewed extensively (3–9). Therefore, we limit ourselves to a discussion of conductance fluctuations in electrolyte solutions (45) and new noise sources that have been identified recently for currents through open ion channels (46, 47).

An excellent review of the early history of noise studies of different ionic systems, such as single pores in thin dielectric films, microelectrodes, and synthetic membranes, is reference 3. The review by Weissman (48) describes several state-of-the-art fluctuation spectroscopy methods that include (1) determination of chemical kinetics from conductivity fluctuations in salt solutions, (2) observation of conductivity noise that arises from enthalpy fluctuations in the electrolyte with high temperature coefficient of resistivity, and (3) detection of large conductivity fluctuations in a binary mixture near its critical point.

Fluctuation phenomena in ionic solutions are a subject of growing interest (49–51). However, for several reasons (48), experimental approaches to studies of conductance fluctuations in liquid phase samples are not as well established as those in the solid state. Strong electric fields that are used to measure conductance fluctuations (to produce noise in excess of the Johnson noise) cause pronounced electroosmotic and electrophoretic complications. As a result, the measurements of conductance fluctuations are usually made with a significant uncertainty factor (cited as 0.4 in reference 52).

In principle, as far as homogeneous and stationary objects are concerned, two alternative methods can be used to measure a single-time correlator of conductance fluctuations. One method is to instantaneously divide the sample volume (using a hypothetical procedure) into a set of identical elements, for instance, cubes. After the conductance G of each of the cubes is determined, the standard deviation of the conductance from the mean value is found. The other method is based on a sufficiently long (unperturbing) observation of the conductance of a particular element that communicates with an outer ion reservoir. Equilibrium exchange of ions between the element and the rest of the sample will give rise to conductance fluctuations, and the standard deviation is obtained from consecutive readings. For ergodic systems, both methods should provide identical answers with an accuracy dependent on the number of elements processed or on the measurement (observation) time.

A method of large-scale conductance fluctuation measurements in flowing ionic solutions was developed (21) recently to measure the space average squared value of these fluctuations with an accuracy of several percent. This

method is similar in nature to the procedure of dividing the electrolyte volume into a set of identical elements. The laminar electrolyte flow consecutively changes elements of the volume in a capillary and determines the fluctuation spectrum by its velocity profile. Parameters of the capillary and the hydrostatic pressure difference can be selected to minimize the effect of diffusion and electrokinetic phenomena. This approach eliminates the uncertainties inherent in other experimental setups and substantially increases the absolute accuracy of the conductance fluctuation measurements.

The foregoing method was used to study fluctuations in solutions of strong electrolytes (45) and in ionogenic and nonionogenic micellar colloids (22). Strong electrolytes were chosen to represent 1:1 electrolytes with nearly equal (NaCl) and significantly different (HCl) mobilities of anions and cations and a 2:1 electrolyte (CaCl₂).

The results of these measurements are shown in Figure 3 as the dimensionless value $\langle(\delta G)^2\rangle/\langle G\rangle^2$. The uppermost solid straight line is drawn so that the relative mean square value of fluctuations is normalized to the total number of dissolved electrolyte molecules, N_M ; that is,

$$\frac{\langle(\delta G)^2\rangle}{\langle G\rangle^2} = \frac{1}{N_M} \quad (7)$$

The central and bottom straight lines are normalized with respect to a double and triple number of molecules, respectively. Analysis of the experimental dependencies shows that as the electrolyte concentration decreases, the fluctuation level approaches the value anticipated for a system of identical noninteracting particles. This trend is observed both for NaCl and HCl, 1:1 electrolytes that yield two ions per dissolved molecule, and for CaCl₂, a 2:1 electrolyte that dissociates into one doubly charged and two singly charged ions.

This "ideal gas behavior" of conductance fluctuations appears to be rather unaccountable. First, electrolyte solutions are systems with pronounced interactions that are attributable to a slow decrease of Coulomb forces between ions; this brings about substantial correlation between mutual positions of ions in space. Second, even in the hypothetical case of weakly interacting charge carriers, the conductance fluctuation level is expected to be equal to the value calculated from the total number of carriers only when the mobilities of different carriers are identical. Indeed, substantial difference in mobilities, say for a 1:1 electrolyte, forces lower mobility carriers to be electrically "invisible" and, thus, the conductance fluctuations must be normalized only to ion species with higher mobility; that is, to the total number of dissolved molecules. Figure 3 shows that this conclusion contradicts the HCl electrolyte experiments in which the mobility of cations is almost five times as large as that of anions. Nevertheless, the level of

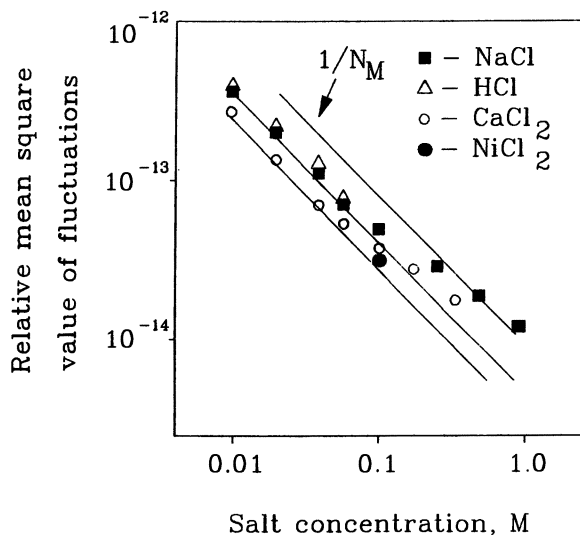


Figure 3. Large-scale conductance fluctuations in aqueous solutions of several strong electrolytes measured by the laminar flow method vs. electrolyte concentration (45). The upper solid line shows the inverse total number of dissolved electrolyte molecules in the sample (that is, in solution volume confined by a fused quartz capillary channel of 13- μm radius and 0.4-mm length). The middle and lower lines correspond to inverse total numbers of ions for 1:1 and 2:1 electrolytes. At small electrolyte concentrations the fluctuation level is within several percent of the inverse number of ions independent of electrolyte type.

conductance fluctuations is close to the value calculated from the normalization that used the total number of ions.

A generalization of the classical result of Lax and Mengert (53) to the case of multicharge ions and combined systems demonstrates that just because of the long-range Coulomb forces between ions, the conductance fluctuation level in dilute simple electrolytes must be normalized to the total number of ions regardless of the electrolyte type and ion mobility difference (45). However, this condition does not hold for complex electrolytes or electrolyte mixtures that contain more than one type of cation or anion. If the mobilities of different types of ions of the same sign are not equal, the fluctuation level would increase so that normalization to the total number of ions in the sample would fail.

A higher fluctuation level compared to the noise of an individual electrolyte was found in the case of NaCl and HCl electrolyte mixtures. The results are presented in Figure 4. Reference solutions of 0.025 M were mixed in different proportions to assure variation of ionic composition while maintaining the total number of ions constant. Mobilities of positive ions, u_{Na} and

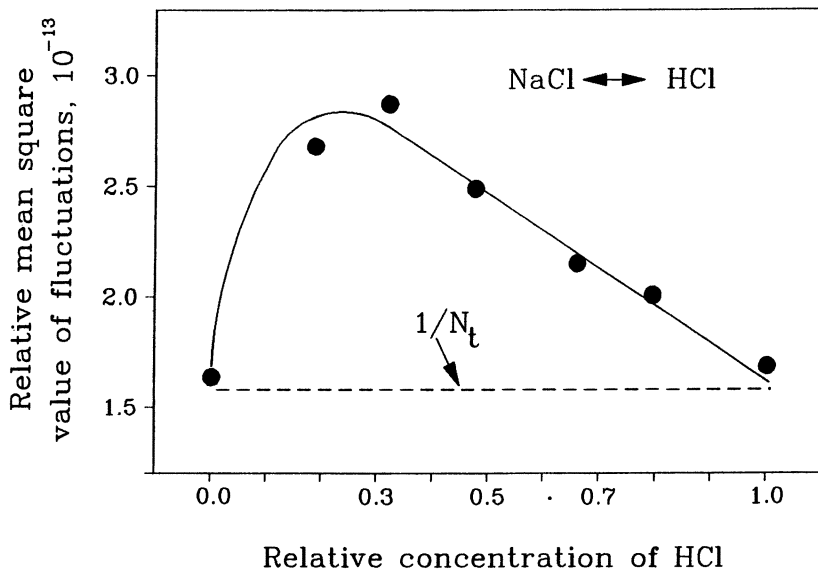


Figure 4. Mixtures of NaCl and HCl electrolytes show higher conductance fluctuations than individual electrolytes (45). The sample composition changes from pure NaCl solution ($K_H = 0.0$) to pure HCl solution ($K_H = 1.0$); the total number of ions is held constant. Experimental points for pure electrolytes are in good agreement with the inverse number of ions in the capillary.

u_H , in dilute solutions of these electrolytes differ approximately by a factor of 7. The solid line is drawn according to theoretical considerations, which give the formula for the deviation of relative conductance fluctuations from the inverse total number of ions in the sample. The ratio θ of fluctuation level in the electrolyte mixture to that in a simple 1:1 electrolyte can be written as (45):

$$\theta = 1 + \frac{2K_H(1 - K_H)(u_H - u_{Na})^2}{[u_{Cl} + u_{Na} + K_H(u_H - u_{Na})]^2} \quad (8)$$

where the relative concentration of HCl is defined through proton and sodium concentrations, $K_H = n_H/(n_H + n_{Na})$.

Indeed, much higher levels of conductance fluctuations were reported for electrolytes that contain polystyrene latex suspensions (21) or micellar colloids (22). Fluctuations were shown to depend on concentration, characteristic size, and the charge of colloid particles. For uncharged nonconductive spherical particles that occupy volume fraction F of the total sample volume

V , excess conductance fluctuations were in agreement with the expression

$$\frac{\langle(\delta G)^2\rangle}{\langle G\rangle^2} = \frac{3}{8} \frac{\pi d^3 F}{V} \quad (9)$$

which directly relates particle diameter d with relative fluctuation level $\langle(\delta G)^2\rangle/\langle G\rangle^2$.

The present results describe an additional source of electrical noise that exists in biological signal transduction media. The contribution of this noise to currents through ion channels can be calculated by considering conductance fluctuations in the region along the convergent ionic paths from the bulk electrolyte medium to the mouth of the channel. Order-of-magnitude estimations show that although electrolyte conductance fluctuations are not important for small single channels where their contribution is significantly below the shot noise level, these fluctuations can be seen in the case of closely packed multichannel arrays and larger transmembrane pores when access resistance (54, 55) is comparable to the resistance of the channel proper.

Two newly identified mechanisms of conductance noise generation in open ion channels were reported recently. Experiments with water-soluble polymers of different molecular weights showed that a "mesoscopic" transmembrane pore formed by alamethicin permits observation of electric noise generated by polymer molecule number fluctuations (46). Alamethicin induces aqueous pores of about 10-Å radius that show several conductance levels. These pores are large enough to transport water-soluble polymers with molecular weights up to several thousand daltons. In polymer-free solutions, noise spectra of open-pore currents are frequency-independent in the 40–4000-Hz range and decrease slightly with conductance level number. The magnitude of this noise in 1-M NaCl solutions at 100-mV membrane voltage is comparable but still larger than shot noise anticipated for corresponding currents.

The addition of water-soluble polymers to electrolyte solutions increases open-channel noise. Fluctuations in the number of polymer molecules in the channel produce a supplementary noise component. For polyethylene glycols with 200–10,000-Da molecular weights, this component was white in the frequency range of several kilohertz. Figure 5 presents the spectral density of the open-channel noise averaged over 200–2000 Hz as a function of polymer weight. In contrast to results for polymer-free solutions, the noise grows as the level number increases. Experimental points for polymers smaller than 4000 Da are in agreement with a simple theory of polymer number fluctuations. The theory takes into account the dependence of polymer partition into the channel on polymer weight obtained from the "macroscopic" effect of the polymer addition on channel conductance and permits the estimation of the characteristic time of polymer diffusion through the channel.

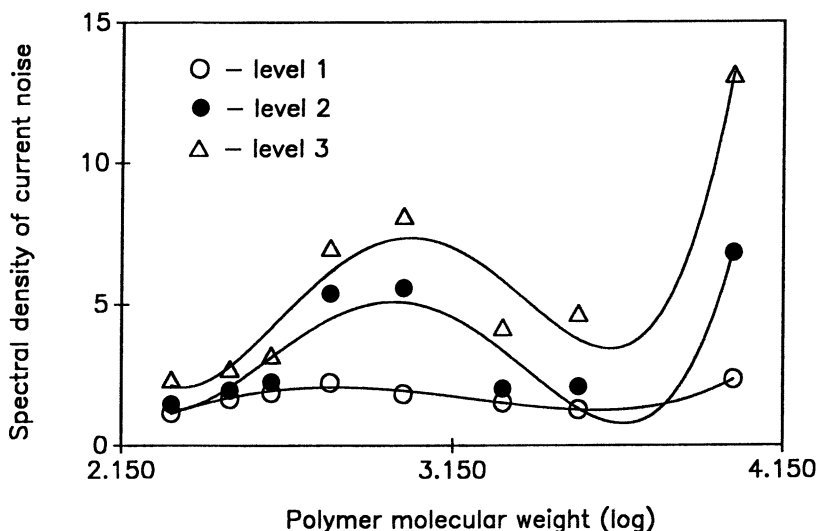


Figure 5. Spectral density of polymer-induced current noise in the open alamethicin channel vs. polymer molecular weight (46). Data represent noise in different channel-conducting levels at 150 mV in the presence of polyethylene glycols of different sizes added to 1-M NaCl aqueous solutions to obtain 15% weight-to-weight concentration. The vertical scale is given in 10^{-27} A²/Hz units.

Studies of single channels formed in lipid bilayers by *Staphylococcus aureus* alpha toxin showed that fluctuations in the open-channel current are pH-dependent (47). The phenomenon was attributed to conductance noise that arises from reversible ionization of residues in the channel-forming molecule. The pH-dependent spectral density of the noise, shown in Figure 6, is well described by a simple model based on a first-order ionization reaction that permits evaluation of the reaction parameters. This study demonstrates the use of noise analysis to measure the rate constants of rapid and reversible reactions that occur within the lumen of an ion channel.

1/f Noise

Noise with a spectral density that is inversely proportional to frequency over a wide frequency range is a well-known phenomenon found in a great number of quite different objects that include biological membranes and other ionic systems. Extensive reviews of earlier works relevant to membrane biophysics can be found in the literature (3, 6, 56).

Multiple reports on the presence of this noise in such a diverse group of systems as carbon resistors, semiconductors, metallic thin films, and aqueous ionic solutions led researchers to believe in the existence of some profound

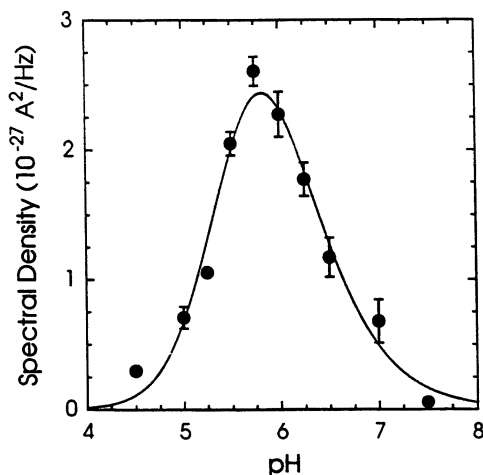


Figure 6. Noise of protonation in the current through an open alpha-toxin channel as a function of pH (47). Spectral density is white at low frequencies and is represented by values averaged over the 200–2000-Hz range. The data were obtained in 1-M NaCl solutions at 150 mV of membrane voltage. The solid line is a two-parameter fit to the first-order ionization reaction that describes a reversible protonation of residues in the channel-forming molecule.

law of nature that applies to all electric conductors and results in $1/f$ noise. This general idea was undoubtedly behind the famous Hooge formula (57) that relates the level of $1/f$ noise in the system to the total number of free charge carriers, N_i , through the empirical parameter α :

$$\frac{S_V(f)}{\langle V \rangle^2} = \frac{S_I(f)}{\langle I \rangle^2} = \frac{\alpha}{N_i f} \quad (10)$$

Equation 10 thus states that any dependence of $1/f$ noise on dimensions and the geometry of a particular object can be reduced to the effective value of N_i . Hooge's formula was the subject of criticism in recent literature on noise (49, 50), but, in our opinion, the formula is still most helpful and a popular way to characterize $1/f$ noise of specific systems. As a matter of fact, only 15 years ago the influence of Hooge's empirical relation was so strong that it was used in attempts to solve the inverse problem; that is, to estimate the number of ions in the membrane channel from membrane $1/f$ noise (58, 59).

In early experiments (60) the results of electrolyte noise measurements were best described by relation 10 if the dimensionless parameter α was assumed to be proportional to the electrolyte concentration and was taken to be equal to 10 for 1-M aqueous solutions of strong electrolytes.

In later experiments with ionic solutions separated by porous membranes, significant deviations of the magnitude of $1/f$ noise intensity from that predicted by Hooge's formula were found (61). For single holes of $\sim 5\text{-}\mu\text{m}$ diameter in $12.5\text{-}\mu\text{m}$ -thick Mylar film in 0.1-M KCl aqueous solution, the $1/f$ noise can be described by the much lower value of $\alpha = 10^{-2}$.

Significant deviations from Hooge's formula also were found for ion channels in biological membranes after special difference procedures (7) for recording fluctuations from specific channels were introduced. For example, for sodium channels modified by batrachotoxin in myelinated nerve (62), the number of mobile ions derived from the formula with the original value of α is nearly 30 times higher than the number of open-membrane channels.

In experiments with amphotericin pores in lipid bilayer membranes (63) and with single macroscopic capillaries (64–66) filled with carefully purified aqueous solutions of potassium chloride, $1/f$ noise was found to be negligible in comparison with other noise components. The conclusion was that $1/f$ noise in electrolytes is absent with an upper limit on α of about 10^{-3} . De Vos et al. (67) suggested that occasionally reported results on measurable $1/f$ noise in electrolytes (*see*, for instance, reference 68) stem from uncontrolled contamination of the samples by inclusions of solid, liquid, or gaseous phases.

The effect of added foreign-phase dispersions on the excess noise in electrolytes was studied (21, 22). From relation 15 of Bezrukov et al. (21), it follows that the mean-square value of the relative conductance fluctuations that originate from nonconducting contaminants does not depend on the electrolyte concentration. Hence, to present the results of the excess noise measurements in the form of Hooge's formula, with the samples equally contaminated on the average, the parameter α must be taken to be proportional to the electrolyte concentration.

Nevertheless, the phenomenon of membrane $1/f$ noise does exist and cannot be viewed as some artifact that stems from nonoptimal data processing or poor sample preparation. Apart from $1/f$ -like spectra reported for thick ($\sim 1\text{-mm}$) synthetic membranes of different types (*see* references 69 and 70 and reviews (3, 6) for earlier works), this noise was found in the current and voltage of lipid bilayer membranes modified by several channel-inducing compounds (71–74). The first extensive study of $1/f$ spectra was conducted on chemically dimerized gramicidin A by Sauve and Bamberg (71). Regular gramicidin A generates a Lorentzian-type power spectrum because of an association–dissociation reaction of transmembrane channel formation. In contrast to regular gramicidin A, the covalently linked dimer exhibits clear $1/f$ noise behavior over several orders of frequency magnitude. The intensity of current noise was proportional to membrane conductance, that is, proportional to the number of channels in the membrane, for three decades of conductance change. Relation 10 well described the current noise intensity if N_i was used to denote the number of channels and $\alpha = 10^{-2}$. Comparison of these results with results obtained for large aqueous pores (61) led to the

conclusion that $1/f$ noise in this system is related to some general phenomenon of ion transport.

The experimental findings of Sauve and Bamberg were reproduced for several chemically dimerized gramicidin A analogs that had different linking chain lengths (72–74). These analogs also produced clear $1/f$ noise. The noise intensity was dependent on the lipid composition of the membrane and proportional to the number of channels over a 100-fold increase in their density in the membrane. The idea of ion transport through the open channel as a source of $1/f$ noise was experimentally tested (72, 73). Given the intensity of $1/f$ noise in a multichannel membrane, $S_1(f)$, the mean current through a single open channel, $\langle i \rangle$, and the mean current through a multichannel membrane, $\langle I \rangle$, we can calculate the level of the root-mean-square current fluctuations in the open channel, $\sqrt{\langle (\delta i)^2 \rangle}$, if we suppose that these fluctuations should account for noise observed in the multichannel membrane. If τ is the time resolution of single-channel recording and τ_0 is the time of observation, we have

$$\langle \delta i \rangle^2 = \frac{\langle i \rangle}{\langle I \rangle} \int_{(2\pi\tau_0)^{-1}}^{(2\pi\tau)^{-1}} S_1(f) df \quad (11)$$

where the multiplier before the integral is equal to the inverse mean number of simultaneously open channels.

The results of this calculation and comparison to a single-channel recording are presented in Figure 7. The root-mean-square level, which is required to explain $1/f$ noise in membrane current by transport phenomena through the open channel, is much higher than the actual level. The conclusion is that $1/f$ noise in an open channel (if it exists) cannot account for $1/f$ noise in a multichannel membrane.

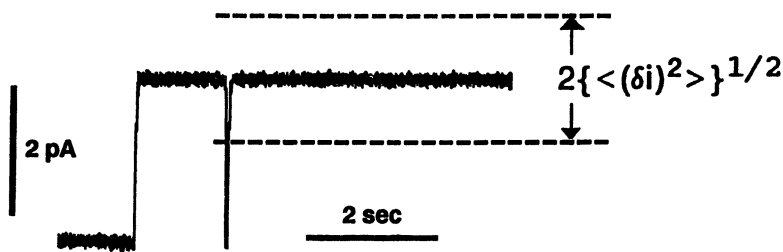


Figure 7. The noise of an open channel formed by chemically dimerized gramicidin A is at least 1 order of magnitude less than the noise required to explain $1/f$ noise in multichannel membranes (72, 73). Glutaryl-bis-desformylgramicidin was applied at 10^{-16} -M concentration in 1-M aqueous KCl solution bathing a bilayer from glycerol monooleate and cholesterol at 100-mV membrane voltage.

The same system (i.e., a glutaryl-bis-desformylgramicidin channel in a lipid bilayer) was used to study the level of $1/f$ noise in a single channel (36, 37). Only a white component, approximately 1 order of magnitude higher than the level predicted by Schottky's formula, eq 2, was found in the 3–300-Hz frequency range. The origin of this component was not clear and was tentatively attributed to unresolved channel switching to a closed state. This experiment set an upper limit for the possible value of the universal (system-independent) $1/f$ noise in ionic conductors (viz. $\alpha \leq 10^{-5}$). The same value for the limit of α can be inferred from the experiments of Heinemann and Sigworth (27, 34), who reported 1 order of magnitude lower values of white noise component in the gramicidin channel but used some correction procedure for their spectra and 1 order of magnitude higher frequency range. Close values for the upper limit were recently reported for macroscopic capillaries filled with electrolyte solutions (*see* reference 75 and references therein).

A model membrane system that also shows reproducible and clear $1/f$ behavior was described by Bezrukov and Brutyan (76). Fluctuations of current through lipid bilayers with one-sided application of three different polyene antibiotics of very close chemical structure (i.e., amphotericin B, nystatin, and mycoheptin) were studied. For one-sided application these antibiotics form channels that are weakly bound to the membrane as compared with the channels of the two-sided action. All three compounds produced pronounced noise component with spectral distribution of $1/f$ type (Figure 8). It was found that the noise intensity scales as the ratio of single channel conductances for amphotericin B, nystatin, and mycoheptin: namely, $h_A:h_N:h_M = 10:5:1$. For mycoheptin the spectrum is described by the function $1/f^{0.86}$ over the whole frequency range used. With two-sided application of these antibiotics, channels are more stable and strongly bound to the bilayer. In this case, significantly lower noise intensities were found; the spectrum for amphotericin B was described by a single Lorentzian spectrum of relatively small amplitude (63).

Based on these and earlier findings, a suggestion was made that $1/f$ noise in membranes can arise from diffusion-induced channel transitions between open and closed states (72–74, 76). Channel switching can be generated not only by channel conformational changes, but also as a result of translational or rotational motion of the whole channel that can bring it to a position where it cannot transport ions through the membrane. For weakly bound and easily washable one-sided polyene channels, this channel switching can be the process of equilibrium transitions of antibiotic molecules between solution and membrane. This hypothesis is supported by the strong dependence of $1/f$ noise on membrane lipid composition reported in references 72–74 and by recent work on fractal properties of biological membranes and membrane protein aggregates (*see* references 77 and 78 and references therein).

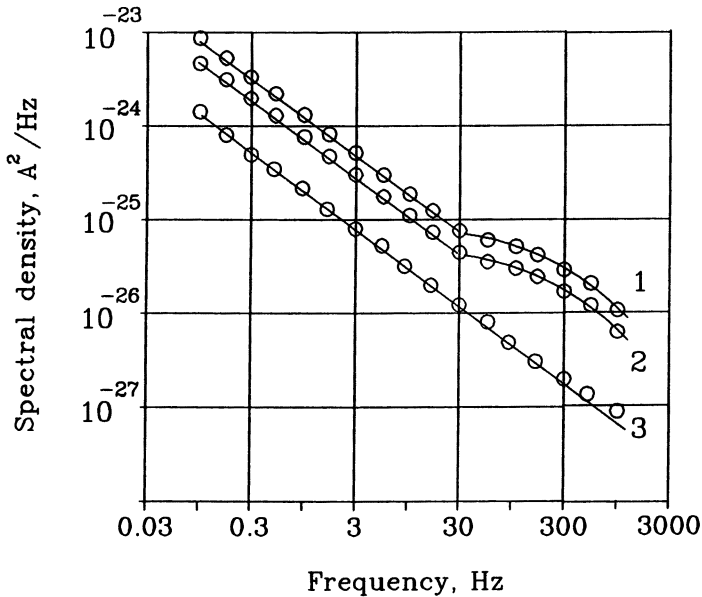


Figure 8. Membrane current noise for one-sided application of three different polyene antibiotics of a very close chemical structure shows $1/f$ -like spectra with intensities proportional to single-channel conductances for these antibiotics (76). Amphotericin B (1), nystatin (2), and mycoheptin (3) spectra refer to the same membrane conductance of 7.1×10^{-8} S at 10 mV.

The idea of diffusion as a source of $1/f$ noise is rather attractive and indeed was explored by many authors (79–81). Diffusion theories that attempted to explain membrane $1/f$ noise by considering fluctuations in the number of charge carriers or diffusion polarization effects were reviewed by Neumcke (56).

Recently Gingl and Kiss (82) studied the noise of one-dimensional diffusion by computer simulation of the process. Coordinate $x(t)$ of a free particle that undergoes diffusion motion was used as an argument of the function $h(x) = \text{sign}(x)[\text{abs}(x)]^{-k}$ to obtain power spectra of $h(x(t))$ at different values of k . The conclusion drawn from this study was that spectral density $1/f$ corresponds to $k = 0.3$. This result seems to be somewhat inaccurate.

Let us consider this process analytically. We shall calculate the spectrum of noise that arises from free one-dimensional diffusion of a particle, whose coordinate determines the value to be measured. First, let this value be defined as a periodical function of a coordinate that changes abruptly from zero to G_0 at equal intervals 2τ . To visualize the model, imagine a single ion channel that undergoes one-dimensional diffusion through the areas where it can transport ions divided by the areas where it cannot transport ions (Figure

9B). We are interested in the spectrum of noise in conductance $G(x(t))$, which is defined by

$$S_G(f) = 4 \int_0^\infty \langle G(x(t))G(x(t+\tau)) \rangle \cos(2\pi f\tau) d\tau \quad (12)$$

For a probability $P(x_0, x, \tau)$ to find a particle (channel) in position x at time τ if it was in position x_0 at $\tau = 0$, we can write

$$D \frac{\partial^2 P(x_0, x, \tau)}{\partial x^2} = \frac{\partial P(x_0, x, \tau)}{\partial \tau} \quad (13)$$

where D is the diffusion coefficient. Because $G(x)$ is an even function with respect to $x = \pm \iota$, we can introduce reflecting walls at these points that do not change the time behavior of $G(x(t))$. This procedure yields conditions $\partial P(x_0, x, \tau) / \partial x = 0$ at $x = \pm \iota$ and permits us to write for the τ -dependent part of the solution of eq 13,

$$P(x_0, x, \tau) = \sum_1^\infty a_n \exp(-\tau/\tau_n) \cos(\pi n x / \iota) \quad (14)$$

where
$$\tau_n = \iota^2 / D (\pi n)^2 \quad (15)$$

We make use of the condition

$$P(x_0, x, \tau) |_{\tau=0} = \delta(x - x_0) \quad (16)$$

to obtain

$$P(x_0, x, \tau) = (1/\iota) \sum_1^\infty \exp(-\tau/\tau_n) \cos(\pi n x_0 / \iota) \cos(\pi n x / \iota) \quad (17)$$

The autocorrelation function in eq 12 can be written in the form

$$\langle G(x(t))G(x(t+\tau)) \rangle = \frac{1}{2\iota} \iint_{-\iota}^{\iota} G(x_0)G(x) P(x_0, x, \tau) dx_0 dx \quad (18)$$

which gives a straightforward expression for the power spectral density:

$$S_G(f) = \frac{2}{\iota^2} \sum_1^\infty \left[\int_{-\iota}^{\iota} G(x) \cos(\pi n x / \iota) dx \right]^2 \frac{\tau_n}{1 + (2\pi f \tau_n)^2} \quad (19)$$

Spectra calculated for several different functions $G(x)$ are presented in Figure 9. The model of noise at free one-dimensional diffusion can describe

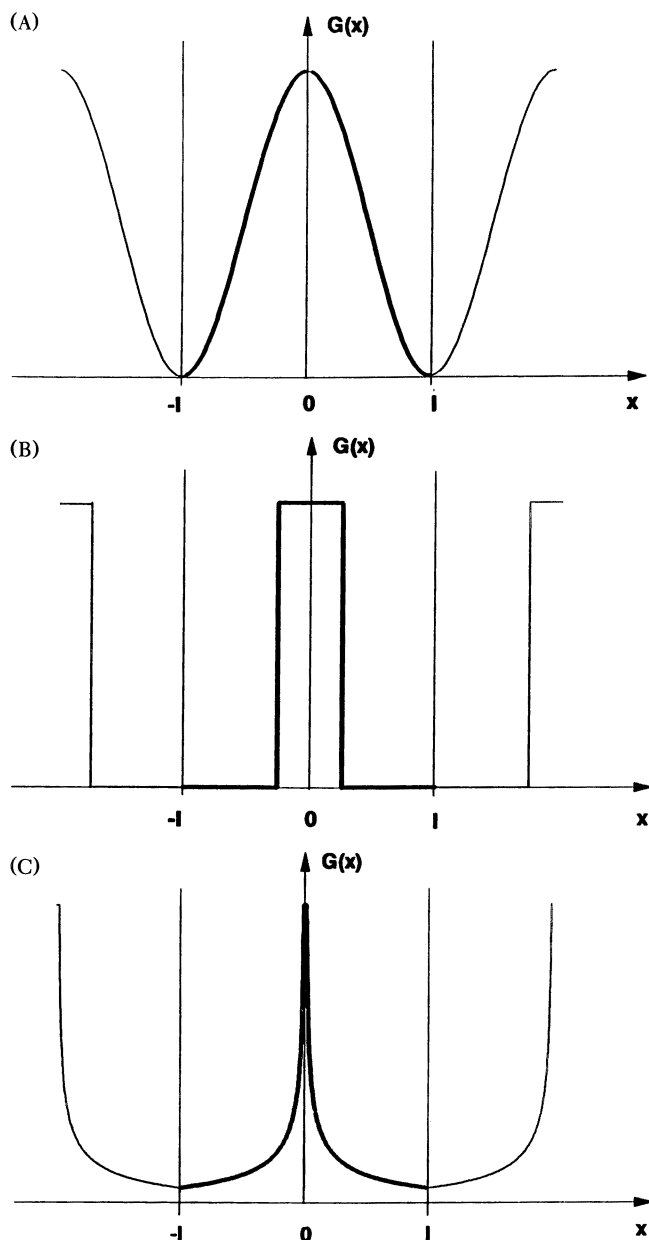


Figure 9. Free one-dimensional diffusion generates fluctuations with practically all types of declining spectra that depend on the choice of the scaling function $G(x)$. The sine wave scaling function gives a Lorentzian spectrum with the f^{-2} high-frequency asymptote (A). The square wave produces a more complex spectrum with an extended $1/f$ -like region and $f^{-3/2}$ high-frequency dependence (B). The $(\text{abs}(x))^{-1/2}$ scaling function generates noise with a $1/f$ spectrum at high frequencies (C). (The actual function used in computations was $(\text{abs}(x) + 10^{-6})^{-1/2}$.)

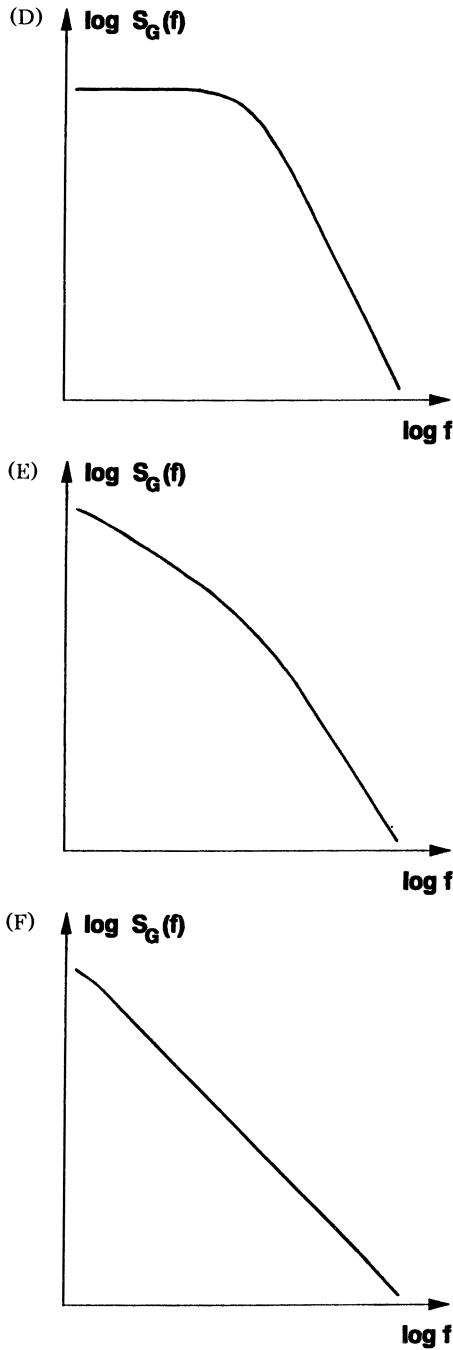


Figure 9. —Continued. All spectra are plotted in a log-log scale over four decades of frequency change. D, E, and F correspond to A, B, and C, respectively.

practically any type of noise with declining spectral density. As can easily be seen from eq 19, a sine function for $G(x)$ will produce a Lorentzian spectrum with a f^{-2} high-frequency tail. A square wave will yield a more complex spectrum with $f^{-3/2}$ high-frequency behavior. Two features are worth mentioning. First, even for the simplest model considered, the spectrum has a much longer $1/f$ -like region than does a Lorentzian spectrum. Second, the characteristic time, or rather set of characteristic times $\tau_n = \iota^2/D(\pi n)^2$, of the spectrum is proportional to the square of characteristic length ι , which means, for example, that the 100-fold range of fractal scaling found experimentally for many objects (83) could lead to 10,000-fold frequency range of $1/f$ noise.

Finally, function $G(x) = (\text{abs}(x))^{-1/2}$ will generate $1/f$ noise at high frequencies. Indeed, try function $G(x) = (\text{abs}(x))^{\mu-1}$. For sufficiently high frequencies (i.e., for large values of n) the integration in eq 19 can be extended to $\pm\infty$, which gives, for the term in square brackets (84),

$$2 \int_0^{\infty} x^{\mu-1} \cos(\pi nx/\iota) dx = \frac{\Gamma(\mu)}{(\pi n/\iota)^{\mu}} \cos\left(\frac{\mu\pi}{2}\right) \quad (20)$$

if $0 < \mu < 1$. Then, high-frequency asymptotic behavior of the spectral density can be evaluated by integration instead of summation in eq 19 and by making the integral dimensionless with respect to f (see also reference 79, page 137). If we omit the details, we have

$$S_G(f) \approx \frac{1}{f^{\mu+1/2}} \quad (21)$$

so that the $1/f$ spectrum corresponds to $\mu = 1/2$.

Acknowledgment

We express our gratitude to V. Ph. Pastushenko for fruitful discussions.

References

1. Johnson, J. B. *Phys. Rev.* **1928**, *32*, 97–109.
2. Stevens, C. F. *Biophys. J.* **1972**, *12*, 1028–1047.
3. Verveen, A. A.; DeFelice, L. J. *Prog. Biophys. Mol. Biol.* **1974**, *28*, 189–265.
4. Conti, F.; Wanke, E. *Q. Rev. Biophys.* **1975**, *8*, 451–506.
5. Neher, E.; Stevens, C. F. *Annu. Rev. Biophys. Bioeng.* **1977**, *6*, 345–381.
6. DeFelice, L. J. *Introduction to Membrane Noise*; Plenum: New York, 1981.
7. Neumcke, B. *Int. Rev. Neurobiol.* **1982**, *23*, 35–67.
8. Fishman, H. M. *Prog. Biophys. Mol. Biol.* **1985**, *46*, 127–162.
9. Fishman, H. M.; Leuchtag, H. R. *Curr. Top. Membr. Transp.* **1990**, *37*, 3–35.
10. Nyquist, H. *Phys. Rev.* **1928**, *32*, 110–113.

11. DeFelice, L. J.; Firth, D. R. *IEEE Trans. Biomed. Eng.* **1971**, *18*, 339–351.
12. DeFelice, L. J.; Michalides, J. P. L. M. *J. Membr. Biol.* **1972**, *9*, 261–290.
13. Bezrukov, S. M.; Vodyanov, I.; Drabkin, G. M.; Preobrazhenskii, N. I. Preprint 295, Leningrad Nuclear Physics Institute, Leningrad, Russia, 1976 (in Russian).
14. Bezrukov, S. M.; Vodyanov, I.; Drabkin, G. M.; Preobrazhenskii, N. I. *Dokl. Biophys. (Engl. Transl.)* **1977**, 232–234, 34–37; *Dokl. Akad. Nauk. SSSR* **1977**, 233, 704–707.
15. Kolb, H.-A.; Lauger, P. J. *Membr. Biol.* **1977**, *37*, 321–345.
16. Szabo, G. *Ann. N.Y. Acad. Sci.* **1977**, *303*, 266–278.
17. Bruner, L. J.; Hall, J. E. *Biophys. J.* **1979**, *28*, 511–514.
18. Kolb, H.-A.; Lauger, P. J. *Membr. Biol.* **1978**, *41*, 167–187.
19. Hedman, K.; Klason, C.; Kubat, J. J. *Appl. Phys.* **1979**, *50*, 8102–8106.
20. Hedman, K.; Klason, C.; Poupetova, D. *Rheol. Acta* **1983**, *22*, 449–454.
21. Bezrukov, S. M.; Drabkin, G. M.; Sibilev, A. I. *J. Colloid Interface Sci.* **1986**, *113*, 194–202.
22. Bezrukov, S. M.; Pustovoit, M. A.; Sibilev, A. I. *J. Colloid Interface Sci.* **1992**, *148*, 375–381.
23. Schottky, W. *Ann. Phys.* **1918**, *57*, 541–567.
24. Thompson, J. D.; Joiner, W. C. H. *Solid State Commun.* **1975**, *16*, 849–851.
25. Habbal, F.; Joiner, W. C. H. *J. Low Temp. Phys.* **1977**, *28*, 83–93.
26. Thompson, J. D.; Joiner, W. C. H. *Phys. Rev. B* **1979**, *20*, 91–104.
27. Heinemann, S. H.; Sigworth, F. J. *Biophys. J.* **1990**, *57*, 499–514.
28. Frehland, E. *Biophys. Chem.* **1978**, *8*, 255–265.
29. Frehland, E.; Stephan, W. *Biochem. Biophys. Acta* **1979**, *553*, 326–341.
30. Frehland, E. *Biophys. Chem.* **1980**, *12*, 63–71.
31. Frehland, E.; Solleder, P. *Biophys. Chem.* **1986**, *25*, 135–146.
32. Solleder, P.; Frehland, E. *Biophys. Chem.* **1986**, *25*, 147–159.
33. Lauger, P. *Electrogenic Ion Pumps*; Sinauer Associates: Sunderland, MA, 1991.
34. Heinemann, S. H.; Sigworth, F. J. *Biophys. J.* **1988**, *54*, 757–764.
35. Sigworth, F. J. *Biophys. J.* **1985**, *47*, 709–720.
36. Bezrukov, S. M.; Irkhin, A. I.; Sibilev, A. I. *Abstracts of Papers*, 37th Meeting of the International Society of Electrochemistry Vilnius; University Press: Vilnius, Lithuania, 1986; Vol. 4, pp 402–404.
37. Bezrukov, S. M.; Irkhin, A. I.; Sibilev, A. I. *Phys. Lett. A* **1987**, *123*, 477–480.
38. Sigworth, F. J.; Urry, D. W.; Prasad, K. U. *Biophys. J.* **1987**, *52*, 1055–1064.
39. Eisenberg, R. S.; Hainsworth, A. H.; Levis, R. A. *J. Physiol. (London)* **1988**, *396*, 84P.
40. Eisenberg, R. S.; Hainsworth, A. H.; Levis, R. A. *J. Physiol. (London)* **1989**, *410*, 18P.
41. Kolb, H.-A.; Frehland, E. *Biophys. Chem.* **1980**, *12*, 21–34.
42. Tyagai, V. A. In *Electrical Phenomena at the Biological Membrane Level*; Roux, E., Ed.; Elsevier: New York, 1977; pp 325–335.
43. Grafov, B. M.; Levich, V. G. *Sov. Phys.-JETP* **1968**, *27*, 507–510.
44. Voss, R. F.; Clarke, J. *Phys. Rev. B* **1976**, *13*, 556–573.
45. Bezrukov, S. M.; Pustovoit, M. A.; Sibilev, A. I.; Drabkin, G. M. *Physica B* **1989**, *159*, 388–398.
46. Bezrukov, S. M.; Vodyanov, I. In *Proceedings of the International Conference on Noise in Physical Systems and 1/f Noise*; Musha, T.; Sato, S.; Yamamoto, M., Eds.; Ohmsha, Ltd.: Tokyo, Japan, 1991; pp 641–644.
47. Bezrukov, S. M.; Kasianowicz, J. J. *Phys. Rev. Lett.* **1993**, *70*, 2352–2355.
48. Weissman, M. B. *Annu. Rev. Phys. Chem.* **1981**, *32*, 205–232.

49. *Noise in Physical Systems and 1/f Noise*; D'Amico, A.; Mazzetti, P., Eds.; Proceedings of the 8th International Conference; North-Holland: Amsterdam, Netherlands, 1986.
50. *Noise in Physical Systems*; van Vliet, C. M., Ed.; Proceedings of the 9th International Conference; World Scientific: Singapore, 1987.
51. *Proceedings of the International Conference on Noise in Physical Systems and 1/f Noise*; Musha, T.; Sato, S.; Yamamoto, M., Eds.; Ohmsha, Ltd.: Tokyo, Japan, 1991.
52. van den Berg, R. J.; de Vos, A.; de Goede, J. In *Noise in Physical Systems*; Proceedings of the 6th International Conference; Meijer, P. H. E.; Meijer, P. H. E.; Mountain, R. D.; Soulen, R. J., Eds.; National Bureau of Standards: Washington, DC, 1981; pp 217–220.
53. Lax, M.; Mengert, P. *J. Phys. Chem. Solids* **1960**, *14*, 248–267.
54. Hille, B. *Ionic Channels of Excitable Membranes*; Sinauer Associates: Sunderland, MA, 1984; pp 181–188.
55. Hall, J. E. *J. Gen. Physiol.* **1975**, *66*, 531–532.
56. Neumcke, B. *Biophys. Struct. Mechanism* **1978**, *4*, 179–199.
57. Hooge, F. N. *Phys. Lett. A* **1969**, *29*, 139–140.
58. van der Berg, R. J.; Beekman, R. E. In *Abstracts*, 18th Dutch Federative Meeting; 1977; p 127.
59. van den Berg, R. J.; Siebenga, E.; de Goede, J.; Moolenaar, W. H.; Verveen, A. A. In *Proceedings of the Symposium on 1/f Fluctuations*; Tokyo, Japan, 1977; pp 97–105.
60. Hooge, F. N. *Physica* **1972**, *60*, 130–144.
61. Dorset, D. L.; Fishman, H. M. *J. Membr. Biol.* **1975**, *21*, 291–309.
62. Khodorov, B. I.; Neumcke, B.; Schwarz, W.; Stampfli, R. *Biochim. Biophys. Acta* **1981**, *648*, 93–99.
63. Bezrukov, S. M.; Drabkin, G. M.; Sibilev, A. I.; Feigin, A. M. *Dokl. Biophys. (Engl. Transl.)* **247–249**, 210–212; *Dokl. Akad. Nauk. SSSR* **1979**, *249*, 730–732.
64. van den Berg, R. J.; de Vos, A.; de Goede, J. *Phys. Lett. A* **1981**, *84*, 433–434.
65. van den Berg, R. J.; de Vos, A.; de Goede, J. *Phys. Lett. A* **1981**, *87*, 98–100.
66. van den Berg, R. J.; de Vos, A. *Phys. Lett. A* **1982**, *92*, 203–206.
67. de Vos, A.; van den Berg, R. J.; de Goede, J. *Phys. Lett. A* **1984**, *102*, 320–322.
68. Musha, T.; Sugita, K. *J. Phys. Soc. Jpn.* **1982**, *51*, 3820–3825.
69. Fang, Y.; Li, Q.; Green, M. E. *J. Colloid Interface Sci.* **1982**, *86*, 185–190.
70. Fang, Y.; Li, Q.; Green, M. E. *J. Colloid Interface Sci.* **1982**, *88*, 214–220.
71. Sauve, R.; Bamberg, E. *J. Membr. Biol.* **1978**, *43*, 317–333.
72. Bezrukov, S. M.; Drabkin, G. M.; Fonina, L. A.; Irkhin, A. I.; Melnik, E. I.; Sibilev, A. I. Preprint 598, Leningrad Nuclear Physics Institute, Leningrad, Russia, 1980.
73. Bezrukov, S. M.; Drabkin, G. M.; Fonina, L. A.; Irkhin, A. I.; Melnik, E. I.; Sibilev, A. I. In *Bilayer Lipid Membranes*; Far East Science Publishers: Vladivostok, Russia, 1983; pp 64–87 (in Russian).
74. Irkhin, A. I.; Bezrukov, S. M.; Melnik, E. I. *Biologicheskije Membrany* **1984**, *1*, 739–749 (in Russian).
75. van den Berg, R. J.; de Vos, A.; de Goede, J. *Phys. Lett. A* **1989**, *139*, 249–252.
76. Bezrukov, S. M.; Brutyan, R. A. *Biophysics (Engl. Transl.)* **1987**, *32*, 573–575; *Biofizika* **1987**, *32*, 526–528.
77. Nonnenmacher, T. F. *Eur. Biophys. J.* **1989**, *16*, 375–379.
78. Dewey, T. G.; Datta, M. M. *Biophys. J.* **1989**, *56*, 415–420.
79. Richardson, J. M. *Bell Syst. Tech. J.* **1950**, *29*, 117–141.

80. van Vliet, K. M.; van der Ziel, A. *Physica* **1958**, *24*, 415–421.
81. Weissman, M. B. *J. Appl. Phys.* **1977**, *48*, 1705–1707.
82. Gingl, Z.; Kiss, L. B. In *Abstracts of Papers*, 10th International Conference on Noise in Physical Systems; Akademia Kiado: Budapest, Hungary, 1989; pp 197–199.
83. Pietronero, L.; Tosatti, E. *Fractals in Physics*; Elsevier Biomedical Press: Amsterdam, Netherlands, 1986.
84. Gradshteyn, I. S.; Ryzhik, I. M. *Tables of Integrals, Series, and Products*; Academic: Orlando, FL, 1965.

RECEIVED for review May 1, 1991. ACCEPTED revised manuscript August 5, 1992.

Laser Doppler Scattering for the Determination of Ionic Velocity Distributions in Channels and Membranes

Felipe Macias and Michael E. Starzak

Department of Chemistry, State University of New York at Binghamton,
Binghamton, NY 13902-6000

The Doppler shift of light scattered from a moving particle provides a direct measure of the velocity of the particle. Laser Doppler velocimetry is applied to the observation of the velocity distribution of potential-driven ions in gramicidin channels in bilayer membranes. The membrane-channel system constrains the ions to a limited range of directions. Because the length of the channel (2.6 nm) is small relative to the wavelength of the scattering light (632.8 nm), the scattering in the channels is constructive and produces a net observable signal as the sum of scattering from multiple, intrachannel ions. The frequency, or velocity, distribution is unimodal, which indicates that the intrachannel velocity is roughly constant as it traverses the channel. Potential binding sites within the channel produce small variations in the intrachannel velocity that are reflected in the width of the velocity-Doppler frequency distribution. For transmembrane potentials from 10 to 150 mV, the intrachannel average velocities range from 0.0375 to 0.238 m/s.

COMplete characterization of the kinetics of membrane channels requires a detailed understanding of channel gating, selectivity, and ion permeation. Ion permeation, the most basic of the three phenomena, has been described with a number of distinct models. Discrete state models postulate one or more binding sites within the channel. The ion then per-

0065-2393/94/0235-0401\$08.00/0
© 1994 American Chemical Society

meates through the channel in a series of discrete kinetic steps. Rate parameters describe motion from binding site to binding site until the ion appears on the opposite side of the membrane (1). Mathematically similar models postulate ion-channel states (e.g., two ions in a single channel) and develop kinetics for the transitions between such stochastic states (2). In such formulations, the transition from a state that defines a channel with a single ion to a second state that defines a channel with two ions is a first-order kinetic process. Additional states might be channel states modified by the action of some binding external to the channels (3, 4). The total number of stochastic states can increase rapidly for complicated systems, and it becomes progressively more difficult to determine whether a good fit of the experimental data using a large number of adjustable rate constants signifies an accurate mechanism for the permeation process.

For multistep intrachannel ion-binding models, the formulation of the rate constants for individual transitions is complicated by the existence of two parameters in the flux expression. Parlin and Eyring (5) and Starzak (6) developed a flux expression for ion flow through membranes or channels that used transition-state theory where the rate constant was characterized by an activation energy barrier. For dimensional consistency, this rate constant, k_i , appeared in conjunction with a length, λ_i , the distance in the channel that the ion must move to cross the energy barrier.

The net flux, J , for ions with concentration c_i at an intrachannel binding site b_i is proportional to the velocity with which these ions progress to the next binding site:

$$J = v_i c_i$$

For consistency, the Eyring-Parlin parameters, λ_i and k_i , must be combined into a single local velocity, v_i , for the transition from state b_i to the next state. The flux is

$$J = \lambda_i k_i c_i = v_i c_i$$

This local velocity, rather than the rate constant, is the parameter of interest. However, the magnitude of the local velocity can still be described by an energy barrier formalism:

$$v_i = v' \exp\left(-\frac{E_i}{RT}\right)$$

where E_i is the barrier height, R is the gas constant, and T is the temperature. A determination of all local velocities for an ion within a channel then provides a complete description of the ion permeation. Stochastic models that focus on stochastic states, which include both the channel and

the ion, must still be formulated using rate constants or transition probabilities and are less amenable to a local velocity analysis.

If ion permeation involves a discrete binding-site mechanism, the number of distinct local velocities that must be determined will increase with the number of binding sites. For example, the permeation of a single ion through a channel with two discrete binding sites requires six local velocities: three that lead the ion through the channel to the opposite bath and three that describe the ion motion in the opposite direction. Under conditions where the reverse velocities make a negligible contribution to the total flux (e.g., in a large electric field that drives the ions to the opposite bath), a velocity distribution for the ion could consist of three separate peaks for (1) the local velocity from the solution to the first binding site, (2) the local velocity from the first intrachannel binding site to the second site, and (3) a final local velocity for the ion as it moves from the second binding site to the opposite bath. If all local velocities for this two-binding-site case are identical, the velocity distribution will coalesce to a single peak.

Discrete state models with binding sites suggest that the ion may physically bind at the intrachannel binding sites. If binding does occur, the velocity distribution can be significantly broadened because of deceleration and acceleration as the ion approaches and leaves the binding site. The local velocity formulation for permeation is more forgiving because it assumes that these accelerations and decelerations are far shorter than the net transit time; that is, the ion is in a steady velocity state for each leg of its journey. The ion approaches the site with one steady local velocity and rapidly assumes the second velocity as it passes the binding site. There is no "binding", merely an abrupt change in velocity.

Although many permeation processes can be described effectively by discrete state binding sites within the channel, they are not the only possible permeation mechanisms. The ion may diffuse through the channel to reach the opposite bath. This diffusional flow can be considered the limit of discrete site diffusion because the number of discrete sites increases. In such a model, the ion cannot make the abrupt changes in velocity that could characterize the finite site, discrete state model. The velocity, however, can change continuously as the ion moves through the channel. A discrete state velocity distribution would evolve naturally to a continuous velocity distribution, where the relative numbers of ions at each velocity in the continuum of velocities could be established.

Continuum models have been studied theoretically (7, 8) and are amenable to computer simulations (9). In addition, continuum models may be more consistent with physical evidence that indicates that each permeating ion is accompanied by a plug of water molecules (10). These water molecules must also move through the channel with local velocities and may act to ensure a more steady continuous ion flow in the channel.

Although the discrete state and continuum models are analyzed in different ways, both models must produce a local velocity distribution for the ions within the channel. A continuum velocity distribution might be characterized by a single peak of finite bandwidth that reflects velocity fluctuations within the channel, whereas a discrete state model might consist of several different peaks in the distribution. Such velocity distributions have been generated from the models used because electrochemical experiments do not yield detailed information on the internal kinetic parameters. These parameters are deduced from the experimental data, which are generally the net currents observed for a series of transmembrane potentials for a variety of bath ionic components and concentrations. More detailed information on the nature of intrachannel kinetics becomes accessible if it is experimentally possible to deduce the velocity distribution of the ions in the channel.

The gramicidin channel is the ideal membrane channel for a detailed study of ion permeation. Two gramicidin molecules dimerize in a bilayer membrane to form an open channel; potential-dependent gating processes to generate an open channel are absent. Random current fluctuations can be observed, however, and have been attributed to changes in the channel itself. These changes include conformation fluctuations of the channel protein (11), channel block (12), and ion entry (13).

Although most univalent ions are permeable in the gramicidin channel, the channel has some conductance properties that suggest that the permeation process may be more complicated than ion motion down a narrow "tube". Channel "block" by divalent cations is mechanistically complicated (14). Also, when Tl^+ ion is present as the sole permeant ion, it is an excellent permeant ion that retains linear behavior to very large transmembrane potentials (15). However, when this ion is present as the minority cation in variable mole fraction solutions of Tl^+ and Na^+ , Tl^+ ion severely limits set channel currents (16). Such anomalous behavior can be elucidated if the local velocity of a specific ion (e.g., Tl^+ ion) can be determined experimentally. In fact, the laser Doppler scattering technique produces a detectable scatter only with the Tl^+ so that ion motions within the gramicidin channels can be differentiated.

Laser Doppler Velocimetry

The elucidation of a mechanism for the permeation of cations in gramicidin channels requires a complete velocity distribution for these cations in the channels. The distribution describes the fractional concentration or probability of finding an ion at a specific local velocity in the channel. An ion that moved through the channel at constant velocity would give an extremely narrow distribution; 100% of the ions are moving at that single local velocity. For a discrete state model with two binding sites, the distributions could

involve three separate peaks in the distribution if the three forward local velocities dominate and are all different. The amplitudes of the distribution peaks provide a direct measure of the probability that the ion moves with a specific velocity; that is, the amplitudes are a measure of the concentrations of ions within an ensemble of channels that have a specific velocity. Such distributions give the full range of local velocities for each set of bath concentrations, potentials, and other experimentally modifiable conditions.

When light is scattered from a moving particle, the incoming light of frequency f is Doppler-shifted to a new scattering frequency f' . This frequency f' is directly proportional to the relative velocity, v , of the moving particle relative to the speed of light, c :

$$f' = f \left(1 - \frac{v}{c} \right)$$

Although the frequency shift

$$\Delta f = |f - f'|$$

is small, it can be detected as a difference frequency when the input frequency, f , and Doppler-scattered frequency, f' , are mixed in a nonlinear detector. The observed difference frequency, Δf , is

$$\Delta f = f \frac{v}{c} = \frac{v}{\lambda}$$

where λ is the wavelength of the input light beam. Because a range of input light wavelengths would generate a range of frequency differences, such Doppler scattering experiments are optimized with narrow bandwidth laser excitation.

For experiments with a reference light beam and the Doppler-shifted scattered light beam, the signal is optimized when the amplitudes of these two signals have approximately equal amplitudes and traverse equal or in-phase path lengths (17). Because balanced amplitudes for the two signals can be difficult to establish experimentally, an alternative experimental configuration is preferable. The laser beam is split into two equal amplitude halves that are then displaced equal distances from the optical axes. These displaced beams are then directed parallel to the optical axis and passed through a lens that refocuses them onto the optical axis at a common point (Figure 1). If the beam angles relative to the optical axis are each α , the two optical beams give positive and negative projections of

$$v \sin \alpha$$

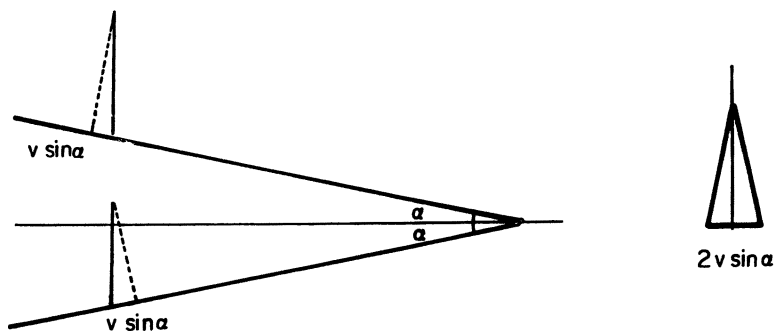


Figure 1. The velocity components required for a net Doppler frequency difference for a crossed-beam system with reference angle α . The net velocity difference $2v \sin \alpha$ gives a Doppler shift $\Delta\nu = 2v \sin \alpha \lambda^{-1}$.

A nonlinear detector will detect the net frequency difference produced by the difference of these two velocity components as

$$\Delta f = \frac{2v \sin \alpha}{\lambda}$$

As illustrated in Figure 1, the frequency difference will be generated by velocity components that are perpendicular to the optical axis of the system.

When a helium-neon (HeNe) laser with $\lambda = 632.8$ nm is used as the input beams and the two equal beams are separated and refocused to give an intersection angle $\alpha = 10.72^\circ$ for each beam, the relative velocity of the scattering particles relates to the observed difference frequency as

$$v = 1.7 \times 10^{-6} \Delta\nu \text{ m/s}$$

Because a normal for the planar bilayer must be oriented at some angle θ relative to the optical axis, only a component of the actual velocity is observed. This component, which is perpendicular to the optical axis of the system, can be converted into the total velocity, v_t , as

$$v_t = \frac{v}{\sin \theta} = \frac{\lambda \Delta f}{\sin \theta}$$

For observations at the standard orientation of 45° for the HeNe laser, the total velocity is related to the observed frequency difference as

$$v_t = 2.4 \times 10^{-6} \Delta f \text{ m/s}$$

Instrumentation

A crossed-beam scattering system (Figure 2) was the preferred method for low-intensity scattering because scattered light background or pedestal (17) can be reduced. The beam from a 20-mW HeNe laser (Jodon) was separated into two equal beams that were displaced 25 mm from the optical axis in opposite directions in the horizontal plane using a beam splitter-displacer (TSI, Inc.). The beams were reflected parallel to the main optical axis in the beam splitter-displacer. A 50-mm lens refocused these beams to a common point on the main optical axis approximately 120 mm from the lens. Because the intersecting beams diverged after the intersection point, they could be masked so that only scattered light was observed on the optical axis. This forward-scattered light was collected with a telephoto lens and focused on a pinhole. The light through the pinhole was detected by a photomultiplier (1P21). Because the photomultiplier acts as a nonlinear detector, the difference frequency between the two frequency components of light scattered by the two displaced beams appeared as a difference frequency in the photomultiplier output. This signal was directed to a kilohertz frequency spectrum analyzer (Hewlett-Packard 3561A). Although a current-to-voltage converter was also used between the photomultiplier and analyzer, this device did not improve the signal-to-noise ratio.

The optical and electronic systems were calibrated using flowing water seeded with colloidal spheres (Dupont Ludox). The constant velocity solution flow was inserted into the beam intersection region with the water flow perpendicular to the optical axis for direct detection of the total velocity for a

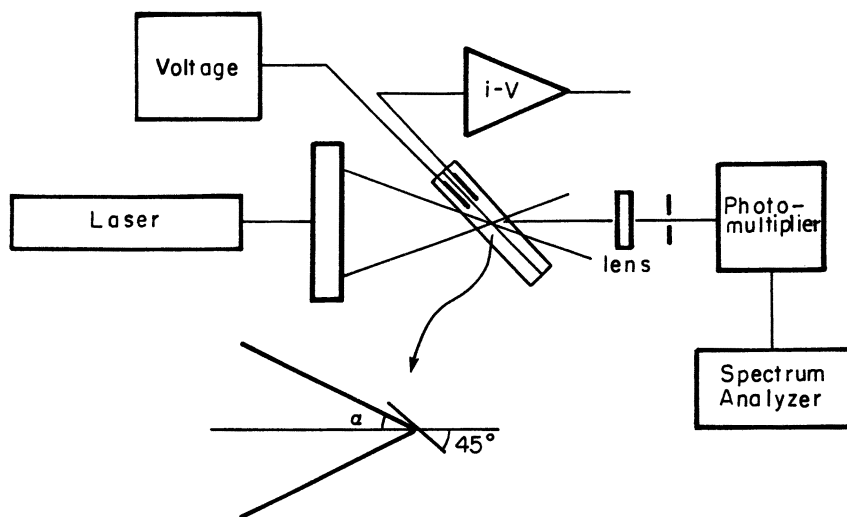


Figure 2. Block diagram of the laser Doppler gramicidin channel system.

single colloidal particle. As each colloidal particle entered the beam intersection region, it produced a "tone burst" spectrum that was captured on a storage oscilloscope (Tektronix). The frequency within each tone burst gave the Doppler difference frequency and the velocity of the colloidal particle that correlated with the known flow velocity of the water.

Because laser Doppler velocimetry has been used extensively to determine the velocity of large charged particles in electrophoresis (18–20), the velocities of charged particles in an applied electric field were studied for further calibration of the experimental configuration. The intersecting beams irradiated a water solution seeded with charged latex microspheres (Interfacial Dynamics). A field was applied to move the microspheres in a direction perpendicular to the main optical axis. The velocity increased linearly with the applied field, which signaled a constant microsphere mobility over the range of fields studied.

These test systems involved large single particles that serve as effective scattering centers. The scattering centers for ion flows in gramicidin channels are the ions themselves. Although individual ions cannot scatter as effectively as a large colloidal sphere or very large protein, these ions will all experience homogeneous, directed velocities when they permeate the gramicidin channels. The membrane constitutes a region of spatial and electrical homogeneity. The channel length is small relative to the wavelength of the light so that scattered light from ions in all parts of the channel is essentially in phase; that is, it interferes constructively. A channel transmits approximately 10^7 ions per second to produce a large number of scattering centers in a small spatial volume. This scattering amplitude enhancement by a large number of scattering centers generates an observable ion scattering signal.

Planar bilayer scattering experiments were initially conducted in a rectangular chamber with quartz windows for both the intersecting input beams and the Doppler-scattered light. The windows and bilayer normal were oriented at different angles relative to the optical axis by placing the cell on a rotating base. The rectangular cell was replaced by a cylindrical cell to permit a greater range of orientation angles. In both cases, the membrane was formed at a pinhole in a support that separated the two solutions. Micrometer-controlled syringes that contained glycerin were used to orient the membrane exactly on the optical axis of the system. Fine adjustment was obtained by maximization of the scattering signal that reached a photodiode that was inserted into the chamber behind the bilayer and support and lay along the optical axis. When alignment was optimal, this photodiode was removed and replaced by a platinized platinum electrode for current measurements. A second electrode in the opposite bath was used to apply the transmembrane potential.

Planar bilayer membranes were formed from solutions of 25 mg of glycerolmonooleate (Sigma Chemical) in 0.9 mL of decane (Wiley). In both chambers, 0.1-M solutions of thallos acetate (TlAc) with a trace of TlCl were

used. Although other univalent ions were used as permeant ions, Tl^+ gave the only observable signal with both membrane chambers. A potential ramp was used to verify the presence of the bilayer membrane and the incorporation of gramicidin channels. The experiments were performed with a constant transmembrane potential produced by a battery-potentiometer arrangement. Currents were recorded using a current-to-voltage converter and were slightly smaller than the currents generated by the ramp potentials. Some electrode polarization may have resulted from the long times at constant potential (10–15 min) required for spectral analysis of the scattered light signal.

Tl^+ ion with the largest atomic number ($Z = 81$) was the only ion that gave consistent observable Doppler scattering. Marginal signals were observed for Cs^+ with the rectangular cell but were not observed with the cylindrical cell. No Doppler scattering was observed for Rb^+ , Ag^+ , or K^+ . The Tl^+ spectrum was also observed using a 10-MHz bandwidth spectrum analyzer (Tektronix) to verify the absence of additional high-frequency bands. The 10-MHz bandwidth encompassed all frequencies possible for the ions at the maximal electric field strength.

Because membrane surface waves can also produce a Doppler scattering signal (21), the frequency distribution for Tl^+ was observed with the cell at a series of angles relative to the optical axis. Because surface waves and ion motions in the channel move in mutually perpendicular directions, it is possible to discern the direction of motion that produces the Doppler shift by observing the change in observed frequency difference with a change in the angle of orientation. As shown in Figure 3, the Doppler frequency increased linearly with the sine of the angle of orientation (Φ) between the optical axis and the membrane normal. The scattering is produced by particle motions normal to the membrane surface; that is, consistent with the motions of ions through channels.

The frequency distributions for each potential constituted a single, connected spectrum. Some of these difference spectra are shown in Figure 4. The average frequencies for these spectra are determined by the spectrum analyzer for the 0.1-M Tl^+ solutions with the chamber oriented at 45° and are tabulated in Table I along with their corresponding average velocities. The single spectral region suggests that the ions move through the channel under a given transmembrane potential at a steady limiting velocity with minimal acceleration and deceleration. The bandwidths of the single spectral regions for each potential ranged from 200 to 1500 Hz, which indicates some velocity fluctuations within the channel. However, these fluctuations appear to be perturbations of a dominant single permeation velocity. If binding sites are present in the region of the channel where the ions produce the observed Doppler scattering, these sites only serve to produce perturbations in the steady velocity of the permeating ion. No distinct spectral regions that indicate different velocities between different binding sites within the channel are observed.

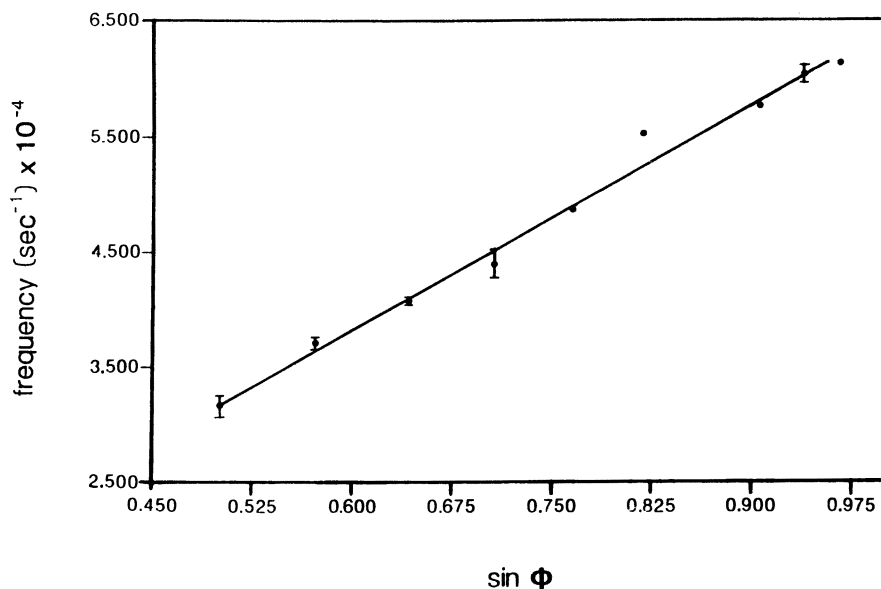


Figure 3. Variation in Doppler frequency with orientation angle of the membrane system. Doppler frequency and ion velocity increase as the motion becomes more perpendicular to the optical axis.

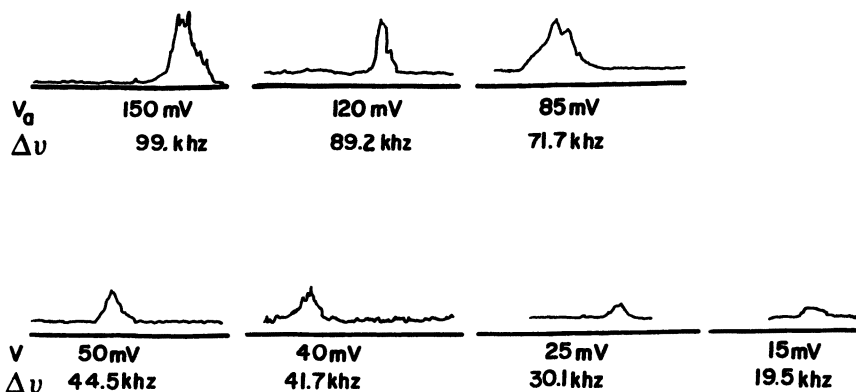


Figure 4. Some typical Doppler spectra for Tl^+ ions in gramicidin channels at different applied potentials. V_0 is the applied constant potential, and Δv is the average Doppler difference frequency.

The interior of the gramicidin channel is postulated to serve as a "waterlike" environment for both the permeant ion and other water molecules in the channel. If the channel interior is similar to bulk water, a permeant ion is expected to have permeability properties similar to those of the ion in water. This condition permits an estimate of the upper limits of ion velocity

Table I. Velocities and Transit Frequencies for Tl(I) Ion in Gramicidin Channels

Potential (mV)	Observations	Doppler Shift (kHz)	Velocity (m/s $\times 10^1$)	Transit Frequency (s ⁻¹ $\times 10^{-7}$)
10	2	15.6 \pm 0.19	0.375	1.44
15	1	19.5	0.469	1.80
20	2	24.2 \pm 1.0	0.582	2.24
25	1	30.1	0.724	2.79
30	2	32.8 \pm 0.8	0.788	3.03
40	3	40.8 \pm 1.3	0.981	3.78
50	2	44.5 \pm 1.4	1.09	4.21
60	2	54.3 \pm 0.1	1.31	5.01
70	2	61.2 \pm 0.2	1.47	5.68
80	3	67.5 \pm 0.5	1.64	6.30
90	3	73.5 \pm 1.3	1.77	6.78
100	3	78.3 \pm 0.6	1.88	7.21
110	3	83.8 \pm 1.4	2.01	7.72
120	3	87.4 \pm 1.2	2.10	8.10
130	3	92.3 \pm 0.5	2.22	8.53
140	3	96.4 \pm 0.6	2.32	8.93
150	1	99.0	2.38	9.14

within the channel. The maximal electric field is the field generated when the membrane acts solely as an insulating barrier. In this case, the maximal electric field is the transmembrane potential divided by the bilayer thickness. If this field is multiplied by the aqueous mobility of the permeant ion (22), the resultant velocity will be a measure of the maximal possible velocity for the ion in the membrane. These velocities range from 0.3 to 4.5 m/s for transmembrane potentials of 10 and 150 mV, respectively. These maximal velocities are clearly an order of magnitude larger than the observed velocities for the channels, so channel permeation is probably more complicated than simple aqueous diffusion. Of course, this hypothesis can only be tested with an accurate determination of the electric field within the channels. The velocity distribution observations do not determine the ion mobility in the channel, which would permit a direct comparison of the motion of the ion in aqueous solution and within the conducting channel.

The intrachannel velocities of the ions are experimentally observable parameters and, as such, can be used to determine other system parameters. Because the detailed velocities of ions within the channels have not been determined using electrochemical techniques, estimates of the motions of ions through channels utilize other parameters such as the transit frequency, the number of ions that pass through a single channel at a given transmembrane potential each second (23, 24). Because the motion through the channels is essentially a constant velocity motion, the transit frequency can be estimated from the observed velocity and the distance traveled during the

observation. For example, if the observed velocity carries the ion the entire width of the membrane, d , an ion transit frequency, v_t , is defined as

$$v_t = \frac{v}{d}$$

The transit frequencies are estimated and tabulated in Table I for a channel length of 2.6 nm. The transit frequencies range from 1.4×10^7 to 9.1×10^7 for applied potentials from 10 to 150 mV, respectively. The results are comparable to those obtained by Andersen and Procopio (23) for large transmembrane potentials. However, it is important to note that the actual distance covered at the observed velocity is not known with certainty. Shorter distances of steady velocity motion will produce a higher transit frequency. At the same time, however, a delay time near the channel mouth while the ion loses some waters of hydration may significantly reduce the net transit frequency. The experiments detect only motions in a region where the ion moves with a constant, directed velocity.

Discussion

Laser Doppler velocimetry permits observation of a velocity distribution for Tl^+ ions within the gramicidin channel. The limited velocity range observed for a given transmembrane potential indicates that the ion probably moves through the channel at a constant velocity. The instrument is ideal for such measurements because it monitors the motions of a large number of ions moving in the same direction in a limited volume of space. Ions in solution or in the interfacial region undergo a general direction motion as well as other velocity and directional variations. Doppler spectra from such ions cannot produce the constructive interference necessary for observable scattering. The technique has the ability to focus only on those ions that are located within the membrane channels.

Techniques that increase scattering amplitude can be used to increase the intensity of the Doppler-scattered signal. For example, replacement of the HeNe laser with an argon-ion laser of shorter wavelength will produce approximately a threefold increase in the scattering amplitude. Such techniques may make it possible to detect scattering from smaller ions in the channels (e.g., K^+ or Na^+). However, the ability of the system to detect only scattering from Tl^+ ions constitutes an advantage in some cases. The total number of ions in a channel each second can be estimated via electrochemical measurements. Because the number of these ions that are Tl^+ can be determined using laser Doppler velocimetry, it is possible to determine the fraction of current carried by each ion in studies with mixed univalent ions.

Because velocities within the channels are the fundamental kinetic parameters, such studies to generate the velocity distribution for these ions

makes it possible to establish the best kinetic mechanism for the permeation of an ion through the channel and the kinetic parameters for this mechanism. Such detailed information can be obtained for more complicated ion-specific channels as well. In each case, the experiments provide detailed new information on the permeation of ions through the channels under the influence of an applied transmembrane potential.

Acknowledgment

The support of the office of Naval Research (Grant 1487K0301) is gratefully acknowledged.

References

1. Lauger, P. *Biochim. Biophys. Acta* **1973**, *311*, 423–441.
2. Finkelstein, A.; Andersen, O. S. *J. Membr. Biol.* **1981**, *59*, 155–171.
3. Sandblom, J.; Eisenman, G.; Neher, E. *J. Membr. Biol.* **1977**, *31*, 383–417.
4. Sandblom, J.; Eisenman, G.; Neher, E. In *Metal Ligand Interactions in Organic and Biochemistry*; Pullman, B., Ed.; Reidel: Dordrecht, Netherlands, 1977.
5. Parlin, R.; Eyring, H. In *Ion Transport in Membranes*; Clarke, H. T., Ed.; Wiley: New York, 1954.
6. Starzak, M. E. *The Physical Chemistry of Membranes*; Academic: Orlando, FL, 1984; pp 230–234.
7. Helfrich, P.; Jordan, P. *Biophys. J.* **1990**, *57*, 1075–1084.
8. Lauger, P. *Biochim. Biophys. Acta* **1976**, *455*, 493–509.
9. Turano, B.; Chen, I.; Busath, D. *Biophys. J.* **1989**, *55*, 503a.
10. Rosenberg, P. A.; Finkelstein, A. *J. Gen. Physiol.* **1978**, *72*, 327–335.
11. Sigworth, F. J. *Biophys. J.* **1985**, *47*, 709–720.
12. Heinemann, S. H.; Sigworth, F. J. *Biophys. J.* **1988**, *54*, 757–764.
13. Heinemann, S. H.; Sigworth, F. J. *Biophys. J.* **1990**, *57*, 499–514.
14. Bamberg, E.; Lauger, P. *J. Membr. Biol.* **1977**, *35*, 351–376.
15. Andersen, O. S. In *Renal Function*; Giebisch, G.; Purcell, E., Eds.; Independent Publishing Group: Port Washington, NY, 1977.
16. Neher, E. *Biochim. Biophys. Acta* **1975**, *401*, 540–544.
17. Drain, L. E. *The Laser Doppler Technique*; Wiley: Chichester, England, 1980; pp 85–118.
18. Haas, D.; Ware, B. R. *Anal. Biochem.* **1976**, *70*, 506–525.
19. Mohan, R.; Steiner, R.; Kaufmann, R. *Anal. Biochem.* **1976**, *70*, 506–525.
20. Uzgiris, E. E. *Rev. Sci. Instrum.* **1974**, *45*, 74–80.
21. Byrne, D.; Earnshaw, J. C. *J. Phys. D* **1979**, *12*, 1145–1157.
22. Robinson, R. A.; Stokes, R. H. *Electrolytic Solutions*; Butterworth: London, 1959; p 463.
23. Andersen, O. S.; Procopio, J. *Acta Physiol. Scand. Suppl.* **1980**, *481*, 27–35.
24. Andersen, O. S. *Annu. Rev. Physiol.* **1984**, *46*, 531–548.

RECEIVED for review March 14, 1991. ACCEPTED revised manuscript November 17, 1992.

Determination of Potassium- and Sodium-Channel Relaxation Times in Squid Nerve Fibers from Membrane Admittance Analysis

Harvey M. Fishman¹ and H. Richard Leuchtag²

¹Department of Physiology and Biophysics, University of Texas Medical Branch, Galveston, TX 77555-0641

²Department of Biology, Texas Southern University, Houston, TX 77004

Complex admittances in the 12.5–5000-Hz frequency range were acquired rapidly (80 ms) and at various times after step voltage clamps of squid giant axons. In a K⁺-conducting membrane (Na⁺ conduction blocked) at 12.5 °C, admittances were in a steady state 100 ms after steps, whereas in a Na⁺-conducting membrane (K⁺ conduction blocked) at 8 °C, admittances were time-invariant in the interval from 20 ms to 1 s after step changes. Admittances determined in the –65- to 0-mV voltage range were fitted by an admittance model to obtain conduction relaxation times for K⁺ and for Na⁺ as a function of voltage. Evaluation of macroscopic conduction in membranes via rapid admittance determinations provides a direct linear analysis that relates to linear theory and to Markovian models of single-channel conduction processes.

CONDUCTION OF IMPULSES along single giant nerve fibers of the squid is powered by two energy sources: a potassium ion gradient that maintains the membrane in an excitable (resting) state, with the axon interior negative (about –65 mV), and a sodium ion gradient that, when Na⁺ conduction is triggered, transiently changes the polarity of the axon interior to a positive value and thereby generates an electrical pulse—the action potential (1). The

0065-2393/94/0235-0415 \$08.00/0
© 1994 American Chemical Society

ion flows are controlled by two ion-conducting systems in the membrane: the K system and the Na system. The conductance of the Na system has a remarkably steep dependence on voltage over a range of voltages just above the resting potential, and depolarization of the membrane triggers the onset of the action potential by allowing Na^+ to flow into the axon.

The ion-conducting systems are based on two specialized macromolecules, the K channel (2) and the Na channel (3), embedded in a relatively inert phospholipid bilayer. These channels differ in ion selectivity, kinetics, and pharmacological sensitivities. However, both channels have at least two states, one conducting and the other nonconducting, and undergo stochastic transitions between states, the probabilities of which depend on membrane voltage (present and recent past) and temperature. In cells that allow direct access to the plasma membrane, unitary currents measured by micropatch techniques reflect transitions to a conducting state (openings) and transitions to a nonconducting state (closings) (4). The smooth currents measured by standard (nonmicropatch) methods represent sums of many unitary currents (5).

In microkinetic analyses of ion conduction through these single channels, transitions between channel nonconducting and conducting states are usually assumed to be described by a Markovian process. Under this assumption a comparable macrokinetic description of ion-channel-conduction relaxation times is available directly from a population of identical (single) channels. This analysis is accomplished by fitting a linear model of membrane driving-point functions (complex impedance or admittance) to low-frequency (1–5000 Hz) admittance determinations made in a steady state during voltage steps (clamps) of the membrane potential. With the advent of methods for rapid determination of the “small-signal” admittance of membranes (6–9), a direct linear analysis of ion conduction in membranes became a viable alternative (8, 10, 11) to conventional voltage clamp analysis, which was shown recently to yield results that are not equivalent to a linear analysis (12).

An expression for the complex admittance, $Y(jf)$, of an axon membrane is obtained by linearizing the Hodgkin–Huxley (HH) equations (1) and by applying a Laplace transformation (13, 14). The membrane admittance is then given by the general expression

$$Y(jf) = j2\pi fC + g_i + \sum \frac{g_p}{(1 + j2\pi f\tau_p)} \quad (1)$$

where $j = \sqrt{-1}$, f is frequency, C is capacitance, g_i is a frequency-independent ion conductance, and the $g_p(1 + j2\pi f\tau_p)^{-1}$ terms are the frequency-domain counterparts of time-domain relaxations of the ion conductances associated with activation and inactivation kinetics of the specific type of ion channel being described.

Description of ion-channel kinetics via admittance analysis provides a framework within which linear kinetic models can be compared to macroscopic data (from a population of channels) in a membrane. Analysis of conduction via driving-point-function determinations also provides proper data (from a true linear analysis) for comparison with the relaxation times obtained from microscopic data from one or a small number of channels in a membrane patch isolated by a micropipette (4). In Markov modeling, the open- and closed-time distributions are fitted to sums of exponential functions (15).

Materials and Methods

Preparation and Solutions. Giant axons from the hindmost stellar nerve of squid, *Loligo pealei*, were used in these experiments. Conventional internal axial-electrode techniques, as described previously (10), were implemented. Axons were placed in a cooled, flowing external artificial seawater (ASW) composed of 430-mM NaCl, 10-mM CaCl₂, 50-mM MgCl₂, 20-mM sucrose, and 5-mM tris(hydroxymethyl)aminomethane hydrochloride buffered to pH 7.4 at 22 °C. To study K⁺ conduction, intact axons (not internally perfused) were used and 1-μM tetrodotoxin (TTX) was added to the ASW to eliminate Na⁺ conduction. For studies of Na⁺ conduction, the ASW contained 50% of the Na⁺ listed and the remaining 50% was replaced with tetramethylammonium ion. The purpose of the reduction in Na⁺ concentration was to facilitate spatial control of the membrane potential. The axons in Na⁺ experiments were internally perfused with a solution composed of 100-mM potassium glutamate, 200-mM cesium glutamate, 40-mM CsF, 400-mM sucrose, and 5-mM TrisCl buffered to pH 7.4 at 22 °C. In addition, 1-mM 3,4-diaminopyridine was added to the perfusate to assure blockage of K⁺ conduction.

Data Analysis. Complex admittance determinations were fitted by an admittance function (13, 14, 16) based on the linearized HH equations (1). Admittance measurements were made under steady-state conditions (see Figures 2 and 4). Series resistance (R_s), the access resistance between the two voltage electrodes and up to the inner and outer surfaces of the axon membrane was not removed from measurements. Instead R_s was included and determined in the fit of the steady-state admittance model to the data. The measured complex admittance, therefore, is

$$Y(jf) = \frac{1}{R_s + [1/Y_m(jf)]} \quad (2)$$

The membrane admittance, $Y_m(jf)$, due to capacitance, leakage, and K^+ and Na^+ conduction, was modeled by

$$Y_m(jf) = (j2\pi f)^\alpha C_m + g_L + Y_K(jf) + Y_{Na}(jf) \quad (3)$$

where the admittance of the potassium system is

$$Y_K(jf) = g_{K\infty} + \frac{g_n}{1 + j2\pi\tau_n} \quad (4)$$

and the admittance of the sodium system is

$$Y_{Na}(jf) = g_{Na\infty} + \frac{g_m}{1 + j2\pi\tau_m} + \frac{g_h}{1 + j2\pi\tau_h} \quad (5)$$

C_m is membrane capacitance, α is a number less than 1 that reflects the constant phase angle character of C_m (17), g_L is the leakage conductance, and $g_{K\infty}$ and $g_{Na\infty}$ are the chord conductances of the respective K^+ and Na^+ systems. The g_n term reflects the kinetic component (activation) of the potassium conductance that relaxes with time constant τ_n and the g_m and g_h terms reflect the kinetic components (activation and inactivation, respectively) of the sodium conductance that relax with time constants τ_m and τ_h , respectively.

The FORTRAN program CPXFIT was used to fit eqs 2 and 3 to complex admittance data obtained on either a K^+ - or a Na^+ -conducting membrane. CPXFIT employed a grid search [GRIDLS (18)] method of least squares to explore the parameter space of the frequency function in these equations. The parameter values that yielded the best fit (minimum chi-square (χ^2) value) was obtained by minimizing the χ^2 of the vector difference (formed by the real and imaginary parts of the admittance) between the model and the data at each frequency. A useful feature of the program was a probe for a local minimum in the following way. Upon approach to a minimum χ^2 , the incremental step size of each parameter was reset to 10% of its value and fitting resumed. This perturbation in step size usually produced sufficient change in the parameter space to proceed to a deeper minimum χ^2 if the prior one was only a local minimum.

Rapid Complex Admittance Measurements. The voltage clamp system, chamber, and axial electrode techniques were described previously (10, 12). By superposing a repetitive small-amplitude (1-mV root mean square) Fourier-synthesized signal (8, 16, 19) onto large step clamps, a current response was acquired during voltage clamp pulses. Immediately

after a response was acquired, a 400-point complex admittance was computed (by software) in the 12.5–5000-Hz frequency range as the ratio of the Fourier-transformed current response to that of the small-amplitude voltage signal previously stored.

Figure 1 shows the timing of the acquisition of admittance data during the current response of a K^+ -conducting axon membrane to a rectangular voltage-clamp pulse. The horizontal dashed line with periodic vertical marks indicates the start of a continuously applied repetitive 1-mV signal. A large voltage step (30 mV), from -65 to -35 mV, was applied so that the response to the small synthesized signal occurred after a specified premeasurement interval (200 ms in this example) and so that one complete cycle of the signal (during the data acquisition window in Figure 1) began precisely after the premeasurement interval. The small amplitude of the synthesized signal was necessary to assure that the response that contained the admittance information reflected primarily the linear properties of the membrane (20).

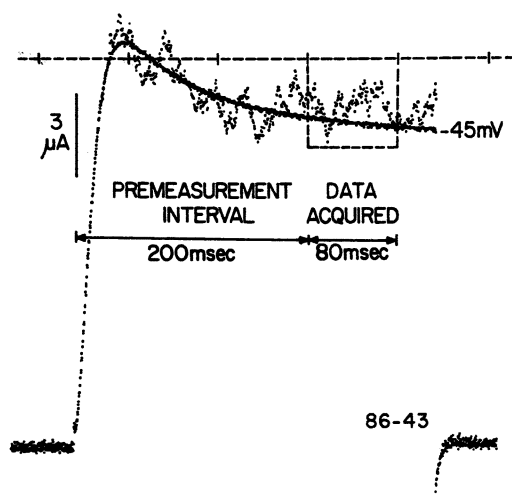


Figure 1. Illustration of the acquisition of a K^+ current response during a voltage-clamp step (not shown) and with a 1-mV (root mean square) Fourier-synthesized signal applied continuously and periodically, as indicated by the ticks on the dashed horizontal line. The K^+ current response to the small voltage perturbation was acquired after a "premeasurement interval" (200 ms) from the onset of a large voltage step from -65 to -35 mV. The Fourier transform of the current response together with the previously stored Fourier transform of the synthesized voltage signal enabled calculation of the complex admittance, $Y(jf)$ given by eqs 2, 3, and 4 with $Y_{Na}(jf) = 0$, during the time indicated by the dashed box (data acquired) after the step change in membrane voltage. (Reproduced with permission from reference 12. Copyright 1991).

The premeasurement interval allowed the membrane to respond to several cycles of the perturbation signal before the data were acquired. This condition enabled satisfaction of the additional requirement that data be obtained in a steady state so that the frequency structure of the admittance would not depend on the time of measurement and thus be interpretable in terms of linear time-invariant processes. In this respect, the frequency components introduced into the admittance function by the slowly decaying phase of the mean-current response in Figure 1 were also eliminated in the time domain. This elimination was accomplished by a coherence elimination method described previously (8) in which a pair of evoked responses was obtained with an inversion (polarity change) of the superposed synthesized signal between acquisition of the paired responses. Time-domain subtraction of the pair of responses eliminated the decaying phase in the mean current, which was common to both responses. The subtraction of paired responses also resulted in reinforcement of the admittance-containing current response because of the intentional inversion of the small voltage signal between response pairs.

Figure 2 illustrates acquisition intervals in a Na^+ -conducting axon membrane during a rectangular voltage-clamp pulse. The crosshatching on V_m indicates the superposed signal, and the crosshatching on I_m represents the current response, which contains the admittance information. The dark horizontal bars are data acquisition periods (80 ms in duration) after three premeasurement intervals of 20, 100, and 200 ms. Admittances at the same membrane potential were determined at these times after steps to establish that the membrane admittance was invariant and thus was in a steady state 20 ms after a step (see Figure 5).

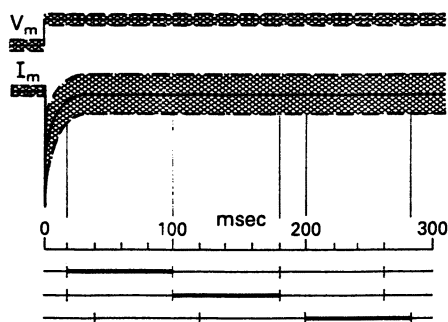


Figure 2. Representative drawing of the Na^+ current (I_m) response to a voltage-clamp step, shown as V_m , with superposed synthesized small perturbation (crosshatching). The acquisition of the current response to the small voltage perturbation, from which the admittance $Y(jf)$ was calculated from eqs 2, 3, and 5 with $Y_K(jf) = 0$, occurred in the three intervals (20–100, 100–180, and 200–280 ms) marked by heavy horizontal lines under the time scale.

Admittance data are plotted in the following two ways:

1. As magnitude,

$$|Y(jf)| = \sqrt{G^2(f) + B^2(f)}$$

and phase,

$$\angle Y(jf) = \arctan \frac{B(f)}{G(f)}$$

functions of frequency.

2. As the reciprocal admittance in the complex impedance plane [$X(f)$ versus $R(f)$],

$$Z(jf) = R(f) + jX(f) = \frac{1}{Y(jf)}$$

where $Y(jf) = G(f) + jB(f)$.

Results

K⁺ Conduction: Determination of $Y_K(jf)$ in a Steady State. Rapid admittance determinations in biological membranes can be used to characterize the linear response of membrane conduction (8-12, 16) provided that (1) the amplitude of the voltage stimulus elicits an insignificant nonlinear response (measured as higher harmonics) and (2) the admittance determination is invariant with time. With respect to provision 1, the amplitude of the voltage perturbation used to obtain admittance data at any given membrane potential in these experiments was chosen to be 1 mV (root mean square), which was shown previously (20) by harmonic analysis to yield essentially a linear response in the squid axon. To satisfy criterion 2, admittance data in a predominantly K⁺-conducting axon were acquired at 0.1 and at 0.5 s after step voltage clamps to membrane potentials ranging from -80 to 10 mV. These data are shown in Figure 3, in which the reciprocal of the admittance is plotted as 400 frequency points in the complex impedance plane. The data were obtained from the same axon at each of the two times after steps to the same indicated voltages. The impedance locus at the two times shows slight differences at membrane voltages greater than -60 mV. Nevertheless, best fits of eqs 2, 3, and 4 with $Y_{Na}(jf) = 0$ (solid curves) to these data yielded estimates of the relaxation time, τ_n , that were nearly identical (Table I). Comparable results were obtained in eight other axons. Thus, for a K⁺-conducting axon the membrane admittance appears to be

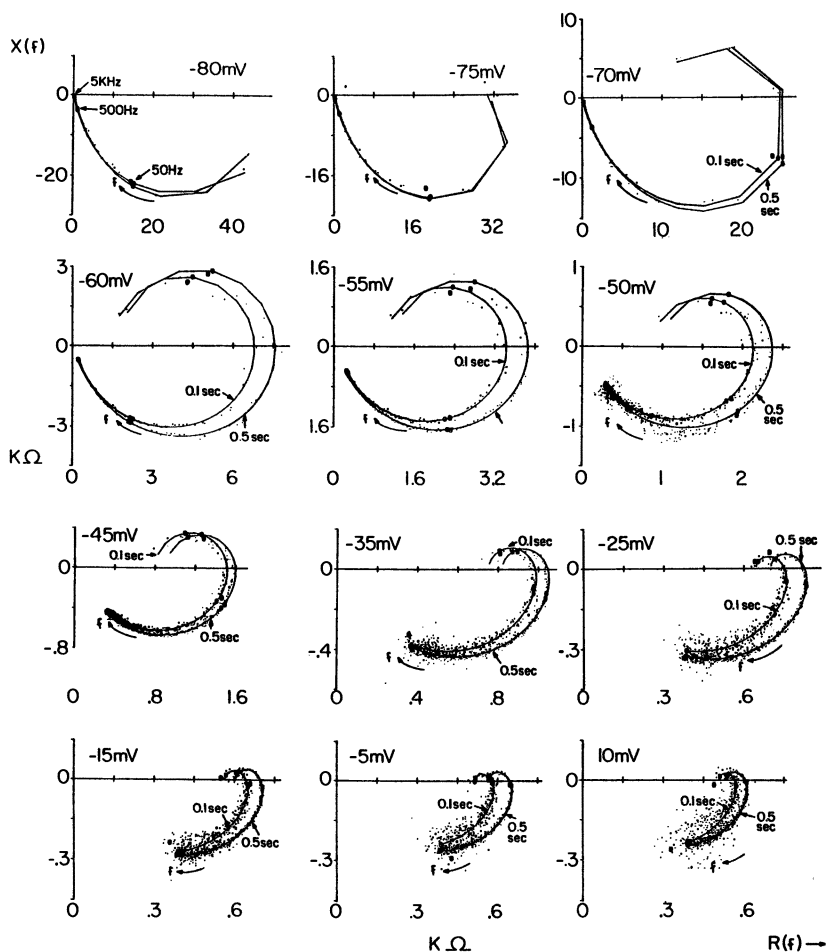


Figure 3. Admittance data from a K^+ -conducting membrane and curve fits (solid curves) of eqs 2, 3, and 4 with $Y_{Na}(jf) = 0$ plotted in the complex plane $[X(f)$ vs. $R(f)]$ as impedance $[Z(jf) = R(f) + jX(f) = Y^{-1}(jf)]$ loci (400 frequency points) over the 12.5–5000-Hz frequency range. These data were acquired rapidly as complex admittance data, as illustrated in Figure 1, at premeasurement intervals of 0.1 and 0.5 s after step voltage clamps to each of the indicated membrane potentials from a holding of -65 mV. The near superposition and similarity in shape of the two loci at 0.1 and 0.5 s, at each voltage, indicates that the admittance data reflect a steady state in this interval after step clamps. Axon 86-41 internally perfused with buffered KF and externally perfused in ASW + TTX at 12°C . The membrane area is 0.045 cm^2 .

Table I. Estimates of τ_n

V (mV)	0.1 s	0.5 s
-75	7.3	6.9
-70	10.1	9.8
-60	12.7	12.1
-55	11.0	10.9
-50	8.3	7.0
-45	5.0	5.3
-35	2.1	2.0
-25	1.0	1.2
-15	0.84	0.86
-5	0.62	0.71
10	0.86	0.67

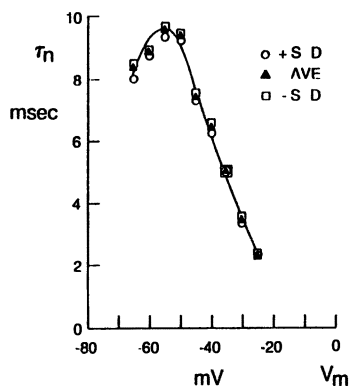
NOTE: All values are given in milliseconds and are taken from fits of the admittance data plotted as impedance loci in Figure 3 at the two premeasurement intervals (PMI) 0.1 and 0.5 s after step changes to membrane voltage, V .

sufficiently time-invariant in the interval between 0.1 and 0.5 s after a step to consider measurements in this interval to reflect a steady-state condition.

Evaluation of $\tau_n(V)$ from Admittance Analysis. Figure 4 shows a plot of the estimates of τ_n obtained from model curve fits to admittances acquired 200 ms after steps and obtained at nine membrane voltages spanning the range from -65 to -25 mV in a K^+ -conducting axon. The three data points plotted at each membrane voltage in Figure 4 were obtained in the following manner. At each membrane potential, eight separate admittance determinations were made. An averaged admittance was calculated by averaging the real and imaginary parts from the eight single determinations. At each frequency the real and imaginary parts (from each of the single admittance determinations that went into the average calculation) were used to calculate the standard deviation of the real and imaginary parts from the corresponding parts of the averaged admittance. Two new admittance functions were then generated by adding (and subtracting) one standard deviation to (from) the real and imaginary parts of the averaged admittance at each frequency. Best fits of eqs 2, 3, and 4 with $Y_{Na}(jf) = 0$ to these three admittance functions at different voltages yielded the values plotted as AVE, +SD, and -SD in Figure 4. Because the data fits involved all 400 points, the AVE points did not always fall between the -SD and +SD points.

The appearance of the admittance-derived $\tau_n(V)$ curve is qualitatively similar to that produced by a HH analysis of large step-voltage responses. However, a quantitative comparison (12) showed significant discrepancies between the values at corresponding potentials and variability in the discrep-

Figure 4. Estimates of the potassium-conductance relaxation time, τ_n , from fits of eqs 2, 3, and 4 with $Y_{Na} = 0$ to admittance determinations at various membrane voltages, similar to those shown in Figure 3. Filled triangles are from fits of the average (AVE) of the real and imaginary parts of eight separate, successive admittance determinations at each voltage. Open circles and squares are from fits of 1 standard deviation added to (+SD) or subtracted from (-SD) the real and imaginary parts of the AVE admittance. Intact axon 87-39 in ASW + TTX ($1 \mu\text{M}$) at 12.5°C .



ancies at different voltages. Thus the functional shapes of $\tau_n(V)$ obtained from the same axon by a HH analysis and by an admittance analysis are different.

Na⁺ Conduction: Determination of $Y_{Na}(jf)$ in a Steady State. Admittance data for a predominantly Na⁺-conducting membrane, acquired after steps to four membrane voltages in the -60- to 0-mV range, are plotted as magnitude and phase angle functions of frequency in Figure 5. At each voltage, data were obtained at the premeasurement intervals (20, 100, and 200 ms) shown in Figure 2 and described therein. The most obvious change in the admittance function with depolarization is the low-frequency asymptotic behavior of the phase function. At -60 mV (near the open-circuit rest potential) the low-frequency end of the phase function tends toward 0° , whereas at depolarized potentials (-40, -20, and 0 mV) the phase exceeds 180° , which is the manifestation of a steady-state negative conductance produced by the Na⁺-conducting system, as described previously (10). The 180° phase angle at depolarized voltages reverted to an angle that approached 0° , as at -60 mV, at all voltages after external application of $1\text{-}\mu\text{M}$ TTX. No significant differences were seen in these data acquired at different times after step changes to the same voltage, and thus the admittances determined 20 ms after steps to a Na⁺-conducting membrane reflected a steady-state condition.

Best Fits of Impedance Data with the $Y_{Na}(jf)$ Model. After the existence of a steady-state condition 20 ms after step clamps was established, we acquired a set of admittance data in the 5–2000-Hz frequency range in a Na⁺-conducting axon at a premeasurement interval of 100

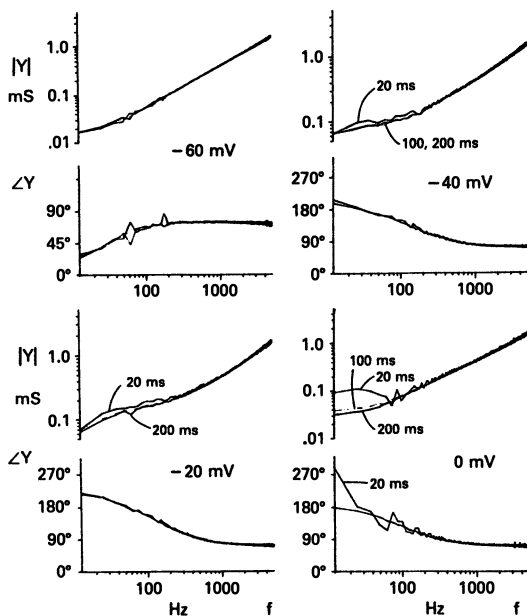


Figure 5. Admittance data plotted as magnitude and phase angle vs. frequency as determined at the three premeasurement intervals (20, 100, and 200 ms) shown in Figure 2 and at the indicated membrane voltages. The superposition of the admittance data at each voltage indicates that the admittance is time-invariant in the interval from 20 to 200 ms after step changes in membrane voltage. Axon 87-19 internally perfused with the perfusate described in the text and externally perfused with ASW at 8 °C.

ms. These data (frequency points) are plotted in the complex impedance plane in Figure 6 at eight membrane voltages ranging from -65 to 0 mV. The solid curves are loci of the best fits of the reciprocal of the admittance function defined by eqs 2, 3, and 5, with $Y_K(jf) = 0$. The striking feature of the loci in the complex impedance plane is the change from a right half-plane [$R(f) > 0$] locus at -65 mV (near rest potential) to a left half-plane [$R(f) < 0$] locus at depolarized membrane voltages. The impedance [$Z(jf) = R(f) + jX(f)$] behavior at depolarized voltages reflects a negative resistance [$R(f) < 0$] process that is characteristic of the Na^+ -conducting system of the axon membrane.

Evaluation of $\tau_m(V)$ and $\tau_h(V)$ from Admittance Analysis.

Application of the averaged admittance methodology to a Na^+ -conducting axon enabled us to obtain three data points at each membrane voltage. Figure 7 shows these data, which were obtained from best fits of eqs 2, 3, and 5 with

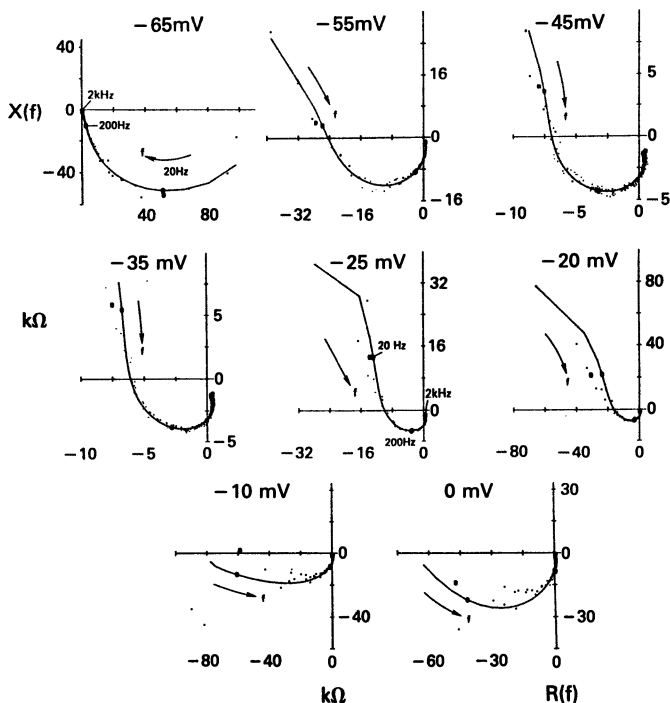


Figure 6. Admittance data from a Na^+ -conducting membrane and curve fits (solid curves) of eqs 2, 3, and 5 with $Y_K(jf) = 0$ plotted in the complex plane $[X(f) \text{ vs. } R(f)]$ as impedance loci (400 frequency points) over the frequency range 5 to 2000 Hz. Same axon and conditions as in Figure 5.

$Y_K(jf) = 0$. The dependence of τ_m and τ_h on κ at voltage has the appearance of time constants derived from a HH analysis. However, as with the K^+ -conducting system, a quantitative comparison indicated discrepancies in the estimates obtained from a HH analysis with respect to estimates obtained from an admittance analysis at all voltages (12).

Discussion

The complex admittance method described here allows data to be analyzed without reference to any particular model. This condition is particularly important at this time, when new data and new concepts are challenging previously accepted concepts. The elucidation of the primary structure of channel proteins (2, 3) has stimulated the development of a number of structurally oriented models (e.g., references 21 and 22). In addition, new physical and mathematical concepts have been brought to bear on the problem of channel gating in excitable membranes. These concepts include

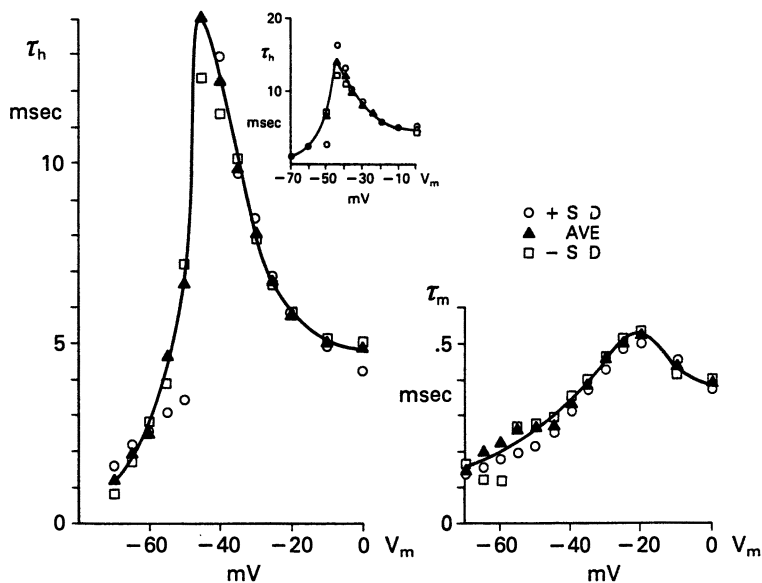


Figure 7. Estimates of the sodium-conductance activation relaxation time, τ_m , and inactivation relaxation time, τ_h , from fits of eqs 2, 3, and 5 $Y_k(jf) = 0$ to admittance determinations at various membrane voltages, similar to those shown in Figure 6. Filled triangles are from fits of the average (AVE) of the real and imaginary parts of eight separate, successive admittance determinations at each voltage. Open circles and squares are from fits of 1 standard deviation added to (+SD) or subtracted from (-SD) the real and imaginary parts of the AVE admittance. Axon 87-37 internally perfused with the perfusate described in text and externally perfused with ASW at 9 °C.

transitions between ferroelectric and superionically conducting states in Na channels (23, 24), fractal kinetics (25), and chaotic rather than stochastic models (26).

Acknowledgments

Work supported in part by ONR Grant N00014-90-J-1137 and by Texas Advanced Technology grant 004952011. H. R. Leuchtag thanks Texas Southern University for a sabbatical leave and the Materials Research Laboratory, Pennsylvania State University, for its hospitality.

References

1. Hodgkin, A. L.; Huxley, A. F. *J. Physiol.* **1952**, *115*, 111-222.
2. Takumi, T.; Ohkubo, H.; Nakanishi, S. *Science (Washington, D.C.)* **1988**, *242*, 1042-1045.

3. Noda, M.; Ikeda, T.; Suzuki, H.; Yakeshima, H.; Takahashi, T.; Kuno, M.; Numa, S. *Nature (London)* **1986**, *322*, 826–828.
4. Hamill, O. P.; Marty, A.; Neher, E.; Sakmann, B.; Sigworth, F. J. *Pflugers Arch.* **1981**, *391*, 85–100.
5. Sigworth, F. J.; Neher, E. *Nature (London)* **1980**, *287*, 447–449.
6. Husimi, Y.; Wada, A. *Rev. Sci Instrum.* **1976**, *47*, 213–219.
7. Poussart, D.; Ganguly, U. S. *Proc. IEEE* **1977**, *65*, 741–747.
8. Fishman, H. M.; Moore, L. E.; Poussart, D. In *The Biophysical Approach to Excitable Systems*; Adelman, W. J., Jr.; Goldman, D. E., Eds.; Plenum: New York, 1981; pp 65–95.
9. Kottra, G.; Fromter, E. *Pflugers Arch.* **1984**, *402*, 409–420.
10. Fishman, H. M.; Leuchtag, H. R.; Moore, L. E. *Biophys. J.* **1983**, *43*, 293–307.
11. Hayashi, H.; Fishman, H. M. *Biophys. J.* **1988**, *53*, 747–757.
12. Fishman, H. M.; Lipicky, R. J. *Biophys. Chem.* **1991**, *39*, 177–190.
13. Chandler, W. K.; FitzHugh, R.; Cole, K. S. *Biophys. J.* **1962**, *2*, 105–127.
14. Mauro, A.; Conti, F.; Dodge, F.; Schor, R. J. *Gen. Physiol.* **1970**, *55*, 497–523.
15. Colquhoun, D.; Hawkes, A. G. In *Single-Channel Recording*; Sakmann, B.; Neher, E., Eds.; Plenum: New York, 1983; pp 135–175.
16. Miyamoto, S.; Fishman, H. M. *Ferroelectrics* **1988**, *86*, 129–146.
17. Cole, K. S. *Membranes, Ions and Impulses*; University of California Press: Los Angeles, CA, 1972; pp 42–43.
18. Bevington, P. R. *Data Reduction and Error Analysis for the Physical Sciences*; McGraw-Hill: New York, 1969; pp 208–213.
19. Nakamura, H.; Husimi, Y.; Wada, A. *Jpn. J. Appl. Phys.* **1977**, *16*, 2301–2302.
20. Moore, L. E.; Fishman, H. M.; Poussart, D. J. *Membr. Biol.* **1980**, *54*, 157–164.
21. Guy, H. R.; Seetharamulu, P. *Proc. Natl. Acad. Sci. U.S.A.* **1986**, *83*, 508–512.
22. Kosower, E. M. *FEBS Lett.* **1985**, *182*, 234–242.
23. Leuchtag, H. R. *J. Physiol.* **1989**, *418*, 10P.
24. Leuchtag, H. R. *1990 International Symposium on Applications of Ferroelectrics*; IEEE: New York, 1991; pp 279–283.
25. Liebovitch, L. S.; Toth, T. I. *Ann. Biomed. Eng.* **1990**, *18*, 177–194.
26. Liebovitch, L. S.; Toth, T. I. *J. Theor. Biol.* **1991**, *148*, 243–267.

RECEIVED for review January 29, 1991. ACCEPTED revised manuscript August 4, 1992.

Electrochemical Model of Voltage-Gated Channels

Martin Blank

Department of Physiology and Cellular Biophysics, Columbia University,
630 West 168th Street, New York, NY 10032

An electrochemical model of protein aggregation has been developed based on changes in surface free energy that accompany changes in molecular surface area and charge density. The surface free energy model quantitatively predicts the disaggregation of hemoglobin tetramers into dimers at alkaline pHs, and also accounts for the energetics of the conformational changes in the reactions of hemoglobin with ligands (e.g., the Bohr effects, the Hill coefficient). Because membrane channels are oligomeric proteins, the model has been applied to channel opening and closing. Many physical properties appear to be direct consequences of this model, including the observed variation of the ion selectivity of voltage-gated channels with gating current and the cooling that accompanies channel opening.

Electrochemical Perspective

The two main threads of recent research on ion channels—investigations of channel structure and channel function—are interrelated in that research in each area illuminates both. Biologists realize that an understanding of function must be based on structure, but it has been difficult to extract clues relevant to function from the very detailed information about amino acid sequences and their arrangements in the channel proteins. This is where the concepts of electrochemistry have proven useful. Consideration of average properties and large populations of channels, rather than specific groups in an individual channel (the focus of much current research), has made it possible

0065-2393/94/0235-0429 \$08.00/0
© 1994 American Chemical Society

to treat channels as charged surfaces of proteins and to develop a macroscopic description of channel function. This approach has provided insights into a number of important problems. In this chapter, we will summarize our research on the energetics and kinetics of channel function and show how the electrochemical model deals with two specific problems: ion specificity and thermal responses that accompany channel opening and closing.

Aggregated Protein Structures

Many membrane processes in cells (e.g., ion pumping, sensory transduction, impulse conduction, energy transduction) involve charge movement across integral protein structures called channels. Channels are composed of subunits that have specialized hydrophilic and hydrophobic regions organized in a cylindrical geometry. There are many structural similarities in groups of protein assemblies with different physiological properties (1), so specific biological properties must be achieved through relatively small variations of physical properties such as the surface charge (2). The opening and closing of all channels requires changes in protein–protein contacts, more accurately changes in the area of protein–water interface, so the gating process depends upon the same physical principles that govern aggregation and disaggregation in oligomeric proteins. These principles are well known.

In line with our knowledge of mass action, proteins of many sizes, shapes, and degrees of aggregation tend to aggregate as the monomer concentration increases. Aggregation decreases as the pH is further away from the isoelectric point and the charge on the molecule increases. Surface charge plays an important role because the surface free energy of dissolved proteins is low and the electrostatic contribution is relatively large (3).

Protein aggregation reactions are generally described as entropy-driven because they proceed spontaneously with the evolution of heat; that is, a positive change of enthalpy (4). Because the net free energy change is negative for a spontaneous process, a large positive entropy change must accompany this reaction, most likely from the release of adsorbed water molecules when the oligomers associate. *The accepted description is correct but incomplete.* The description does not indicate why aggregation occurs only in particular ranges of pH. To understand the pH dependence the aggregation process should be considered in terms of *surface* free energy, which varies with the surface charge. Because aggregation does not involve molecular rearrangements within the subunits, but rather interactions between the subunit surfaces, we can approximate the total free energy change in these processes by the surface free energy. The loss of adsorbed waters upon oligomer aggregation is equivalent to the loss of interfacial area, and disaggregation involves the formation of additional protein–water interface.

Surface Free Energy Changes in Protein Aggregation

The surface free energy, F_s , of the protein can be calculated in terms of two parameters: A , the area of the molecule in contact with the solution, and σ , the surface charge density (σ = charge per A):

$$F_s = (f_0 - \pi) A \quad (1)$$

where A is the molar area of the protein surface, f_0 is the free energy per unit area of an uncharged protein surface, and π is the surface pressure due to the charged surface layer, where $\pi < f_0$. At low surface charge density (below 10 charges per 100 nm²), $\pi = k\sigma^2$, where $k = 0.016$ if σ is in charges per nanometer squared and π is in ergs per centimeter squared. Therefore,

$$F_s = (f_0 - k\sigma^2) A \quad (2)$$

and a small change in F_s ,

$$\Delta F_s = (f_0 - k\sigma^2) \Delta A - 2k\sigma A \Delta\sigma \quad (3)$$

From the positive ΔA term in eq 3, it appears that increases in area lead to a positive ΔF_s , so this process will not occur spontaneously. The unfavorable free energy that accompanies an increase in area can be overcome by an increase in σ (i.e., $\Delta\sigma > 0$), which contributes directly to a negative ΔF_s and also contributes indirectly by decreasing the magnitude of the ΔA term. This principle is in action in the disaggregation of hemoglobin, which involves an energetically unfavorable increase in surface area. However, as the hemoglobin tetramer becomes positively or negatively charged, there is a compensatory decrease in surface free energy when the charge is spread over a greater area, and this decrease leads to disaggregation into dimers.

In general, processes involve a change of both charge density (due to a change of pH or the binding of an ion) and area (due to changes in aggregation). Such changes alter the free energy minimum and shift the disaggregation constant, K_D :

$$\Delta \ln K_D = \frac{\Delta F_s}{RT} \quad (4)$$

where R is the universal gas constant and T is the absolute temperature. Substituting for ΔF_s from eq 3, we can obtain an expression relating $\Delta \ln K_D$ to the change in surface charge density.

Hemoglobin Disaggregation

To test the quantitative predictions of the model, we measured the disaggregation of the hemoglobin tetramer by the increase in osmotic pressure with pH (5). When the pressure is compared to that observed in solutions of bovine serum albumin (BSA; a protein of comparable molecular weight that does not disaggregate), we can ascribe the difference in pressure to disaggregation. In the titration of both protein solutions, the minimum pressure occurs at the isoelectric point (IEP), which is 6.82 ± 0.06 for hemoglobin at 25.0°C .

The osmotic pressures obtained during alkaline titration are shown in Figure 1 for hemoglobin and BSA as functions of the molecular charge. The BSA curve represents the osmotic pressure of a charged biopolymer in a complex Gibbs–Donnan equilibrium. Because the hemoglobin solution should give the same osmotic pressure as BSA at the same molar concentration and biopolymer charge, the higher pressure is due to the increase in concentration caused by disaggregation. The difference between the two curves (the dashed curve) indicates that disaggregation occurs at all degrees of charge, and that above 25 charges per molecule or $\text{pH} = 9.5$, disaggregation goes beyond the dimer to the monomer.

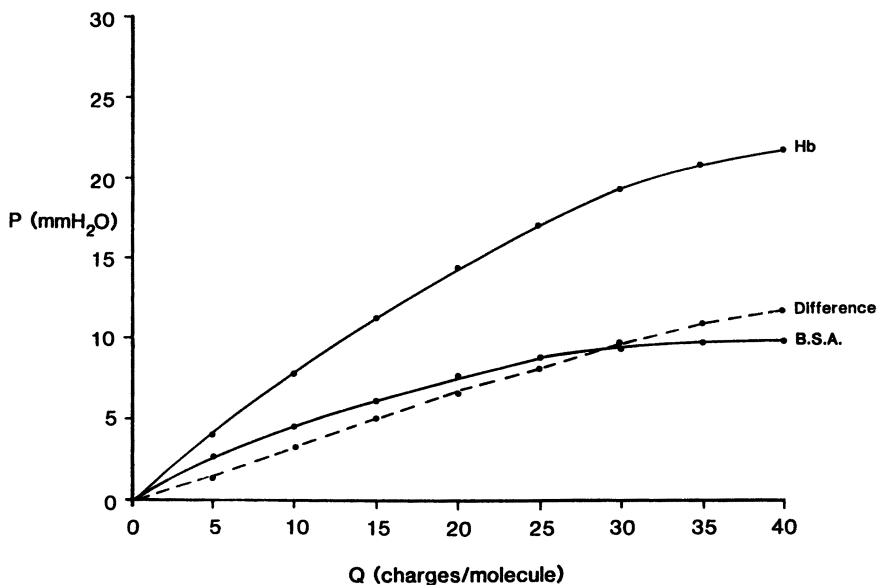


Figure 1. The colloid osmotic pressure (in millimeters of water) as a function of the charges per molecule in the alkaline region of hemoglobin (Hb) and BSA. The difference between the two protein solutions at comparable charges per molecule is the dashed line labeled difference. (Reproduced with permission from reference 5. Copyright 1987.)

The excess concentration of osmotically active molecules, C , can be calculated from the dashed curve. The ratio of C to the initial concentration, C_0 , is a direct measure of the degree of disaggregation and can be used to calculate the equilibrium constant, K_D :

$$K_D = \frac{4M(C/C_0)^2}{(1 - C/C_0)}$$

where M is the molar concentration of dissolved hemoglobin tetramer. A plot of $\log K_D$ versus the molecular charge, Q , is given in Figure 2. The slope appears to be constant below 10 charges per molecule, and extrapolation to the IEP determines $K_D = 2.0 \times 10^{-7}$ mol/L at zero charge. Ackers (6)

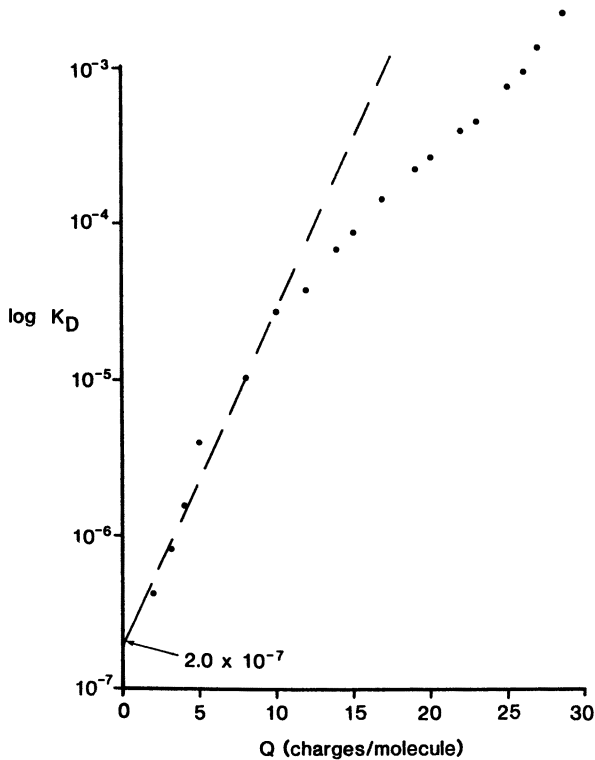


Figure 2. A semilog plot of the disaggregation equilibrium constant, K_D , as a function of the charge on the molecule, Q . The slope of the initial part of the curve is 0.21 per charges per molecule and the intercept is 2.0×10^{-7} (Reproduced with permission from reference 5. Copyright 1987.)

used somewhat different conditions to find a value of 1.08×10^{-6} mol/L at pH 7.4. At pH 7.4, our value is $K_D = 3.0 \times 10^{-6}$ mol/L. In addition to determining the pHs at which tetramers disaggregate into dimers, the calculations agree with observations in regard to the effects of oxygenation and ionic strength (3).

The aggregation of sickle hemoglobin, which differs from normal hemoglobin by only one amino acid on the beta chain, proceeds markedly under certain conditions. If we assume that aggregation beyond the tetramer stage can also occur in normal hemoglobin, it is possible to explain the unusually large increase in viscosity that occurs in hemoglobin solutions at high concentration (7). Assuming that hemoglobin associates isodesmically, we can calculate the concentrations of the different oligomeric species and their contributions to the viscosity. The calculations show an increasing viscosity with concentration and also suggest a change from flexible chain to rigid rod as a result of head-to-tail interactions in the same chain when it becomes longer.

Conformational Changes in Hemoglobin Reactions

Conformational changes are frequently invoked to describe biochemical mechanisms qualitatively. With the surface free energy model, it is possible to evaluate the energetic consequences of conformational changes in proteins. We have done this for the ligand-binding reactions of hemoglobin (8).

The oxygen binding curve of hemoglobin is sigmoidal in shape, which indicates a change in the affinity with degree of oxygenation. The curve also shifts with pH (the Bohr effect). Both properties are due to the conformational changes in the hemoglobin molecule upon oxygenation. We can estimate the free energy of these changes along the lines indicated in Figure 3, which is a diagram of the changes that occur in hemoglobin as a result of combination with oxygen. The results of these calculations, shown in Figures 4 and 5, indicate that the oxygen-binding constant of hemoglobin varies with pH, as in the acid and alkaline (physiological) Bohr effects, and also with the ionic strength. In Figure 4, the binding constant is calculated to be a maximum below the IEP, as has been observed.

Because the free energy of the hemoglobin system varies as a result of both the subunit aggregation reactions and the combination with ligands, the two processes should be linked; that is, oxygenation should affect aggregation and vice versa. This linking is one of the characteristics of hemoglobin reactions, and it is possible to understand it quantitatively with the aid of the surface free energy model (3).

The surface free energy model also suggests a simple physical meaning for the Hill coefficient, which is the empirical constant used to describe

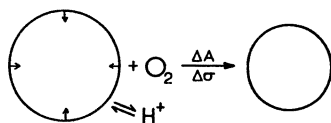


Figure 3. A model for calculating the energetics of the conformational change of hemoglobin when it reacts with oxygen or another ligand. The decrease in area (ΔA) is due to the relative movement of the chains of the hemoglobin tetramer toward each other. The change in surface charge density ($\Delta\sigma$) is due to the changes in ionization of the histidine groups that are affected by the movements of the chains. The magnitudes of these two changes have been estimated from published X-ray and titration data. (Reproduced with permission from reference 8. Copyright 1975.)

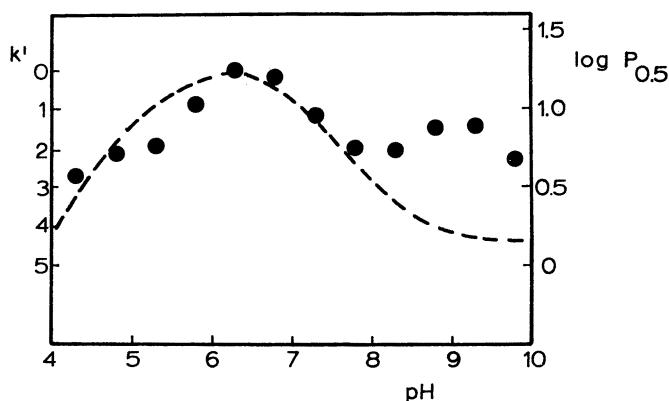


Figure 4. The calculated values of the equilibrium constant (\bullet) in units of $k' = \Delta F_s / RT$, the surface free energy change due to the conformational change, superimposed upon the dashed curve of the Bohr effect in units of $\log P_{0.5}$, the oxygen pressure for half saturation of hemoglobin. The sets of values are made to coincide at pH 6.3 and are in the same units over the same pH range. (Reproduced with permission from reference 8. Copyright 1975.)

cooperative oxygen binding. Ordinary binding is usually described by a simple equation that is based on a balance between the rates of binding and release. For a ligand at concentration C that reacts with a fraction y of available binding sites, the equilibrium binding constant

$$K = \frac{y}{(1-y)} \frac{1}{C} \quad (5)$$

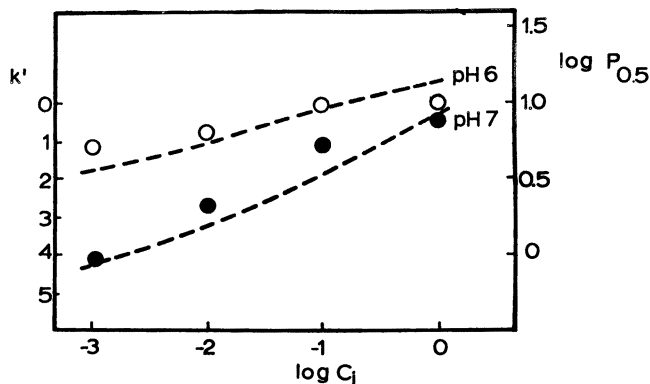


Figure 5. The calculated values of the equilibrium constant at pH 6.3 (○) and at pH 7.3 (●) in units of K' , the surface free energy change due to the conformational change, as a function of the logarithm of the ionic strength. The measured values at pH 6 and pH 7 are shown as dashed lines in units of $\log P_{0.5}$. The calculated and observed values are made to coincide at pH 6.3 and $\log C_1 = -1$. (Reproduced with permission from reference 8. Copyright 1975.)

where $y/(1 - y)$ is the ratio of reacted to unreacted sites. The affinity is related to ΔG^0 , the free energy change per mole due to the binding reaction:

$$K = \exp - \frac{\Delta G^0}{RT} \quad (6)$$

Additional changes in free energy (ΔG_s) that occur as a result of the conformational changes of hemoglobin cause a displacement of the affinity to a new value:

$$K' = \exp - \frac{\Delta G^0 + \Delta G_s(y)}{RT}$$

$$K' = K \exp - \frac{\Delta G_s(y)}{RT} \quad (7)$$

When ΔG_s is negative, the affinity increases, and because ΔG_s varies with y , there is a gradual change of affinity during a reaction. In the Hill equation for the combination of oxygen with hemoglobin, the affinity is assumed to remain constant at a new value, K_e , and the increase in binding is accomplished by raising the concentration to the power n , where $n > 1$ for $\Delta G_s < 0$:

$$K_e = \frac{y}{(1 - y)} \frac{1}{C^n} \quad (8)$$

When $n > 1$ the interaction is termed cooperative.

Equations 5, 7, and 8 provide two equivalent expressions for the effect of a cooperative process on the fraction of sites bound. In eq 9, the extra free energy change is handled empirically with the exponent n , and in eq 10 the extra free energy change is included explicitly:

$$\Delta G^0 + RT \ln \frac{y}{(1-y)} - nRT \ln C = 0 \quad (9)$$

$$\Delta G^0 + \Delta G_s(y) + RT \ln \frac{y}{(1-y)} - RT \ln C = 0 \quad (10)$$

If we differentiate the two equations with respect to $\ln C$ and subtract one from the other,

$$n - 1 = - \frac{d \Delta G_s(y)}{RT d \ln C} \quad (11)$$

$(n - 1)$ has the form of a surface excess in the Gibbs equation and can be interpreted simply as a higher concentration of ligand that results from the extra free energy change. A plot of $(n - 1)$ versus C has the same form as graphs of surface excess in a classical interfacial system (9). Note that n is not constant but varies with y and is equal to unity at the extremes of the range, $y = 0$ and $y = 1$, as has been observed for hemoglobin oxygenation.

The agreement between our predictions and the measurements shows that surface free energy changes are a good measure of the total free energy change that occurs in hemoglobin reactions. The surface free energy model has reasonable predictive value and appears to be particularly useful to describe the energetics of aggregation equilibria and conformational changes.

Channel-Gating Processes

Membrane channels are made up of protein subunits in a cylindrical array, so the opening of voltage-gated channels can be thought of as the partial disaggregation of oligomeric proteins triggered by changes in the surface charge density. Because the interactions between the parts of the channel proteins exposed to the aqueous phase are similar to those of the subunits of globular proteins in solution, we can assume that changes in the equilibrium constant can be estimated from the disaggregation of hemoglobin tetramers into dimers. The fraction of channels that are open, α , would be similar to the fraction of tetramers disaggregated based on the surface free energy change given in eq 3, except that the equilibrium would not involve an increase in the number of species.

The equilibrium constant for the channel-opening reaction is independent of the number of channels and can be written as

$$K_0 = \frac{\alpha}{1 - \alpha} \quad (12)$$

Solving for α ,

$$\alpha = \frac{K_0}{1 + K_0} \quad (13)$$

From Figure 2 we see that at zero charge $K \ll 1$, so α is essentially equal to K_0 . However, as the charge increases, K_0 and α increase and diverge. The variation of α as a function of the surface charge density is shown in Figure 6. The magnitude of α is very close to zero up to about 20 charges per 100 nm², and there is a relatively large increase in the range of 25–35 charges per 100 nm².

We do not know the charge on the channel proteins in the squid axon, but the overall sigmoid dependence of the fraction of open channels, α , on the charge density, σ , shown in Figure 6 is reminiscent of the fraction of sodium channels available in the steady-state squid axon as a function of the membrane potential (10). (The charge density is expected to change with the membrane potential.) We do know that the membrane has a much higher

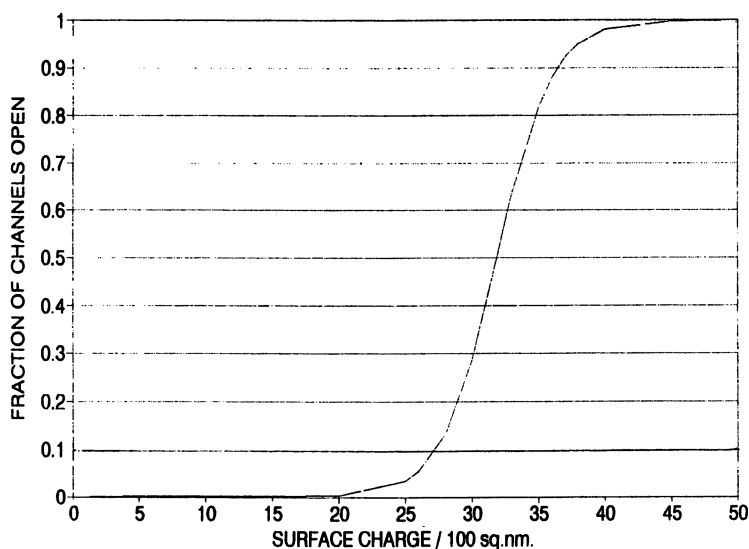


Figure 6. The fraction of oligomeric channels open as a function of the surface charge density (in charges per 100 nm²). The equilibrium constant for the channel-opening reaction is assumed to be equal to that of hemoglobin disaggregation, which is also a function of the charge.

negative charge on the outside (about 60 nm^{-2}) than on the inside (about 10 nm^{-2}). If the charge densities are uniform, we would expect the subunits of the channels to be disaggregated (i.e., open) on the outer surface, where the charge is high, and aggregated (i.e., closed) on the inner surface, where the charge is low. See Figure 7 (11). Depolarization would be expected to shift some negative gating charges from the outer to the inner surface and cause the channel to open when about 25 charges per nanometer squared are reached. (The outer surface would still have a high enough charge density to remain open.)

These better than 1 order of magnitude estimations of the properties of a voltage-gated ion channel (12) are in line with observations on squid axons in terms of (1) the steady-state distribution of charge; (2) the charge flow during depolarization; (3) the range of surface charge where opening occurs; (4) the cation selectivity of the open channel; and (5) the cation binding. Other observations on nerves, such as the increase in excitability with an increase in charge brought about by higher intracellular pH and membrane phosphorylation or the decrease in excitability brought about by the binding of multivalent (toxic) cations, can also be explained qualitatively in terms of this model.

Channel gating may arise from any mechanism that leads to changes in the surface charge; that is, the movement of mobile (e.g., gating) charges with changes in polarization, the binding of ligands, or charge movements associated with enzymatic [e.g., Na, K-adenosinetriphosphatase (ATPase)] reactions. The acetylcholine receptor, a ligand-gated channel that binds the neurotransmitter acetylcholine, can be considered in terms of the same channel-opening mechanism. Under normal conditions, the acetylcholine receptor is negatively charged and binds about 60 calcium ions. When acetylcholine binds to the receptor, $\sim 4-6$ of the calcium ions are released (13). A displacement of calcium ions from the receptor by acetylcholine ions could lead to an increase in the total negative charge on the protein and trigger the partial disaggregation (i.e., opening) of the receptor protein. The change in surface charge due to ion displacement could be the basis of channel opening and closing for ligand gating as well as voltage gating.

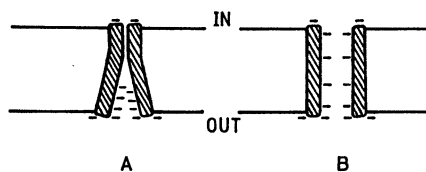


Figure 7. Model of a voltage-gated oligomeric channel in cross section. In the resting state (A), the asymmetric charge distribution causes the outer face to be open and the inner face to be closed. Upon depolarization (B), a shift of charge causes the inner face to open. (Reproduced with permission from reference 11. Copyright 1982.)

Voltage Gating and Channel Specificity

To study the effects of electrochemical properties on passive ion transport processes, we developed a model that focuses on ionic processes at membrane and channel surfaces (14). The surface compartment model (SCM) is based on a Helmholtz electrical double layer, where the enhanced concentration of counterions and the depletion of co-ions at charged surfaces is described by straight line gradients. Treatment of the electrical double layer as a compartment greatly simplifies the calculation of ion transport.

The set of nonlinear independent differential equations of the SCM is derived by application of the principles of conservation of mass and charge during current flow to the surface compartments, and application of the principles of chemical reaction kinetics to ion binding at the surfaces. In the equations, the fluxes are driven by electrochemical potential differences given by Nernst-Planck equations.

For the steady state, the SCM shows a tight relation between surface charge, membrane potential, and ionic flux that is useful to explain the interlinked changes that occur in these properties (14, 15). The recent finding by Richard and Miller (16) that channel properties are affected by ion gradients is an example of such coupling.

To study non-steady-state systems, we applied the SCM to the problem of excitation, where, based on the macroscopic concentrations of ions and electrical potentials, it is generally accepted that the ion fluxes do not follow the classic electrodiffusion equations. When the surface concentrations and surface potentials at the charged membrane surfaces are used, the ion fluxes are given by the same electrodiffusion equations that apply to ions in solution (14).

The voltage-gated channels of the SCM (described before) are based on a charge-dependent oligomer aggregation mechanism where gating currents trigger the opening of the channels. The dependence of channel opening on surface charge (Figure 6), approximated by three linear regions in the SCM program, has σ equal to the charge density on the inside surface of the membrane where the channel is constricted. The conductance is assumed to be constant at high and low σ , and directly proportional to σ in the intermediate range. During depolarization, the gating currents shift negative charge from the outer to the inner surface, which increases the charge and causes the channel to open. The conductances to sodium and potassium ions in each channel change from the steady-state values (a K-Na conductance ratio of 10:1) toward the values in free solution (a K-Na conductance ratio of 1.5:1).

Because the magnitude of σ depends on the degree of depolarization, the permeability increase is voltage-dependent. Also, when the inward sodium flux decreases and the membrane potential starts to return to resting conditions, the resultant shift causes the channel to close and the ion permeability

to decrease as in "inactivation". Inactivation can also occur when the charged groups on proteins react with ions as a result of changes in ionic species and concentrations in the electrical double-layer regions. This phenomenon has been observed in "inactivation" processes during voltage clamp; that is, channel closing due to ionic reactions that lead to reductions in surface charge (17). The qualitative features of the permeability changes that occur in excitable membranes during an action potential are therefore demonstrated by this mechanism.

The channels are assumed to be permeable to *both* sodium and potassium ions at all times. Despite this assumption, the channels show an apparent ion selectivity that depends on the gating current needed to open the channel. Figure 8 shows that a "sodium channel" results from rapid gating currents and a "potassium channel" results when the gating currents are much slower. The difference of over 1 order of magnitude in the gating currents of the sodium and potassium channels of excitable membranes predicted by the model is about the same magnitude as has been observed. A membrane with fast and slow channels gives currents observed during voltage clamp of squid axons and described by electrodiffusion equations. Note that the changes in Na channels exposed to batrachotoxin (18), as well as the recent electrophysiological studies of different forms of the K channel (19), show a variation of ion selectivity with rate of opening as suggested by the SCM results.

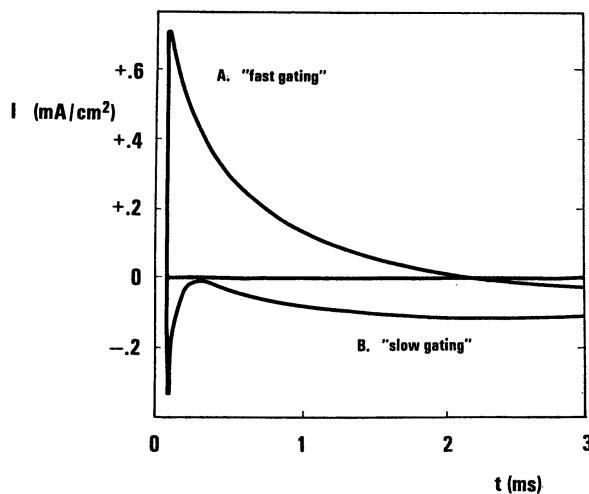


Figure 8. The ionic current (in milliamperes per centimeter squared) across a voltage-gated channel as a function of time (in milliseconds) for different gating currents. The fast gating curve has a conductance that is 15 times greater than the slow gating, and this difference leads to a change in the direction of the ionic current. (Reproduced with permission from reference 12. Copyright 1984.)

The effects of oscillating electric fields on ion accumulation processes are also explained by SCM calculations (20). The oscillations lead to periodic changes in the ionic concentrations that are functions of the frequency, but the percentage change is greatest in those concentrations with the lowest steady-state values. In particular, sodium on the inner surface and potassium on the outer surface show maximal changes at about 100–200 Hz. These two ionic concentrations normally control the activity of the Na, K-ATPase of cell membranes, and increases could stimulate the enzyme.

We recently showed that low-frequency alternating currents (ac) through Na, K-ATPase vesicle suspensions change enzyme activity (21). The ac signals decrease adenosine 5'-triphosphate (ATP) splitting by the normal enzyme, with the maximum effect at about 100 Hz, and increase the enzyme activity when the activity is lowered in different ways, including the introduction of ouabain. Both inhibition and activation by ac signals can be explained by variations in ion activation (22, 23). The frequency dependence is related to the ion mobilities and reaction rate constants in the electrical double layers (20).

In summary, a fuller understanding of the physicochemical processes at membrane and channel surfaces has shown the following:

1. Steady-state properties are linked through the surface charge.
2. Ionic currents in channels follow electrodiffusion theory.
3. Channel selectivity is controlled by the kinetics of channel opening.
4. Oscillating electric fields cause ion concentration changes that can change ion pump activation.

Energetics of Channel Opening and Closing

Because the processes of excitation are largely dissipative (i.e., the flow of ions down existing electrochemical gradients and the use of chemical bond energy to restore the ionic gradients), a net evolution of heat would be expected. This evolution is observed, but measurements of the heat associated with excitation of nerve fibers (24) or electric organs (25) indicate three distinct phases in the heat flow during an action potential:

1. An initial warming phase that is short-lived and small.
2. A longer cooling phase that is comparable in amplitude.
3. A still longer warming phase that has the largest amplitude and most probably is associated with recovery mechanisms.

The net heat evolved is actually small in comparison with the initial heating and cooling, which suggests that the net heat is a measure of the dissipative processes, whereas the other quantities are due to reversible processes such as channel opening and closing.

Because opening of the sodium channel could be interpreted as partial disaggregation of the subunits, we can estimate the expected heat from the number of sodium channels per unit area of membrane. Data on the concentration of sodium channels in unmyelinated C fibers of rabbit vagus nerve (24) indicate 110-nmol/kg wet weight. Estimation of the diameter of the C fibers as 0.5–1 μm and assumption of a density of Na^+ channels comparable to the squid axon (26) make it possible to estimate the measured heat per gram. Taking into account the interference due to the temporal and spatial overlap of positive and negative heat, the estimated positive heat is 25 $\mu\text{cal/g}$ and the negative heat is 22 $\mu\text{cal/g}$. If the major part of the ΔH is due to the oligomeric reactions of the channels, the negative heat is a better measure of the largely reversible ΔH for channel opening and closing. In that case, the reversible channel process involves a ΔH of about 6 kcal/mol of channel protein (molecular weight 270 kD) or about 0.02 cal/g of channel. The ΔH for the aggregation reaction of tobacco mosaic virus (TMV) protein [the classic model for the study of oligomeric reactions (4)] is about 0.7 cal/g. This value implies that only about 3% of the protein surface is involved in the reactions that affect channel opening and closing.

A positive ΔH for channel closing should coincide with the falling phase of the action potential, and channel opening should be associated with a negative ΔH or heat absorption. The measured heat in nerve fibers appears to be at odds with the model, but the temporal and spatial resolution of the heat measurements is difficult. (The overlap of many axons with different propagation rates in a single nerve fiber and the presence of sodium and potassium channels with different time constants in a single fiber means that the closing of sodium channels may coincide with the opening of potassium channels. In studies of electric organs, the heat of the ion channels of nerve fiber may overlap with the heat of the acetylcholine receptor channels on the opposite cell surface.)

However, the following statements are clearly true:

- There is a net heat evolution as expected in a dissipative process.
- There is a heat absorption phase (channel opening) that precedes a heat evolution phase (channel closing).
- The magnitude of the reversible heat, about 0.02 cal/g of channel protein, suggests an involvement of about 3% of the protein surface in gating.

These observations suggest that the energetics of protein aggregation reactions can explain channel energetics. It is also possible to explain recent experiments on the heating of nerves by exposure to microwaves (27), where a rapid temperature rise results in a decrease in the firing rate of a nerve. This effect could be mediated through the ΔH changes associated with channel opening and closing. Because channel closing evolves heat, additional heat input would inhibit channel closing (by LeChatelier's principle), prolong electrical activity, and slow down the firing rate. An explanation of these observations in terms of the ion shifts brought about by the temperature changes (28) appears reasonable, but channel processes may also be involved.

Insights into Active Transport

The Na, K-ATPase is the cation-activated membrane enzyme that "pumps" Na^+ and K^+ ions across cell membranes when ATP is split. The hydrolysis of ATP provides enough energy to transport the ions against their electrochemical gradients, but the mechanism is not understood. Because the protein components of the enzyme operate across the membrane, the physical chemistry of channel processes discussed here may provide some insight into possible mechanisms.

One proposal to explain ion pumping (29) suggests that the ATPase undergoes conformational changes that cause an ion-binding surface of the enzyme to alternately contact the aqueous compartments on the two sides of the membrane. With this scheme, the enzyme surface exposed to the outside would have to bind K^+ ions preferentially and exchange the K^+ ions for Na^+ ions when exposed to the inside. There is supporting experimental evidence to indicate preferential binding at the activation sites on the two surfaces, as well as the occlusion (i.e., unavailability for exchange) of particular ions during part of the cycle.

The channel model used in the SCM suggests how a change of exposure to the two different solutions could occur on the molecular level. As in Figures 6 and 7, assume a total charge of 60 per 100 nm^2 that is divided between the inner and outer surfaces at 25 and 35 per 100 nm^2 , respectively. Given the probabilities, one face would be open and the other face would be closed. A shift of charge, at a constant total charge, would shift the average probabilities in a way that would appear coupled. The probability of opening at one surface would increase and the probability at the other surface would decrease. In this scheme, the ATPase would cause a shift of charge like the gating charge that follows changes of polarization in voltage gating. (The shift of charge would also have to change the ion-binding specificity, which reverses the normal binding preferences of the outer surface for K^+ and the inner surface for Na^+ .) One consequence of this picture is that a change in total charge, by a change in pH, would uncouple the probabilities and make

such a mechanism less efficient. This would be in line with the pH optimum of the Na, K-ATPase at physiological pH (30).

The SCM also suggests other electrochemical processes in channels that could lead to ion pumping. For example, Figure 8 shows that the direction of a flux depends on the magnitude of the gating current. It may be possible to have an ionic flux in a channel move in a direction opposite to the direction predicted from macroscopic electrochemical potentials. In the SCM, a shift of charge from a high-charge density region to a low-charge density region, in response to a depolarizing stimulus, causes a channel to open. The same charge shift affects the ionic gradients by freeing bound counterions in the high-charge region and binding counterions in the low-charge region. The two changes can result in a reversed local concentration gradient for driving ions through the opened channel at the same time as there is a diminished electrical gradient across the channel. With specific ion adsorption, a local gradient of a particular ion could be created. Here again the ATPase would function by way of charge shifts between the two enzyme surfaces.

Charge transfer within channel proteins, comparable to the gating current in the sodium channel, accompanies changes in polarization, which in turn are affected by the ambient ion concentrations. The ATPase may have an additional ability to transfer charge by virtue of its catalytic function. The splitting of ATP releases redox energy that is comparable to electron shifts or changes in the ratios of redox couples. The reverse reaction, the formation of ATP from adenosine 5'-diphosphate and phosphorus, is driven by redox processes in the inner mitochondrial membrane. The correlation between the nonspecific inhibitory ability of a cation and its redox potential (31), as well as parallels with the mitochondrial ATPase, suggest a role for redox processes and rapid charge conduction within the Na, K-ATPase.

Acknowledgment

We thank the Office of Naval Research and Electric Power Research Institute for their support.

References

1. Stevens, C. F. *Nature (London)* **1987**, 328, 198–199.
2. Doring, C.; Colombini, M. J. *Membr. Biol.* **1985**, 83, 81–86.
3. Blank, M. *Colloids Surf.* **1980**, 1, 139–149.
4. Lauffer, M. A. *Entropy Driven Processes in Biology*; Springer: New York, 1975.
5. Blank, M.; Soo, L. *Bioelectrochem. Bioenerg.* **1987**, 17, 349–360.
6. Ackers, G. K. *Biophys. J.* **1980**, 32, 331–346.
7. Blank, M. J. *Theor. Biol.* **1984**, 108, 55–64.
8. Blank, M. J. *Theor. Biol.* **1975**, 51, 127–134.
9. Blank, M. J. *Colloid Interface Sci.* **1973**, 43, 557–563.
10. Hodgkin, A. L.; Huxley, A. F. *J. Physiol.* **1952**, 117, 500–544.

11. Blank, M. *Bioelectrochem. Bioenerg.* **1984**, *13*, 317–327.
12. Blank, M. *Bioelectrochem. Bioenerg.* **1982**, *9*, 615–624.
13. Chang, H. W.; Neumann, E. *Proc. Natl. Acad. Sci. U.S.A.* **1976**, *73*, 3364–3368.
14. Blank, M. *Biochim. Biophys. Acta* **1987**, *906*, 277–294.
15. Blank, M.; Britten, J. S. *Bioelectrochem. Bioenerg.* **1978**, *5*, 528–540.
16. Richard, E. A.; Miller, C. *Science (Washington, D.C.)* **1990**, *247*, 1208–1210.
17. Blank, M. *Bioelectrochem. Bioenerg.* **1983**, *10*, 451–465.
18. Khodorov, B. I.; Revenko, S. V. *Neuroscience* **1979**, *4*, 1315–1330.
19. Wei, A.; Covarrubias, M.; Butler, A.; Baker, K.; Pak, M.; Salkoff, L. *Science (Washington, D.C.)* **1990**, *248*, 599–603.
20. Blank, M. *J. Electrochem. Soc.* **1987**, *134*, 1112–1117.
21. Blank, M.; Soo, L. *Bioelectrochem. Bioenerg.* **1989**, *22*, 313–322.
22. Blank, M.; Soo, L. *Bioelectrochem. Bioenerg.* **1990**, *24*, 51–61.
23. Blank, M. *FASEB J.* **1992**, *6*, 2434–2438.
24. Howarth, J. V. *Philos. Trans. R. Soc. London Ser. B* **1975**, *270*, 425–432.
25. Keynes, R. D.; Aubert, X. *Nature (London)* **1964**, *203*, 261–264.
26. Levinson, S. R.; Meves, H. *Philos. Trans. R. Soc. London Ser. B* **1975**, *270*, 349–352.
27. Wachtel, H.; Seaman, R.; Joines, W. *Ann. N.Y. Acad. Sci.* **1975**, *247*, 46–62.
28. Barnes, F. S. *Bioelectromag.* **1984**, *5*, 113–115.
29. Glynn, I. M.; Karlisch, S. J. D. *Annu. Rev. Biochem.* **1990**, *59*, 171–205.
30. Britten, J. S.; Blank, M. *Biochim. Biophys. Acta* **1968**, *159*, 160–166.
31. Britten, J. S.; Blank, M. *J. Colloid Interface Sci.* **1973**, *43*, 564–570.

RECEIVED for review January 29, 1991. ACCEPTED revised manuscript October 6, 1992.

Theory of Electroporation

James C. Weaver

Harvard–MIT Division of Health Sciences and Technology, Massachusetts Institute of Technology, Cambridge, MA 02139

Electroporation is a dramatic cell membrane phenomenon that is of growing importance to biology, biotechnology, and medicine. Electroporation caused by short pulses occurs at a transmembrane voltage of about 1000 mV for many different types of cell and artificial membranes. Here we describe the development of a theoretical model that predicts measurable quantities. An underlying theme of our general approach is the hypothesis that electroconformational or structural changes of (1) the membrane itself, (2) membrane macromolecules, and (3) membrane–macromolecule complexes can provide a general basis for electric field interactions with cells. Electroporation theory is presently based on the membrane itself and can be expected to also involve membrane–macromolecule complexes. In related nonelectroporation work, we hypothesized that membrane macromolecules are relevant to understanding possible weak electric field interactions, and we have estimated the threshold field, $E_{e,\min}$ associated with the thermal noise limit for the response of living cells to weak electric fields.

Electroconformational Changes as a General Membrane Phenomenon

At low frequencies the quasistatic approximation can be used to separately describe both the electric field, $\mathbf{E}(t)$, and the magnetic field, $\mathbf{B}(t)$. Very generally, cells are heterogeneous with respect to their electrical properties (1) but uniform with respect to their magnetic properties (excluding specialized magnetic material such as magnetite and ferritin) (2). Specifically, the permittivity and electrical conductivity of the membrane is significantly different from the permittivity and conductivity of the intra- and extracellular

0065–2393/94/0235–0447 \$09.08/0
© 1994 American Chemical Society

media. These differences in electrical properties result in interfacial polarization, which, through the cell geometry, leads to an amplification in which a change in the external electric field, ΔE_e , causes a much larger change in the transmembrane field, $\Delta E_m = \Delta U/d$ (3, 4). Two relatively simple cell shapes are often considered and illustrate the basic concept: (1) a spherical cell, for which $\Delta U = 1.5E_e R_{\text{cell}} \cos \theta$ if θ is the angle between the direction of \mathbf{E}_e and the point of interest on the cell membrane, and (2) an elongated cell, for which $\Delta U_{\text{max}} \approx E_e L/2$ if L is the characteristic long dimension of the cell and the cell is parallel to \mathbf{E}_e .

With this in mind, we first focus on the hypothesis that because of an increased U , electroconformational changes occur in the membrane itself (Table I). Of specific interest to electroporation theory are those membrane electroconformation changes that lead to pore formation. The earliest studies known to us considered the overall compression of a membrane in response to forces normal to the membrane (5). In such models, an increase in U causes compression that leads to a mechanical instability and an associated critical transmembrane voltage, U_c , for membrane rupture. This early prediction agreed with experiments on solvent-containing planar membranes, but not with experiments on the less compressible biological membranes. More sophisticated treatments of instabilities have been developed (18, 19), but do not describe the subsequent behavior of the transmembrane voltage, $U(t)$, the membrane conductance, $G(t)$, or the number of transported molecules, $N_s(t)$, that are crucial to an understanding of electroporation. Moreover, bulk electrocompression models cannot distinguish between rupture and reversible electrical breakdown, both of which have been observed experimentally in oxidized cholesterol planar membranes (20). These two very different outcomes are now believed to depend on the relative dynamics of pore population changes and membrane discharge through the pore population.

Table I. Membrane-Related Electroconformational Change Candidates

<i>Type of Electroconformational Change</i>	<i>Significant Feature</i>
Overall membrane compression	Rupture and REB not actually described (5)
Lipid-domain interface fluctuations	Suggested alternative to transient pores (6)
Free volume fluctuations	Transport of nonpolar species (7)
Local depressions and distortions	Possible precursors to hydrophilic pores (8, 9)
Transient hydrophobic pores	Possible precursor to hydrophilic pores (10)
Transient hydrophilic pores	Key to quantitative descriptions (10–16)
Foot-in-the-door hydrophilic pores	Candidate metastable pores ^a
Composite hydrophilic pores	Candidate metastable pores
Membrane enzyme changes	Coupling to membrane macromolecules (17)
Membrane macromolecule protrusion changes	Candidate signaling change mechanism

SOURCE: Data are taken from reference 23A.

The important reversible nature of electroporation that is often observed in cell membranes is also not treated.

In contrast, pore models consider the pore-expanding forces that are parallel to the membrane and that arise from normal forces acting on pores as U is increased. Pore models can quantitatively account for both rupture and reversible electrical breakdown (REB) in planar membranes and reversible behavior in cells. For this reason, our discussion will emphasize localized electroconformational changes, particularly hydrophilic pores. The modeling of electroporation using such pores was first presented in an impressive series of seven back-to-back papers; only the first paper is cited here (10).

The last entry in Table I, "membrane macromolecule protrusion changes," ought to be a general phenomenon. Recently it has been considered theoretically (21A, 21B), although it was earlier identified as a possibility in an experimental study (22). Viewed from a macroscopic, continuum perspective, the mean molecular protrusion should reflect a force balance that involves electrostatic and hydrophobic interactions that changes as the transmembrane voltage is varied. For example, as U changed, the electrostatic free energy of the membrane-immersed portion changes. The mean protrusion should, therefore, vary with U , which may alter the accessibility of binding sites on the protruding molecule (e.g., a receptor) or at nearby sites on the membrane. This protrusion provides a candidate mechanism for coupling electric fields to biochemical pathways of the cell and, therefore, could alter cell function because of an external electric field.

Strong Electrical Fields: Electrical Behavior Due to Electroporation

Most biological studies and applications of electroporation involve short pulses ($10^{-6} < t_{\text{pulse}} < 10^{-3}$ s) because longer pulses often lead to nonthermal cell killing and to intolerable heating in physiological electrolytes. A striking aspect of electroporation is that time scales that differ by many orders of magnitude are involved (*see* Table II). Both planar membranes and closed membranes (cells and vesicles) have been studied. Because the geometry is simpler, we first consider electroporation in artificial planar bilayer membranes, some of which (e.g., oxidized cholesterol) exhibit four different outcomes by variation of the properties of the electrical pulse only (Table III).

Reversible electrical breakdown (REB) is particularly striking. (REB is actually a rapid discharge due to the high ionic conductivity caused by the gentle structural membrane rearrangement of multiple pore formation.) In our models, subcritical pores (i.e., nonrupture-causing pores) are responsible for this high conductance state (11). Our first quantitative description of REB (33, 34) correctly predicted many key features of $U(t)$ and $G(t)$ but had

Table II. Time Scales Involved in Electroporation

<i>Time Scale (s)</i>	<i>Significance</i>	<i>How Known</i>
10^{-11}	Molecular collision times within lipid membrane	Statistical mechanics (11, 23B)
10^{-7} – 10^{-6}	Cell and planar membrane charging times	Optical, microelectrode measurements consistent with theory (20, 24–26)
10^{-7} – 10^{-6}	Membrane discharging times (reversible electrical breakdown)	Optical, microelectrode measurements; consistent with theory (16, 20, 24, 25)
10^{-6} – 10^{-5}	Membrane discharging times (planar membrane rupture)	Electrical measurements; consistent with theory (16, 24)
10^{-4} – 10^{+4}	Phenomena that occur after the membrane has discharged (e.g., metastable pore phenomena, membrane recovery)	Optical, chemical, scanning electron microscopy (SEM), and electrical measurements (27–32)

Table III. Four Observed (20) Outcomes for an Oxidized Cholesterol Planar Bilayer Membrane

<i>Characteristic Electrical Behavior</i>	<i>Pulse Magnitude</i>
REB; membrane discharge to $U = 0$	Largest
Incomplete REB; discharge halts at $U > 0$	Smaller
Rupture (mechanical); slow, sigmoidal electrical discharge	Still smaller
Membrane charging without dramatic behavior of U	Smallest

several unsatisfactory assumptions. The most recent description (List 1 and Table IV) overcomes these difficulties and provides a quantitative description of $U(t)$ for all four outcomes for charge injection conditions (Figures 1 and 2) (16). A description of REB alone, which occurs in closed membranes [e.g., vesicles (35)], is actually less challenging.

A general approach to modeling, in which general hypotheses are interrelated in a modular form (List 1 and Table IV), is used. This approach allows modules (e.g., a physical model of the pore free energy) to be separately modified, whereas all of the other features of the simulation are retained. The elements given in List 1 are presently formalized by using the physical ingredients identified in Table IV. Table V lists the simulation parameters and their values.

Hydrophilic pores are assumed to be created by transitions from hydrophobic pores (Figure 3) (10). The details of this process are not known.

List 1. Elements of the General Electroporation Model

1. A membrane contains an equilibrium population (small at $U = 0$) of hydrophilic pores
 2. The membrane conductance, $G(t)$, is due to the pores; a cell membrane also has channels
 3. Changes in the transmembrane voltage, $U(t)$, cause changes in the pore population
 4. Transient behavior is determined by calculating how the pore population changes because of changes in $U(t)$
 5. Feedback between $U(t)$ and $G(t)$ involves both the pore population and external conduction pathways of the experimental system (membrane environment)
 6. Reversible electrical breakdown (REB) is caused by large ionic conduction through the transient pore population
 7. Rupture of a planar membrane is caused by the appearance of one or more large, unstable pores; the closed membranes do not allow cell rupture (35), except by portions of the membrane that are bounded by other cellular structures (e.g., cytoskeleton) because these portions may behave like small planar membranes and therefore can rupture
-

**Table IV. Physical Ingredients in a Recent Version
of the Theory (16, 36)**

<i>Ingredient</i>	<i>Significance</i>
\dot{N}_c	Rate of pore creation (pores of radius r_{\min})
\dot{N}_d	Rate of pore destruction (pores of radius r_{\min})
$n(r, t)$	Pore density function that describes a wide range of pore sizes
$\dot{n}(r, t)$	Dynamic behavior of the heterogeneous pore population
$\sigma_p(r)$	Born energy-modified conductivity within pores
$H(r, r_i)$	Hindered transport through pores [Renkin equation (37)]
$U_p \leq U$	Local transmembrane voltage reduced by the spreading resistance
$R_E + R_N$	Membrane charging through external resistances
Circuit equation	Coupling to the pulse generator, electrodes, and electrolyte (Figure 4)
η_s	Transport of charged molecules through pores by electrical drift ^a

^a Barnett, A.; Weaver, J. C., unpublished.

Unless explicitly stated otherwise, the term “pore” hereafter refers to hydrophilic pores, because they are believed to provide pathways for ionic and molecular transport. A quantitative description of pore creation and destruction is essential, even if it cannot be made completely from first principles [e.g., by molecular dynamics (38)]. Generally a “pore free energy”, $\Delta E(r)$, is used in which the pore is approximated as a circular cylinder of radius r . Both mechanical (39, 40) and electrical (10–12) contributions are considered: The contributions are emphasized by the form $\Delta E(r, U_p)$, where U_p is the local transmembrane voltage at the site of the pore. We use $\Delta E = \Delta E_M$

+ $\Delta E_E + \Delta E_0$, where ΔE_M is the mechanical contribution, ΔE_E is the electrical contribution, and ΔE_0 is an arbitrary constant. The mechanical contribution is

$$\Delta E_M = 2\pi\gamma r - \pi\Gamma r^2 \quad (1)$$

where Γ is the surface energy density of the membrane-water interface and γ is the pore edge energy (39, 40). In the case of a planar membrane, rupture is believed to occur if one or more pores achieve radii $r > r_c$, where the critical radius for rupture is $r_c = \gamma/\Gamma$.

The electrical contribution ΔE_E treats the pore as an electrical capacitor that explicitly includes conduction through the pore and external region near

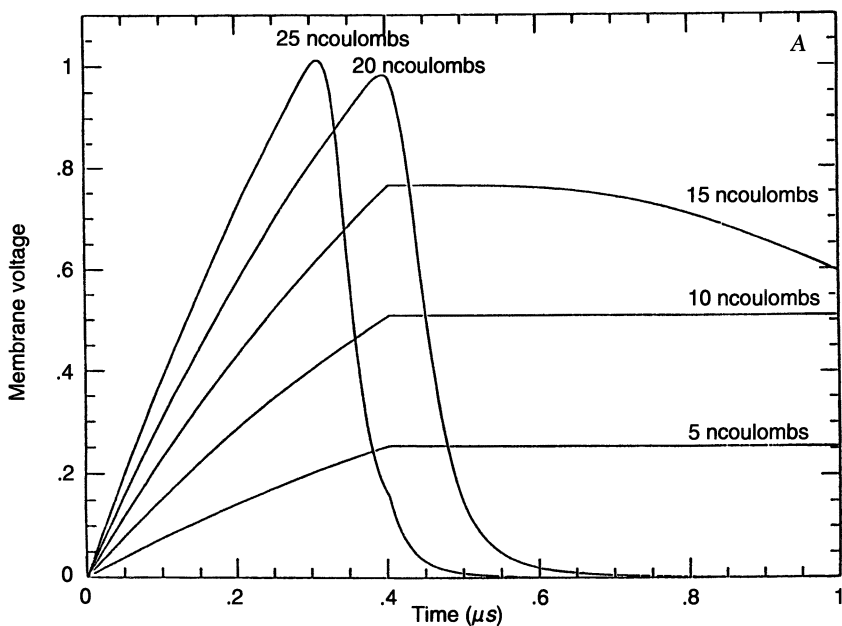


Figure 1A. Short time scale (0–1 μ s) behavior of the transmembrane voltage $[U(t)]$ predicted by a recent version of the theoretical model for a planar bilayer membrane exposed to a single very short (0.4- μ s) pulse; that is, “charge injection” conditions (16). The key features of reversible electrical breakdown (REB) are predicted by the model, as is the occurrence of incomplete reversible electrical breakdown. In the case of incomplete reversible electrical breakdown, the membrane discharge is incomplete because $U(t)$ does not reach zero after the pulse. Each curve is labeled by the corresponding value of the injected charge Q . The curves for $Q = 25$ and 20 nC show REB, whereas the other curves do not.

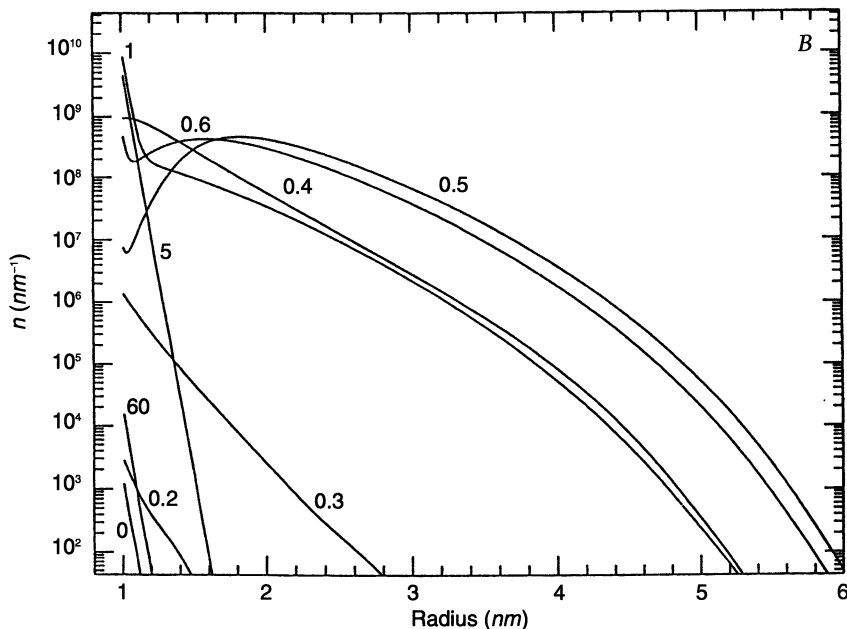


Figure 1B. Corresponding computed pore population distribution (probability density), $n(r, t)$ (16). Each curve is labeled by the corresponding value of the injected charge Q . For $Q = 25$ and 20 nC (cases for which REB occurs), N increases to about 10^8 in less than $0.5 \mu\text{s}$ and then decays exponentially with a time constant of $\approx 4.5 \mu\text{s}$. For $Q = 15$ nC, N increases rapidly to about 10^5 and remains almost constant for about $4 \mu\text{s}$ before the exponential decrease. For $Q = 10$ nC, N increases to about 2×10^3 in about $5 \mu\text{s}$ and remains almost constant for about $30 \mu\text{s}$ before the decay phase. The membrane in this case ruptures. For $Q = 5$ nC, N increases to about 40 in $80 \mu\text{s}$. N will return to its initial value as the membrane discharges with a time constant of about 2 s.

the pore mouth (13, 14). This gives

$$\Delta E_E = - \frac{\pi(\epsilon_w - \epsilon_l)U^2}{h^2} \int_{r_{\min}}^r \alpha^2 r dr$$

where

$$\alpha(r) = \left[1 + \frac{\pi r \kappa_p(r)}{2h\kappa_e} \right]^{-1} \quad (2)$$

The function $\alpha(r)$ contains the “voltage divider” effect associated with the spreading resistance external to a pore and the internal pore resistance. We assume that pores have a minimum radius, $r_{\min} = 1.0$ nm, because head-group packing constraints require r_{\min} to be somewhat greater than the size of the

hydrophilic head groups (≈ 0.7 nm) that make up the inner surface of the pore, and the pore wall must contain at least several phospholipid molecules (35). We also assume that the number of pores changes because of the creation and destruction of pores with radius r_{\min} (10), which yields a boundary condition at $r = r_{\min}$ for the flux of pores in radius space:

$$J_p = \dot{N}_c - \dot{N}_d \quad \text{at } r = r_{\min} \quad (3)$$

Here \dot{N}_c and \dot{N}_d are the pore creation and destruction rates, and the pore flux is

$$J_p = -D_p \left(\frac{\partial n}{\partial r} + \frac{n}{kT} \frac{\partial \Delta E}{\partial r} \right) \quad (4)$$

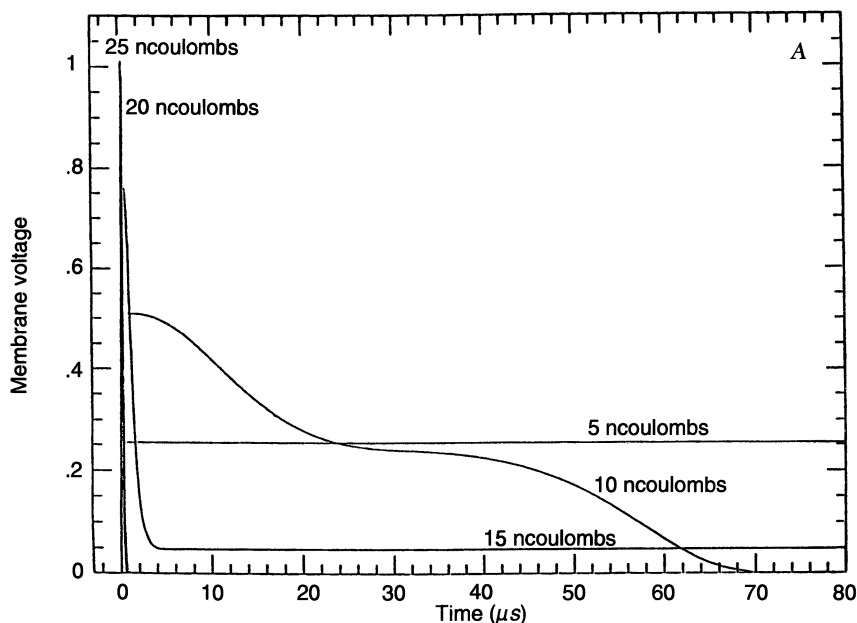


Figure 2A. Longer time scale (0–80 μ s) electrical behavior, predicted by the same model that shows rupture and simple charging of an artificial planar bilayer membrane (16). The characteristic sigmoidal behavior of $U(t)$ is predicted by the model (16), but the time scale is somewhat shorter than found in experiments (61). Each curve is labeled by the corresponding value of the injected charge Q . The curves for $Q = 25$ and 20 nC are the spikes at $t = 0$. The curve for $Q = 15$ nC shows that the membrane underwent REB at $t = 2$ μ s, but the membrane recovered before it had time to discharge completely. The curve for $Q = 10$ nC shows rupture, whereas the curve for $Q = 5$ nC shows that the membrane conductance did not increase enough to discharge the membrane.

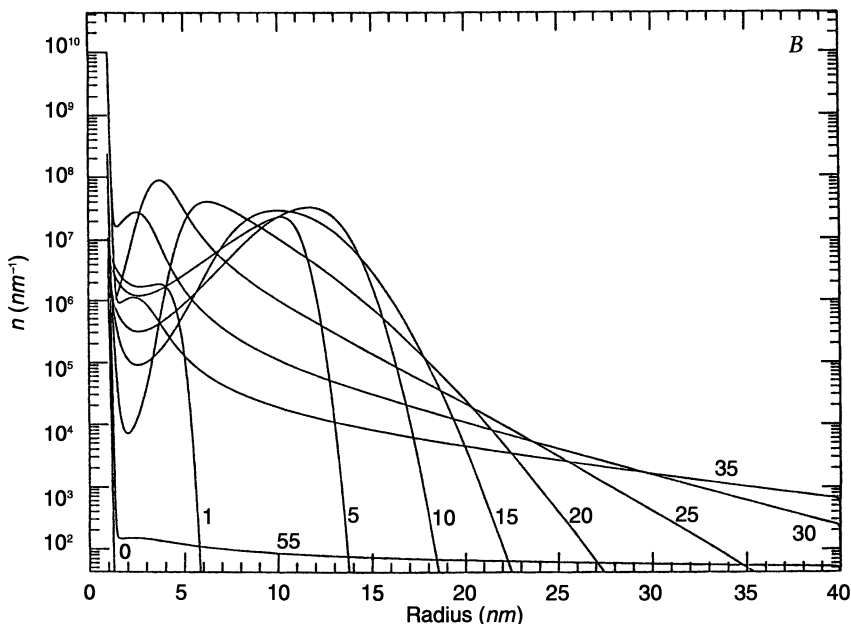


Figure 2B. Corresponding pore population distributions as described by $n(r, t)$ (16). Each curve is labeled by the corresponding value of the injected charge Q . For $Q = 25$ and 20 nC (cases for which REB occurs), N increases to about 10^8 in less than $0.5 \mu\text{s}$ and then decays exponentially with a time constant of $\approx 4.5 \mu\text{s}$. For $Q = 15$ nC, N increases rapidly to about 10^5 and remains almost constant for about $4 \mu\text{s}$ before the exponential decrease. For $Q = 10$ nC, N increases to about 2×10^3 in about $5 \mu\text{s}$ and remains almost constant for about $30 \mu\text{s}$ before the decay phase. The membrane in this case ruptures. For $Q = 5$ nC, N increases to about 40 in $80 \mu\text{s}$. N will return to its initial value as the membrane discharges with a time constant of about 2 s.

During pore formation the membrane achieves energetically unfavorable configurations; that is, an energy barrier, Λ , is overcome. Although the important details are unknown, we assume that Λ depends on the transmembrane voltage U . The contribution of permanent dipoles associated with pore structures (41) is presently neglected, so Λ is assumed to depend on U^2 (viz. $\Lambda = \delta_c - aU^2$, where δ_c and a are constants). The corresponding absolute rate estimate is

$$\dot{N}_c = \nu \exp\left(-\frac{\delta_c - aU^2}{kT}\right) \quad (5)$$

where ν is an attempt rate based on an attempt rate density, ν_0 , and the volume of the membrane (11). To provide continuity within our work, we have used the barrier contained in eq 5 and have not yet attempted to include

Table V. Simulation Parameters and Values

<i>Parameter</i>	<i>Description</i>	<i>Value</i>
<i>a</i>	Coefficient of U^2 in Λ	1.9×10^{-20} F
A_m	Membrane area ^a	1.45×10^{-6} m ²
<i>C</i>	Capacitance of membrane	9.61×10^{-9} F
D_p	Diffusion constant in pore radius space ^a	5×10^{-14} m ² /s
dt	Time step size (in units of $D_p/(\Delta r)^2$)	0.5
<i>h</i>	Membrane thickness ^a	2.8 nm
kT	Boltzmann's constant times temperature	4×10^{-21} J
R_E	Series resistance of electrolyte, electrodes, and wires	30 Ω
R_N	Internal resistance of current source (pulse generator)	50 Ω
r_{max}	Large pore initial size	40 nm
r_{min}	Minimum pore radius ^a	1 nm
r_+	Radius of positive ions	0.2 nm
r_-	Radius of negative ions	0.2 nm
<i>t</i>	Time	s
t_{pulse}	Pulse length	0.4 μ s
z_+	Charge of positive ions (in units of proton charge)	+1
z_-	Charge of negative ions (in units of proton charge)	-1
γ	Pore edge energy density ^a	2×10^{-11} J/m
Γ	Membrane surface energy ^a	1×10^{-3} J/m ⁻²
δ_c	Pore creation energy barrier ^a	2.04×10^{-19} J
δ_d	Pore destruction energy barrier ^a	2.04×10^{-19} J
Δr	Numerical grid spacing of simulation	0.0195 nm
ϵ_l	Dielectric constant of lipid ^a	$2.1\epsilon_0^b$
ϵ_w	Dielectric constant of water	$80\epsilon_0^b$
ν	Pore creation rate prefactor ^a	10^{28} s ⁻¹
K_e	Conductivity of bulk solution	0.98 Ω /m
χ	Pore destruction rate prefactor ^a	5×10^{16} m/s

^a Parameters that characterize the membrane (16).

^b $\epsilon_0 \equiv 8.85 \times 10^{-12}$ F/m.

other estimates (15) of the barrier. Although pore destruction is also not understood in detail, we assume that the probability that a pore of radius r_{min} is destroyed is independent of U . This assumption gives

$$\dot{N}_d = \chi n(r_{min}) \exp\left(-\frac{\delta_d}{kT}\right) \quad (6)$$

where χ is a constant.

A combination of physical forces and diffusion governs pore evolution. As a result, pores with a wide range of sizes appear in the membrane. This distribution of sizes is described by a "pore population function," that is, a probability density function, $n(r, t)$. At any time t , there are $n(r, t) \Delta r$ pores with radii between r and $r + \Delta r$.

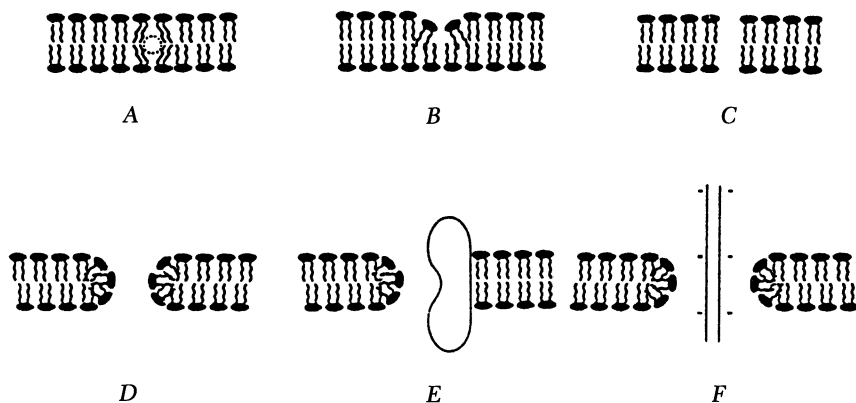


Figure 3. Hypothetical structures of transient and metastable membrane conformations that are believed relevant to electroporation (17). A, Free volume fluctuation believed to be involved in the transport of nonpolar molecules across membranes (7) and a possible early precursor to a hydrophilic pore. B, Aqueous protrusion or “dimple” that is envisioned as a more direct precursor to a hydrophilic pore (8). C, Hydrophobic pore, a high-energy transient structure that is believed to be a direct precursor to a hydrophilic pore (10). D, Hydrophilic pore that is believed to be the primary participant in short-term electrical behavior and probably involved in molecular transport (10). E, Composite pore with one or more proteins at the inner pore edge, a speculative possibility that might account for a metastable pore that persists after U has decayed because of reversible electrical breakdown (58). F, Composite pore due to a “foot-in-the-door” mechanism, which involves insertion of a linear charged macromolecule into a hydrophilic pore, such that screened coulombic repulsion prevents shrinkage of the pore. This is another candidate for a metastable pore, which can persist and transport small ions and molecules long after U has decayed to a small value by reversible electrical breakdown. The present view of electroporation assumes that transitions from $A \rightarrow B \rightarrow C \rightarrow D$ have a nonlinear increased frequency of occurrence as U is increased. Similar transitions may lead to E and F. Partially anchored cytoplasmic molecules, components of extracellular matrix, and “in transit” transported molecules are examples of pore-entering molecules that may lead to persistent pores of type F. Indeed, observation of enhanced transport of a small charged molecule due to electroporative uptake of DNA (a charged molecule “in transit” during uptake) has been reported (53).

The kinetics of the pore population are quantitatively described by Smoluchowski's equation (14, 42):

$$\frac{\partial n}{\partial t} = D_p \left[\frac{\partial^2 n}{\partial r^2} + \frac{\partial}{\partial r} \left(\frac{n}{kT} \frac{\partial \Delta E}{\partial r} \right) \right] \quad (7)$$

Here D_p is the effective diffusion constant for the pore radius (43). One of our previous models showed that D_p should be independent of pore radius,

but the model used an estimate in which water was treated as an ideal gas (14) and gave a value of D_p that was 20 times larger than the present value (which assumes that molecular interactions will decrease D_p). ΔE is important because $-(\partial \Delta E / \partial r)_U$ is the effective driving force that acts to change the pore size. Equation 7 is valid for $r_{\min} \leq r \leq r_{\max}$ (we used $r_{\max} = 2r_c$ in our simulations). Relatively few pores are predicted for small $U(t)$. However, for large $U(t)$ a tremendous number of rapidly changing pores with a wide range of sizes is predicted, and this phenomenon corresponds to "electroporation." To quantitatively describe metastable pores (not yet accomplished), additional interactions will be needed.

We assume that the transport of ions across the membrane occurs by passage through pores large enough to accommodate small hydrated ions (e.g., Na^+ and Cl^-). However, the presence of ions within small pores requires that the "Born energy" (44) and hindered motion both be considered. The bulk electrolyte conductivity σ_e is a function of the concentrations, c_i , and of the mobilities, η_i , of its ions:

$$\sigma_e = \sum_i (z_i e)^2 \eta_i c_i \quad (8)$$

Here $e = 1.6 \times 10^{-19}$ C, z_i is the charge of the i th type of ion, and the sum is over the different ion types of the electrolyte. In contrast, the conductivity within a pore, σ_p , is reduced:

$$\sigma_p(r) = \sum_i (z_i e)^2 \eta_i c_i H(r, r_i) \exp\left(\frac{\mu_i^0}{kT}\right) \quad (9)$$

Here $H(r, r_i)$ is a steric hindrance factor (see following text) and μ_i^0 is the standard chemical potential of an ion of type i inside the pore. We use a previously obtained estimate (13)

$$\mu_i^0 = \frac{(z_i e)^2}{4\pi \epsilon_1 r} P\left(\frac{\epsilon_1}{\epsilon_w}\right) \quad (10)$$

which is based on a point charge on the axis of an infinite cylindrical cavity. Here ϵ_1 and ϵ_w are the dielectric constants of the lipid and the water, respectively, and the Parsegian function P has a maximum value of 0.25 (44).

Hindrance of movement within a pore is described by using Renkin's equation (37):

$$H(r, r_i) = \left[1 - \left(\frac{r_i}{r}\right)^2\right] \left[1 - 2.1\left(\frac{r_i}{r}\right) + 2.09\left(\frac{r_i}{r}\right)^3 - 0.95\left(\frac{r_i}{r}\right)^5\right] \quad (11)$$

for $H \rightarrow 0$ as $r_i \rightarrow r$.

An additional complication is that a heterogeneous electric field exists within the electrolyte near the pore entrances. The associated potential drop in the electrolyte is estimated by consideration of "spreading resistance" (45), $R_s(r)$, given by $R_s \approx 1/2\sigma_e r$. The spreading resistance results in a smaller transmembrane voltage, U_p , at the site of pore. The internal resistance of a pore is estimated by using the reduced conductivity, $\sigma_p(r)$, so that $R_p = h/\pi r^2 \sigma_p(r)$ (13, 14). These two resistances act in series and create a "voltage divider" so that $U_p \leq U$. This divider reduces both the electrical driving force and ΔE , with the consequence that large pores expand more slowly. The current through a pore is $I_p = U/R_s(r) + R_p(r)$, so that the total current I through the membrane and the conductance, $G(t)$, are

$$I = U \int_{r_{\min}}^{\infty} \left[\frac{n(r, t)}{R_s(r) + R_p(r)} \right] dr \quad (12a)$$

$$G(t) = \int_{r_{\min}}^{\infty} \left[\frac{n(r, t)}{R_s(r) + R_p(r)} \right] dr \quad (12b)$$

as $r_{\min} > r_i = r_+ = r_-$. $G(t)$ is used self-consistently with an equation for the external circuit (*see* following text) to determine the membrane electrical behavior.

The circuit of Figure 4 shows the relationship between the pulse generator, the charging pathway resistance, and the membrane, which is treated as the parallel combination of the membrane capacitance, C . The capacitance changes negligibly during electroporation, because only a small fraction of the membrane is occupied by aqueous pores (Freeman, S. A.; Wang, A. M.; Weaver, J. C., unpublished). However, the membrane resistance, $R(t) = 1/G(t)$, changes by orders of magnitude. In a charge pulse experiment a current pulse of amplitude I_i passes through R_N to create a voltage pulse, V_0 (Figure 4). For $0 < t < t_{\text{pulse}}$, current flows into or across the membrane, and at $t = t_{\text{pulse}}$ the pulse is terminated by opening the switch. Because the generator is then disconnected, membrane discharge can occur only through the membrane for a planar membrane [not so for a cell, which has a circumcellular discharge pathway (Weaver, J. C.; Barnett, A.; Wang, M. W.; Bliss, J. G., unpublished)]. For planar membrane experiments the appropriate circuit differential equations are

$$C \frac{dU}{dt} = \begin{cases} \frac{I_p R_N}{R_E + R_N} - U \left(+ \frac{1}{R_E + R_N} \right) & \text{if } t < t_{\text{pulse}} \\ -\frac{U}{R} & \text{if } t > t_{\text{pulse}} \end{cases} \quad (13)$$

subject to the initial condition $U(0) = 0$. A modified treatment approximates a cell by considering two "polar regions" as planar membranes (Weaver,

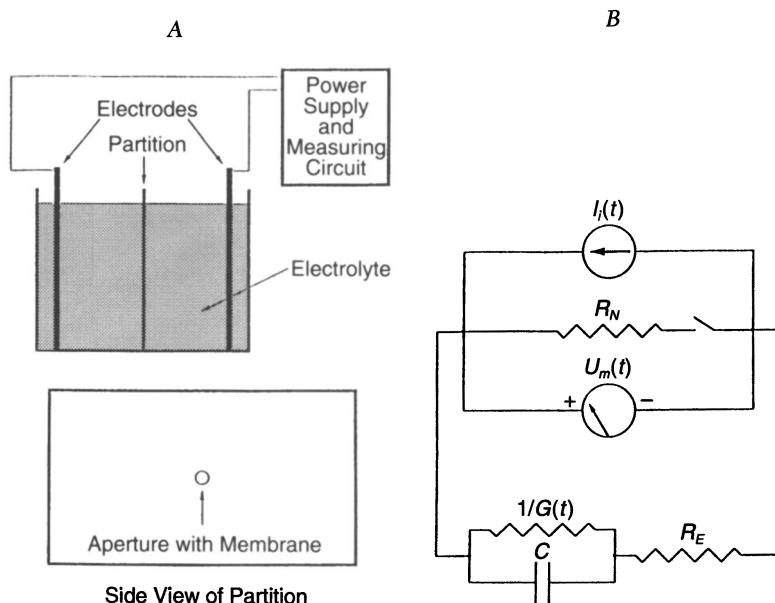


Figure 4. A, Experimental configuration for studying artificial planar bilayer membranes. A vessel that contains a bathing electrolyte is separated into two compartments by an insulating partition. On each side there is a planar electrode connected to a voltage source (pulse generator) and a measuring circuit. The membrane spans an aperture of area A_m in the partition. B, Equivalent circuit for a charge pulse experiment using the configuration in A (14, 16). The pulse generator is modeled by the current source $I_i(t)$ in parallel with the resistor R_N , which corresponds to a voltage pulse, V_0 . The electrolyte, electrodes, and wires are modeled by the resistor R_E , and the membrane is modeled by the capacitor C in parallel with the resistor $1/G(t)$. The switch is opened at the end of the current pulse, and the discharge current is forced to flow through the membrane. The voltmeter measures the potential difference $U_m(t)$ between the electrodes. The membrane initially charges with a time constant of $\pi_{chg} = (R_N + R_E)C$ (16), which is typically a few microseconds; that is, a result of the finite resistance of the bathing electrolyte, electrodes, and pulse generator output resistance. This value is of the same order of magnitude as for many isolated cells (59, 60).

J. C.; Barnett, A.; Wang, M. W.; Bliss, J. G., unpublished). A self-consistent numerical solution to these equations is used to provide an electroporation simulation.

Strong Electrical Fields: Molecular Transport Due to Electroporation

During and within about 10^{-4} s of a pulse, electrical interactions probably dominate pore behavior. For this reason, treatment of electrical behavior is

crucial to understanding electroporation. However, greatly enhanced molecular transport across cell membranes is the primary motivation for most electroporation applications (46–48) and is far more important to biology than membrane electrical behavior. To treat molecular transport, we have extended the model to include one contribution to molecular transport across a planar membrane, that of electrical drift (36). Other basic molecular transport mechanisms (viz. diffusion and convection) should be included in future versions. The possibility of endocytosis, either as a primary membrane event or as a secondary, electroporation-stimulated effect, should also be considered as a molecular transport mechanism (49). In electroporative transport we expect that water-soluble molecules of effective radius r_s are transported through the pores that have $r \geq r_s$. This expectation is equivalent to the assumption that the electroporated membrane is a rigid sieve. It remains for future experiments to include the possibility that the approach and entry of a molecule might cause additional membrane conformational changes that assist or inhibit molecular transport. Hindered transport is expected for all three types of transport through pores, because many pores are only slightly larger than r_s . For each type of transport the characteristic time for relaxation into a steady-state transport is important, because, if it is justified, a steady-state description is generally much simpler.

For a charged molecule of type s , the drift current across the membrane is larger than the diffusion current as long as U is greater than the Nernst voltage for species s : $U_{\text{Nernst},s} > kT/z_s e \ln[c_{s,1}/c_{s,2}]$, where z_s is the charge on a molecule of type s and the argument of the logarithm is the ratio of the concentrations on the two sides of the membrane. We also limit our treatment to those cases in which the associated electric current is small compared to the current carried by the small ions of the bathing electrolyte. This limitation allows us to neglect the effect of molecular transport on the electrical behavior of the membrane but provides an estimate of the electrical drift flux, \dot{N}_s , of charged molecules of type s across the membrane:

$$\dot{N}_s(t) = U \int_{r_s}^{\infty} \left[\frac{n(r, t)}{X_s(r) + X_p(r)} \right] dr \quad (14)$$

Note that only pores with $r > r_s$ participate, because the hindrance factor is zero for $r = r_s$ (eq 11). The net number of molecules transported across the membrane is the time integral of \dot{N}_s over the duration of the simulation and is a quantity that should be measurable for different experimental conditions, particularly different pulse magnitudes, durations, and shapes. The terms

$$X_s = \frac{1}{(z_s e) \eta_s \bar{c}_s r} \quad \text{and} \quad X_p = \frac{h}{\pi (z_s e) \eta_s \bar{c}_s H_s \exp(\mu_s^0/kT) r^2} \quad (15)$$

are the analogs to the spreading resistance and internal pore resistance for the small ions. Here η_s is the electrical mobility of a molecule of type s and

\bar{c}_s is their concentration on the supply side. As is the case for conduction by small ions, μ_s^0 is the chemical potential of a molecule of type s inside a pore, which is approximated by its Born energy, and $H = H(r, r_s)$ is the steric hindrance factor.

In a recent set of simulations, we used the potential energy of a point charge on the axis of an infinite cylinder cavity for the Born energy. However, this value is too large because two significant contributions were not included. First, a hydrophilic pore is lined with phospholipid head groups that have an effective dielectric constant that is intermediate between that of lipid and water; this lowers the Born energy. Second, a membrane-spanning pore has finite length, so that the infinite cylinder approximation is too large; this also lowers the Born energy. For this reason, here we have used the results of Jordan, who has treated finite pores lined with material of intermediate dielectric constant (50, 51). Thus we have used a reduced estimate, in which eq 10 has been multiplied by the factor $0.02(h/r)$. This approximation still treats the charge as a point charge, which is a reasonable approximation for a small ion but far less so for a larger molecule. For this reason, we have also used an effective value for z_s^2 (e.g., $z_{s,\text{eff}}^2 = z^{1.5}$) that is less than z_s^2 . To test the sensitivity of molecular transport to molecular size and charge we have initially assumed a spherical molecule.

During a simulation of electrical behavior the quantities $U(t)$ and $n(r, t)$ are progressively computed (16). \dot{N}_s is simultaneously estimated, and the cumulative flux is computed as the simulation progresses to provide a prediction of the average net transport, \bar{N}_s . To date, molecular transport estimates involve (1) a driving force proportional to z , (2) repulsion due to a Born energy effect, and (3) geometrically reduced transport through hindrance (which explicitly includes sieving). The integrated flux of several different hypothetical spherical molecules with different sizes and charge was computed for a simulated charge-pulse experiment (Figures 5 and 6). Initially we used the bulk molecular concentration, \bar{c}_s , to estimate the availability of molecules for pore entry, but in future versions the locally elevated or depressed concentration within the double layer near a charged membrane should be included.

Our initial estimates of molecular transport based on electrical drift should be extended by including convection [e.g., electroosmosis (31)] and diffusion (52). The same general strategy is reasonable: A dynamic pore population will be computed, in which electrical interactions are the dominant source of pore creation and expansion. In the case of a planar membrane with no osmotic or hydrostatic pressure gradient, the final stages of pore population expansion and collapse should also be governed by purely electrical interactions. By following the pore population over its development, the contribution of each transport mechanism can be estimated. For cell membranes, a nonzero pressure difference will usually exist. In this case, pores of

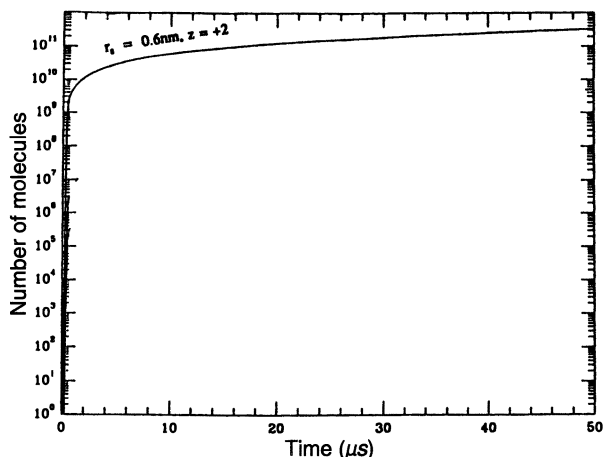


Figure 5. Theoretical estimate of the transport of propidium iodide (PI) across an artificial planar bilayer membrane. The molecule was treated as a circular disk with charge $z_s = +2$. Only transient aqueous pores are used in this version of the model. Future versions should include metastable pores and estimates of the contributions of diffusion and convection.

electrical origin may be further expanded. The very large pores in red blood cell membranes visualized by rapid freeze electron microscopy (29) may have been generated in this way. The very large size (40–100 nm) and relatively long lifetime (10–40 ms) of these pores suggest that (1) they should contribute significantly to molecular transport, but based on our theoretical model (and also optical (25) and microelectrode measurements (24) in other cells), (2) it is difficult to believe that these large pores are the “primary pores” caused by elevated transmembrane voltages, because $U(t)$ decays to zero within 10^{-3} s or less after the pulse.

The effect of metastable pores with lifetimes greater than 10^{-3} s should also be considered, for example, by extending the model to include interactions that “trap” one or more of the transient large pores. Although the mechanism is not yet understood in detail, there is growing experimental evidence that a significant number of cells retain an ability to take up large numbers of macromolecules long after $U(t)$ should have decayed to zero. Experiments that show a decaying number of cells, each with an undiminished ability for large amounts of uptake (30 and Harrison, G. I.; Bliss, J. G.; Weaver, J. C., unpublished), are particularly suggestive of metastable pores. For example, protrusion of cytoplasmic macromolecules into pores could provide a coulombic repulsion that prevents pore shrinkage to r_{\min} . Similarly, the entry of a charged linear molecule (e.g., DNA) should provide a “foot-in-the-door” effect, in which the pore remains open until the molecule either is expelled or transported. This mechanism is consistent with the observation of

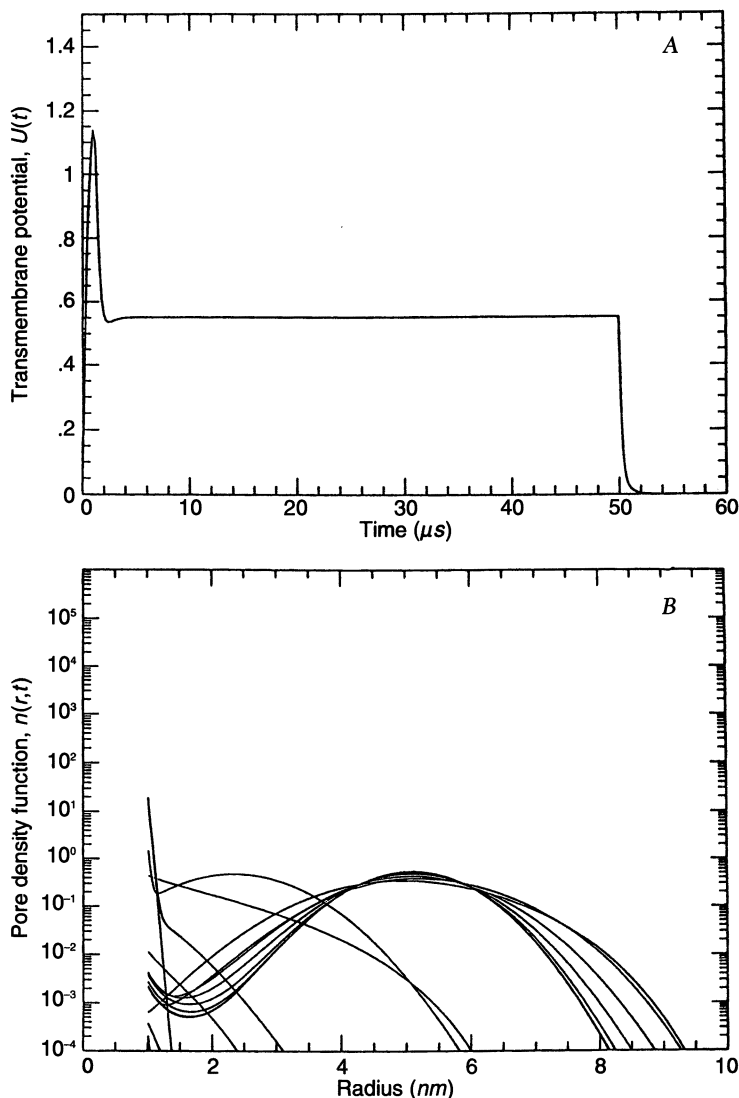


Figure 6. A, Theoretical prediction of $U(t)$ for a cubic cell model. This extension of a planar bilayer membrane model assumes that the participating membrane regions are two planar areas on opposite sides of a cell. Unlike the planar membrane, the cubic cell correctly gives a rapid discharge of the transcellular potential difference even if there is negligible electroporation. Here the behavior was simulated by providing a single $50\text{-}\mu\text{s}^2$ pulse of amplitude $V_0 = 4\text{ V}$. B, Corresponding behavior of $n(r,t)$. Note the continued evolution of the pore population to include progressively larger pores while the pulse is on. At the same time the transmembrane voltage has reached an approximate plateau. Unlike planar membranes that achieve this transmembrane voltage, rupture does not occur for cell membranes.

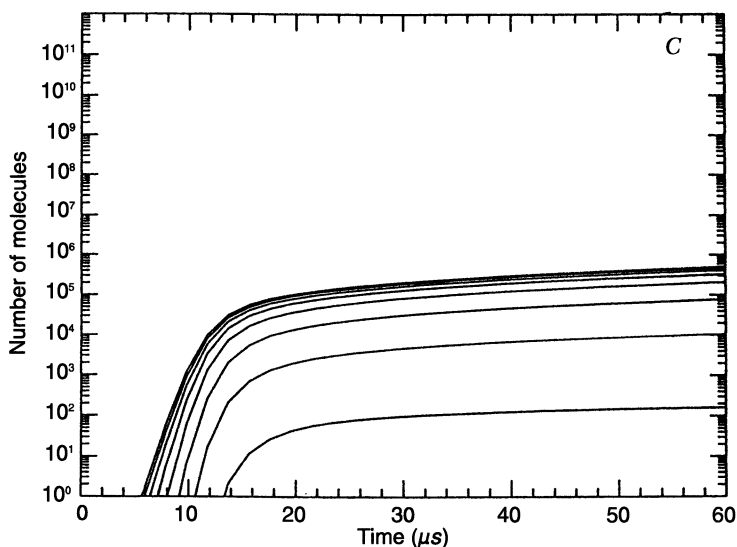


Figure 6.—Continued. C, Predicted electrical drift contribution to molecular transport across one of the two cubic cell membranes. (Weaver, J. C.; Barnett, A.; Wang, M. W.; Bliss, J. G., unpublished). A hypothetical series of molecules, all with unit charge ($z_s = 1$) was used to test the relative importance of different size pores in the pore population. More realistic predictions would use estimates of the size (radius r_s), shape (a form factor), and the Born energy repulsion ($z_{s,eff}^2 = z^m$, where m is a number in the range $1 < m < 2$).

increased transport of small molecules during DNA introduction by electroporation (53). Capture of membrane proteins at a pore edge (Figure 3) or interaction with the cytoskeleton might also lead to metastable pores. Similarly, transport of a cytosolic or extracellular molecule into an expanded transient pore, and subsequent binding or adsorption of the molecule to the pore edge, could lead to repulsive interactions within the pore that prolong the lifetime of the pore.

Cubic Cell Model for Electroporation

The topologies of planar and cell membranes are significantly different. Planar membranes can discharge only through the membrane (or the external circuit if the pulse generator remains connected). In contrast, cells can discharge either by conduction through the membrane or by an extracellular pathway. Thus cells have a short discharge time, π_{dis} , even for electric field pulses that do not cause electroporation. A cubic cell model for electroporation has been developed that assumes that (1) only a portion of the cell membrane significantly participates in electroporation and (2) this portion can be approximated by two planar membranes (Weaver, J. C.; Barnett, A.;

Wang, M. W.; Bliss, J. G., unpublished). This extension of the planar model provides a better description of cell membrane electrical behavior during electroporation and provides a more realistic basis for describing molecular transport.

Weak Electrical Fields: Estimates of Thresholds

Electroporation occurs for very large increases in U , such that the change, ΔU , is extremely large compared to the background fluctuations (“noise”) in the transmembrane voltage. In preliminary consideration of this fact, we noted that application of a basic signal-to-noise ratio criterion might provide an estimate of the minimum electric field, $E_{e, \min}$, to which a cell should respond (54). This approach led to the following broadband estimate for a spherical cell:

$$E_{e, \min} = \frac{2(\delta U)_{kT}}{3r_{\text{cell}}} = \frac{2}{3} \left[\frac{kTd}{\pi \epsilon_0 K_m} \right]^{1/2} \frac{1}{r_{\text{cell}}^2} \quad (16)$$

This approach to estimating thresholds can be applied to other cell shapes (e.g., elongated cells) and can be extended by considering mechanisms that lead to limited frequency bands of response and the possibility of “signal averaging” by the accumulation of transported molecules via the mechanism of electroconformational coupling (55). Such “narrow banding” and signal accumulation (a type of signal averaging) is a fundamental attribute of membrane enzyme electroconformational coupling (56). This constraint on noise leads to lower threshold predictions:

$$E_{\min, \Delta f} \approx \frac{4\sqrt{RkT \Delta f}}{L_{\text{cell}}} \approx 2 \left[\frac{\rho_m kTd \Delta f}{\pi} \right]^{1/2} \frac{1}{L_{\text{cell}} R_{\text{cell}}} \quad (17)$$

where Δf is the frequency bandwidth (e.g., within which the electroconformational coupling mechanism functions) and R is the resistance of the cell membrane. The Δf associated with electroconformational coupling is ordinarily not extremely small and has its origin in the relaxation times of the enzyme-catalyzed reaction, rather than a “resonance” phenomenon (56).

Transient Aqueous Pores as Enzymes

Transient hydrophilic pores can be regarded as excitations of the membrane because their frequency-of-occurrence is dependent on thermal fluctuations, the local transmembrane voltage, and the local composition of the membrane, and any participating membrane macromolecules. As pathways for ionic conduction, hydrophilic pores act much like ion channels, but with the

significant differences that (1) they can achieve many different sizes and (2) they usually exist for only a short time.

Eisenberg recently noted that channels function as entities that catalyze transmembrane transport and, in this sense, can be regarded as enzymes (57). Eisenberg notes that channels stabilize the transition state between substrate (*S*) and product (*P*) if the channel transition state is regarded as the state with an ion within the channel. This stabilization occurs because the channel is polarizable, with a channel aqueous interior dielectric constant and a channel wall dielectric constant that both exceed the lipid dielectric constant, so that the barrier to ion transport is lowered. This transport-enhancing function of transient pores has, of course, been explicitly considered by many investigators of electroporation. In this case a solubilized ion passes through the membrane because of the reduced Born energy. The pore size often exceeds the simple geometric requirement of $r > r_i$, so that the Born energy barrier is reduced even more.

Here we suggest that ions or molecules temporarily bound to the membrane surface may have their transmembrane movement enhanced by pore formation and that this possible mechanism also has catalytic features. This additional hypothesis envisions that local membrane conformational changes can result from both the local transmembrane voltage and the surface binding of a transported molecule (*S*). That is, a pore–substrate complex is formed. One possible outcome is transmembrane transport in which *S* is temporarily bound to the inner surface of a pore, with subsequent electrical lateral motion (relative to the pore inner surface) by diffusion or lateral drift to the other side. Alternatively, as a pore shrinks and closes, *S* is presented to the other side of the membrane. In either case, upon dissociation, transport of *S* will have been accomplished.

In summary, a pore may function as an enzyme, with transport enhanced (“catalyzed”) in two ways:

1. Reduction of the Born energy barrier for a soluble ion or molecule (the usual role attributed to pores during electroporation).
2. Transient binding and transport of an ion (or molecule) in a three step process:
 - (a) Binding to the exposed interior surface of the pore.
 - (b) Moving with respect to the membrane midplane because of further pore conformation changes or lateral transport along the interior surface of the pore.
 - (c) Unbinding from the pore on the other side of the membrane.

This hypothetical process might also occur if a membrane macromolecule resides at the “edge” of a composite pore, such that portions of the macro-

molecule are exposed and are able to temporarily bind the transported molecules. In this case, following a conformational change that increases the probability of release on the other side of the membrane, the molecule unbinds. This second type of transport process should have greater specificity than the transport of completely dissolved species that never bind to the membrane or to the interior surface of the pore.

Summary

Electroporation has been modeled by consideration of membrane electroconformational changes, with emphasis on hydrophilic pores. We recognize that we should be cautious in applying relatively simple physical models to complex biological cells. However, the common short pulse experiments that cause electroporation almost universally observe dramatic effects in artificial and cell membranes for a transmembrane voltage of 1 V. This universal behavior strongly suggests that many aspects of the onset and short-term behavior of electroporation can be described by models that involve a few key parameters. Progress to date is encouraging because reasonable quantitative descriptions of the time-dependent transmembrane voltage, the membrane conductance, and some aspects of molecular transport have been achieved. Likewise, limited but encouraging results for the interaction of weak electric fields with cells has been obtained by consideration of signal-to-noise ratio issues and the invocation of membrane enzyme electroconformational coupling. This approach has led to estimates of the minimum electric field to which cells might respond.

Acknowledgments

We thank K. T. Powell, G. I. Harrison, J. G. Bliss, D. C. Bartoletti, A. Barnett, and R. D. Astumian for many stimulating and helpful discussions. This work was supported mainly by Office of Naval Research Contract N00014-87-K-0479 and partially by National Institutes of Health Grant ES06010.

References

1. Polk, C.; Postow, E., Eds. *CRC Handbook of Biological Effects of Electromagnetic Fields*; CRC Press: Boca Raton, FL, 1986.
2. Kirschvink, J. L.; Kirschvink, A. K.; Woodford, B. J. *Proc. Natl. Acad. Sci. U.S.A.* **1992**, *89*, in press.
3. Foster, K. R.; Schwann, H. P. In *CRC Handbook of Biological Effects of Electromagnetic Fields*; Polk, C.; Postow, E., Eds.; CRC Press: Boca Raton, FL, 1986; pp 27-96.
4. Neumann, E. In *Electroporation and Electrofusion in Cell Biology*; Neumann, E.; Sowers, A.; Jordan, C., Eds.; Plenum, New York, 1989; pp 61-82.

5. Crowley, J. M. *Biophys. J.* **1973**, *13*, 711–724.
6. Cruzeiro-Hansson, L.; Mouritsen, O. G. *Biochim. Biophys. Acta* **1988**, *944*, 63–72.
7. Potts, R. O.; Francoeur, M. L. *Proc. Natl. Acad. Sci. U.S.A.* **1990**, *87*, 3871–3873.
8. Chizmadzhev, Yu. A.; Arakelyan, V. B.; Pastushenko, V. F. *Bioelectrochem. Bioenerg.* **1979**, *6*, 63–70.
9. Bach, D.; Miller, I. R. *Biophys. J.* **1980**, *29*, 183–188.
10. Abidor, I. G.; Arakelyan, V. B.; Chernomordik, L. V.; Chizmadzhev, Yu. A.; Pastushenko, V. F.; Tarasevich, M. R. *Bioelectrochem. Bioenerg.* **1979**, *6*, 37–52.
11. Weaver, J. C.; Mintzer, R. A. *Phys. Lett.* **1981**, *86A*, 57–59.
12. Sugar, I. P. *J. Physiol. (Paris)* **1981**, *77*, 1035–1042.
13. Pastushenko, V. F.; Chizmadzhev, Yu. A. *Gen. Physiol. Biophys.* **1982**, *1*, 43–52.
14. Powell, K. T.; Weaver, J. C. *Bioelectrochem. Bioelectroenerg.* **1986**, *15*, 211–227.
15. Glaser, R. W.; Leikin, S. L.; Chernomordik, L. V.; Pastushenko, V. F.; Sokirko, A. I. *Biochim. Biophys. Acta* **1988**, *940*, 275–287.
16. Barnett, A.; Weaver, J. C. *Bioelectrochem. Bioenerg.* **1991**, *25*, 163–182.
17. Tsong, T. Y.; Astumian, R. D. *Bioelectrochem. Bioelectroenerg.* **1986**, *15*, 457–476.
18. Dimitrov, D. S.; Jain, R. K. *Biochim. Biophys. Acta* **1984**, *779*, 437–468.
19. Dimitrov, D. S. *J. Membr. Biol.* **1984**, *78*, 53–60.
20. Benz, R.; Beckers, F.; Zimmermann, U. *J. Membr. Biol.* **1979**, *48*, 181–204.
21. (A) Weaver, J. C. In *Charge and Field Effects in Biosystems*; Allen, J.; Cleary, S. F.; Hawkrigde, F. M., Eds.; Plenum: New York, 1992; Vol. 3, pp 475–496. (B) Mycue, D.; Zahn, J.; Zahn, M.; Weaver, J. C. In *Proceedings of the First World Conference for Electricity and Magnetism in Biology and Medicine*; Blank, M., Ed.; San Francisco Press: San Francisco, CA, 1993.
22. Balázs, M.; Matkó, J.; Szöllösi, J.; Mátyus, L.; Fulwyler, M. J.; Damjanovich, S. *Biochem. Biophys. Res. Commun.* **1986**, *140*, 999–1006.
23. (A) Weaver, J. C. In *Proceedings of the First World Conference for Electricity and Magnetism in Biology and Medicine*; Blank, M., Ed.; San Francisco Press: San Francisco, CA, 1993. (B) Reif, F. *Fundamentals of Statistical and Thermal Physics*; McGraw-Hill: New York, 1965.
24. Benz, R.; Zimmermann, U. *Bioelectrochem. Bioenerg.* **1980**, *7*, 723–739.
25. Hibino, M.; Shigemori, M.; Itoh, H.; Nagayama, K.; Kinosita, K. *Biophys. J.* **1991**, *59*, 209–220.
26. Farkas, D. L. In *Electroporation and Electrofusion in Cell Biology*; Neumann, E.; Sowers, A. E.; Jordan, C. A., Eds.; Plenum: New York, 1989; pp 409–431.
27. Mehrle, W.; Zimmermann, U.; Hampp, R. *FEBS Lett.* **1985**, *185*, 89–94.
28. Sowers, A. E.; Lieber, M. R. *FEBS Lett.* **1986**, *205*, 179–184.
29. Chang, D. C.; Reese, T. S. *Biophys. J.* **1990**, *58*, 1–12.
30. Tsoneva, I.; Tomov, T.; Panova, I.; Strahilov, D. *Bioelectrochem. Bioenerg.* **1990**, *24*, 41–49.
31. Dimitrov, D. S.; Sowers, A. E. *Biochim. Biophys. Acta* **1990**, *1022*, 381–392.
32. Tekle, E.; Astumian, R. D.; Chock, P. B. *Proc. Natl. Acad. Sci. U.S.A.* **1991**, *88*, 4230–4234.
33. Powell, K. T.; Derrick, E. G.; Weaver, J. C. *Bioelectrochem. Bioelectroenerg.* **1986**, *15*, 243–255.
34. Weaver, J. C.; Powell, K. T. In *Electroporation and Electrofusion in Cell Biology*; Neumann, E.; Sowers, A.; Jordan, C., Eds.; Plenum: New York, 1989; pp 111–162.
35. Sugar, I. P.; Neumann, E. *Biophys. Chem.* **1984**, *19*, 211–225.

36. Weaver, J. C.; Barnett, A. In *Guide to Electroporation and Electrofusion*; Chang, D. C.; Chassy, B. M.; Saunders, J. A.; Sowers, A. E., Eds.; Academic: New York, 1992; pp 91–117.
37. Renkin, E. M. *J. Gen. Physiol.* **1954**, *38*, 225–243.
38. Karpplus, M.; Petsko, G. A. *Nature (London)* **1990**, *347*, 631–639.
39. Litster, J. D. *Phys. Lett.* **1975**, *53A*, 193–194.
40. Taupin, C.; Dvolaitzky, M.; Sauterey, C. *Biochemistry* **1975**, *14*, 4771–4775.
41. Neumann, E.; Schaefer-Ridder, M.; Wang, Y.; Hofschneider, P. H. *EMBO J.* **1982**, *1*, 841–845.
42. Pastushenko, V. F.; Chizmadzhev, Yu. A.; Arakelyan, V. B. *Bioelectrochem. Bioenerg.* **1979**, *6*, 53–62.
43. Deryagin, B. V.; Gutop, Yu. V. *Kolloidn. Zh.* **1962**, *24*, 370–374.
44. Parsegian, V. A. *Nature (London)* **1969**, *221*, 844–846.
45. Newman, J. J. *Electrochem. Soc.* **1966**, *113*, 501–502.
46. Neumann, E.; Rosenheck, K. *J. Membr. Biol.* **1972**, *10*, 279–290.
47. Potter, H. *Anal. Biochem.* **1988**, *174*, 361–373.
48. *Electroporation and Electrofusion in Cell Biology*; Neumann, E.; Sowers, A.; Jordan, C., Eds.; Plenum: New York, 1989.
49. Zimmermann, U.; Schnettler, R.; Klöck, G.; Watzka, H. *Naturwissenschaften* **1990**, *77*, 543–545.
50. Jordan, P. C. *Biophys. J.* **1983**, *41*, 189–195.
51. Jordan, P. C. *Biophys. J.* **1984**, *45*, 1091–1100.
52. Weaver, J. C.; Powell, K. T.; Mintzer, R. A.; Sloan, S. R.; Ling, H. *Bioelectrochem. Bioelectroenerg.* **1984**, *12*, 405–412.
53. Klenchin, V. A.; Sukharev, S. I.; Serov, S. M.; Chernomordik, L. V.; Chizmadzhev, Yu. A. *Biophys. J.* **1991**, *60*, 804–811.
54. Weaver, J. C. In *Mechanism of Field/Cell Interactions*; Blank, M.; Findl, E., Eds.; Plenum: New York, 1987; pp 249–270.
55. Weaver, J. C.; Astumian, R. D. *Science (Washington, D.C.)* **1990**, *247*, 459–462.
56. Robertson, B.; Astumian, R. D. *J. Chem. Phys.* **1991**, *94*, 7414–7419.
57. Eisenberg, R. S. *J. Membr. Biol.* **1990**, *115*, 1–12.
58. Teissie, J.; Tsong, T. Y. *J. Membr. Biol.* **1980**, *55*, 133–140.
59. Kinoshita, K., Jr.; Ashikawa, I.; Saita, N.; Yoshimura, H.; Itoh, H.; Nagayama, H.; Ikegami, A. *Biophys. J.* **1988**, *53*, 1015–1019.
60. Lojewski, Z.; Farkas, D. L.; Ehrenberg, B.; Loew, L. L. *Biophys. J.* **1989**, *56*, 121–128.
61. Benz, R.; Zimmermann, U. *Biochim. Biophys. Acta* **1980**, *597*, 637–642.

RECEIVED for review February 26, 1991. ACCEPTED revised manuscript November 6, 1992.

Cytochrome c_3 : Properties and Recent Insights

M. A. Cusanovich¹, J. H. Hazzard¹, and G. S. Wilson²

¹Department of Biochemistry, University of Arizona, Tucson, AZ 85721

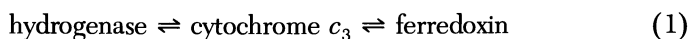
²Department of Chemistry, University of Kansas, Lawrence, KS 66045

The cytochromes c_3 from the sulfate-reducing bacteria of the genus Desulfovibrio comprise a class of c-type cytochromes that are distinguished from the more familiar mitochondrial cytochromes c in two important respects. First, cytochromes c_3 contain four heme groups, rather than one, bound to a single polypeptide of less than 120 amino acid residues. In addition, the redox potentials of the multiple hemes are very low (-165 to -400 mV) in contrast to $+260$ mV for mitochondrial cytochrome c. Importantly, the electrochemical and electrical properties of the cytochromes c_3 are unique among biological redox proteins. The cytochromes c_3 modify electrodes in a way that facilitates heterogeneous electron transfer and in dry films have the ability to change resistivity by up to 10 orders of magnitude in going from the fully oxidized to fully reduced states. The structural properties, oxidation-reduction potentials, heterogeneous and homogeneous electron-transfer kinetics, electrical properties of protein films, and the utilization of site-directed mutagenesis in understanding the structure and function of the cytochromes c_3 are discussed. The focus is on new information and insights that further our understanding of the cytochromes c_3 as well as define the issues that must be addressed to exploit fully this important and interesting protein.

THE CYTOCHROMES c_3 ARE CLASS III c-TYPE CYTOCHROMES (1) that were originally isolated in 1954 from *Desulfovibrio* (2, 3). Although widely distributed amongst the *Desulfovibrio*, cytochromes c_3 have only recently been found in other species; for example, in the purple phototrophic bacterium H1R (T. E. Meyer, personal communication) and in *Desulfuromonas acetoxi-*

0065-2393/94/0235-0471 \$08.00/0
© 1994 American Chemical Society

dans (4). Functionally, in the *Desulfovibrio*, the cytochromes c_3 mediate electron transfer between hydrogenase and the iron-sulfur protein ferredoxin, as shown schematically (5)



Reduced ferredoxin reacts with proteins that participate in the dissimilatory reduction of sulfate to sulfide; oxidized ferredoxin reacts with pyruvate dehydrogenase that catalyzes the conversion of pyruvate to acetyl CoA (phosphoroclastic reaction). In sulfate reduction, molecular hydrogen is the electron source, and in the phosphoroclastic reaction, protons are the terminal electron acceptor and hydrogenase mediates electron transfer between cytochrome c_3 and protons or molecular hydrogen.

Cytochrome c_3 is distinct from the class I c -type cytochromes (for example, mitochondrial cytochrome c) and class II c -type cytochromes (for example, cytochrome c') in terms of out-of-plane ligation. The class III cytochromes have histidine in both the fifth and sixth heme coordination positions versus his-met (class I) or his-vacant (class II) and also differ in the number of covalently bound heme groups per peptide chain: four heme groups for class III versus one heme group for classes I and II. Moreover, the cytochromes c_3 have a number of unusual properties that make them valuable experimental materials for understanding biological electron transfer.

To date, the cytochromes c_3 from four species have been extensively studied in terms of both structural and physicochemical properties. These species are cytochrome c_3 from *Desulfovibrio vulgaris* Miyazaki (Miyazaki), *Desulfovibrio vulgaris* Hildenborough (Hildenborough), *Desulfovibrio desulfuricans* Norway (Norway), and *Desulfovibrio gigas* (Gigas). The structural properties, oxidation-reduction potentials, site-directed mutagenesis, electrical properties, and homogeneous and heterogeneous redox kinetics of cytochrome c_3 will be discussed, and the prospects for future insights will be described.

Structure

The amino acid sequences of four examples of cytochromes c_3 (Miyazaki, Hildenborough, Gigas, and Norway) are presented in Figure 1. A number of features are notable. Although there is substantial amino acid sequence homology between Hildenborough and Miyazaki cytochrome c_3 (85%), there is much less homology among the other cytochromes c_3 . For example, Norway and Miyazaki cytochrome c_3 have only 35% sequence homology.

The amino acid sequence identity matrix for cytochromes c_3 from six *Desulfovibrio* species are as follows:

- Gigas
- 53 Miyazaki
- 53 85 Hildenborough
- 31 39 37 *D. desulfuricans* El Agheila
- 32 39 37 67 *D. saleigens* British Guiana
- 30 35 34 40 44 Norway

The percent identity in amino acid sequence is given using the insertions and deletions shown in Figure 1. Only a small number (25) of sequence positions are conserved among the four sequences shown. However, 16 of these 25 are associated with heme binding (cys and his); hence only nine side chains are conserved. This lack of amino acid sequence homology among the cytochromes c_3 as a family allows for substantial differences in physicochemical properties while retaining structural homology.

Figure 1 also provides information on heme attachment. The heme numbering corresponds to heme designation in the Miyazaki cytochrome c_3 crystal structure. For two of the four hemes (heme III and heme II), the heme binding sequence is cys followed by two amino acids and then cys-his. This binding sequence is typical of *c*-type cytochromes: The histidine serves as one of the axial ligands. However, the other two hemes have the unusual sequence cys followed by four, rather than two, amino acids and then cys-his. Moreover, it is quite apparent that the distal histidine, because of its distance from the heme binding site in the amino acid sequence (Figure 1), plays a key role in determining the three-dimensional structure of the class III cytochromes.

As far as electrostatics are concerned, Gigas and Norway cytochromes c_3 are acidic (pI = 5.2) (6) and neutral (pI = 6.9) (7), respectively, whereas Miyazaki and Hildenborough cytochrome c_3 are basic (pI = 10.5) (6). These electrostatic properties result from a net apoprotein charge of +8, +8, +4, and +4 for Miyazaki, Hildenborough, Norway, and Gigas cytochrome c_3 , respectively. Based on amino acid composition sequence and the fact that the four hemes provide eight propionates, we can infer that at least four propionates should be ionized at a pH 7.0 to yield the observed isoelectric points, assuming that some of the uncertainties in the Gigas cytochrome c_3 sequence are acidic. It is also notable that reduction of all four hemes of the cytochrome c_3 is accompanied by a protein net charge decrease of 4 because the formal heme iron charge will change from +1 to 0. This last observation suggests that ionic strength could have a very large effect on the redox

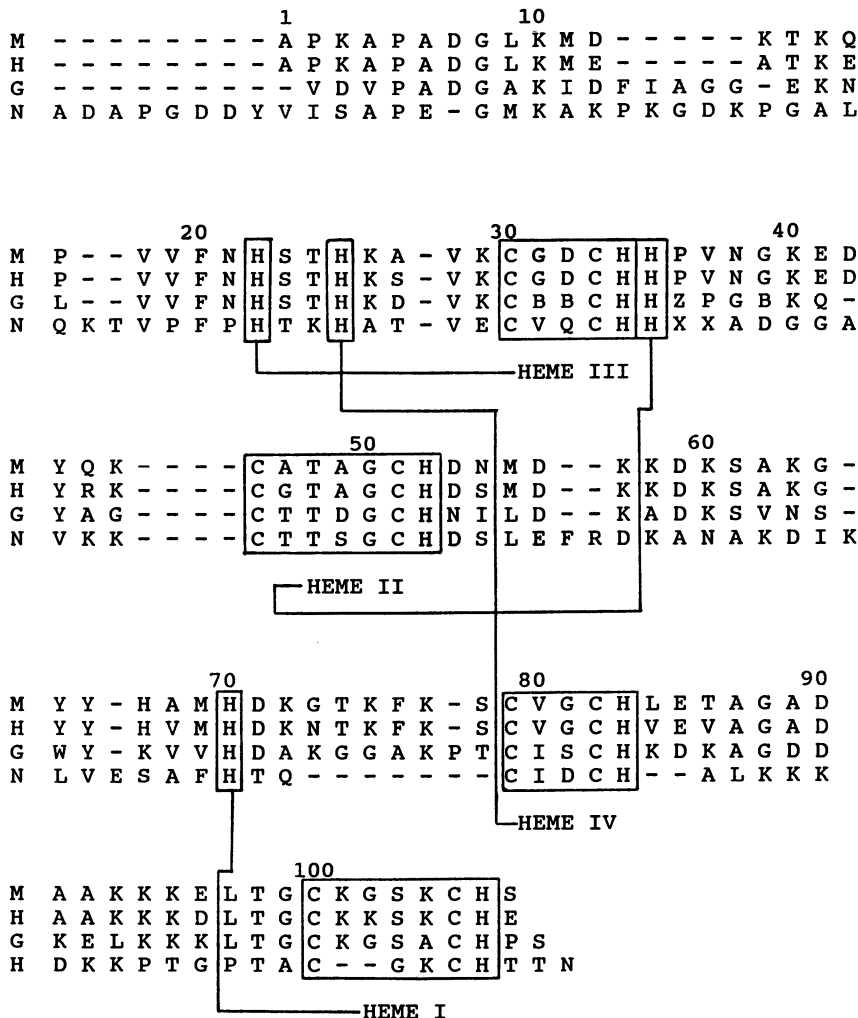


Figure 1. Cytochrome c_3 amino acid sequences. Amino acid sequences are given for Miyazaki (M), Hildenborough (H), Gigas (G), and Norway (N). Numbering is for Miyazaki cytochrome c_3 . Heme labeling is consistent with assignments from the Miyazaki cytochrome c_3 three-dimensional structure (Figure 2).

potential of the cytochrome c_3 hemes and that partial reduction should greatly influence subsequent reduction steps.

The three-dimensional structures of the four cytochromes described here are known (8–10; N. Yasuoka, personal communication). The Miyazaki cytochrome c_3 X-ray structure is solved to the highest resolution (1.8 Å) (8). Because the cytochromes c_3 are structurally homologous, only the Miyazaki

cytochrome c_3 structure will be discussed in detail. Figure 2 presents three different stereo representations of the Miyazaki structure. In the top panel, a ribbon diagram shows the backbone folding and heme positioning, which establishes the relative orientation of the four hemes and their relation to the molecular surface. The heme numbering is consistent with that of Figure 1 and will be used throughout this discussion. A space-filling representation in the middle panel of Figure 2 demonstrates the exposure of heme II (in green) to solvent. The axial histidine ligands (magenta) are clearly visible. Hemes I and IV are partially visible on the left and right, respectively. Oxygen atoms of glutamic acid and aspartic acid residues are identified by red (heme propionate oxygens are pink) and lysine (NZ) by blue. Some of these residues participate in salt bridges or in hydrogen bonding and, thus, do not contribute to the surface electrostatic field, which is shown in the bottom panel. This representation illustrates the electrostatic fields that would be experienced by an approaching reactant at an ionic strength of 0.01 M and an energy of 2 kT, and is calculated using the modified Tanford–Kirkwood method of Matthew (11, 12). The positive fields are blue, and the negative fields are red. A number of structural features are notable. The iron-to-iron distances vary from 17.8 to 11.0 Å, and the angles between the heme planes vary from 22 to 89° (Table I) (8).

As can be seen in the top panel of Figure 2, there is no obvious regular relationship among all four hemes, although interheme planar angles of near 90° (80–89°) are most common (Table I). The exposure of each of the hemes to solvent in terms of accessible surface area is 127, 168, 136, and 136 Å² for hemes I–IV, respectively (8). Two points are apparent. First, relative to the class I c -type cytochromes where the accessible surface area is typically 32–49 Å², the cytochrome c_3 heme exposure is quite large. Second, heme II is substantially more exposed than the other three hemes, which suggests that it may have some unique properties. In terms of electrostatics, it is quite apparent that the Miyazaki cytochrome c_3 has an asymmetric charge distribution and the region in the vicinity of heme I and the C-terminus has a large positive field. This asymmetric electrostatic field may play an important role in the functional and electrical properties of the cytochrome c_3 as we shall discuss later. Lysine residues at positions 15, 57, 58, 72, 94, 95, and 101 make up much of the electrostatic field in the heme I and C terminus region. Reference to the amino acid sequences given in Figure 1 shows that positive charges at positions 15, 57, 95, and 101 are conserved among Miyazaki, Hildenborough, and Gigas cytochrome c_3 , which suggests that the asymmetrical charge distribution is also conserved. This feature persists despite the fact that Miyazaki and Gigas cytochrome c_3 have net protein charges of opposite sign. In contrast, a comparison of Miyazaki and Norway cytochrome c_3 sequences yields conserved lysines only at positions 15 and 58. Thus, the positive field observed for the Miyazaki cytochrome is absent in the Norway cytochrome. Indeed, the calculated electrostatic map for the Norway cy-

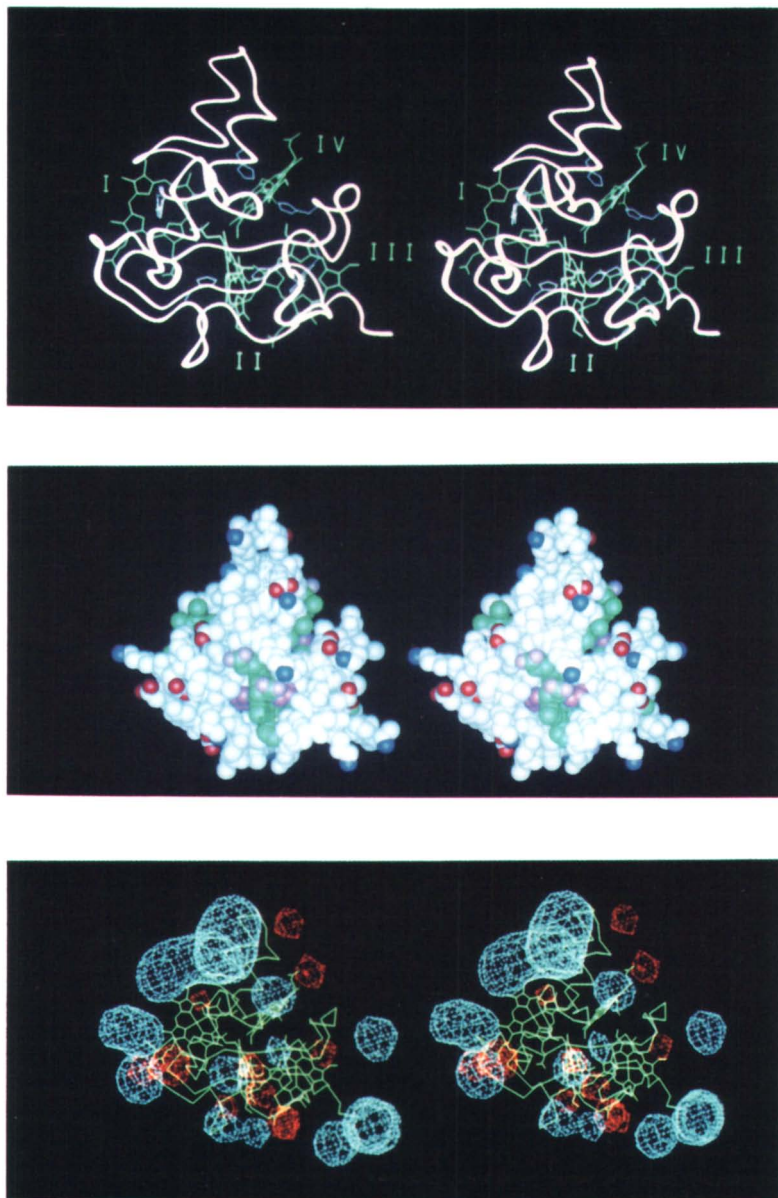


Figure 2. Stereo views of Miyazaki cytochrome c_3 showing the C backbone folding pattern (top panel), the space-filling view of the relative solvent exposure of heme II (middle panel), and the distribution of the electrostatic fields on the protein surface (lower panel). The views in all three panels are of the same x, y, z orientation as displayed on an Evans and Sutherland model PS390 graphics system using software packages Insight (top and middle) and Frodo (lower).

Table I. Iron–Iron Distances and Heme–Heme Angles for Miyazaki Cytochrome c_3

Heme	I	II	III	IV
I		16.4 Å	17.8 Å	12.0 Å
II	73°		12.2 Å	15.8 Å
III	22°	88.7°		11.0 Å
IV	80°	59.1°	80.3°	

NOTE: The upper right quadrant gives Fe–Fe distances. The lower left quadrant gives angles between heme planes. The heme nomenclature is that used in Figures 1 and 2.

SOURCE: Data are taken from reference 8.

tochrome is also asymmetric; all four hemes are in a negative field, and only a small positive field remains at the C terminus.

In summary, the cytochromes c_3 are structurally homologous and have a compact structure with little secondary structure. Clearly, the folding is dictated by the presence of the four six-coordinate hemes. In general, the cytochromes c_3 have an asymmetric charge distribution, and all four hemes are substantially more exposed to solvent than in the more typical class I high potential c-type cytochromes.

Oxidation–Reduction Potentials

A characteristic of the cytochromes c_3 is a very low oxidation–reduction potential. Moreover, it is obvious from the multiheme nature of these cytochromes that the redox properties should be complex. In the simplest situation, four individual redox potentials could be expected, one for each heme. In addition to the axial ligands on the hemes, a number of factors are anticipated to influence the individual heme redox potentials. First and foremost, the environment of each heme can exert an influence on its oxidation–reduction potential. This influence will be manifested in two ways: the packing of the specific amino acid side chains about each heme and the extent of solvent exposure of each heme. It is quite apparent from the structural data (Figures 1 and 2) that the four hemes, which are in nonequivalent environments, are expected to have different oxidation–reduction potentials. Moreover, at least with Miyazaki cytochrome c_3 , one of the hemes (heme II) is substantially more exposed to solvent, which may result in a lower oxidation–reduction potential (13). Finally, it is apparent that in a small molecule that contains four hemes within close proximity (< 18 Å), heme–heme interactions, principally as a result of electrostatic interactions, are likely to influence oxidation–reduction potentials (14). Indeed, on electrostatic grounds the redox state of one heme should influence another. This influence results from the fact that addition of electrons changes the formal

charge due to each heme iron from plus to zero, so the electrostatic field experienced by adjacent hemes will be significantly altered.

In biological redox proteins containing two or more redox centers two types of oxidation–reduction potentials can be defined. The formal potential of the molecule will result in a *macroscopic redox potential* for each of the four hemes, which reflects the fact that five macroscopic states exist: S_0 , fully oxidized; S_1 , one electron reduced; S_2 , two electron reduced; S_3 , three electron reduced; and S_4 , fully reduced (Figure 3) (14). However, each individual heme has a definable oxidation–reduction potential (the *microscopic potential*), which may vary depending on the redox state of its neighbors. As shown in Figure 3 for cytochrome c_3 , a total of 32 microscopic potentials may exist. These potentials can be thought of as descriptions of the distribution of electron density as electrons partition among the four hemes. From the microscopic potential, an interaction potential between any two hemes (heme i and heme j) can be defined as the change in the midpoint redox potential of heme i caused by the oxidation of heme j . For example, the interaction potential between the hemes with the two highest macroscopic potentials, heme 1 and heme 2, is the difference between the redox

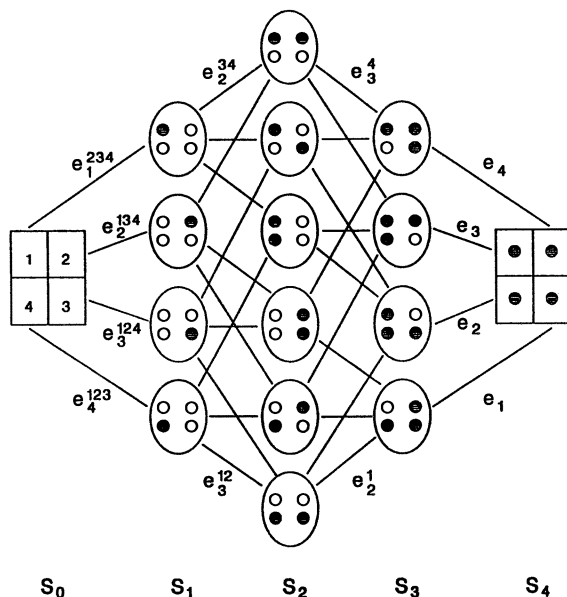


Figure 3. Electron distribution for cytochrome c_3 . S_0 – S_4 define the five macroscopic states (see text). The 16 microscopic states are shown. Open circles represent oxidized heme, and solid circles represent reduced heme. The microscopic redox potentials of heme i are given by e_i^{jkl} where j, k, l represent hemes that remain oxidized. For clarity only, 12 of the 32 microscopic redox potentials are labeled.

potential of heme 1 (e_1) and the redox potential of heme 1 when heme 2 is oxidized (e_1^2), which is termed I_{12} (15). The nomenclature used here is from Santos et al. (15) and is illustrated in Figure 3. The heme notation does not relate to structural assignments (Figures 1 and 2) but to redox potential only.

Table II summarizes the macroscopic redox potentials for the four cytochromes c_3 . As expected from the strong amino acid sequence homology, the Miyazaki and Hildenborough cytochromes c_3 have redox potentials that are very similar and have a redox potential span of 110–120 mV between heme 1 and heme 4. In sharp contrast, Norway cytochrome c_3 has a redox potential span of approximately 235 mV. Clearly, the differences in macroscopic redox potentials among the various cytochromes c_3 result from the different amino acid sequences and, thus, different heme environments. To date, little can be said about the specific reasons for differences in macroscopic redox potentials among the cytochromes c_3 , but in view of the large amount of structural information that is accumulating, much progress can be expected in the future.

In terms of the microscopic potentials, the interaction potentials are of particular interest because they provide information on the interaction of the individual hemes with each other (15–19). Table III presents interaction

Table II. Cytochrome c_3 Macroscopic Oxidation–Reduction Potentials

Source	E'_0 (mV) ^a				Reference
	1	2	3	4	
Miyazaki	–260	–312	–327	–369	14
Hildenborough	–263	–321	–329	–381	16
Norway	–165	–305	–365	–400	17
Gigas	–235	–235	–306	–315	18

^a Potentials referred to the normal hydrogen electrode at pH values near 7.

Table III. Interaction Potentials from Microscopic Redox Potentials

Interaction Potentials (mV)	Miyazaki Cytochrome c_3 ^a pH 7.1	Gigas Cytochrome c_3 ^b pH 7.2
I_{12}	5	19
I_{13}	–21	–26
I_{14}	–35	6
I_{23}	43	42
I_{24}	–11	–24
I_{34}	–7	–18

^a Reference 19.

^b Reference 15.

potentials for the Miyazaki and Gigas cytochromes. Given the very different macroscopic potentials, the similarities between the Gigas and Miyazaki interaction potentials are striking. Only I_{14} shows a different sign, and the actual values of the other interaction potentials are quite similar given the precision of these difficult measurements.

Electrochemistry cannot provide direct information about the individual hemes and, thus, a spectroscopic technique is needed. In monitoring the redox state of each heme during titration to produce diamagnetic Fe(II), it is possible to take advantage of the paramagnetic properties of the Fe(III) heme core using NMR spectroscopy (15, 19, 20). This methodology has also been used to establish a lower boundary for the rate constant for intramolecular electron transfer in cytochrome c_3 . With Gigas the intramolecular electron-transfer rate constant must be greater than 10^5 s^{-1} (15), and recent work suggests a rate constant of approximately 10^8 s^{-1} for Miyazaki cytochrome c_3 (K. Kimura, S. Nakajima, and K. Niki, personal communication). The rate of intermolecular electron transfer for Miyazaki cytochrome c_3 is much lower, which makes it possible to distinguish intramolecular from intermolecular processes (19). This distinction will prove to be a valuable property for fundamental studies. Moreover, using NMR, Fan et al. (14) concluded that heme 1 (the highest potential heme) in the redox studies can be related to heme I in the crystal structure, and that Heme 3 in the macroscopic redox titrations is heme IV in the structure. Thus, we will adopt the nomenclature heme I(1) and heme IV(3) to relate macroscopic redox potential to structure.

Although complex, the ability to assign microscopic redox potentials and to determine interaction potentials sets the stage for the analysis of the redox data in terms of the structure of cytochrome c_3 . This approach should greatly expand our understanding of biological redox potentials and facilitate efforts to exploit and understand the electrochemical, electrical, and kinetic properties of cytochrome c_3 .

Heterogeneous Electron Transfer

A striking feature of the cytochromes c_3 is their ability to modify an electrode surface in such a way as to facilitate subsequent electron transfer (21). Among the different cytochromes studied to date, only cytochrome c_3 can be oxidized and reduced with high electrochemical reversibility at an electrode-solution interface without any mediator or promoter (16, 21). This reversibility contrasts with the more usual situation in which the protein adsorbs on the electrode surface, thus preventing further electron transfer. Alternatively, rather slow ($k^0 < 10^{-3} \text{ cm/s}$) heterogeneous electron transfer rates are observed. Using Miyazaki cytochrome c_3 and a mercury electrode on which specific adsorption of cytochrome c_3 is known to occur, the ad-

sorbed film of the protein remains electrochemically active and continues to facilitate heterogeneous electron transfer between the electrode and the soluble protein.

Because the heterogeneous electron-transfer rate was extremely fast, it was not possible to evaluate it by conventional techniques such as cyclic voltammetry. Instead, the galvanostatic double pulse method was employed (21). From these measurements, a heterogeneous rate constant of 1.2 cm/s ($\alpha = 0.48$) was obtained. To our knowledge, this is the first example of a directly measured protein heterogeneous rate constant of such a large magnitude. Differential capacitance measurements suggest that monolayer coverage of cytochrome c_3 is achieved and that electron transfer occurs through the adsorbed protein layer that possesses essentially "native" properties. The electrode is therefore "modified" by the electroactive species itself. To consider whether this kind of model is reasonable, it is necessary to estimate the rate of electron transfer through the film. From NMR measurements, the intra- and intermolecular electron-transfer rate constants can be estimated. These values are $k_{\text{intra}} = 1.5\text{--}7.8 \times 10^8 \text{ s}^{-1}$ and $k_{\text{inter}} = 1 \times 10^4 \text{ M}^{-1}/\text{s}$, respectively (K. Kimura, S. Nakajima, and K. Niki, personal communication). The upper limit for the heterogeneous rate constant can be estimated from Marcus theory (eq 2):

$$k^0 \leq Z_{\text{hetero}}(k_{\text{ex}}/Z_{\text{ex}})^{1/2} \quad (2)$$

where Z_{hetero} and Z_{ex} are the collision frequencies of a molecule with an electrode (heterogeneous) and in solution (homogeneous), respectively (22). In this case $k_{\text{ex}} = k_{\text{inter}}$, and the estimation concludes that $k^0 \leq 3 \text{ cm/s}$. The steric and molecular association terms are assumed to be unity.

An electron-transfer reorganization energy, λ , of 0.94 eV (21) was also calculated from Marcus theory (22). This value is very close to that of the Fe(III)–Fe(II) system in acidic medium (23) and to cytochrome c (0.7 eV) and cytochrome b_5 (1.2 eV) from measurements of self-exchange (24). As far as we are aware, this is the first example of a consistent λ value for a heme protein measured electrochemically and by self-exchange measurements.

Recently it was proposed that the apparently slow heterogeneous electron-transfer rates for such proteins as cytochrome c , cytochrome b_5 , plastocyanin, and ferredoxin are an artifact of the experimental approach (25). Instead of assuming that protein molecules react at a planar and essentially homogeneous surface, it is assumed instead that movement of the protein occurs predominantly by radial diffusion to very small, specific sites. These sites are presumed to facilitate very rapid electron transfer at the reversible potential while the rest of the surface remains inactive. Thus, the modified electrode surface behaves like an array of microelectrodes. If this theory is used to treat previous data, much higher electron-transfer rate constants are obtained. Although this theory deserves more detailed scrutiny, it may serve

as a contrast to the case of cytochrome c_3 where the entire surface is “active” and, therefore, classical models of macroscopic planar or spherical diffusion can be applied.

Adsorbed layers of cytochrome c_3 have also been used to facilitate electron transfer of molecules that otherwise would not yield high electron-transfer rates. Facilitated electron transfer has been observed for flavodoxin and ferredoxin on cytochrome c_3 modified basal plane pyrolytic graphite (26).

Surface Spectroscopy

Because cytochrome c_3 films have unique properties, an effort has been made to study such deposits by spectroscopic techniques, especially surface-enhanced Raman spectroscopy (SERS). When Miyazaki cytochrome c_3 is adsorbed on a suitably treated silver electrode, SERS spectra may be obtained. Marker bands at 1380 and 1375 cm^{-1} have been used to characterize the redox state of the adsorbed protein (27). If the potential applied to the electrode is varied, an apparent redox potential for the adsorbed film can be measured. A value of -260 mV versus the normal hydrogen electrode (NHE) was obtained. This value corresponds to the highest of the four macroscopic redox potentials for Miyazaki cytochrome c_3 (-260 mV). Because the SERS effect is most pronounced for the interactions of the protein with the surface over distances of about 5 Å, it may be assumed that the observed interaction is dominated by the heme closest to the surface. This conclusion is consistent with the environment around this heme, which is least “exposed” and is also in a high lysine environment—conditions likely to promote chemisorption and interaction because the electrode is operated on the negative side of the point of zero charge. Based on the structural information available, this would suggest that cytochrome c_3 is oriented on the surface and heme I (Figure 1) is the closest to the surface. In contrast, if silver colloid is deposited on a Miyazaki cytochrome c_3 film adsorbed on a silver electrode, the SERS signal is dominated by the colloid interaction and a much lower (-300 mV versus NHE) potential is obtained. This lower potential would fall in the middle of the range of macroscopic potentials for Miyazaki cytochrome c_3 . It is, therefore, likely that the colloid measures all heme sides, whereas the silver electrode itself reveals more specific interactions. The foregoing arguments assume that interaction of the silver with the protein does not perturb the redox potentials, an assumption that may not be valid. The resonance Raman spectrum of Hildenborough cytochrome c_3 adsorbed on a highly oriented pyrolytic graphite electrode is very weak. However, when silver colloid is deposited on the adsorbed protein, a signal nearly as large as that previously noted is observed. Though these results are preliminary, they indicate the possibility of determining apparent redox

potentials by following the intensity of marker bands as a potential is applied to a substrate (electrode surface) that is essentially SERS-inactive. The use of SERS to study the properties of adsorbed films of cytochrome c_3 is being pursued at the present time.

It should be noted that resonance Raman studies of cytochrome c_3 show evidence of band splittings in partially reduced solutions (28). This observation suggests either nonequivalence of the four hemes or an exciton-like splitting of vibrational modes. Heme-heme interactions are clearly important.

Electrical Properties of Protein Films

Films of cytochrome c_3 show more than 10 orders of magnitude change in resistivity (10^{12} – $57 \Omega\text{-cm}$) when they pass from the fully oxidized to the fully reduced state (29). There have been a number of studies of electrical conductivity of proteins and protein films. This conductivity can result from electric-field-induced diffusion of charge carriers: cations and anions, protons, electrons, and holes. In the case of cytochrome c_3 , the large difference in resistivity can be due to a change or changes in polarization energy, changes in electronic states of heme clusters, and interactions between hemes. The presence of adsorbed water, which can comprise a significant part of the protein volume, can have a strong influence on the electrical properties. Rosenberg (30) measured the conductivity of hemoglobin as a function of adsorbed water and explained the increase in conductivity as a result of a change in dielectric constant coincident with absorption of water. However, this explanation is controversial. Eley (31) has suggested that conduction in “wet” protein is ionic. Takashima and Schwan (32), who studied crystalline powders of proteins, found that the increase in dielectric constant is proportional to the increase in adsorbed water until the first adsorption layer is completed. Above two or three layers, the dielectric constant does not increase further. Presently, it is assumed (30) that below 15% adsorbed water, the conductivity of a protein is almost entirely electrical in nature. Electronic conduction can be intrinsic or extrinsic and can be promoted by charge transfer or by tunneling (33). Previous studies suggested that some hydrated proteins can behave like semiconductors. As a semiconductor, a protein can be expected to show increasing conductivity with increasing temperature. Oxidized cytochrome c_3 shows exactly the opposite effect, which suggests behavior like an ionic conductor. However, reduced cytochrome c_3 in dry films does show an increase in conductivity with an increase in temperature that is consistent with a semiconductor (34). Some particular changes of resistivity of cytochrome c_3 with temperature have been observed. Below the temperature of 292 K and under 200-kPa hydrogen pressure, ferrocyanochrome c_3 has an activation energy of 2.15 eV, which reflects the semiconductor nature of the protein. Above this temperature,

both ferri- and ferrocycytochrome forms are believed to exist (34). Above a critical temperature of 346 K, the activation energy drops to 1.55 eV. This drop causes the difference in resistivity between the oxidized and reduced forms. At the present time, the behavior of cytochrome c_3 in dry films is not well understood in molecular terms. However, an in-depth understanding of the electrical properties of cytochrome c_3 may be most useful in preparing biological materials for applications in bioelectronics.

Homogeneous Electron Transfer

The kinetics of oxidation and reduction of the cytochromes c_3 provide a means to better understand their physicochemical and functional properties. However, because of the complexity of multiple hemes, low redox potentials, and sensitivity to molecular oxygen, kinetic studies have been limited compared with other c -type cytochromes and redox proteins. Nevertheless, some information is available that provides insight into the mechanism of action of cytochrome c_3 .

The reduction of both Hildenborough and Norway cytochrome c_3 by $S_2O_4^{2-}$ ($SO_2^{\bullet-}$) is biphasic, and both phases are second order ($SO_2^{\bullet-}$ is the reactive species) (35, 36). At pH 9.1 the two kinetic phases are approximately equal in magnitude, which suggests that the four hemes can be divided into two groups of two, with rate constants of 6.8×10^6 and 2.1×10^6 M^{-1}/s , respectively (35). At pH 7.0 the fast phase accounts for 86% of the reaction with Norway cytochrome c_3 ($k = 1 \times 10^7$ M^{-1}/s) and 72% with Hildenborough cytochrome c_3 ($k = 3.2 \times 10^6$ M^{-1}/s) (36). The slow phase was found to be 10- to 20-fold smaller than the fast kinetic phase at pH 7. The problem is that the biphasic kinetics suggest a slow intramolecular electron transfer. This result is in conflict with the NMR data that indicate fast intramolecular electron transfer (15, 19). Dithionite is notoriously difficult to use and causes a variety of difficulties. In view of foregoing difficulties, the NMR results, and (as will be shown) the very different results with other reactants (including the physiological reactant ferredoxin), it is probably best to view the dithionite results as an artifact.

Using the methylviologen cation radical ($MV^{\bullet+}$) formed by pulse radiolysis, monophasic kinetics of cytochrome reduction are observed with a rate constant of 4.5×10^8 M^{-1}/s (1.1×10^8 M^{-1}/s on a per heme basis) at pH 8.0 with the Hildenborough cytochrome (36). This very fast second-order process approaches the diffusion controlled limit. Moreover, the reverse reaction can be estimated to be 7.8×10^4 M^{-1}/s , which suggests that the reaction takes place primarily with the highest potential heme (the $\Delta E'_0$ between heme I and $MV^{\bullet+}$ is 190 mV, consistent with an equilibrium constant of approximately 10^3). Interestingly, the kinetics with $MV^{\bullet+}$ are ionic strength dependent, which is consistent with a plus-plus interaction,

and suggest a net charge of $+4.7 \pm 0.7$ on Hildenborough cytochrome c_3 , which is a result consistent with that expected from the isoelectric point. Moreover, the $MV^{\bullet+}$ results are consistent with fast intramolecular electron transfer, as predicted with NMR.

Recently we carried out kinetic studies with Hildenborough and Miyazaki cytochrome c_3 using deazariboflavin semiquinone (dRf^\bullet), $MV^{\bullet+}$, and propylene diquat ($PDQ^{\bullet+}$), produced by laser flash photolysis, as reductants (37). Initially, all three reactions were accurately second order, consistent with all hemes being reduced with the same rate constant or with a single site reduced, followed by fast intramolecular electron transfer to reduce the remaining three hemes. However, by measuring reduction kinetics with cytochrome c_3 poised at different extents of reduction, the kinetics of reduction of individual hemes could be resolved. Thus, reduction of cytochrome c_3 in approximately 5% steps and application of the known macroscopic redox potentials (*see* previous section) enabled calculation of the concentration of each heme (c_i) at each stage of reduction. The plot of k_{obs} versus percent reduction can thereby be fitted to solve for the rate constant for each heme (k_i):

$$k_{obs} = \sum c_i k_i \quad (3)$$

Using the macroscopic potentials of Hildenborough cytochrome c_3 at low ionic strength (16 mM), the rate constant for reduction of the high potential heme by dRf^\bullet is $1 \times 10^9 \text{ M}^{-1}/\text{s}$ and for the other three hemes is $4.2 \times 10^8 \text{ M}^{-1}/\text{s}$. Similarly, for Miyazaki cytochrome c_3 rate constants of 8×10^8 and $5.2 \times 10^8 \text{ M}^{-1}/\text{s}$ were obtained. With $PDQ^{\bullet+}$, the lowest and highest potential hemes have the same kinetics ($k_1 = k_4 = 1.6 \times 10^8 \text{ M}^{-1}/\text{s}$) and are resolvable from the two intermediate potential hemes ($k_2 = k_3 = 0.6 \times 10^8 \text{ M}^{-1}/\text{s}$) for Hildenborough cytochrome c_3 . Moreover, the reduction kinetics with $MV^{\bullet+}$ and $PDQ^{\bullet+}$ are ionic strength dependent and the rate constant increases with increasing ionic strength as expected for a plus-plus electrostatic interaction. However, we find that the reduction kinetics with dRf^\bullet are also ionic strength dependent, which is unexpected because dRf^\bullet is uncharged under the experimental conditions used. This unexpected result establishes that electrostatic analysis of the cytochromes c_3 is complicated by an effect of ionic strength on the redox potential of one or more hemes or an ionic-strength-induced structural change. Nevertheless, results to date establish that by controlling the driving force (i.e., redox potential of the reductant), the electrostatics (charge on the reductant as well as ionic strength), and the extent of reduction of cytochrome c_3 , the interaction domains of individual hemes can be probed. This type of approach has been applied to a wide variety of redox proteins to yield information on the topology and electrostatics of their molecular surface (38, 39). Clearly, the cytochromes c_3 are more

complex than systems containing a single prosthetic group, but they are amenable to analysis.

Based on our kinetic analysis and the finding that the lowest potential heme is either as reactive as the intermediate potential hemes (dRf^\bullet) or more reactive ($PDQ^{\bullet+}$), we can conclude that the low potential heme is the most exposed heme (heme II, Figure 2). This assignment is supported by the fact that solvent exposure tends to stabilize the oxidized form of hemes relative to the reduced form and results in a lower midpoint potential (13). Thus, completing the relation of redox potential to structure [heme I(1) and heme IV(3)], we can make additional assignments: heme II(4) and, by deduction, heme III(2). This relationship between heme macroscopic redox potential and structure should greatly facilitate future kinetic studies that relate structure to function. These assignments differ from those reported for the Norway cytochrome based upon EPR measurements (40), where the highest potential heme is heme IV, followed by heme I(2) and heme III(3). The only consistency between the Norway and Miyazaki heme-redox potential assignments is for heme II, which has the lowest redox potential. Although the specific reasons for these differences are not yet understood, the apparent lack of agreement is not surprising in light of the low sequence homology.

Cytochrome c_3 can form stable complexes with its physiological reactant ferredoxin (dissociation constant on the order of $1 \mu M$) (41). The reactions of oxidized ferredoxin with reduced cytochrome c_3 and reduced ferredoxin with oxidized cytochrome c are rapid ($> 10^7 M^{-1}/s$) (36). Moreover, electron transfer within the ferredoxin-cytochrome c_3 complex can be measured and is approximately $150 s^{-1}$ (36). Recently, hypothetical complexes between cytochrome c_3 and ferredoxin were prepared using molecular graphics (41). Complementary charge interactions were found that are consistent with relatively strong binding constants at low ionic strength. Moreover, no severe steric restrictions are found that prevent relatively close approach of prosthetic groups. Although not definitive, computer-generated models provide a basis for designing experiments to elucidate the interactions mediating complex formation.

The kinetic studies completed to date support the notion of rapid intramolecular electron transfer. Most importantly, kinetic studies establish that under appropriate conditions the kinetics of individual hemes can be probed. However, to exploit fully the cytochrome c_3 system, we need a detailed understanding of the perturbations caused by changing the ionic strength. This area will be a major focus of future studies.

Site-Directed Mutagenesis

An important vehicle to exploit and understand the unique properties of the cytochromes c_3 is site-directed mutagenesis. This approach allows perturba-

tion of specific features of cytochrome c_3 . In combination with structural studies (X-ray and NMR), redox titrations, kinetic properties, and electrical properties, site-directed mutagenesis can be employed as a powerful tool for elucidating the role of specific amino acid side chains. To this end, we recently cloned and expressed cytochrome c_3 from Hildenborough (42). The Hildenborough gene was isolated some time ago (43), but *Desulfovibrio* is not a convenient host for site-directed mutagenesis. Hildenborough cytochrome c_3 can be expressed in *E. coli*, but only the apoprotein is produced (44). We have now expressed Hildenborough cytochrome c_3 in *Rhodobacter sphaeroides*, where it is properly processed and has properties identical with wild-type cytochrome c_3 (42).

Mutants are currently being prepared to alter the properties of cytochrome c_3 . To illustrate this approach, several examples can be described: replacement of his-70 by met and ala, substitution of lys-15 with asp, and mutation of phe-20 to leu. Replacement of his-70 will alter the ligation of heme I(1) and force high spin (ala substitution) or high potential (met substitution). These changes should substantially alter the redox potential of heme I(1) and thus affect kinetic and electrical properties. Similarly, replacement of lys-15 by asp will alter the positive electrostatic field in the vicinity of heme I(1). This mutation should affect the ability of cytochrome c_3 to interact on metal surfaces and may alter its properties in dry films. Phe-20 is conserved in the amino acid sequence of all tetraheme *Desulfovibrio* cytochromes c_3 and is positioned between the two intermediate redox potential hemes, heme III(2) and heme IV(3). Thus, this mutation may have profound effects on intramolecular electron transfer in cytochrome c_3 . Obviously, a large number of mutations can be prepared that may play critical roles in understanding the cytochromes c_3 and addressing the questions posed here.

Summary

Although complex, the cytochromes c_3 provide the opportunity to obtain information that will greatly extend our knowledge of biological electron transfer and the interaction of redox centers in multiheme proteins. Moreover, because of unique electrochemistry and electrical properties, the cytochromes c_3 provide the opportunity to develop a system useful as a model for bioelectronic devices. Much research remains to be done to understand fully the redox properties of the cytochromes c_3 . However, the data discussed clearly define interesting and important issues, which include (1) the paths by which electrons move between hemes; (2) how electrons enter and exit the cytochrome c_3 molecule during physiological electron transfer; (3) the nature of the factors that control the interaction potentials between hemes; (4) the factors responsible for the observed behavior on metal surfaces; and, importantly, (5) the specific molecular features responsible for the behavior of

cytochrome c_3 in dry films. From the structural data discussed here, an intuitive model can be described that may explain some of the properties of the cytochromes c_3 . Given the asymmetric charge distribution on the cytochrome c_3 surface (Figure 2) and the close proximity of the metal centers within the molecule, it is plausible that the molecule can orient on metal surfaces or in films in an ensemble of plus-minus interactions that create what could be viewed as an oriented heme (Fe) wire. Although much more work must be done to prove this concept, it does provide a basis for experimental design.

Acknowledgment

This work was supported by a grant from the Office of Naval Research.

References

1. Ambler, R. P. In *From Cyclotrons to Cytochromes*; Robinson, A. B.; Kaplan, N. O., Eds.; Academic: New York, 1982; pp 263–280.
2. Postgate, J. R. *Biochem. J.* **1954**, *56*, xi–xii.
3. Ishimoto, M.; Koyama, J.; Nagai, Y. *Bull. Chem. Soc. Jpn.* **1954**, *27*, 564–565.
4. Ambler, R. P.; Bruschi, M.; LeGall, J. *FEBS Lett.* **1971**, *18*, 347–350.
5. Suh, B. J.; Akagi, J. M. *J. Bacteriol.* **1969**, *99*, 210–215.
6. Postgate, J. R. *The Sulphate Reducing Bacteria*, 2nd ed.; Cambridge University Press: Cambridge, U.K., 1984; pp 74–75.
7. Hatchikian, E. C.; Papavassiliou, P.; Bianco, P.; Haladjian, J. *J. Bacteriol.* **1984**, *159*, 1040–1045.
8. Higuchi, Y.; Kusunoki, M.; Matsuura, Y.; Yasuoka, N.; Kakudo, M. *J. Mol. Biol.* **1984**, *172*, 109–139.
9. Haser, R.; Pierrot, M.; Frey, M.; Payan, F.; Astier, J. P.; Bruschi, M.; LeGall, J. *Nature (London)* **1979**, *282*, 806–810.
10. Kissinger, C. R. Ph.D. Thesis, University of Washington, Seattle, 1989.
11. Matthew, J. B. *Annu. Rev. Biophys. Chem.* **1985**, *14*, 387–417.
12. Matthew, J. B.; Richards, F. M. *Biochemistry* **1982**, *21*, 4989–4996.
13. Kassner, R. J. *Proc. Natl. Acad. Sci. U.S.A.* **1972**, *69*, 2263–2267.
14. Fan, K.; Akutsu, H.; Niki, K. *J. Electroanal. Chem.* **1990**, *278*, 295–306.
15. Santos, H.; Moura, J. J. G.; Moura, I.; LeGall, J.; Xavier, A. V. *Eur. J. Biochem.* **1984**, *141*, 283–296.
16. Nakahara, Y.; Kimura, K.; Inokuchi, H.; Yagi, T. *Chem. Phys. Lett.* **1980**, *73*, 31–34.
17. Bianco, P.; Haladjian, J. *Electrochim. Acta* **1981**, *26*, 1001–1004.
18. Xavier, A. V.; Moura, J. J. G.; LeGall, J.; DerVartanian, D. V. *Biochimie* **1979**, *61*, 689–695.
19. Fan, K.; Akutsu, H.; Kyogoku, Y.; Niki, K. *Biochemistry* **1990**, *29*, 2257–2263.
20. Guerlesquin, F.; Brushi, M.; Wuthrich, K. *Biochim. Biophys. Acta* **1985**, *830*, 296–303.
21. Sagara, T.; Nakajima, S.; Akutsu, H.; Niki, K.; Wilson, G. S. *J. Electroanal. Chem.* **1991**, *297*, 271–282.
22. Marcus, R. A. *Annu. Rev. Phys. Chem.* **1982**, *15*, 155–196.
23. Delahay, P. *Chem. Phys. Lett.* **1982**, *90*, 425–429.

24. Dixon, D. W.; Hong, X.; Woehler, S. E.; Mauk, A. G.; Sishta, B. P. *J. Am. Chem. Soc.* **1990**, *112*, 1082–1088.
25. Bond, A. M.; Hill, H. A. O.; Page, D. J.; Psalti, I. S. M.; Walton, N. J. *Eur. J. Biochem.* **1990**, *191*, 737–742.
26. Bianco, P.; Manjaoui, A.; Haladjian, J. *J. Electroanal. Chem.* **1988**, *249*, 241–252.
27. Niki, K.; Kawasaki, Y.; Kimura, Y.; Higuchi, Y.; Yasuoka, N. *Langmuir* **1987**, *3*, 982–986.
28. Verma, A. L.; Kimura, K.; Nakamura, A.; Yagi, T.; Inokuchi, H.; Kitagawa, T. *J. Am. Chem. Soc.* **1988**, *110*, 6617–6623.
29. Sagara, S. Ph.D. Thesis, University of Tokyo, 1987.
30. Rosenberg, B. *J. Chem. Phys.* **1962**, *36*, 816–823.
31. Eley, D. D.; Spivey, D. I. *Trans. Faraday Soc.* **1960**, *56*, 1432–1442.
32. Takashima, S.; Schwan, H. P. *J. Phys. Chem.* **1965**, *69*, 4176–4182.
33. Lipinski, B. *Electronic Conduction and Mechanoelectrical Transduction in Biological Materials*; Marcel Dekker: New York, 1982.
34. Ichimura, K.; Kimura, K.; Nakahara, Y.; Yagi, T.; Inokuchi, H. *Chem. Lett.* **1982**, *1*, 19–22.
35. Favaudon, V.; Ferradini, C.; Pucheault, J.; Gilles, L.; LeGall, J. *Biochem. Biophys. Res. Commun.* **1978**, *84*, 435–440.
36. Capeillère-Blandin, C.; Guerlesquin, F.; Brushi, M. *Biochim. Biophys. Acta* **1986**, *848*, 279–293.
37. Akutsu, H.; Hazard, J. H.; Bartsch, R. G.; Cusanovich, M. A. *Biochim. Biophys. Acta* **1992**, *1140*, 144–156.
38. Tollin, G.; Meyer, T. E.; Cusanovich, M. A. *Biochim. Biophys. Acta* **1986**, *853*, 29–41.
39. Cusanovich, M. A.; Hazzard, J. T.; Meyer, T. E. *J. Macromol. Sci. Chem.* **1989**, *A26(283)*, 433–443.
40. Guigliarelli, B.; Bertrand, P.; More, C.; Haser, R.; Gayda, J. P. *J. Mol. Biol.* **1990**, *215*, 161–166.
41. Cambillau, F.; Frey, M.; Mossé, J.; Guerlesquin, F.; Bruschi, M. *Proteins* **1988**, *4*, 63–70.
42. Cannac, V.; Caffrey, M. S.; Voordouw, G.; Cusanovich, M. A. *Arch. Biochem. Biophys.* **1991**, *286*, 629–632.
43. Voordouw, G.; Brenner, S. *Eur. J. Biochem.* **1986**, *159*, 347–351.
44. Pollock, W. B. R.; Chemerika, P. J.; Forrest, M. E.; Beatty, J. T.; Voordouw, G. *J. Gen. Microbiol.* **1989**, *135*, 2319–2328.

RECEIVED for review January 29, 1991. ACCEPTED revised manuscript July 22, 1992.

Evaluation of Surface-Bound Membranes with Electrochemical Impedance Spectroscopy

Jianguo Li, Nancy W. Downer, and H. Gilbert Smith*

TSI Corporation, 57 Union Street, Worcester, MA 01608

Membrane structures that contain the visual receptor protein rhodopsin were formed by detergent dialysis on platinum, silicon oxide, titanium oxide, and indium-tin oxide electrodes. Electrochemical impedance spectroscopy was used to evaluate the biomembrane structures and their electrical properties. A model equivalent circuit is proposed to describe the membrane-electrode interface. The data suggest that the surface structure is a relatively complete single-membrane bilayer with a coverage of 0.97 and with long-term stability.'

COMMUNICATION IN LIVING ORGANISMS is governed by the cell bilayer membrane, which selectively recognizes specific chemical messengers and responds accordingly. Receptor proteins located in cellular membranes have evolved for highly specific recognition functions and are the natural sites of action for a wide variety of biologically active chemical components, including hormones, neurotransmitters, odorants, and many drugs.

Biosensors based on membrane receptors require the protein to be coupled both functionally and structurally with electrical substrates. The interface between the biological recognition element and the solid substrate must allow electrical signal transduction and provide an environment conducive to biological function. Both requirements are demanding. A significant barrier to production of this type of sensor has been the tremendous difficulty of preparing functional and stable lipid-protein bilayer membranes linked to

* Corresponding author: 104 Foster Street, Littleton, MA 01460

surfaces. Such membranes should be functionally equivalent to free-standing membranes and must (1) provide a "blocking" interface to prevent unintended permeabilities, (2) be chemically and mechanically stable on solid substrates, and (3) incorporate specific protein receptors.

Integral membrane receptor proteins normally function as part of the lipid bilayer membrane that separates intracellular and extracellular aqueous compartments. Proteins in natural membranes are thus exposed to regions of two different compositions: the high-dielectric aqueous media on both sides of the membrane and the low-dielectric hydrophobic hydrocarbon region at the core of the lipid bilayer.

Several procedures have been developed to form artificial membranes that retain properties of natural biological membranes (1, 2). These procedures rely on the self-assembly properties of the membrane components (lipids and proteins) to form functioning membrane structures. Lipid bilayer structures have been formed by sonicating suspensions of lipids to form vesicles (3), spreading dissolved lipids across an orifice to form planar bilayers (4), and by using Langmuir-Blodgett techniques to serially add monolayers to a surface (5). Although Langmuir-Blodgett techniques offer good control in deposition of a lipid phase onto solid surfaces, the techniques for incorporating membrane proteins are less well developed. A number of workers have attached proteins to lipid monolayers and bilayers on solid surfaces by anchoring the protein with a hydrophobic tail or by covalently attaching the protein to the lipid head groups. Other researchers have formed bilayers by adsorbing vesicles containing proteins onto surfaces or by incorporating proteins into Langmuir-Blodgett films at an air-water interface and then depositing that film onto a surface (for reviews, *see* references 6 and 7).

We have reported the formation of surface-bound lipid membranes that contain receptors on planar electrode surfaces by a modified detergent dialysis technique (8, 9). This technique is an adaptation of procedures previously used to incorporate membrane proteins into free-standing lipid bilayer structures. Detergent dialysis has been used to directly form protein-containing bilayer membrane vesicles from solubilized protein-lipid mixtures (10, 11). This approach allows the simultaneous incorporation of lipid and protein, and it often retains protein functionality. Other approaches to forming free-standing membrane structures include the fusion of protein-containing vesicles with planar lipid bilayers (12) and the use of detergent dilution techniques to insert proteins into unilamellar vesicles (13).

To assemble the surface-bound membrane structure, we first form a hydrophobic monolayer by using alkylsilanization to covalently attach long-chained hydrocarbon chains to hydroxyl groups in the oxide layer on the electrode surface. Such a hydrophobic surface can be thought of as one leaflet of a membrane bilayer. Alkylsilane-modified surfaces have been widely used as substrates for lipid monolayers deposited by Langmuir-Blodgett techniques. The lipids in these monolayers have mobilities like those of lipids

in natural membranes (14). Huang formed lipid multilayers on such surfaces by dialysis from deoxycholate solutions of lipid and found that when palmitoyl-modified antibodies were included in the detergent solution they also became associated with the surface structures (15). Huang found that the lipid diffused rapidly but that the antibody was relatively immobile.

We simultaneously incorporate both lipid and protein by using dialysis to remove detergent from a solubilized lipid-protein mixture in the presence of the alkylsilanated substrate. Under our conditions, from the evidence in this paper and elsewhere (9), the surface structures appear to be single bilayer membranes. Our hypothesis is that the hydrocarbon chains attached to the surface serve as initiation sites for a lipid bilayer membrane to form as the detergent is slowly removed. The model is of a membrane that is anchored to the surface by hydrophobic interactions with the surface-bound hydrocarbon layer. Integral membrane proteins are retained in these structures by their interaction with the hydrophobic core of the membrane without being directly attached to the electrode surface.

Membranes containing the visual pigment rhodopsin, a G-protein-linked receptor, were chosen as a model system for this work. Rhodopsin was one of the first integral membrane proteins whose amino acid sequence was determined (16–18). More than 40 receptors have been reported to have structural and functional homologies with rhodopsin (19). This chapter describes the use of electrochemical impedance spectroscopy to evaluate lipid bilayer membranes containing rhodopsin formed on electrode surfaces.

Experimental Details

Chemicals and Biochemicals. Acetonitrile (ACN, 99%), tetrabutylammoniumtetrafluoroborate (TBAF, 99%), tetracyanoethylene (TCNE, 98%), and anhydrous *n*-hexadecane (99%) were used as received from Aldrich. Chloroform (American Burdick & Jackson) and carbon tetrachloride (Mallinckrodt) were dried over aluminum oxide (Water Associates, Framingham, MA) for at least 48 h before use. Octadecyltrichlorosilane (OTS) and dimethyloctadecylchlorosilane (DMOCS) were from Petrach Systems, Inc. (Bristol, PA). KCl, H₂SO₄, and HF (52%) of analytical reagent grade were obtained from Mallinckrodt. *N*-2-Hydroxyethylpiperazine-*N'*-ethanesulfonic acid (HEPES), p*K*_a 7.55 was from Sigma. Octyl-β-D-glucopyranoside (OG) used as the detergent was from Calbiochem (La Jolla, CA). Disk membranes containing rhodopsin (Rh) were isolated from rod outer segments from bovine retinas (J. A. Lawson, Co., Lincoln, NE) by flotation on 5% polysucrose (Ficoll 400) (20). Platinum sheet (99.99%) and titanium rod (99.99%) were purchased from Johnson Matthey, p-Si (24–36-Ω cm) and n-Si (100-Ω cm) wafers with a silica layer thickness of 950 Å on the polished side and a gold film evaporated on the other side were provided by EG & G Reticon (Sunnyvale, CA). The indium-tin oxide (100–500-Å-thick) coated glass substrates (ITO) were from Donnelly Co. (Holland, MI).

Electrode Preparation. Pt electrodes were polished with alumina polishing powder (1, 0.3, and 0.05 μm) to a mirror finish and cleaned electrochemically by cycling the potential between hydrogen and oxygen evolution potentials in 1-M

H₂SO₄ until the characteristic clean Pt wave pattern of hydrogen adsorption was observed. The electrode was next poised at 1.1 V versus a saturated calomel electrode (SCE) until the current decayed to less than 1 μ A, which indicates complete oxidation of the electrode surface.

The titanium electrodes were polished with diamond paste (1 and 0.3 μ m) in mineral oil and washed in acetone followed by deionized water wash. The TiO₂ film was formed on titanium in 1-M H₂SO₄ while the potential was swept slowly in a positive direction at a sweep rate of 1 mV/s. The thickness of the anodic film was proportional to the applied growth voltage. Anodizing ratios for titanium at 1-mV/s sweep rate are reported to be 6 nm/V up to 2 V and 3.6 nm/V above 2 V (21). In this work, the growth potential was 31 V versus SCE, and the thickness was estimated to be 15 nm.

The silicon oxide electrodes were 5- \times 5-mm chips cut from a Si-SiO₂ wafer. The ohmic contact was made by connection of a wire to the gold film on the rear side of the chip with silver conducting epoxy. The chip was then mounted on a glass tube and sealed along its edge with epoxy. An etching process to reduce the SiO₂ thickness was carried out in 5% HF at room temperature.

The ITO electrode was made of a 5- \times 5-mm slice cut from ITO sheet. A copper wire was attached to the ITO film with silver conducting epoxy. The ITO slice was mounted on a glass tube with epoxy. All electrodes were washed thoroughly with deionized water and dried in a vacuum oven for 12 h at 100 $^{\circ}$ C before alkylsilanization.

Alkylsilanization. Alkylsilanization of electrode surfaces was carried out by a modification of the procedure of Sagiv (22). The anhydrous solvent was prepared with 80:12:8 hexadecane-chloroform-carbon tetrachloride under dried nitrogen in a glove bag (relative humidity < 4%). The dried electrodes were silanized by reaction in stirred 3% (v/v) OTS solution for 3 h or 6% (v/v) DMOCS solution for 6 h. The silanized electrode surface was rinsed with dry solvent and then with chloroform and cured in a vacuum oven at 100 $^{\circ}$ C for 12 h.

Detergent Dialysis. The technique of detergent dialysis, which is often used to form functional membrane vesicles (10, 11), was adopted to assemble membrane-mimetic structure onto electrode surfaces (9). The dialysis unit used in this work had two compartments separated by a dialysis membrane filter (Spectra/Pro 6 membrane, molecular weight cutoff 3500, Los Angeles, CA). The electrode was mounted in one compartment that contained detergent solubilized disk membranes. Dialysis was against a flowing stream of detergent-free buffer driven by a peristaltic pump (type 2232, Microperpex s, LKB, Sweden). Rod outer segment disk membranes were solubilized with 30-mM OG to a final rhodopsin concentration of 1 mg/mL. Care was taken to avoid bubbles in the dialysis compartments. The detergent dialysis was carried out at 4 $^{\circ}$ C in the dark or under red light filtered through a safe light filter (Kodak 2, Eastman Kodak Co.). The detergent dialysis was at a flow rate of 100 μ L/min for 20-30 h.

Electrochemical Measurements. Cyclic voltammetry and alternating current (ac) impedance spectroscopy were performed using an ac impedance system (EG & G Princeton Applied Research model 378) that included a potentiostat-galvanostat (model 273), a two-phase lock-in analyzer (model 5208), and an IBM PS/2 computer. For ac impedance measurements, a 5-mV sine wave was superimposed on an applied voltage bias from the potentiostat. The reference electrodes were saturated calomel electrodes (SCE; Fisher) for measurements in aqueous solution and silver electrodes

for measurements in nonaqueous solution. All potentials are reported with respect to SCE.

Results and Discussion

Surface Modification with Organosilanes. Chromatographic (23) and other studies indicate that the order of reactivity of halosilanes with silica is $X_3SiR > X_2SiR_2 > XSiR_3$. This relationship was also observed with SnO_2 surfaces (24) based on electron spectroscopy for chemical analysis (ESCA). Organosilanes with more than one reactive group have the potential to bind to more than one surface site but also can cross-react to form polymers. For instance, during the immobilization of diphenylphosphine groups on silica, Oswald et al. (25) demonstrated that the trichlorosilane reagent claimed slightly less than two sites per silane. The fate of the remaining silane reactive group is important to the surface structure formed. Aue et al. (26, 27) claim that linear siloxane polymers form that are bound to the silica surface at only a few sites. After a dichloro- or trichlorosilane forms one $-Si-O-Si-$ surface link, polymer formation can occur if a second $Si-Cl$ bond becomes hydrolyzed by water-forming $-Si-O-Si(OH)-$. If this event occurs in the presence of unreacted solution chlorosilane, a polymer chain can be initiated at the $Si(OH)$ site. Such polymer formation can occur on most metal oxide surfaces.

Pt electrode anodization in sulfuric acid at 1.1 and 1.9 V versus SCE yields an approximate monolayer of PtO and a surface layer of predominantly PtO_2 , respectively (28, 29). Reportedly, Pt electrodes anodized at 1.1 V can be silanized under anhydrous conditions (30) to produce surface $Pt-O-Si-$ bonds. We have used the X_3SiR and $XSiR_3$ silanes, OTS and DMOCS, to modify the surface of our electrodes. X_3SiR silane was found to produce a more stable and reproducible silane layer on electrode surfaces. Therefore, we employed octadecyltrichlorosilane (OTS) to obtain high surface coverages for supporting the reconstituted membrane structure. OTS has a C_{18} carbon chain with a length of 26.5 Å, which is approximately equivalent to a single lipid layer of a membrane bilayer structure. To form a single layer of OTS on the electrode surfaces we attempted to minimize polymer formation by utilizing dry solvents and by carefully and thoroughly washing excess silane from the electrode with fresh solvent before exposing the electrode to moisture.

Electrochemical Analysis of PtO-OTS Electrodes. OTS forms a neutral and low dielectric silane layer and is electrochemically inert. The OTS layer formed on Pt electrodes acts as an insulating layer to block the active Pt surface. Electrochemical examination of the PtO-OTS electrode provides information on the structure of the OTS layer on which the lipid-protein membrane is to be formed. We examined the PtO-OTS

electrode surface in a nonaqueous electrolyte (to avoid reduction of PtO) using tetracyanoethylene (TCNE) as the model redox species.

Cyclic voltammograms of TCNE at Pt oxide and PtO-OTS electrodes measured at the sweep rate of 40 mV/s in 0.1-M TBAF in acetonitrile are shown in Figure 1. The well-defined pair of chemically reversible waves measured at the PtO electrode, which represents reduction of TCNE to its anion and reoxidation of the anion to TCNE, exhibits the 60-mV peak potential separation and wave symmetry expected for a reversible electrochemical reaction. For the PtO-OTS electrode, the reduction and oxidation peak currents of TCNE decrease dramatically. The peak potential separation increases to 180 mV which indicates irreversibility of TCNE at the PtO-OTS electrode. The Pt electrode is still accessible to reduction and oxidation of TCNE after OTS coating, but the effective (microscopic) electrode area is lowered by the covalent bonding of OTS to the Pt surface. The smaller microscopic area gives rise to higher current densities, an increased charge transfer rate limitation, and irreversibility. This series of events suggests that a porous OTS layer is formed on the PtO electrodes.

The porous structure of the OTS layer on PtO was confirmed by the electrochemical impedance spectra of TCNE. Figure 2 shows the complex plane plots of TCNE reduction at PtO and PtO-OTS electrodes at -0.4 V, near the TCNE reversible potential, where Z' and Z'' are the real and

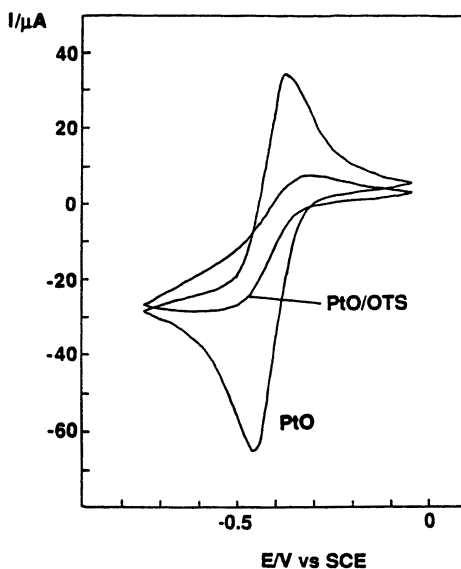


Figure 1. Cyclic voltammetry of tetracyanoethylene (TCNE) on the PtO and PtO-OTS electrodes at 40 mV/s. 5-mM TCNE in acetonitrile containing 0.1-M TBAF.

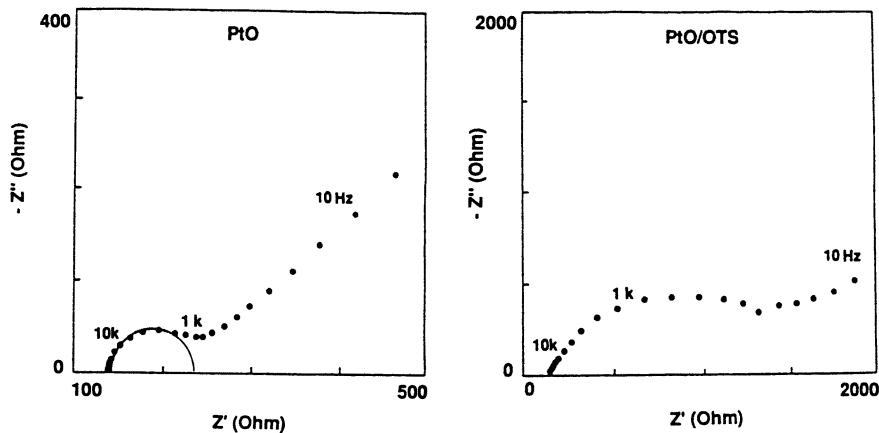


Figure 2. Complex plane plots of TCNE reduction on the PtO and PtO-OTS electrodes at 0.4 V in 5-mM TCNE in acetonitrile containing 0.1-M TBAF.

imaginary components of the measured impedance, respectively. A complex plane plot with a semicircle and a 45° tail was measured at the PtO electrode. This plot is the normal plot expected for a charge transfer process at a smooth electrode surface (31–33). The PtO-OTS electrode, however, gave a sunken semicircle in the measured complex plane plot. This result may be indicative of a porous electrode surface. Due to the uncontrolled nature of surface roughness, it is difficult to describe a rough electrode surface mathematically. Fractal analysis has been used to describe diffusion at a rough electrode surface, and sunken semicircular curves have been simulated (34–36). The sunken semicircle measured with the PtO-OTS electrode may suggest fractal surface features with pores of different sizes and shapes permeating through the OTS layer to the electrode surface.

The effective area of the OTS-coated PtO electrode can be derived if the charge transfer resistance (R_{ct}) is known. R_{ct} can be obtained from impedance data measured at a potential near the reversal potential (37, 38): $R_{ct} = RT/(nFAI_0)$, where R is the universal gas constant, T is absolute temperature, n is the number of electrons transferred per molecule of TCNE, F is Faraday's constant, I_0 is the exchange current density, and A is the effective surface area. Because the impedance spectra of the PtO and PtO-OTS electrodes were measured under the same conditions, the value of R_{ct} may be assumed to be affected only by the effective surface area. In Figure 3, the impedance data are replotted as Z' versus $1/\omega^{1/2}$, where ω is the angular frequency ($2\pi f$). R_{ct} is estimated from the intercept on the Z' axis by extrapolation. The R_{ct} values are 95 and 980 Ω for PtO and PtO-OTS, respectively. An OTS coverage factor, θ , can then be estimated from $(1 - \theta) = R_{ct(\text{PtO})}/R_{ct(\text{PtO-OTS})}$. In this case $\theta = 0.9$.

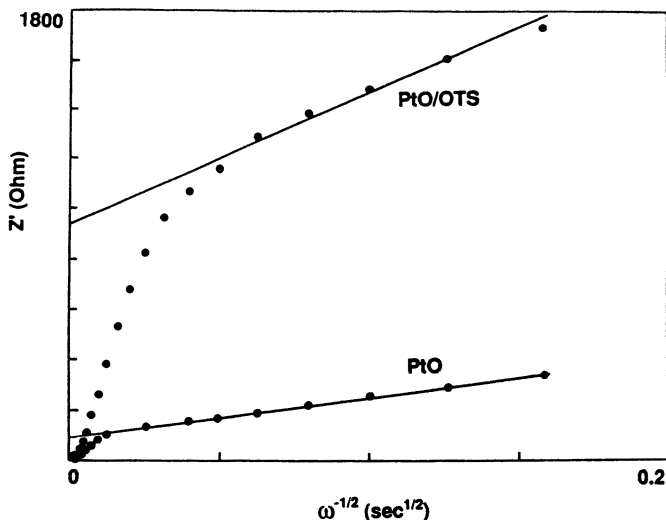


Figure 3. Z' vs. $\omega^{-1/2}$ plots for the impedance data from Figure 2. The uncompensated electrolyte resistance of $150\ \Omega$ is subtracted.

The electrochemical stability of PtO-OTS in aqueous saline solution was tested by measuring cyclic voltammograms of PtO and PtO-OTS electrodes in 0.1-M KCl, pH 6.8 (Figure 4). The electrode capacitances that correspond to the cyclic voltammograms are shown in Figure 5. These capacitances were measured at 1000 Hz. The OTS layer can be described as a planar capacitor in series with the PtO and double-layer capacitances. Formation of the OTS layer decreased the capacitance; however, the PtO beneath the OTS layer was still reduced when the potential was swept below 0.3 V. This observation again is evidence that the OTS layer on PtO is somewhat porous. The onset potential of PtO reduction in aqueous solution is pH-dependent.

The OTS layer was chemically unstable at pH > 9. At this pH, the capacitance immediately increased to the value of the bare PtO electrode, which suggests that the OTS layer dissolves in basic solutions. The hydrolysis of silane on SiO_2 was previously observed in 0.1-M NaOH (24). The silane-PtO is reported to be resistant to most solvents, including dilute aqueous acid (for a few minutes) (30). Our measurements confirm the stability on PtO at neutral pH.

To characterize the membrane-coated PtO electrodes we have chosen a potential window from 0.3 to 0.6 V where PtO is electrochemically stable and passive according to the cyclic voltammograms in Figure 4. The pH was 6.8.

Electrochemical Properties after Membrane Deposition. A rhodopsin-containing membrane was deposited on PtO-OTS electrodes by dialysis, as described in the experimental details section. After dialysis, the

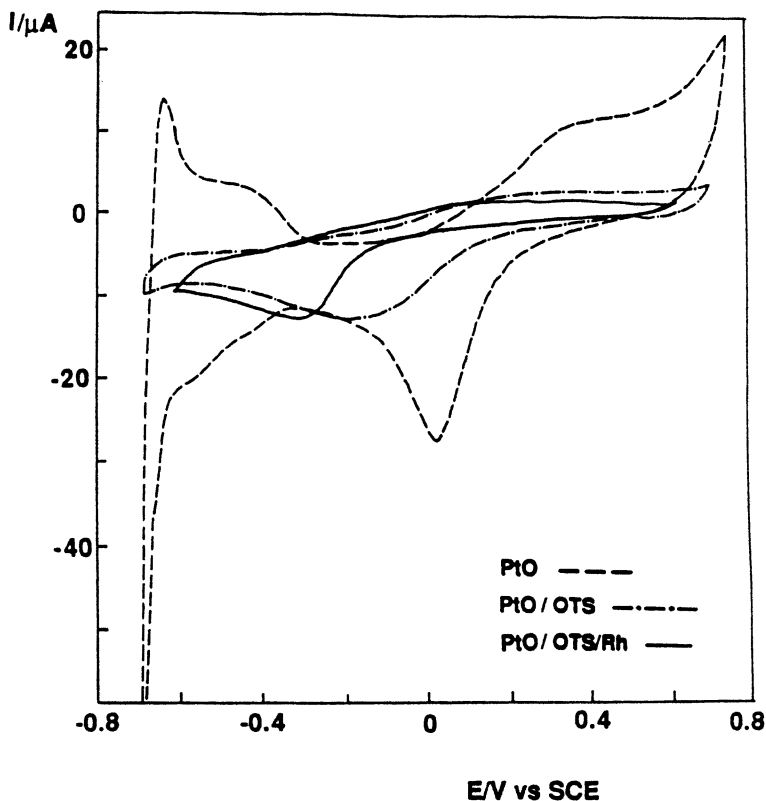


Figure 4. Cyclic voltammetry of the PtO, PtO-OTS, and PtO-OTS-Rh electrodes in 0.1-M KCl containing 20-mM HEPES, pH 6.8. The sweep rate is 20 mV/s.

electrodes were gently rinsed with saline buffer to wash off excess vesicles on the surface before electrochemical measurements. The changes in the cyclic voltammogram and the capacitance are illustrated in Figures 4 and 5. Deposition of the membrane on the electrode surface brought about further “blocking” of the effective area of PtO, which resulted in a further suppression of the PtO reduction (*see* Figure 4). The capacitance decreased further as the result of an additional capacitance due to the rhodopsin-containing membrane in series with the existing capacitance of oxide and OTS layers (*see* Figure 5).

Impedance spectra were recorded in 0.1-M KCl, pH 6.8, at 0.4 V versus SCE. Figure 6 shows the Bode plots of $\log|Z|$ versus $\log f$ and phase angle (θ) versus $\log f$, where $|Z|$ is the impedance magnitude, f is the frequency, and phase angle θ is the arctangent of the ratio of the imaginary and real parts of the measured impedance. The magnitude of the impedance in-

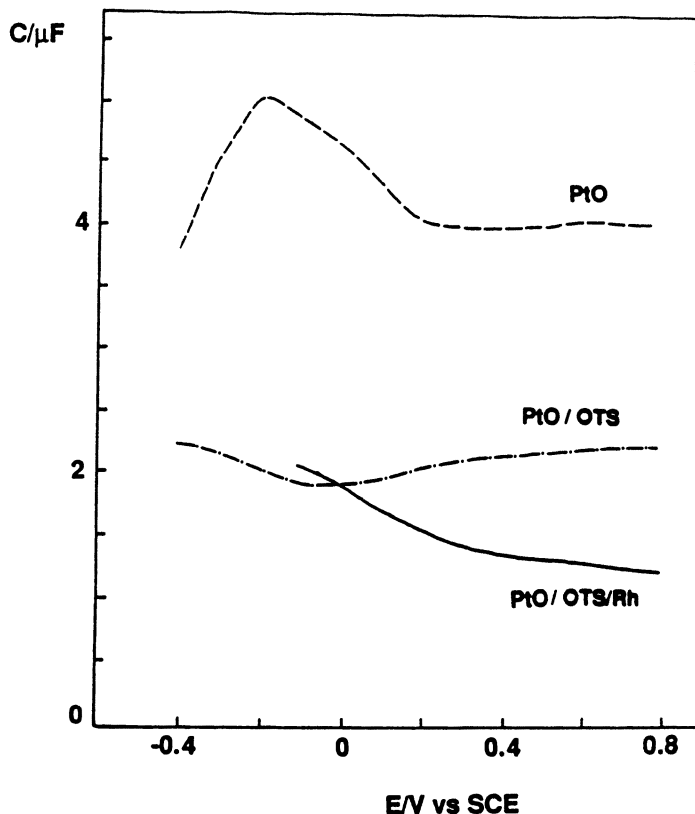


Figure 5. Capacitances of the PtO, PtO-OTS, and PtO-OTS-Rh electrodes measured at 1000 Hz in 0.1-M KCl containing 20-mM HEPES, pH 6.8.

creased upon membrane formation, and the phase angle was also sensitive to membrane deposition. A broad phase-angle maximum plateau appeared in the frequency range > 500 Hz but disappeared after washing the electrode with 30 mM OG to dissolve the deposited membrane (see the half-opened dotted curve in Figure 6). These results are consistent with the formation of a protein-lipid membrane on the OTS-treated PtO electrode by detergent dialysis.

Model of Surface-Bound Membrane on Pt Electrode. From the foregoing discussion of experimental results we can develop a physical model of the surface-bound membrane that consists of two layers, as schematically depicted in Figure 7. The porous, hydrophobic OTS layer provides a structure to anchor the reconstituted membrane layer. Protein molecules with bound lipid may insert into the pores in the OTS layer. The

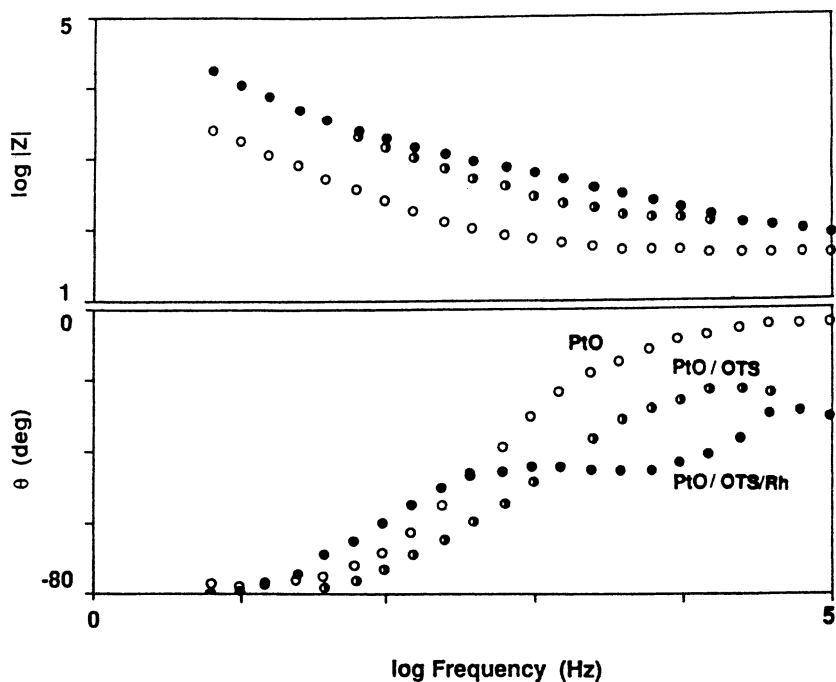


Figure 6. Bode plots for the PtO, PtO-OTS, and PtO-OTS-Rh electrodes measured at 0.4 V in 0.1-M KCl containing 20-mM HEPES, pH 6.8.

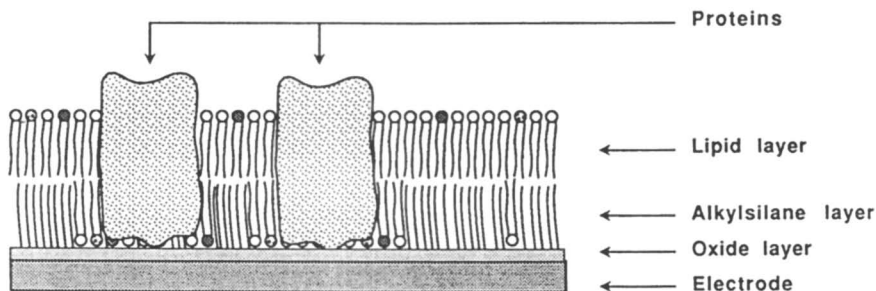


Figure 7. Model of a single surface-bound membrane formed by detergent dialysis on an alkylsilanated electrode surface.

model assembly is essentially a bilayer membrane immobilized on the electrode surface.

More detailed information on the physical structure and electrical properties can be obtained by analysis of the impedance spectra, as presented in Figure 6. An electrical equivalent circuit [resistance-capacitance (RC) circuit] was used by Fare (38) to interpret the capacitance and conductance data of

lipid bilayers measured at low frequencies (e.g., 0.5 Hz). Fare's equivalent circuit consists of a parallel combination of conductances and capacitances for the portion of the electrode coated with a Langmuir-Blodgett membrane and for the uncoated portion of the electrode, but it does not include the polar region of the bilayer. The concept of a coverage factor was introduced into the equivalent circuit by Stelzel and Sackmann (39). Yoshida et al. (40) added elements for the polar region of a lipid layer by using an equivalent circuit that consisted of two pairs of RC elements in series for the hydrocarbon core and the hydrophilic surface region, respectively.

An equivalent circuit can be derived for the surface-bound membrane formed in this work similar in a manner to the approach taken for porous anodic films and porous electrodes (41-46). An equivalent circuit network, proposed in Figure 8a, corresponds to the model in Figure 7. This network has three RC subnetworks that represent the oxide layer, the surface-bound membrane layer, and the double layer. C_{ox} and R_{ox} are the capacitance and resistance of oxide. C_{dl} and R_{dl} are the double-layer capacitance and the polarization resistance, known as the charge transfer resistance at the membrane-water interface. For the subnetwork of the surface-bound membrane layer, one branch represents a tightly packed alkylsilane and lipid bilayer in series, and the other branch represents the pores and defects through the bilayer. C_{alk} , C_{lip} and R_{alk} , R_{lip} are the capacitances and resistances of

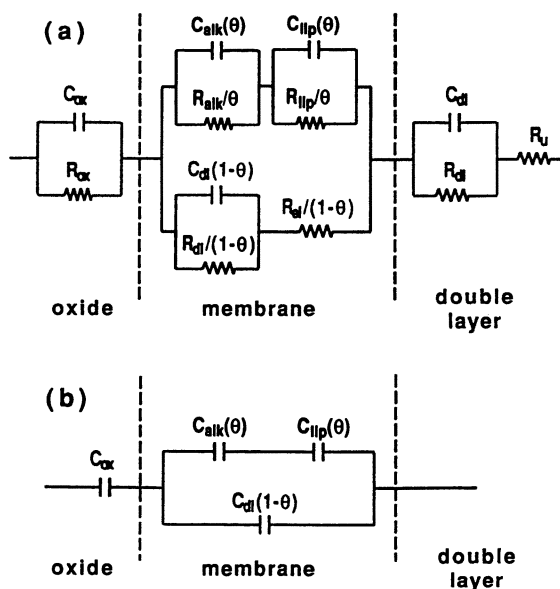


Figure 8. (a) Proposed equivalent circuit for surface-bound membrane electrode interface. (b) Simplified equivalent circuit valid at higher frequency region.

alkylsilane and lipid layers. R_{el} is the resistance of electrolyte in series with the RC circuit of the double layer at the oxide-water interface in the pores. R_u is the series resistance of the electrolyte. θ is defined as the coverage factor for the tightly packed bilayer on the surface, and $(1 - \theta)$ is the fractional area covered by pores and defects.

The simulation spectra of the PtO electrodes with and without the surface-bound membrane are shown in Figure 9 for comparison with the experimental data of Figure 6. The parameters used in the simulation are listed in Table I. The first column lists the values used for curve fitting the experimental spectra, and the second column gives the corresponding values normalized for unit area.

This simulation reproduces the essential features of the experimental data. A calculated capacitance for the tightly packed part of the surface-bound membrane (C_{bl}) can be obtained by treating C_{alk} and C_{lip} in series. The resistance can be similarly calculated from R_{alk} and R_{lip} . The calculated values of $0.52 \mu\text{F}/\text{cm}^2$ and $1325 \Omega \text{ cm}^2$ are in good agreement with literature values for natural membranes (47-48). The best curve fit for the coverage factor, θ , was 0.97, which indicates formation of a relatively complete membrane by the detergent dialysis approach.

Capacitance values of the PtO, C_{ox} , from the best curve fit is lower for the membrane-coated electrode than for the bare PtO electrode. Also the resistance, R_{ox} , is higher for the membrane-coated electrode than for the

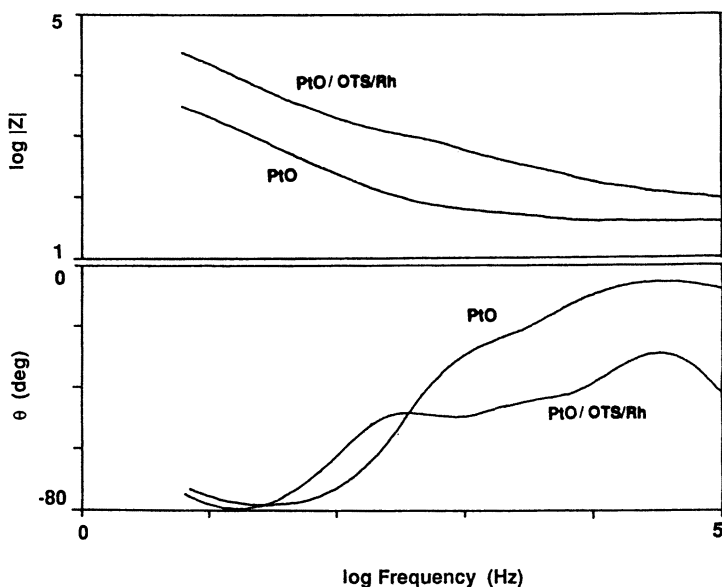


Figure 9. Theoretical simulation of impedance spectra from the proposed equivalent circuit in Figure 8a for curve fit to the spectra in Figure 6.

Table I. Parameters for Best Fit to Impedance Spectra (Figure 6)

<i>Parameters</i>	<i>Values for Model</i>	<i>Normalized Values</i>
PtO-Membrane		
C_{dl}	2.5 μF	10 $\mu\text{F}/\text{cm}^2$
C_{ox}	1.0 μF	4.0 $\mu\text{F}/\text{cm}^2$
C_{alk}	0.25 μF	1.0 $\mu\text{F}/\text{cm}^2$
C_{lip}	0.27 μF	1.1 $\mu\text{F}/\text{cm}^2$
R_{ox}	800 Ω	200 $\Omega \text{ cm}^2$
R_{alk}	3000 Ω	1200 $\Omega \text{ cm}^2$
R_{lip}	500 Ω	125 $\Omega \text{ cm}^2$
R_{dl}	80,000 Ω	20,000 $\Omega \text{ cm}^2$
R_u	120 Ω	30 $\Omega \text{ cm}^2$
R_{el}	12 Ω	3 $\Omega \text{ cm}^2$
θ	0.97	
Bare PtO Electrode		
C_{dl}	6.0 μF	24 $\mu\text{F}/\text{cm}^2$
C_{ox}	3.0 nF	12 $\mu\text{F}/\text{cm}^2$
R_{dl}	5000 Ω	1250 $\Omega \text{ cm}^2$
R_{ox}	40 Ω	10 $\Omega \text{ cm}^2$
R_u	80 Ω	20 $\Omega \text{ cm}^2$

bare PtO electrode. This analysis suggests that the structure of the oxide is altered by alkylsilanization and membrane deposition. It is likely that hydration of the oxide layer differs between the bare electrode where the oxide has direct contact with water and the membrane-coated electrode where the oxide is protected by the alkylsilane and protein-lipid layers.

At frequencies below 63 Hz, the double-layer capacitance began to dominate the overall impedance of the membrane electrode. The electric potential profile of a bilayer membrane consists of a hydrocarbon core layer and an electrical double layer (49). The dipolar potential, which originates from the lipid bilayer head-group zone and the incorporated protein, partially controls transmembrane ion transport. The model equivalent circuit presented here accounts for the response as a function of frequency of both the hydrocarbon core layer and the double layer at the membrane-water interface. The value of C_{dl} from the best curve fit for the membrane-coated electrode is lower than that for the bare PtO interface. For the membrane-coated electrode, the model gives a polarization resistance, R_{dl} , of 80 k Ω compared with 5 k Ω for the bare PtO electrode. Formation of the lipid membrane creates a dipolar potential at the interface that results in higher R_{dl} . The incorporated rhodopsin may also extend the double layer, which makes the layer more diffuse and, therefore, decreases C_{dl} .

The impedance response of each layer on the electrode surface can be attributed to elements of the spectrum in terms of frequency. Although the

broad phase-angle maximum plateau induced by the formation of the surface-bound membrane on the PtO electrode is attributed to several RC constants, the total impedance is dominated by the admittance of the surface-bound membrane for frequencies > 500 Hz. Typical double-layer capacitances are usually in the range of $10\text{--}40 \mu\text{F}/\text{cm}^2$, which is at least 1 order of magnitude greater than the membrane capacitance. Thus at higher frequencies, the double-layer capacitance behaves like a short circuit and can be neglected. In addition, R_{ox} , R_{alk} , R_{lip} , and R_{dl} are usually in the range of $200\text{--}20,000 \text{ k}\Omega \text{ cm}^2$, and are higher than the impedances of the capacitance components in the equivalent circuit. These resistances can be treated as open circuits at higher frequencies. R_{el} is small and can be treated as a short circuit. R_{u} can be either compensated experimentally or subtracted in the data analysis. The equivalent circuit in Figure 8a can therefore be simplified as shown in Figure 8b.

In this simplified form, the membrane capacitance, C_{m} , is in series with C_{ox} . Thus, $C_{\text{m}} = C_{\text{ox}} C_{\text{t}} / (C_{\text{t}} - C_{\text{ox}})$, where C_{t} is the total capacitance of the surface-bound membrane electrode and C_{ox} is the measured capacitance of the electrode before membrane formation. The membrane capacitance, C_{m} , can thus be estimated at a single frequency. Further, the capacitance of the tightly packed bilayer, C_{bl} , can be calculated from C_{m} if the coverage factor and the double-layer capacitance are known: $C_{\text{bl}} = (C_{\text{m}} - (1 - \theta)C_{\text{dl}}) / \theta$.

By using the imaginary component of the measured impedance data for PtO-OTS and PtO-OTS-Rh electrodes (Table II) at a frequency of 1000 Hz (after subtracting R_{u}), the calculated C_{m} is $867 \text{ nF}/\text{cm}^2$ and C_{bl} is thus $584 \text{ nF}/\text{cm}^2$ using $C_{\text{dl}} = 10 \mu\text{F}/\text{cm}^2$ and $\theta = 0.97$, which are close to the theoretical values derived from the best curve fit simulation. We conclude that the simplified equivalent circuit may be adequate for the surface-bound membrane electrode. The thickness of the tightly packed membrane bilayer, d , can be calculated from $d = \epsilon_0 \epsilon / C_{\text{bl}}$, where ϵ is the dielectric constant of

Table II. Capacitances for Membranes Formed on Various Electrodes

Type of Electrode	C_{total} (nF/cm^2) ^a		C_{layer} (nF/cm^2) ^b		C_{bl}^c (nF/cm^2)	Thickness ^d (\AA)	
	Bare	OTS	OTS-memb.	OTS-memb.			
PtO	10,260	1100	800	1232	867	584	46.8
TiO ₂	1,681	1120	607	3358	950	670	40.8
ITO	3,020	1423	710	1490	926	645	42.4
p-Si-SiO ₂	62.95	60.1	57	1330	610	320	85.4
n-Si-SiO ₂	40.7	39.7	39	1627	793	508	53.8

^a Capacitance measured at 1000 Hz for unmodified electrode (bare), after alkylsilylation (OTS), and after membrane deposition (OTS-memb.).

^b Calculated capacitance for each surface layer.

^c Calculated capacitance of membrane using $C_{\text{dl}} = 10 \mu\text{F}/\text{cm}^2$ and $\theta = 0.97$.

^d Calculated using $\epsilon = 3$.

the bilayer. The calculated thickness of the membrane bilayer on the PtO electrode is 46.8 Å using a dielectric constant of 3.

Surface-bound membranes formed on PtO electrodes were chemically and mechanically stable. The PtO-OTS-Rh electrodes were monitored by measuring the capacitance while the electrodes were kept in buffer at 4 °C for 11 days. Any dissolution of the surface-bound membrane would result in an increase in capacitance. Little change in capacitance was observed, which indicates that the membranes are stable.

Surface-Bound Membrane on SiO₂, TiO₂, and ITO Electrodes. The detergent dialysis procedure was also used to deposit membranes on SiO₂, TiO₂, and ITO electrodes. The planar Si-SiO₂ electrode is a solid-state capacitor with the n- or p-type silicon substrate forming one "plate" of the capacitor and the electrolyte at the surface forming the other plate. The insulating SiO₂ layer and surface-bound membrane form the dielectric. Although the planar Si-SiO₂ electrode is a simple device, it has the same fundamental physical structure as other solid-state devices, such as field effect transistors (FETs), but it allows a simpler approach to analyze the device characteristics. For example, the FET sensor relies on changes in its gate voltage caused by a change in the surface charge density upon exposure to an analyte. The gate of the FET is operated under inversion conditions and can be represented by an equivalent circuit of space-charge capacitance, silicon oxide layer capacitance, and membrane capacitance in series. All three capacitances must be considered during analysis of the device response. In contrast, the Si-SiO₂ electrode can be operated under accumulation conditions and only the silicon oxide and membrane capacitances need to be considered. SiO₂ is extremely stable in most biological solutions and suitable for alkylsilylation. The capacitance of a 950-Å-thick SiO₂ layer is typically 35 nF/cm², which is 1 order of magnitude lower than the capacitance of the surface-bound membrane. The total impedance of the electrode is therefore dominated by the SiO₂ capacitance.

TiO₂ formed by electrochemical anodization on a polished titanium surface is usually an n-type semiconductor. In the potential window where it is passive, TiO₂ is in a depletion condition. The capacitance of TiO₂ is the space-charge capacitance described by the Mott-Schottky equation.

ITO electrodes behave electrochemically similar to Pt electrodes, and the double-layer capacitance can be neglected at higher frequencies to allow easily calculation of the membrane capacitance.

The simplified equivalent circuit in Figure 8b was used to evaluate surface-bound membranes on SiO₂, TiO₂, and ITO electrodes. Figures 10 and 11 present the capacitance curves for n-Si-SiO₂ and TiO₂ electrodes with and without OTS- and rhodopsin-containing lipid membranes in KCl buffer. As with the PtO electrodes, the capacitance decreases upon formation of an OTS layer and the membrane on the oxide surface. Table II lists the

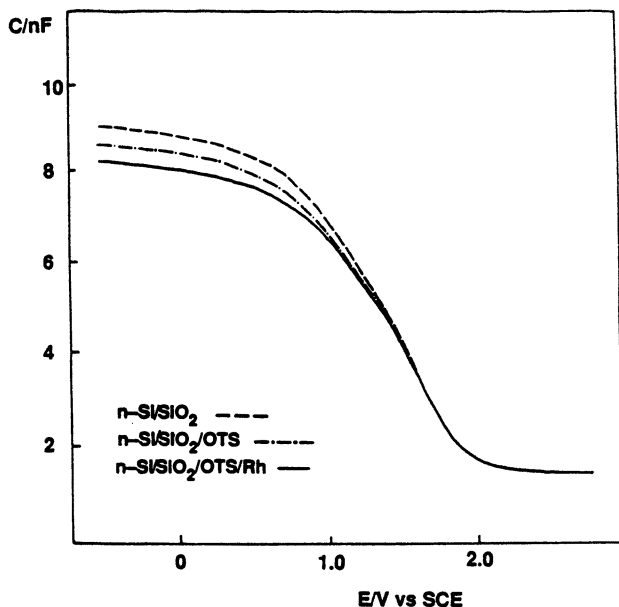


Figure 10. Capacitances of the $n\text{-Si-SiO}_2$, $n\text{-Si-SiO}_2\text{-OTS}$ and $n\text{-Si-SiO}_2\text{-OTS-Rh}$ electrodes measured at 1000 Hz in 0.1-M KCl containing 20-mM HEPES, pH 6.8.

measured capacitances (C_{total}) for the unmodified electrodes and for the electrodes after alkylsilanization and membrane deposition. From these measured values we have used the simplified equivalent circuit of Figure 8b to calculate the capacitance of the OTS layer and the combination of the OTS layer and deposited membrane. Adjusting the OTS-membrane composite for the surface coverage, θ , provides the capacitance of the tightly packed bilayer, C_{bl} , from which the thickness of the surface-bound membrane is calculated. These results are all consistent with formation of a single membrane bilayer on the electrode surfaces.

Because the surface-bound membrane capacitance is in series with the oxide layer capacitance, the change in the total capacitance induced by the surface-bound membrane is a function of both the dielectric properties and the thickness of the oxide layer. The dielectric constants for TiO_2 and ITO are 10–15 times higher than for SiO_2 ; thus, a larger change in capacitance is observed when the membrane is formed on TiO_2 and ITO electrodes than with the SiO_2 electrode (see Table II). The SiO_2 thickness of the p-Si- SiO_2 electrode was 550 Å (reduced from 950 Å by etching in HF). The n-Si- SiO_2 electrode had a 950-Å oxide layer. As shown in Table II, the thinner the SiO_2 on the p-type silicon electrodes, the larger the change in capacitance upon membrane formation. The calculated capacitance of the surface-bound mem-

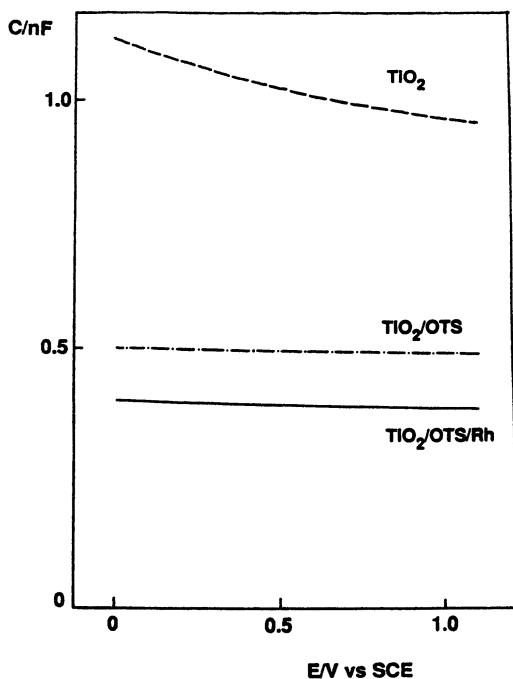


Figure 11. Capacitances of the TiO_2 , $\text{TiO}_2\text{-OTS}$, and $\text{TiO}_2\text{-OTS-Rh}$ electrodes measured at 1000 Hz in 0.1-M KCl containing HEPES, pH 6.8.

brane itself on the p-Si-SiO₂ electrode is lower than for the other electrodes. This observation may indicate formation of a tighter membrane bilayer. The etching may provide a cleaner hydrated surface for better alkylsilanization and membrane deposition.

Summary and Conclusions

Electrochemical impedance spectroscopy provides a sensitive means for characterizing the structure and electrical properties of the surface-bound membranes. The results from impedance analysis are consistent with a single biomembrane-mimetic structure being assembled on metal and semiconductor electrode surfaces. The structures formed by detergent dialysis may consist of a hydrophobic alkyl layer as one leaflet of a bilayer and the lipid deposited by dialysis as the other. Proteins surrounded by a bound lipid layer may simultaneously incorporate into pores in the alkylsilane layer by hydrophobic interactions during deposition of the lipid layer. This model is further supported by the composition of the surface-bound membranes and by Fourier transform infrared analyses (9).

These structures appear well suited for investigations of intramembrane charge redistributions associated with receptor protein function and for applications that use receptors as the active element in biosensor systems. The receptor protein is retained in these structures by its hydrophobic interaction with the core of the membrane, and the environment around the receptor mimics that of a natural membrane. The receptor protein is thus free to undergo rotational and translational diffusion in the plane of the membrane. This should aid in retention of function relative to systems in which the receptor is directly immobilized on a surface.

The system is, of course, not totally natural in that one surface of the membrane is blocked by the electrode. Interactions may exist between the receptor and the electrode surface that inhibit functionality. We have, however, found that aspects of the function of several receptors, including rhodopsin (8), the nicotinic acetylcholine receptor, and the Ca-ATPase from sarcoplasmic reticulum can be retained in these systems (unpublished results).

Acknowledgments

This research was supported in part by the Office of Naval Research.

References

1. Darszon, A. J. *Bioenerg. Biomemb.* **1983**, *15*, 321.
2. Montal, M. *Biochim. Biophys. Acta* **1979**, *559*, 231.
3. Huang, C. *Biochemistry* **1969**, *8*, 344.
4. Mueller, P.; Rudin, O. O.; Tien, H. T.; Westcott, W. C. *Nature (London)* **1962**, *194*, 979.
5. Procarione, W. L.; Kauffman, J. W. *Chem. Phys. Lipids* **1974**, *12*, 251.
6. Tiede, D. M. *Biochim. Biophys. Acta* **1985**, *811*, 357.
7. McConnell, H. M.; Watts, T. H.; Weis, R. M.; Brian, A. A. *Biochim. Biophys. Acta* **1986**, *864*, 95–106.
8. Smith, H. G.; Li, J.; Downer, N. W.; DeLuca, L. W. *Proc. IEEE/Engineering in Medicine and Biology Society* **1989**, *11*, 1329.
9. Downer, N. W.; Li, J.; Penniman, E. M.; DeLuca, L. W.; Smith, H. G. *Biosensors Bioelectr.* **1992**, *7*, 429–440.
10. Madden, T. O. *Chem. Phys. Lipids* **1986**, *40*, 207.
11. Kagawa, Y.; Racker, E. *J. Biol. Chem.* **1971**, *246*, 5477.
12. Miller, C. *Physiol. Rev.* **1983**, *63*, 1209.
13. Jackson, M. L.; Litman, B. J. *Biochemistry* **1982**, *21*, 5601.
14. Tamm, L. K.; McConnell, H. M. *Biophys. J.* **1985**, *47*, 105–113.
15. Huang, L. *Biochemistry* **1985**, *24*, 29–34.
16. Ovchinnikov, Y. A.; Abdulaev, N. G.; Feigina, M. Y.; Artamonov, I. D.; Zolotarev, A. S.; Kostina, M. B.; Bogachuk, A. S.; Miroshnikov, A. I.; Martinov, V. I.; Kudelin, A. B. *Bioorg. Khim.* **1982**, *8*, 1011.
17. Hargrave, P. A.; McDowell, J. H.; Curtis, D. R.; Wang, J. K.; Juscak, E.; Fong, S.-L.; Rao, J. K. M.; Argos, P. *Biophys. Struct. Mech.* **1983**, *9*, 235.
18. Nathans, J.; Hogness, D. S. *Cell* **1983**, *34*, 807.

19. Birnbaumer, L.; Abramowitz, J.; Brown, A. M. *Biochim. Biophys. Acta* **1990**, *1031*, 1063.
20. Smith, H. G.; Litman, B. J. *Enzymology* **1982**, *81*, 57.
21. McAleer, J. F.; Peter, L. M. *Faraday Disc. Chem. Soc.* **1980**, *70*, 67.
22. Sagiv, J. *J. Am. Chem. Soc.* **1980**, *102*, 92.
23. *Bonded Stationary Phases in Chromatography*; Grushka, E., Ed.; Ann Arbor Science Publishers: Ann Arbor, MI, 1974.
24. Moses, P. R.; Wier, L.; Murray, R. *Anal. Chem.* **1975**, *47*, 1882.
25. Oswald, A. A.; Murrel, L. L.; Boucher, L. J. *Abstracts of Papers*, 168th Meeting of the American Chemical Society, Los Angeles, CA; American Chemical Society: Washington, DC, 1974; PETR.
26. Aue, W. A.; Hastings, C. R.; Augl, J. M.; Norr, M. K.; Larsen, J. V. *J. Chromatogr.* **1971**, *56*, 295.
27. Aue, W. A.; Hastings, C. R. *J. Chromatogr.* **1969**, *42*, 319.
28. Allen, G. C.; Tucker, P. M.; Capon, A.; Parsons, R. *J. Electroanal. Chem.* **1974**, *50*, 335.
29. Kim, K. S.; Winograd, N.; Conway, R. E.; Davis, R. E. *J. Am. Chem. Soc.* **1971**, *93*, 6296.
30. Lenhard, J. R.; Murray, R. W. *J. Electroanal. Chem.* **1977**, *78*, 195.
31. de Levie, R.; Pospisil, L. *J. Electroanal. Chem.* **1969**, *22*, 277.
32. de Levie, R. *J. Electroanal. Chem.* **1990**, *261*, 1.
33. Maritan, A.; Toigo, F. *Electrochim. Acta* **1990**, *35*, 141.
34. de Gennes, P.-G. *Comptes Rendus* **1982**, *295*(2), 1061.
35. Nyikos, L.; Pajkossy, T. *Electrochim. Acta* **1985**, *30*, 1533.
36. de Levie, R.; Vogt, A. *J. Electroanal. Chem.* **1990**, *278*, 25.
37. Bond, A. M. *Modern Polarographic Methods in Analytical Chemistry*; Marcel Dekker: New York, 1980.
38. Fare, T. L. *Langmuir* **1990**, *6*, 1172.
39. Stelzel, M.; Sackmann, E. *Biochim. Biophys. Acta* **1989**, *981*, 135.
40. Yoshida, T.; Mori, T.; Ueda, I. *J. Colloid Interface Sci.* **1983**, *96*, 39.
41. *Impedance Spectroscopy*; Macdonald, J. R., Ed.; Wiley: New York, 1987.
42. Madon, M. J.; McKubre, M. C. H. *J. Electrochem. Soc.* **1983**, *130*, 1056.
43. Lenhart, S. L.; Macdonald, D. D.; Pound, B. G. *J. Electrochem. Soc.* **1988**, *135*, 1063.
44. Mansfeld, F.; Kendig, M. W. *J. Electrochem. Soc.* **1988**, *135*, 828.
45. Hoar, J. P.; Wood, G. C. *Electrochim. Acta* **1962**, *7*, 333.
46. Hitzig, J.; Juttner, K.; Lorenz, W. J.; Paatsch, W. *Corros. Sci.* **1984**, *24*, 945.
47. Ti Tien, H. *Bilayer Lipid Membranes (BLM): Theory and Practice*; Marcel Dekker: New York, 1974.
48. Cole, K. S. *Membranes, Ions and Impulses: A Chapter of Classical Biophysics*; University of Calif. Press: Berkeley, CA, 1968.
49. Ti Tien, H. In *Thin Liquid Films*; Ivanov, I. B., Ed. Marcel Dekker: New York, 1988; p 927.

RECEIVED for review February 20, 1991. ACCEPTED revised manuscript July 10, 1992.

Electronic Processes and Redox Reactions in Bilayer Lipid Membranes

H. Ti Tien

Membrane Biophysics Laboratory, Giltner Hall, Department of Physiology,
Michigan State University, East Lansing, MI 48824

Electron transfer plays the key role in many areas of biomembrane phenomena ranging from simple redox reactions to the complicated conversion and storage of solar energy via the thylakoid membrane in chloroplast photosynthesis. The use of artificial bilayer lipid membranes (BLMs) as an experimental model of biomembranes such as the thylakoid membrane and the cristae membrane of the mitochondrion have provided a rational understanding for the energy conversion process of natural systems. The advance in the theoretical and experimental investigations of light energy transduction and of electron mechanisms via membrane reconstitution has been particularly relevant. This chapter will focus on two aspects of BLM studies in relation to biomembranes: membrane electrochemistry and membrane photochemistry. Some attention will be paid to the basic principles of electrochemistry as applied to membrane research. Recent experiments with BLMs and their potential applications in areas of biosensor development, biomolecular electronic devices, and solar energy conversion will also be summarized.

CHARGE GENERATION, SEPARATION, AND TRANSLOCATION are the main concern of electrochemistry. To relate these phenomena to membranes, the principal focus of research deals with the mechanisms of reactions through the membrane proper and at, as well as across, the solution–membrane interface. The electrical double layer at the interface plays a crucial role. The reconstituted planar bilayer lipid membrane (BLM) that separates two aqueous solutions was first reported in 1961. The BLM has proven to be an excellent model for biomembranes; it permits charge separation and translo-

0065-2393/94/0235-0513 \$08.00/0
© 1994 American Chemical Society

cation to be measured directly by modern electrochemical techniques (1, 2). In this chapter we shall describe the essential aspects of the BLM system, including a description in some detail of the latest methodology for formation of BLMs on solid supports (s-BLMs). The emphasis of this review will be on redox reactions and light-induced charge separation and electron transfer in experimental BLMs. In connection with BLM research, the large number of papers dealing with methods for incorporating membrane proteins and for studying single-channel conductance will only be mentioned in passing because of space limitations. Membrane channel reconstitution experiments (3, 4) and other topics not covered here, such as thickness determination, interfacial chemistry, permeability to water, and nonelectrolytes, can be found in several comprehensive reviews on the subject matter (5–13).

The Conventional BLM System

The usual picture of a BLM interposed between two aqueous solutions consists of a liquid hydrocarbon phase sandwiched between two hydrophilic regions. The electrical properties of BLMs have been extensively investigated. Such investigation usually entails the measurements of membrane resistance (R_m or conductance, $C_m = 1/R_m$), capacitance (C_m), potential (E_m), dielectric breakdown voltage (V_b), and current–voltage (I/V) characteristics. Unmodified BLMs (i.e., BLMs formed from phospholipids or oxidized cholesterol dissolved in an *n*-alkane solvent in 0.1-M KCl solution) have typical intrinsic values of R_m greater than $10^8 \Omega \text{ cm}^2$, $C_m = 5000 \text{ pF}$, $E_m = 0$, $V_b = 200 \pm 50 \text{ mV}$, and I/V curves obeying Ohm's law. The structure of the BLM is a thin slab of liquid crystals in two dimensions (14) that has a $\sim 3\text{--}4\text{-nm}$ -thick fluid hydrocarbon core. This liquid-crystalline portion of the BLM is an excellent insulator, but its electrical conductance can be drastically altered by incorporation of a variety of compounds such as iodine, valinomycin, enzymes, 2, 4-dinitrophenol, chlorophyll and its related compounds, dyes, organic metals, and semiconductor particles (2, 5, 7, 14).

Experimentally, bilayer lipid membranes (BLMs) are formed easily across a hole in a poly(tetrafluoroethylene) (PTFE; Teflon) partition interposed between two chambers filled with aqueous solution (e.g., 0.1-M KCl). The lipid solution (e.g., 20 mg of phosphatidyl choline per milliliter of decane) is introduced onto the hole via a small brush, a glass rod, or a microsyringe, and it thins spontaneously, which results in a bilayer lipid leaflet (i.e., a BLM). In addition to the conventional technique just described, a BLM can also be formed from two monolayers at the air–water interface according to a method first used by Takagi et al. in 1965 (see reference 14, Figure 11-3, page 477) and improved by others (14, 16–18). This method is based on the Langmuir–Blodgett technique and involves two steps: First, lipid monolayers are spread at the air–water interface of two solutions separated by a hy-

drophobic barrier that contains a small aperture. Second, the barrier is lowered through the monolayers, which forms a BLM in the aperture under favorable conditions. Pretreatment of the aperture with a number of solvents such as hexadecane, squalene, or petrolatum in pentane is usually recommended to enhance the formation and stability of the BLM (2, 7, 14).

The New BLM System

In contrast to the conventional BLM system just described, a novel yet extremely simple method for formation of a stable BLM was recently developed in our laboratory (19–23). The technique involves the formation of self-assembled lipid bilayers on solid supports. The supported BLM (s-BLM) has a greatly improved mechanical stability (lasting indefinitely) and has desirable dynamic properties. One of the methods of formation of a s-BLM consists of two distinct steps. In the first step, the tip of a PTFE-coated platinum wire is cut off. To provide the best cut of the platinum wire, we constructed a miniature guillotine (Figure 1) where the sharp knife moves vertically onto the wire placed on the flat base. The cut is performed while the wire is immersed in a drop of lipid solution so that the initial contact of the newly exposed wire surface is with the lipid solution. In the second step, this newly cut lipid-coated PTFE-covered platinum wire is transferred into an aqueous bathing solution. This two-step self-assembled lipid bilayer works because the freshly cut metal surface is hydrophilic and attracts the polar groups of the lipid molecules. Thus, a lipid monolayer is tenaciously formed on the nascent metallic surface. Immersion of the lipid-coated wire into an aqueous solution spontaneously thins the lipid layer to a BLM that is anchored on one side to the solid support and is exposed to water on the other side. Further details of this method are available in the literature (19–23, 41).

Evidence for Electronic Processes in Biomembranes

In 1941 Albert Szent-Gyorgyi suggested the role of solid-state electronic processes in biology (for a review, *see* references 2 and 24–27). Many attempts have been made during the intervening years to demonstrate that such electronic processes can occur in biomembranes and their constituents such as proteins and lipids (*see* reference 24). The concept of electronic processes in membranes and related systems was first reviewed in 1971 (14, 28), and the phenomenon known as electrostenolysis was stressed. In this connection, the term “electrodeics” has been proposed (10, 28). In the language of membrane electrochemistry, electrostenolysis simply means that a reduction reaction takes place on the side of the membrane (or barrier) where the positive electrode is situated and oxidation occurs on the other side

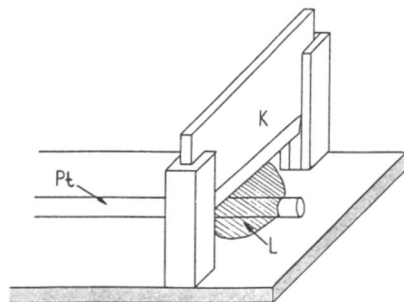


Figure 1. Schematic diagram of guillotine for cutting metallic wires that are immersed in a droplet of lipid solution. Key: Pt, platinum wire; K, knife; L, lipid droplet. (Adapted from reference 21.)

of the membrane facing the cathode. Although electronic processes in BLM in the dark have been discussed since 1970 (*see* reference 24), no conclusive evidence has been shown. This lack of evidence is because an unmodified BLM is an excellent insulator (resistivity $> 10^{15} \Omega$) and thus incapable of either ionic or electronic conduction. To demonstrate electronic conduction in BLM the membrane must be modified to function as a redox or semiconductor electrode. Additionally, an appropriate method must be found to study electronic processes that can be applied to the BLM system.

Basics of Cyclic Voltammetry. Electrochemical techniques such as cyclic voltammetry (CV) and linear sweep voltammetry (LSV) are most appropriate to the study of electronic processes and redox reactions. These techniques are conceptually elegant and experimentally simple; thus they are popular for studying redox reactions at the electrode–solution interfaces and have been increasingly employed by electrochemists (2, 7). Several remarks regarding the cyclic voltammograms of electron-conducting BLM should be made.

1. Mass transfer by migration of electroactive species under the influence of an applied voltage is rendered negligible by using a high concentration of supporting electrolyte (e.g., 0.1-M KCl).
2. The principal mode of mass transport of electroactive species at the surface of BLM is assumed to be diffusion that occurs as a result of the electrochemical potential difference developed between the BLM–solution interface and the bulk solution.
3. Electron-transfer reactions can be directly related to the voltammograms. This relationship arises because the redox products generated near or in the BLM are available for further redox reaction as the scan direction is reversed. During the cathodic scan ($-E$ or increasingly negative), more and more electrons are available for reduction to the species adjacent to the BLM; that is, one side of the BLM becomes a

stronger reducing electrode. Conversely, as the potential is increased toward the positive direction, the other side of the BLM becomes a better oxidizing electrode, with positive holes, so to speak, increasingly ready for oxidation (2, 24).

Electronic Conduction across BLM in the Dark. One of the most striking changes of BLM electrical properties was observed when I_2 and I^- were added to the bathing solution. The usually very high electrical resistivity of the BLM (in the range of 10^8 – 10^{12} Ω cm^2) dropped by several orders of magnitude as observed by Finkelstein, Cass, and others (*see* reference 24). One possible explanation is that the membrane became more permeable to I^- or polyions of iodine. Another possibility is that the conductivity changes were due to electron conduction across the membrane (14). More specifically, conductivity changes are due to charge-complex formation at the interface between the membrane and the bathing solution, and due to the transfer of electrons across the membrane. After capacitance and conductivity changes of BLM were measured as a function of the frequency of the applied field and the concentrations of KI and I_2 in the bathing solution, it was shown that I_3^- was able to enter the BLM and act as an electron donor. Furthermore, the electrons in the membrane were transferred between donor and acceptor centers by a hopping mechanism (*see* reference 24). In similar experiments, Boguslavski reported (29) that an exchange of electrons took place at the membrane–bathing solution interface and that holes were the charge carriers inside the membrane. Karvaly and Pant (30) also found that current transferred across the membrane was independent of ^{131}I (up to a specific flux level). From voltages generated by varying the iodine concentration in one of the compartments while $[I^-]$ was kept constant and from current–voltage characteristics taken under the same conditions as with tracer measurements, Karvaly and Dancshazy (31) concluded that, although some contribution of ionic conductivity could not be excluded, the current carriers across the membrane were primarily electrons and that the membrane–bathing solution interface behaved like a semiconducting electrochemical electrode. The same conclusion was drawn on the basis of voltages observed in systems where the concentration of the ferric ion in one of the compartments was varied. In a different kind of experiments, Feldberg et al. (32) observed electronic conductivity across BLMs formed from glycerol monooleate in *n*-hexadecane and magnesium etiochlorin. The bathing solution contained a buffer and ferro–ferricyanide redox couples on both sides of the BLM. The value of the redox potential of the couples could be changed by varying the ratio between ferrocyanide and ferricyanide present in the bathing solution. Three different methods of detecting the electron current flowing across the BLM were used by measuring the open-circuit voltage when the redox potentials of the couples on both sides of the membrane were changed. The density of the current flowing across the

BLM was proportional to the magnesium etiochlorin in the membrane. When the magnesium etiochlorin concentration was kept constant and the redox potential of the couples was changed, the resultant current across the membranes followed the magnitude and sign of the changes. All three methods showed that the predominant charge carriers of current across the BLM were electrons.

Thus far, we have used the classical concept of electrochemistry to describe the various phenomena associated with membranes; only hydrated ions and ions surrounded by other ions (ionic cloud) were involved. At physiological temperatures, ions undergo ceaseless motion or random walk; they get nowhere by random walk alone (their time average displacement is zero). A net transport of ions is possible by (1) the presence of an electrical field and (2) by chemical potential gradient. Thus, a net drift is superimposed on the random walk. When ions reach the interface, properties change abruptly; the anisotropy of the forces compels ions to adopt new configurations unknown in bulk solution. Here, a variety of phenomena occurs: charge separation, potential gradient, adsorption, and orientation of water dipoles. At present, modern electrochemistry is focused on the transfer of charges across the interface, in particular, the electrified interface (2, 7, 10). The involvement of the electrical double layer, therefore, is self-evident.

The charges that we are concerned with here are the electronic charges (electrons and holes). For charges of this type to be transported across the interface, electrochemical reactions must take place. In the presence of a membrane that is impermeable to ions, what will happen then? Here, the membrane must serve at least two functions: (i) a pathway for electronic charges and (ii) an electrode surface for chemical transformation (reduction and oxidation or redox reactions).

Electrical Properties of BLM in the Absence of Light. Literature references prior to 1980 are available elsewhere (34). Here it is sufficient to state that, due to its ultrathinness (< 7 nm), an electric field of 100,000 V/cm is easily developed across the BLM. This very high field strength greatly modifies charge separation and transport properties as well as hydrocarbon solubility in BLMs. White (35) studied the physical chemistry of the BLM and reported how electric fields alter *n*-alkane solubility in the bilayer, which causes a shift from the bilayer to the Plateau-Gibbs border and microlenses. The solubility of *n*-alkanes in BLMs was investigated by Gruen and Haydon (36), who reported that the *n*-alkanes dissolve primarily into the central core of a BLM and significantly alter the BLM thickness. Contrary to expectation, *n*-alkanes with increasing chain length have less solubility. This phenomenon has also been considered at length by McIntosh et al. (37), based on the results obtained by the combined use of differential scanning calorimetry, X-ray diffraction, and monolayer techniques. To complete the picture, we also mention the paper by Sugar and Neuman (38), who

proposed a stochastic model for electric field-induced pores in membranes (termed electroporation). At subcritical electric fields, the average pore size is stationary and very small. At supercritical field strengths, the pore radius increases and, when it reaches a critical pore size, dielectric breakdown occurs. However, if the electric field is turned off before the membrane ruptures, the pore apparently completely reseals itself; hence, the BLM survives. In this connection the paper by Zimmermann is of interest (39).

To apply the powerful CV technique to the BLM system, a conceptual effort has to be made; that is, one side of the BLM must be considered as the working electrode, while the other side provides the connection to the external circuit. As already mentioned, an unmodified BLM behaves essentially as an excellent insulator and does not function as a working electrode. Therefore, the BLM must be modified for it to function as a metallic or semiconductor electrode. To impart electronic properties, we have discovered that incorporation of organic semiconductors (synmetals), such as TCNQ (7,7,8,8-tetracyanoquinodimethane) or TTF (tetrathiafulvalene), enables the BLM to become electron-conducting (33, 40). In the absence of TCNQ in the BLM but with other experimental conditions the same, the current–voltage (I/V) plot is linear; it practically coincides with the x axis on the scale used. In the absence of redox couples in the bathing solution, but with TCNQ in the BLM, the I/V curve remains linear. To show more clearly that the redox reactions occur across the TCNQ-containing BLM, the following experiment was carried out. To one side of a TCNQ-containing BLM we added a high concentration of equimolar ferri–ferrocyanide solution, whereas to the other side, aliquots of ascorbic acid of known concentration were introduced (2, 40). The membrane potentials (E_m) after each addition of ascorbic acid were measured concurrently. It is most interesting to note that the extrapolated value of E at the equal molar concentrations of the two redox couples agrees very well with the difference of the two standard redox potentials ($E^\circ = 300$ mV). The highly asymmetrical current–voltage curves are reminiscent of the curves of a p – n junction diode, which permits an electron current flow in a forward-bias direction only. In our TCNQ–BLM system, oxidation occurs at the membrane–solution interface that contracts the ascorbic acid solution and reduction of ferricyanide to ferrocyanide takes place on the other side of the BLM, which has a negative polarity. Implicit in this interpretation is the assumption that transmembrane movement of electrons occurs via the TCNQ molecules imbedded in the lipid bilayer; that is, the whole system has the properties of a p – n junction with the TCNQ–BLM acting as a rectifier.

To demonstrate that the TCNQ–BLM behaves like a metallic electrode (e.g., Pt, which is frequently used in CV), a comparative experiment was carried out: Cyclic voltammograms of quinhydrone were obtained using either Pt or TCNQ-containing BLM under very similar conditions. The cathodic portions of the voltammograms were found to be quite similar,

which substantiates that the TCNQ-BLM functioned as a working electrode. In this connection, a cyclic voltammogram of horse-heart ferricytochrome *c* was also obtained by means similar to that reported by Eddowes and Hill in 1977 (*see* references 2, 10, 11), who used a gold working electrode. Thus, to be consistent with the theory of CV, the TCNQ-BLM must function as a redox electrode in the usual practice of electrochemistry.

The significant advantages of the CV technique are simplicity, good precision of measurement, the involvement of the lipid bilayer, and the capability for future development. Because the electron-transfer chain components are closely associated with the lipid bilayer, the values thus determined by the usual Pt electrode may be quite different from the actual values in the membrane. Therefore, the technique described here offers a new approach to the determination of E° of membrane-bound biomolecules, such as the cytochromes and other redox enzymes, using modified BLM as the working electrode. Further, this new type of electronically conducting BLM coupled with the CV technique may be useful in the study of membrane bioenergetics (40) and in the design of molecular electronic devices based on ultrathin films (41).

Membrane Photochemistry

Light-Induced Electron Transfer. In green plant photosynthesis, the primary event and its subsequent redox reactions are believed to take place in and across the thylakoid membrane. On the basis of evidence from electron microscopy, the structure of a thylakoid membrane is that of a lipid bilayer with embedded pigment-protein complexes (42, 43). To effect light transduction, certain membrane-bound "machineries" have evolved in nature. The details of these machineries (or transducers) in biological membranes for light transduction are largely uncertain, but they are definitely made of lipids, proteins, and pigments. To explain the light-driven redox reactions from water to NADP (nicotinamide adenine dinucleotide phosphate), the so-called Z scheme, with two photosystems (PS-I and PS-II), was proposed in the 1960s (44, 45). Mitchell's chemiosmotic hypothesis, established in the 1970s, accounted for electron transfer and photophosphorylation via an ion-impermeable lipid membrane. As a result of Mitchell's hypothesis, PS-I and PS-II of the Z scheme were incorporated into the thylakoid membrane in the late 1970s (44-47). Concurrently with the aforementioned developments, the BLM system was developed in the early 1960s. In 1968, photoelectric effects in chlorophyll-containing BLM were observed (14, 25, 48). These past accomplishments have enhanced our understanding of light transduction processes in the thylakoid membrane and have set the stage for future experiments.

Summary of Recent Experiments. BLM containing chlorophylls and related compounds have been studied by several groups of investigators (44, 48). For references prior to 1980, a number of reviews are available (25, 44). To elicit appreciable photoelectric effects, asymmetrical conditions across the pigmented BLM are necessary. These conditions can be manifest as differences in pH, electrical potential, composition, or concentration of electron acceptors and donors present in the bathing solutions. For electron-transfer and charge separation studies, we have formed BLMs from lipid solutions containing chlorophyll (Chl) or porphyrins with and without added modifiers, such as quinones and carotenes. The addition of quinones or carotenes is due to well-documented evidence that quinones serve as the primary electron acceptor and carotenes serve as effective light-gathering accessory pigments. Therefore, it seems highly probable that a close proximity between a donor species (e.g., chlorophyll or porphyrin) and an electron acceptor molecule (e.g., quinone) is a prerequisite. To test this hypothesis, several groups of workers have synthesized covalently linked porphyrin-quinone and porphyrin-carotene complexes (49). As a model for the initial photophysicochemical event in reaction centers of photosynthesis, incorporation of these molecularly designed compounds into reconstituted BLM is of interest and has been carried out by several groups of investigators. The photopotentials obtained on some of these BLM systems are indeed interesting in that they are larger by at least a factor of 3 (the highest values hitherto reported) than those of chlorophyll-containing BLMs. In this connection, the experiment reported recently by Rich and Brody (50) is of interest because they found that the Chl BLM in the presence of dihydroxy carotenoids gave rise to much greater photocurrents than either the simple carotenes or the diketocarotenoids. BLMs formed using pheophytin (a magnesium-free chlorophyll) generate very small photocurrent regardless of the carotenoids used. This observation is explained in terms of a lack of interaction between pheophytin and carotenoids. The negligible photocurrent in pheophytin BLM might also be due to the mismatched redox potential between pheophytin and ferricyanide, which prevents the reduction of ferricyanide by pheophytin. The interaction between chlorophyll and beta-carotene in BLM has also been studied by Vacek et al. (51), who observed a decrease of photopotential on repeated flash excitation that may arise from lipid oxidation. The kinetics of photopotential was studied in more detail by Liu and Mauzerall (52, 53), who explained the decay by a rate constant that decreases exponentially with distance between pigment cation and reduced acceptor (e.g., ferrocyanide). Another observation from their study is that the pigment cation does not transverse the BLM in less than 10 ms. Instead of using ferricyanide, ferric chloride (FeCl_3) was used earlier as an electron acceptor. The photoconductivity of the Chl BLM with added beta-carotene was studied as a function of wavelength. The highest efficiency, 541 nm, was obtained with the photoelectrospectrometry described by Lopez and Tien (*see* reference 2). This tech-

nique combines the classic photoelectric effect with optical spectroscopy. Thus far, only a range of UV and visible wavelengths has been reported (25, 54, 55). For example, Putvinskii (55) reported the influence of UV light on the stability of BLM formed from mitochondrial lipids and explained his results in terms of photoperoxidation of unsaturated fatty acid chains of phospholipids. Kadoshnikov and Stolovitsky (56) reported the results of spectral photoelectrochemical investigations of Chl BLM and liposomes. Chlorophyll in these membranes has monomeric (640 nm) and crystalline (740 nm) forms. The linewidth of the electron paramagnetic resonance (EPR) signal of monomeric Chl cation-radical is 8–9 G; that of the crystalline form is 1.7 G with the g factor = 2.0024. The same authors also reported that about 25 Chl molecules are incorporated in the aggregates. The BLM, with incorporated Chl and pheophytin, generated photopotentials of opposite signs.

In a novel experiment, Koyama et al. (57) obtained a spectrum of carotenoid BLM by resonance Raman spectroscopy—a major advance in BLM spectroscopy. For efficient charge transfer, the orientation of chlorophyll molecules at the membrane–solution interface is important. Brasseur et al. (58) developed a procedure for conformation analysis to define the position of chlorophyll in BLM. They found that the porphyrin ring is orientated at an angle of $45 \pm 5^\circ$ to the plane of the BLM, which is in excellent agreement with the value reported previously (44).

In an interesting study, Hattenbach et al. (59) raised the question “Does phytochrome interact with lipid bilayers?” Phytochrome, a plant chromoprotein purported to respond reversibly to red light of different wavelengths (667 and 725 nm), has been incorporated into a BLM. Hattenbach and colleagues (59) found no detectable change in membrane conductance during illumination with red light (660 nm). This finding in BLM, however, does not rule out the regulatory role of phytochrome in plant membranes.

A unique feature of the BLM system is that a coupled photosensitized redox reaction may be independently activated at the two interfaces of the BLM. This reaction, which mimics the Z-scheme of photosynthesis (2, 44, 61–63), can be accomplished by using zinc tetraphenylporphyrin (TPP) (or MgTPP) as the photoabsorber in the BLM in conjunction with tris(2,2'-bipyridine) ruthenium ion ($\text{Ru}(\text{bpy})_3^{2+}$) methylviologen (MV; 1,1'-dihexadecyl-4,4'-bipyridium) as the electron acceptor, EDTA (ethylenediamine- N,N,N',N' -tetraacetate) as the electron donor, and vitamin K (VK) as a hydrogen carrier (63). The presence of ZnTPP in the BLM greatly enhances the response, which implies facilitated electron transport. Photoexcitation of $\text{Ru}(\text{bpy})_3^{2+}$ or ZnTPP leads to viologen reduction, as evidenced by the polarity of the photopotentials. Because the acceptor (MV or Fe) and donor (EDTA) are physically immobilized, some transmembrane redox reactions must take place. The most direct interpretation of the data is that the reduction of $\text{Ru}(\text{bpy})_3^{2+}$ occurs on the side containing EDTA; the transmem-

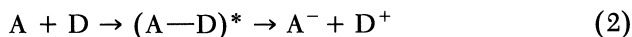
brane electron tunneling is facilitated by ZnTPP and VK. The drop in photocurrent may be caused by the diffusion of reduced MV, which could become more soluble in the membrane phase. In analogy to the Z scheme of photosynthesis, this two-step electron-transfer system should be further studied.

It should be mentioned that BLMs and liposomes have been employed to aid the understanding of *H. halobium* at the molecular level. Incorporation of bacteriorhodopsin (BR) into planar BLMs has been carried out successfully for electrical measurements by several groups of investigators since 1976. Karvaly's group (60, 61) appears to be the first to report both photovoltaic effects and photoconductivity in BR-containing BLMs (for earlier references, see reference 44 and reviews by Hong and Dratz in this volume).

Photochemical Redox Reactions. From the preceding experiments, it appears that a large number of very rapid processes occur from the excited state of a given molecule. The only way for a reaction to occur from an excited state is for it to take place on a time scale very nearly the same as the processes with which it must compete. The overriding factor of quantum mechanics and its influence on macroscopic behavior is the law of probabilities. If a process is very slow compared to others, it certainly will not be a dominating process. It is not enough for a process to yield stable products; it also must be very fast to occur photochemically. Electron transfer is among the fastest type of chemical process. Therefore, photochemistry consists almost exclusively of charge or electron-transfer reactions, which may be summarized as follows:



or



where A and D denote an electron-poor (acceptor) and an electron-rich (donor) species, respectively, and A^- and D^+ are the reduced A and oxidized D. The asterisk denotes an excited state of A^* , D^* , or $(A-D)^*$ as shown in eq. 2, which is known as an exciplex. The driving force or Gibbs free energy change (ΔG) of these reactions is caused by the absorption of photons by the species indicated (2, 63).

In a photoredox process, an electron is excited to a higher energy level, which alters both the electron donor and electron acceptor properties of the molecule (P). The excitation of the electron leaves a positive hole in its previous location in the orbital and may permit the excited molecule (P^*) to accept an electron. Alternatively, the excited molecule may now have an electron energetically favorable for transfer to another molecule (oxidation).

Reverse reactions, which would result in charge recombination and subsequent deexcitation, must be prevented for a photochemical charge-transfer reaction to proceed with any efficiency. Prevention of reverse reactions may be accomplished by separating the products in some way. A simple example of product separation is the charge separation process that occurs at semiconductor junctions. If *p*- and *n*-type semiconductors are sandwiched together, an interface, called a junction, is formed between them. When light falls on the interface, an electron-hole pair is formed across the junction, which results in charge separation and a voltage difference (63).

The semiconductor model is analogous to processes created in a system of redox reactants; namely, after a redox reaction occurs the products must be moved apart as quickly as possible. The processes of diffusional mass transport or convection are the only means of separating the products in solution, and these processes are slow compared to the mechanism involved in semiconductors. To enhance mass transport, it is possible to introduce intermediates so that the oxidant and reductant are separated by fast electron-transfer reactions. In this case, recombination is prevented (to some extent) by the physical separation of oxidant and reductant using intermediary donors and acceptors (63).

Potential Applications

An experimental bilayer lipid membrane less than 7 nm thick that separates two aqueous solutions is a miraculous structure in itself. However, it has not been made into a practical device thus far, although there have been many attempts. The past, present, and future efforts in the exploitation of the BLM system, especially s-BLMs, for practical applications (2) are worthy of summary.

Specific Electrodes. Many ionophores, such as valinomycin and other macrocyclic compounds (9, 24), have been incorporated into BLMs and have made these membranes ion-specific as well as selective. Another system of interest is iodine-containing BLM, which is specific to iodide (2). The presence of other ions such as Cl^- , SO_4^{2-} , or F^- does not interfere with the "electrode" response to I^- . The behavior of iodine-containing BLM is reminiscent of metallic electrodes that are reversible to ions or their salts (e.g., Ag, Ag^+ , and AgCl). A variety of compounds can and have been incorporated into BLM to make them useful in biosensor devices (14, 24, 64).

Biosensors. Biosensors are essentially a special class of devices that transduce a bioreaction into an electrical signal. In terms of membrane research, the heart of a biosensor is a modified BLM that serves as a model

for the biomembrane. A number of investigators (9, 65–68) have exploited the BLM system for laboratory use. We envision that, for detection in biological environments, the sensing element should be biocompatible and biomembrane-like. Thus, the BLM system has great potential and is an ideal choice for developing a new class of electrochemical biosensors. With electrical methods, detection sensitivities less than 10^{-13} M easily can be achieved and are quite comparable to what is now available using radioimmunoassay techniques.

For biosensing purposes, however, BLMs formed by the conventional method have a number of problems, the most serious of which is the extreme fragility of the BLM. This shortcoming greatly limits the usefulness of the BLM as a practical device because it cannot be easily fabricated and will not sustain rugged laboratory use. One successful attempt to overcome this fragility problem was achieved in our laboratory by forming BLMs on solid supports (s-BLMs), as previously described. We found that the electrical properties of s-BLMs are consistent with those of conventional BLMs. To illustrate our approach to the development of a biosensor for taste discrimination, for example, we would extract and isolate taste buds from bovine tongues for incorporation into supported BLMs. Similarly, we would isolate receptor proteins from olfactory organs to construct biosensors for odor detection. Whether a new class of biosensors using s-BLMs can be developed remains to be seen, but the advantages of specificity and biocompatibility of BLMs make such an endeavor exciting (41, 63, 67–72).

Biomolecular Electronic Devices. The basis for molecular electronic device (MED) concepts was the topic of MED workshops and symposia organized by Carter in the 1980s (69). These proceedings provided a first step toward the design and construction of a “molecular” diode (or rectifier). Using the CV technique and a TCNQ-containing BLM, we have shown that flow from the cathode to the anode via the well-known organic conductors TCNQ (tetracyano-*p*-quinodimethane) and TTF (tetrathiofulvalene) is accomplished by a tunneling mechanism. To date, one problem in relation to MED is the concern that molecules in Langmuir–Blodgett films of bilayer thickness have exhibited no interesting electronic properties (e.g., nonlinear I/V curves). We speculate that one of the reasons lies in the substrate–film contact, which could be full of pinholes at the bilayer dimension. This problem could be overcome by using the BLM techniques. In this connection, mention must be made of the work by Potember, Poehler, and Cowan (*see* reference 69), who have been working with polycrystalline films of Cu or Ag salts of TCNQ. They have shown that such thin films (5–10 μM thick) sandwiched between metal electrodes can switch from a low to a high level of conductance in response to an applied voltage. A similar effect also could be observed with a laser instead of a voltage. Thus, Potember et al. (*see* references 2 and 69) have constructed an optically driven switch that uses

5–10 μm films. In comparison with a bilayer lipid membrane (5 nm thick), a factor of 1000 times larger is involved. Thus, what new kinds of phenomena could be observed as one approaches molecular sizes with TCNQ-containing BLMs? One way to find out is to form a TCNQ-TTF system using the new BLM technique. Experiments along this line currently are being carried out.

Solar Energy Transduction. Photoelectric effects in BLM, discovered in 1968, have been extensively investigated (63). Lately, photoactive BLMs have found their place in the field of photochemical conversion and storage of solar energy (for reviews, see references 63 and 73–79). For instance, with suitable electron acceptors and donors in the bathing solution separated by a pigmented BLM, light-induced redox reactions can occur at opposite interfaces. It may be possible to couple BLMs of this type in such a way as to effect photolysis of water into hydrogen and oxygen (25, 63). However, the ultrathin lipid films in the form of BLM that are described in this chapter have not been developed into practical devices for energy transduction. The chief attraction of photoactive BLM to many scientists is that the system mimics, to some extent, the photosynthetic thylakoid membranes of green plants, through which solar energy is harvested and processed. Investigations of photoactive BLM may provide insight on the mechanism of light-initiated redox reactions in photosynthesis, from which we may learn the basic conditions that must be fulfilled for efficient photoelectrochemical utilization of solar energy. Such knowledge may aid in the design and construction of practical devices for producing electricity and for splitting water to hydrogen by sunlight.

Indeed, based on experience gained in pigmented BLM research in artificial photosynthesis, a novel type of photoelectric cell, termed a semiconductor septum electrochemical photovoltaic (SC-SEP) cell, has been developed. In a SC-SEP cell, a semiconductor septum (e.g., CdSe) is used in place of a pigmented BLM to separate two aqueous solutions. When light shines on the semiconductor membrane, photoinduced redox reactions are observed (82–84). Operation under short-circuit conditions allows the cell to be used for photolysis of water using solar energy (85).

Acknowledgments

The work reviewed here was supported by the Office of Naval Research Contract N00014-85-0399 and by the National Institutes of Health Grant GM-14971. Jane Reid is thanked for consistent secretarial assistance.

References

1. In *Proceedings of the Symposium of the Electrochemical Society*, Blank, M., Ed.; Plenum: New York, 1986; pp 149–166.

2. Tien, H. T. In *Thin Liquid Films*; Ivanov, I., Ed.; Dekker: New York, 1988; pp 927–1057.
3. Krueger, B. K.; Worley, J. F.; French, R. J. *Nature (London)* **1983**, 303, 172.
4. Vassilev, P. M.; Tien, H. T. In *Artificial and Reconstituted Systems*; Harris, J. R.; Etemadi, A.-H., Eds.; Plenum: New York, 1989; pp 97–147.
5. Blumenthal, R.; Klausner, R. D. In *Membrane Reconstitution*; Poste, G.; Nicholson, G. L., Eds.; Elsevier: New York, 1982; p 43.
6. Ahlers, M.; Muller, W.; Reichert, A.; Ringsdorf, H.; Venzmer, J. *Angew. Chem. Int. Ed. Engl.* **1990**, 29, 1269.
7. Antonov, V. F.; Rovin, Y. G.; Trofimov, L. T. *A Bibliography of Bilayer Lipid Membranes*; All Union Institute for Scientific and Technical Information: Moscow, Russia, 1979.
8. Akabas, M. H.; Cohen, F.; Finkelstein, A. *J. Cell Biol.* **1984**, 98, 1063–1071.
9. *Water Transport in Biological Membranes*; Benga, G., Ed.; CRC Press: Boca Raton, FL, 1989; p 41.
10. *Modern Bioelectricity*; Marino, A. A., Ed.; Dekker: New York, 1988; p 181.
11. Davison, S. G. *Prog. Surf. Sci.* **1985**, 19(3), 169–274.
12. *International Symposium on Solution Behavior of Surfactants*; Mittal, K. L., Ed.; Plenum: New York, 1990; Vol. 8, p 133.
13. *International Symposium on Solution Behavior of Surfactants*; Mittal, K. L.; Shah, D. O., Eds.; Plenum: New York, 1992; Vol. 11, pp 61–80.
14. Tien, H. T. *Bilayer Lipid Membranes (BLM): Theory and Practice*; Dekker: New York, 1974.
15. Vodyanoy, V.; Halverson, P.; Murphy, R. B. *J. Colloid Interface Sci.* **1982**, 88, 247.
16. Ring, A. *Pflugers. Arch. Eur. J. Physiol.* **1992**, 420, 264–268.
17. Tancrede, P.; Paquin, P.; Houle, A.; LeBlanc, R. M. *J. Biochem. Biophys. Methods* **1983**, 7, 299.
18. Wang, E.-K. *J. Chem. Soc. Faraday Trans.* **1991**, 86, 2243–2247.
19. Tien, H. T.; Salamon, Z. *Bioelectrochem. Bioenerg.* **1989**, 22, 211.
20. Wardak, A.; Tien, H. T. *Bioelectrochem. Bioenerg.* **1990**, 24, 1.
21. Martynski, T.; Tien, H. T. *Bioelectrochem. Bioenerg.* **1991**, 25, 317.
22. Zviman, M.; Tien, H. T. *Biosensors Bioelectron.* **1991**, 6, 37.
23. Schulmann, W.; Heyn, S.-P. *Adv. Mater.* **1991**, 3, 388–391.
24. *Bioelectrochemistry and Bioenergetics*; Milazzo, G., Ed.; Wiley: New York, 1983; Vol. 5, pp 157–224.
25. Tien, H. T. *Photochem. Photobiol.* **1976**, 24, 95–207.
26. Lewis, T. J. *Phys. Med. Biol.* **1982**, 27, 335–352.
27. Taylor, D. M.; Mahboubian-Jones, M. G. B. *Thin Solid Films* **1982**, 87, 167–172.
28. Bockris, J. O'M.; Diniz, F. B. *J. Electrochem. Soc.* **1988**, 135, 1947–1954.
29. Boguslavski, L. In *Modern Aspects of Electrochemistry*; White, R. E.; Bockris, J. O'M.; Conway, B. E., Eds.; Plenum: New York, 1986; Vol. 18, p 113.
30. Karvaly, B.; Pant, H. *Stud. Biophys.* **1972**, 33, 51.
31. Karvaly, B.; Dancshazy, Z. *FEBS Lett.* **1977**, 76, 45.
32. Feldberg, S. W.; Armen, G. H.; Bell, J. A.; Chang, C. K. *Biophys. J.* **1980**, 34, 149.
33. Ward, M. D. *Electroanal. Chem.* **1990**, 16, 181–312.
34. *Membranes and Transport*; Martonosi, A. N., Ed.; Plenum: New York, 1982.
35. White, S. *Science (Washington, D.C.)*, **1980**, 207, 1075.
36. Gruen, D. W. R.; Haydon, D. A. *Pure Appl. Chem.* **1980**, 52, 1229.
37. McIntosh, T. J.; Simon, S. A.; MacDonald, R. C. *Biochem. Biophys. Acta* **1980**, 597, 445; 645, 318.

38. Sugar, I. P.; Neuman, E. *Biophys. Chem.* **1984**, *19*, 211.
39. Zimmermann, U. *Biochim. Biophys. Acta* **1982**, *694*, 227–277.
40. *Redox Chemistry and Interfacial Behavior of Biological Molecules*; Dryhurst, G.; Niki, K. Eds.; Plenum: New York, 1988.
41. *Molecular Electronics: Biosensors and Biocomputers*; Hong, F. T., Ed.; Plenum: New York, 1989.
42. Olson, J. M.; Hind, G. *Brookhaven Symp. Biol.* **1976**, *28*, 105–131.
43. *Photosynthetic Oxygen Evolution*; Metzner, H., Ed.; Academic: New York, 1978; pp 411–438.
44. *Photosynthesis in Relation to Model Systems*; Barber, J., Ed.; Topics in Photosynthesis 3; Elsevier: New York, 1979; pp 115–173.
45. *Solar Power and Fuels*; Bolton, J. R., Ed.; Academic: New York, 1977; pp 167–225.
46. Tien, H. T. *Photochem. Photobiol.* **1976**, *24*, 95–207.
47. Yonezawa, H.; Fujiwara, Y.; Sato, T. *Thin Solid Films* **1992**, *210*, 736–738.
48. *Transport in Membranes: Model Systems and Reconstitution*; Antolini, R.; Gliozzi, A.; Gorio, A., Eds.; Raven: New York, 1982; pp 57–75.
49. Connolly, J. S.; Bolton, J. R. In *Photoinduced Electron Transfer*; Fox, M. A.; Cannon, M., Eds.; Elsevier: Amsterdam, The Netherlands, 1989; pp 303–393.
50. Rich, M.; Brody, S. S. *FEBS Lett.* **1982**, *143(1)*, 45.
51. Vacek, K.; Valent, O.; Skuta, A. *Biophys.* **1982**, *2*, 135.
52. Mauzerall, D. In *Light-Induced Charge Separation in Biology and Chemistry*; Gerischer, H., Ed.; Verlag-Chimie: Berlin, Germany, 1979; pp 241–254.
53. Liu, T. M.; Mauzerall, D. *Biophys. J.* **1985**, *48*, 1.
54. Lambardt, A.; Janot, J. M.; Bienvenue, E.; Miquel, G.; Seta, P. *Bioelectrochem. Bioenerg.* **1992**, *27*, 449–463.
55. Putvinskii, A. V. *Biofizika* **1977**, *22*, 725.
56. Kadoshnikov, S. I.; Stolovitsky, Yu. M. *Bioelectrochem. Bioenerg.* **1982**, *9*, 79.
57. Koyama, Y.; Komori, M.; Shiomi, K. *J. Colloid Interface Sci.* **1982**, *90*, 293.
58. Bresseur, R.; Meutter, J. D.; Ruyschaert, J.-M. *Biochim. Biophys. Acta* **1984**, *764*, 295.
59. Hattenbach, A.; Gundel, J.; Hermann, G.; Haroske, D.; Mueller, E. *Biochem. Physiol. Pflanz.* **1982**, *177*, 611.
60. Schreckenbach, T. *Photosynthesis in Relation to Model Systems*; Barber, J., Ed.; Elsevier Biomedical Press: New York, 1979; Chapter 6.
61. Ormos, P.; Dancshazy, Z.; Karvaly, B. *Biochim. Biophys. Acta* **1978**, *503*, 304.
62. Fox, M. A. *Top. Curr. Chem.* **1991**, *159*, 67–101.
63. Tien, H. T. *Prog. Surf. Sci.* **1989**, *30*, 1–200.
64. Koryta, J. *Ions, Electrodes and Membranes*; Wiley: New York, 1982; p 197.
65. Tien, H. T.; Salamon, Z.; Kochev, V.; Ottova, A.; Zviman, M. In *Proceedings of the Symposium on Molecular Electronics: Biosensors and Biocomputers*; Hong, F. T., Ed.; Plenum: New York, 1989; pp 259–268.
66. Krull, V. J.; Thompson, M.; Wong, M. E. In *Fundamentals and Applications of Chemical Sensors*; Schuetale, D.; Hammerle, R.; Butler, J. W., Eds.; American Chemical Society: Washington, DC, 1986; p 351.
67. Reichert, W. M.; Bruckner, J.; Joseph, J. *Thin Solid Films* **1987**, *152*, 345.
68. Yamada, H.; Matsue, T.; Uchida, I. *Denki Kagaku* **1992**, *60*, 664–665.
69. *Molecular Electronic Devices*; Carter, F. L.; Siatkowski, R. E.; Wohltjen, H., Eds.; North-Holland, Amsterdam, The Netherlands, 1988; p 685.
70. *Active Materials and Adaptive Structures*; Knowles, G. J., Ed.; Proceedings of ADPA, AIAA/ASME/SPIE, November 1991, Alexandria, VA; Institute of Physics Publishing: Bristol, England, 1991; pp 27–32.

71. Tien, H. T. *J. Clin. Lab. Anal.* **1988**, *2*, 256–264.
72. Olsher, U.; Frolow, F.; Bartsch, R. A.; Pugia, M. J.; Shoham, G. *J. Am. Chem. Soc.* **1989**, *111*, 9217–9222.
73. Porter, G.; Archer, M. D. *Interdisc. Sci. Rev.* **1976**, *1*, 119.
74. Patsis, A. V.; Seanor, D. A. *Photoconductivity in Polymers*; Technomic Publishing: Westport, CT, 1976; pp 309–328.
75. Bolton, J. R.; Hall, D. O. *Ann. R. Energ.* **1979**, *4*, 353.
76. Gerischer, H. *Top. Appl. Phys.* **1979**, *31*, 115.
77. *Solar Energy: Chemical Conversion and Storage*; Hautala, R. R.; King, R. B.; Kutal, C., Eds.; Humanities Press: Atlantic Highlands, NJ, 1979; pp 203–235.
78. Gratzel, M. *Ber. Bunsenges. Ges.* **1980**, *84*, 981.
79. Chen, W. L.; Gross, E. L.; Pan, R. L. *Botan.* **1992**, *33*, 9–15.
80. Seta, P.; Bienvenue, E. *Imag Chim. Suppl.*, Centre National de la Recherche Scientifique: Paris, France, 1985; pp 65–70.
81. Seta, P.; Bienvenue, E.; Moore, A. L.; Moore, T. A.; Gust, D. *Electrochim. Acta* **1989**, *34*, 1723–1727.
82. Mureramanzi, S.; Tien, H. T. *Int. J. Ambient Energy* **1986**, *7*(1), 3.
83. Summers, L. A. *J. Heterocycl. Chem.* **1992**, *28*, 827–842.
84. Malinski, T.; Ciszewski, A.; Fish, J.; Kubszewski, E.; Czuchajo, L. *Adv. Mater.* **1992**, *4*, 354–357.
85. Tien, H. T. *Adv. Mater.* **1990**, *2*, 263.

RECEIVED for review March 5, 1991. ACCEPTED revised manuscript September 1, 1992.

Electrochemical Processes in Membranes That Contain Bacteriorhodopsin

Felix T. Hong

Department of Physiology, Wayne State University, School of Medicine,
Detroit, MI 48201

Pulsed-light illumination of reconstituted bacteriorhodopsin membranes elicits a fast photoelectric signal as a result of light-induced rapid charge separation. This signal is similar to the early receptor potential in a visual membrane. Nonelectrochemical interpretation of this type of signal reported in the literature has led to discrepancies in data reported by various laboratories and to conclusions that contradict established facts. This problem is addressed by applying the Gouy–Chapman diffuse double-layer theory to the electrokinetic process of rapid charge separation and recombination. This electrochemical analysis leads to a universal equivalent circuit that offers a coherent interpretation of data, simple explanations for a number of otherwise inexplicable observations, and a predictive power that was lacking in the nonelectrochemical analysis. The interpretation is further extended to include photosynthetic and visual membranes and the design principles of molecular electronic devices.

BACTERIORHODOPSIN IS UNIQUE AMONG MEMBRANE PROTEINS because of its central role in many different scientific disciplines and its use as the proving ground for many different scientific approaches such as laser spectroscopy, membrane biophysics, and molecular biology (1–6). In addition, bacteriorhodopsin has attained a new prominence, not only because it is used as a model of membrane ion pumps, but also because it is increasingly important for such technological applications as advanced photonic and photoelectronic

0065-2393/94/0235-0531 \$10.70/0
© 1994 American Chemical Society

materials (7–9). In this chapter, we will illustrate the power of electrochemistry to elucidate both the molecular and the underlying physicochemical processes so as to enhance our understanding of the basic mechanism of bacteriorhodopsin function. We will also discuss possible technological applications.

Bacteriorhodopsin, the only protein component of the purple membrane of *Halobacterium halobium*, belongs to a family of membrane proteins that form seven α -helical loops across the membrane and that contain vitamin A₁ as the chromophore (10, 11). Rhodopsin, the first known member of this family, is the visual pigment in the rod receptor cells of vertebrates and in the rhabdomeres of invertebrates. Rhodopsin has been known for more than 100 years. Although it was known (12) that a single photon absorbed by a single rhodopsin molecule is sufficient to elicit a neural excitation of the visual membrane, the biochemical mechanism of visual phototransduction has only recently been elucidated (for reviews, see references 13–18). In view of this new understanding, the absorbed photon energy serves merely as a trigger to unleash stored energy in the form of a sodium ion gradient, and the visual membrane functions as a photon signal transducer like a phototransistor. In contrast, bacteriorhodopsin functions as a photon energy converter like a silicon photodiode. The absorbed photon energy is converted to electrochemical energy in the form of a transmembrane proton gradient, similar to the role of the photosynthetic thylakoid membrane of chloroplasts of green plants. In other words, *Halobacterium halobium* uses a visual pigment to perform photosynthesis. However, unlike the reaction center of a phototrophic purple bacterium or the two reaction centers of higher plants, the reaction center of *Halobacterium halobium* consists of a single molecular component: bacteriorhodopsin.

The structural simplicity and the unique relationship of bacteriorhodopsin to the two major photobiological systems—vision and photosynthesis—allow us to consider several questions of scientific and technological importance. What is the minimum requirement of a light energy converter? Does Nature utilize a common design for vision and for photosynthesis? How can we technologically exploit bacteriorhodopsin by “reverse engineering”? Although definitive answers may not always be available, we will illustrate that a deeper insight is feasible by using the power of electrochemistry to analyze the relaxation kinetics of electric signals elicited from a bacteriorhodopsin membrane when it is illuminated with a brief (microsecond or shorter) flash of visible light. The electric signals so generated belong to a class of bioelectric signals known as displacement currents; the gating current of a squid axon is the best known example. Unlike other types of bioelectric signals, displacement currents are not generated by ion diffusion in water, but rather are generated by charge displacements in the membrane. The light-induced displacement currents are also known as the fast photoelectric signals. Specifically, by invoking electrochemistry, a phenomenological de-

scription of electrophysiology can be transformed into a rigorous molecular description of the underlying physicochemical processes. Thus, some seemingly inexplicable phenomena will have simple explanations based on electrochemistry.

Fast Photoelectric Effect

The fast photoelectric effect is the manifestation of light-induced rapid charge separation in the direction perpendicular to the membrane surface (19–23). Because the photopigments maintain a preferential orientation with respect to the membrane, the charge separation is vectorial in nature and, therefore, can be detected macroscopically as a photovoltage under open circuit conditions or as a photocurrent (known as a displacement photocurrent) under short-circuit conditions. The best known example of fast photoelectric signals is the early receptor potential (ERP) found in the retina of the cynomolgus monkey (24, 25). However, earlier reports of the early receptor potential and the ERP-like signal in reconstituted bacteriorhodopsin membranes were plagued with inconsistencies and paradoxes. For example, the R2 component of the ERP was correlated with the acid–base reaction of the metarhodopsin I to metarhodopsin II transition (25), yet the R2 component was reported to have no significant pH dependence (26), which thus defies the law of mass action. More recently, we pointed out a striking discrepancy in the relaxation time data reported by various laboratories on the ERP-like signal from reconstituted bacteriorhodopsin membranes (Table I). As we will show, these difficulties can be resolved by an electrochemical analysis. In fact, an electrochemical analysis of light-induced charge separation and recombination predicts these heretofore inexplicable observations.

Electrochemical Basis of the Fast Photoelectric Effect

Our electrochemical analysis is based on a major conclusion from decades of investigation of the ERP: The ERP is the electrical manifestation of light-induced rapid charge displacements and the transient photocurrent satisfies the condition of a zero time integral (33). In other words, the displacement photocurrent is not generated by diffusion of ions through an aqueous channel in the membrane, but rather by rapid charge separation and recombination. Thus, the light-induced forward charge movement is subsequently compensated by an equal and reverse charge movement in the opposite direction that results in no net charge transport across the membrane and, therefore, satisfies the zero time-integral condition.

Charge recombination is a widely recognized phenomenon in photosynthesis and solar energy conversion research that, until recently, was less appreciated in bacteriorhodopsin research. Charge recombination dissipates

Table I. Relaxation Time Constants of Bacteriorhodopsin Photosignals

Reference	τ_1 (μs)	τ_2 (μs)	τ_3 (ms)	τ_4 (ms)
27	1.3	17	0.06	0.9
28	25	150	2.4	5.8
29	4.4	81	2.5	8
30	<i>a</i>	57	1.06	13
31 ^b	<i>a</i>	115	4.5	640
32	< 0.2	200	2	1000

^a τ_1 not reported.

^b Derived from Figure 1d in reference 31.

SOURCE: Reproduced with permission from reference 39. Copyright 1986.

the converted photon energy before it can be further stored as a more stable and readily utilized form of energy such as a transmembrane electrochemical gradient of protons. The conspicuous manifestation of charge recombination in the form of the ERP possesses no conceptual difficulty in a visual membrane. However, displacement photocurrents that are capacitative do not lead to a net transmembrane charge transport [direct current (dc) photocurrent] and no light energy is converted to a stable form during the process. The kinetic analysis that follows will show that the net proton transport does occur despite the ever-present charge recombination. A striking observation is that displacement photocurrents are much more prominent in magnitude than the dc photocurrent if a brief (microsecond) light pulse is used to stimulate the membrane. Thus, an overwhelming fraction of separated charges appear to recombine. Only a negligible fraction is converted to the form of a proton gradient. On the other hand, if a long rectangular light pulse is used, a displacement current can be observed only briefly upon the onset and upon the cessation of the light pulse; only the net charge transfer (forward transfer minus reverse transfer) is observed during the steady state. Why the magnitude of displacement photocurrents tends to be out of proportion when it is elicited by a brief light pulse can be explained by a universal equivalent circuit model that will be described later.

The ERP was often attributed to intramolecular charge displacement. Because light-induced conformational changes of rhodopsin are accompanied by rapid charge separation and because rhodopsin maintains a fixed orientation in the membrane, a transient array of electric dipoles with net moments in the direction perpendicular to the visual membrane will appear upon illumination. By virtue of the zero time-integral condition, such an electric dipole array must vanish as separated charges recombine upon cessation of illumination. This process is tantamount to charging and discharging of a capacitor. This mechanism will be referred to as the *oriented dipole mechanism* (OD mechanism in Figure 1) (34). However, this is not the only kind of

charge separation and recombination that can be found in the visual membrane and in the purple membrane of *H. halobium*.

The metarhodopsin I–metarhodopsin II transition, which occurs concurrently with the R2 signal, is a key step in the photobleaching of rhodopsin. In this reaction, one proton is bound to the pigment (35). Such a proton binding reaction is required for proton pumping in the purple (bacteriorhodopsin) membrane. If we assume that a reverse reaction exists in each and every biochemical reaction, then a proton binding reaction must be accompanied by a reverse reaction in which the bound proton is released into the adjacent aqueous phase; that is, the proton is released into the same aqueous phase whence it was bound previously. Upon light-induced proton binding by the pigment, the counterions must be left behind in the adjacent aqueous phase. This abandonment constitutes another kind of charge separation. The reverse interfacial proton transfer can thus be regarded as charge recombination. Such interfacial proton transfer reactions and the accompanying reverse reactions are also tantamount to charging and discharging of a capacitor. We refer to this mechanism as the *interfacial proton transfer mechanism* (IPT mechanism in Figure 1).

Because the objective of proposing these models is to understand the macroscopically measured displacement photocurrents in terms of the underlying mechanistic and molecular processes, the connection between macroscopic electrical parameters and microscopic parameters must be demonstrated. This linkage can be provided by an analysis based on the Gouy–Chapman diffuse double layer theory and the derivation of an equivalent circuit. As documented elsewhere (34, 36), analysis of the two models shown in Figure 1 gives rise to a space charge density profile and an electrical potential profile across the membrane. The equations that describe these profiles can be reinterpreted as charge–potential relationships in terms of three fundamental capacitances: a geometric capacitance (C_g) and two double layer capacitances (C_d). This interpretation allows the spatial relationship of these capacitances and the (microscopic) photovoltage source (E_p') and its internal resistance (R_p) to be deduced. Two slightly different equivalent circuits that were obtained for the two mechanisms could be further reduced to a common irreducible equivalent circuit, in which a composite capacitance, C_p , is connected in series with the macroscopically measured photoelectromotive force (photoemf), E_p . Contrary to conventional wisdom, this capacitance, which we named *chemical capacitance*, is physically distinct from the ordinary membrane capacitance. A detailed argument, published elsewhere (20), proves this point of view. Here it suffices to point out that whereas an ordinary membrane capacitance is in parallel with the photoemf, the capacitance C_p is in series with the photoemf. In other words, the photosignal is ac-coupled (alternating-current coupled) through a built-in series capacitance, which, together with the internal resistance R_p , forms a high-pass filter for the photosignal.

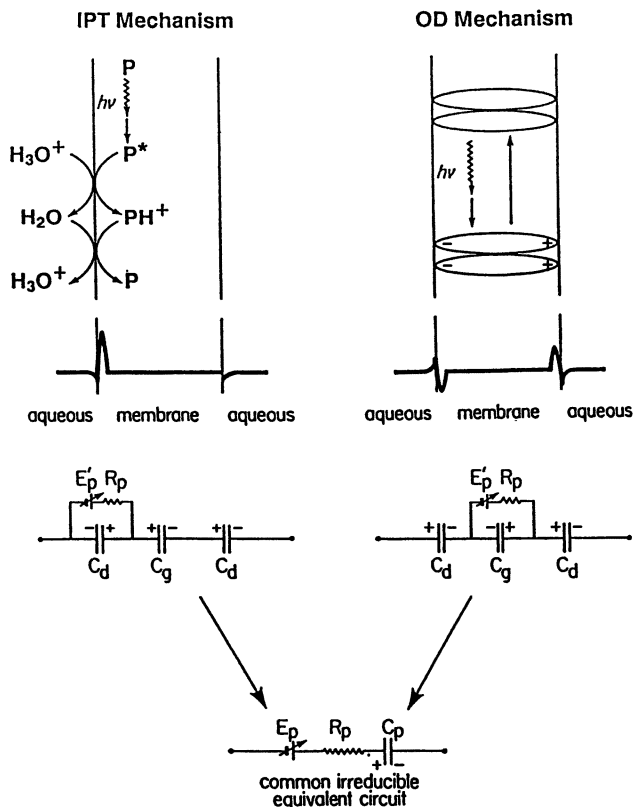


Figure 1. Two types of photoinduced charge separation (upper diagrams). The interfacial proton transfer (IPT) mechanism applies both to cytoplasmic proton binding and extracellular proton release at the membrane surface (only proton binding is shown). The oriented dipole (OD) mechanism applies to charge separation inside the membrane (or rather, inside bacteriorhodopsin). The thick curve across the membrane shows the space charge density profile, which, together with the potential profile across the membrane (not shown), allows us to deduce the two microscopic equivalent circuits shown in the lower diagrams. The two slightly different microscopic equivalent circuits are equivalent to the same irreducible equivalent circuit. (Reproduced with permission from reference 34. Copyright 1978.)

The high-pass filter effect of C_p dictates that the faster the charge separation and recombination, the greater the magnitude of the observed photocurrent. This relationship explains why a photocurrent induced by a brief light pulse appears to represent largely charge separation and recombination and why the prominent photocurrent spikes appear only upon the onset and the cessation of a long rectangular light pulse. In fact, these events are typical responses of a high-pass filter to a voltage pulse.

Another consequence of the presence of the series capacitance, C_p , is the reduction of the source impedance of the membrane in the high-frequency range. Because of this peculiar effect, a short-circuit measurement is harder to achieve in the high frequency range than in a steady state because a lower input impedance is required to achieve a short-circuit condition. Sometimes a commercial picoammeter is used to measure displacement photocurrents under a presumed short-circuit condition. However, such instruments often have an input impedance on the order of 100 k Ω in the megahertz frequency range. In view of the much reduced source impedance of a reconstituted purple membrane, these measurement conditions are actually closer to an open circuit than to a short-circuit condition. The measurement is often accompanied by a telltale observation that the measured current is the first time derivative of the measured photovoltage (26). A detailed analysis of this problem is presented elsewhere (19, 20).

As suggested by the common equivalent circuit shared by both the OD and the IPT mechanism, the macroscopically measured photosignals that arise from these two mechanisms are superficially indistinguishable. Differentiation between the two mechanisms is possible, however, by virtue of a chemical manipulation. Whereas the charge recombination is most likely a first-order (monomolecular) process in the OD mechanism, recombination is a bimolecular process (second order or pseudo first order) in the ICT mechanism. Thus, the photosignal that arises from an interfacial proton binding process is expected to be sensitive to the pH of the adjacent aqueous phase. The absence of such pH dependence of the ERP as reported in the literature prompted some investigators to conclude that the ERP is generated by an oriented dipole mechanism. However, the R2 component of the ERP has been shown to be correlated with a proton binding reaction. This paradoxical behavior can be explained by the universal equivalent circuit model (*see* succeeding text).

The revelation that C_p is indeed a novel capacitance requires the inclusion of two capacitances in the equivalent circuit shown in Figure 2 (36, 37). In essence, with the exception of a genuine short-circuit measurement, the macroscopically measured photosignal is a manifestation of the interaction of two circuits in parallel: One circuit represents the photochemical event associated with bacteriorhodopsin, and the other circuit represents the resistance-capacitance (RC) relaxation event of the inert supporting structure—the membrane dielectric.

It can be visualized readily in Figure 2 that the photocurrent generated in the circuit has two parallel paths to follow: one path is formed by the resistance (R_m) and the capacitance (C_m) of the inert supporting structure; the other path is through the external measuring device. The partition of these two fractions of photocurrent depends primarily on the relative magnitude of the access impedance (R_e) and the impedance of the inert supporting structure.

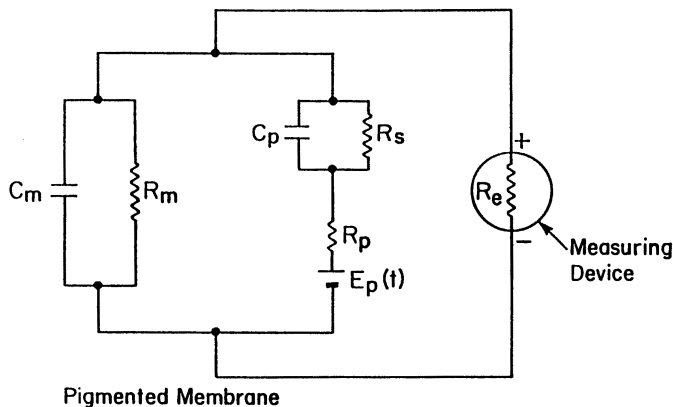


Figure 2. Equivalent circuit of a bacteriorhodopsin membrane that includes the circuit parameters of the inert supporting structure and the access impedance of the measuring system. R_e is the access impedance, which includes the input impedance of the measuring device, the electrode impedance, and the electrolyte impedance between the membrane and the electrodes. R_m and C_m are the resistance and the capacitance of the membrane, C_p is the chemical capacitance, R_p is the internal resistance of the photoelectric voltage source, $E_p(t)$, which is a function of the illuminating light power, and R_s is the transmembrane resistance encountered by the dc photocurrent. (Reproduced from reference 19. Copyright 1980 American Chemical Society.)

Under a true short-circuit condition, the photocurrent will be diverted exclusively to the external measuring device and there will be no interaction with the inert supporting structure. Thus, upon illumination with a brief light pulse (ideally with a delta function time course), charges will separate and a surge of forward photocurrent will be generated. Upon the cessation of illumination, charge recombination ensues and the photocurrent reverses direction immediately; the reversed current will decline with a single exponential time course if the recombination is a first-order or pseudo-first-order process (shown in Figure 3) (19).

If, however, the access impedance is substantially different from zero, the partition of photocurrent between the external circuit and the internal membrane RC network will lead to a surge of forward photocurrent that is followed by a biexponential decay, as can be shown analytically by solution of a second-order differential equation (36). In the extreme case of an open circuit measurement in which the fraction of photocurrent following through the external circuit is negligibly small and in which the electrical signal is necessarily reported as a photovoltage, almost all of the photocurrent will proceed to the membrane RC network. It is quite apparent that the photocurrent relaxation necessarily will be slow because it is dominated by the RC relaxation of the inert supporting structure ($R_m C_m$). This conclusion indicates that the long relaxation time constant τ_4 reported by Drachev et al.

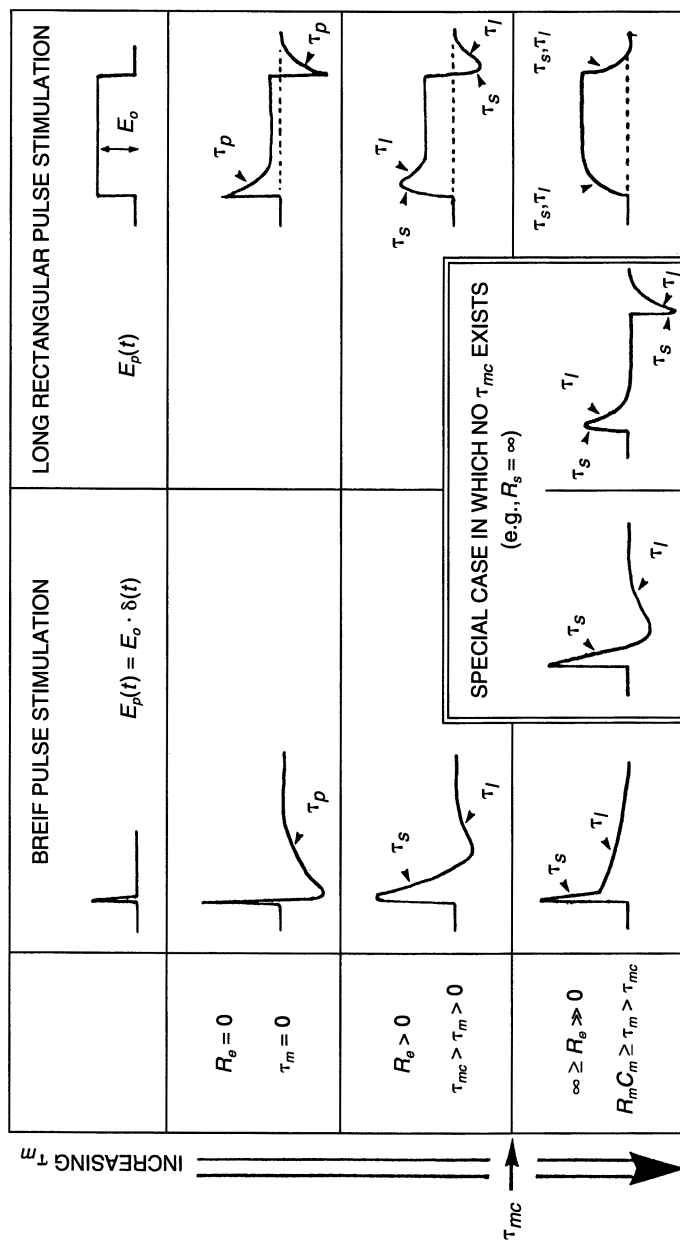


Figure 3. Relaxation time course of a pulsed-light-induced photoelectric signal with a single component. Both responses to a brief light pulse and to a long rectangular light pulse are shown, but only the brief light pulse is discussed in the text. The parameter τ_m is the characteristic RC relaxation time of the system that depends on R_m , R_e , and C_m shown in Figure 2. τ_{mc} is the critical value around which the time course is changed from monotonic to biphasic and vice versa (not discussed in the text). (Reproduced from reference 19. Copyright 1980 American Chemical Society.)

(32) under open circuit conditions is indeed the membrane RC relaxation (Table I). This effect was recognized and reported by Drachev et al. (32), but the distortion of the remaining time constants was not appreciated. Because almost all reported ERP data in the literature are measured under open circuit conditions, this effect explains, at least partially, why the R2 component of the ERP was found to be insensitive to pH changes in the aqueous phases. A similar problem can also be identified in the literature of bacteriorhodopsin: the ERP-like signal from a reconstituted bacteriorhodopsin membrane is insensitive to pH in the physiological range (32). Hong and Montal (38) have demonstrated that such a lack of pH sensitivity in bacteriorhodopsin membranes is, in part, due to the commonly used open circuit measurement method. We found that at least two chemically distinct components exist in a reconstituted bacteriorhodopsin membrane: a B1 component that is insensitive to both temperature and pH changes and is thus analogous to the R1 component of the ERP, and a second temperature sensitive component, B2, that is analogous to the R2 component, which was found to be highly sensitive to pH under a near short-circuit condition but that is insensitive to pH under an open circuit condition (Figure 4).

Component Analysis

The preceding analysis clearly indicates that the practice of decomposing a photosignal in terms of its individual components as shown in Table I is not recommended. In fact, our analysis indicates that a photosignal that represents a single exponential relaxation will be manifest as a biexponential decay except under true short-circuit conditions. Thus, decomposition of the photosignal into components that correspond to the underlying chemical processes must be based on the equivalent circuit analysis and taken into account the presence of a nonzero access impedance. The equivalent circuit analysis indicates that all of the circuit parameters can be either determined experimentally or derived by computation using measurable parameters and are, therefore, not freely adjustable (*see* Appendix III in reference 36).

Thus, unlike some kinetic models with many parameters that must be determined implicitly by curve fitting, the present equivalent circuit model offers a stringent test of the validity of our electrochemical analysis. The previously published (34, 36) derivation of the equivalent circuit implies that the equivalent circuit is intended for a photocurrent that arises from a single relaxation process; that is, either first-order or pseudo-first-order processes. Thus, a composite photosignal that consists of both B1 and B2 is not expected to agree with the equivalent circuit. Therefore, a prerequisite to test the validity of the equivalent circuit analysis is to devise a successful method to separate the two components, for example, by elimination of the B2 component completely but leaving the B1 component intact.

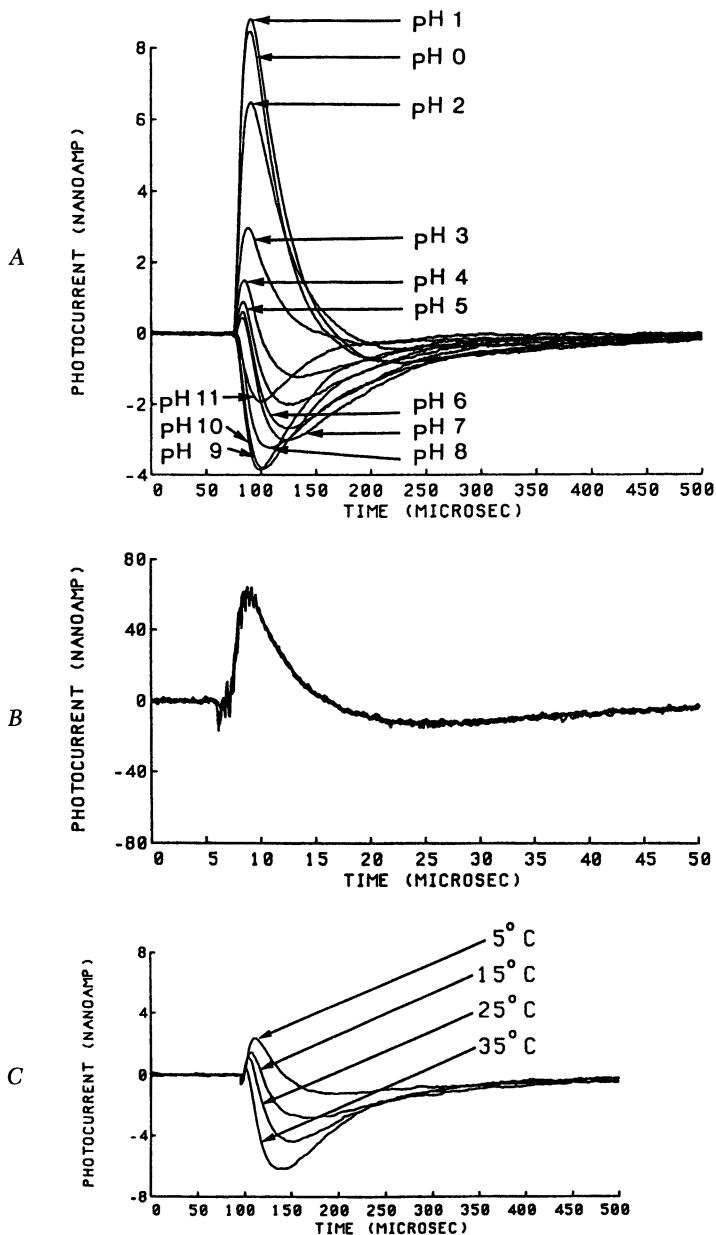


Figure 4. Temperature and pH dependence of the B1 and the B2 components. The photosignals generated in Trissl-Montal films are shown in A and in C for their pH and temperature dependence, respectively. The corresponding photosignals obtained from a multilayered thin film are shown in B and in D. The plot in B shows superposition of photosignals obtained from the same film at pH 7, 8, 9, and 10. Continued on next page.

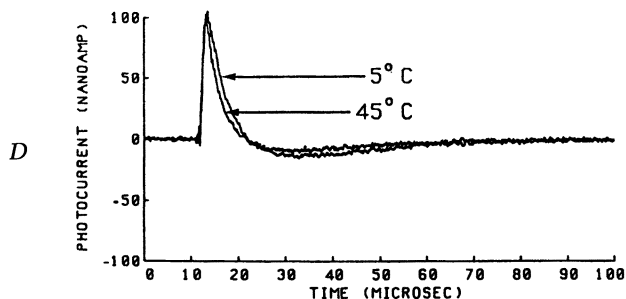


Figure 4.—Continued. The small temperature dependence shown in *D* corresponds to an activation energy of 2.5 kcal/mol. (Reproduced with permission from references 39 and 41. Copyrights 1986 and 1987.)

One such method was reported by Okajima and Hong (39). Multiple layers of purple membrane sheets were first deposited onto a thin (6- μm) Teflon film that had been previously coated with a mixture of azolectin and *n*-octadecylamine. This thin film assembly was allowed to dry for at least two days, then mounted in a two compartment chamber, and then rehydrated. Pulse light stimulation consistently gave rise to a photosignal that was pH insensitive (Figure 4B) and that was consistently in agreement with the equivalent circuit (Figure 5). In fact, when the access impedance was varied, the change of the photosignal time course could be fully predicted by the equivalent circuit analysis (Figure 5 in reference 39).

However, if the purple membrane sheets are deposited onto the Teflon film by means of a method originally developed by Trissl and Montal (40), a photosignal of considerably smaller magnitude is observed; this photocurrent consists of both a temperature- and pH-insensitive component and a temperature- and pH-sensitive component (Figure 4A and C). Here, a composite signal with at least two components (B1 and B2) is being dealt with, and the decomposition can be tricky. The foregoing analysis indicates that each of the two components decays in two exponentials, as shown in Figure 6. Because of the partial overlap of the decay of B1 and the rise of B2 and because of their opposite polarities, inhibition of B2 alone also can be interpreted as a concurrent inhibition of B2 and enhancement of B1 (cf., Figure 4A and C). In fact, the concurrent inhibition and enhancement was the interpretation presented by Drachev et al. (32). This interpretation further contributes to the apparent lack of pH dependence of the B2 component, because part of the pH dependence of B2 was attributed to B1 instead. Our use of two separate methods of reconstitution and our electrochemical analysis permit us to avoid this pitfall.

Thus, if we define the pH-insensitive photosignal found in the multilayered thin film as the B1 component and the pH-sensitive portion of the

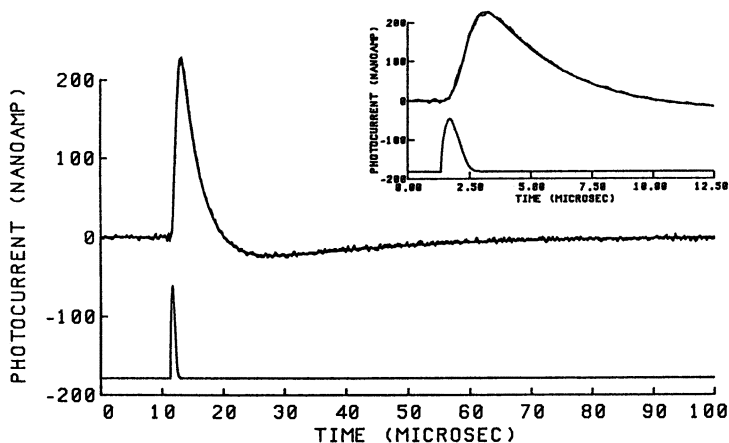


Figure 5. Comparison of the computed photosignal and the measured photosignal obtained from a dried multilayered film of oriented purple membranes. The bathing electrolyte solutions contained 0.1-M KCl and 0.01-M L-histidine buffered at pH 2. The measurement was made at an access impedance of $39.2 \text{ k}\Omega$ and an instrumental time constant of $0.355 \mu\text{s}$. The lower trace is the power versus time function of the light source (dye laser; output at 590 nm). The inset shows the same data at an expanded time scale. See text for further explanation. (Reproduced with permission from reference 39. Copyright 1986.)

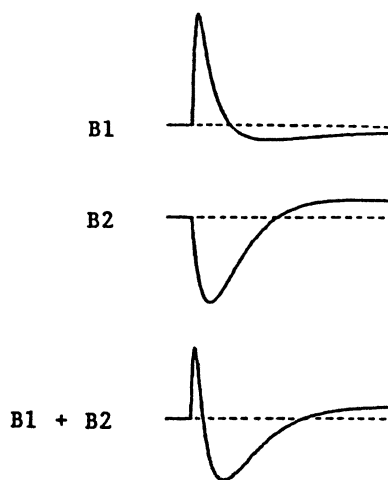


Figure 6. Schematic diagrams that show the decomposition of a composite signal with two displacement current components of opposite polarities when the access impedance is not zero. Each component decays in two exponentials as dictated by the equivalent circuit. Notice that inhibition of the B2 component results in a decrease of the negative peak, but an increase of the positive peak. The sole inhibition of B2 could be misinterpreted as a concurrent increase of B1. (Reproduced with permission from reference 38. Copyright 1979.)

photosignal observed in a Trissl-Montal-type thin film as the B2 component, then a pattern appears. The B2 component is sensitive to D_2O substitution and to changes of ionic strength, whereas the B1 component is not (20, 39, 41). The B2 component can be suppressed with the treatment of a surface chemical label, fluorescamine, whereas the B1 component is not altered by

such a treatment (41). These observations suggest that the B1 component is a natural entity consistent with the underlying photochemistry. Our observations are also consistent with the assignment of the OD mechanism to the B1 signal and the IPT mechanism to the B2 signal. One obvious question is "Why does a dried multilayered bacteriorhodopsin film lose its ability to generate a B2 signal?"

The working hypothesis is as follows (Figure 7). The observation that the pure B1 signal obtained in a multilayered bacteriorhodopsin film is usually 5–10 times larger in peak amplitude than the composite B1 and B2 signal from a Trissl–Montal film suggests that the multiple layers of purple membrane sheets must maintain a high degree of orientation, which results in additivity of the B1 signal. Such additivity would not be expected of the B2 component, because the B2 generation requires access to aqueous protons and only the top layer of the multilayered assembly has such access. This differential effect can lead to enhancement of the B1 signal relative to the B2 signal, but cannot completely eliminate the B2 contribution. The near perfect

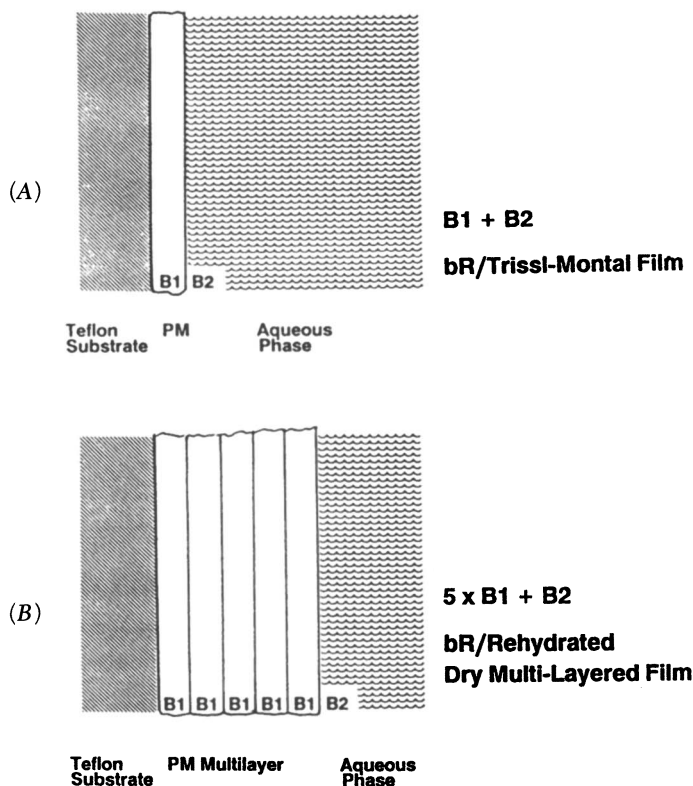


Figure 7. Schematic diagrams that show the difference of a Trissl–Montal film (A) and a rehydrated dry multilayered film (B).

agreement with the equivalent circuit suggests that an additional factor may be responsible for the complete elimination of the B2 signal. We found that prolonged drying of the multilayered bacteriorhodopsin film is necessary to completely eliminate the pH sensitivity. If, however, the film has been dried for less than two days, pH sensitivity, though less conspicuous, is retained. The following series of experiments (42) demonstrates that the additivity of the B1 component serves to diminish the pH sensitivity by virtue of diminishing the B2 contribution to the overall signal and that prolonged drying impairs the mechanism of the B2 generation but not the B1 generation.

In a freshly prepared dried multilayered bacteriorhodopsin film, we observed the magnitude of the photosignal is about 100 nA as compared with 10–20 nA found with a Trissl–Montal bacteriorhodopsin film. We also found that the temperature and pH sensitivity in this film is still evident though less conspicuous than a typical Trissl–Montal bacteriorhodopsin film. This observation indicates a diminished relative contribution of B2. If, however, we attempted to remove the multiple layers by stripping the film with a cotton swab, the photosignal was not completely eliminated but was reduced to about 10–20 nA; the resultant photosignal became indistinguishable from a typical Trissl–Montal bacteriorhodopsin film in terms of its temperature and pH sensitivity (Figure 8A). Apparently, stripping with a cotton swab fails to remove the very bottom layer that adheres tightly to the Teflon substrate.

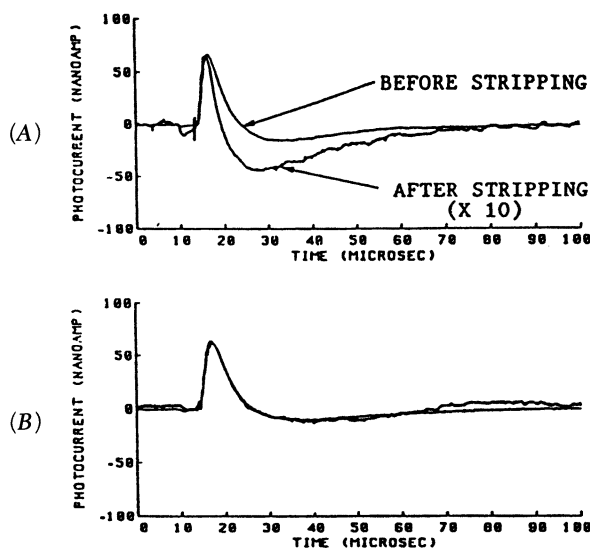


Figure 8. Photoelectric signals from a fresh (A) and an aged (B) multilayered film before and after stripping with a cotton swab. Both records are taken at 26 °C. The signal obtained after stripping is magnified 10 times in A and 6.5 times in B. (Reproduced with permission from reference 42. Copyright 1989.)

A similar experiment using a dried multilayered bacteriorhodopsin film older than 4 days was carried out to determine the effect of prolonged drying. No trace of pH sensitivity could be found in this preparation. Subsequent removal of the multiple layers using a cotton swab reduced the photosignal to an amplitude comparable to that found in a Trissl–Montal bacteriorhodopsin film, but no detectable pH sensitivity could be observed. In fact, this diminutive signal had the same time course as the photosignal before stripping, as shown in Figure 8B.

Independent support for the validity of the foregoing component analysis is provided by experiments carried out with a mutant bacteriorhodopsin. Purple membranes were isolated from a mutant strain of *Halobacterium halobium* in which a point mutation at residue 212 (aspartic acid replaced by asparagine) was carried out by a new method of site-directed mutagenesis and expression (43, 44). The photosignal was found to be pH-independent in the range of pH 4–11 (45, 46). This photosignal was found to be a pure B1 component because its time course could be superimposed, after normalization, with that of the pure B1 component observed in a multilayered mutant bacteriorhodopsin film. Thus, Nature does indeed decompose the photosignal in accordance with the outlined component analysis. In other words, the B1 component as defined is indeed a natural entity.

Concept of Local Reaction Conditions

The apparent symmetry of proton uptake and release on either side of the purple membrane suggests that proton release at the extracellular side and its reverse reaction may be manifest as a displacement photocurrent (a hypothetical B2' component). This signal is blocked in a Trissl–Montal bacteriorhodopsin film because the Teflon film precludes access of aqueous protons at the extracellular side. If, however, bacteriorhodopsin is reconstituted in a lipid bilayer membrane, this hypothetical component, which represents proton release at the extracellular side, might be observable. A complication arises from the expected polarity of the B2' signal, which should be the same as that of the B2 component (both are of opposite polarity to the B1 component). Therefore, a method must be devised to distinguish the B2' from the B2 component. The following kinetic analysis provides the rationale for such a method.

The currently prevailing thought about proton translocation in the purple membranes stipulates a proton conduction channel formed by a series of proton binding sites that consist of the carboxylic group of aspartic acids (47, 48) (Figure 9). For example, Asp96 is considered to be the immediate proton donor to the Schiff base that links the chromophore to the ϵ -amino group of Lys216. Thus, a model that is consistent with our present view of displacement current generation is shown in Figure 10.

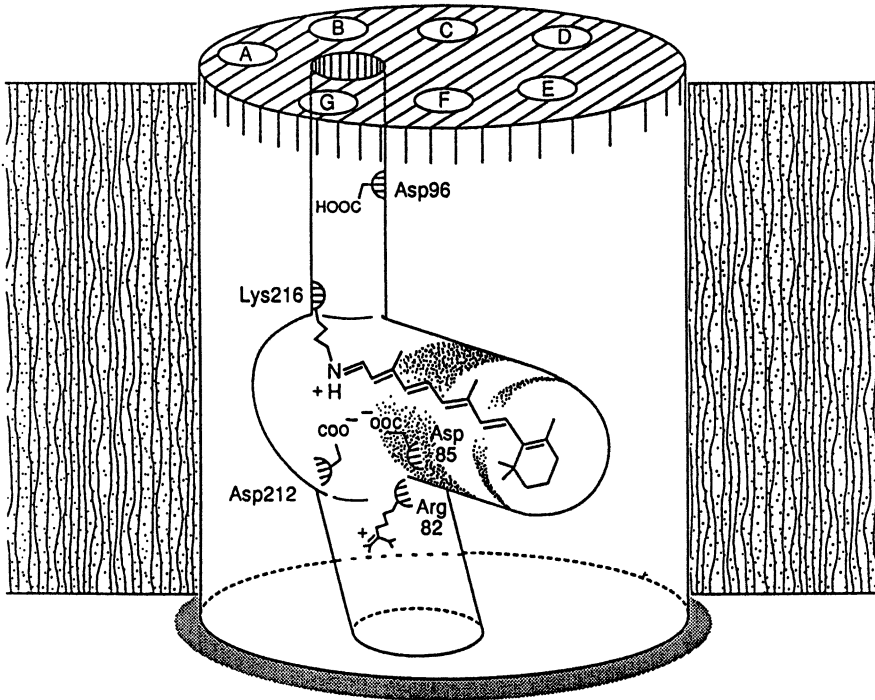


Figure 9. Proton conduction pathway as revealed by cryoelectron microscopy. The letters A, B, C, D, E, F, and G refer to the seven α -helices that span the membrane. Notice that the C terminus and the cytoplasmic side of the purple membrane are at the top of the diagram. (Reproduced with permission from reference 48. Copyright 1990.)

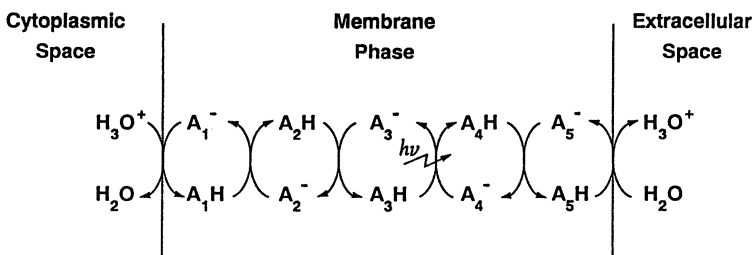


Figure 10. Coupled consecutive proton transfer pathway across the membrane. The actual number of binding sites is not known. For simplicity, only five binding sites (A_1 through A_5) are shown. Site A_3 designates the Schiff base proton binding site. It is understood that the Schiff base is neutral when deprotonated and carries a positive charge when protonated. The reverse reactions are not shown but are important for the discussion. (Reproduced with permission from reference 82. Copyright 1990.)

The model in Figure 10 depicts a sequence of proton transfer reactions between adjacent proton binding sites; the reactions are coupled in a linear fashion. This model resembles the reaction scheme in the photosynthetic reaction center of *Rhodospseudomonas viridis* except that protons instead of electrons are transferred (49, 50). An essential ingredient of the model is the reverse reaction of each and every proton transfer reaction. A simple kinetic analysis reveals that the minimum requirement for the scheme to work as a light-driven proton pump is to have one of the forward proton transfer steps be driven by light, but the absence of a reverse reaction in this step is not required. The driving force for proton translocation is generally accepted to be derived from a light-induced pK_a decrease (or rather, pK_b increase) of the Schiff base proton binding site (A_3), which causes a proton to be transferred from site A_3 to site A_4 . By virtue of the law of mass action, the equilibrium will shift toward the extracellular side. Eventually deprotonation of site A_5 releases a proton into the extracellular aqueous phase. On the other hand, deprotonation of the Schiff base (site A_3) creates a vacancy for a proton (a "negative" hole). By the same token, the increasing tendency to fill this vacant site will shift the equilibrium away from the intracellular surface. Eventually, the surface binding site A_1 will refill its vacancy by binding a proton from the intracellular aqueous phase.

The analysis of the OD and the IPT mechanisms indicates that for each pair of forward and reverse proton transfer reactions, there is an associated displacement current. As explained before, equivalent circuit analysis indicates that the faster the forward and reverse reactions, the more prominent the displacement current. Several laboratories observed that the initial (B1) component represents a current from the extracellular space to the intracellular space (27–32, 51, 52). Thus, the B1 component represents movement of positive charges in the direction opposite to that of the physiological proton translocation or movement of negative charges in the direction of the physiological proton translocation. Regardless of the interpretation, the observation suggests that there is at least a slow forward proton transfer reaction in the direction of physiological proton translocation that is interposed between the Schiff base binding site and either of the two surface proton binding sites. Thus, in the microsecond time scale, the two interfacial proton transfer reactions represented by the B2 and the B2' components, respectively, are chemically decoupled. Again by virtue of the law of mass action, the B2 component will be insensitive to the extracellular pH although it is dependent on the intracellular pH. Likewise, the hypothetical B2' component is expected to be dependent on the extracellular pH but not on the intracellular pH. Thus, an interfacial proton transfer reaction depends solely on the local reaction conditions at the vicinity of the surface proton binding site at the microsecond time scale. This dependence is because there is insufficient time for the effect of changing reaction conditions at the opposite side of the

membrane to propagate via the proton conduction channel. This effect is summarized as the concept of *local reaction conditions* (53).

Following this reasoning, by variation of the electrolyte compositions on the two aqueous phases independently, the B2 and the hypothetical B2' components may be separated. An experimental test of this idea is shown in Figure 11 (41). Bacteriorhodopsin was first reconstituted into a lipid bilayer with both aqueous phases maintained initially at pH 7. Acidification of the cytoplasmic aqueous phase caused reversible inhibition of the negative phase as expected for the known behavior of the B2 component. Subsequent acidification of the extracellular aqueous phase leads to the appearance of a new negative phase that has a different time course. Furthermore, this negative component has a pH dependence that is opposite to the pH dependence of the known B2 component and is enhanced by acidification. This new component is thus identified with the hypothetical B2' component.

The foregoing analysis highlights an important feature of the operation of the purple membrane. Whereas many experiments were performed with purple membrane aqueous suspensions, the working environment of the purple membrane is highly anisotropic because its action creates a proton concentration gradient as well as a transmembrane electric potential that are not present in an aqueous suspension. We believe this is at least part of the reason why some experiments reported by different laboratories cannot be reconciled. A detailed discussion in this regard has been published elsewhere (53).

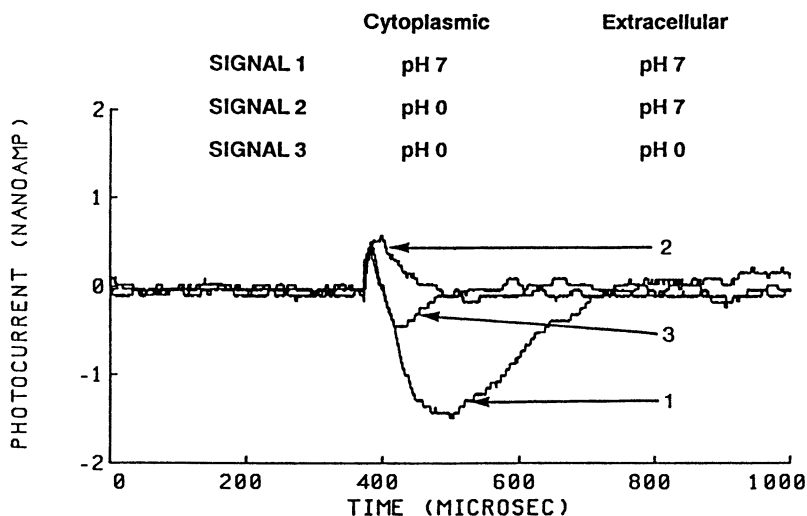


Figure 11. An experiment that shows the presence of two pH sensitive components, B2 and B2'. (Reproduced with permission from reference 41. Copyright 1987.)

The Concept of Intelligent Materials

The interfacial proton transfer reactions responsible for both the B2 and the B2' component are bimolecular reactions. According to the law of mass action, the relaxation of the photosignal is dependent on three factors:

1. The concentration of occupied or unoccupied surface proton binding sites, which is dependent on light intensity and illumination conditions.
2. The pK_a of the surface proton binding sites.
3. The proton concentration of the adjacent aqueous phase.

Consider the last factor: The B2 component is expected to be enhanced by decreased pH, whereas the B2' component is expected to be inhibited by decreased pH. The data shown in Figure 11 are contrary to this expectation. Thus, we conclude that the primary effect of the aqueous pH is to alter the pK_a of the surface proton binding sites.

This postulated pH effect on the pK_a of the surface proton binding sites reveals the sophistication of Nature's design of a proton pump. Like any mechanical pump, the efficiency of a proton pump can be diminished as a result of its action. Proton pumping by the purple membrane results in an increase of the intracellular pH and a corresponding decrease of the extracellular pH. If the pK_a of the surface proton binding groups on either side of the membrane were pH-independent, the pumping efficiency will be significantly reduced by the changing proton concentrations on both sides of the membrane as a result of proton pumping. If, however, the pK_a of the intracellular proton binding group is increased as the cytoplasmic pH rises, the equilibrium of the interfacial proton transfer reaction will be shifted in favor of proton uptake from the cytoplasmic aqueous phase. Likewise, if the pK_a of the extracellular proton binding (or rather releasing) group is decreased as the extracellular pH declines, the equilibrium will be shifted in favor of proton release into the extracellular aqueous phase. This feature, which has an apparent survival value, fits the description of intelligent materials as proposed by the Science and Technology Agency (STA) of Japan: "substances/materials with the ability to respond to environmental conditions intelligently and manifest their functions" (54, 55).

The concept of intelligent materials was first developed for materials science. The original idea was to design or synthesize materials with microstructures so that both sensors and actuators were embedded throughout. The advantage of such materials for the construction of machines is the possibility of massively parallel and distributed signal processing, which results in significant relief of the burden of the central processor. Biological

materials such as bacteriorhodopsin represent the ultimate intelligent materials because the desired intelligence resides in a single molecule.

Generality of the Electrochemical Analysis

The foregoing analysis is restricted to membranes that contain bacteriorhodopsin. However, we believe the electrochemical approach can be applied to other pigment-containing membranes. In fact, the previously outlined electrochemical method was first developed for and successfully applied to an artificial membrane system that contains a magnesium porphyrin and is coupled to a redox gradient. In this system, the transported charge is an electron instead of a proton (36, 37). Figure 12 shows that the electrochemical analysis also may be applicable to reconstituted reaction centers immobilized on a thin film (56). The waveform of the pulsed-light photoelectric signal is similar to that of the B1 component. This similarity suggests that the signal is a displacement photocurrent. The record in Figure 12 indicates that the photocurrent was not measured under a genuine short-circuit condition (i.e., the access impedance was not negligibly small as compared with the source impedance); otherwise, the photocurrent should have reversed its polarity upon cessation of illumination. For a more detailed analysis, the interested reader is referred to publications elsewhere (19, 36). The existence of the apparent relaxation time course in the millisecond range suggests that the signal may have been distorted by the interaction of the photochemical event and the membrane RC relaxation mentioned earlier. In fact, we have observed a similar change of time course in purple membranes oriented and immobilized on a solid substrate (57). Other important factors known to affect the charge recombination, such as temperature, the distance between the electron donor-acceptor pairs, and their relative orientation, may also

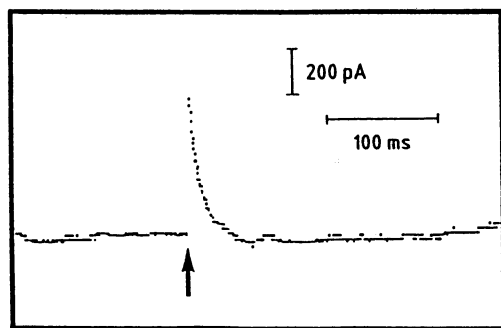


Figure 12. Light-induced current response in a thin film reconstituted from purified bacterial reaction centers. (Reproduced with permission from reference 56. Copyright 1990.)

come into play. We believe that a detailed equivalent circuit analysis of the photosignal may help to clarify the relative importance of these factors.

The generality of the equivalent circuit model suggests that, with suitable modifications, it should also be applicable to a reconstituted halorhodopsin membrane. Halorhodopsin is the second most abundant of the retinal proteins in *Halobacterium halobium* (4, 6, 58). Instead of pumping protons, a halorhodopsin membrane pumps chloride ions across the membrane upon illumination. The modified electrochemical model predicts the existence of a fast photosignal that represents interfacial chloride ion transfer, which should be sensitive to chloride ion concentration rather than to pH. The prediction is experimentally verified as shown in Figure 13 (59), in which there is a photosignal component (named H2) that depends on the Cl^- concentration in a reversible fashion. In addition, there is a photosignal (H1) that persists in a halorhodopsin multilayered dry film that is insensitive to the change of chloride ion concentration.

Although the visual membrane (that contains rhodopsin) does not function as a photosynthetic membrane, the fast photoelectric signal is similar and indeed analogous to the signal from a reconstituted bacteriorhodopsin membrane. In fact, the names B1 and B2 were chosen primarily on the basis of their similarity in temperature dependence to the R1 and the R2 components of the ERP, respectively: Both B1 and R1 are temperature insensitive, but both B2 and R2 are inhibited by low temperature. The ERP data published by Ostrovsky's and Skulachev's groups (60, 61) suggest that the equivalent circuit model may be applicable to the analysis of the ERP. These authors considered possible physiological roles of the ERP. However, the majority of

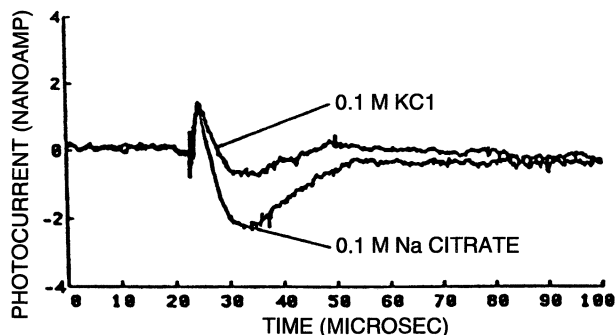


Figure 13. Photoelectric signals from a Trissl-Montal-type halorhodopsin thin film. The change of the photosignal is reversible when the aqueous solution is changed from KCl to sodium citrate and vice versa. The pH was 6, and the temperature was 25 °C. The H1 component has a positive polarity, and the H2 component has a negative polarity. The H1 component alone appears in a multilayered dry film (not shown) and is not sensitive to the replacement of medium. (Reproduced with permission from reference 59. Copyright 1990 Institute of Electrical and Electronics Engineers, Inc.)

visual physiologists dismissed the ERP as an epiphenomenon unrelated to visual phototransduction.

Our analysis of the two mechanisms of displacement photocurrent generation suggests otherwise. The oriented dipole mechanism is operative whenever there is a light-induced charge separation in the oriented membrane-bound pigments. Both photosynthetic and visual membranes contain membrane-bound photopigments that maintain a fixed orientation with respect to the membrane. In the photosynthesis literature, light-induced charge separation is well recognized as the primary event. Likewise, in the vision literature, it is generally thought that the photon energy absorbed by the visual pigment is temporarily stored as charge separation and is subsequently used to drive a conformational change of the visual pigment to achieve the desired signal transduction (62). Thus, the R1 component may be the electrical manifestation of this important step of charge separation.

The interfacial proton transfer mechanism is operative whenever there is a rapid transfer of protons across the membrane-water interface. Such an event is essential for the establishment of a proton gradient in a photosynthetic membrane, whether the membrane is chlorophyll- or bacteriorhodopsin-based. Interfacial proton transfer also occurs in a visual membrane; its physiological role is not apparent because a visual membrane is not a photon energy converter as is the purple membrane. The initially absorbed photon energy is negligible compared to the energy that is being regulated with regard to the sodium ion current that is associated with visual excitation. Thus, a photon acts merely as a trigger to initiate a sequence of biochemical and neurophysiological events during which photon energy is amplified 100,000-fold via the so-called cyclic GMP (cyclic 3',5'-guanosine monophosphate) cascade (14, 15). Thus, there is no need for the visual membrane to transport protons all the way across the visual membrane and, in fact, it does not transport protons. The latter conclusion follows from work of Ostrovsky's group (61, 63), who showed protons are bound from the cytoplasmic surface but are not released into the intradisc space in the rod outer segment.

The presence of intracellular proton binding and the absence of intradisc release suggests that the R2 signal may play an important role in visual transduction. This possibility is supported by several additional observations. Metarhodopsin II is known to be the key photointermediate of the rhodopsin photobleaching sequence and it activates transducin (G protein); therefore, it is linked directly to the cyclic GMP cascade (64). As mentioned earlier, a proton is bound to rhodopsin during the metarhodopsin I to II transition and during the appearance of the ERP R2 component. This binding suggests that the R2 component may be generated by an interfacial proton uptake at the cytoplasmic surface just like the B2 component of bacteriorhodopsin. Previous objections to this idea that were based on the apparent lack of pH effect are no longer valid (20, 65, 66).

Thus, the binding of transducin to metarhodopsin II coincides with the appearance of a positive surface potential. This positive surface potential, which is associated with proton binding, has been postulated by us (34) and observed experimentally by Cafiso and Hubbell (67). Furthermore, this positive surface potential appears on the cytoplasmic surface where transducin is bound and activated. This observation leads us to postulate that the positive surface potential associated with the R2 signal may "trigger" phototransduction by enhancing the binding and activation of transducin (66). A negative surface potential also appears at the cytoplasmic surface at a later stage because of the phosphorylation of numerous serine and threonine residues on the cytoplasmic surface of rhodopsin (68). This negative surface potential may be a mechanism to actively turn off the transduction process because expenditure of energy in the form of adenosine 5'-triphosphate (ATP) is required.

The preceding surface potential-based trigger mechanism for visual transduction requires experimental verification. However, as demonstrated in a report by Drain and Mauzerall (69), such a mechanism may actually work. These investigators studied the diffusion of hydrophobic ions such as tetrphenylborate or tetraphenylphosphonium ions across an artificial lipid bilayer membrane under the influence of an externally imposed transmembrane potential. In addition, the lipid bilayer also contains magnesium octaethylporphyrin, but the membrane separates two aqueous phases that contain equal concentrations of an electron acceptor. Upon illumination, positive surface potentials of equal magnitudes appear on both membrane surfaces. The resultant surface potentials enhance the partition of tetrphenylborate into the membrane and, therefore, increase the conductivity of the membrane to these ions. In contrast, because of the negative charges borne by tetraphenylphosphonium ions, the light-induced surface potential decreases the ionic conductivity.

Conclusions and Perspectives

Nature utilizes different types of chromophores in constructing photobiological systems. However, there are several important features in common. First, most photopigments are membrane-bound and oriented with respect to the membrane surface. The primary response of photopigments to light stimulation is charge separation. Most photobiological membranes bind or release charges at the membrane-water interface, which is why our electrochemical analysis (interfacial charge transfer mechanism or oriented dipole mechanism) is applicable to so many systems. The essence of our analysis is to recognize the anisotropic nature of the media where chemical reactions occur. In contrast to most solution phase chemistry, chemical reactions occur across the boundary of different phases of media that have different dielectric

constants, viscosities, and electrolyte compositions. The resulting charge movement in these media is not only anisotropic, but also unidirectional (vectorial charge transport). The spatial scale within which the chemical events take place is neither microscopic nor macroscopic; it is often referred to as mesoscopic. As a result of the spatial scale, new and perhaps unexpected phenomena appear. These phenomena must either be regarded as paradoxes or be dismissed as something beyond our existing knowledge of physics and chemistry. In the present context, we have shown that some of these "apparent" paradoxes (investigators with firm mechanistic orientation claim that there are no real paradoxes, only our own temporary confusion) are actually logical consequences of electrochemistry as applied to these systems.

Electrochemistry is probably the branch of existing science that mainstream biologists most neglect. This neglect is primarily because major advances in biochemistry (biological chemistry) have been made in the area of solution phase chemistry. However, life processes are carried out within the framework of a complex structure in which solution phases are compartmentalized by an intricate scaffold of membranes. Nevertheless, electrochemistry has enjoyed some success especially in membrane-related phenomena (70). In view of the importance of biological functions based on interactions that involve forces other than covalent bonding, the electrochemical interaction may be just as important as such well-known mechanisms as the van der Waals interaction and hydrogen bonding. Important phenomena such as self-assembly, antigen-antibody reactions, cell-to-cell recognition, enzyme substrate interactions, and receptor recognition, to name a few, may require electrochemistry for further mechanistic elucidation.

With the advent of molecular electronics as the science and technology of the future, understanding these processes is no longer of mere academic interest (71-76). Molecular electronics evolves from the increasing recognition that the microelectronic revolution will eventually come to a halt because the physical limit of miniaturization imposed by quantum and thermal effects is being approached rapidly. Devices constructed with molecular materials offer hope; living organisms utilize molecular machines with physical dimensions in the nanometer scale (nanobiology). Unlike conventional microelectronic circuits that operate primarily on the basis of bulk properties of materials, biomachinery utilizes the mesoscopic properties of biomaterials and exploits both the underlying physics as well as chemistry for its functions. The rich repertoire of chemical reactions in carbon-containing molecules provides virtually unlimited possibilities for fine-tuning molecular functions and allows intelligent materials to evolve.

Biomaterials are seldom suitable for device construction, but with the advances in synthetic chemistry and in genetic engineering (site-directed mutagenesis), raw biomaterials can be modified to suit the technological needs. Owing to its extraordinary stability, bacteriorhodopsin was one of the first biomaterials to be successfully utilized for device construction. Vsevolodov

and his colleagues (7) developed image storage devices that utilized bacteriorhodopsin with a modified chromophore embedded in a polymer matrix. Hampp and his colleagues (9) utilized a mutant bacteriorhodopsin as a holographic medium. The possible use of bacteriorhodopsin to construct a high-speed high-density optical random access memory is being pursued by Birge's group (77). All these applications utilize the photochromic properties of bacteriorhodopsin. In addition, bacteriorhodopsin also has attractive photoelectric properties that can be exploited for sensor construction (8, 78).

Site-directed mutagenesis as applied to bacteriorhodopsin was a difficult and labor-intensive procedure that used *E. coli* as the expression system (79, 80). Recently, Needleman's group successfully developed a new expression system that uses a bacteriorhodopsin-deficient mutant strain of *H. halobium* (43, 44). Preliminary results were quite encouraging. Unlike the mutants expressed in *E. coli*, the new method produces mutant bacteriorhodopsins with properties that differ from the protein expressed by *E. coli*. Presumably this difference occurs because correct folding into three-dimensional structures is more likely in the natural host than in its surrogate. Denaturation of the mutant proteins is further avoided because reconstitution is unnecessary. Our preliminary results show that the fast photoelectric signal can be drastically altered by a judiciously chosen point mutation.

In addition to the use of bacteriorhodopsin as building blocks to construct devices, an enhanced understanding of the design principles of molecular devices can be achieved by reverse engineering of photobiological membranes. Our analysis suggests that the minimum requirement for a light-driven ion pump can be deduced. As a workable light-driven proton pump, Figure 10 shows an array of proton binding sites that span the entire thickness of the membrane. Protons can move from one aqueous phase to the other via a series of consecutive coupled proton transfer reactions. The only additional requirement for such a pump to work is to have at least one of the proton movement steps be driven by light; a one-way proton transfer reaction is not required. In other words, unidirectional proton pumping against an existing gradient can be achieved in the presence of reverse reactions in each and every step of the consecutive reactions. Reverse reactions (charge recombination) undoubtedly will reduce the efficiency of the pump. Therefore, additional elaboration of the pump will minimize the impact of reverse reactions.

Kuhn (81) has proposed a detailed analysis for the bacterial reaction center of *Rhodospseudomonas viridis* that explains how Nature managed to minimize the effect of charge recombination by a judicious arrangement of the relative locations and distances between various prosthetic groups. In the case of bacteriorhodopsin, our analysis indicates that the pH-dependent pK_a changes of the surface proton binding groups counteract the increasing rates of reverse interfacial proton transfers caused by the emerging proton gradient that the pump generates. In addition, the two interfacial forward proton transfer reactions may be light-assisted (82, 83). These additional effects are

possible because the entire proton pump resides in a single molecule so that these effects can be accomplished by subtle conformational changes. These "purposeful" effects are the hallmark of intelligent materials (84).

Our analysis of the possible role of the ERP suggests another attribute of intelligent materials; that is, modular design of molecular functions. The ability of bacteriorhodopsin to bind protons from the cytoplasm upon light stimulation serves as a critical step in proton translocation. The same event in rhodopsin, however, may serve an entirely different function; it triggers the cyclic GMP cascade. Thus, Nature could well have utilized a common design for vision and for photosynthesis (85). The same design principle may be implemented with completely different types of molecules or materials. On the other hand, the same molecular event may be exploited for different purposes.

This chapter summarizes work on bacteriorhodopsin done in the laboratories of the author and his collaborators. Our work has benefited by the application of electrochemistry. Not only can a simpler and more coherent picture be obtained from an electrochemical approach than from a nonelectrochemical approach, but the predictive power of electrochemistry further allows us to design new experiments. In contrast, when a nonelectrochemical approach is used, an ad hoc model must be concocted to fit each particular set of experiments. Such models often lack internal consistency (e.g., reference 86).

To be able to provide simple explanations for complex biological phenomena is most gratifying and reinforces our resolve to pursue the mechanistic understanding of life processes. However, we refrain from a proclamation of the victory of the mechanistic approach because we believe the debate between the mechanistic approach and the neovitalistic approach is endless and futile. Whereas it is impossible to prove the validity of the mechanistic approach by a finite number of successful attempts, it is equally impossible to prove the validity of the neovitalistic approach by the sheer absence of available mechanistic explanations to a specific problem. An abundance of historic lessons show that when the capability of existing sciences is about to be exhausted, lingering puzzles actually usher in new sciences. In our present case, the solutions to our puzzles do not even require a new science, but rather a new perspective and a new point of view that use the existing knowledge of electrochemistry.

Acknowledgments

This research was supported by a contract from the Office of Naval Research (N00014-87-K-0047) and a contract from the Naval Surface Warfare Center (N60921-91-M-G761). The author wishes to acknowledge the contributions of his collaborators, Janos Lanyi, Lowell McCoy, Mauricio Montal, and

Richard Needleman. The experimental work that forms the basis of this review was performed by Man Chang, Albert Duschl, Filbert Hong, Sherie Michaile, Baofu Ni, and Ting L. Okajima.

References

1. Oesterhelt, D.; Stoeckenius, W. *Nature (London)* **1971**, *233*, 149–152.
2. Stoeckenius, W. *Sci. Am.* **1976**, *234(6)*, 38–46.
3. Stoeckenius, W. *Trends Biochem. Sci.* **1985**, *10*, 483–486.
4. Stoeckenius, W. In *Molecular Electronics: Biosensors and Biocomputers*; Hong, F. T., Ed.; Plenum: New York, 1989; pp 159–163.
5. Stoeckenius, W.; Bogomolni, R. A. *Annu. Rev. Biochem.* **1982**, *51*, 587–616.
6. Lanyi, J. K. In *Bioenergetics*; Ernster, L., Ed.; Elsevier: Amsterdam, The Netherlands, 1984; pp 315–350.
7. Vsevolodov, N. N.; Druzko, A. B.; Djukova, T. V. In *Molecular Electronics: Biosensors and Biocomputers*; Hong, F. T., Ed.; Plenum: New York, 1989; pp 381–384.
8. Rayfield, G. W. In *Molecular Electronics: Biosensors and Biocomputers*; Hong, F. T., Ed.; Plenum: New York, 1989; pp 361–368.
9. Hampp, N.; Bräuschle, C.; Oesterhelt, D. *Biophys. J.* **1990**, *58*, 83–93.
10. Ovchinnikov, Yu. A.; Abdulaev, N. G.; Feigina, M. Yu.; Kiselev, A. V.; Lobanov, N. A. *FEBS Lett.* **1979**, *100*, 219–224.
11. Khorana, H. G.; Gerber, G. E.; Herlihy, W. C.; Gray, C. P.; Anderegg, R. J.; Nihei, K.; Biemann, K. *Proc. Natl. Acad. Sci. U.S.A.* **1979**, *76*, 5016–5050.
12. Hecht, S.; Schlaer, S.; Pirenne, M. H. *J. Gen. Physiol.* **1942**, *25*, 819–840.
13. Chabre, M. *Annu. Rev. Biophys. Biophys. Chem.* **1985**, *14*, 331–360.
14. Stryer, L. *Annu. Rev. Neurosci.* **1986**, *9*, 87–119.
15. Stryer, L. *Sci. Am.* **1987**, *257(1)*, 42–50.
16. Liebman, P. A.; Parker, K. R.; Dratz, E. A. *Annu. Rev. Physiol.* **1987**, *49*, 765–791.
17. Yoshizawa, T.; Shinozawa, T.; Shichida, Y.; Matuoka, S.; Ioshida, S.; Kandori, H.; Sokabe, M. In *Retinal Proteins*; Ovchinnikov, Yu. A., Ed.; VNU: Utrecht, The Netherlands, 1987; pp 75–84.
18. McNaughton, P. A. *Physiol. Rev.* **1990**, *70*, 847–883.
19. Hong, F. T. In *Bioelectrochemistry: Ions, Surfaces, Membranes*; Blank, M., Ed.; ACS Advances in Chemistry 188; American Chemical Society: Washington, DC, 1980; pp 211–237.
20. Hong, F. T.; Okajima, T. L. In *Electrical Double Layers in Biology*; Blank, M., Ed.; Plenum: New York, 1986; pp 129–147.
21. Tien, H. T. *Prog. Surface Sci.* **1989**, *30*, 1–200.
22. Keszthelyi, L.; Ormos, P. *J. Membrane Biol.* **1989**, *109*, 193–200.
23. Trissl, H.-W. *Photochem. Photobiol.* **1990**, *51*, 793–818.
24. Brown, K. T.; Murakami, M. *Nature (London)* **1964**, *201*, 626–628.
25. Cone, R. A.; Pak, W. L. In *Handbook of Sensory Physiology 1: Principles of Receptor Physiology*; Loewenstein, W. R., Ed.; Springer: Berlin, Germany, 1971; pp 345–356.
26. Trissl, H.-W. *Photochem. Photobiol.* **1979**, *29*, 579–588.
27. Fahr, A.; Läger, P.; Bamberg, E. *J. Membrane Biol.* **1981**, *60*, 51–62.
28. Dér, A.; Hargittai, P.; Simon, J. *Biochem. Biophys. Methods* **1985**, *10*, 295–300.
29. Keszthelyi, L.; Ormos, P. *FEBS Lett.* **1980**, *109*, 189–193.
30. Rayfield, G. W. *Biophys. J.* **1983**, *41*, 109–117.

31. Trissl, H.-W. *Biochim. Biophys. Acta* **1983**, 723, 327–331.
32. Drachev, L. A.; Kaulen, A. D.; Khitrina, L. V.; Skulachev, V. P. *Eur. J. Biochem.* **1981**, 117, 461–470.
33. Hagins, W. A.; McGaughy, R. E. *Science (Washington, D.C.)* **1967**, 157, 813–816.
34. Hong, F. T. *Bioelectrochem. Bioenerg.* **1978**, 5, 425–455.
35. Matthews, R. G.; Hubbard, R.; Brown, P. K.; Wald, G. J. *Gen. Physiol.* **1963**, 47, 215–240.
36. Hong, F. T. *Photochem. Photobiol.* **1976**, 24, 155–189.
37. Hong, F. T.; Mauzerall, D. *Proc. Natl. Acad. Sci. U.S.A.* **1974**, 71, 1564–1568.
38. Hong, F. T.; Montal, M. *Biophys. J.* **1979**, 25, 465–472.
39. Okajima, T. L.; Hong, F. T. *Biophys. J.* **1986**, 50, 901–912.
40. Trissl, H.-W.; Montal, M. *Nature (London)* **1977**, 266, 655–657.
41. Hong, F. T.; Okajima, T. L. In *Biophysical Studies of Retinal Proteins*; Ebrey, T. G.; Frauenfelder, H.; Honig, B.; Nakanishi, K., Eds.; University of Illinois Press: Urbana-Champaign, IL, 1987; pp 188–198.
42. Michaile, S.; Hong, F. T. *Abstracts of Papers*, Proceedings of the 11th Annual International Conference, IEEE Engineering in Medicine and Biology Society, Seattle, WA; Kim, Y.; Spelman, F. A., Eds.; Institute of Electrical and Electronics Engineers, Inc.: Washington, DC, 1989; pp 1333–1335.
43. Ni, B.; Chang, M.; Duschl, A.; Lanyi, J.; Needleman, R. *Gene* **1990**, 90, 169–172.
44. Needleman, R.; Chang, M.; Ni, B.; Váró, Gy.; Fornés, J.; White, S. H.; Lanyi, J. K. *J. Biol. Chem.* **1991**, 266, 11478–11484.
45. Hong, F. H.; Ni, B.; Chang, M.; Needleman, R. B.; Hong, F. T. *Abstracts of Papers*, Proceedings of the 4th International Symposium on Bioelectronic and Molecular Electronic Devices, Miyazaki, Japan; Aizawa, M., Ed.; R & D Association for Future Electron Devices: Tokyo, Japan, **1992**, 90–93.
46. Hong, F. T.; Hong, F. H.; Needleman, R. B.; Ni, B.; Chang, M. In *Molecular Electronics—Science and Technology*; Aviram, A., Ed.; American Institute of Physics: New York, 1992; pp 204–217.
47. Engelman, D. M.; Henderson, R.; McLachlan, A. D.; Wallace, B. A. *Proc. Natl. Acad. Sci. U.S.A.* **1980**, 77, 2023–2027.
48. Henderson, R.; Baldwin, J. M.; Ceska, T. A.; Zemlin, F.; Beckmann, E.; Downing, K. H. *J. Mol. Biol.* **1990**, 213, 899–929.
49. Deisenhofer, J.; Michel, H.; Huber, R. *Trends Biochem. Sci.* **1985**, 10, 243–248.
50. Deisenhofer, J.; Michel, H. *Science (Washington, D.C.)* **1989**, 245, 1463–1473.
51. Holz, M.; Lindau, M.; Heyn, M. P. *Biophys. J.* **1988**, 53, 623–633.
52. Liu, S. Y. *Biophys. J.* **1990**, 57, 943–950.
53. Hong, F. T. *J. Electrochem. Soc.* **1987**, 134, 3044–3052.
54. *The Concept of Intelligent Materials and the Guidelines on R & D Promotion*; Takagi, T., Ed.; Science and Technology Agency, Government of Japan: Tokyo, Japan, 1989.
55. Hong, F. T. *Intelligent Material Newsletter (Intelligent Materials Forum, Tokyo)* **1992**, 2(2), 15–18.
56. Hara, M.; Majima, T.; Miyake, J.; Ajiki, S.; Sugino, H.; Toyotama, H.; Kawamura, S. *Appl. Microbiol. Biotechnol.* **1990**, 32, 544–549.
57. Hong, F. T. *Biosyst.* **1986**, 19, 223–236.
58. Lanyi, J. K. *Physiol. Rev.* **1991**, 70, 319–330.
59. Michaile, S.; Duschl, A.; Lanyi, J. K.; Hong, F. T. *Abstracts of Papers*, Proceedings of the 12th Annual International Conference, IEEE Engineering in Medicine and Biology Society, Philadelphia, PA; Oranal, B.; Pedersen, P. C., Eds.; Institute of Electrical and Electronics Engineers, Inc.: Washington, DC, 1990; pp 1721–1723.

60. Drachev, L. A.; Kalamkarov, G. R.; Kaulen, A. D.; Ostrovsky, M. A.; Skulachev, V. P. *Eur. J. Biochem.* **1981**, *117*, 471–481.
61. Ostrovsky, M. A. In *Molecular Electronics: Biosensors and Biocomputers*; Hong, F. T., Ed.; Plenum: New York, 1989; pp 187–201.
62. Birge, R. R.; Cooper, T. M. *Biophys. J.* **1983**, *42*, 61–69.
63. Shevtchenko, T. F.; Kalamkarov, G. R.; Ostrovsky, M. A. *Sensory Systems (USSR Acad. Sci.)* **1987**, *1*, 117–126 (in Russian).
64. Emeis, D.; Kühn, H.; Reichert, J.; Hofmann, K. P. *FEBS Lett.* **1982**, *143*, 29–34.
65. Hong, F. T. *Abstracts of Papers*, Proceedings of the 9th Annual Conference, IEEE Engineering in Medicine and Biology Society, Boston, MA; Newbower, R. S.; Foster, K. R.; Laxminarayan, S., Eds.; Institute of Electrical and Electronics Engineers, Inc.: Washington, DC, 1987; pp 60–62.
66. Hong, F. T. *J. Mol. Electron.* **1989**, *5*, 163–185.
67. Cafiso, D. S.; Hubbell, W. L. *Biophys. J.* **1980**, *30*, 243–264.
68. Wilden, U.; Kühn, H. *Biochemistry* **1982**, *21*, 3014–3022.
69. Drain, C. M.; Mauzerall, D. *Bioelectrochem. Bioenerg.* **1990**, *24*, 263–268.
70. McLaughlin, S. *Curr. Top. Membr. Transp.* **1977**, *9*, 71–144.
71. *Molecular Electronic Devices*; Carter, F. L., Ed.; Marcel Dekker; New York, 1982.
72. *Molecular Electronic Devices II*; Carter, F. L., Ed.; Marcel Dekker; New York, 1987.
73. *Molecular Electronic Devices*; Carter, F. L.; Siatkowski, R. E.; Wohltjen, H., Eds.; North-Holland: Amsterdam, The Netherlands, 1988.
74. *Molecular Electronics: Biosensors and Biocomputers*; Hong, F. T., Ed.; Plenum: New York, 1989.
75. *Molecular Electronics: Materials and Methods*; Lazarev, P. I., Ed.; Kluwer Academic Publishers: Dordrecht, The Netherlands, 1991.
76. *Molecular Electronics—Science and Technology*; Aviram, A., Ed.; American Institute of Physics: New York, 1992.
77. Birge, R. R.; Zhang, C. F.; Lawrence, A. F. In *Molecular Electronics: Biosensors and Biocomputers*; Hong, F. T., Ed.; Plenum: New York, 1989; pp 369–379.
78. Miyasaka, T.; Koyama, K.; Itoh, I. *Science (Washington, D.C.)* **1992**, *255*, 342–344.
79. Dunn, R. J.; Hacket, N. R.; McCoy, J. M.; Chao, B. H.; Kimura, K.; Khorana, H. G. *J. Biol. Chem.* **1987**, *262*, 9246–9254.
80. Nassal, M.; Mogi, T.; Karnik, S. S.; Khorana, H. G. *J. Biol. Chem.* **1987**, *262*, 9264–9270.
81. Kuhn, H. *Phys. Rev. A* **1986**, *34*, 3409–3425.
82. Hong, F. T. In *Biomedical Engineering in the 21st Century*; Wang, C.-Y.; Chen, C.-T.; Cheng, C.-K.; Huang, Y.-Y.; Lin, F.-H., Eds.; Center for Biomedical Engineering, National Taiwan University, Taipei, Taiwan, 1990; pp 85–95.
83. Hong, F. T. *Nanobiol.* **1992**, *1*, 39–60.
84. *Proceedings of the 1st International Conference on Intelligent Materials*; Takagi, T.; Takahashi, K.; Aizawa, M.; Miyata, S., Eds.; Technomic: Lancaster, PA, 1993; 516 pp.
85. Hong, F. T. In *Molecular Electronics: Materials and Methods*; Lazarev, P. I., Ed.; Kluwer Academic Publishers: Dordrecht, The Netherlands, 1991; pp 291–310.
86. Hong, F. T. *Proceedings of the 13th Annual Northeast Bioengineering Conference*; Foster, K. R., Ed.; Institute of Electrical and Electronics Engineers, Inc.: Piscataway, NJ, 1987; pp 304–307.

RECEIVED for review July 26, 1991. ACCEPTED revised manuscript November 9, 1992.

Electroconformational Coupling

Enforced Conformational Oscillations of a Membrane Enzyme for Energy Transduction

Tian Y. Tsong

Department of Biochemistry, University of Minnesota College
of Biological Sciences, St. Paul, MN 55108

We have studied, at the molecular level, how a cell can interact with an applied electric field and how an endogenous electric field may be used by a cell to regulate its internal activities and to exchange information with other cells. Molecules of the cell membrane play an important role because an electric field, either of endogenous or exogenous origin, is greatly amplified at the site of a cell membrane. This field amplification by a membrane enables a cell to receive, process, and transmit weak electric signals. Several laboratories have shown that membrane adenosine triphosphatase can absorb energy from an applied electric field and use it to perform different types of chemical work. To interpret these results, an electroconformational coupling model has been proposed. The model postulates that there are at least two catalytically and electrically active forms of the enzyme: one with its cation binding site exposed to one side of the membrane and the other with its binding site exposed to the opposite side. The two forms exhibit different affinities for the ligand. An oscillating electric field of appropriate amplitude and frequency can turn the catalytic wheel of the enzyme by enforcing conformational oscillations among its different catalytic states. Analysis of the model reproduces many features of experimental results, including the observed optimal frequency for field stimulation. To obtain precise values of electric potential across a cell membrane, electric parameters of several cell membranes have also been measured.

0065-2393/94/0235-0561 \$08.00/0
© 1994 American Chemical Society

ALL SURFACES ARE ELECTRIFIED (1), and a cell membrane is no exception. This property of a cell membrane makes it well suited for processing electric energy and signals. Early studies on electrical properties of cell membranes are documented in the monographs of Cole (2) and Tien (3). More recent studies have focused on single-channel measurements of membrane patches or purified channels reconstituted into bilayer lipid membranes (BLM) (*see* Chapter 15 in this volume). The reconstitution of purified membrane channels, enzymes, and receptors into lipid vesicles for biophysical characterizations is also a common approach. Our work focuses on the direct exposure of cells, organelles, or proteoliposomes, in suspension, to a direct current (dc) pulse, an alternating current (ac) field, or a dc-shifted radio-frequency field. For convenience, this last technique will be called the pulsed electric field (PEF) method (4, 5).

Electric-Field-Induced Transmembrane Potential

A PEF can induce a transmembrane electric potential, $\Delta\psi_m$, or an effective electric field across the membrane lipid bilayer of $E_m = \Delta\psi_m/d$, where d is the thickness of the bilayer (5–8 nm). For a cell of spherical shape, the relationship between $\Delta\psi_m$ and the applied field, E_a , is (6–11)

$$\Delta\psi_m = 1.5 R_{\text{cell}} E_a \cos \theta \quad (1)$$

where R_{cell} is the radius of the cell and θ is the angle between the field line and the normal to a point of interest on the cell membrane. Equation 1 is applicable to a dc type of PEF or an ac field (12). For an ac field of the type $E_a = E_{\text{ac}}^0 \sin(\omega t)$, the transmembrane potential generated will not only depend on θ but will oscillate with a frequency $f = \omega/2\pi$ (ω is the angular frequency and t is time). E_{ac}^0 is the amplitude of the ac field. For most cells, if the frequency of an ac field is below 100 Hz, eq 1 can still apply. However, when the frequency of an ac field approaches the relaxation time of the cell membrane, τ_m , a phase shift will occur between E_a and E_m that results in the reduction of effective field, and eq 1 is no longer valid. In such a case, the Schwan equation should apply (6, 12):

$$\Delta\psi_m = 1.5 R_{\text{cell}} E_a \cos \theta / [1 + (\omega\tau)^2]^{1/2} \quad (2)$$

Here $\omega = 2\pi f$, where f is the frequency of the ac field.

When the maximal transmembrane potential is considered ($\theta = 0^\circ$), eqs 1 and 2 become, respectively,

$$\Delta\psi_{\text{max}} = 1.5 R_{\text{cell}} E_a \quad (3)$$

$$\Delta\psi_{\text{max}} = 1.5 R_{\text{cell}} E_{\text{ac}}^0 / [1 + (\omega\tau)^2]^{1/2} \quad (4)$$

This applicability of equations 1–4 has been verified for many types of cells and lipid vesicles by fluorescence imaging techniques (7–9) and for the measurement of critical breakdown field strength (10–12).

Interaction of a Membrane Protein with an Electric Field

Most membrane proteins are electrically active. If a membrane-spanning protein has a conformational change that involves translocation or displacement of charges, or change in the molar electric moment (ΔM_e), then a transmembrane electric field will shift its chemical equilibrium to favor states that have higher electric moments (M_e). The quantitative relationships for the effect of an electric field on the chemical equilibrium represented by eq 5 are given in eqs 6–8 (13, 14):

$$P_1 \rightleftharpoons P_2 \quad (5)$$

$$K_{12, \text{elec}} = K_{12,0} \exp[\Delta M_e E_m / RT] \quad (6)$$

$$k_{12, \text{elec}} = k_{12,0} \exp[r \Delta M_e E_m / RT] \quad (7)$$

$$k_{21, \text{elec}} = k_{21,0} \exp[(r - 1) \Delta M_e E_m / RT] \quad (8)$$

In these equations, P_1 and P_2 are the two conformational states of the transport protein, and equilibrium constants (K) and rate constants (k) in an electric field are shown to be these constants in zero field multiplied by a nonlinear term that is the product of ΔM_e and the electric field across the membrane, E_m . The r in these equations is the apportionation constant and has a value between 0 and 1 (14). This property of a membrane protein has been explored, and a model called electroconformational coupling has been proposed to interpret data on the electric activation of membrane enzymes (13–17). A four-state membrane-facilitated transport model has been analyzed and shown to absorb energy from oscillating electric fields to actively pump a substrate up its concentration gradient (*see* the section entitled Theory of Electroconformational Coupling).

Another mode of protein–electric field interaction has been proposed by Blank (18–21). Blank considers that the effects of an electric field on membrane protein mainly arise from its effect on the electric double layer at the water–membrane interface. In other words, an electric field can change the concentration of ions near a membrane protein, which results in a stimulation or a reduction in its activity. The surface compartmental model has been used to interpret the ac stimulated adenosine triphosphate (ATP) splitting of Na, K-ATPase (adenosine triphosphatase) and ribonucleic acid (RNA) synthesis in various types of cells (19–21).

Two types of experiments have been reported: One uses a low amplitude (less than 1 mV/cm) ac field, and the other uses an ac amplitude larger than

1 V/cm. Low-field experiments have been prompted by environmental concern and high-field experiments have been done to understand molecular mechanisms of field interactions with cell membranes (14, 21, 22). The medium-field experiments should also be relevant to the development of biosensors and molecular electronics (23). Our experiments used moderately high field strength (a few volts to many kilovolts per centimeter). The choice of a field strength was dictated by mimicking the endogenous field of the enzyme under consideration. For example, inhibition of the Na, K-ATPase of human erythrocytes leads to a depolarization of several millivolts (24), which implies that cation pumping by the enzyme is responsible for an equivalent amount of membrane potential. The applied field strength of 20 V/cm is required to generate 10 mV of $\Delta\psi_m$ in a human erythrocyte. When F_0F_1 ATPase of submitochondrial particles is considered, a 10-kV/cm applied field would be required to generate about 200 mV of $\Delta\psi_m$ required for ATP synthesis (14).

Use of a high field to activate a membrane enzyme was first reported by Witt et al. (25) in 1976. They used dc pulses of approximately 1 kV/cm and of 1-ms duration to induce ATP synthesis by the chloroplast ATPase. Following this initial work, there have been many reports on 1-kV/cm dc field-induced ATP synthesis in different ATP synthetic systems (*see* the literature cited in references 13 and 14). The main conclusion from these studies is that an applied field-induced transmembrane potential can facilitate ATP release from the enzyme; whether a PEF can affect enzyme turnover is not clear. Because 1-kV/cm dc fields also cause severe Joule heating of a sample suspension, thermal effects cannot be easily avoided except when very short electric pulses (microseconds) are used. Thus, the method has limited utility for electroactivation experiments. The PEF method is, however, quite popular for the study of electroporation and electrofusion of cell membranes (*see* the chapter by J. Weaver in this volume), electroinsertion of membrane proteins (26), and electrotransfection of cells (27).

Electric Activation of Na, K-ATPase

A summary of the salient features of our experimental results (28–30) on Na, K-ATPase follows.

Na, K-ATPase of human erythrocytes can respond to the stimulation of an ac field of approximately 20 V/cm to pump Na^+ , K^+ , and Rb^+ against their respective concentration gradients. There was no irreversible damage of the membrane permeation barrier after the erythrocytes were exposed for several hours to this magnitude of ac field. After the field was turned off, the erythrocytes behaved very much like fresh erythrocytes in terms of their cell shape, volume, and normal ion permeation properties.

At, 4 °C, no ATP-dependent Na⁺, K⁺, or Rb⁺ pumping activities sensitive to ouabain were detected. An ac electric field stimulated active efflux of Na⁺ and influx of K⁺ and Rb⁺ but not the passive influx of Na⁺ and efflux of K⁺ and Rb⁺. This ac-stimulated active transport of cations was completely inhibited by 0.2 mM of ouabain. At 26 °C, the enzyme hydrolyzed ATP to pump Na⁺ and K⁺. An ac stimulation further increased the rate of pumping. At 37 °C, the ATP hydrolysis of the enzyme was at its maximum and an ac stimulation did not escalate the rate of active pumping of these ions.

The optimal field strength for activating both the Na⁺ and the K⁺ pumps was 20 V/cm (peak-to-peak). This applied field would generate a $\Delta\psi_m$ of 12 mV, or an effective transmembrane electric field, E_m , of 24 kV/cm. Other field strengths led to reduced activities.

When the optimal field strength, 20 V/cm, was used, the optimal frequency for the Na⁺ pump was 1.0 MHz, whereas it was 1.0 kHz for the K⁺ or Rb⁺ pump. The wide separation of the optimal frequencies for the two pumps clearly indicates that they can function independently of each other. With a 20-V/cm field and a frequency of 1 kHz, the K⁺ pump, but not the Na⁺ pump, would be activated. Likewise, at 1 MHz the Na⁺ pump, but not the K⁺ pump, would be activated. Whether phosphorylation of the enzyme is responsible for coupling the two pumps *in vivo* remains to be tested.

Under optimal conditions, the net ac-stimulated Na⁺ pumping was 15–30 ions per enzyme per second and Rb⁺ pumping was 10–20 ions per enzyme per second. The ratio for the two was roughly 3:2. The agreement of this value with the generally observed transport ratio may be coincidental. It is, however, possible to select a frequency of the ac field for which the ratio of Na⁺ to K⁺ transport would be 3:2.

The ac-stimulated cation pumping apparently did not require hydrolysis of ATP. At 4 °C there was no significant ATP hydrolysis, but there was stimulated activity. This stimulated activity was almost identical in ATP-containing (600–800- μ M ATP) and ATP-depleted (<10- μ M ATP) erythrocytes.

The Michaelis–Menten constant, K_M , of internal Na⁺ for the Rb⁺ uptake and the Na⁺ efflux was 8 mM, and that for the external K⁺ was 1.5 mM, with a Hill coefficient of approximately 1.5. These values agree with ATP-dependent pumping activity of the enzyme.

Other inhibitors of the enzyme also had similar effects on the ac-stimulated activity. Ouabain (50% inhibition at 0.35 μ M), oligomycin (8.0 μ M), ouabagenin (3 μ M), and vanadate (20 μ M) all inhibited the ac-stimulated pumping activity. 4,4'-Bis(isothiocyano)-2,2'-distilbenesulfonate (DIDS), an inhibitor of band 3 protein-mediated Li⁺/Na⁺ exchange, had no effect, nor did phloretin at micromolar concentrations. These results show that Na, K-ATPase is responsible for the observed effects.

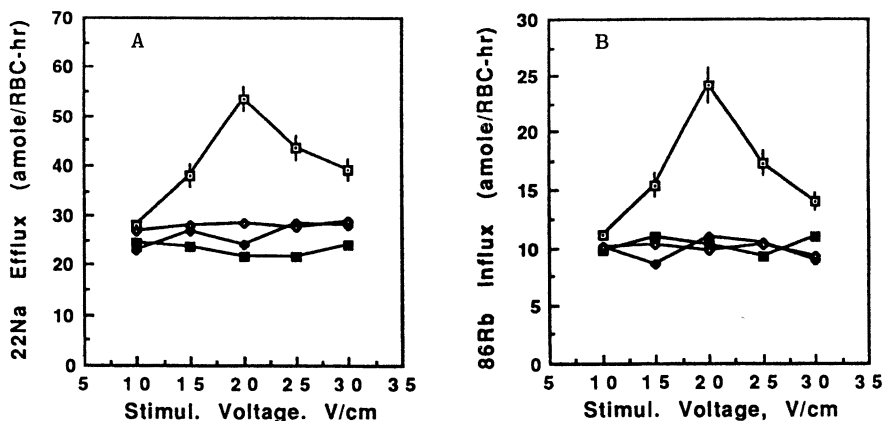


Figure 1. Amplitude dependence of electric-field stimulated Na^+ pumping (A) and Rb^+ pumping (B). Na^+ efflux was measured with the ac field at 1 MHz and Rb^+ influx was measured at 1 kHz. 1 MHz and 1 kHz are the optimal frequencies of the Na^+ pump and the Rb^+ pump, respectively. Key: ◆, sample not stimulated with ac field; □, sample stimulated with ac field; ■, sample not stimulated with ac field, in the presence of 0.2-mM ouabain; ◇, sample stimulated with ac field, in the presence of 0.2-mM ouabain. 1 amole/RBC-hr = 0.0108 mmol/L of cells per hour, where RBC is red blood cell count. These measurements were done at 3 °C. (Adapted from reference 30.)

Because the stimulated transport of cations did not require ATP hydrolysis, the enzyme must be able to absorb free energy from the applied electric field. Only an oscillatory field of defined frequency and amplitude was effective. Figures 1 and 2 show the dependence of these ion pumping activities on the field strength and on the frequency of the applied ac field, respectively.

An ac field could also stimulate ATP hydrolysis activity of sheep kidney Na, K-ATPase and Ecto nucleotide diphosphohydrolase, at 37 °C (31). ATP hydrolysis does not require energy input. The increase in the ATP splitting activity reflects the sensitivity of chemical rate constants to an electric field as in eqs 7 and 8. Figure 3 shows the ATP hydrolysis activity of Ecto ATPase at 37 °C as a function of frequency when a 5.0-V/cm (peak-to-peak) ac field was used. As mentioned, Blank and Soo used 1-mV/cm ac fields to stimulate the ATP splitting activity of Na, K-ATPase (19, 20). Their results are also presented here.

Theory of Electroconformational Coupling

To interpret experimental data on ac activation of Na, K-ATPase, F_0F_1 ATPase, and other related membrane phenomena based on the concept of electrocon-

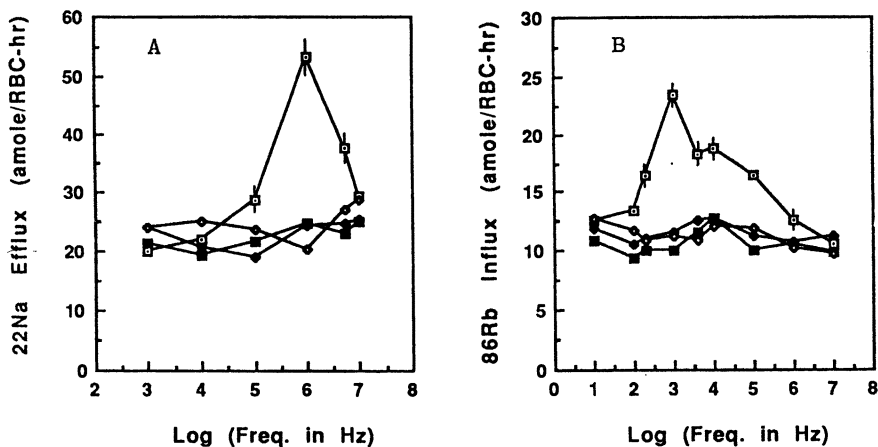


Figure 2. Frequency dependence of electric-field-stimulated Na^+ pumping (A) and Rb^+ pumping (B). A field strength of 20 V/cm (peak-to-peak) was used in both cases. Symbols are the same as in Figure 1. These measurements were done at 3 °C. (Adapted from reference 30.)

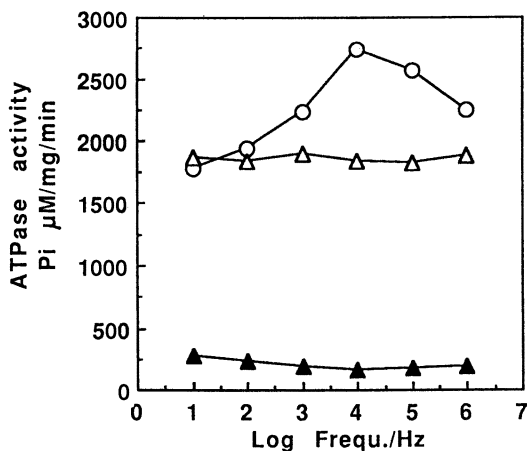
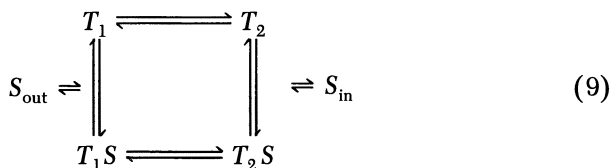


Figure 3. Frequency dependence of electric-field-stimulated ATP hydrolysis activity of a highly purified Ecto nucleotide diphosphohydrolase. The ATP splitting activity of the detergent-solubilized Ecto enzyme was measured at 37 °C in the absence of ac field (Δ), in the presence of 5.0-V/cm (peak-to-peak) ac field (\circ), and in the presence of 10-mM vanadate (\blacktriangle). Buffer: 0.1% of detergent NP40, 30-mM histidine, 4-mM ATP, 4-mM Mg^{2+} , at pH 7.4. The optimal amplitude of stimulation is 5.0 V/cm with a 10-kHz ac field. (Adapted from reference 31.)

formational coupling discussed earlier, we have used a four-state membrane transport, reaction 9, to analyze thermodynamics of ion pumping in an oscillating electric field (13-17):



Results of our analysis indicate that any Michaelis-Menten type of enzyme has the ability to become a free energy transducer under certain specified conditions (14). In the absence of an electric field, reaction 9 is a facilitated membrane transport system; that is, the transporter, T, can carry the substrate S across the membrane from the compartment with higher concentration of S (out) to the compartment with lower concentration of S (in). However, when an ac field is turned on, T can pump S from in to out, up the concentration gradient.

An enzyme or transporter must be able to interact with an electric field. This simply means that there is charge displacement in its structure that is associated with the T_1 to T_2 transition. An electric field favors a state with greater electric moment (assuming T_2) than a state with smaller electric moment (assuming T_1). If the T_1 to T_2 transition changes the molar electric moment of the transporter by ΔM_e , an electric field of E_m will effect a shift in the equilibrium according to eq 6.

When an oscillating electric field, $E_a = E_{ac}^0 \sin(\omega t)$, is applied, the enzyme will be forced to oscillate among its various conformational states. These oscillations will drive the catalytic cycle of reaction 9 to turn either clockwise or counterclockwise. The direction of flux depends on the affinity of T for S. If T_2 has higher affinity for S_{in} than T_1 has for S_{out} , then the ac field will turn the wheel clockwise to pump S from right to left. Otherwise, the ac will turn the wheel counterclockwise to pump S from left to right. Figure 4 shows an example of ac field driven conformational oscillations of reaction 9. State occupancies of different species of the transporter are plotted as a function of the ac cycle. As seen, each species oscillates with periodicity coincident with the ac frequency. In other words, the enzyme oscillation is enforced by the ac field. Figure 5 reproduces the frequency dependence of Na^+ and Rb^+ pumping by Na, K-ATPase using suitable kinetic parameters.

For this process to occur efficiently, the frequency of the ac field must match the kinetic characteristics of reaction 9. Numerical analysis indicates

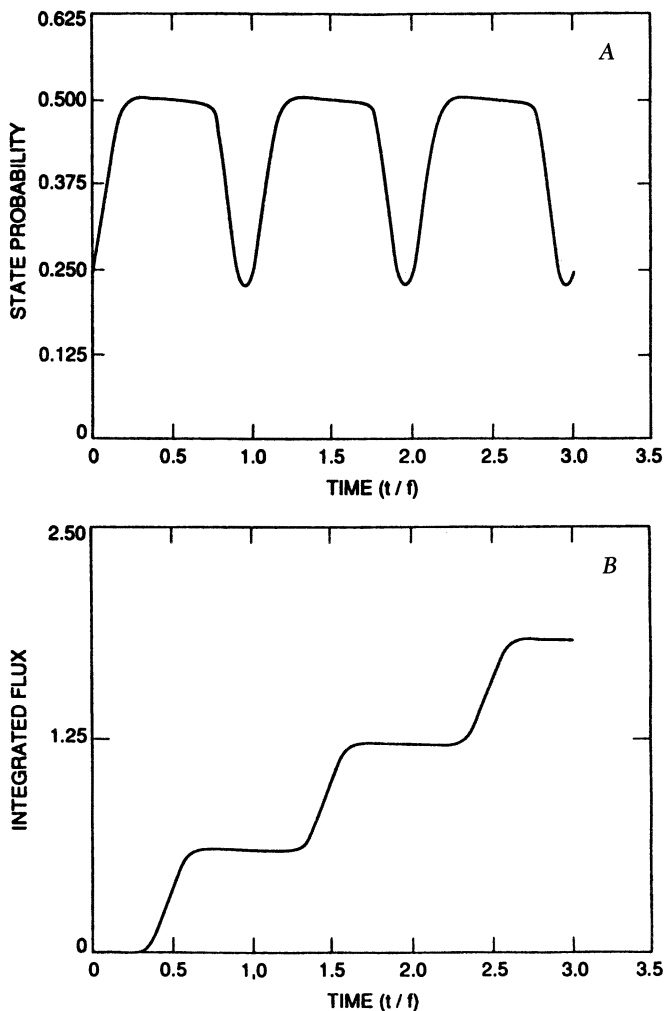


Figure 4. *ac*-induced conformational oscillations of enzyme states in reaction 9. The state occupancy of T_2S is plotted as a function of the *ac* cycle (A). The net clockwise flux of *S* is integrated (B). The set of parameters used for the calculation are given in Liu et al. (30).

that the system can be tuned to an optimal set of conditions for a maximal energy conversion.

For a neutral ligand, the efficiency of energy conversion (i.e., the ratio of power absorption and power output) approaches the theoretical maximum 100% (in practice, it is less than 100%) if

$$r_{\text{conf}} \gg r_e \gg r_b \quad (10)$$

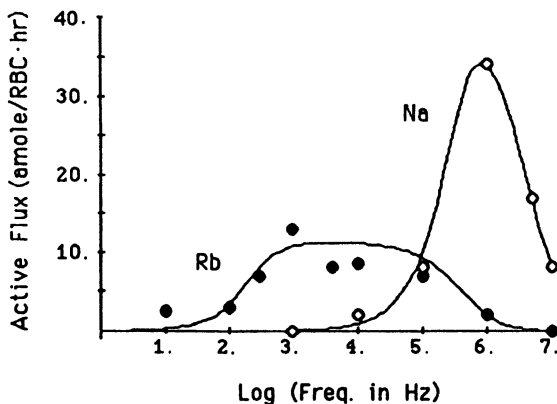


Figure 5. Simulation of the ac-stimulated cation pumping of Figure 2 by the electroconformational coupling model. The filled circles are experimental points and the solid lines are calculated curves according to reaction 9. (Reproduced with permission from reference 32. Copyright 1991.)

Here r_{conf} , r_e , and r_b are, respectively, the rate of the T_1 to T_2 (or T_1S to T_2S) transition, the rate of the rise of electric field, and the rate of the binding of S_{in} to T_2 (or S_{out} to T_1). When this inequality is met, the system will respond to the oscillating field at nearly equilibrium conditions and, as a result, the efficiency of energy conversion reaches its maximal value.

Any membrane transport system may be classified into one of the six categories:

1. A transporter without gating charges and a neutral ligand.
2. A transporter with gating charges and a neutral ligand.
3. A transporter without gating charges and a charged ligand.
4. A transporter–ligand complex without gating charges; that is, the gating charges of the transporter are neutralized by the charges of the ligand.
5. A transporter and its complex with the ligand having gating charges of opposite signs.
6. A transporter with gating charges of the same sign as the charged ligand.

System 1 is electrically inactive and cannot be coupled to an ac field for energy transduction. All other systems absorb energy from an ac field to actively transport the ligand. System 2 has been examined in greater detail

elsewhere (13–17). For systems 2 and 6, the efficiency of energy transduction can approach 100% when a large-amplitude ac field is used and when the condition specified by eq 10 is satisfied. The maximal efficiency is only 50% for systems 3 and 4. In these two systems, reverse energy transduction (i.e., the conversion of chemical potential energy into an electric energy) cannot be achieved. In system 5, the maximal efficiency is a mere 8.7%. The active pumping of ligand in systems 3, 4, and 5 is mainly due to the rectification. In all cases except system 1, the active flux depends strongly on the frequency of the field and on the concentration of the ligand, and there are windows both on the frequency and the concentration axes. By measuring the windows, rate constants and equilibrium constants of reaction 9 can be determined (32). Figure 6 gives a three-dimensional relationship of the active flux, the ac frequency, and the ligand concentration. The presence of a concentration window remains to be verified by experiment.

Energy transduction by a membrane protein is not limited to electric signals. Any potential energy that can interact with a protein and that exhibits similar properties of an oscillating field should also be able to transmit energy to the protein to drive an endergonic reaction (14, 22). For example, if the T_1 to T_2 transition involves a volume change or a change in its area in the lipid bilayer, it should be able to transduce acoustic signals. The former is called PV coupling, and the latter is called γA coupling (33). We have investigated how such a mechanosensitive membrane transport system can absorb energy from an acoustic signal to pump an ion and, thus, convert acoustic energy into electric potential energy (33). Likewise, temperature oscillations and concentration oscillations can also be used for energy and signal transductions. The temperature oscillations require a ΔH (enthalpy of reaction) and the concentration oscillations require a ΔG (free energy of reaction) for the T_1 to T_2 transition (14).

Measurements of Membrane Electric Parameters

For the analysis of data using the electroconformational coupling model, we need to know electric parameters of cell membranes. The transmembrane potential generated by an ac field can be calculated using the Schwan equation (eq 2). To test whether the equation is applicable to cell membranes, we have measured the critical breakdown potential, $\Delta\psi_{\text{crit}}$, of myeloma cell membranes using an ac field of frequencies from 100 Hz to 300 kHz. When an ac-induced $\Delta\psi_m$ equaled $\Delta\psi_{\text{crit}}$, the membrane was punctured with pores and a fluorescence probe (propidium iodide) permeated the cell. The dye bound specifically to DNA and gave rise to a red color (emission maximum 639 nm). Figure 7 gives an example of the measurement of E_{crit} using propidium iodide. The field intensity that induced a $\Delta\psi_{\text{crit}}$, E_{crit} , was

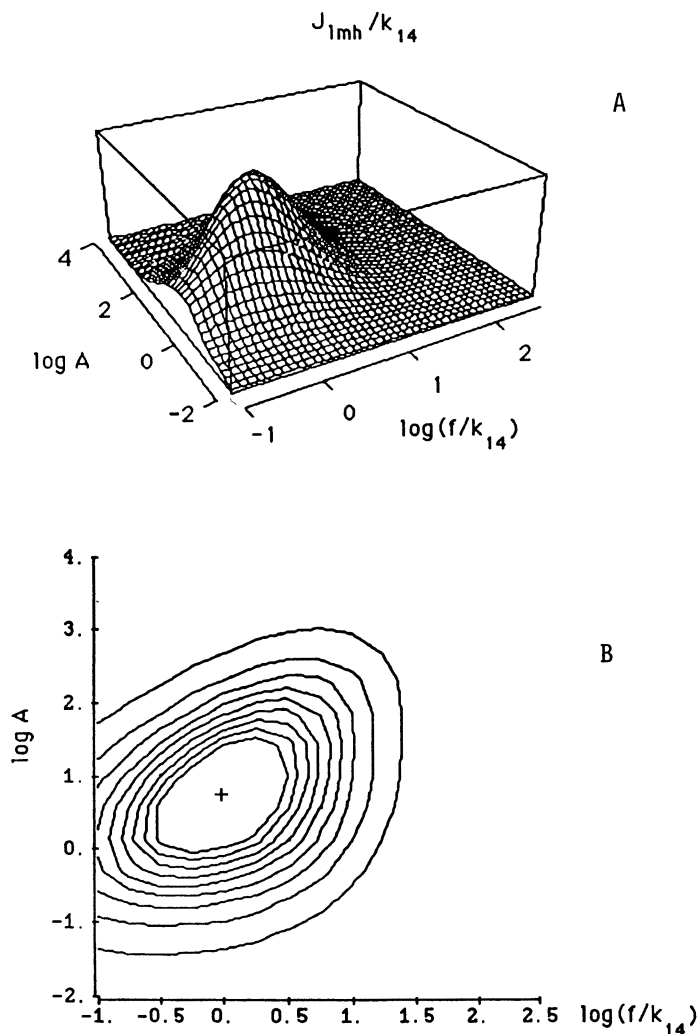


Figure 6. The ac-stimulated flux, J_{1mh} , as a function of dimensionless frequency, f/k_{14} , and ligand concentration A (A) and contour maps of the same plot (B). Data from Markin and Tsong (32).

plotted as a function of the ac frequency in Figure 8. These curves fitted nicely to the Schwan equation, which indicates that the Schwan equation is applicable to cell membranes (12). The dielectrophoresis method has also been used to obtain the membrane capacitance and the membrane dielectric constant (34).

The electroconformational coupling method measures the force acting on a cell by a nonuniform oscillating electric field. Depending on the frequency

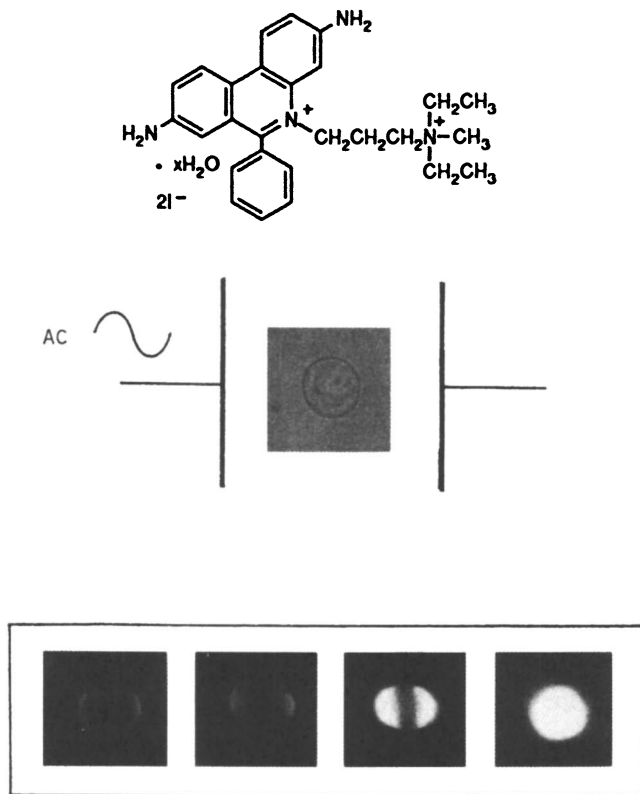


Figure 7. Measurement of the critical breakdown potential of a myeloma cell membrane using an ac field. The chemical formula of propidium iodide is shown in the upper figure. The middle figure shows a typical myeloma cell under the microscope (bright field). The relative positions of the platinum electrodes are indicated. The lower figure gives some photographs taken at different times after a cell was electroporated by an ac field E_{crit} . Within 1–3 s, two narrow, fluorescent bands appeared at the two loci facing the electrodes (the leftmost photo). The next three photos, from left to right, were taken at 20 s, 1 min, and 3 min, respectively, after the application of a 200-ms ac field of 1 kV/cm at 100 kHz. (Reproduced with permission from reference 12. Copyright 1990.)

of the ac, the cell may be attracted either toward higher or lower field intensity. At a critical frequency, f_{crit} , the net force acting on the cell is zero; that is, the cell stops moving in either direction. According to Saver (35), this frequency depends on electric parameters of the cell membrane and the conductivity of the external medium. Experimentally, f_{crit} is determined in media of different conductivities. By regression analysis the dielectric constant and the membrane conductivity can be determined (34).

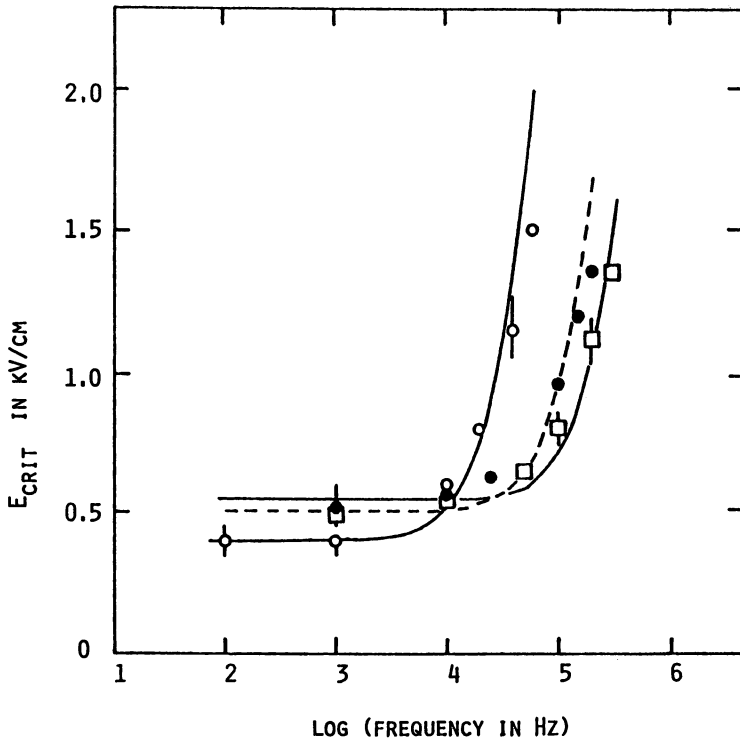


Figure 8. Critical ac field strength, E_{crit} , for electroporation of myeloma cells as a functions of ac frequency. Data were obtained in media of different resistivities: 52,600 Ω cm (○); 7050 Ω cm (●); 2380 Ω cm (□). The curves drawn through these data points were obtained by calculation (○) or optimization (● and □) according to the Schwan equation. (Reproduced with permission from reference 12. Copyright 1990.)

Developmental Bibliography

The conceptual development of the theory of electroconformational coupling can be traced by referring to the following list of publications.

1987

- Tsong, T. Y.; Astumian, R. D. Electroconformational coupling and membrane protein function. *Prog. Biophys. Mol. Biol.* 50, 1-45.
- Tsong, T. Y.; Chauvin, F.; Astumian, R. D. Interaction of membrane proteins with static and dynamic electric fields via electroconformational coupling. In *Mechanistic Approaches to Interaction of Electromagnetic Fields with Living Systems*; Blank, M.; Findl, E., Eds.; Plenum: New York; pp 187-202.

Westerhoff, H. V.; Kamp, F.; Tsong, T. Y.; Astumian, R. D. Interaction between enzyme catalysis and nonstationary electric fields. In *Mechanistic Approaches to Interaction of Electromagnetic Fields with Living Systems*; Blank, M.; Findl, E., Eds.; Plenum: New York; pp 203–215.

1988

Tsong, T. Y. Active cation pumping of Na,K-ATPase and SR Ca-ATPase induced by an electric field. *Methods Enzymol.* 157, 240–251.

Tsong, T. Y.; Astumian, R. D. Electroconformational coupling: An efficient mechanism for energy transfection by membrane-bound ATPases. *Ann. Rev. Physiol.* 50, 273–290.

Tsong, T. Y.; Tomita, M.; Lo, M. M. S. Pre-selection of B-lymphocytes by antigen for fusion to myeloma cells by pulsed electric field method. In *Molecular Mechanisms of Membrane Fusion*; Oki, S. et al., Eds.; Plenum: New York; pp 223–236.

Astumian, R. D.; Chock, P. B.; Chauvin, F.; Tsong, T. Y. Electroconformational coupling and the effects of static and dynamic electric fields on membrane transport. In *Electromagnetic Fields and Biomembranes*; Markov, M.; Blank, M., Eds.; Plenum: New York; pp 59–74.

1989

Tsong, T. Y. Electroporation of cell membranes: Its mechanisms and applications. In *Electroporation and Electrofusion in Cell Biology*; Neumann, E. et al., Eds.; Plenum; New York; pp 149–163.

Lo, M. M. S.; Tsong, T. Y. Producing monoclonal antibodies by electrofusion. In *Electroporation and Electrofusion in Cell Biology*; Neumann, E. et al., Eds.; Plenum: New York; pp 259–270.

Tsong, T. Y. Deciphering the language of cells. *Trends in Biochem. Sci.* 14, 89–92.

Tsong, T. Y.; Liu, D. S.; Chauvin, F.; Astumian, R. D. Resonance electroconformational coupling: A proposed mechanism for energy and signal transduction by membrane proteins. *Biosci. Rep.* 9, 13–27.

Tsong, T. Y. Electroconformational coupling: A fundamental process of biomolecular electronics for signal transduction. In *Molecular Electronics*; Hong, F., Ed.; Plenum: New York; pp 83–95.

Tsong, T. Y.; Astumian, R. D. Charge-field interactions in cell membranes and electroconformational coupling: Transduction of electric energy by membrane ATPase. In *Charge-Field Effects in Biosystems*; Allen, M. J., Ed.; Plenum: New York; Vol. II, pp 167–177.

Astumian, R. D.; Robertson, B.; Tsong, T. Y. Charge-field interactions in cell membranes and electroconformational coupling: Theory for the interactions between dynamic electric fields and membrane enzymes. In *Charge-Field Effects in Biosystems*; Allen, M. J., Ed.; Plenum: New York; Vol. II, pp 179–190.

- Robertson, B.; Astumian, R. D.; Tsong, T. Y. Nonlinear effects of periodic electric fields on membrane proteins. In *Charge-Field Effects in Biosystems*; Allen, M. J., Ed.; Plenum: New York; Vol. II, pp 191–209.
- Astumian, R. D.; Chock, P. B.; Tsong, T. Y.; Westerhoff, H. V. Effects of oscillations and energy-driven fluctuations on the dynamics of enzyme catalysis and free energy transduction. *Phys. Rev. A* 39, 6416–6435.

1990

- Liu, D. S.; Astumian, R. D.; Tsong, T. Y. Activation of Na and the Rb pumping modes of Na,K-ATPase by an oscillating electric field. *J. Biol. Chem.* 265, 7260–7267.
- Tsong, T. Y. Electric modulation of membrane proteins: Enforced conformational oscillation and cellular energy and signal transductions. *Annu. Rev. Biophys. Biophys. Chem.* 19, 83–106.
- DeBustros, A.; Lee, R. Y.; Compton, D.; Tsong, T. Y.; Baylin, S. B.; Nelkin, B. D. Different cis-acting DNA elements regulate expression of the human calcitonin gene in cultured lines of lung carcinoma and medullary thyroid carcinomas. *Mol. Cell Biol.* 10, 1773–1778.
- Xie, T. D.; Sun, L.; Tsong, T. Y. Study of mechanisms of electric field induced DNA transfection I: DNA entry by surface binding and diffusion through membrane pores. *Biophys. J.* 58, 13–19.
- Xie, T. D.; Tsong, T. Y. Study of mechanisms of electric field-induced DNA transfection II: Transfection by low-amplitude, low-frequency alternating electric fields. *Biophys. J.* 58, 897–903.
- Markin, V. S.; Tsong, T. Y.; Astumian, R. D.; Robertson, B. Energy transduction between a concentration gradient and an alternating electric field. *J. Chem. Phys.* 93, 5062–5066.
- Marszalek, P.; Liu, T. S.; Tsong, T. Y. Schwan equation and transmembrane potential induced by alternating electric field. *Biophys. J.* 58, 1053–1058.
- Tsong, T. Y. On electroporation and some related cell membrane phenomena. *Bioelectrochem. Bioenerg.* 24, 271–295.
- Tomita, M.; Tsong, T. Y. Selective production of hybridoma cells: Preselection of B-lymphocytes by antigen for electrofusion with myeloma cells. *Biochim. Biophys. Acta* 1055, 199–206.

1991

- Prudovsky, I.; Tsong, T. Y. Fusion of fibroblasts with differentiated and non-differentiated leukemia cells resulting in blockage of DNA synthesis. *Dev. Biol.* 144, 232–239.
- Marszalek, P.; Zielinsky, J. J.; Fikus, M.; Tsong, T. Y. Determination of electric parameters of cell membranes by a dielectrophoresis method. *Biophys. J.* 59, 982–987.

- Markin, V. S.; Tsong, T. Y. Reversible mechanosensitive ion pumping as a part of mechano-electrical transduction. *Biophys. J.* **59**, 1317–1324.
- Markin, V. S.; Tsong, T. Y. Frequency and concentration windows for the electric activation of a membrane active transport system. *Biophys. J.* **59**, 1308–1316.
- Markin, V. S.; Tsong, T. Y. Electroconformational coupling of ion transport in oscillating electric field: Rectification versus pumping. *Bioelectrochem. Bioenerg.* **26**, 251–276.

References

1. Bockris, J. O'M.; Reddy, A. K. N. *Modern Electrochemistry*; Plenum: New York, 1970; Vols. I and II.
2. Cole, K. S. *Membranes, Ions and Impulses*; University of California Press: Berkeley, CA, 1972.
3. Tien, H. T. *Bilayer Lipid Membranes*; Dekker: New York, 1974.
4. Tsong, T. Y. *Biosci. Rep.* **1983**, *3*, 487.
5. Kinoshita, K.; Tsong, T. Y. *Proc. Natl. Acad. Sci.* **1977**, *74*, 1923.
6. Schwan, H. P. In *Biological Effects and Dosimetry of Nonionizing Radiation*; Grandolfo, M.; Michaelson, S. M.; Rindi, A., Eds.; Plenum: New York, 1983; p 213.
7. Gross, D.; Loew, L. M.; Webb, W. W. *Biophys. J.* **1986**, *50*, 339.
8. Kinoshita, K.; Ashikava, I.; Staita, N.; Yoshimura, H.; Itoh, H.; Nagayama, K.; Ikegami, A. *Biophys. J.* **1988**, *53*, 1015.
9. Ehrenberg, B.; Farkas, D. L.; Fluhler, E. N.; Lojewski, Z.; Loew, L. M. *Biophys. J.* **1987**, *51*, 833.
10. Teissie, J.; Tsong, T. Y. *Biochemistry* **1981**, *20*, 1548.
11. El-Mashak, M. E.; Tsong, T. Y. *Biochemistry* **1985**, *24*, 410.
12. Marszalek, P.; Liu, D. S.; Tsong, T. Y. *Biophys. J.* **1990**, *58*, 1053.
13. Tsong, T. Y.; Astumian, R. D. *Bioelectrochem. Bioenerg.* **1986**, *15*, 457.
14. Tsong, T. Y. *Annu. Rev. Biophys. Biophys. Chem.* **1990**, *19*, 83.
15. Robertson, B.; Astumian, R. D. *Biophys. J.* **1990**, *57*, 689.
16. Astumian, R. D.; Chock, P. B.; Tsong, T. Y.; Westerhoff, H. V. *Phys. Rev. A* **1989**, *39*, 6416.
17. Markin, V. S.; Tsong, T. Y.; Astumian, R. D.; Robertson, B. *J. Chem. Phys.* **1990**, *93*, 5062.
18. Blank, M. *J. Electrochem. Soc.* **1987**, *134*, 1112.
19. Blank, M.; Soo, L. *Bioelectrochem. Bioenerg.* **1989**, *22*, 313–322.
20. Blank, M.; Soo, L. *Bioelectrochem. Bioenerg.* **1990**, *24*, 51–61.
21. *Mechanistic Approaches to Interactions of Electric and Electromagnetic Fields with Living Systems*; Blank, M.; Findl, E., Eds.; Plenum: New York, 1987.
22. Tsong, T. Y. *Trends Biochem. Sci.* **1989**, *14*, 89.
23. Tsong, T. Y. In *Molecular Electronics*; Hong, H. T., Ed.; Plenum: New York, 1989; p 83.
24. Hoffman, J. F.; Kaplan, J. H.; Callahan, T. J. *Fed. Proc., Fed. Am. Soc. Exp. Biol.* **1979**, *38*, 2440.
25. Witt, H. T.; Schlotter, E.; Graber, P. *FEBS Lett.* **1976**, *69*, 272.
26. Mounieime, Y.; Tosi, P. F.; Gazitt, Y.; Niolau, C. *Biochem. Biophys. Res. Commun.* **1989**, *159*, 34.

27. Neumann, E.; Sowers, A. E.; Jordan, C. A. *Electroporation and Electrofusion in Cell Biology*; Plenum: New York, 1989.
28. Serpersu, E. H.; Tsong, T. Y. *J. Membrane Biol.* **1983**, *74*, 191.
29. Serpersu, E. H.; Tsong, T. Y. *J. Biol. Chem.* **1984**, *259*, 7155.
30. Liu, D. S.; Astumian, R. D.; Tsong, T. Y. *J. Biol. Chem.* **1990**, *265*, 7260.
31. Liu, D. S. et al. *Abstract*, FASEB Annual Meeting, 1991.
32. Markin, V. S.; Tsong, T. Y. *Biophys. J.* **1991**, *59*, 1308.
33. Markin, V. S.; Tsong, T. Y. *Biophys. J.* **1991**, *59*, 1317.
34. Marszalek, P.; Zielinsky, J. J.; Fikus, M.; Tsong, T. Y. *Biophys. J.* **1991**, *59*, 982.
35. Sauer, F. In *Interactions between Electromagnetic Fields and Cells*; Chiabrera, A.; Grattarola, M.; Vivani, R., Eds.; Plenum: New York, 1985; p 181.

RECEIVED for review January 29, 1991. ACCEPTED revised manuscript August 17, 1992.

Author Index

- Akeson, M., 41
Berkowitz, Max L., 3
Beusen, Denise D., 259
Bezrukov, S. M., 375
Blank, Martin, 429
Brumfeld, V., 107
Colombini, Marco, 245
Colombo, Marcio, 177
Cusanovich, M. A., 471
Deamer, D. W., 41
Downer, Nancy W., 491
Fishman, Harvey M., 415
Grove, Anne, 329
Gruner, Sol M., 129
Gutman, Menachem, 27
Haber, J. E., 315
Harris, Andrew L., 197
Harris, S. L., 315
Hazzard, J. H., 471
Hong, Felix T., 531
Huang, Huey W., 83
Iwamoto, Takeo, 329
Korenstein, R., 107
Leuchtag, H. Richard, 415
Li, Jianguo, 491
Liebovitch, Larry S., 357
Loew, Leslie M., 151
Macias, Felipe, 401
Marrer, Stephan, 329
Marshall, Garland R., 259
Miller, I. R., 107
Monk, B. C., 315
Montal, Mauricio, 329
Montal, Myrta S., 329
Na, S., 315
Parsegian, V. Adrian, 177
Perlin, D. S., 315
Raghavan, K., 3
Rand, R. Peter, 177
Rau, Donald C., 177
Seto-Young, D., 315
Smith, H. Gilbert, 491
Starzak, Michael E., 401
Tien, H. Ti, 513
Tomich, John M., 329
Tsong, Tian Y., 561
Vanysek, Petr, 55
Vodyanoy, Igor, 375
Weaver, James C., 447
Wilcox, Michael J., 225
Wilson, G. S., 471

Affiliation Index

- Brandeis University, 315
Brock University, 177
Columbia University, 357, 429
The Johns Hopkins University, 197
Massachusetts Institute of Technology, 447
Michigan State University, 513
National Institutes of Health, 41, 177
Northern Illinois University, 55
Office of Naval Research, 375
Princeton University, 129
The Public Health Research Institute, 315
Rice University, 83
State University of New York at Binghamton, 401
Tel Aviv University, 27, 107
Texas Southern University, 415
TSI Corporation, 491
University of Arizona, 471
University of California at Davis, 41
University of California, San Diego, 329
University of Connecticut Health Center, 151
University of Kansas, 471
University of Maryland, 245, 375
University of Minnesota College of Biological Sciences, 561
University of New Mexico, 225
University of North Carolina, 3
University of Southern California Medical School and Children's Hospital, 329
University of Texas Medical Branch, 415
Washington University, 259
Wayne State University, 531
The Weizmann Institute of Science, 107

Subject Index

A

- α -helix
 band parameters for CD, 92*t*
 conformation in polypeptide, 86–87
 use of polarization to determine orientation, 87
- ac-stimulated flux, function of
 dimensionless frequency, 572*f*
- Access impedance, partition of
 photocurrent, 538
- Acetylcholine (ACh)
 structure and activity, 292–293
 transmembrane or amphipathic sequences, 292
- Acetylcholine receptor (AChR) channel
 neuronal, 348
 selects against anions, 332
Torpedo complex subunits, 333–334
- Acoustic signals, energy transduction by a
 membrane protein, 571
- Activation energy barriers
 globular proteins, 369–370
 kinetics of channel switching between
 different states, 368*f*
 statistical properties of single-channel data, 367
 transitions, 366
- Active transport, ions across cell
 membranes, 444–445
- Adenosine triphosphate (ATP) release from
 enzyme, applied field-induced
 transmembrane potential, 564
- Adenosine triphosphate (ATP) synthesis
 adequate proton supply, 51
 characteristics of proton flux, 48
 proton-conducting channel, 41
 rate of proton conductance, 49
- Admittance data
 acquisition of a K⁺ current response, 419*f*
 data analysis, 417–418
 determination of K- and Na-channel
 relaxation times, 415–428
 K⁺-conducting membrane, 422*f*
 magnitude and phase angle vs. frequency,
 425*f*
 Na⁺-conducting membrane, 426*f*
 Na⁺ current response to a voltage-clamp
 step, 420*f*
 plotting calculations, 421
 rapid complex, 418–421
- Adsorbed protein, redox state, 482
- Adsorption of proteins, water–nitrobenzene
 interface, 72–78
- Aggregated protein structures, channels, 430
- Aggregation
 conductance states in planar lipid bilayers, 264
 peptide ion channels, 300–301
 preparation of peptide aggregates, 302–303
- Alamethicin
 α -helical form, 88–89
 aligned multilayers of DPhPC, OCD
 spectra, 90*f*
 association with membranes, 83–106
 asymmetric current–voltage curve, 273–274
 bridge through self-aggregation, 264
 CD spectra for different electric
 potentials, 118–119
 conductance, 302*f*
 conformation at different membrane
 potentials, 120*t*
 current–voltage curves, 275*f*
 DLPC vesicles, CD spectrum, 89*f*
 DPhPC vesicles, CD spectrum, 93*f*
 embedded in PC vesicles, CD spectra, 118*f*
 helix dipole model, 277*f*
 in DOPC, phase diagram, 96*f*
 in DPhPC, phase diagram, 95*f*
 incorporation into lipid vesicle
 membranes, 110–111
 inserted and surface state helices, 94
 molar ellipticity as a function of
 Donnan potential, 119*f*
 multistate conductance, 267*f*
 nonconducting state, 94
 optimize solvent and dipole interactions
 with membrane, 272*f*
 pore models, 270
 structure and mechanisms, 270–271
 voltage-gating channel model, 271*f*
- Alamethicin dimer, oligomers, 301*f*
- Alamethicin monomers, structural description, 93
- Alignment, X-ray diffraction samples, 85
- Alkanes, spontaneous curvatures, 141
- n*-Alkanes, electric fields and solubility
 in BLMs, 518
- Allosteric control, water as a variable, 185–186
- Amino acids
 cytochrome *c*₃ sequence, 472–474*f*
 VDAC sequences, 249*f*
- Amphipathic helix
 residue arrangements, 262*f*–263*f*
 sodium channel, 291
- Amphipathic α -helix
 inner bundle of channel proteins, 332–333
 plausible unifying structure, 351
 structural motif in ion channels, 331

- Amphipathic peptides, conductance events, 349
- Amphipathicity, peptide ion channels, 300
- Amphiphilic molecules, structure of aqueous vs. integral membrane proteins, 129
- Anion-selective channel, mitochondrial voltage-dependent, 245–258
- Anions, permeability of liposomes, 46
- Anisotropy in the protein environment, lipid bilayer, 131
- Antibiotics
1f noise, 391
 membrane current noise, 392*f*
 peptide, 260–285
- Anticorrelations in transport events, shot noise, 380
- Apamin, structure and activity, 288–289
- Aqueous–membrane interface, electrostatic forces, 4
- Artificial membranes
 electrochemical approach, 551
 formation procedures, 492–495
- Artificial photosynthesis, pigmented BLM research, 526
- Averaged surface reconstruction, three-dimensional representation, 248*f*
- Axon membrane, expression for the complex admittance, 416
- Axon system, dye characterization, 168–170
- Axon terminal, voltage coupling across gap junctions, 238–242
- Azo dyes, characteristics, 152
- B**
- β -sheet structures, gramicidin A, 261
- β -sheet wall, VDAC, 246–248
- Back diffusion, quantitative interpretation, 122–124
- Bactericidal activity, magainin, 276
- Bacteriorhodopsin
 absorbance, 110
 description and activity, 532
 device construction, 555–556
 mutant strain, 546
 photovoltaic effects and photoconductivity, 523
 reconstitution in lipid vesicles, 109–110
 ultimate intelligent material, 551
 vision and photosynthesis, 532
- Bacteriorhodopsin film
 ability to generate a B2 signal, 542–545
 prolonged drying to eliminate pH sensitivity, 545
- Bacteriorhodopsin membranes
 electrochemical processes, 531–560
 equivalent circuit, 538*f*
 lack of pH sensitivity, 540
 temperature and pH dependence of components, 541*f*–542*f*
- Bacteriorhodopsin photosignals, relaxation time constants, 534*t*
- Bacteriorhodopsin reconstituted vesicles, CD spectrum, 116*f*
- Bee venom
 apamin, 288–289
 mast cell degranulating (MCD) peptide, 288–289
 melittin, 285–287
- Bending energy, monolayers of a lamellar bilayer, 139
- Beryllium plate, high quality diffraction patterns, 98
- Biexponential decay, second-order differential equation, 538
- Bilayer(s), force measurement, 187–189
- Bilayer channels, sucrose-permeable liposomes, 210–215
- Bilayer curvature elasticity, membrane protein activity, 129–148
- Bilayer lipid membranes (BLM)
 description of system, 514–515
 electrical properties in absence of light, 518–520
 electrical resistivity in presence of iodine, 517
 electronic processes and redox reactions, 513–529
 formation methods, 514–515
 fragility, 525
 metallic electrode behavior, 519–520
 potential applications, 524–526
- Bilayer thermal motion, separation of neutral bilayers, 188
- Binding agents, channel behavior, 255
- Binding kinetics, dyes, 164
- Binding sites
 ion permeation, 401
 number of distinct local velocities, 403
 symmetry, 100
- Biological functions, electrochemistry, 555
- Biological ionic systems, conductance noise, 382
- Biological membranes
 electronic noise sources, 375–399
 estimates of proton permeability, 46–47
 proton channels, 47–49
 significant deviations from Hooge's formula, 389
- Biological redox proteins, oxidation–reduction potentials, 478

- Biological signal transduction media,
source of electrical noise, 386
- Biomembrane(s)
dynamics of proton transfer reactions, 27
evidence for electronic processes, 515–520
interaction of protons with surface
groups, 31–33
study approaches, 39
- Biomembrane lipids, diversity, 131–133
- Biomembrane molecules, computer modeling,
14–23
- Biomembrane structures, electrochemical
impedance spectroscopy, 491–510
- Biomembrane surfaces
concentration of counterions, 6
solvation force behavior, 7
- Biomolecular electronic devices, lack of
electronic properties, 525
- Biosensors
modified BLM, 524–525
specific recognition functions, 491
specificity and biocompatibility, 525
- Biphasic reduction, cytochrome c_3 , 484
- Bipolar cell, dendritic integration, 226
- Boltzmann distribution, Gouy–Chapman
theory, 4–5
- Born energy
calculation of actual ion flux, 45
ions within small pores, 458
simulations, 462
- Boundary lipid, nonspecific coupling with
protein, 143
- Bovine serum albumin (BSA)
adsorbed, effect of pH, 77–78
adsorbing material, 72
methods of study, 55
- Bragg reflections, phases determined by
swelling method, 98
- Buffer(s), measurement of reaction rates, 43
- Buffer molecules
enhanced interaction with membrane
surface groups, 31–32
proton diffusion, 31
- Bulk electrocompression models, rupture
and reversible electrical breakdown, 448
- ## C
- Calcium channel
proteins that mimic, 333
single-channel conductance, 345
- Calcium channel modulators, binding sites, 331
- Calibration, laser Doppler instrumentation,
407–408
- Capacitance
double-layer, 505–506
function of pH at interface, 78*f*
membrane, 459
source impedance of the membrane, 537
surface-bound membranes, 506–508
- Carbocyanine dyes, potentiometry on the
water–nitrobenzene interface, 59–72
- Carotenes, light-gathering accessory
pigments, 521
- Carrier-mediated ion transport,
nonequilibrium noise, 381
- Carrier molecule, covalent attachment of
peptide segments, 333
- Catalytic wheel, enzyme, 561
- Cation pumping, ac-stimulated, 570*f*
- Cationic peptides, basic residues, 298–299
- Cecropins, 283–284
- Cell bilayer membrane, communication in
living organisms, 491
- Cell membranes
electrical properties, 562
endogenous or exogenous electric field, 561
topology, 465
- Cell physiology, potentiometric membrane
dyes, 151
- Channel(s)
aggregated protein structures, 430
determination of ionic velocity, 401–413
formed by connexin, prospects for
biophysical study, 203–205
- Channel closure in VDAC, process, 251–253
- Channel conductance, potential dependence, 125
- Channel conformation, change as transition
across activation energy barrier, 366
- Channel formation in membranes, peptides,
259–314
- Channel-forming peptides, uniformly
aligned multilayers of membranes, 83–106
- Channel-forming polypeptides, membrane
potential, 126
- Channel-forming proteins, conservation in
secondary structures, 246–248
- Channel gating
changes in channel structure, 184
mechanism, 439
- Channel-gating processes, membranes, 437–439
- Channel kinetics
characteristics, 361
effective kinetic rate constant, 361–365
- Channel mechanisms, fractal analysis, 357–374
- Channel opening, dependence on surface
charge, 440
- Channel opening and closing, energetics,
442–444

- Channel proteins
coherent patterns of motion, 373
extensive sequence conservation, 351
four-helix bundles as model of pore structure, 334–337
functional elements of pore-forming structure, 349
functional elements responsible for pore properties, 332
functional properties, 331
hydrophobic sequences, 347–348
structure and inferences, 330–331
- Channel selectivity, electrostatic environment within the pore, 250
- Channel specificity, voltage gating, 440–442
- Channel switching, sources, 391
- Channel transitions, sucrose-permeable liposomes, 211
- Chaos, switching of conformational states of ion channel, 371–372
- Chaotic system, definition, 371–372
- Charge, transient generation, 124
- Charge density, fraction of open channels, 438
- Charge displacement, enzyme or transporter, 568
- Charge recombination
bacteriorhodopsin, 556
converted photon energy, 533–534
net proton transport, 534
- Charge separation
photoinduced, 536f
response of photopigments to light stimulation, 554
vectorial, 533
- Charge shift
ionic gradients, 445
probability, 444
- Charge-shift probes, spectroscopic and binding properties, 166t–167t
- Charge transfer resistance, effective area of OTS-coated PtO electrode, 497
- Chemical capacitance, definition, 535
- Chemical dehydration of head groups, osmotic pressure, 139
- Chemical free energies, hydration forces, 179–181
- Chemical potential gradient, net transport of ions, 518
- Chemically specific lipid requirements, membrane proteins, 131
- Chloride, permeability of liposomes, 46
- Chloride ion, halorhodopsin membrane, 552
- Chlorophyll
form in BLM, 522
in bilayer lipid membranes, 521
- Cholesterol, membrane thickness buffer, 104
- Chromophore, insertion into defined microenvironments, 28
- Chromophore modification, potentiometric dyes, 153
- Circular dichroism (CD) spectroscopy, secondary structures of proteins, 86–93
- Cleavage protocols, peptide–resin mixture, 343
- Colicins
model of mechanism of action, 303
voltage-gated monovalent ion channels, 303
- Complementary surfaces, attractive force, 192
- Complex admittance method, generalized data analysis, 426
- Component analysis, photosignal, 540–546
- Compound eyes
fluorescence micrograph, 237f
individual retinas, 226
interference contrast micrograph, 228f
light micrograph of a few facets, 232f
scanning electron micrograph, 227f
- Computer modeling, biomembrane molecules, 14–23
- Conductance, open and closed VDAC, 250–253
- Conductance disparity, oligomeric size, 348
- Conductance fluctuations
aqueous solutions of strong electrolytes, 384f
measurement methods, 382–383
mixtures of NaCl and HCl electrolytes, 385f
- Conductance noise
generation mechanisms, 386
modulation of ion transport, 381–387
pH-dependent spectral density, 387
- Conductance properties, neutral peptide sequences, 264–265
- Conductivity, proteins and protein films, 483
- Conductivity changes, transfer of electrons across the membrane, 517
- Configuration space, motion of membrane molecules in liquid crystalline phase, 20–23
- Confocal microscopy, magnitude of mitochondrial membrane potential, 163
- Conformational changes, energetic consequences in proteins, 434–437
- Conformational constraints, α, α -dialkyl amino acids, 267
- Conformational geometries, lipid matrix, 144
- Conformational states
channel proteins, 357
switching, 358
- Conformational studies, peptides in solvents, 295
- Conformational switches, peptide structures, 271–276
- Connexin
definition, 198
immunoaffinity purification, 205

- Connexin—*Continued*
 suitable for reconstitution, 205
- Connexin-32
 bilayer conductance, 216*f*
 effects of preparation methods, 217
 pore in liposomes, 208–210
 selection by sucrose permeability, 208
- Connexin channels
 biophysical questions, 218–219
 composition, 201–202
 identification, 204–205
 liposomes, 206–208
 problems regarding reconstitution, 218
 schematic drawings, 199*f*
- Connexin-32 channels
 activity, 211*f*
 reversal potentials for bilayers, 214
 structural form, 215
 through one or two membranes, 197–223
 voltage dependence, 212*f*
 voltage-dependent kinetics, 214*f*
- Connexin protein
 gated pore through two membranes, 198
 importance for electrochemical studies, 198–203
- Contact value theorem, surface charge density, 5–6
- Contingent gating, state-dependent alteration of field across a protein, 201
- Continuum models, ion permeation, 403–404
- Correlation function, inhomogeneous boundaries, 11–12
- Coupling
 ATP hydrolysis and proton transport, 327
 function in retina, 229
 neural elements, 229
- Coupling ratio, definition, 239
- Crossed-beam system
 low-intensity scattering, 407
 velocity components, 406*f*
- Crystal, images of VDAC, 246
- Crystallization, water-soluble proteins and membrane proteins, 130
- Cubic cell model
 electroporation, 465–466
 transmembrane voltage, 464*f*
- Current-voltage behavior, H⁺-ATPase in yeast, 320
- Current flow, comparison between electrode and ITIES, 56, 57*f*
- Current noise, calculations, 379
- Curvature energy, chains of lipid hydrocarbon, 140
- Curvature stress
 lipid bilayers of biomembrane systems, 147
 nonlamellar-prone lipids, 133
 polar and nonpolar region, 144
- Cyanine dyes, delocalized positive charge, 157, 162
- Cyclic voltammetry
 basics, 516–517
 modification of BLM, 519
 significant advantages, 520
- Cylindrical geometry, changes in lattice dimension, 137–138
- Cytochrome *c*₃
 amino acid sequences, 474*f*
 asymmetric electrostatic field, 475
 biphasic reduction, 484
 changes of resistivity, 483–484
 electron distribution, 478*f*
 electrostatic properties, 473
 iron-iron distances and heme-heme angles, 477*t*
 kinetics of intramolecular electron transfer, 485
 macroscopic oxidation-reduction potentials, 479*t*
 oxidation-reduction potentials, 477–480
 properties and insights, 471–489
 stereo views, 476*f*
 structure, 472–477
 surface spectroscopy, 482–483
- Cytolytic peptides, cationic site adjacent to a hydrophobic surface, 299

D

- Decay constant
 nature of the interface, 12
 nature of the surface, 11
- Decay length, strength of hydration force, 12–14
- Decomposition of a composite signal, schematic diagrams, 543*f*
- Defects
 lipid bilayers, measurements of cation permeability, 45
 lipid sample, 85
- Defensins
 consensus sequence, 281*f*
 dimer crystal structure, 283*f*
 selected sequences, 282*t*
 structure, 280–281
- Dehydration energy, gramicidin channel, 104
- Dendrites, monopolar, 239
- Dendritic integration, bipolar cell, 226
- Depolarization, voltage dependence, 440
- Derjaguin-Landau-Verwey-Overbeek (DLVO) theory, van der Waals and electrostatic forces, 3
- Designed proteins, amphipathic α -helices, 329

- Desulfovibrio*, cytochrome *c*₃, 471–489
- Detergent-solubilized protein, VDAC, 250
- Detergent dialysis
formation of a relatively complete membrane, 503
formation of surface-bound lipid membranes, 492–495
procedure with membranes on SiO₂, TiO₂, and ITO electrodes, 506
structures formed, 508
- Deterministic process, switching between different conformational states, 372
- Dielectric breakdown, strength of electric field, 519
- Difference frequency, Doppler scattering, 405–406
- Difference spectra, bacteriorhodopsin, 115
- Difference X-ray diffraction, direct measurement of ion locations, 98
- Diffraction patterns, membrane multilayers, 97
- Diffusion
protons within thin water layers, 28–31
source of *1/f* noise, 392
- Diffusion current, charged molecule, 461
- Diffusion dynamics, shift from 3-D to 2-D space, 34
- Diffusional membrane potential, application, 110
- Diffusional relaxation
calculation, 124
curve, 125*f*
- Dilauroylphosphatidylethanolamine (DLPE)
molecules
atom densities, 17*f*
spacing in gel phase, 16
- Dioleoylphosphatidylcholine (DOPC), alamethicin, 96
- Dioleoylphosphatidylethanolamine (DOPE)
temperature dependence of basis vector length, 136*f*
water extraction, 138
- Dipalmitoylphosphatidylcholine (DPPC)
protrusions of phospholipid molecules in bilayer, 22, 23*f*
simulations of liquid crystalline phase, 20–23
–water interface, simulation of atom and water densities, 20*f*, 22*f*
- Dipolar potential, transmembrane ion transport, 504
- Disaggregation
equilibrium constant as function of charge on the molecule, 433*f*
hemoglobin, 432–434
- Disaggregation constant, change in charge density and pH, 431
- Discrete state models, ion permeation, 403–404
- Displacement current
bacteriorhodopsin membrane, 532
extracellular to intracellular space, 548
- Displacement photocurrent
hypothetical B2' component, 546
light pulse to stimulate membrane, 534
photosynthetic and visual membranes, 553
pulsed-light photoelectric signal, 551
- Dissipative resistance, fluctuations in a nonlinear steady state, 381
- DNA
hydration energies, 193–194
repulsion and attraction, 191–192
- Donnan potential
calculation, 111–112
conformational changes in alamethicin, 107
gradient, generation across the membrane, 111–112
- Doppler frequency, variation with orientation angle of membrane system, 410*f*
- Doppler scattering, determination of ionic velocity distributions in channels and membranes, 401–413
- Doppler spectra, thallium ions in gramicidin channels, 410*f*
- Doppler velocimetry, 404–406
- Double helix, repulsion and attraction, 191–192
- Double-layer interaction, electrostatic force, 6–7
- Double-layer problem, Gouy–Chapman theory of the interface,
- Double minimum potential well, enhancement of proton activity indication, 32–33
- Drift current, charged molecule, 461
- Drift flux, calculation, 461
- Dye
3,3'-diethylthiodicarbocyanine (DisC₂), 112
diffusion in thin water layers, 28
fluorescence of carbocyanine as potential-sensitive probes, 59–60
need for supporting electrolytes, 66
nonaqueous phase on reference interface, 63
optimal for particular purpose, 170
potentials of transfer, 66
- Dye binding to the membrane, kinetics, 164–165
- Dye characterization, potentiometric probe in biological applications, 163–170
- Dye concentration, membrane-bound vs. free aqueous forms, 164
- Dye coupling
compartmentalization of tissue, 238
experimental results, 237–238
photoreceptors, 235–238
- Dye design
fast dyes, 152–157
slow dyes, 157–163

Dye indicators, membrane potential, 151–173
 Dye partitioning, interfacial potential, 59–60
 Dye-potential studies, limits on linear range, 72

E

- Early receptor potential (ERP)
 definition, 533
 inconsistencies and paradoxes, 533
 lack of pH sensitivity, 540
 paradoxical behavior, 537
- Effective kinetic rate constant
 definition, 363
 potassium channel in corneal endothelium, 364*f*
- Egg phosphatidylcholine, model for membrane-bound dyes, 163–164
- Elastic curvature stress, lamellar–nonlamellar phase boundaries, 129–148
- Elastic properties, liquid crystalline bilayer, 130
- Elastic stress field, interaction with membrane proteins, 143
- Electric field effect
 CD spectra of alamethicin added to PC vesicles, 118–120
 CD spectra of bacteriorhodopsin, 114–117
 membrane proteins, 124
 proteins and channel forming polypeptides in the membrane, 107–128
- Electric-field-stimulated ATP hydrolysis, frequency dependence, 567*f*
- Electric-field-stimulated Na⁺ and Rb⁺ pumping amplitude dependence, 566*f*
 frequency dependence, 567*f*
- Electric mobility, apparent, 107
- Electric parameters, cell membranes, 571
- Electric potential gradient, effect on membrane protein, 108
- Electrical behavior, simulation, 462
- Electrical conductance, conventional BLM system, 514
- Electrical coupling
 compartmentalization of tissue, 238
 gap junctions, 234
 quantification, 241
 six terminals in a neuroomatidium, 234
- Electrical drift, molecular transport across planar membrane, 461
- Electrical fields
 behavior due to electroporation, 449–460
 BLM property modification, 518
 estimates of thresholds, 466
 molecular transport due to electroporation, 460–465
 net transport of ions, 518
- Electrical noise
 equilibrium conditions, 377
 sources, biological membranes and relevant ionic systems, 375–399
- Electrical potential, effect on CD intensity of bacteriorhodopsin reconstituted vesicles, 115
- Electroactive impurity, influence on interfacial potential–dye concentration relationship, 71*f*
- Electroactive species, mode of mass transport, 516
- Electrochemical analysis
 generality, 551–554
 PtO–OTS electrodes, 495–498
- Electrochemical impedance spectroscopy, evaluation of surface-bound membranes, 491–510
- Electrochemical model, voltage-gated channels, 429–446
- Electrochemical processes, bacteriorhodopsin membranes, 531–560
- Electrochemical proton gradients, proton pumps, 47
- Electrochemical reversibility, cytochrome *c*₃, 480
- Electrochemical stability, PtO–OTS in aqueous saline solution, 498
- Electrochemistry
 biological functions, 555
 liquid–liquid interfaces, 55–56
- Electrochromic dye, internal charge migration, 156*f*
- Electrochromism, fast dyes, 153
- Electroconformational changes, membranes, 447–449
- Electroconformational coupling
 developmental bibliography, 574–577
 electric activation of membrane enzymes, 563
 energy transduction, 561–578
 force acting on a cell, 572–573
 model, analysis of data, 571
 theory, 566–571
- Electrode
 adsorption of cytochrome *c*₃, 480–481
 surface roughness, 497
- Electrogenic proton transport
 genetic probing, 317–318
 membrane-embedded helices, 325–326
 yeast H⁺-ATPase, genetic approaches, 315–328
- Electrogenicity, H⁺-ATPase, 320
- Electrolyte(s), 1/*f* noise, 389
- Electrolyte compositions, separation of components, 549
- Electrolyte solutions, conductance fluctuations, 384–386

- Electron conduction, across BLM in the dark, 517–518
- Electron density profiles, gramicidin–DLPC bilayers, 100, 102*f*, 103*f*
- Electron transfer
effect of electrode surface, 481
heterogeneous, 480–482
homogeneous, 484–486
intermolecular, 480
reorganization energy, 481
- Electroneutrality
apparent, 322
mutant H⁺-ATPase, 320–323
- Electronic charges, transport across interface, 518
- Electronic inhibition, lateral current through gap junctions, 239–241
- Electronic processes, bilayer lipid membranes, 513–529
- Electrophoretic mobility
quantitative interpretation, 122–124
steady state conditions, 107–108
- Electrophoretic propagation of PSI particles, 114*f*–115*f*
- Electrophotoluminescence (EPL)
back diffusion, 113–114
measurement procedure, 113–114
relative change, 120
- Electroporation
behavior of strong electrical fields, 449–460
cubic cell model, 465–466
general model, 451*t*
hypothetical structures of membrane conformations, 457*f*
membrane electroconformational changes, 468
molecular transport, 460–465
myeloma cells, functions of ac frequency, 574*f*
physical ingredients of the theory, 451*t*
simulation parameters and values, 456*t*
theory, 447–470
time scales, 450*t*
- Electroretinogram, electrode position in the eye, 235–236
- Electrostatic concepts, interaction forces between membrane surfaces, 3–25
- Electrostatic force
description, 3
double-layer interaction, 6–7
effect on geminate recombination, 38*f*
Gouy–Chapman theory, 4–6
intermembranal water phase, 37
- Electrostatic model
analysis, 9
hydration forces, 8–10
- Electrostatic repulsion, interplay of forces, 188
- Electrostenolysis, definition, 515
- Ellipticity
alamethicin, 118–120
bacteriorhodopsin reconstituted in vesicles, 117*f*
function of calculated transmembrane potential, 119
- End-on interactions, peptide ion channels, 296
- Endocytosis, molecular transport mechanism, 461
- Energy barrier, local velocity of ion permeation, 402
- Energy transduction
efficiency, 571
enforced conformational oscillations of a membrane enzyme, 561–578
- Entropic forces, molecular assembly, 192
- Entropy
 L_s – H_n transitions, 135
protein aggregation, 430
- Enzyme
catalytic wheel, 561
time dependence of energy structure, 370
transient aqueous pores, 466–468
- Enzyme function, perturbation, 326
- Enzyme inhibitors, effects on ac-stimulated activity, 565
- Enzyme oscillation
ac-induced, 569*f*
enforced by ac field, 568
- Equilibrium electrical noise, Johnson noise, 376–378
- Equilibrium separations in excess water, degree of swelling, 187
- Equivalent circuit
capacitance and conductance data of lipid bilayers, 501–502
change of photosignal time course, 542
decomposition of photosignal, 540
reconstituted halorhodopsin membrane, 552
surface-bound membrane electrode interface, 502*f*
theoretical simulation of impedance spectra, 503*f*
- Excess noise, measurable, 377
- Excitable cell preparations, dye characterization, 168–170
- Expression system, mutant bacteriorhodopsin, 556
- Extracellular voltage, high impedance, 241

F

- 1/*f* noise
diffusion theories, 392

1/f noise—*Continued*

- open channel and multichannel membrane, 390
- spectral density inversely proportional to frequency, 387–396
- upper limit in ionic conductors, 391
- Facet lenses, illumination, 239
- Facilitated electron transfer, cytochrome c_3 , 482
- Fast dyes
 - differences in membrane potential of a single cell, 170
 - electrochromic mechanism, 153
 - fluorescence response, 153
 - individual electrical events, 151
 - merocyanine chromophore, 153–156
 - oxonol chromophore, 153
 - potential-dependent intramolecular rearrangements, 152–153
 - representative sampling, 154f–155f
 - styryls, 156–157
- Fast photoelectric effect
 - electrochemical basis, 533–540
 - light-induced displacement currents, 532
 - light-induced rapid charge separation, 533
- Fast photoelectric signal, point mutation, 556
- Ferredoxin, reactions, 472
- Ferredoxin–cytochrome c_3 complex, electron transfer, 486
- Ferric ion, electronic conductivity across BLMs, 517
- Field amplification, cell membrane, 561
- Field direction, reversal, 111–112
- Field effect transistors, device characteristics, 506
- Field strength, experiment design, 563–564
- Flip-flop gating mechanism
 - helix rods, 273
 - schematic diagram, 274f
- Fluctuation phenomena, ionic solutions, 382
- Fluorescence
 - carbocyanine dyes, 59–60
 - function of lipid concentration, 164
- Fluorescence dynamics
 - function of excitation wavelength, 169f
 - pyranine trapped in aqueous layers, 34–37
- Fluorescence intensity, magnitude of
 - mitochondrial membrane potential, 163
- Fluorescence quenching, time dependence, 113f
- Fluorescence response, fast dyes, 153
- Flux
 - ion flow through membranes or channels, 402
 - ions across a liposome membrane, 42
 - mechanism for permeation of protons and other cations, 42–43
- Fly, photoreceptor axon terminals, 225–243
- Force measurements, swelling pressures and free energies, 181–182
- Foreign-phase dispersions, effect on excess noise in electrolytes, 389
- Formation of surface-bound lipid membranes, detergent dialysis technique, 492–495
- Four-helix bundles
 - pore structure of channel proteins, 334–337
 - synthesis and purification, 337–343
- Fractal(s)
 - mathematical properties, 359–360
 - self-similarity, 359–360
 - Sierpinski triangle, 360f
- Fractal analysis
 - channel mechanisms, 357–374
 - controversy over physical properties of ion channel protein, 370–371
 - properties of globular proteins, 369–370
 - rough electrode surface, 497
- Fractal kinetics
 - large ranges of time scales, 367
 - logarithmic relationship, 363
- Fractal properties, single-channel data, 372
- Fractal scaling
 - continuous distribution of activation energy barriers, 367
 - relationship between kinetic rate constants, 365–366
- Fragments, proteins that interact with membranes, 290–293
- Free energy approach, hydration forces, 10–14, 179–181
- Free energy of activation, simulation, 268–270
- Free energy of interaction, entropic and enthalpic parts, 192
- Free one-dimensional diffusion,
 - fluctuations, 394f–395f
- Frequency shift, light from moving particle, 405
- Frustrated energy, quantitative value, 143
- Functional control, water at the
 - macromolecular surface, 177–196
- Fungal antibiotics, peptaibols, 264

G

- Cap junction(s)
 - electrical coupling, 234
 - gating mechanism, 235
 - in axon terminals, voltage coupling, 238–242
 - light adaptation, 241
 - photoreceptor axon terminals of the fly, 225–243
- Cap junction channels
 - connexin protein, 197
 - function, 198
 - importance for electrochemical studies, 198–203
 - permeability, 200

- Gap junction channels—*Continued*
 prospects for biophysical study, 203–205
 reconstitution into liposomes and planar phospholipid bilayers, 204
 structure, 198
 transjunctional voltage sensitivity, 200–201
- Gated channels, connexin protein, 197
- Gating, changes in channel structure, 184
- Gating current
 ion pumping, 445
 sodium and potassium channels, 441
- Gating potential, orientation of helices, 303–304
- Gating processes, VDAC protein, 250–253
- Gaussian bands, helices parallel and perpendicular to the light, 90–92
- Gel-solidified probes, ease of handling, 79
- Genetic mapping
 hygromycin B resistance, 325
 mutations, 323–325
- Genetic probing, electrogenic proton transport, 317–318
- Geometric constraints, proton binding dynamics, 33–38*f*
- Globular proteins
 fractal interpretations consistent with known properties, 369–370
 shallow local energy minima, 369
 time dependence of energy structure, 370
- Gouy–Chapman theory
 electrostatic force, 4–6
 linkage between macroscopic and microscopic electrical parameters, 535
 phase boundary, 4
 rapid charge separation and recombination, 531
- Gramicidin
 membrane thickness buffer, 104
 proton-conducting channel, 49–52
- Gramicidin A
1/f spectra, 389
 crystallized from ethanol, 265*f*
 noise of an open channel, 390*f*
 schematic models, 264*f*
 structure and function, 260–261
- Gramicidin channel
 description, 97
 energy requirements for ion diffusion, 45
 ion binding site, 103–104
 ion permeation, 404
 location of ion binding sites, 83–106
 mechanism and conductance, 49–52
 proton conductance, 41, 52
 proton currents in HCl solutions, 50
 shot noise, 380
 velocity distribution for cations, 404–406
 waterlike environment, 410
- Gramicidin–DLPC multilayers, X-ray diffraction patterns, 99*f*
- Graphite electrode, protein redox potentials, 482
- Guillotine, formation of supported BLM, 516*f*

H

- H⁺-ATPase
 electrogenicity, 320
 membrane topography, 324*f*
 model system, 316–317
 mutations, 327
- Halobacterium halobium*, bacteriorhodopsin as reaction center, 532
- Halorhodopsin membrane
 interfacial chloride ion transfer, 552
 photoelectric signals, 552*f*
- Halosilanes, order of reactivity with silica, 495
- Head-group atoms
 phospholipid molecules, 16–18
 properties of water molecules, 18
- Heat flow, channel opening and closing, 442–444
- Helical conformation, crystal structures, 268
- Helical hinge region, translocation of a mitochondrial signal peptide, 298
- Helical rod, models, 273
- Helix
 inserted and surface state, 94
 orientation, 88–93, 303–304
 properties, 269*t*
 realignment mechanism for gating, 304*f*
 reorientation, 273
 rigid reorientation in response to electrical potential forms, 273
 structures, 269*f*
- Helix–hairpin mechanism, schematic diagram, 299*f*
- Helix–hairpin model, membrane protein insertion, 298
- Heme
 oxidation–reduction potential, 477–478
 solvent exposure, 475, 486
- Heme attachment, cytochrome *c*₃, 473–474*f*
- Heme groups, cytochrome *c*₃, 472
- Hemichannels
 composition, 202
 formation of junctional channels, 202–203
 function in cells, 200
 interactions, 218
 lateral interactions, 202
 reconstituted connexin-32, 215
 structure, 198

- Hemoglobin
colloid osmotic pressure vs. charges per molecule, 432*f*
conductivity, 483
conformational changes, 434–437
disaggregation, 432–434
model for calculating energetics of conformational change, 435*f*
molecular osmometer, 185
osmotic stress associated with oxygen binding, 186*f*
- Heterogeneous rate constant, upper limit, 481
- Hexagonal lattice, basis length vs. temperature, 136
- Hexagonal phase, structural dimensions and stress, 189*f*
- High-affinity site, homologous regions from subunits, 332
- High-pass filter effect, photocurrent magnitude, 535–536
- High-resolution lamellar diffraction, ion binding sites in gramicidin channel, 97–104
- H_{II} phase
cross section, 141*f*
osmotically dehydrated, 139*f*
- Hildenborough gene, cytochrome c_3 , 487
- Hindered motion, ions within small pores, 458
- Hodgkin–Huxley model, currents measured across cell membranes, 358–359
- Holographic medium, mutant bacteriorhodopsin, 556
- Homology, amino acid sequence, 472–473
- Hooge formula, 1*f* noise, 388–389
- Human erythrocytes
applied field strength, 564
Na, K-ATPase, 564–565
- Hydrated surface, etching, 508
- Hydration
DNA attractive force, 192
importance in biological processes, 192–193
stress on solvent-exposed surfaces, 194
- Hydration energies, DNA, 193–194
- Hydration force
chemical free energies, 179–181
description, 3
electrostatic models, 8–10
experimental results, 7–8
free energy approach, 10–14
mathematical forms and language, 178–179
phospholipid molecules, first computer simulations, 14–15
protrusion model, 14
- Hydration layer, curve calculated for actual width, 37
- Hydration repulsion
bilayer interactions, 187
equilibrium swelling of bilayers, 187–188
- Hydrocarbon chains
biomembrane lipids, 131–132
initiation sites for a lipid bilayer membrane, 493
lipid hydrocarbon, 140
- Hydrocarbon packing energy, removal, 140
- Hydrocarbon thickness, changes in lattice dimension, 136–138
- Hydrogen-bonded water molecules
adequate proton supply, 50–51
potential proton translocators, 48–52
proton selectivity, 51
proton translocation, 41
rate of proton transport, 50
- Hydrogen ion, pH gradients, 42
- Hydrophilic pores, source, 450
- Hydroxide ion, membrane translocation, 42
- Hygromycin B resistant mutants, within the bilayer, 325*t*
- Hyperacuity
anatomical substrate, 231–234
definition, 228
mechanism, 228–229
- I
- Ideal gas behavior, conductance fluctuations, 383
- Ideal linear potentiometric response, theoretical slope, 68–69
- Ideally polarizable interface, supporting electrolyte, 64–65
- Image potential, gramicidin channel, 104
- Image repulsion, static van der Waals interaction, 9
- Image storage devices, bacteriorhodopsin with modified chromophore, 556
- Immiscible electrolyte solutions, apparatus used for potentiometric and voltammetric studies on the interface, 58*f*
- Immiscible liquids, interfacial ion transport, 55–81
- Immiscible solutions, microinterface, 78–79
- Immune peptides, death of the invading organism, 279–285
- Immunoaffinity purification, connexin, 205
- Impedance
function of concentration of BSA, 76*f*
membrane electrode, 504–506
- Impedance data, best fits with the admittance model, 424–425
- Impedance frequencies, surface-bound membrane, 504–505

- Impedance measurement
 dependence on applied interfacial potential, 73–74
 function of BSA concentration, 74
 indication of adsorption, 72
- Impurity, interfacial potential, 70–71
- Inactivation, ion permeability, 441
- Independent axes, substrate for hyperacuity, 231
- Information processing, retina, 226–231
- Inhomogeneous boundaries, correlation function, 11–12
- Input impedance, short-circuit condition, 537
- Insect defensins, effective against Gram-positive bacteria, 281
- Instrumentation, laser Doppler scattering, 407–412
- Integral membrane proteins, fragments, 290–293
- Intelligent materials
 concept, 550–551
 definition, 550
 modular design of molecular functions, 557
 purposeful effects, 557
- Interaction forces, between membrane surfaces, 3–25
- Interaction potential
 definition, 478
 microscopic redox potentials, 479*t*
- Interface between two immiscible electrolyte solutions (ITIES), similarity to conventional electrode electrochemistry, 56
- Interfacial capacitance
 3-D surface plot, 77*f*
 calculation, 74–77
- Interfacial curvature, lamellar–nonlamellar phase transition, 134
- Interfacial ion transport
 evidence, 57–59
 immiscible liquids, 55–81
 liquid–liquid interfaces, 56–59
- Interfacial polarization, transmembrane field, 448
- Interfacial potential
 dye partitioning, 59–60
 function of dye concentration, 67*f*
 logarithm of initial dye concentration, 70*f*
 reference interface, 62–63
 relative concentration, 67
- Interfacial proton transfer
 mechanism, 535
 photosynthetic and visual membranes, 553
- Interfacial reactance, calculation, 76
- Interfering ions, potentiometry, 69–71
- Interior positive membrane potentials, systems used to generate and measure, 321*f*
- Internal kinetic parameters, deduced from experimental data, 404
- Interstitial chain density, transition temperature, 142
- Intrachannel ion-binding models, rate constants for individual transitions, 402
- Intrachannel velocities, ion mobility, 411–412
- Intramolecular bridging polar groups, energies, 186–187
- Intramolecular electron transfer, cytochrome *c*₃, 485
- Iodine, electrical resistivity of BLM, 517
- Ion(s), passage through pores, 458
- Ion binding sites, location in gramicidin channel, 97–104
- Ion channel(s)
 biophysical properties, 369
 definition, 357
 ion distribution determination, 84
 measurement of current, 358
 osmotic stress from excluded species, 184
 permeability, 200
 reconstitution into liposomes and planar phospholipid bilayers, 204
 structure fluctuations in coherent patterns of motion, 357
- Ion channel conformational states
 chaos, 371–372
 deterministic process, 372
- Ion channel gating, calcium-sensitive mechanisms, 330
- Ion channel protein
 controversy over physical properties, 370–371
 physical properties, 365–369, 372
- Ion channel states, broad continuum, 365
- Ion-conducting channels, planar lipid membranes, 48–49
- Ion-conducting systems, potassium and sodium, 415–416
- Ion counterflow, mutant H⁺-ATPase, 320–323
- Ion flux
 electrodiffusion equations, 440
 energy requirement, 44–45
- Ion permeation
 binding-site mechanism, 403
 binding sites, 401
 fluid lipid bilayer, 41–42
- Ion pumping
 field strength and frequency of applied ac field, 566
 possible mechanisms, 444–445
 thermodynamics in an oscillating electric field, 568
- Ion selectivity, gating current, 441
- Ion specificity, specific electrodes, 524

Ion transit frequency, gramicidin channel, 411–412
 Ion transport across membranes, assumptions, 293
 Ion transport through open channel, source of $1/f$ noise, 390
 Ionic channel across a low dielectric lipid bilayer, osmotic stress measurements, 182–184
 Ionic conduction, muscle neuronal AChR and synthetic protein, 347*t*
 Ionic current, voltage-gated channel, 441*f*
 Ionic strength, effect on redox potential, 485
 Ionic systems, electronic noise sources, 375–399
 Ionic velocity distributions in channels and membranes, laser Doppler scattering, 401–413
 Irreversible ion transport, immiscible electrolyte solutions, 58
 ITIES theory, applications, 79
 ITO electrodes, device characteristics, 506

J

Johnson noise, thermal motion of charged particles in conductors, 376–378
 Junctional channel formation, 202–203
 identification, 204–205
 prospects for biophysical study, 203–205
 structure, 199–200
 junctional membranes, splitting, 218
 Junctional pore, permeability, 200

K

K^+ conductance, ATPase-mediated, 323*f*
 Kornyshev–Leikin theory, decay length, dependence on interface, 19

L

L_a-H_{II} transition curvature, 143
 entropy, 135
 geometrically frustrated free energies, 140
 lattice dimensions, 135
 mean interfacial molecular area, 135
 L_a-H_{II} transition temperature, hydrophobic chains, 141

Lag period, before back diffusion, 124
 Lamellar–nonlamellar phase boundaries, elastic curvature stress, 129–148
 Lamina cartridges, neural circuitry, 234
 Landau-type expansion, justification on molecular grounds, 13
 Lantibiotics class of antibiotics, 279
 structure, 278
 Laser beam, experimental configuration, 405–406
 Laser Doppler gramicidin channel system, block diagram, 407*f*
 Laser Doppler scattering determination of ionic velocity distributions in channels and membranes, 401–413
 instrumentation, 407–412
 Laser Doppler velocimetry, 404–406
 Laser-induced proton pulse, knowledge of proton diffusion, 28
 Lateral tension profile, protein conformations, 142
 Lattice size, water core radius plus a constant, 141
 Ligand sensitivity, junctional channels, 201
 Ligands, transition-effecting action, 185
 Light, scattering frequency, 405–406
 Light adaptation, gating mechanism, 235
 Light-driven proton pump requirements, 548
 reverse engineering of photobiological membranes, 556
 Light-induced current response, reconstituted thin film, 551*f*
 Light-induced electron transfer, redox reactions in and across the thylakoid membrane, 520
 Light-induced rapid charge separation, photoelectric signal, 531
 Light-induced redox reactions, BLM, 526
 Line tensions, exchange of free energy with the bilayer matrix, 131
 Lipid(s) effect on alamethicin phase transition, 96–97
 force measurement, 187–192
 impact of environment on structure, 295
 lateral mobility, 109
 smectic defects, 85
 Lipid assemblies, phase transitions, 190
 Lipid bilayer(s) anisotropy in the protein environment, 131
 conductance states, 264
 correspondence between noise and impedance, 377
 fluctuations of current, 391
 interactions with membrane proteins, 143
 proton permeability, 44–47

- Lipid bilayer(s)—*Continued*
 repulsive forces, 7–8
 transient hydrated defects with
 selectivity for protons, 43
 Lipid bilayer matrix, structure and
 physical properties, 130
 Lipid bilayer membrane, ion-conducting
 channels, 48–49
 Lipid compositions, biomembranes, 132
 Lipid curvature elasticity, 133–143
 Lipid effects, chemically specific, 131
 Lipid hydrocarbon chain layer, thermal
 energy, 135
 Lipid mesomorphic tendencies, cell
 membrane function, 146
 Lipid monolayers
 curvature, effect on membrane proteins,
 144–145
 cylindrical geometry of the HII phase as
 a geometric amplifier, 137*f*
 Lipid phase, water concentration change,
 135–136
 Lipid–protein bilayer membranes linked to
 surfaces, biosensor requirements, 491–492
 Lipid systematics, mesomorphic behavior, 145
 Lipid vesicles, dye characterization, 163–165
 Lipid–water phases, cross section, 134*f*
 Liposome(s)
 connexin-32, 197, 210–215
 detergent-induced conductances, 215
 sucrose-permeable, 206
 Liposome membranes, potassium ion flux, 42
 Liquid–liquid interfaces
 electrochemistry, 55–56
 interfacial ion transport, 56–59
 Liquid crystalline lipid mesomorphs,
 fundamental construction units, 134
 Local reaction conditions, concept, 546–549
 Local velocities, ion within a channel, 402
 Localized electroconformational changes,
 hydrophilic pores, 449
 Lumen of the pore, polar-neutral residues, 337
 Luminescence, measurement, 113–114
- M**
- MA- β peptide, synthetic, 349–350
 Macromolecular energies, surface energies, 186
 Macromolecular surface, water, 177–196
 Macromolecules, interactions, 190–192
 Macroscopic redox potential
 cytochrome c_3 , 479
 hemes, 478
- Magainin
 analogs, 278
 structure, 276
 voltage-dependent channels in lipid bilayers, 276
 Magnesium etiochlorin, electronic
 conductivity across BLMs, 517–518
 Mammalian defensins, bactericidal activity, 281
 Marcelja–Radic theory
 nature of hydration force, 10–11
 pictorial representation, 11*f*
 Markov model
 constant probability per second of
 switching states, 359
 physical properties of ion channel
 protein, 365–371
 properties of channel protein, 365
 sharply defined time scales, 367
 Mast cell degranulating (MCD) peptide,
 structure and activity, 288–289
 Mastoparan, structure and activity, 287–288
 Mechanistic approach, explanations for
 complex biological phenomena, 557
 Mechanistic themes, membrane proteins, 130
 Melittin
 structure and activity, 285–287
 tetramer crystal structure, 286*f*
 Membrane(s)
 1*f* noise, 387–392
 channel-forming peptides in uniformly
 aligned multilayers, 83–106
 channel-gating processes, 437–439
 containing bacteriorhodopsin,
 electrochemical processes, 531–560
 determination of ionic velocity, 401–413
 electroconformational changes, 447–449
 on PtO electrodes, stability, 506
 one-dimensional structure, 84–85
 role of water in proton conductance, 41–54
 uniformly aligned multilayer samples, 85–86
 Membrane-active proteins, fragments, 290–293
 Membrane admittance
 determination of K- and Na-channel
 relaxation times, 415–428
 general expression, 416
 Membrane-bound dye, response to directly
 applied voltage, 165, 168*f*
 Membrane conductance, single-channel
 current records, 348
 Membrane dielectric, two circuits in
 parallel, 537
 Membrane electric parameters,
 measurements, 571–574
 Membrane electrodes
 capacitances, 505*t*
 impedance, 504–506

- Membrane fusion, nonlamellar phases, 133
- Membrane ion channels, protein function and dynamics, 197–223
- Membrane photochemistry, 520–524
- Membrane potential
determination by potential-sensitive fluorescent dye, 112
differences between mutant and wild-type cells, 318–320
dye indicators, 151–173
effect on biological activity, 108
relationship to ATP hydrolysis, 322*f*
secondary structure of membrane proteins, 125
- Membrane potential maps, types, 170
- Membrane protein(s)
curvature stress modulation, 147
in electric fields, conformation and mobility, 107–128
interaction with an electric field, 563–564
mechanistic themes, 130
modes of interaction with the embedding lipid bilayer, 131
nonlamellar-prone lipids, 133
structure, function, and location, 369
- Membrane protein activity, bilayer curvature elasticity, 129–148
- Membrane protein reconstitution, accuracy, 145–146
- Membrane protein structures, uncertainty, 129–130
- Membrane RC relaxation, long relaxation time constant, 538–540
- Membrane receptors, specific recognition functions, 491
- Membrane surface, interaction forces, 3–25
- Membrane surface waves, Doppler shift, 409
- Membrane thickness, effect of transmembrane potential, 296
- Membrane transport system
categories, 570–571
mechanosensitive, 571
- Mercury electrode, adsorption of cytochrome c_3 , 480–481
- Merocyanine dyes
fast potential-dependent absorbance changes, 153
mechanisms, 156
- Mesomorphic phase transitions, theory, 133–143
- Metarhodopsin
binding of transducin, 554
visual transduction, 553
- Metastable pores, uptake, 463–465
- Methylation of the surface, magnitude of hydration repulsion, 187
- Micellar colloids, conductance fluctuations, 385–386
- Michaelis–Menten enzyme, free energy transducer, 568
- Microelectronic revolution, physical limit of miniaturization, 555
- Microinterface
immiscible solutions, 78–79
study applications, 79
voltammetric determination of lauryl sulfate, 79*f*
- Microscopic equivalent circuits, space charge distribution profile, 536*f*
- Microscopic redox potentials, interaction potentials, 479–480
- Mitochondria
ATP synthesis, 51
binding agents and channel behavior, 255
structure and function, 245–246
- Mitochondrial ATP synthetase transmembrane fragment, structure and activity, 293
- Mitochondrial membranes, proton conductance, 46
- Mitochondrial outer membrane vesicle, freeze-fracture electron micrograph, 256*f*
- Mitochondrial porin, osmotic stress, 183–184
- Mitochondrial voltage-dependent anion-selective channel, 245–258
- Models
alamethicin pore, 270
computer simulation technique, 14–23
currents across cell membranes, Hodgkin–Huxley, 358–359
fractals, Markov, 359–371
gramicidin channel, 261
helical rod, 273
synthetic pore proteins, 334–337
- Molecular assembly, entropic forces, 192
- Molecular dynamics simulations, oscillatory force, 15–20
- Molecular dynamics unit cell, DLPE molecules in gel phase, 15*f*
- Molecular electronics
lack of electronic properties, 525
nanobiology, 555
- Molecular osmometer, hemoglobin, 185
- Molecular transport
electrical drift contribution, 465*f*
electroporation, 460–465
estimates based on electrical drift, 462
- Molecules in solution, shape and volume changes, 184
- Monolayer bending energy, water removal, 138
- Monolayer curvature stress, ultimate source, 144
- Monopolar dendrite, encoding, 239

Multilayer sample, X-ray diffraction study, 85
 Multilayered bacteriorhodopsin film, prolonged drying to eliminate pH sensitivity, 545
 Multilayered film, photoelectric signals, 545f
 Multilayers
 membranes, structural order, 84
 uniformly aligned, 83–106
Musca domestica, gap junctions in
 photoreceptor axon terminals, 225–243
 Mutagenesis
 site-directed, 486–487
 site-directed and random, 317
 Mutant(s), properties of cytochrome *c*₃, 487
 Mutant enzymes
 electroneutral H⁺ transport, 327
 isolation, 317
 membrane potential depolarization, 318–320
 uptake of [¹⁴C]TPP, 318f
 Mutant H⁺-ATPase, ion counterflow, 320–323
 Mutant strain, bacteriorhodopsin, 546
 Mutation(s)
 genetic mapping, 323–325
 hygromycin B resistance, 325
 Mutational analysis,
 transmembrane-spanning domain, 296
 Mycoplasma, lipid adjustments, 146–147
 Myeloma cell membrane, critical breakdown potential, 573f
 Myoglobin, time course of the binding of CO, 369–370

N

Na, K-ATPase
 electric activation, 564–566
 human erythrocytes, inhibition, 564
 Nanobiology, molecular electronics, 555
 Negative hole, proton binding site, 548
 Neovitalistic approach, explanations for complex biological phenomena, 557
 Nerstian indicators, environmental insensitivity, 162–163
 Nerve fibers
 determination of K- and Na-channel relaxation times, 415–428
 measured heat, 443
 Net drift, superimposed on random walk, 518
 Net proton flux, uncertainty about protons or hydroxide ions, 43–44
 Neural circuitry, lamina cartridges, 234
 Neural elements, coupling, 229
 Neuronal AChRs, classes of subunits, 348
 Neuronal signaling, synaptic junctions, 330

Neuroommatidium
 divergence of optical axes, 231
 electrical coupling of axon terminals, 234–235
 fluorescent dye, 231–233
 Neurosuperposition
 photoreceptors, 231
 staining pattern of photoreceptor terminals, 233f
 Nicotinic AChR channel, proteins that mimic, 333
 Nitrobenzene, relative permittivity, 59
 Nitrobenzene–water interface
 ion transport, 57–59
 potentiometry in the presence of oxacyanine dyes, 59–72
 Noise
 biological membranes and relevant ionic systems, 375–399
 one-dimensional diffusion, computer simulation, 392–396
 protonation, function of pH, 388f
 source classification, 376
 Nonequilibrium noise, carrier-mediated ion transport, 381
 Nonexcitable cells, quantitative microscopy, 170
 Nonhelical molecules, orientational circular dichroism (OCD), 87–88
 Nonlamellar-prone lipids, biomembranes, 133
 Nonpolarizable interface, salt concentration, 63–64

O

Octadecyltrichlorosilane (OTS)
 porous structure, 496
 protein molecules with bound lipid, 500–501
 supporting reconstituted membrane structure, 495
 unstable in basic solutions, 498
 Oligomer size, determinant of single-channel conductance, 348–349
 Oligomeric channel, fraction open as function of surface charge density, 438f
 Oligomeric channel proteins, design principles and chemical synthesis, 329–354
 Open channel, single membranes, 217
 Open-channel noise levels
 addition of water-soluble polymers to electrolyte solutions, 386
 shot noise, 380–381
 Optical random access memory,
 bacteriorhodopsin, 556
 Order near the interface, water molecules, 10–11

Order parameter, orientational polarization of water, 11

Organic dyes, changes in membrane potential, 151

Organosilanes, surface modification, 495

Orientational polarization
DLPE molecules, 18
monotonic behavior of water, 22
origin of the hydration force, 11
water between DLPE bilayers, 19f
water between DPPC bilayers, 21f

Oriented circular dichroism (OCD)
helices, 88–93
nonhelical molecules, 87–88
orientation of α -helices, 84
theory and applications, 86–93

Oriented dipole mechanism, definition, 534

Oscillating electric field
enzyme, 568
ion accumulation processes, 442

Oscillating polarization profiles, short runs, 15

Osmotic pressures
hemoglobin and BSA, 432
water removal, 139

Osmotic stress
application to a functioning protein, 185
energetics of a molecular array, 182f
energetics of nonbilayer assemblies of phospholipids, 189–190
intermacromolecular force vs. molecular distance, 191f
loading oxygen onto hemoglobin, 185, 186f
measurement of energies in molecular assemblies, 177
molecular dimensions and intermolecular spacings, 182
motion of interacting molecules, 181
net repulsive pressure between membranes, 188f
structural dimensions of hexagonal phase, 189f
voltage dependent anion channel, 183–184
water associated with opening and closing of a membrane channel, 183f

Out-of-plane ligation, cytochrome *c*₃, 472

Oxocyanine dyes
potential sensors, 71
potentiometry on the water–nitrobenzene interface, 59–72

Oxidation–reduction potentials, cytochromes *c*₃, 477–480

Oxonol dyes
binding promoted by depolarization, 162
fast potential-dependent absorbance changes, 153

Oxygen binding, hemoglobin, calculations, 435–437

Oxygen binding affinity, delocalized energy, 186

Oxygenation, conformational changes in the hemoglobin molecule, 434

Oxygenation energy, protein–protein interaction, 186

P

Packing energy, chains of lipid hydrocarbon, 140

Patch clamp technique
protein conformational states, 372
sequence of open and closed states of an individual ion channel, 358

Peptaibols
amino acid sequences, 266t
charge movement across membranes, 271–273
voltage-dependent conductance, 264

Peptide(s)
 α -helix conformation, 86–87
channel-forming, 83–106
impact of environment on structure, 295
sequences that represent functional segments, 332
transition to transmembrane component, 294–295

Peptide aggregate, molten globule, 303

Peptide antibiotics
gramicidin A, 260–261
immune peptides
cecropins, 283–284
defensins, 280–283
tachyplesin, 284–285
lantibiotics, 278–279
magainins, 276–278
peptaibols, 264–276

Peptide blocks, assembly, 342–343

Peptide fragments, chemical modification and studies, 290

Peptide ion channels
amphipathicity, 300
beta-sheet as a structural motif, 300
conditions for characterization, 293–294
end-on interactions, 296
structural basis of formation, 259–314
structure and mechanism, 293–304
width of the bilayer, 295–296

Peptide residues, interaction with negatively charged lipids, 350

Peptide spectra, π - π^* and n - π^* transitions, 86–87

Permeability
excitable membranes, 441
potassium ion and protons, 44

- Permeability—*Continued*
 protons and other ions in model and biological membranes, comparison, 46*t*
- Permeation mechanism
 fluid lipid bilayer, 41–42
 through the channel, 403
- pH, effect on adsorbed BSA, 77–78
- pH gradients, liposome membranes, 42
- pH sensitive components, aqueous phases, 549*f*
- Phage lytic factors, protein interaction with the membrane, 290
- Phase change reversibility, alamethicin samples, 94
- Phase transition
 alamethicin in a membrane, 95–97
 L_s-H_{II} , 134
 lipid assemblies, 190
- Phosphatidylcholine (PC)
 bilayers, measurement of forces, 7
 phase behavior, 134–143
- Phosphatidylethanolamine (PE), phase behavior, 134–143
- Phospholipid, enhancement of proton activity indication, 32–33
- Phospholipid bilayer, ion-conducting systems, 416
- Phospholipid head group, effect on protonation dynamics, 32*f*
- Phospholipid membranes, characteristics of thin water layers, 27
- Phospholipid molecules, density and location of atoms, 16–18
- Photochemical conversion, BLM, 526
- Photocurrent
 partition, 537
 short-circuit condition, 538
- Photodynamic damage, usefulness of a dye, 168
- Photoelectric signal, light-induced rapid charge separation, 531
- Photon energy converter, bacteriorhodopsin, 532
- Photopotential
 chlorophyll BLMs, 521
 kinetics, 521
- Photoreceptor(s)
 dye coupling, 235–238
 gating mechanism, 235
 optical disparity, 241
 stimulus intensity and voltage, 239
- Photoreceptor axon terminals
 fly, gap junctions, 225–243
 interference contrast micrograph, 229*f*
 traces of intracellular recordings, 240*f*
- Photoredox process, description, 523–524
- Photosignal
 component analysis, 540–546
 relaxation, 550
- Photosynthesis, redox reactions in and across the thylakoid membrane, 520
- Photosystem I (PSI)
 accumulation and depletion on poles, 121*f*
 accumulation on one pole, 121*f*
 mobility in plane of vesicular thylakoid membrane, 120–122
- Phototransduction, positive surface potential, 554
- Phytochrome, role in plant membranes, 522
- Pigment-containing membranes, electrochemical approach, 551
- Planar bilayer(s), connexin-32, 197
- Planar bilayer membrane
 electroporation, 449–460
 experimental configuration, 460*f*
 longer time scale electrical behavior, 454*f*
 oxidized cholesterol, 450*t*
 transport of propidium iodide, 463*f*
- Planar bilayer scattering experiments
 instrumentation, 408
 results, 409
- Planar lipid bilayer
 reconstitution, 343–345
 single-channel conductance, 345
 single-channel recordings, 346*f*, 347*f*
- Planar lipid membrane, ion-conducting channels, 48–49
- Planar membrane
 circuit differential equations, 459
 topology, 465
- Planar phospholipid membrane, sensitivity, 252
- Poisson's equation, Gouy–Chapman theory, 4–5
- Polar and nonpolar region, curvature stress, 144
- Polarization
 charge transfer within channel proteins, 445
 parallel and antiparallel, 120
 water, DLPE surface, 18*f*
- Polarization profile, water, 21
- Polarization resistance, PtO electrodes, 504
- Polished beryllium plate, high quality diffraction patterns, 98
- Polyanion, influence on gating processes, 253
- Polycrystalline films, sandwiched between metal electrodes, 525
- Polyethylene imide affected alamethicin vesicles, CD spectra, 118*f*
- Polymer-covered surfaces, steric force, 14
- Polymer formation, halosilanes, 495
- Polymer(s) in electrolyte solutions, open-channel noise, 386

- Polymer-induced current noise vs. polymer molecular weight, 387*f*
- Polypeptide, α -helix conformation, 86–87
- Polysaccharides
characteristics and repulsive forces, 190–191
permeability in mitochondria, 245
- Polystyrene latex suspensions, conductance fluctuations, 385–386
- Pore
function as an enzyme, 467
transient hydrophilic, 466–468
- Pore creation and expansion, electrical interactions, 462–463
- Pore flux, calculation, 454
- Pore formation
electroconformational changes, 448
role of lipid composition, 294
- Pore-forming properties, sequence-specific motifs, 350
- Pore-forming proteins, design, 332–334
- Pore free energy, calculation, 451–453
- Pore-lining segments, identification, 331–332
- Pore models, pore-expanding forces parallel to membrane, 449
- Pore population distribution
calculated, 455*f*
computed, 453*f*
range of pore sizes in membrane, 456
- Pore population kinetics, 457–458
- Pore production rate, effect of transmembrane potential, 296
- Pore structure of channel proteins, four helix bundles, 334–337
- Porphyrins, in bilayer lipid membranes, 521
- Potassium channel
current, 358*f*
determination of relaxation times in squid nerve fibers, 415–428
- Potassium conduction, determination of admittance in a steady state, 421–424
- Potassium ions
flux across liposome membranes, 42
pH gradients, 42
- Potential–concentration relationships, water:nitrobenzene volume ratios, 67–68
- Potential-dependent spectral changes, apparatus for measuring, 168*f*
- Potential energy minimum, PE and PC lipid bilayers, 135
- Potential of zero charge (PZC)
calculation, 74
water–nitrobenzene interface, 75*f*
- Potentiometric membrane dyes
characterization, 151–173
relative affinities, 164
- Potentiometry
concluding remarks, 71–72
experimental procedure, 65–66
insensitivity to pH, 72
interfering ions, 69–71
results, 66–72
water–nitrobenzene interface, carbocyanine dyes, 59–72
- Power law, fractal kinetics, 364
- Premeasurement interval, membrane response, 419–420
- Prepolarization, diffusional relaxation, 122*f*
- Prepulse
amplitudes, 113
effect on EPL signal, 113
- Primary pores, elevated transmembrane voltages, 463
- Probability density function, range of pore sizes in membrane, 456
- Proline, role in activity of membrane-active peptides, 297–298
- Protein(s)
designed and synthesized, 329
effect on capacitance, 77
lateral mobility, 109
orientational order, 84
predetermined conformational properties, 332–333
semiconductor nature, 483–484
synthetic, mimic pore-forming structure, 333
VDAC, 246
- Protein activity
mesomorphic tendencies of the lipid, 146
phase tendency of the lipid, 146
- Protein adsorption
impedance measurements, 72–74
water–nitrobenzene interface, 72–78
- Protein aggregation
electrochemical model, 429–446
entropy-driven reactions, 430
surface free energy changes, 431
- Protein assemblies, structural similarities, 430
- Protein attachment, VDAC, 254–255
- Protein conformations
frustrated monolayer elastic curvature, 143–144
stress–depth distribution, 142
- Protein–electric field interaction, concentration of ions near a membrane protein, 563
- Protein films
electrical properties, 483–484
redox state, 482
- Protein loops, VDAC protein, 255
- Protein mechanisms, evaluation and testing of models, 131

- Protein properties, fractal interpretation, 365–369
- Protein–protein interaction, oxygenation energy, 186
- Protein receptors, function, 492
- Protein structure dynamics, proton transport, 316
- Protein surface, solvation–desolvation, 193
- Proton(s)
- interaction with surface groups, 31–33
 - measurement of diffusion, 28
- Proton antenna, enhancement of proton activity indication, 33
- Proton binding
- geometric constraints, 33–38*f*
 - positive surface potential, 554
- Proton conductance
- bilayers, models, 44–47
 - hydrogen-bonded waters, 49–52
 - model and biological membranes, role of water, 41–54
- Proton-conducting channel
- biological membranes, 47–49
 - chain of hydrogen-bonded water molecules across membrane, 43
 - gramicidin, 49–52
- Proton conduction pathway, cryoelectron microscopy, 547*f*
- Proton diffusion at a water–membrane interface, time-resolved dynamics, 27–40
- Proton diffusion coefficient
- buffering moieties on membrane surfaces, 31–32
 - calculation, 29–30
 - near a surface, 31
- Proton flux
- across bilayers, characteristics, 43–44
 - independence of pH values, 44
- Proton permeability, comparison with permeability of other cations in lipid bilayers, 45–47
- Proton permeation of lipid bilayers, conclusions, 47
- Proton pump
- electrochemical proton gradients, 47
 - pH effect on pK_a of surface proton binding sites, 550
 - reverse engineering of photobiological membranes, 556
- Proton release, extracellular side, 546
- Proton selectivity
- amino acid interaction with protons, 52
 - hydrogen-bonded water molecules, 51
 - water chains, 51–52
- Proton transfer, purple membranes, 546–549
- Proton transfer pathway, coupled consecutive, 547*f*–548
- Proton transport
- dilemma, 318–320
 - electrogenic, 315–328
 - mechanism, 315–316
 - mutation in the cytoplasmic ATP hydrolysis domain, 323–325
- Proton wire, amino acid residues of membrane proteins, 48
- Protrusion model, hydration force, 14
- PtO effective area, blocking, 499
- PtO electrodes
- Bode plots, 501*f*
 - capacitance and resistance values, 500*f*, 503–504
 - cyclic voltammetry, 499*f*
 - parameters for best fit to impedance spectra, 504*t*
 - polarization resistance, 504
 - simulation spectra, 503
- PtO–OTS electrodes, electrochemical analysis, 495–498
- PtO–OTS in aqueous saline solution, electrochemical stability, 498
- Pulsed electric field (PEF) method, definition, 562
- Pulsed-light induced photoelectric signal, relaxation time course, 539*f*
- Purple membrane
- computed and measured photosignal, 543*f*
 - fragments as source of
 - bacteriorhodopsin, 109–110
 - proton pump, 550
 - sheets on Teflon film, photosignals, 542
 - working environment, 549
- Pyranine
- fluorescence decay dynamics in bulk water, 34, 35*f*
 - measurement of reprotonation, 29*f*
 - model for water layers in membranes, 28
 - reaction space for proton-excited anion recombination, 34*f*
 - reprotonation rate vs. 2-D concentration, 30*f*

Q

- Quasistatic approximation, electric field and magnetic field, 447
- Quinones, primary electron acceptor, 521

R

- Radius of curvature, lipid monolayers, 189–190
- Randles equivalent circuit, diagram, 75*f*

Random walk, ionic motion, 518
 Reaction space, proton diffusion between membranes, 34
 Receptor protein
 cellular membranes, specific recognition functions, 491
 function, 492
 rotational and translational diffusion, 509
 Reconstituted channels, structural form, 215
 Reconstitution
 material requirements, 205
 system for study of channels formed by connexin-32, 206–215
 Redox potential
 cytochromes c_3 , 479
 effect of ionic strength, 485
 Redox reactions
 bilayer lipid membranes, 513–529
 coupled photosensitized, 522
 light-driven, 520
 photochemical, 523–524
 Reduction kinetics, cytochrome c_3 , 485
 Reference interface
 addition of other ions, 63
 inequality condition, 62–63
 interfacial potential, 63
 Rehydrated dry multilayered film,
 schematic diagram, 544*f*
 Relative permeabilities, potassium ion and protons, 44
 Relaxation time
 estimates of sodium–conductance activation and inactivation, 427*f*
 evaluation by admittance analysis, 425–426
 fits of admittance data plotted as impedance loci, 423*t*
 potassium conductance, 424*f*
 sodium and potassium channels, 415–428
 Reorganization energy, electron transfer, 481
 Repartitioning
 equilibrium potential, 65
 salt concentrations, 62
 Repulsive force, electrical double layers, 6
 Repulsion force, electrostatic model, 8
 Repulsive force, polysaccharides, 190
 Resistance, conventional BLM system, 514
 Resistance–capacitance (RC) relaxation event, photosignal, 537
 Retina
 information processing, 226–231
 photoreceptor matrix, 231
 Reverse reactions, prevention, 524
 Reversible electrical breakdown (REB)
 definition, 449
 pore models, 449

Rhabdomere
 microscopic observation, 229–230
 optical waveguide, 229
 tips in a living animal, 230*f*
 Rhodamine dyes, mitochondrial membrane potential, 162
 Rhodopsin
 description and activity, 532
 formed on electrode surfaces, 493
 photobleaching, 535
 Rhodopsin-containing membrane on PtO–OTS electrodes, electrochemical properties, 498–500
 Rupture, pore models, 449

S

Salt concentration, interfacial potential, 63–64
 Scattering amplitude, Doppler spectra, 412
 Scattering centers, ion flows in
 gramicidin channels, 408
 Scattering density profiles, structure factors, 100
 Schottky formula, shot noise, 379
 Schwan equation, cell membranes, 571
 Self-similarity
 property of a fractal, 359–360
 time, 361
 Semiconductor model, redox reactants, 524
 Semiconductor septum electrochemical photovoltaic (SC–SEP) cell, separation of aqueous solutions, 526
 Sensor construction, bacteriorhodopsin, 556
 Sequence homology
 channel proteins, 331
 negatively charged or polar residues, 332
 Sequence information, voltage- and ligand-gated channel proteins, 331
 Sequence-specific motifs, pore-forming properties, 350
 Sequence specificity, synthetic proteins, 345–348
 Serine–leucine peptides, ion-conducting channels, 48–49
 Short-circuit condition, input impedance, 537
 Shot noise
 charge transfer, 378
 damping in a simple model circuit, 380*f*
 multistep charge transfer, 379
 Si–SiO₂ electrodes
 capacitances, 507*f*
 device characteristics, 506
 Sickie hemoglobin, aggregation, 434
 Signal averaging, accumulation of transported molecules, 466

- Signal peptides
 applications, 290–291
 helix stability, 297
 protein interaction with the membrane, 290
- Signal processing, massively parallel and distributed, 550
- Silica plate, high quality diffraction patterns, 98
- Silver electrode, protein redox potentials, 482
- Single-channel conductance
 oligomer size, 348–349
 planar lipid bilayers, 345
- Single-channel properties, König's polyanion, 253*t*
- Single-channel recordings, fractal properties, 361–365
- Single crystal diffraction method, ion binding sites in gramicidin channel, 97
- Single membranes, open channels, 217
- Single molecules, in solution, 184–187
- Site-directed mutagenesis
 bacteriorhodopsin, 556
 properties of cytochromes *c*, 486–487
- Slopes of potential vs. logarithm of dye concentration, 69*t*
- Slow dyes
 mechanism, 157, 162
 potential-dependent redistribution, 151
 representative sampling, 160*f*–161*f*
- Sodium, permeability of liposomes, 46
- Sodium channel
 conductance, 292
 determination of relaxation times in squid nerve fibers, 415–428
 heat of disaggregation, 443
 homologous repeats, 291
 synthetic peptides, 291–292
- Sodium conduction, determination of admittance in a steady state, 424
- Software
 AMBER, 16
 CPXFIT, 418
 DISCOVER, 334
 INSIGHT, 334
 TK-Plus Solver, 62
- Solar energy
 photolysis of water, 526
 transduction, 526
- Solvated phospholipid bilayer, electrostatic problem, 8
- Solvation, controlling oxygen uptake, 185
- Solvation energy, water at the macromolecular surface, 177–196
- Solvent-accessible surface, overlapping surface density, 337
- Spatial constraints, peptide interactions, 333
- Spatial orientation, template amino acids, 334–337
- Spatial scale, apparent paradoxes, 555
- Spectral density, noise at free one-dimensional diffusion, 393–396
- Spectral density of voltage
 calculation, 376–377
 valinomycin-modified phospholipid bilayers, 378*f*
- Spherical cell, broadband estimate, 466
- Spherical lipid bilayer, dye characterization, 165–168
- Splitting, junctional membranes, 218
- Spontaneous curvature
 limitations, 142
 molecular volume subjected to a torque, 135
 relative magnitudes, 141
 variation with stoichiometry, 142
- Squid, determination of K- and Na-channel relaxation times, 415–428
- Squid axon, dye characterization, 168–170
- Standard potential of transfer value determination, 60–62
 water and nitrobenzene, 61*t*
- State-dependent alteration of field across a protein, contingent gating, 201
- Steric force, polymer-covered surfaces, 14
- Stochastic behavior, switching of conformational states, 371–372
- Stoichiometry of components, spontaneous curvature, 142
- Streaming potentials, ion flux, 49–50
- Stress, ultimate source, 144
- Stress–depth distribution, protein conformations, 142
- Stress field, interaction with membrane proteins, 143
- Structural theme, membrane proteins, 130
- Structure, cytochromes *c*, 472–477
- Structure factor
 H₂O swelling experiments, 101*f*
 inhomogeneous contribution to hydration pressure, 12
- Styryl dyes
 engineered to meet specific experimental demands, 158*f*–159*f*
 fluorescent potentiometric indicators, 153
 lipid concentration and spectral characteristics, 164, 166*t*–167*t*
 variable overall charge and hydrophobicity, 156–157
- Sucrose permeability
 identification of protein responsible, 208
 liposomes, 207*f*
 mitochondria, 245

Sucrose permeability—*Continued*
 protein from junctional membrane, 206
 selection for full-length connexin-32, 208
 selection for liposomes containing
 full-length connexin-32, 209f
 Sucrose-permeable liposomes, bilayer
 channels, 210–215
 Sulfate-reducing bacteria, cytochrome c_3 ,
 471–489
 Supported BLM (s-BLM), formation and
 characteristics, 515
 Supporting electrolyte
 dye separation, 66
 ideally polarizable interface, 64–65
 potential, 65
 potential–dye concentration relationship, 69f
 potentiometric response, 64
 relationship between interfacial
 potential and dye iodide, 68f
 Surface-bound membranes
 alkylsilanated electrode surface, 501f
 capacitance, 506–508
 detergent dialysis technique, 492–495
 electrochemical impedance spectroscopy, 508
 evaluation, 491–510
 Pt electrode, model, 500–506
 SiO₂, TiO₂, and ITO electrodes, 506–508
 Surface compartment model, effects of
 electrochemical properties on passive
 ion transport, 440
 Surface domain, structural evidence, 255
 Surface free energy
 calculations, 431
 hemoglobin system, 434–437
 protein aggregation, 430–431
 Surface groups, interaction with protons, 31–33
 Surface modification, organosilanes, 495
 Surface spectroscopy, cytochrome c_3 films,
 482–483
 Switching region
 colloidal osmotic pressure of the medium, 254
 voltage-gating process of a channel, 252–254
 Synaptic terminals, gap junctions, 226
 Synergistic effect, polyanions and osmotic
 pressure, 254
 Synporins, synthetic pore-forming molecules, 333
 Synthetic channel proteins, reversed-phase
 HPLC, 344f
 Synthetic peptides
 ability to self-assemble in lipid bilayers, 350
 characteristics, 291–292
 pore structure of channel proteins, 349–350
 sequences that represent functional
 segments, 332
 transmembrane segment, 351

Synthetic proteins
 computer-generated molecular model,
 334f–336f
 mimic pore-forming structure, 333
 pore-forming capability, 350
 sequence specificity, 345–348

T

Tachyplexin
 antibiotic activity, 285
 structure, 284
 Tangential electric fields
 lateral movements of membrane
 components, 107
 origin and effect, 108
 TCNE reduction on PtO and PtO–OTS
 electrodes
 complex plane plots, 497f
 impedance data, 498f
 Template amino acids, spatial orientation,
 334–337
 Template-assembled synthetic protein (TASP),
 covalent attachment of peptide segments, 333
 Template lysines, orientation relative to
 four-helix bundles, 337
 Tetracyanoethylene (TCNE) on PtO and
 PtO–OTS electrodes, cyclic
 voltammetry, 496f
 Tetramethicin
 conductance, 302f
 oligomers, 301f
 Thallium ion, membrane permeation, 404
 Thallium ions in gramicidin channels
 Doppler spectra, 410f
 velocities and transit frequencies, 411t
 Thermal energy, lipid hydrocarbon chain
 layer, 135
 Thermal fluctuations, separation of neutral
 bilayers, 188
 Threshold estimation, weak electrical fields,
 466
 Thylakoid membrane
 solar energy harvest and processing, 526
 structure, 520
 Thylakoid membrane proteins, integral
 membrane spanning complexes, 108–109
 Thylakoid vesicles, preparation, 112
 Ti–TiO₂ electrodes, device characteristics, 506
 Time axis of histogram, fractal scaling
 relationship, 362f
 Time-dependent rate constant, changing
 energy structure of channel protein, 366

- Time-domain subtraction, admittance-containing current response, 420
- TiO₂ electrodes, capacitances, 508*f*
- Torsional angles, residues and crystal structures, 268*f*
- Toxins
 apamin, 288–289
 δ-hemolysin, 289–290
 mastoparan, 287–288
 melittin, 285–287
- Transient aqueous pores, enzymes, 466–468
- Transient defects in lipid bilayers, measurements of cation permeability, 45
- Transient photocurrent, zero time integral, 533
- Transit frequencies, gramicidin channel, 411–412
- Transitions
 channel nonconducting and conducting states, 416
 peptide spectra, 86–87
- Transjunctional voltage sensitivity, gap junction channels, 200–201
- Translocation mechanism, proton conductance, 41
- Transmembrane channels, proton diffusion, 48
- Transmembrane electric field
 polypeptide insertion into lipid bilayer, 120
 quantitative relationships, 563
- Transmembrane electron tunneling, two-step electron transfer, 522–523
- Transmembrane helix
 amino acid sequence and molecular model, 326*f*
 functional channels, 332
 integral membrane proteins, basic conclusions, 297
 sodium channel, 291
 width of the bilayer, 295–296
- Transmembrane ion channel, gramicidin, 97
- Transmembrane ion transport
 dipolar potential, 504
 osmotic stress measurements, 182–184
- Transmembrane potential
 electric-field-induced, 562–563
 intrachannel average velocities, 401
- Transmembrane segments
 electrogenic H⁺ transport, 325
 electrogenic proton transport and coupling to ATP hydrolysis, 327
 length requirements, 296
- Transmembrane sequences, fragments, 290
- Transmembrane signaling, insulin receptor, 270
- Transmembrane transport
 catalytic pore formation, 467
 channels as catalysts, 467
- Transmembrane voltage
 cubic cell model, 464*f*
 effects in artificial and cell membranes, 468
 electrostatic and hydrophobic interactions, 449
 short time scale behavior, 452*f*
 spreading resistance, 459
- Transmitter release, calcium-sensitive mechanisms, 330
- Transport mechanisms, studies of shot noise, 380–381
- Transport noise, nonequilibrium systems, 378–381
- Transport protein, molecular architecture at high resolution, 316
- Trissl–Montal film
 schematic diagram, 544*f*
 signal from multiple layers of purple membrane sheets, 543–545
- Two-dimensional space, reactivity of proton with surface group, 34

U

- Ultramicroelectrodes, solution resistance difficulties, 78
- Uniformly aligned multilayer samples, membranes, 85–86

V

- Valinomycin
 effect on bacteriorhodopsin spectra, 115
 K⁺ diffusion potential, 165
- Valinomycin-doped membranes, spectral density of voltage, 377
- van der Waals force
 description, 3
 dipole correlations and dielectric images, 9
- Velocimetry, laser Doppler, 404–406
- Velocity distribution
 ion mobility in the channel, 411–412
 number of binding sites, 403
 potential-driven ions in gramicidin channels in bilayer membranes, 401–413
 thallium ions within gramicidin channel, 412
- Venoms
 apamin, 288–289
 δ-hemolysin, 289–290
 mast cell degranulating (MCD) peptide, 288–289
 mastoparan, 287–288
 melittin, 285–287

- Vesicle formation, phosphatidyl choline, 111–112
- Viologen reduction, polarity of photopotentials, 522
- Viral fusion factors, protein interaction with the membrane, 290
- Viscosity, hemoglobin solutions, 434
- Visual membrane
analogous to signal from bacteriorhodopsin membrane, 552–553
photon energy, 553
- Visual phototransduction, rhodopsin, 532
- Visual transduction
metarhodopsin, 553
surface potential-based trigger mechanism, 554
- Voltage
membrane-bathing solution interface, 517
restricted extracellular space, 241
- Voltage coupling, gap junctions in axon terminals, 238–242
- Voltage dependence
electric field effect on partition between aqueous and membrane phases, 264
mitochondrial channels, 250–253
- Voltage-dependent anion-selective channel (VDAC)
aluminum hydroxide, 254
computer model for open state, 247
dimer in detergent solution, 249–250
highly charged polymers, 253
mitochondrial, 245–258
modulation, 252–254
modulator, rate and extent of VDAC channel closure, 254
molecular basis for selectivity, 250
monomeric channel, 248–249
osmotic stress, 183–184
properties in mitochondria, 246
properties of open and closed state, 252
protein attachment, 254–255
residues lining the wall of the pore, 250
reversal potential vs. charge within the pore, 251*f*
structure, 246–250
two-dimensional crystals, 247*f*
voltage dependence, 252*f*
- Voltage-dependent pores, lantibiotics, 279
- Voltage divider
external and internal pore resistance, 453
pore expansion, 459
- Voltage-gated channels
conduction and propagation of nerve signals, 330
cross section model, 439*f*
electrochemical model, 429–446
- Voltage gating
channel specificity, 440–442
conformation of membrane proteins, 108
- Voltage perturbation, admittance data, 421
- Voltage-sensitive behavior, ATP hydrolysis, 320
- Voltage sensitivity
determination, 212–215
gap junction channels, 200–201
reconstituted channels, 211–215
- Voltage spectral density, calculation, 376–377
- Voltammograms, electron-transfer reactions, 516–517

W

- Wasp venom, mastoparan, 287–288
- Water
chemical hydration of lipid head groups, 138
macromolecular surface, 177–196
orientational polarization, 21
relaxation of curvature of monolayers, 136
role in proton conductance across model and biological membranes, 41–54
- Water chains, proton selectivity, 51–52
- Water layer, dynamics approximated by two-dimensional space, 29
- Water–membrane interface, proton diffusion dynamics, 27–40
- Water molecules
order near the interface, 10–11
transition-effecting action, 185
- Water–nitrobenzene interface
adsorption of proteins, 72–78
complex plane impedance plots, 73*f*
interfacial potential, 60–62
ion transport, 57–59
nonpolarizable, 63–64
potentiometry in the presence of oxocyanine dyes, 59–72
protein adsorption, 72–78
reference interface, 62–63
- Water oxygen, distribution of densities, 16*f*
- Water polarization
between DLPE bilayers, 19*f*
DLPE surface, 18*f*
- Water removal, free energy consequence, 194
- Water solubility, decrease in chain length, 157
- Water soluble dye, pyranine, 28
- White noise, gramicidin channel, 391
- Wild-type and mutant cells
effect of KCl on medium acidification, 319*f*
voltage-sensitive behavior, 320

X

X-ray determination, multilayer membrane structure, 84

Y

Yeast
electrogenic proton transport, 315–328
H⁺-ATPase as a model system, 316–317

Yeast—*Continued*

lipophilic distribution probe, 318

Z

Zero time integral, transient photocurrent, 533
Zwitterions, correlation vs. exponential decay, 8

Indexing: Colleen P. Stamm
Production: Paula M. Bérard and Margaret J. Brown
Acquisition: Robin Giroux
Cover design: Jack Ballestero

Typeset by Technical Typesetting Inc.
Printed and bound by Maple Press, York, PA